AEROELASTIC RESPONSE AND STABILITY OF TILTROTORS WITH ELASTICALLY-COUPLED COMPOSITE ROTOR BLADES

Mark W. Nixon

Dissertation submitted to the Faculty of the Graduate School
of The University of Maryland in partial fulfillment
of the requirements for the degree of
Doctor of Philosophy
1993

Advisory Committee:

Professor Inderjit Chopra, Advisor
Associate Professor Roberto Celi
Associate Professor Anthony J. Vizzini
Associate Professor J. Gordon Leishman
Professor David Schelling (Dean's Representative)

Acknowledgements

Abstract

Title of Dissertation: AEROELASTIC RESPONSE AND STABILITY OF TILTROTORS WITH ELASTICALLY-COUPLED COMPOSITE ROTOR BLADES

Mark W. Nixon, Doctor of Philosophy, 1993

Dissertation directed by: Dr. Inderjit Chopra, Professor
Department of Aerospace Engineering

There is a potential for improving the performance and aeroelastic stability of tiltrotors through the use of elastically-coupled composite rotor blades. To study the characteristics of tiltrotors with these types of rotor blades it is necessary to formulate a new analysis which has the capabilities of modeling both a tiltrotor configuration and an anisotropic rotor blade. Background for these formulations is established in two preliminary investigations. In the first, the influence of several system design parameters on tiltrotor aeroelastic stability is examined for the high-speed axial flight mode using a newly-developed rigid-blade analysis with an elastic wing finite element model. The second preliminary investigation addresses the accuracy of using a one-dimensional beam analysis to predict frequencies of elastically-coupled highly-twisted rotor blades. Important aspects of the new aeroelastic formulations are the inclusion of a large steady pylon angle which controls tilt of the rotor system with respect to the airflow, the inclusion of

elastic pitch-lag coupling terms related to rotor precone, the inclusion of hub-related degrees of freedom which enable modeling of a gimballed rotor system and engine drive-train dynamics, and additional elastic coupling terms which enable modeling of the anisotropic features for both the rotor blades and the tiltrotor wing. Accuracy of the new tiltrotor analysis is demonstrated by a comparison of the results produced for a baseline case with analytical and experimental results reported in the open literature. Two investigations of elastically tailored blades on a baseline tiltrotor are then conducted. One investigation shows that elastic bending-twist coupling of the rotor blade is a very effective means for increasing the flutter velocity of a tiltrotor, and the magnitude of coupling required does not have an adverse effect on performance or blade loads. The second investigation shows that passive blade twist control via elastic extension-twist coupling of the rotor blade has the capability of significantly improving tiltrotor aerodynamic performance. This concept, however, is shown to have, in general, a negative impact on stability characteristics.

Contents

B Rigid Blade Flap Model Including Free-Flight   401

List of Tables

List of Figures

xi

Nomenclature

a	reference lift curve slope
$\hat{A}$	stability matrix
b, c, t	wing beam, chord, and torsion modes
c	blade chord
c_0	lift coefficient at zero angle of attack
c_1	lift curve slope
c_d	drag coefficient
c_l	lift coefficient
C_{l_α}	lift curve slope
c_m	pitching moment coefficient
$\hat{C}$	damping matrices
C_T	rotor thrust coefficient
D_{ij}	nonlinear stiffness matrix
D_F	fuselage drag force
e_A	chordwise offset of tension axis ahead of elastic axis
e_d	chordwise offset of aerodynamic center behind elastic axis
e_g	chordwise offset of mass c.g. ahead of elastic axis
E	Young's modulus
EA	extensional stiffness
EI_f	local flap bending stiffness

EI_c	local lag bending stiffness
EET	extension-twist-coupled stiffness
ETC	twist-chordwise-bending stiffness
ETF	twist-flapwise-bending stiffness
EES_c	extension chordwise-shear stiffness
EES_f	extension flapwise-shear stiffness
EFS_c	flapwise-bending chordwise-shear stiffness
ECS_f	chordwise-bending flapwise-shear stiffness
EI_b	wing section beamwise stiffness
EI_c	wing section chordwise stiffness
F_A	blade axial force
F_{cor}	blade Coriolis force
F	hub forces, or blade forces as indicated by subscript
G	shear modulus
GA_c	chordwise shear stiffness
GA_f	flapwise shear stiffness
GJ	wing section torsional stiffness
h	distance from pylon pivot point to center of rotation
H	shape functions
I_β^*	blade cyclic-mode flap inertia
$I_{\beta_0}^*$	blade collective-mode flap inertia
$I_{\zeta_0}^*$	blade collective-mode lag inertia
I_ζ^*	blade cyclic-mode lag inertia
$I_{\zeta\alpha}^*$	blade-pylon-coupled lag inertia
I_0^*	rotor speed perturbation inertia
$I_{\beta\alpha}^*$	blade-pylon-coupled flap inertia
$I_{\zeta_0\alpha}^*$	rotor-pylon-coupled lag inertia

k_A	area radius of gyration
k_m	mass radius of gyration
k_{m_1}, k_{m_2}	blade mass radius of gyration in flap and lag
k_β	kinematic pitch-flap coupling
k_ζ	kinematic pitch-lag coupling
$\hat{K}$	stiffness matrices
L	section lift forces in the undeformed system
$\bar{L}$	section lift forces in the deformed system
m	section mass per unit length
m_0	reference section mass per unit length
M_b^*	blade mass
M	Mach number
M_i	Moments on blade or hub as indicated by subscript
$\hat{M}$	mass matrices
m_P^*	mass of pylon
N	number of spatial finite elements
N_b	number of blades
N_t	number of time finite elements
$\hat{p}$	modal displacement vector
$\hat{q}$	nodal displacement vector of beam elements
$\hat{Q}$	blade load vector
Q'_{ij}	material stiffness matrix
r	blade radial station
R	blade radius
s	local time coordinate
S_{ij}	flexibility matrix
S_w^*	first mass moment of pylon

S_w	wing area
S_ζ^*	blade lag first mass moment
S_β^*	blade cyclic-mode flap first mass moment
$S_{\beta_0}^*$	blade collective-mode flap first mass moment
t	time
T	rotor thrust, kinetic energy
$[T]$	transformation matrices as indicated by subscript
u	axial deformation
u_e	elastic axial deformation
u_F	elastic axial deformation associated with forshortening
U	relative wing velocity as indicated by subscript, strain energy
v	lag deformation
V^*	flight velocity normalized by blade tip speed
V_f^*	V^* at flutter
V	forward flight velocity
V_i	velocity as indicated by subscript
w	flap deformation
W	aircraft weight or work done
x	nondimensional radial station, or other distances by subscript
x_{ac}	nondimensional chordwise location of aerodynamic center
$\bar{x}_h$	vector of discrete hub displacements
α_h	pylon pitch
α	angle of attack
α_p	pylon angle of attack
α_y, α_z	pylon rotations in rigid-blade analysis
β_G	gimbal angle in rotating system
β_{GC}, β_{GS}	gimbal angles in fixed-frame

β_p	precone angle
β_0	rotor collective flap degree of freedom
β_{1c}	rotor cyclic flap degree of freedom
β_{1s}	rotor cyclic flap degree of freedom
$\beta+1$	high-frequency rotor flap mode
$\beta-1$	low-frequency rotor flap mode
γ	Lock number
δ	variation of
δ_3	blade pitch-flap coupling angle
ϵ	parameter of bending rotation order of magnitude
ϵ_{xx}	axial strain
$\epsilon_{x\eta}, \epsilon_{x\zeta}$	shear strains
ζ	percent critical damping, or flatwise distance within cross section
ζ_0	rotor collective lag degree of freedom
$\dot{\zeta}_0$	rotor collective lag velocity
ζ_{1c}	rotor cyclic lag degree of freedom
ζ_{1s}	rotor cyclic lag degree of freedom
$\zeta+1$	high frequency rotor lag mode
$\zeta-1$	low frequency rotor lag mode
ζ_h	pylon yaw
η	chordwise distance within cross section
η_r	distance from elastic axis to 3/4 chord
θ	blade pitch angle
$\hat{\theta}$	rotor vector of controls
θ_y, θ_z	local beam rotations
λ, λ_i	rotor induced inflow
Λ	wing sweep angle, negative forward

μ	nondimensional forward flight velocity
ν_β	blade flap rotating in-vacuum frequency
ν_ζ	blade lag rotating in-vacuum frequency
Π	total energy
ρ	air or material density
σ	rotor solidity
ϕ_h	pylon roll
ϕ	elastic twist
$[\Phi]$	matrix of modal vectors
ψ	azimuth angle, or warping as indicated by subscript
ω	natural frequency
Ω	Rotor rotational speed
$[\mathrm{p}]$	progressive mode
$[\mathrm{r}]$	regressive mode
$()^A$	aerodynamic quantity
$()_b$	blade quantity
$()_c$	cross section variable
$()_C$	circulatory quantity
$()_{CC}$	constant coefficient quantity
$()_{NC}$	non-circulatory quantity
$()_R$	rotor quantity
$()_{75}$	quantity at .75R
$()'$	derivative with respect to span, or effective stiffness

Chapter 1

Introduction

1.1 Problem Statement

The tiltrotor aircraft has been a subject of considerable interest because of its ability to combine vertical take-off and landing capability with efficient long-range and high-speed cruise flight capability. This aircraft is similar to a conventional fixed-wing aircraft, but has a large-diameter rotor system mounted to a pylon at each wing tip. The pylons are rotated to change between airplane and helicopter flight modes.

In high-speed axial flight (airplane mode), the tiltrotor is subject to an instability known as proprotor whirl flutter. In this configuration, high inflow through the rotor results in large inplane motion-dependent rotor forces. The inplane forces for a tiltrotor are much larger than those typically associated with conventional propeller-driven aircraft because of the flexible blades undergoing flap and lag motions. The motion-dependent rotor forces act to reduce damping in the wing, resulting in greater wing motion and therefore greater pylon and hub motion. The rotor forces and wing/pylon motion augment each other with increasing airspeed to the point where the rotor forces may become destabilizing, ultimately driving the rotor/pylon/wing system unstable.

In helicopter flight, the tiltrotor is subject to the same harsh dynamic environment as a conventional helicopter. There is the possibility of aeroelastic instabilities associated with flutter, divergence, and air resonance. However, blade flexibility is an important characteristic for the aeroelastic interactions, and generally the more flexible the blade becomes, the more likely that an instability may occur. Because tiltrotor blades tend to be shorter and stiffer than helicopter blades, the likelihood of an instability is lessened for a tiltrotor in the helicopter flight mode compared to its conventional counterpart.

The operational change between airplane and helicopter flight modes leads to a compromise in tiltrotor design for aerodynamic performance. The conventional rotor blade planform and twist distribution cannot be optimized for both high-inflow airplane flight and low-inflow helicopter flight simultaneously. As such, the hover performance of tiltrotors is generally sacrificed in favor of axial flight performance which is the flight regime where this vehicle holds a large advantage over helicopters.

The discussion to this point has focused on problems which are inherent to the tiltrotor configuration. In summary, the tiltrotor has performance losses associated with compromise in design between two extreme flight regimes, and is subject to whirl flutter in high speed flights because the rotor system is mounted on an elastic wing. There is a potential for improving the performance and aeroelastic stability, as well as the vibration characteristics, of tiltrotors through the use of elastically-coupled composite rotor blades. The aerodynamic performance may be improved if the blade can be tailored to deform such that the geometry becomes optimum in each flight regime. The system aeroelastic stability may be improved if blade modes are elastically-coupled so that high damping in one mode may be transferred into a lower damped mode. The investigation of potential uses for elastically-coupled composite rotor blades on tiltrotor aircraft requires sophisticated, comprehensive

2

analytical capabilities which do not currently exist. While adequate analyses exist for modeling tiltrotor aeroelastic behavior, they do not provide a capability for modeling elastically-coupled rotor blades.

The focus of this dissertation is on the development of an aeroelastic tiltrotor analysis which has anisotropic composite rotor blade modeling capability. The theory required to model anisotropic rotor blades is developed, as is the theory required to aeroelastically model a tiltrotor configuration in all its flight modes. The basis of the tiltrotor theory development is the current aeroelastic theory used for helicopter modeling in the University of Maryland Advanced Rotor Code (UMARC). Following the analytical development, an investigation is carried out to examine the use of elastically-coupled composite rotors blades for the simultaneous improvement of the performance and aeroelastic stability characteristics of tiltrotor aircraft.

1.2   Background and Motivation

This dissertation addresses two research topics which have not previously been considered together: stability aspects of tiltrotor configurations and elastically-coupled composite rotor blades. Each topic has itself a full history involving separate motivations and analytical developments. This section first addresses the reasons why the tiltrotor configuration has become a viable concept. It then discusses some important aspects of tiltrotor design, followed by a review of the history of tiltrotor experimental and analytical development. State-of-the-art developments in anisotropic composite rotor blade modeling is also presented. Lastly, the potential uses for elastically tailored composite blades are discussed, including an application for the tiltrotor.

3

1.2.1 Advantages of the Tiltrotor Configuration

The reasons for considering a tiltrotor configuration lie in the desire to merge high-speed airplane flight with vertical takeoff and low-speed helicopter flight capability. A conventional helicopter with its large-diameter, slow-turning rotor is the most efficient vehicle for vertical flight, but it is limited in range and forward flight velocity. High-speed flight, say over 250 knots, requires some variation to the basic helicopter design concept. There are several configurations which have been considered for this purpose. These include the tiltrotor, the tilt-wing, the compound helicopter, stopped-rotor configurations, fan-in-wing configurations, and vectored-thrust jets. The configuration of choice depends on the mission, but if efficient hover and vertical flight is truly an important part of a high-speed mission, then the tiltrotor is perhaps the best choice.

The tiltrotor is an efficient hovering configuration because of its low disc loading. The plot of Figure 1.1 shows the hover efficiency versus the disc loading for several V/STOL configurations. The advantages associated with hovering at a low disc loading are many: low downwash velocity allow these vehicles to operate from unprepared field areas, low tip-speed and low downwash produce favorable noise levels, and low power requirements lead to low fuel consumption and greatly increased range.

Some aspects of the tilt-wing configuration have advantages over the tiltrotor. First, the wing chord remains in line with the rotor flow field, which reduces the wing interference effect experienced by a tiltrotor in hover. Second, on liftoff, the wing has its chord, the stronger of the wing directions, oriented in the direction of lift so that less overall wing structure is required to support the fuselage. This leads to thinner and more efficient wings for high-speed flight. Further, the tilt-wing does not have the control mechanisms of a tiltrotor. There is no need for the complexity and weight of conventional helicopter-type cyclic controls on a tilt-wing

4

because with its high disc loading it cannot hover for a long period of time, and it cannot fly efficiently at low speed in a helicopter mode because of the high wing drag. Because of these characteristics, the tilt-wing has a very narrow conversion corridor (speed and altitude at which the wing can be tilted into or back from airplane mode) which makes it more difficult to operate than a tiltrotor.

Stopped-rotor configurations and compound helicopters have never been able to achieve efficiency in both hover and forward flight as successfully as has the tiltrotor. The stop-rotor type configurations, such as X-wing, suffer from the requirements of 1) the additional weight and complexity of a circulation control system and/or 2) the loss of efficiency in hover associated with thick, high-chord, stiff rotor blades of elliptical cross section. Similarly, compound helicopters carry a rather large weight penalty in an auxiliary propulsion device, and tend to have stub-wing designs which degrade hover efficiency. The combination of these two penalties has proved too much to overcome in compound helicopter designs to date.

The last two V/STOL configurations mentioned, the fan-in-wing and the vectored-thrust jets do not compete for the same missions with a tiltrotor. These aircraft can have supersonic capabilities for forward flight, but are extremely inefficient in hover and vertical flight. The main goal of these designs is simply to have the ability to take-off vertically and get to forward flight as quickly as possible. In military missions these configurations are fighters and attack aircraft, while a tiltrotor is a troop transport, scout, and search and rescue aircraft.

The tiltrotor has great potential for both military and civil missions. For the military missions, the high-speed aspect gives the tiltrotor quicker response times in comparison to conventional helicopters. The tiltrotor also has a greater range with capabilities to penetrate and rescue over 400 miles into enemy territory. This capability would greatly increase U.S. military strength in the types of air wars it has been involved in over the last few decades. In rescue operations, the vertical

5

flight capability is extremely important. The tiltrotor has the additional benefit of reaching rescue sites two to three times faster than present rescue aircraft in use. On the commercial side, tiltrotor aircraft may enhance short-haul operations of less than 800 miles. Passengers will benefit from increased accessibility to heliports which can be located around and inside metropolitan areas, decreasing time and expense of travel to and away from current congested airports. Remote locations currently serviced by helicopters, such as off-shore oil rigs, could be reached in about half the time it currently takes.

1.2.2   Important Considerations in Tiltrotor Design

The tiltrotor is a unique aircraft which requires some special design considerations beyond those of conventional helicopters and fixed-wing propeller airplanes. This section discusses some important considerations for tiltrotors related to aerodynamics, wing download, control loads, noise, gust response, and vibratory loads. Aeroelastic stability is also an important consideration, but, as it is the focus of the present research, this subject is discussed in greater detail in a separate section.

First, it is advantageous to understand the important aerodynamic design considerations which have been identified in the development of the XV-15 Advanced Technology Blades (ATB) and V-22 (formerly JVX) rotor blades [1,2]. Many of the difficulties experienced in the aerodynamic design of these blades stem from the differences in rotor inflow and thrust requirements between helicopter hover mode and high-speed airplane flight. In hover, the inflow is comparatively small, and the blade loading is high since the rotor system is supporting the entire weight of the aircraft and its payload. The hover thrust must also overcome the download produced by the rotor wake impinging on the wing below. The wing download can itself be as large as 10-15 percent of the total rotor thrust [3]. The thrust available in hover must be able to overcome the maximum allowable gross weight and the

6

wing download, and still have an adequate margin to provide roll control without stalling the rotor. In high-speed airplane flight, the inflow is high, and the blade loading is comparatively low since the thrust only has to overcome the aircraft drag. Because the rotor thrust efficiency generally increases with disc loading, the blade aerodynamic design in the airplane flight regime is strongly dependent on the blade twist and planform selections.

Several parameters have been considered in the aerodynamic design of tiltrotor blades. Aerodynamic design of the V-22 blades considered diameter, number of blades, tip speed, airfoils, twist, chord, and taper ratio [2]. For this design, the diameter was set at 38 feet because of storage clearance considerations (requirement for shipboard operations), and the number of blades was set at 3 because of the level of experience in dealing with the rotor dynamics of this system and because of the storage clearance considerations. Thus, no trade-off studies were conducted for these two important parameters. The rotor tip speed was selected based mainly on maximizing thrust for a given power level. In the hover mode, the variation of thrust with tip speed near the maximum thrust is fairly flat so a non-optimum tip-speed may be selected for auxiliary benefits. An important concern for tiltrotors is noise during landing and take-off, so it is possible to select a tip speed slightly lower than that associated with the theoretical optimum to improve the acoustic characteristics without a noticeable loss in hover efficiency. In high-speed airplane flight, the rotor tip speed must be reduced because of compressibility effects at the blade tips. For this flight regime the tip speed may be selected based on maximum airspeed, service ceiling, maximum range, maximum range airspeed, or a combination of these parameters. As an example, the airplane mode tip speed is lower than the hover tip speed by about 16 percent for the V-22 and by about 20-percent for the XV-15. Tiltrotor airfoils are selected depending on their radial location. The inboard blade sections require a thick airfoil to accommodate root

structure build-up, the middle sections are selected for maximum lift to drag ratio (generally 12 to 15 percent thick), and the outboard sections require a thin airfoil (about 9 percent thick) because these are efficient over a large range of attack angles and have low drag divergence Mach numbers. The airfoil sections are selected subject to a constraint on pitching moment coefficients which must be low for acceptable control system loads and vibration characteristics, just as for helicopter blades. The blade twist and chord distributions are selected based on a compromise between figure of merit in hover mode and propeller efficiency in airplane mode at the design forward flight velocity. The aerodynamic design process begins by approximating a chord and twist through parametric study. Once approximate planform and twist is defined, which will hopefully meet both hover and cruise flight requirements, the final distribution can be defined with consideration to which flight mode is more important for the design. The compromise required for a typical tiltrotor twist design is illustrated in Figure 1.2. The chord selection is subject to requirements for low-speed maneuver capability which is assessed by maximum load factor at a given velocity and altitude in helicopter mode. A chord taper ratio may also be included in the design to improve hover efficiency. However, taper tends to reduce propeller efficiency. If the final chord distribution is significantly different from initial assumptions, the design process may need to be restarted with the new chord values.

As mentioned above, noise is an important consideration for tiltrotors. The key issues associated with tiltrotor noise are discussed in a recent study by Huston, Golub, and Yu [4]. These issues seriously impact the viability of a civil tiltrotor where interior noise affects passenger comfort and exterior noise affects public acceptance of vertiports. The noise associated with tiltrotor airplane mode operations is similar to that of a conventional turboprop aircraft, which is a favorable characterization for this flight mode. This noise is less than that associated with

8

helicopters in forward flight. Tiltrotors in hover also tend to produce less noise than helicopters (mainly because of the absence of a tail rotor on the tiltrotor), but tiltrotors in transition from helicopter to airplane mode can produce substantially more noise than a helicopter [5]. The high transition noise is created by blade-vortex interaction resulting from high pylon angles at high airspeeds. The transition noise may also lead to unsuccessful marketing of a civil tiltrotor. Some of the concepts which have been considered for reducing the tiltrotor noise signature are: reducing the individual blade loads by increasing the number of blades and reducing the sonic cylinder at the blade tip by using chord taper and thin airfoils.

Gust response of the tiltrotor is another important consideration which can impact the rotor system design and the marketability of a civil transport. In high-speed airplane flight, vertical gusts result in design-limit blade bending loads and anti-symmetric gusts result in design-limit drive train loads [6]. The marketability aspect is defined by the cabin accelerations resulting from the gusts. Cabin response to vertical gusts are about the same as for conventional turboprop aircraft, but response to lateral and longitudinal gusts are higher than that associated with conventional turboprop aircraft [7]. Research efforts devoted to alleviating this problem have generally focused on use of active controls [8].

Reduction of vibratory loads is another important aspect of the tiltrotor which can create problems for the pylon and wing. In helicopter mode, the tiltrotor has some distinct advantages over conventional rotorcraft regarding vibratory loads. The wing dynamics provide vibration absorption and the rotors can be tilted to minimize the wake-induced vibration at low speeds [9]. In airplane mode, large 2/rev pylon loads have been experienced in flight tests of the XV-15 Tilt Rotor Research Aircraft (3 blades) [10]. Here, the source of excitation was the second cyclic rotor mode loads acting at 1/rev and 3/rev through the gimbal. This excitation

was reduced by optimizing the cyclic controls to maintain zero flapping at high speeds. The wing aerodynamic interference in airplane mode can produce large n/rev shear forces at the rotor hub, where n is the number of blades. Large 3/rev pylon accelerations were experienced in testing of the Bell Model 266 (3 blades) which were shown to increase with forward flight velocity [6]. The cabin response to these accelerations, however, tends to be low because of the inherent damping of the wing.

1.2.3 History of Tiltrotor Development

The first successful demonstrations of the tiltrotor concept occurred in the early 1950's with aircraft developed by the Transcendental Aircraft Corporation and Bell Helicopter. These early demonstration aircraft were then referred to as tilt-proprotors or convertiplanes. The Transcendental Model 1-G, a 3-bladed 17-foot diameter fully-articulated convertiplane, made its first free flight at Bellanca Field, New Castle, Delaware, on July 6, 1954. The rotors were successfully tilted forward for airplane flight in December, 1954, and the Model 1-G completed 23 hours of air time in over 100 flights before suffering major airframe damage in an accident on July 20, 1955. Although the Model 1-G was designed and built without government support, the United States Air Force awarded a contract to Transcendental in June, 1952, for the purpose of obtaining data on blade, rotor shaft and control stresses, and on blade motions under various conditions of ground operation. Tests conducted under this contract indicated that mechanical instability would be an important consideration during conversion mode. The Transcendental Model 2 was built under phase one of an Air Force contract in 1956, and was of the same basic design of the Model 1-G, but with more powerful engines. The final phase of this contract was a flight test program in which the stability and control characteristics of the Model 2 were to be determined in all flight regimes, but this phase was never

10

initiated due to a termination of funding.

While a concern of mechanical instability developed during testing of the Transcendental Model 1-G, it was flight testing of the Bell XV-3 which lead to the discovery of the whirl flutter instability on tiltrotors. The first XV-3, with a three-bladed fully-articulated rotor system, was built under an Air Force/Army contract awarded in 1951, but this aircraft was badly damaged in a 1956 accident related to a blade oscillation problem. A second XV-3 was designed with a two-bladed semi-rigid (teetering) rotor system which successfully eliminated the blade oscillation problem of the first design. This aircraft established its first full conversion in December 1958, but subsequent testing identified problem areas associated with high-speed airplane mode of flight. The transient blade flapping during maneuvers and low levels of longitudinal stability near the dive speed were unacceptable [11]. The low stability margins were found to be related to the inplane forces generated by the combination of blade flapping and aircraft pitching motions. As a result of these observations, full-scale wind-tunnel tests were conducted in 1962 in the NASA Ames 40 x 80-foot wind tunnel. It was during these tests that whirl flutter instability was first experienced on a tiltrotor system.

Around this same time frame, knowledge of the devastation associated with whirl flutter on fixed-wing aircraft became well known. On the night of September 29, 1959, a Lockheed Electra turboprop aircraft, belonging to Braniff International Airways, disintegrated in the air near Buffalo, Texas. A second Electra, belonging to Northwest Airlines, lost a wing and crashed near Tell City, Indiana, on March 17, 1960. The cause of these two fatal accidents remained unknown until it was established in 1963, from NASA Langley wind-tunnel investigations [12], that whirl flutter could occur in an Electra if the engine nacelle stiffness was greatly reduced, as by structural failure . While not conclusive, this explanation is generally accepted as the best explanation of the Electra crashes. Because of the experiences

11

with the Lockheed Electra and Bell XV-3, whirl flutter became an important design consideration and a research topic of great interest in the 1960's and early 1970's.

The U. S. Army began the Composite Aircraft program in 1965 with the objective of developing a rotary-wing research vehicle which could combine the hovering capabilities of a helicopter with the high-speed cruise capabilities of a fixed-wing aircraft. While the program was terminated after a brief two-year period, one of Bell's contributions to this program, an aeroelastic model of the Model 266, was given to NASA Langley. Subsequently, a joint NASA/Bell study of tiltrotor stability, dynamics, and loads was pursued and tests of the model were conducted in the Langley Transonic Dynamics Tunnel [6]. These tests helped foster an expertise in tiltrotor design which lead to improved stability and loads characteristics in later model aircraft.

In 1968, Bell began development of a 25-foot diameter, 3-bladed gimbaled hub tiltrotor designated as the Model 300. Dynamic rotor/pylon stability investigations, both model and full-scale, showed the Model 300 rotor was stable with margins well beyond the aircraft dive speed. In April 1973, NASA and the Army selected Bell to design and manufacture two tiltrotor research aircraft which were originally designated the Model 301, and later became known as the XV-15. These aircraft were intended to demonstrate the feasibility of a generic tiltrotor configuration [13]. The XV-15 employs slightly forward swept wings to provide adequate clearance for blade flapping. Stability margins were maximized by use of a stiff wing, use of a stiff pylon-to-wing attachment, and minimization of the rotor hub to wing distance. Airplane flight mode stability was maintained to 370 knots with a 20-percent reduction in wing and pylon stiffness.

A great deal of aeroelastic knowledge was gained from the XV-15 wind tunnel and flight tests which were conducted by NASA and Bell Helicopter since 1978.

The capability of CAMRAD to predict the XV-15 performance, loads, and stability was assessed by Johnson [14]. Good agreement was achieved between analytical predictions and experimental results of frequency and damping of the wing modes for the XV-15 rotor mounted on a cantilevered wing and tested in a wind tunnel. CAMRAD also produced reasonable predictions of wing mode frequencies and damping of the XV-15 flight tests. Predictions were greatly improved with use of post-test values for the frequencies and structural damping over those obtained using NASTRAN frequencies and a uniform one-percent structural damping. The flight test stability results also indicated a general trend of lower damping for all the symmetric wing modes in comparison to the cantilevered wing stability results. Some problems associated with the XV-15 data were also discussed by Johnson [14]. Most notably, the data obtained showed significant scatter in most cases, and were not acquired at consistent operating conditions (flight altitude and speed varied). Stability measurements were obtained far away from the stability boundaries which created difficulties in the assessment of analytical predictive capabilities.

The first production tiltrotor will be the V-22 Osprey being developed for use by the United States Military. The V-22 development program (formerly a Joint Services program and designated the JVX) was started in April 1983. Six of these aircraft have been developed as part of a 1985 full-scale development program contracted to Bell Helicopter Textron Inc. and Boeing Helicopter Company. Tests of a 1/5-scale semi-span aeroelastic model of the V-22 were conducted in the NASA-Langley Transonic Dynamics Tunnel (TDT) during 1984 [15]. The purpose of these tests was to obtain data to aid full-scale development and establish a data base for analytical validation. The influence of many important design parameters, such as compressibility, wing stiffness, rotor control stiffness, pitch-flap coupling, and coning on the system stability were experimentally determined. Analytical comparisons of CAMRAD and DYN4 (Bell Helicopter's proprotor aeroelastic analysis

which is similar to PASTA [16]) were made with the experimental data [15]. The correlation efforts for these codes were extensive and lead to improvements in each code. General agreement of the CAMRAD and DYN4 codes with the test data was poor, but specific areas of improvement were identified: for DYN4 the modeling of pitch-flap coupling and control system stiffness require improvement while for CAMRAD compressibility effects at high Mach numbers and coning hinge modeling required further investigation. PASTA was in good agreement with all data obtained in the TDT tests.

The first production tilt-wing aircraft is currently under development by Ishida Aerospace Research, Inc. This civil aircraft is designated the TW-68, and is a 14-passenger high-speed V/STOL tilt-wing with two propeller-nacelle systems and four turbo-prop engines. Little information on development of this aircraft, which has been conducted completely in-house, is currently available.

1.2.4   Elastic Tailoring of Composite Rotor Blades

Since the 1960's, there has been a slow changeover from the use of metal to the use of composite blades for both manufacturing and structural performance reasons. This section will discuss some of the advantages associated with composite rotor blades, including some recent advanced concepts for elastic tailoring.

The manufacturability of rotor blades has been greatly improved with the advent of composites. Construction techniques used for metal blades, for cost reasons, limit the complexity of the blade geometry. Metal rotor blades are generally designed with a thin-wall spar wrapped in a semi-monocoque skin. Thin-wall construction is obviously required for weight and structural efficiency, but this type of construction is costly for metal parts which must be stamped or rolled into the desired shape. If the blade geometry varies along the span, then the machine tooling becomes more elaborate and more expensive. It is common for metal rotor blades

to be almost uniform along the span. Linear rotor blade twist is often introduced by mechanically deforming the clamped blade after construction is completed.

Composite construction techniques are fundamentally different from those associated with metal blades. Composite blades are built up from layers of material laid down or filament wound onto a solid mandrel. In some instances, laminates are laid up on flat surfaces and then formed against female clam-shell tooling during cure. In either case, the cost of manufacturing a geometrically complex and precise component is negligibly different from the cost of manufacturing a simple one. The manufacturing cost of a composite rotor blade set is competitive with metal blades, and considering that more complex rotor blade geometries can be designed within budgetary constraints using composites, the majority of new blade designs have shifted to composite construction.

With the increased flexibility in planform design associated with composite rotor blades, researchers and designers have pursued new aerodynamic performance benefits. The spanwise distribution of airfoil sections are now routinely altered to optimize performance. This capability is important for rotor blades because of the significant changes in local velocity which occur along the span. Generally, thick airfoil sections with large chord are desired inboard to increase lift where velocity is low, and thin airfoils with small chord are desired outboard to reduce Mach effects where velocity is high. Detrimental effects associated with blade stall can also be improved through variation of the planform, and induced drag can be reduced with nonlinear twist distributions. These aerodynamic performance improvements, made economically feasible by using composite materials, have expanded the flight envelope of the helicopter.

In the structural performance area, the advantages of composite blades include stiffness, strength, fatigue life, damage tolerance, corrosion tolerance, and elastic tailorability. Composite materials generally have much higher strength-to-weight

and stiffness-to-weight ratios than metals. These properties allow blades to be designed for minimum weight within autorotational inertia constraints. However, minimum weight designs have not yet been considered for production rotors because of limited experience with composite blades and susceptibility to low-impact damage. With limited experience, blades must be designed very conservatively, far away from design limits. Low-impact damage is a problem which undermines some of the structural advantages composites have over metals. This type of damage is characterized by microscopic cracking or delamination which propagates during cyclic loading. The initial damage is undetectable by visual inspection and has no immediate impact on strength or stiffness, but can have a large impact on both in a relatively short period of time. Metals are generally not susceptible to damage which cannot be revealed by visual inspection, so lower factors of safety are required for metal blades. For these reasons, composite blades have generally been *over-designed* with respect to strength and stiffness requirements.

The fatigue life of rotor blades has increased dramatically with the shift to composite construction. Composite materials are inherently resistant to fatigue damage because they are essentially multiple-load-path systems at the microscopic level (many overlapping fibers). If there is damage due to cyclic loading, the load shifts into undamaged (stiffer) areas which slows propagation of the damage and increases fatigue life. An adverse characteristic of composite blades is the possibility of delamination between ply layers. After delamination is initiated, damage generally spreads quickly and can lead to catastrophic failure. Fatigue in rotor blades eventually leads to delamination, but it is very difficult to predict this behavior because of its dependence on both geometry and loading. While fatigue lives of composite rotor blades have been increased to the point where blades can outlast the airframe, it is still difficult to predict the actual lives of these blades.

Damage tolerance and corrosion resistance of rotor blades have also improved

16

with use of composite materials. Composites retain a greater percentage of their original strength after damage than do metals. This attribute is related to the multiple load path system and the high strength to weight ratio inherent in composites. Composites can also be tailored to absorb large amounts of energy through crushing, as demonstrated in crashworthiness-designed components. Corrosion of metal blades has been shown to reduce strength and fatigue life. Composite rotor blades are much less susceptible to corrosion and so do not require the corrosion-protectant coatings that metal blades do.

Many of the advantages of composite materials have been exploited in rotor blade designs as discussed in the above paragraphs. More advanced structural design concepts are now being considered which take advantage of composite material anisotropy to tailor rotor blade stiffness properties (broadly referred to as elastic tailoring). Elastic tailoring becomes an attractive when stiffness properties must be simultaneously controlled in multiple modes or directions, so as to achieve both a desired chord and flapwise bending stiffness, for example. This is where composites have a great advantage over metals in rotor design.

Composite materials are composed of fibers, typically graphite, Kevlar, or fiberglass, embedded in a matrix, generally some type of epoxy resin. Unidirectional laminates have fibers running in only one direction which is much stiffer than the cross direction which is dominated by the matrix properties. Thus, composite materials have a directional nature which can be used to build laminates, substructures, and rotor blades with desired directional properties as well. The anisotropy of composites may also be used to create elastic couplings in structures, such as extension-twist, bending-twist, or bending-shear. Composite materials, thus, may be used to tailor structures for a particular environment with relative ease and cost-efficiency as compared to metals.

A practical example of elastic tailoring in rotor blades is the introduction

17

of the composite flexbeam in hingeless and bearingless helicopter rotor systems. Flexbeams are designed to provide appropriate stiffnesses in the bending directions, and for bearingless systems must additionally maintain low torsional stiffness for pitch control. These designs eliminate expensive and fatigue-prone hinges and bearings used in articulated rotor systems. The advantages of the hingeless and bearingless designs are decreased production costs, improved aerodynamic performance (reduced parasite drag), and increased maneuverability (higher flap/lag stiffness quickens control response). With the increased bending stiffnesses associated with these designs, however, come larger blade loads. With composite materials, flexbeams can be tailored to achieve the desired stiffnesses while achieving acceptable strength margins with the blade loads involved.

A more demanding form of elastic tailoring is the *introduction* of elastic couplings. For rotor blades, anisotropic layups may be used to couple elastic modes such as bending to twist, extension to twist, or bending in one plane to shear in the other. There are several reasons why such coupling is desirable in a rotor blade. Elastic couplings can be used in the same manner, and generally with less complexity, as kinematic couplings. An example of the use of kinematic couplings is found in tiltrotors where pitch-flap coupling is used to reduce blade flapping response. Elastic and kinematic couplings have also been considered to improve stability characteristics of helicopters. One study has shown that negative pitch-lag coupling has a stabilizing influence on air resonance [17]. Elastomeric dampers, generally used to avoid ground and air resonance instabilities in bearingless rotor designs, may be eliminated if appropriate pitch-lag elastic coupling is designed into the rotor system.

The use of anisotropic composite rotor blades to reduce vibration and improve aeroelastic and aeromechanical stability characteristics of hingeless rotor helicopters was recently addressed by Smith [18]. For this study, a finite element

18

with shear degrees of freedom was formulated and implemented into UMARC. The analysis produced good correlation of frequencies with experimental results for several elastically-coupled box-beam specimens. The aeroelastic results showed that, for the elastic couplings considered, the steady flap and lag responses and the corresponding root bending moments and shears were not significantly altered by the elastic couplings. This is because the rotational stiffness contribution is large and is unaltered by the elastic couplings. However, the shaft-fixed aeroelastic stability was significantly altered by the elastic couplings. Use of negative pitch-lag coupling resulted in a 300% increase in lag mode damping compared to the baseline system. Elastic couplings were also shown to have a significant influence on ground and air resonance. The blade design with negative pitch-lag elastic coupling increased the regressive lag mode damping in air resonance conditions, but greatly decreased damping for ground resonance stability. Other types of coupling were also found to destabilize the system in the ground resonance condition.

There have also been studies which show that elastic tailoring may be used to improve tiltrotor performance [19]. In these studies, the deformation of the rotor blade is passively controlled to obtain an optimum twist in both the helicopter and airplane flight modes. The rotor blades of this study are extension-twist coupled where elastic twist deformation results from changes in centrifugal forces associated with two rotor speed settings. The design has one rotor speed and associated twist distribution which are ideal for hover, and a second rotor speed and associated twist distribution which are ideal for cruise flight. These studies have shown that significant performance improvements can be gained with realistic extension-twist-coupled blade designs based on structural strength constraints. The dynamic and stability aspects of these designs have not been investigated.

1.3 Survey of Tiltrotor Aeroelastic Research

Much of the history of tiltrotor development has concentrated on predicting and avoiding whirl flutter instability. Whirl flutter is a self-excited instability resulting from precession-generated aerodynamic loads in high-speed flight. This phenomenon has occurred in both conventional fixed-wing propeller aircraft and tiltrotors, but the tiltrotor is more susceptible to this instability because of higher levels of rotor blade flapping, bending, and control system flexibility. The possibility that whirl flutter could occur on aircraft with propeller systems was first mentioned by Taylor and Brown in 1938 [20]. The phenomenon was only accorded academic interest because of high margins of safety in the aircraft of the time. Little attention was given to the subject until it became a topic of renewed research interest around 1960.

Several early investigations of the aeroelastic behavior of tiltrotor aircraft having straight wings were performed using pylon-pivot models. These models approximate the wing as a system of springs and masses located at the effective pylon pivot point. The earliest work with application to tiltrotors was directed at hinged or flexible propeller systems [21, 22]. The analysis developed through this research effort, as well as other analyses of the time, had difficulty predicting forward whirl flutter in several instances in which it was obtained experimentally with small models. These problems were highlighted in the review made by Reed [23]. A study by Young and Lytwyn [24] showed that the fundamental (in-vacuum) blade flapping frequency could be tuned to maximize stability of a tiltrotor system. The optimum tuning was approximately 1.1 to 1.2 per-rev, which implies a requirement for an increase in flapping restraint for an articulated or gimbaled rotor system. Because an increase in flapping restraint increases blade loads, the applicability of blade tuning is limited [25]. The results of an experimental and analytical investigation conducted on a scaled model of the XV-3 tiltrotor were

reported by Edenborough [26]. His analysis used a math model which included a wing beamwise translation degree of freedom in addition to the conventional pylon pitch and yaw freedoms. The effects of several major parameters on stability were identified: an increase in pylon pitch and yaw stiffnesses is stabilizing, use of blade pitch-flap coupling (δ_3) is destabilizing, and increased flapping restraint is stabilizing. These trends were substantiated analytically by DeLarm [27] using a similar mathematical model. A study of the effects of steady-state coning angle and hinge damping by Kaza [28] showed that these parameters can also have a significant influence on stability. The results of extensive parametric studies were reported by Kvaternik [16, 29, 30]. The axial flight math model used in these latter studies included all six degrees of freedom at the pylon pivot point, but generally only the pylon pitch, yaw, and beam (vertical translation) degrees of freedom were used. These studies verified trends discussed previously and reported some important new trends: wing aerodynamic forces are stabilizing, unsteady aerodynamic forces are stabilizing, windmilling configuration is conservative (power-on case is more stable), high precone is destabilizing, both positive and negative δ_3 are destabilizing, and blade lag dynamics can have an important influence on stability. The analytical model of these studies was later extended to include additional degrees of freedom and a modal representation of the airframe structure, and was then formalized into a code called PASTA (Proprotor Aeroelastic STability Analysis).

A more comprehensive math model which included a modal representation for the wing was developed by Johnson [31]. This model was applicable only to axial flight and included nine degrees of freedom: six for the three-bladed rotor system (including gimbal capability) and three for the three fundamental wing modes. Analytical results obtained with this model correlated well with the results of full-scale proprotor tests. Johnson later extended this math model to include elastic blade characteristics and helicopter and conversion modes of operation [32,33].

21

These models formed the basic theory for the tiltrotor model in CAMRAD [34], which is one of the few comprehensive rotorcraft codes to allow treatment of a tiltrotor aircraft.

In 1985, Johnson assessed some of the recent developments in tiltrotor dynamics [9]. In this review, Johnson expressed concern in the ability of tiltrotor analyses to model some of the new rotor configurations being considered, such as bearingless designs. Concern over the treatment of high-speed aerodynamics was also expressed. Rotor loads are still an important aspect of tiltrotor design because these loads can restrict the conversion corridor. Experience with tiltrotor fuselage vibration showed that wing dynamics provide some vibration absorption, and the ability of the rotors to tilt forward can be used to minimize the wake-induced vibration at low speeds. Thus, fuselage vibration does not seem to be as great a concern for tiltrotors as for helicopters. Johnson consistently emphasizes the influence of pitch-lag and pitch-flap coupling on tiltrotor stability, pointing out that pitch-lag coupling is a problem because of large precone. Precone is chosen to improve blade loads in tiltrotor hover mode, but a large precone at low thrust in airplane mode produces a negative, destabilizing pitch-lag coupling. Johnson also mentions that with a soft-inplane rotor, air resonance is possible at low-flight speeds where aerodynamic damping is low. More details of this phenomenon are discussed in reference [9].

The dynamics associated with the rotor rotational speed degree of freedom (collective lag mode) have been shown to have a large influence on whirl flutter stability [9, 31, 35]. If the rotor speed is assumed to be constant, then the wing roll motion is transmitted to the rotor, which increases the wing beam bending mode damping. This, however, is not an accurate model of the tiltrotor physics. If a rotor is windmilling, the rotor speed is independent of the wing motion, and the wing beam mode damping is reduced. In the powered case, it has been shown that the

engine and rotor-speed governor add little resistance so that the windmilling model is a good representation of the powered case [35]. This is true for a cantilevered wing model and the symmetric modes of a free-flight tiltrotor. This is not true for the antisymmetric modes of a free-flight tiltrotor (one wing bending up while the other is bending down) because stiffness is added to the drive system from the interconnect shaft. The interconnect shaft is a safety device which connects the two rotors so that both may be run off of the power of a single engine. In symmetric modes the shaft creates perturbation of rotor speed in the same direction for both rotors and thus has no stiffness effect. In antisymmetric modes the shaft creates perturbation of rotor speed in opposite directions, adding a stiffness to the rotor speed perturbation modes. The resulting drive system dynamics have a frequency of the same order as the fundamental wing modes, and can thus have an influence on the system stability.

Johnson also discusses the predictive capability of rigid-blade linear analyses for tiltrotor stability [9]. Successful predictions may be made with these analyses even for hingeless and bearingless rotor designs as long as the effective pitch-lag, pitch-flap, and flap-lag couplings are included properly. These types of analyses are effective for a tiltrotor in high-speed airplane flight because of the high-inflow aerodynamics. With high inflow, both the flap and lag bending motions produce a first-order change in the blade angle of attack, and the blade lift has large components both in and out of the rotation plane. As a result, the lift-curve-slope terms dominate the aerodynamic contributions to the system matrices (even in the lag terms), and the aerodynamic loading associated with the deflected trim position has only a small influence on the system stability. Conversely, for a helicopter the inflow is much smaller and the blade lift is mainly in the out-of-plane direction. Thus, the inplane forces are much smaller, and the inplane motion is highly influenced by the blade loads associated with the deflected trim position.

The ability of rigid-blade linear analyses with kinematic couplings to accurately predict whirl flutter stability may be reduced for more advanced blade designs because the elastic coupling can involve significant nonlinear deformations. Another disadvantage of rigid-blade analyses would be their inability to accurately predict rotor dynamics in helicopter or conversion mode where the trim deflection has a more significant influence on the system.

The most accurate and general analyses for aeroelastic stability are based on elastic flap,lag, and torsion blade models. The earliest known elastic-blade aeroelastic analysis which included a tiltrotor configuration capability was developed by Johnson [33] and later became part of CAMRAD [34]. CAMRAD is capable of analyzing conventional helicopter configurations with articulated, hingeless, gimbaled and teetering rotors. The gimbal rotor system is, of course, most useful for the tiltrotor configuration which, as mentioned above, is also included in CAMRAD. Bearingless rotor systems, however, cannot be accurately modeled in CAMRAD because they involve multiple load paths (torque tube and flexbeam), and in CAMRAD the blades are essentially formulated for a single load path. For bearingless rotors, it is better to use a finite-element-based blade analysis. The elastic blade model of CAMRAD is reduced to several flap-lag-coupled and uncoupled-torsion modes, and the kinematic couplings may be input directly or calculated internally based on the control system geometry. Because the analysis is based on a flap-lag rotor model, the flap-lag elastic couplings associated with geometry (such as twist) are included as part of the modal solution. CAMRAD cannot, however, model a general coupled anisotropic rotor blade built up from composite materials. Further, modifications to include this capability would be a difficult task because the CAMRAD blade model is not finite element based, torsion modes are uncoupled, and the blade model does not include an axial degree of freedom which may be elastically coupled with the flap, lag, or torsion modes for composite blades.

24

The CAMRAD rotor aerodynamics formulation is based on two-dimensional tabular data, and includes corrections for Mach number, three-dimensional effects, unsteady flow, and dynamic stall. Prescribed and free-wake models are also available. The CAMRAD airframe consists of six rigid-body degrees of freedom, ten elastic modes, and a drive system with interconnect shaft option and a rotor speed perturbation option. The airframe aerodynamics are based on fuselage/wing/tail steady incidence angles and angle rates. Rotor-body and body-tail interference effects may be included in these calculations. Both free-flight and wind-tunnel modeling options are available.

The predictive capabilities of CAMRAD have been discussed in several studies, and correlations with experimental data have generally been favorable [14,15,36, 37]. The study by Popelka, Sheffler, and Bilger [15] was based on tests of a 1/5-scale semi-span aeroelastic model of the V-22 which were conducted in the NASA-Langley's Transonic Dynamics Tunnel. The influence of many important design parameters, such as compressibility, wing stiffness, rotor control stiffness, pitch-flap coupling, and coning, on the system stability were experimentally determined. Analytical comparisons of CAMRAD and DYN4 (Bell's Proprotor Aeroelastic Analysis which is similar to PASTA) were made with the experimental data. The correlation of calculated results based on pretest data were generally poor for the CAMRAD and DYN4 analyses. Coding errors in the DYN4 analysis were found and corrected, and the analysis was modified to include pitch-lag coupling terms. The CAMRAD model of the coning hinge hub was modified, and the blade airfoil data tables were updated based on the wind tunnel test results. These post-test modifications lead to improved whirl flutter stability predictions for the CAMRAD and DYN4 codes. Compressibility effects were investigated by testing the V-22 model in both air and Freon. An investigation of the variation of the stability boundary with rotor speed showed that while both DYN4 and CAMRAD

could predict the flutter boundaries in air accurately, the CAMRAD error was higher in Freon at high rotor speeds. This error was believed to be related to a local Mach problem in the CAMRAD airfoil tables. CAMRAD and DYN4 were shown to predict the damping of the wing beam mode at and near the point of instability very well (with post-test modifications). The effect of pitch-flap coupling was tested over a range of values from -15 to -10 degrees. The correlation efforts of the remaining parametric studies associated with the V-22 wind tunnel test showed good agreement for both analyses. These studies included variation of wing and control system stiffnesses, and use of a coned hub. An important aspect of the Popelka, Sheffler, and Bilger study was that it demonstrated comparable predictive capabilities of whirl flutter for the rigid-rotor-based DYN4 and the elastic-rotor-based CAMRAD.

Comparisons of aeroelastic analyses with XV-15 flight tests were made by Acree and Tischler [38]. In these flight tests, modal frequencies and damping were determined using curve fits to frequency response data obtained for an XV-15 with metal blades. The frequency and damping determined from the flight data were compared to predictions from two analyses, CAMRAD and ASAP (a new proprietary analysis developed by Bell, replacing DYN4, but still similar to PASTA). ASAP and CAMRAD produced similar predictions, but generally agreed with each other better than the flight test data. Both the frequency and damping predictions of the analyses were in general significantly different from the flight test results. The analytical models used wing natural frequencies, mode shapes, and generalized masses as developed by NASTRAN models, with structural and aerodynamic wing damping estimates based on wind tunnel tests of a V-22 wing aeroelastic model. The study implies that the predictions would improve with the inclusion of better estimates of the wing structural damping.

An improved version of CAMRAD, known as CAMRAD/JA, was completed in

1988 by Johnson [39]. This version of CAMRAD was used in a study by Kottapalli and Meza [40] to investigate fundamental differences between the XV-15 stability with metal blades as compared to the XV-15 with the ATB (Advanced Technology Blades). The ATB are a composite blade set developed for improved tiltrotor performance. This study showed that in airplane flight with the XV-15 metal blades the isolated rotor system is inherently stable, while with the XV-15 ATB blades the isolated rotor system experiences pitch-flap flutter due to an adverse chordwise mass distribution. The study also addresses aspects of the control system stiffnesses which have been shown to have an important influence on the whirl flutter stability.

Some aspects of tiltrotor aeroelasticity were discussed in a study related to development of the XV-15 Advanced Technology Blades [41]. This study was conducted by Boeing under contract with NASA Ames Research Center. The XV-15 ATB design focused on improving the rotor aerodynamic performance which resulted in an increase in solidity from .089 for the metal blades to .103 for the composite blades. Since the rotor diameters are the same for both sets, increased solidity translates to an increased blade chord and thereby increased torsional inertia and lower torsion frequencies for the ATB blades. The lower torsional frequency tends to reduce the whirl flutter stability margins. To overcome this reduction, aft sweep outboard of the pitch bearings was introduced into the design. At high collective settings, such as are experienced in high-speed airplane flight, the sweep reduces blade precone which, in turn, lowers the steady blade bending moments and the related pitch-lag coupling. As has been discussed previously, the pitch-lag coupling generally has a destabilizing influence on whirl flutter stability. The Boeing study showed that about one degree of aft sweep would restore the stability margins degraded by the increase in blade solidity.

The development of the ATB blades also fostered a feasibility study by Bauchau,

Loewy, and Bryan [42] which is relevant to the topic of the present dissertation. The objective of this analytical study was to design a rotor to change twist distribution between hover and forward flight modes by about two degrees. The twist change was to be accomplished using an extension-twist-coupled rotor blade, taking advantage of the 15-percent change in rotor speed between the two flight modes of interest. To maintain favorable dynamic characteristics, the design was constrained relative to the ATB baseline design as follows: same chordwise location of the center of gravity at all blade sections, same placement of fundamental blade in-vacuum frequencies, and same ratio of applied to allowable stresses. The approach taken in the study for matching the fundamental frequencies was to maintain the same mass and stiffness distribution as the baseline ATB, rather than to allow either one to shift and be compensated by the other. This required the elastically-coupled rotor to have the same effective beam properties as the ATB baseline which is a difficult assignment given that the coupling tends to reduce the bending stiffnesses. Under these constraints, the resulting design achieved only about a half of a degree of predicted elastic twist change. The study then considered an approach which relaxed the constraints of frequency matching, resulting in significant amounts of elastic twist. The associated flap and torsion stiffnesses were far below the ATB baseline, however. The aeroelastic stability characteristics associated with these designs could not be determined with available analyses.

Improvements to tiltrotor whirl flutter through active control has also been considered. In a recent a study by Nasu [43], control laws were developed based on harmonic balance algorithms and feedback of wingtip velocity and accelerations. Stability was improved through application of cyclic pitch controls defined by the closed-loop system. There is some question of the correctness of the model used because the initial design did not experience an instability at any velocity and, after reducing wing stiffnesses to one-eighth of their original values, the system

did not experience an instability until an advance ratio of about 1.5, which is far above a realistic value. Nevertheless, application of the feedback control law was shown to improve the damping of this mode.

1.4 Survey of Anisotropic Blade Modeling

There is a potential for improving the performance, aeroelastic stability, and vibration characteristics of rotorcraft through the use of elastically-coupled composite rotor blades. To accomplish these gains, one needs to develop aeroelastic analyses. Currently, comprehensive aeroelastic rotorcraft codes, because of their complexity and size, are limited to modeling the elastic rotor blade using a one-dimensional (beam) theory. Thus, there has been recent emphasis on deriving one-dimensional generally anisotropic beam theories which can capture the important characteristics of a rotor blade, a structure which is more readily defined using two and three-dimensional theories. The theory must also be nonlinear so that the important rotational effects may be included. The developments leading to nonlinear generally anisotropic beam theories are examined in this section. Important considerations for modeling composite rotor blades are addressed first. Developments in general anisotropic beam theories are then addressed, followed by an examination of theories developed specifically for rotor blade use.

1.4.1 Important Considerations in Rotor Blade Analysis

A beam theory developed for modeling a specific structure, such as a rotor blade, can be greatly simplified by taking advantage of certain geometric features. This section will discuss some of the important effects which must be included, as well as those which can be ignored, in the modeling of rotor blades as beams.

Rotor blades have traditionally been modeled as Euler-Bernoulli (classical)

beams because they are long and slender. When rotor blades are constructed of metals, the Euler beam is an adequate blade model because effects associated with in-plane warping, elastic coupling, and transverse shear deformation are generally negligible. The effect of torsion-related out-of-plane warping, which significantly decreases the torsional stiffness of a noncircular beam, has been well understood, and many cross-section analyses use a free-warping assumption (St. Venant) to obtain the effective torsional stiffness for an Euler beam model. This approach has proven adequate for static analysis of rotor blades because blades are usually of closed-cell construction. For closed sections, free-warping may be assumed everywhere except for very near a clamped blade root. The boundary condition restrains the warping of the beam, greatly increasing the torsional stiffness in the region where the restraint is significant. This region is often referred to in terms of a decay length, and the effect of warping restraint decays very quickly as one moves away from the boundary of closed-cell beams. Beams with open cross-sections can have very long warping decay lengths so beam modeling for these structures must accurately account for warping.

Beam modeling of composite rotor blades is significantly more complex than modeling of metal rotor blades because of effects associated with material anisotropy. Composites are a nonhomogeneous material (fibers and matrix) which are modeled as a homogenous material in laminate theory. The properties of the fiber and matrix are "smeared" together as a thin orthotropic lamina or ply. When multiple plies are bonded together in a laminate, the plies may be arranged so that the structure as a whole exhibits anisotropic behavior. By variation of the laminate stacking sequence and the fiber directions of the plies, elastic couplings can be developed between bending, twist, shear, and extension of the laminate. Rotor blades built up from composite laminates can also be designed to exhibit this anisotropic behavior. Some form of laminate theory is generally used in cross-section analyses

to calculate beam stiffness properties for composite rotor blades. Finite element formulations based on laminate theory have also been established here. The effect of transverse shear deformation can be significant in composite rotor blades because the classical stiffnesses may be elastically-coupled to the beam shear stiffnesses. This coupling can have a significant effect on blade flexibility in the coupled directions. Poisson effects can be substantially larger in composite beams which leads to significant in-plane warping of the cross-section. The in-plane warping can influence the beam stiffness properties just as torsion-related warping influences the beam torsional stiffness. The effects discussed in this paragraph must be considered in beam modeling for composite blades.

Rotational effects must also be considered in development of beam theories for composite blades. Nonlinear isotropic-beam theories have been developed to model rotor blade dynamics including effects associated with rotation. The pioneering formulation of elastic rotor blade modeling was developed by Houbolt and Brooks [44] assuming linear strains and small deformations. Although rotor blade strains are assumed small, deflections may be moderate to large. Several studies in the early 1970's considered the nonlinear behavior associated with moderate deflections in rotor blades [45-47]. Dynamic and aeroelastic analyses based on moderate deflection nonlinear beam theory are now state-of-the-art for rotor blades. It is common in these types of analyses to reduce the number of degrees of freedom using reduced-basis modal techniques. Inaccuracies associated with use of modal reduction on highly nonlinear problems have been identified in studies by Bauchau and Liu [48] and Bauchau and Guernsey [49]. These studies demonstrate the importance of formulating a nonlinear composite rotor blade theory using kinematic variables which minimize the nonlinearity of the formulation if modal techniques are to be used. Such rationale for selection of kinematic variables were identified by Kaza and Kvaternik [50].

31

The formulation for rotating beams is more involved than that for nonrotating beams because the rotation effects can only be included through use of the geometrically nonlinear theory of elasticity. For a general anisotropic beam, accounting for all the possible nonclassical beam effects in a nonlinear formulation is undesirable because of size and complexity considerations. One approach for simplifying the formulation is to split the equations associated with the geometrically nonlinear three-dimensional theory of elasticity into a nonlinear one-dimensional set of equations and a linear two-dimensional set of equations (nonlinear beam theory and linear cross-section analysis). This approach has theoretically been shown appropriate for twisted nonhomogeneous anisotropic blades through use of a variational-asymptotical method by Hodges and Atilgan [51].

1.4.2 General Anisotropic Beams

In one of the earliest investigations of anisotropic beams, the equations of elasticity were developed for anisotropic cylindrical shells [52]. This study produced fully-coupled stiffness matrices for both open and closed thin-walled cross-sections, but did not produce analytical results. Other investigators have considered the behavior of general anisotropic beams of *arbitrary* cross-section. A theoretical formulation was developed by Iesan [53] based on an assumed displacement field in one early study, but no results were given. Other studies developed *approximate* solutions using a two-dimensional anisotropic cross-section model which was solved using the Ritz method. In one such approach [54] the local and global (spanwise) deformations were uncoupled, and the two resulting sets of equations were solved simultaneously. In another such approach [55,56], the global beam problem was solved using Saint-Venant's inverse method followed by a solution for the local cross-section deformations. The latter work, while producing equivalent results to the previous approach, demonstrated that the global beam equations can be solved

32

independently of the local cross-section equations. This has special implications for beam modeling of elastic blades in comprehensive aeroelastic rotor codes, as will be discussed later. Kosmatka extended this work to include the effects of initial pretwist on anisotropic beam behavior [57]. This study showed that the elastic twist developed by an axial load applied to a pretwisted extension-twist-coupled beam could be dramatically increased or decreased by the location of the initial twist axis.

The influences of shear deformation and warping in nonrotating *dynamic* analysis of coupled beams have been investigated by Kosmatka [58] and Kosmatka and Ie [59]. These studies demonstrated the importance of out-of-plane shear-dependent warping and in-plane warping (anticlastic deformations) in the free-vibration analysis of beam modes in which shear deformation has significant effects, such as bending modes of short beams and high-frequency bending modes of long beams. Shear deformation also is an important consideration for beams with bending-shear elastic couplings. Based on the work of Kosmatka and Ie [59], it appears necessary to include the shear-related warping effects for an accurate prediction of frequencies of bending-shear coupled beams.

1.4.3   Anisotropic Beam Modeling for Rotor Blades

Early anisotropic beam theories developed specifically for rotor blades concentrated on development of the basic equilibrium, compatibility, and constitutive relations for static analysis of an anisotropic beam [60]. These theories were simplified by assuming a thin-walled construction so that composite laminate characteristics could be easily incorporated through integration around the contour. The influence of the shear deformation on the effective beam stiffnesses was considered, but the influence of cross-section warping was not considered. The importance of the shear deformation and its effect on anisotropic beam bending was emphasized by

33

Rehfield [61] who put forth a clear and concise extension of the Mansfield and Sobey [60] theory. Rehfield also discussed the influence of torsion-related warping on the stiffness parameters [62]. The capabilities and limitations of the Rehfield theory were determined in a series of analytical and experimental studies [19,63,64]. These studies showed that the Rehfield theory could accurately predict the global response of elastically-coupled thin-walled beams, but errors in bending prediction increased with laminate thickness. The predictions of stress and strain distribution through the cross-section were shown to be in error which is attributable to the thin-wall assumptions.

Composite modeling capabilities were introduced in aeroelastic rotor analyses by researchers at the University of Maryland. Hong and Chopra modeled composite rotor blades as laminated thin-walled beams [65,66]. These studies represented hingeless and bearingless rotors as either rectangular cross-section box beams composed of four separate laminates or as I-beams. Laminate theory was used to calculate the effective cross-section properties for the beam model which used displacements associated with classical beam theory. Neither in-plane warping effects nor transverse shear deformation were considered in the analysis. The nonlinear governing equations were derived using a finite element formulation, and the effects of elastic coupling on aeroelastic stability in hover were investigated. This model was extended by Panda and Chopra to examine the dynamics associated with composite rotor blades in forward flight [67]. Here, the effects of ply orientation and elastic coupling on vibration levels and isolated rotor stability were addressed. An important contribution of this work was the solution of the blade periodic response using the finite element in time procedure. The effects of shear deformation on rotating beam dynamics were examined by Smith and Chopra [68] in a study which extended the rotor analysis known as UMARC (University of Maryland Advanced Rotor Code, Hong and Chopra [65,66]) to include explicit

shear degrees of freedom. Results of this study showed improvements in the prediction of lower mode frequencies for bending-shear coupled beams. It is clear from this study that shear deformation effects must be included in the beam analysis to obtain accurate frequencies of bending-shear coupled beams, but the approach of using explicit shear degrees of freedom increased the size and complexity of the formulation. Smith [18] later examined the influence of significant amounts of elastic coupling on helicopter aeroelastic response and aeromechanical stability.

A nonlinear composite beam theory for blades with curved elastic axes was developed by Kosmatka [58]. A refined theory for determination of the composite blade shear center was also presented. The theory accounted for out-of-plane torsion-related warping , but did not consider shear deformations or in-plane warping. Results of the study showed excellent agreement in frequency predictions for some composite curved beams.

The linear periodic response of thin-walled composite rotor blades in forward flight have been investigated by Rand [69,70]. This study used a detailed model for cross-section warping, and examined response, loads, and stresses for blades with extension-torsion and bending-torsion couplings.

Some recent endeavors in the area of composite rotor aeroelastic analyses have also been made. Fulton [71] developed a composite rotor stability analysis based on a finite element formulation of the intrinsic, mixed dynamic equations of Hodges [72] which include the effects associated with shear deformation. Stability results are presented for a helicopter in hover with hingeless extension-torsion-coupled rotor blades. Yuan and Friedmann [73] developed a hovering aeroelastic stability analysis for composite rotor blades with tip sweep and anhedral. This study included transverse shear deformation and torsion-related warping restraint effects in a twenty-three degree-of-freedom beam element. Comparisons of this work are made with results of Hong and Chopra [65]. Kim and Dugundji expanded the

previous large-displacement nonlinear beam formulation of Minguet and Dugundji [74,75] to examine stability in hover.

1.5 Scope of the Present Research

The present research examines the performance, response, and aeroelastic stability of a tiltrotor with elastically-coupled composite rotor blades. As the analytical tools required to perform this task do not currently exist, the focus of this research will be on the development of an appropriate comprehensive aeroelastic analysis which has the required capabilities: tiltrotor configuration modeling and anisotropic blade modeling. These capabilities are added to an existing version of UMARC which is limited to helicopter configuration modeling and isotropic blade modeling.

The research presented in this dissertation consists of four major parts. The first three parts address the theoretical development of an anisotropic-blade aeroelastic tiltrotor theory. In the first part, an understanding of the basic stability mechanisms of a tiltrotor in high-speed axial flight is established using a rigid-blade analysis. The second part addresses the accuracy of using a one-dimensional analysis to predict frequencies of elastically-coupled highly-twisted rotor blades. Here, a new anisotropic beam finite element is developed which uses the same assumed displacement field as the UMARC Euler-beam element. In the third part, the final anisotropic blade and tiltrotor configuration aeroelastic theory is developed and implemented in UMARC. The fourth part of the research encompasses validation of the analysis and investigation of some elastically-coupled blade concepts. The following sections describe in more detail what is accomplished in each of these four parts.

1.5.1 Fundamental Study of Tiltrotor Stability

The basic stability mechanisms of a tiltrotor in high-speed axial flight are investigated in Chapter 2. While the studies mentioned in Section 1.3 describe most of the tiltrotor dynamic behavior trends, physical explanation of many phenomena are not available. In addition, there has been limited investigation of the role of lag dynamics in stability. Further, although wing sweep has been recently considered as a means of increasing tiltrotor cruise velocities [76], there apparently has been no consideration of the influence of wing sweep on aeroelastic stability.

The objective of Chapter 2 is to ascertain the tiltrotor system design parameters which are important to aeroelastic stability and to determine their influence on stability in the high-speed axial flight mode using a rigid-blade linear analysis. This chapter first addresses the math model and theory underlying the analysis development, and then focuses on a discussion of the results obtained using the analysis. In particular, the discussion includes the frequency and damping characteristics of a baseline system, the Bell 25-ft diameter proprotor mounted on a cantilever wing [31], as well as the effects of several key system design parameters on stability of the baseline system. These include: blade frequencies, wing stiffnesses, wing sweep, and blade pitch-flap coupling. All cases assume that the rotor is operating in the windmilling state, which means that the rotor torque does not transfer to the wing and that the wing vertical bending rotation degree of freedom at the wing tip (pylon roll) does not contribute to rotor inplane motion.

It should be noted that the study of Chapter 2 is based entirely on a flap-lag rigid-blade gimballed rotor mounted on a cantilevered wing. Some limitations of this model are the exclusion of: blade torsion dynamics, coupled flap-lag blade elastic motion, and fuselage rigid-body motion. These factors limit the applicability of the model in the prediction of free-flight tiltrotor stability.

1.5.2 Dynamic Analysis of Elastically-Coupled Blades

Chapter 3 addresses the accuracy of using one-dimensional analysis for the prediction of rotating beam frequencies of elastically-coupled, highly twisted rotor blades. There are three objectives for this study: 1) show that the degrees of freedom associated with shear deformation may be statically condensed from the analysis, 2) show that the nonclassical influences associated with cross section warping, which may become significant as a result of elastic coupling, can be accounted for without the incorporation of these effects explicitly in the rotating beam analysis, and 3) determine the potential improvement in efficiency by using higher-order displacement approximations in a finite element implementation.

A rotating beam analysis was developed based on a formulation of nonlinear equations of motion and a finite element implementation. The formulation is derived from basic principles to show how shear deformation and warping enter the theory. The formulation is nonlinear as is required to capture the essential centrifugal stiffening effects even in the linearized form of the equations. The degrees of freedom associated with shear deformation are eliminated through static condensation of the linear force-displacement relationships. The linear part of the formulation is implemented as a p-version beam finite element such that the degree of polynomial approximation for the bending, torsion, and axial displacements may be independently selected. This implementation is described in the chapter along with the results of a convergence study. This convergence study will show the efficiency of certain displacement approximations for a bending-twist-coupled beam.

Results of the rotating beam analysis are compared with those calculated by Smith and Chopra [68] for a set of elastically-coupled rotor blades. This will help to prove the validity of static condensation of the shear degrees of freedom for different modes. Attention is then focused on nonclassical effects (shear deformation

and warping) and their influence on the prediction of both rotating and nonrotating frequencies for elastically-coupled and highly twisted beams. Comparisons are made with experimental results obtained by Chandra [77], 1-D analytical results obtained with UMARC as presented by Smith and Chopra [68], and 3-D analytical results obtained using the analysis of Hinnant [78]. The formulation is then implemented in UMARC, and results are validated for several helicopter rotor blade configurations.

1.5.3 Tiltrotor Aeroelastic Theory Development

A new finite-element-based tiltrotor aeroelastic theory is derived based on Hamilton's principle. The derivation involves the development of elastic strain energy, kinetic energy, and virtual work and is similar to previous derivations of UMARC [79], but involves new degrees of freedom and terms not previously considered. Some of the new terms are related to the anisotropic beam modeling, some to a new formulation for inclusion of important precone effects, and some to the tiltrotor configuration modeling. There are three new degrees of freedom added to the five hub degrees of freedom considered in past UMARC derivations, one of these is associated with blade yaw motion and the other two are associated with a gimballed rotor system. Also, a large steady angle transformation is introduced to account for the rotor pylon angle setting, and an elastic wing model is derived from the elastic blade model. The new structural formulations for the blade, hub, and wing structural model are derived in Chapter 4, and the new aerodynamic formulations are derived in Chapter 5. Chapter 6 addresses other modifications to the UMARC helicopter theory necessary to accommodate the tiltrotor configuration: a rigid analysis for estimating initial controls, linear interpolation of elastic blade properties, and new coupled trim analyses. Chapter 7 addresses the assembly of the wing, hub, and blade matrices and other aspects of tiltrotor stability analysis.

1.5.4 Comparison Studies

The remainder of the dissertation focuses on results obtained with the new aeroelastic tiltrotor analysis, and these results are reported in Chapter 8. The analytical results obtained for a baseline configuration are compared with published analytical and experimental results. Following an assessment of the capabilities of the new aeroelastic tiltrotor analysis, two elastically-coupled rotor blade concepts are investigated. In one study, the potential use of bending-twist-coupled rotor blades to enhance tiltrotor stability characteristics is investigated. The influence of these blades on performance and loads is also considered. In the second study, the potential use of extension-twist-coupled rotor blades to improve aerodynamic performance is invetigated. Here, the influence of these rotor blades on stability characteristics is also considered.
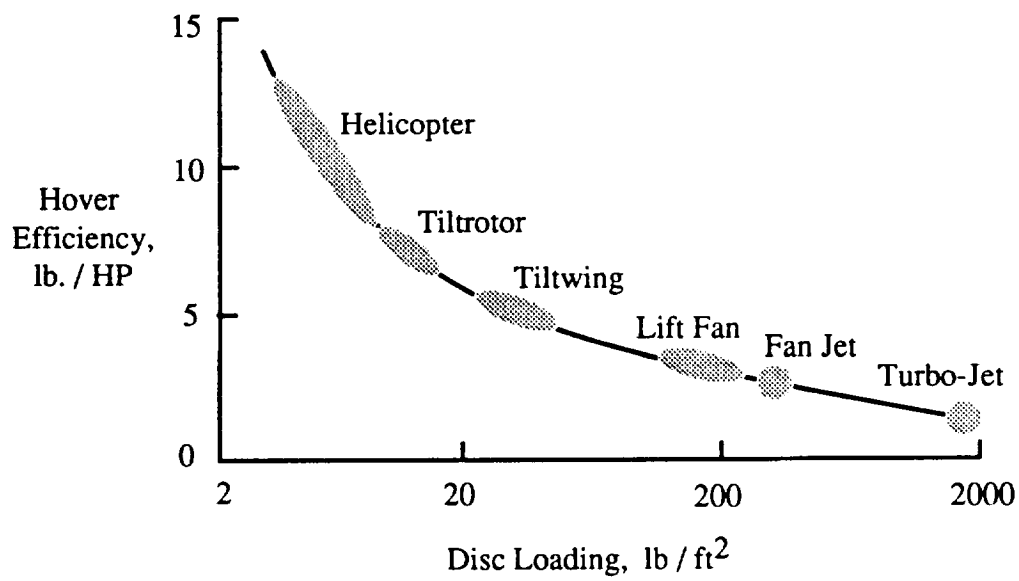
Figure 1.1: Hover efficiency as a function of disc loading.
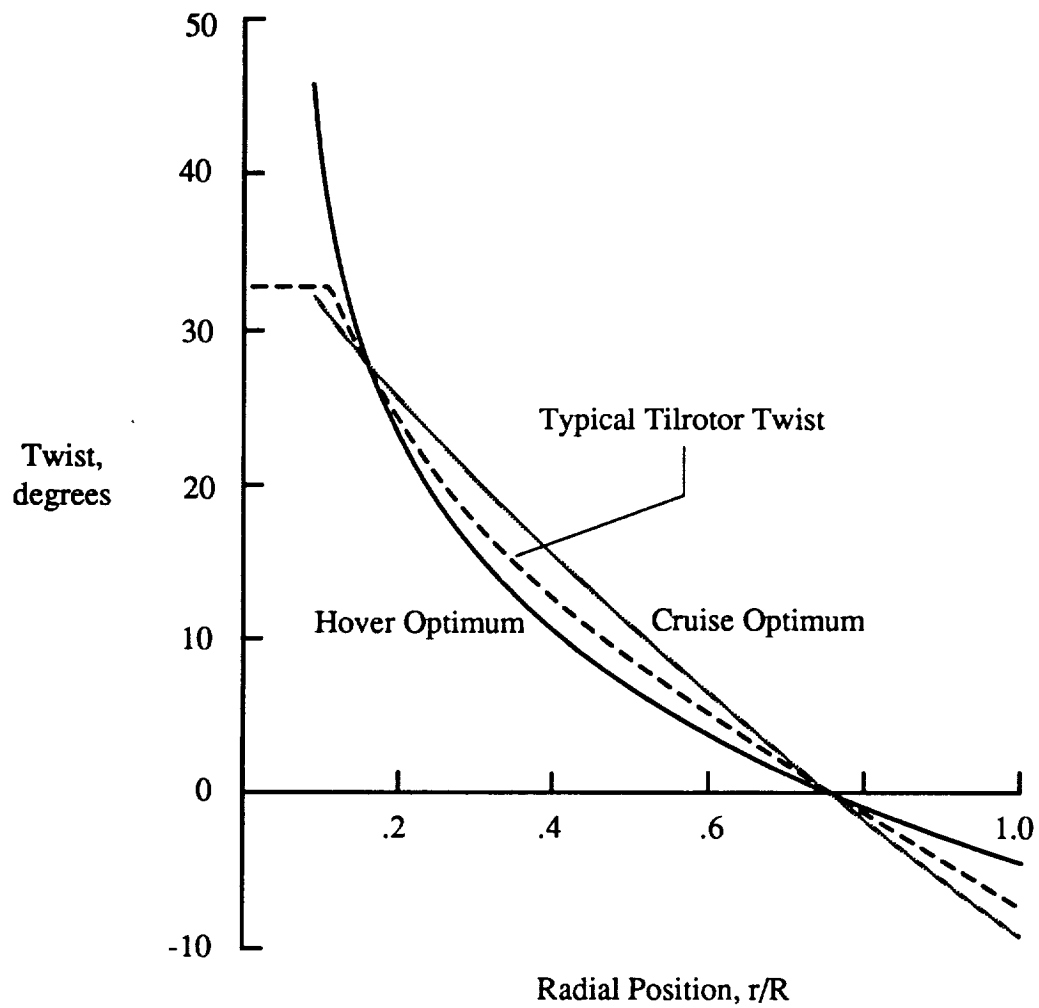
Figure 1.2: Twist distributions optimized for various tiltrotor flight modes.

Chapter 2

Fundamental Study of Tiltrotor Whirl Flutter

In this chapter, the aeroelastic theory for a tiltrotor in high-speed axial flight is derived and implemented as a rigid-blade linear analysis for fundamental studies of whirl flutter stability. The objective is to gain an understanding of important whirl flutter characteristics, and examine how system design parameters influence these characteristics. The present chapter first describes the math model and theory underlying the analysis, then focuses on a discussion of the results obtained using the analysis. In particular, the discussion includes the frequency and damping characteristics of a baseline system, the Bell 25-ft diameter proprotor mounted on a cantilevered wing [31], as well as the effects of several key system design parameters on stability of this baseline system. These include: blade frequencies, wing stiffnesses, wing sweep, and blade pitch-flap coupling. All cases assume that the rotor is windmilling, which means that the rotor torque does not transfer to the wing and that the wing vertical bending slope degree of freedom at the wing tip (pylon roll) does not contribute to rotor inplane motion.

While the tiltrotor studies desribed in Section 1.2.3 discuss many tiltrotor dynamic behavior trends, they do not always provide a physical explanation for the

observed behavior. The present chapter will attempt to provide some of these explanations. In addition, there has been limited investigations on the role of lag dynamics in stability. Further, although wing sweep has been recently considered as a means of increasing the tiltrotor cruise velocities [76], there apparently has been no consideration of the influence of wing sweep on aeroelastic stability.

It should be noted that the study of this chapter is based entirely on a flap-lag rigid-blade gimballed rotor mounted on a cantilevered wing. Some limitations of this model are the exclusion of blade torsion dynamics, coupled flap-lag blade elastic motion, and fuselage rigid body motion. These factors limit the applicability of the model in the prediction of free-flight tiltrotor stability.

2.1   Description of the Math Model

A detailed derivation of the math model is provided in Appendix A. The following paragraph provides a brief description of the math model and some of the important assumptions used in its development.

A three-bladed gimballed rotor system is assumed. The rotor aerodynamic model is quasi-steady and assumes a constant lift curve slope with Mach number corrections. The structural model is a rigid-blade flap-lag model. For a gimballed rotor system in flap, the rotor tip-path-plane may tilt like an articulated system hinged at the center of rotation, but must cone like a hingeless system about a virtual flap hinge. In cyclic lag, the rotor acts like a hingeless system with deflections defined about a virtual lag hinge, but in collective lag the blades are free. Perturbations of the rotor speed are considered which have been shown in past studies to have a significant influence on tiltrotor stability. The rotor system has six degrees of freedom (β_0, β_{1c}, β_{1s}, ζ_0, ζ_{1c}, ζ_{1s}) and associated equations of motion. The wing-tip motion contributes terms to the rotor equations, and the net rotor forces are in-turn applied to the wing tip. The wing model is represented

by beam finite elements having vertical bending, chordwise bending, and torsional degrees of freedom. The wing lift is included in the wing equations through a quasi-steady aerodynamic model with Mach number corrections. The wing and rotor systems are coupled through the degrees of freedom associated with the wing-tip. The force terms of both the rotor and wing equations contain motion dependent terms which are brought into the system mass, damping and stiffness matrices. The steady forces are then set to zero and the resulting system of equations is solved using standard eigenvalue techniques to obtain its frequency and damping characteristics. The accuracy of the analysis was verified through comparison of results with those reported by Kvaternik [16] and Johnson [31].

2.2   Frequency and Damping Characteristics of the Baseline System

The important in-vacuum frequencies of the baseline wing and rotor system are listed in Table 2.1. The rotating lag frequency changes with collective pitch (and therefore forward flight velocity) so its value for the baseline configuration is represented by a curve as shown in Figure 2.1. The in-vacuum cyclic flap frequency is related to the gimbal dynamics, and does not change with collective pitch. The collective flap frequency is dominated by the rotational stiffness contribution, and thus changes very little with the collective pitch. Since this mode has a high frequency, the changes as a function of collective pitch setting are neglected. Additional data for the rotor system are reported by Johnson [31] and are also given in Table 2.2. A finite element model for the wing was developed with the equivalent mass and stiffness characteristics of Johnson's modal wing model. The model parameters for the finite element wing are listed in Table 2.3.

Now consider the system with aerodynamics. The frequency and damping

of the wing and rotor modes for the baseline system are shown as a function of forward flight velocity in Figure 2.2. The terms $\beta-1$ and $\beta+1$ represent the low and high frequency modes of the fixed-frame blade flapping response, respectively, and similarly $\zeta-1$ and $\zeta+1$ represent the low and high frequency fixed-frame blade lag response. Since ν_β is less than 1.0 in air, the $\beta-1$ mode is progressive.

The frequencies of the $\beta-1$ and $\zeta-1$ modes cross the fundamental wing mode frequencies and affect the damping of the wing modes. Abrupt changes of damping occur in the beam and chord modes where $\zeta-1$ crosses those wing frequencies, and the beam and chord mode damping decrease rapidly as the $\beta-1$ frequency approaches those wing frequencies. The wing chord mode has a damping valley because the $\zeta-1$ mode damping is lower than the chord mode damping at the velocity where the frequencies cross. Conversely, the beam mode has a damping peak because the $\zeta-1$ mode damping is greater than the beam mode damping at the velocity where those frequencies cross. Further indication of this transfer of damping from the lag mode is offered in Figure 2.3, where the baseline lag frequency curve has been arbitrarily shifted up by a factor of 1.05. As shown, the increase in lag frequency shifts the crossing with the chord frequency to a higher velocity where the corresponding chord mode damping is now lower than the $\zeta-1$ mode damping. The result is a damping peak rather than a damping valley in the chord mode.

2.3   Rotor Frequency

In this section, the influence of rotor in-vacuum flap and lag frequencies on tiltrotor stability is examined in more detail. The mass and inertia properties are held fixed, so the increase in the in-vacuum flap frequency can be developed only through an increase in the gimbal hub spring. The lag frequency increase would be obtained through increases in the blade stiffnesses (both flap and lag). The baseline flap

46

frequency is parametrically varied from .9 to 2.5 of its original value (the lower factor of .9, while physically unobtainable for flap in vacuum, is used to provide continuity of the trends). Because the lag frequency changes as a function of velocity, for this study the lag frequency was varied by shifting the baseline lag frequency *curve* by a factor ranging from .9 to 2.5. Extreme variations of flap and lag frequency are unlikely to be obtainable in design practice, but they are of academic interest so that physical reasoning of the trends within the design range may be established. The in-vacuum flap and lag frequency variations were performed independently, meaning that the flap frequency was held at its baseline value while lag frequency was varied, and vice versa. In addition to showing the direct effects of flutter speed as a function of flap and lag frequency, this study will provide insight into the flutter mechanism. By better understanding this mechanism, the rotor and wing properties may be selected to enhance tiltrotor stability.

The results of sweeping through values of ν_β and ν_ζ on the baseline tiltrotor configuration are illustrated in Figure 2.4 and Figure 2.5, respectively. Several observations based on these plots are described in the following numbered paragraphs (italicized). The paragraphs also include explanations (non-italicized) which are based on a sequence of frequency and critical damping plots reflecting parametric changes in the flap and lag frequencies. The results of changing flap frequency are shown in Figures 2.6 and 2.7 while the results of changing lag frequency are shown in Figures 2.8 and 2.9.

1. *As shown in Figure 2.4, the beam and chord mode V_f^* rise sharply with an increase in ν_β at low values of ν_β (ν_β factors .9 to 1.2).* There are two effects working here. One is a decrease in the $\beta - 1$ frequency, and the other is an increase in the wing torsion frequency. The decrease of the $\beta - 1$ frequency increases the velocity at which it crosses above the $\zeta - 1$ frequency (note sequence of Figures 2.2,

47

2.6, 2.7). As long as the $\zeta-1$ frequency remains between the beam mode frequency and the $\beta-1$ frequency there is little interaction between the flapping and wing motions. The low lag frequency acts like a barrier, preventing coalescence of the low flap frequency with the beam mode, until the low flap frequency is able to cross above it. Notice that the $\beta-1$ mode changes from a progressive mode at $1.0\nu_\beta$ (Figure 2.2) to a regressive mode at higher ν_β and low velocities (Figures 2.6, 2.7). This is because the δ_3 effect is small at low velocities, so the effective rotating frequency is above 1.0 until the δ_3 effect lowers it. As ν_β increases it takes progressively higher velocities to lower the effective flap frequency, which is why the transition from the regressive to progressive flap mode occurs at increasingly higher velocities. The increase in torsion frequency further separates the beam and torsion modes, which is stabilizing as will be shown later in the wing frequency study.

2. *As shown in Figure 2.4, a $\zeta+1$ mode instability occurs at high ν_β factors (ν_β factor above 1.2). The flutter speed ,V_f^*, drops sharply over the range $1.2\nu_\beta$ to $1.6\nu_\beta$ then increases over the range $1.6\nu_\beta$ to $2.5\nu_\beta$. The rotor instability shifts from a $\zeta+1$ mode to a $\beta+1$ mode at about $1.9\nu_\beta$.* A $\zeta+1$ rotor instability occurs above about $1.2\nu_\beta$ because of a flap and lag frequency coalescence in the rotating frame. In the fixed frame, the high frequency modes cross which results in an instability in the highest frequency rotor mode, $\zeta+1$. As ν_β increases beyond $1.6\nu_\beta$(these plots not shown), the $\beta+1$ frequency first crosses the $\zeta+1$ frequency curve then coalesces weakly with it as it falls below the $\zeta+1$ frequency. The weakening of the coalescence gives a higher V_f^* for the $\zeta+1$ instability. Further increases in ν_β result in the rotor instability shifting from the $\zeta+1$ mode to the $\beta+1$ mode. This occurs at the ν_β where the $\beta+1$ frequency becomes higher than the $\zeta+1$ frequency.

3. *As shown in Figure 2.4, the wing beam mode does not become unstable above about $1.4\nu_\beta$.* There are two reasons for this. First, the flap and lag modes become

highly coupled due to the coalescence of those frequencies (as discussed above) so there is only a slight destabilizing influence of the blade flap mode on the beam mode. The second reason is the increased separation of the wing beam and torsion frequencies which has a stabilizing effect on the wing mode (notice increase in torsion frequency in sequence of Figures 2.2, 2.6, 2.8 even at low velocities). As ν_β increases, the torsion frequency also increases because of mechanical coupling between the rotor flap and wing torsion motions.

4. *As shown in Figure 2.4, the wing chord mode can become unstable even at high ν_β factors.* This is because the chord mode is not strongly coupled to any other modes. Its flutter speed continues to increase as ν_β increases due to decreasing interaction with the rotor flapping mode. It should be noted that the chord mode may be more strongly coupled with the beam and torsion modes in the free flight condition (not considered in the present study) through inertial coupling.

5. *As shown in Figure 2.5, the chord mode V_f^* increases with increases in ν_ζ factor, until about $1.5\nu_\zeta$, then does not increase further.* At low values of ν_ζ factor the damping in the chord mode is strongly influenced by the location of the $\zeta - 1$ frequency with respect to the chord frequency, particularly when there are no other frequencies between the two. Each subsequent change in the lag frequency creates a large change in the chord mode V_f^* (notice where the $\zeta - 1$ frequency crosses the chord frequency in the sequence of Figures 2.2, 2.8, 2.9). As the lag frequency factor increases above 1.5, the $\zeta - 1$ frequency becomes higher than the torsion frequency for most velocities, so there is little influence of further increases in ν_ζ factor on the chord mode instability.

6. *As shown in Figure 2.5, the beam mode V_f^* first increases with ν_ζ factor, reaches a maximum, then decreases with ν_ζ factor to a value lower than that for the baseline configuration ($1.0\nu_\zeta$).* The beam mode V_f^* initially increases with ν_ζ factor because damping of this mode is increased through coalescence of the beam

frequency with the $\zeta-1$ frequency (note where the $\beta-1$ and $\zeta-1$ frequencies cross in relation to the beam mode frequency in the sequence of Figures 2.2, 2.8, 2.9). As the lag frequency increases, the $\zeta-1$ mode crosses the beam mode at higher velocity, where there is more damping available to be transferred to the beam mode. With further increases in ν_ζ factor the $\beta-1$ frequency coalesces with the beam frequency without any interference from the $\zeta-1$ frequency (Figure 2.9). The coalescence between the beam and $\beta-1$ frequencies becomes dominant as ν_ζ continues to increase, resulting in a large decrease in the beam mode V_f^*. Also of interest is the trend of the beam mode flutter curve with respect to ν_ζ in comparison with that of the chord mode (see Figure 2.5). As noted previously, the beam mode instability becomes flap mode dominated at about $1.3\nu_\zeta$, which corresponds to the peak in its flutter curve. The chord mode instability becomes flap mode dominated at about $1.7\nu_\zeta$, which corresponds to the plateau in its flutter curve. The instability of the beam mode becomes flap mode dominated at a lower ν_ζ factor than the chord mode because its frequency is closer to the $\beta-1$ frequency than is the chord mode frequency. The beam mode flutter curve eventually levels off at a very high ν_ζ factor, above that at which the chord mode levels off, because the beam mode is coupled to the torsion mode through the wing-chordwise mass offset. The beam mode flutter continues to be influenced by the lag frequency until the $\zeta-1$ frequency ceases to cross or coalesce with the torsion frequency.

7. *As shown in Figure 2.5, the chord V_f^* is lower than the beam V_f^* over the range of $1.0\nu_\zeta$ to $1.4\nu_\zeta$.* This is because there is increased damping in the beam mode due to its interaction with the lag mode. As shown in the sequence of Figures 2.2 and 2.8 the $\zeta-1$ frequency crosses the beam mode frequency at increasingly higher velocities as the ν_ζ factor is increased in this range (1.0 - 1.4 ν_ζ). With higher velocity there is greater damping in the lag mode, some of which is transferred to the beam mode during the frequency coalescence. Little increase

in damping is introduced into the chord mode because of the low velocity at which those frequencies cross. Thus, for the cited range of ν_β factor, the chord mode instability occurs before the beam mode instability.

The most significant results of the rotor frequency study are that optimum flap and lag frequencies exist which can significantly increase the flutter velocity of tiltrotor systems. The flutter velocity is shown in Figure 2.4 to increase from 1.23 to about 1.42 by increasing the flap frequency by a factor of 1.35, and in Figure 2.5 from 1.23 to about 1.33 by increasing the lag frequency by a factor of 1.35. These represent increases in flutter velocity of about 13% for the flap case and about 8% for the lag case. The results associated with tuning of the lag frequency are especially important because tuning of the lag frequency has more practical relevance than does tuning of the flap frequency. This is because tiltrotor systems have been stiff-inplane so that an increase in inplane stiffness would not have a severe impact on loads.

It is also important to note that the stability improvements presented above came about because of the coalescence of certain frequencies. The low rotor frequencies ($\beta-1$ and $\zeta-1$) are important system design parameters, as their placement with respect to each other as well as the fundamental wing modes can greatly improve or degrade the stability of the system. Based on the rotor frequency study, a general rule is to design the $\zeta-1$ frequency to fall between the $\beta-1$ frequency and the lowest fundamental wing mode in the velocity range preceding the flutter velocity. The lag frequency in this case couples with the flap frequency, delaying its interaction with the wing modes. An even better solution is to have the low lag frequency cross the lowest fundamental wing mode just as that mode begins to coalesce with the low flap frequency. In this case, the damping of the wing mode is increased by the lag mode, delaying the instability to a higher velocity. For maximum influence, the lag frequency should cross the wing mode at the high-

est possible velocity (but before the flap mode drives an instability). This will maximize the damping in the lag mode which is then available to be transferred.

Based on the results of the above study, as well as results of other studies not reported here, there are three main mechanisms which are responsible for instability. These may be described as lag-dominated whirl flutter, flap-dominated whirl flutter, and rotor resonance. In lag-dominated whirl flutter, the lag mode weakens the coupling of the flap and wing modes while increasing the coupling between the flap and lag motions themselves. As a result, the stability of the system is more sensitive to lag-motion-related forces than to flap-motion-related forces. In flap-dominated whirl flutter, the flap motion becomes highly coupled with one or more wing modes and there is negligible coupling with the lag motion. Rotor resonance is characterized by coalescence of the high-frequency flap and lag modes, which results in an instability of the higher frequency mode.

2.4 Wing Frequency

The effects of the wing beam, chord, and torsion frequencies on tiltrotor stability are examined in this section. The wing frequencies, as given in Table 2.1, are altered through parametric variation of the wing baseline stiffnesses. In the first part of this study, the variations are performed independently, as they were in the rotor frequency study. In the second part of this study, combined changes in wing stiffnesses are examined.

The results of independent variations of the three wing stiffnesses by factors of .50 to 1.50 of the baseline value are shown in the plots of Figures 2.10-2.12. The plots show the change in flutter speed for each of the three wing modes for each case. These results indicate that the flutter velocity is more dependent on the placement of the wing frequencies relative to each other than on the placement of the wing frequencies relative to the rotor frequencies. This is most evident for

52

the case of torsional stiffness variation (Figure 2.10). The beam mode stability is greatly reduced by a reduction in the torsion stiffness. The rotor frequency study showed that the beam stability changes relative to changes in the beam or rotor frequencies. Since the rotor frequencies and beam mode frequency are unchanged for variations of torsion stiffness, the reduced beam mode stability must instead be due to placement of the torsion frequency relative to the beam frequency. Based on the above reasoning, the beam mode flutter speed would be expected to decrease rather than increase with an increase in beam stiffness. This is indeed the case as is illustrated in Figure 2.11.

The chord mode flutter velocity is shown to increase with an increase in chord stiffness in Figure 2.12, while the flutter velocities of the beam and torsion modes remain relatively constant. The change in flutter velocity of the chord mode is less dramatic than was shown for the beam mode in the previous two cases. This is because the chord mode is not highly coupled to either of the other two wing modes, and the extent of stiffness variation does not move the chord frequency above or below the other wing frequencies. Since the chord mode is not highly coupled to either the beam or torsion modes, placement of the chord mode frequency with respect to the other wing frequencies is less important.

As was shown in Figure 2.2, the flutter velocity of the baseline tiltrotor system is about 1.23. In the next study, the combinations of wing stiffness required to maintain flutter at $V^* = 1.23$ are examined. Three flutter boundaries, corresponding to constant beam stiffness values ranging from .50 to 1.50 of the baseline value, are shown in Figure 2.13. Each curve represents the combination of torsion and chord stiffness (shown as a factor of the baseline value) required to maintain the baseline flutter velocity. As the beam stiffness is increased the minimum required torsion stiffness also increases (for EI_c above the 1.0 factor). This supports earlier findings that stability is improved through increased separation between the beam

and torsion frequencies. The plot also shows that the chord stiffness requirements are almost constant for GJ factors above about 0.8.

The most significant result of the wing frequency study is that the wing torsion to beam frequency ratio is an important design parameter for a tiltrotor system. It is clear that the separation between these frequencies has greater importance than the placement of the beam frequency relative to the rotor frequencies. If this were not the case then the flutter velocity would increase with an increase in beam frequency (because of an increased separation between the flap and beam frequencies) rather than decrease (because of increased participation of torsion in the beam mode). It is also noteworthy that the chord frequency significantly influences only the chord mode V_f^*. Thus, it is possible to improve the chord mode V_f^* independently of the beam mode V_f^*, and vice versa. Since the chord mode instability occurs at a velocity very close to that associated with the beam mode, any design changes aimed at increasing the stability of the complete system must take both modes into account.

2.5   Forward Swept Wing

This study examines the effects of sweeping the baseline wing forward. The pylon and rotor system remains oriented in the flow direction the same as for a straight wing. The sweep is varied while maintaining wing length (measured along the elastic axis), streamwise chord length, and rotor radius constant. While both wing length and rotor radius cannot be maintained constant with sweep on an actual tiltrotor aircraft due to rotor-fuselage clearance requirements, this assumption is employed in the analysis to isolate the effects of forward sweep. Divergence of the system was considered, but was found to occur at velocities much higher than those associated with flutter, even at high wing sweeps. This is not surprising beacuse 1) the wing stiffnesses associated with tilt rotors are much higher than

54

that associated with conventional fixed wing aircraft, and 2) the flutter boundaries associated with tilt rotors are lower than those associated with conventional fixed wing aircraft (primarily due to the large rotor flapping motion).

The influence of wing forward sweep on flutter is illustrated in Figure 2.14. This plot shows that the beam and chord mode V_f^* come together for the swept wing, with a reduction in system flutter velocity of about 8 percent over a sweep from zero to -45°. The cause of this reduction has two possible sources: the change in wing frequencies due to a shift in pylon mass or the change in perturbation force components due to reorientation of the rotor with respect to the wing. The wing frequencies are altered by the change in pylon first and second mass moments of inertia in pitch about the wing elastic axis. This primarily effects the wing torsion frequency which increases with sweep. Based on the wing frequency parametric study, this should increase the beam mode V_f^* because of the increased separation between the beam and torsion frequencies. The plot of Figure 2.14 shows that the beam mode V_f^* is not increased. Hence, the wing frequency change must not be the dominating influence for the beam or chord mode instabilities. This is confirmed in Figure 2.15 which shows the beam mode instability boundaries for two cases: one with the normal orientation of the wing pylon in the flow direction (and a corresponding decrease in torsion frequency) and one with the pylon mass distribution remaining the same as for the straight wing (as if the pylon orientation with respect to the wing was unchanged by sweep) such that the wing frequencies are nearly constant with respect to sweep. As shown, the beam mode V_f^* decreases even further with the baseline wing frequencies, indicating that the wing frequency changes associated with sweep have a stabilizing influence. The decrease in flutter velocity must then be attributed to a change in the destabilizing forces from the rotor.

In Figures 2.16 and 2.17, the stiffness changes required to maintain the straight

55

wing flutter velocity ($V_f^* = 1.23$) for the swept wing are shown. The plot of Figure 2.16 shows that a substantial increase in chord stiffness is required to maintain $V_f^* = 1.23$, while only a slight increase in torsional stiffness is required. The chord stiffness increase maintains the chord mode V_f^* while the torsion stiffness increase maintains the beam mode V_f^*. Based on the results of the previous section, it might be assumed that an increase in beam stiffness is required to overcome the additional destabilizing force components associated with wing sweep if one desires to maintain the straight wing flutter velocity. However, the plot of Figure 2.17 shows that a *decrease* in beam stiffness of roughly 10-15% is required. The two plots of Figures 2.16 and Figure 2.17 suggest that the ratio of wing torsion to beam frequency is still an important factor even with wing sweep. The additional destabilizing forces associated with wing sweep couple these two modes more than for the straight wing case. While the coupling between the torsion and beam modes is through the pylon and rotor mass offset for the straight wing, these modes are additionally coupled through the rotor system forces when wing sweep is introduced. With increased coupling, the requirement for frequency separation between the modes is increased. The wing sweep tends to increase the frequency separation, but not enough to overcome the rotor force coupling effects, so the net effect is decreased flutter velocities. The torsion and beam modes remain largely uncoupled from the chord mode. For the chord mode, a substantial increase in chord stiffness is the only alternative for maintaining straight wing flutter velocity at large forward wing sweep angles.

2.6   Pitch-Flap Coupling

Pitch-flap coupling is an important and necessary parameter for basic tiltrotor designs because of flap clearance considerations. There are four basic methods for obtaining adequate flap clearance of the blade from the wing. One is an adjustment

of the mast length, the second is an increase of flapping restraint, the third is use of forward wing sweep, and the fourth is employment of kinematic pitch-flap coupling. Extension of the mast length is very destabilizing while increase of flapping restraint drives blade loads to an unacceptable level. The destabilizing effects of forward wing sweep have been discussed in the previous section. The employment of pitch-flap coupling can significantly reduce blade flapping with negligible effect on the blade loads, but it also has a destabilizing effect on stability. Positive pitch-flap coupling (here defined as blade flap up producing blade pitch up) is given by negative δ_3 and decreases flap frequency while negative pitch-flap coupling is given by positive δ_3 and increases flap frequency.

The plot of Figure 2.18 shows the flutter velocity boundaries associated with changes of δ_3 (the baseline configuration has $\delta_3 = -15°$). This plot shows that positive δ_3 is more suitable with respect to stability considerations than negative δ_3, which is generally true for stiff-inplane rotor systems as reported by Gaffey [6]. As shown, positive δ_3 results in a rotor instability at relatively low values of δ_3. This instability is best explained by considering the blade frequencies in the rotating system. The rotor instability is caused by resonance of the blade flap and lag frequencies. The resonance occurs because the lag frequency of a stiff-inplane rotor decreases with velocity (discussed in rotor frequency section) while the flap frequency increases (because of positive δ_3) until at some velocity the two coincide. With negative δ_3 the effective flap frequency decreases with velocity, so it never meets the lag frequency in the velocity range of interest.

The plot of Figure 2.18 also shows that the mode of instability changes from a chord mode at small negative δ_3 to a beam mode at large negative δ_3. While both the chord and beam modes are stabilized with decreasing negative δ_3, the beam mode is stabilized more than the chord mode because of increased separation between the torsion and beam frequencies (decreased negative δ_3 increases the flap

57

frequency which increases the torsion frequency). Consequently, there is a range of negative δ_3 where the chord mode instability becomes critical.

2.7 Summary

The influences of several key system design parameters on tiltrotor aeroelastic stability in the high-speed axial flight mode have been examined. The findings have substantiated earlier work performed by other researchers as well as identified some new trends and the physical reasonings behind them. Some of the important past conclusions which have been substantiated are as follows:

1. Beam and torsion frequency separation has a large influence on stability of the beam mode.

2. Negative δ_3 is more effective than positive δ_3 with respect to stability considerations for a stiff-inplane rotor system.

The results of this study have also identified and explained at least two important effects which have not been previously discussed in the open literature:

1. Lag frequency tuning appears to be a practical method for increasing axial flight flutter velocities. The blade lag frequency may be selected to reduce the coupling of the $\beta-1$ and wing beam modes, thereby increasing the wing beam mode damping.

2. An increase in forward wing sweep is destabilizing. This is because of an increase in the rotor destabilizing force components in the beam and chord directions. The wing frequency changes associated with the reorientation of the pylon with sweep have a stabilizing influence on the beam mode, but this effect is dominated by the rotor force changes.

Table 2.1: Frequencies of the baseline system.

Rotating Blade Freq. (per rev) In Vacuum	
ν_β	1.02
$\nu_{\beta 0}$	1.85
ν_ζ	see Figure 2.1
$\nu_{\zeta 0}$	0
Wing Freq. (per rev)	
beam	0.42
chord	0.70
torsion	1.30

Table 2.2: Important parameters of the baseline system.

Number of blades	3
Radius	12.5 ft.
Lock number	3.83
Solidity	.089
Lift curve slope	5.7
Pitch/flap coupling	-.268
Tip speed	600 ft/sec
Rotational speed	48.0 rad/sec
Blade Inertias	
I_b	105 slug-ft^2
I_β^*	1.0
$I_{\beta_0}^*$	.779
I_ζ^*	.670
$I_{\zeta_0}^*$	.670
I_0^*	1.0
$I_{\beta\alpha}^*$	1.0
$I_{\zeta_0\alpha}^*$	.787
S_ζ^*	1.035
$S_{\beta_0}^*$	1.212
M_b^*	6.160
Blade Inertias for windmilling	
$I_{\zeta_0}^*$	1.0
$I_{\zeta_0\alpha}^*$	1.0
$\nu_{\zeta 0}$	0.0

60

Table 2.3: Important parameters of the baseline wing.

	Value	Root Element	2nd Element	3rd Element	Tip Element (+ Pylon)
Span, y_w/R	1.333				
Chord, c_w/R	.413				
Mast height, h/R	.342				
No. of Elements	4				
Length, l/R	4.55	4.55	4.55	3.
$I_{cg} * \left(\frac{N I_b}{2}\right)$	1.	1.	1.	$63.3 \cos^2 \Lambda$
$S_\alpha * \left(\frac{N I_b}{2}\right)$	.05	.05	.05	$9.09 \cos \Lambda$
Mass $* \left(\frac{N I_b}{2}\right)$	1.	1.	1.	14.54
$EI_b * \left(\frac{N I_b \Omega^2}{2}\right)$	3.13e7	3.13e7	3.13e7	3.13e7
$EI_c * \left(\frac{N I_b \Omega^2}{2}\right)$	8.48e7	8.48e7	8.48e7	8.48e7
$GJ * \left(\frac{N I_b \Omega^2}{2}\right)$	1.62e7	1.62e7	1.62e7	1.62e7
Aero. Center, e/c	.051	.051	.051	0.
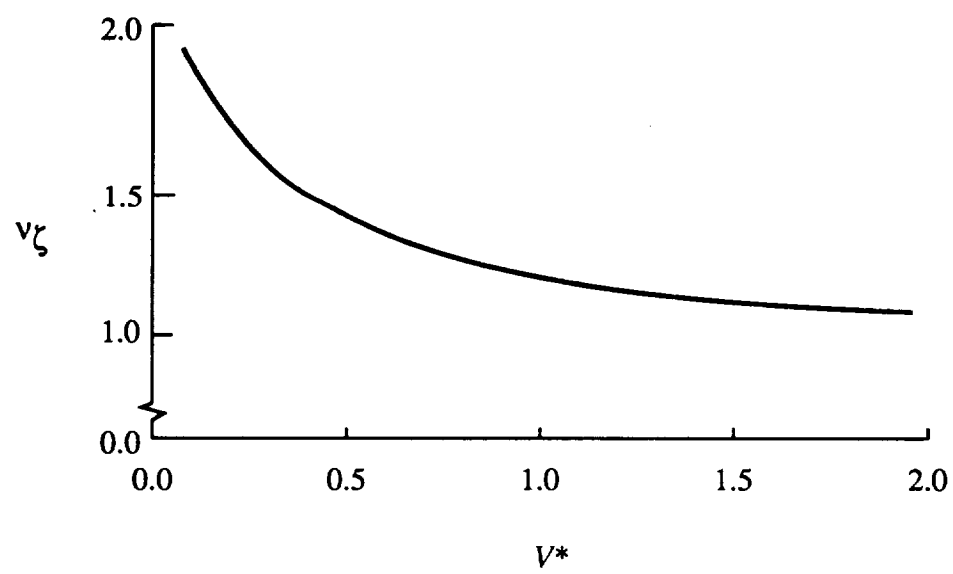
Figure 2.1: Blade lag frequency as a function of velocity.

(a) Frequency.
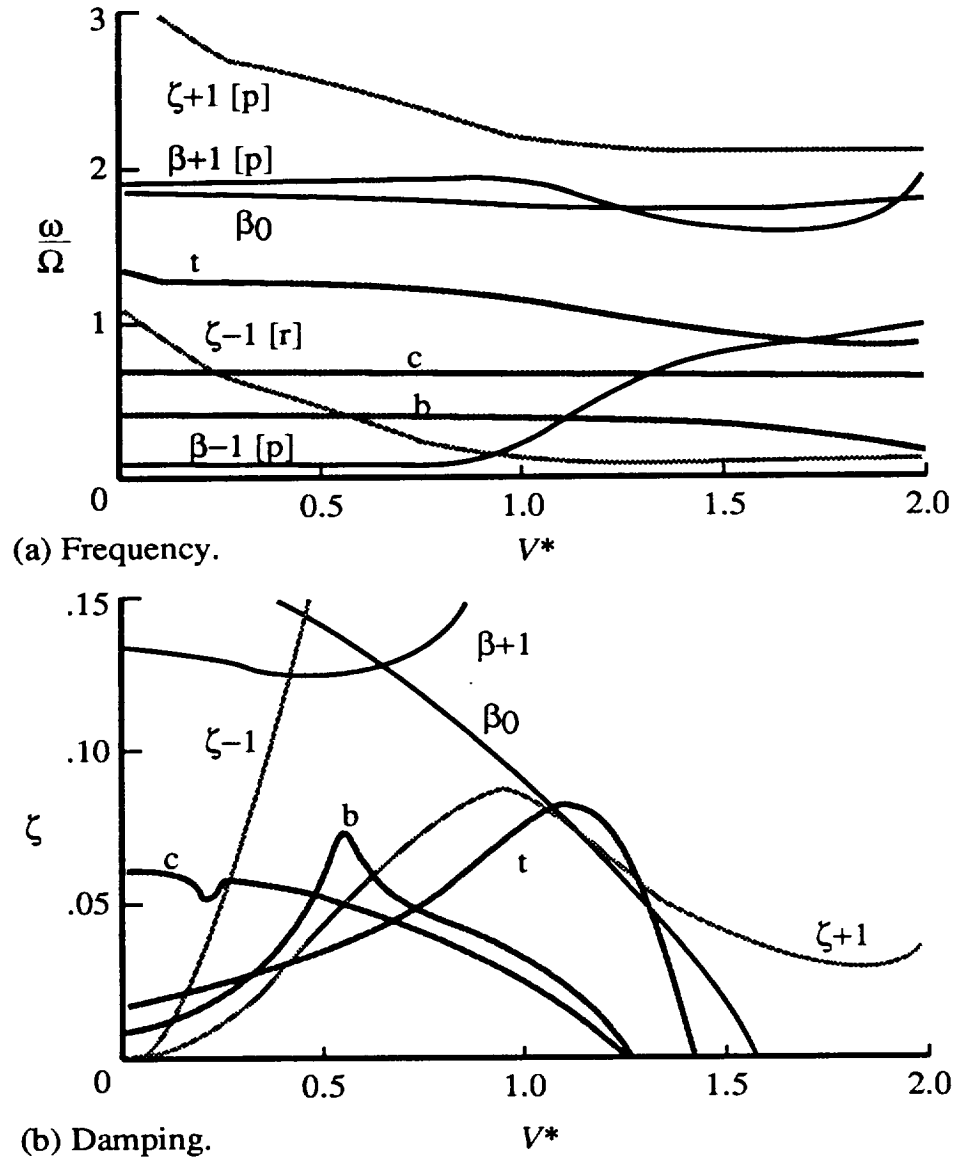
(b) Damping.

Figure 2.2: Frequency and damping as a function of velocity for the baseline $(1.0\nu_\beta, 1.0\nu_\zeta)$ system.

(a) Frequency.
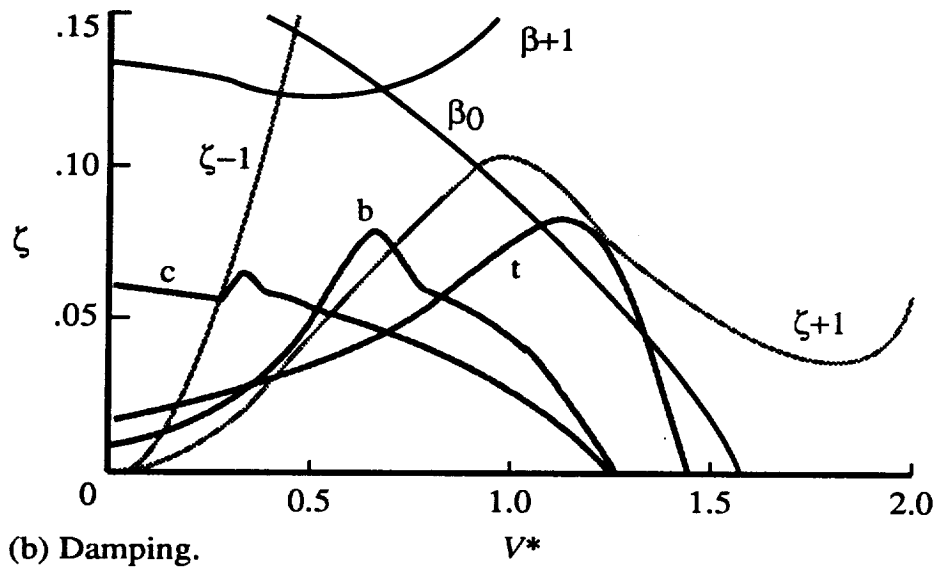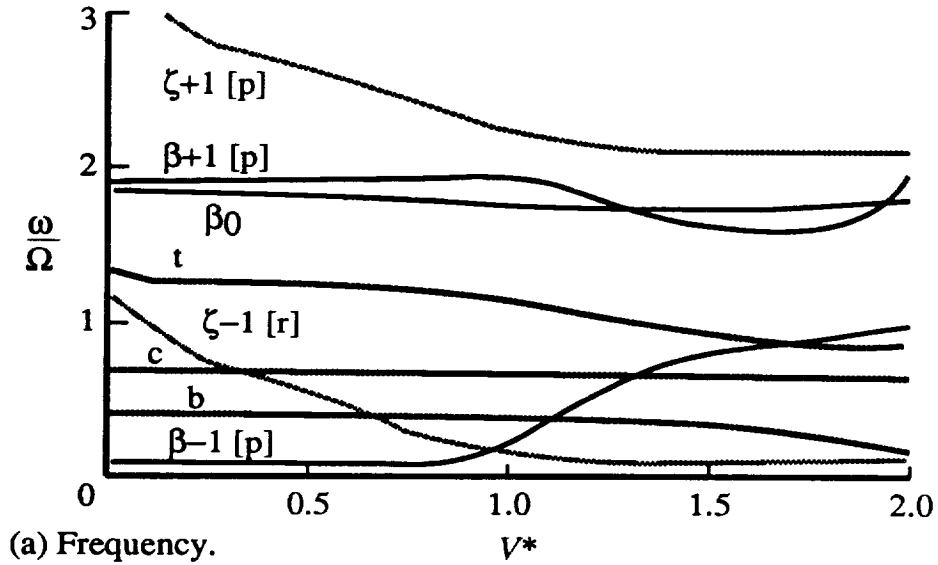
(b) Damping.

Figure 2.3: Frequency and damping as a function of velocity for ν_ζ increased by the factor 1.05.
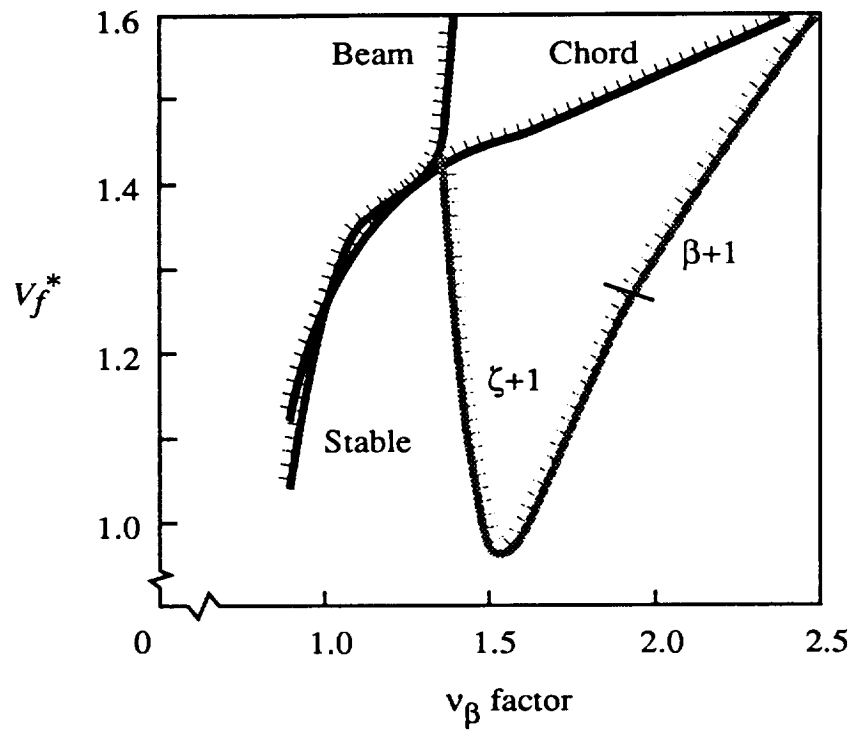
Figure 2.4: Flutter velocity as a function of ν_β factor.
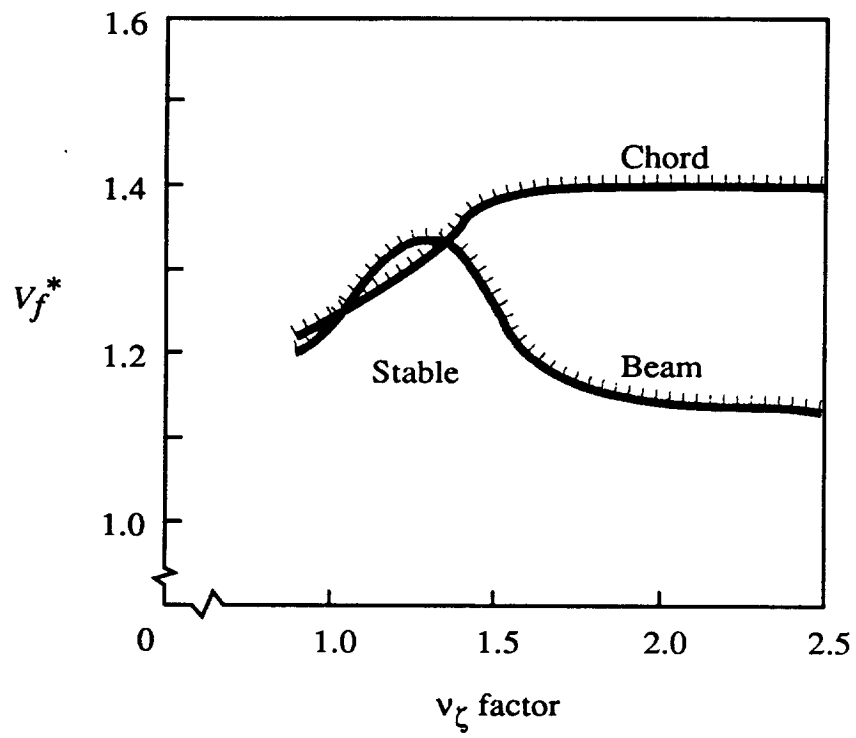
Figure 2.5: Flutter velocity as a function of ν_ζ factor.

(a) Frequency.
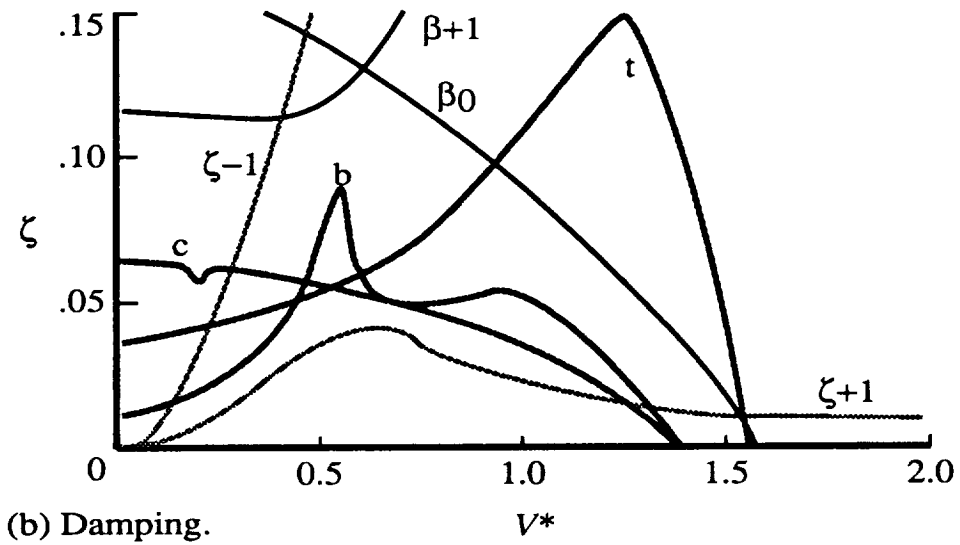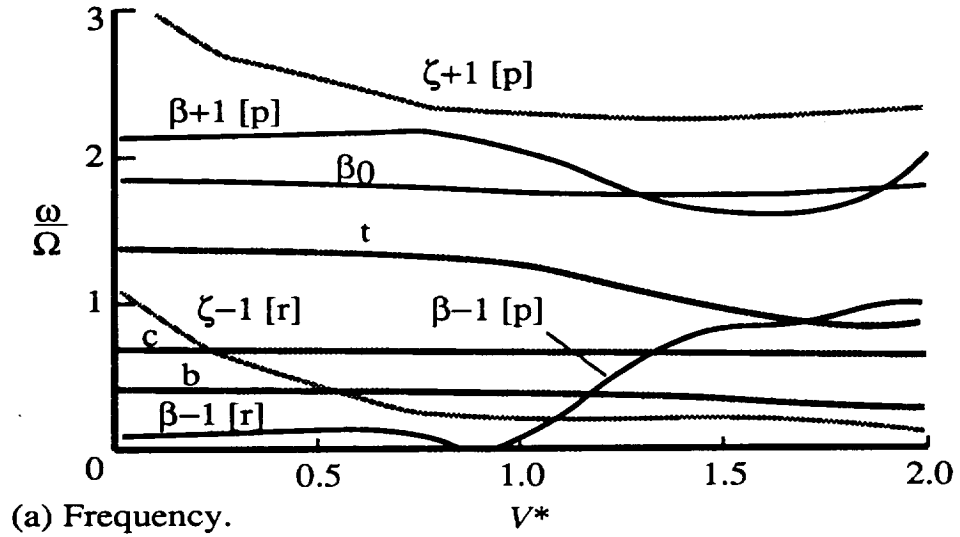
(b) Damping.

Figure 2.6: Frequency and damping as a function of velocity for $1.2\nu_\beta$.

(a) Frequency.
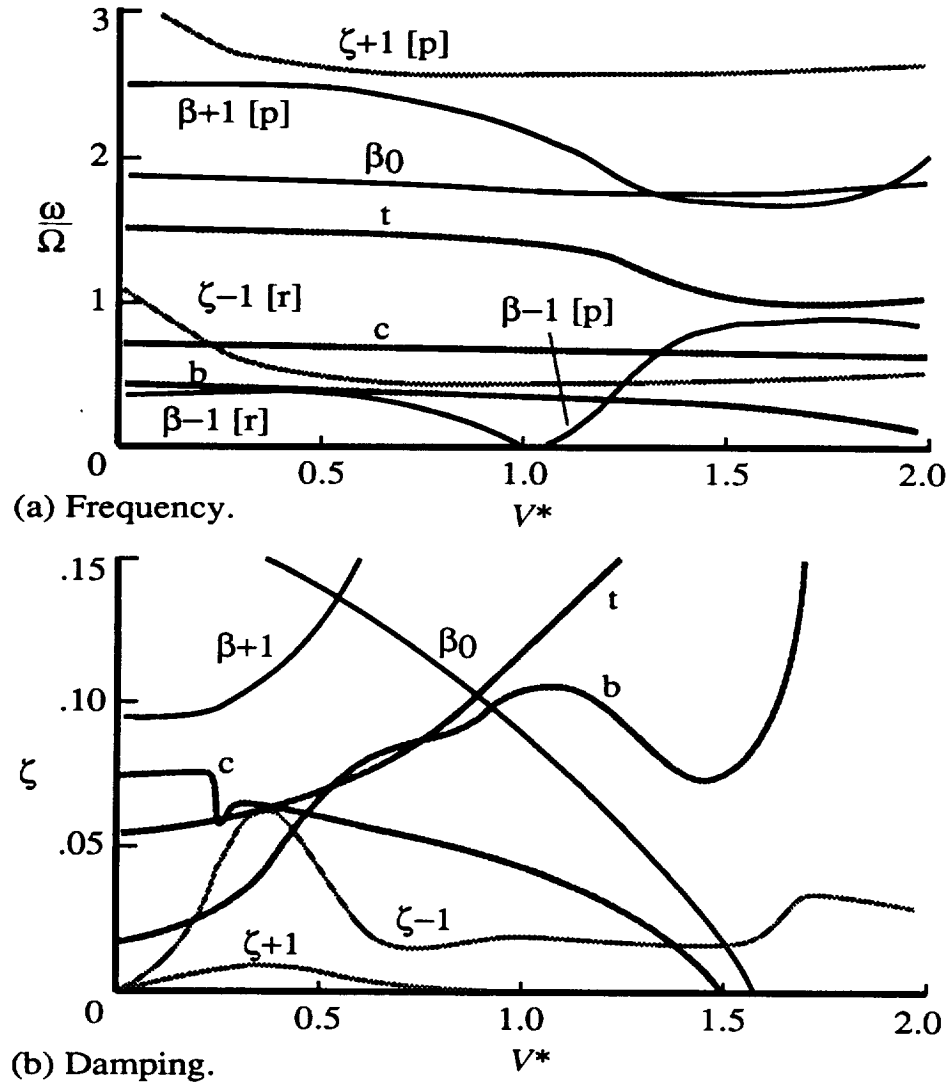
(b) Damping.

Figure 2.7: Frequency and damping as a function of velocity for $1.5\nu_\beta$.

68
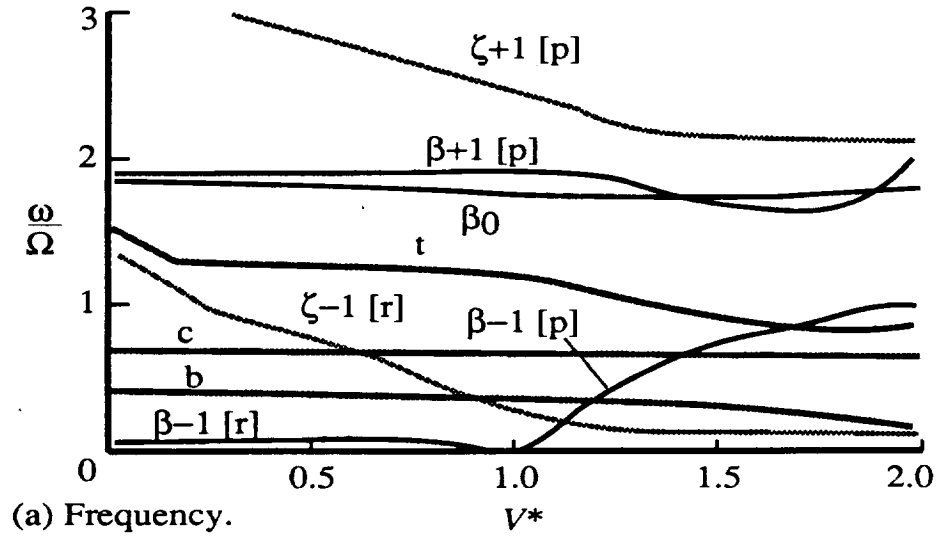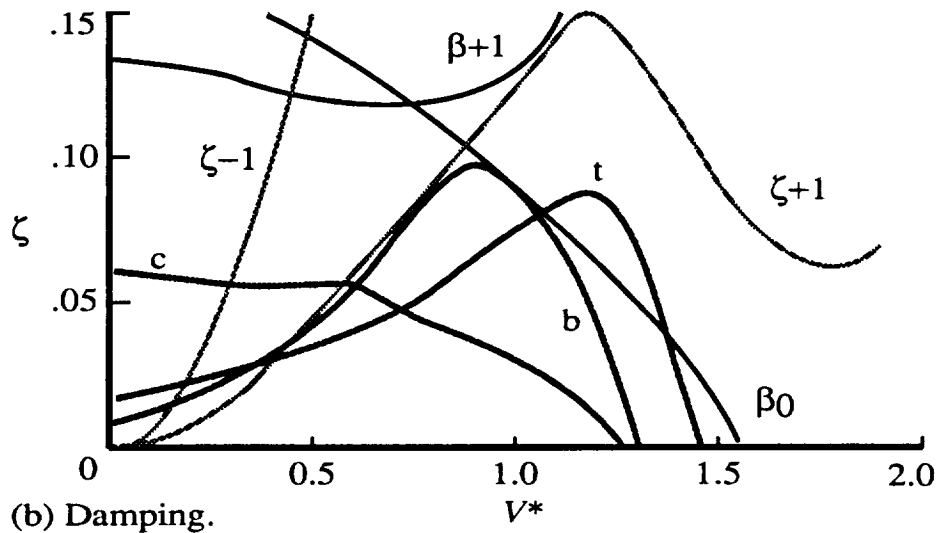
(a) Frequency.

(b) Damping.

Figure 2.8: Frequency and damping as a function of velocity for $1.2\nu_\zeta$.

69

(a) Frequency.
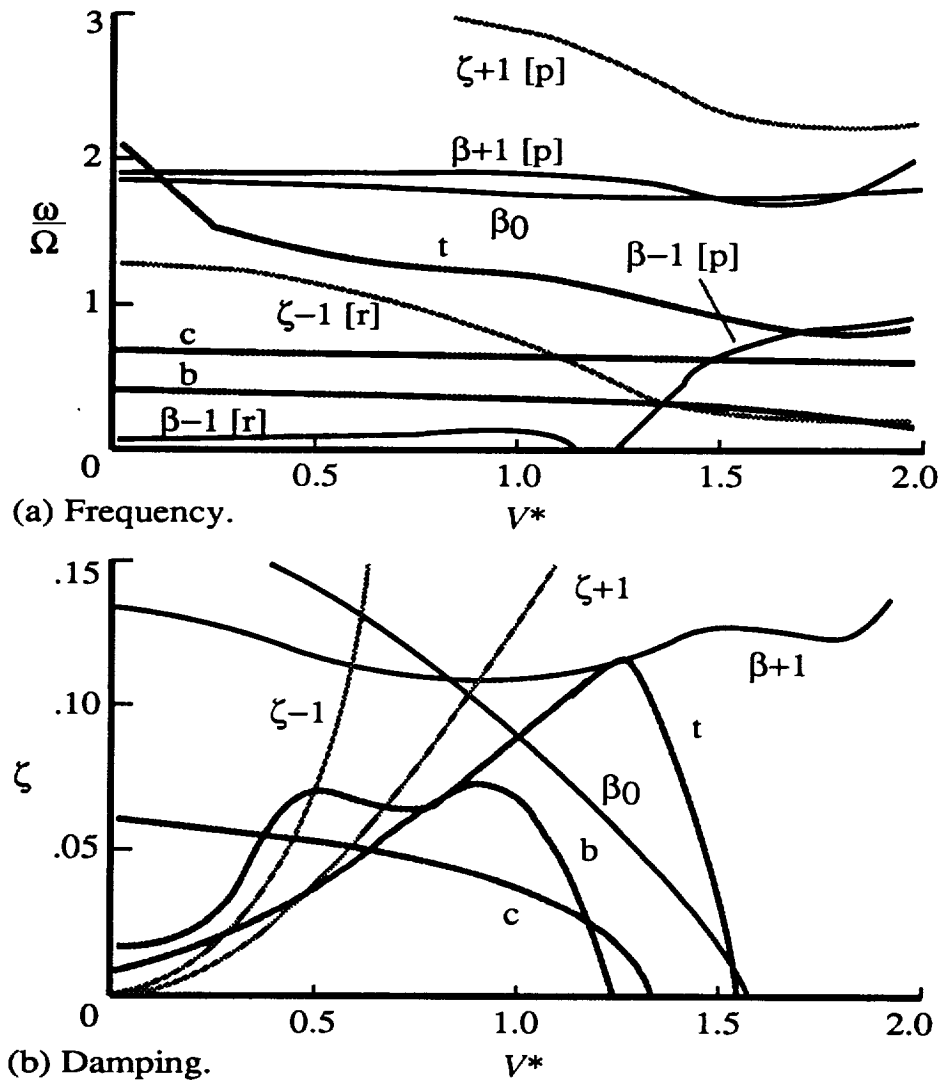
(b) Damping.

Figure 2.9: Frequency and damping as a function of velocity for $1.5\nu_\zeta$.

70
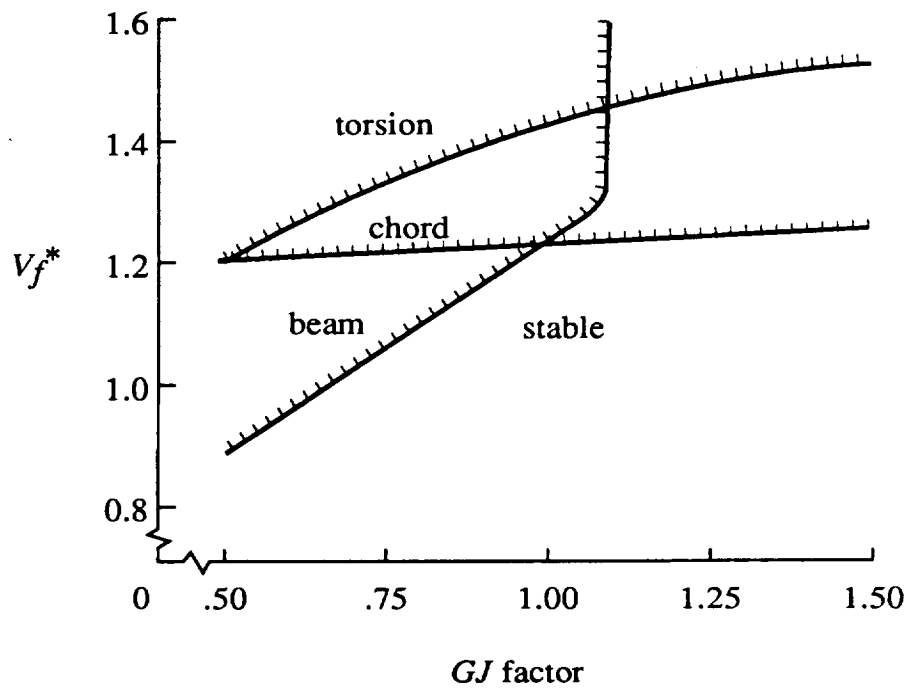
Figure 2.10: Flutter velocity of the wing modes with parametric variations of wing torsion stiffness.
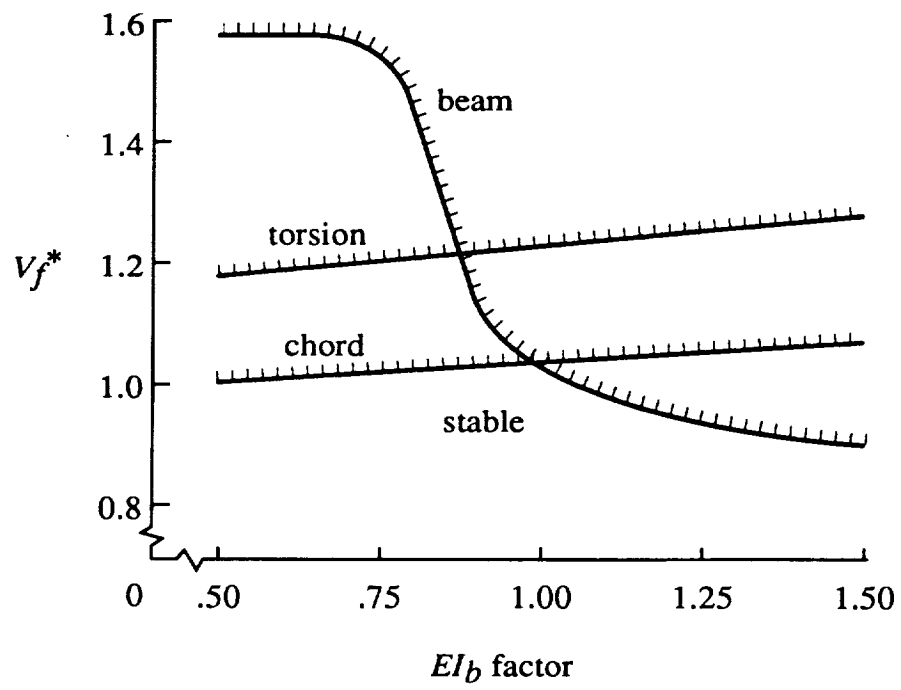
Figure 2.11: Flutter velocity of the wing modes with parametric variations of wing beam stiffness.
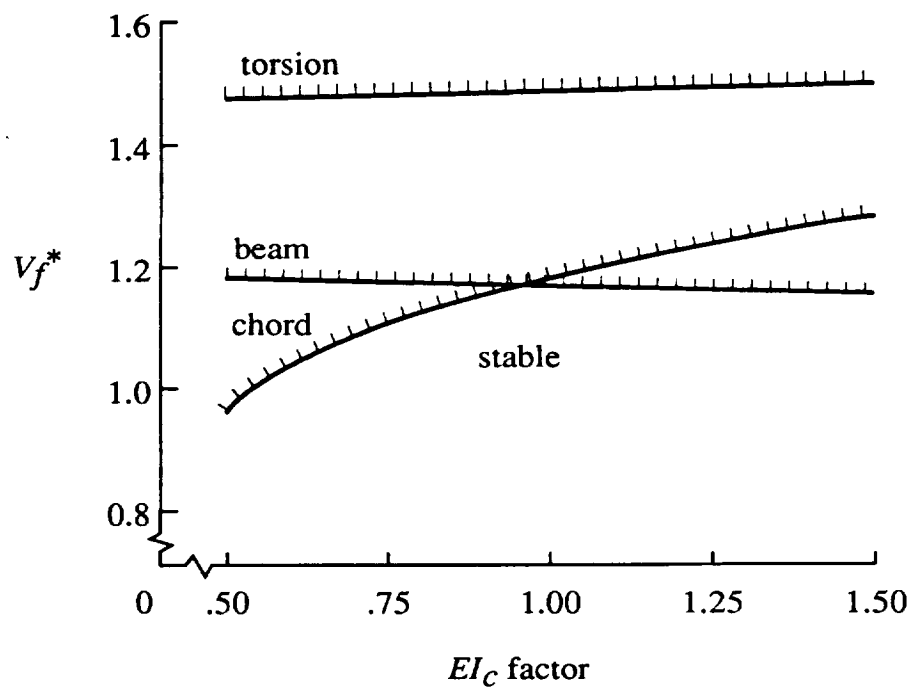
Figure 2.12: Flutter velocity of the wing modes with parametric variations of wing chord stiffness.

73

C-2
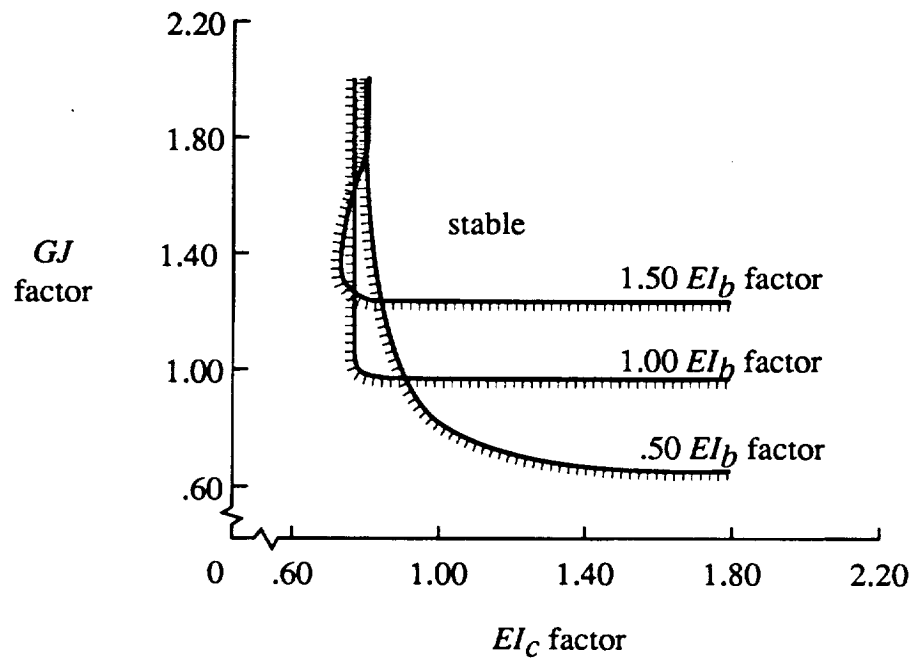
Figure 2.13: Stability boundaries of constant $V_f^* = 1.23$ for combined stiffness variations.
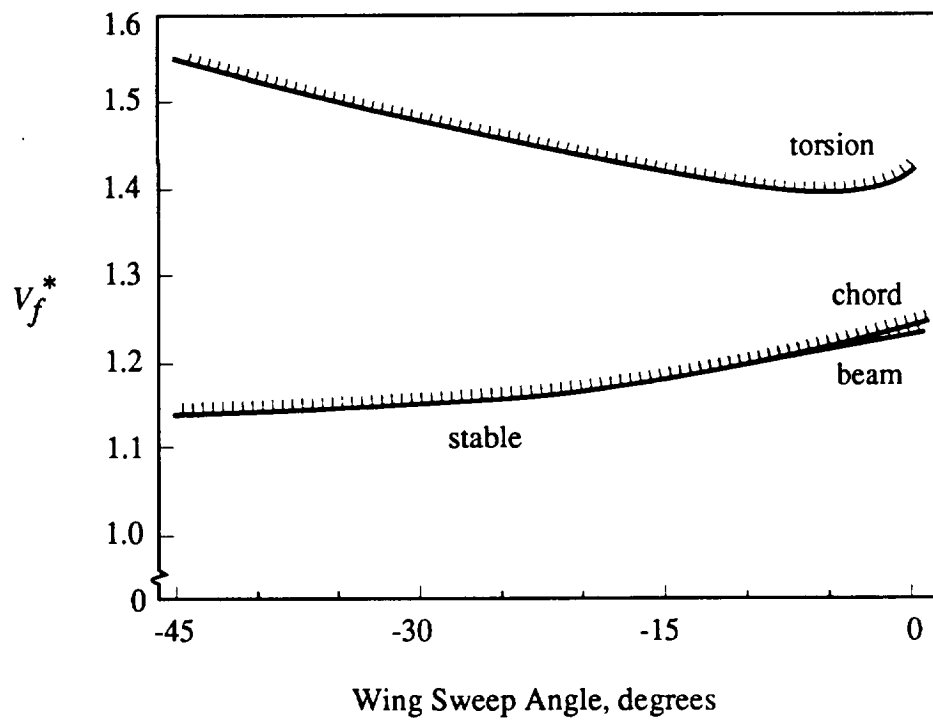
Figure 2.14: Flutter of the swept forward wing.
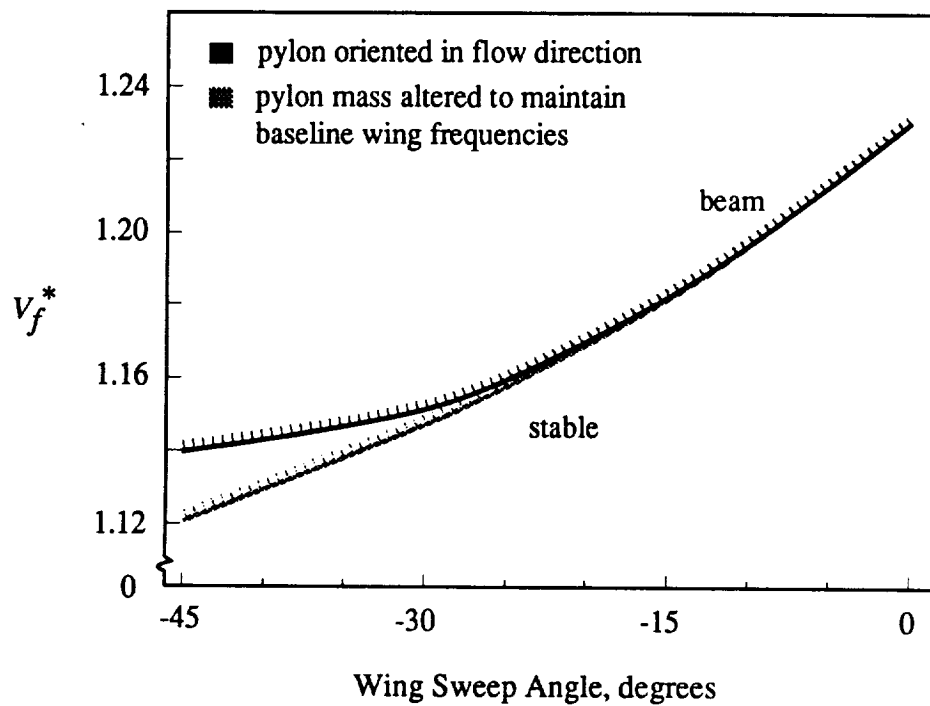
Figure 2.15: Beam mode flutter of the swept wing for two pylon orientation cases.
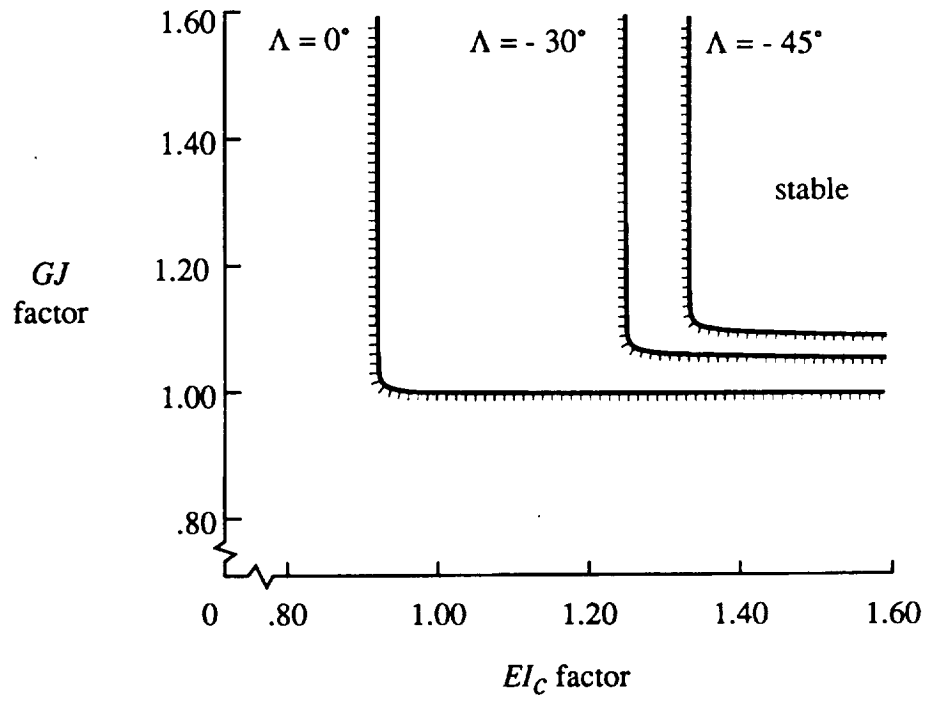
Figure 2.16: Torsion and chordwise stiffness requirements for maintaining straight-wing flutter velocity ($V_f^* = 1.23$, EI_b at baseline).
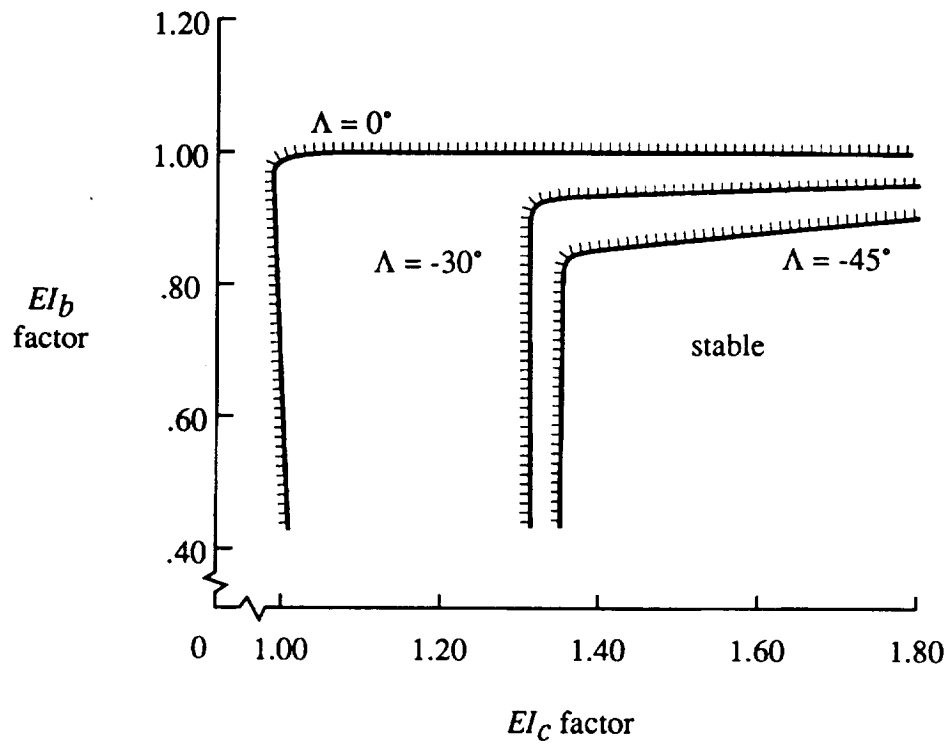
Figure 2.17: Beamwise and chordwise stiffness requirements for maintaining straight-wing flutter velocity ($V_f^* = 1.23$, GJ at baseline).
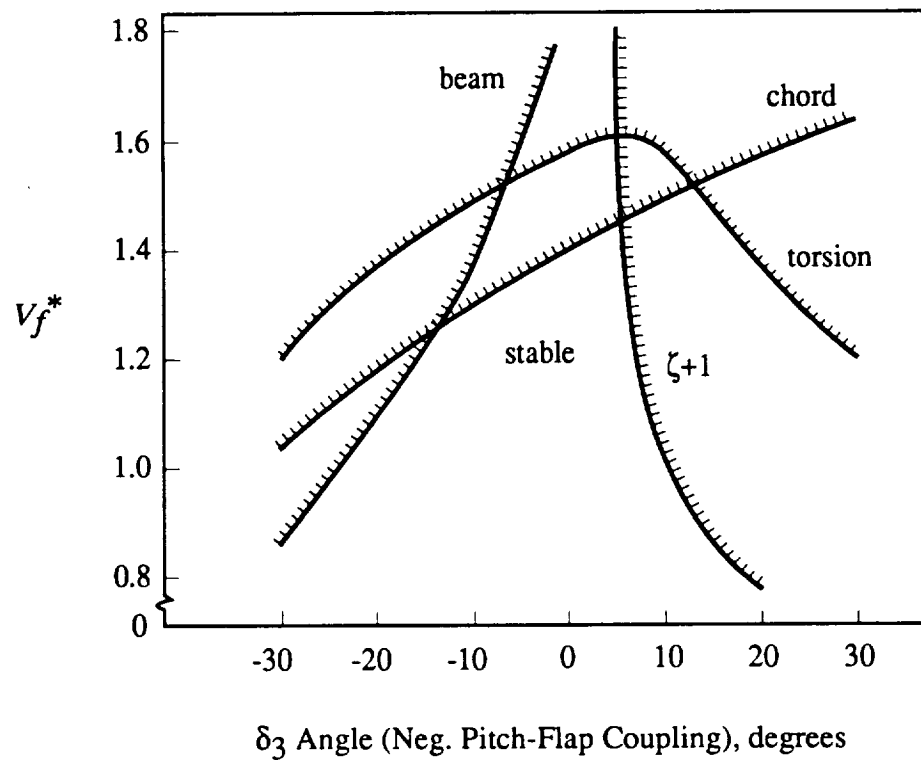
Figure 2.18: Flutter velocity boundaries as a function of the pitch-flap coupling.

Chapter 3

Dynamic Analysis of Pretwisted Elastically-Coupled Rotor Blades

This chapter will address the accuracy of using one-dimensional analysis for the prediction of rotating beam frequencies of elastically-coupled, highly-twisted rotor blades. There are three objectives for this study: 1) show that the degrees of freedom associated with shear deformation may be statically condensed from the analysis, 2) show that the nonclassical influences associated with cross-section warping, which may become significant as a result of elastic coupling, can be accounted for without the incorporation of these effects explicitly in the rotating beam analysis, and 3) determine the potential improvement in efficiency by using higher-order displacement approximations in a finite element implementation. Because of these objectives, a new rotating blade analysis is formulated which is not associated with the UMARC analysis. This new analysis is used to test the present formulation so that only those concepts which prove effective are used in the next level of forumlation, the full aeroelastic tiltrotor model derived in Chapters 4-7.

The potential for decoupling the local analysis from the global analysis was discussed in Section 1.1.1. An explicit formulation for this approach is proposed in the present chapter which considers the influence of nonclassical effects only on

the effective beam stiffness properties and eliminates degrees of freedom associated with shear deformation through static condensation. This formulation leads to a rotating beam analysis based on only those degrees of freedom which have been used for classical beam analyses. A second analysis, which should consider all the possible nonclassical influences, but may be based on linear theory, is used to determine the effective beam properties for the first analysis. If such an approach is accurate for geometries and materials typical of rotor blades, then rotor analyses based on isotropic materials and classical beam theory may be modified to incorporate composite materials and nonclassical effects.

A rotating beam analysis was developed based on a formulation of nonlinear equations of motion and a finite element implementation. The formulation is derived to show how shear deformation and warping enter the theory. The formulation is nonlinear as is required to capture the centrifugal stiffening effects even in the linearized form of the equations. The degrees of freedom associated with shear deformation were eliminated through static condensation of the linear force-displacement relationships. The linear part of the formulation was implemented as a p-version beam finite element such that the degree of polynomial approximation for the bending, torsion, and axial displacements may be independently selected. This implementation is described along with the results of a convergence study. This convergence study shows the efficiency of certain displacement approximations for a bending-twist-coupled beam.

Results of the present rotating beam analysis are compared with those produced by Smith and Chopra [68] for a set of elastically-coupled rotor blades to show that static condensation of the shear degrees of freedom is valid for the modes considered. Attention is then focused on nonclassical effects (shear deformation and warping) and their influence on the prediction of both rotating and nonrotating frequencies for elastically-coupled and highly-twisted beams. Comparisons are

81

made with experimental results obtained by Chandra [77], 1-D analytical results obtained with UMARC as presented by Smith and Chopra [68], and 3-D analytical results obtained using the analysis of Hinnant [78].

3.1 Energy Formulations

For the formulation of strain and kinetic energy, the blade is assumed to be a long and slender beam, and constructed from anisotropic materials such that displacement modes may be elastically coupled. The blade may deform in extension u_e, lag bending v, flap bending w, and torsion ϕ, and both built-in pretwist and elastic twist deformation may be large. The equations of motion are formulated based on the form of Hamilton's variational principle typically used in rotor analysis,

$$\delta\Pi = \int_{t_1}^{t_2} (\delta U - \delta T - \delta W)\, dt = 0 \qquad (3.1)$$

The potential energy variation δU is developed entirely by the elastic strain of deformation, the kinetic energy variation δT is developed from blade velocity terms, and the work variation δW is zero in the present formulation (no external loading is considered, the system is conservative).

As the formulation presented here is nonlinear and explicit, the number of terms in the energy expressions can quickly grow to an unmanageable size. Further, many of the terms may be negligible compared to other important terms. To reduce the number of terms to only those of significance, an ordering scheme is employed where terms of $O(\epsilon^{n+2})$ and higher are eliminated in the presence of terms of $O(\epsilon^n)$. All displacement variables defined in this formulation are assigned an order of ϵ with two exceptions. The axial displacement u_e is of order ϵ^2 and the twist deformation ϕ is of order one. The latter exception results from making the analysis accurate for rotor blades with very large elastic couplings associated with twist deformation.

3.1.1 Geometry and Coordinates

The present formulation considers only the shaft-fixed response (no hub degrees of freedom. The hub motion and other tiltrotor related parameters will be considered in Chapters 4-7. The shaft-fixed formulation requires four coordinate systems. The inertial coordinate system is aligned with the shaft as shown in Figure 3.1. A rotating reference frame $(\hat{I}_r, \hat{J}_r, \hat{K}_r)$ has the same origin as the inertial reference frame, but rotates with the blade such that its x-axis is in the plane of rotation. An undeformed-blade reference frame $(\hat{I}_u, \hat{J}_u, \hat{K}_u)$ is defined with its x-axis directed along the elastic axis of the undeformed blade as shown in Figure 3.2. The elastic part of the blade is offset from the center of rotation a distance $h_x \hat{I}_U$. A cross-section reference frame $(\hat{I}_c, \hat{J}_c, \hat{K}_c)$ is defined with origin at an arbitrary position $(h_x + x)\hat{I}_u$ along the elastic axis of the blade, and with origin on that axis acting as the reference point for the cross section. The unit vector $\hat{J}_c$ is directed along the chord direction of the blade cross section while $\hat{K}_c$ is defined by the cross product of $\hat{I}_c$ and $\hat{J}_c$. Thus, the cross-section system is an orthonormal vector set which is rotated by the amount of twist associated with an arbitrary spanwise location of the undeformed blade. A deformed reference frame $(\hat{I}_d, \hat{J}_d, \hat{K}_d)$ is identical to the cross-section set before deformation, but translates and rotates with the bending and twist of the rigid cross section plane to a new position after deformation.

The unit vector triads of each coordinate system are related by the following equations:

$$\left\{ \begin{array}{c} \hat{I}_r \\ \hat{J}_r \\ \hat{K}_r \end{array} \right\} = [T_{ri}] \left\{ \begin{array}{c} \hat{I}_i \\ \hat{J}_i \\ \hat{K}_i \end{array} \right\} \tag{3.2}$$

$$\left\{ \begin{array}{c} \hat{I}_u \\ \hat{J}_u \\ \hat{K}_u \end{array} \right\} = [T_{ur}] \left\{ \begin{array}{c} \hat{I}_r \\ \hat{J}_r \\ \hat{K}_r \end{array} \right\} \tag{3.3}$$

$$\left\{ \begin{array}{c} \hat{I}_c \\ \hat{J}_c \\ \hat{K}_c \end{array} \right\} = [T_{cu}] \left\{ \begin{array}{c} \hat{I}_u \\ \hat{J}_u \\ \hat{K}_u \end{array} \right\} \qquad (3.4)$$

$$\left\{ \begin{array}{c} \hat{I}_d \\ \hat{J}_d \\ \hat{K}_d \end{array} \right\} = [T_{dc}] \left\{ \begin{array}{c} \hat{I}_c \\ \hat{J}_c \\ \hat{K}_c \end{array} \right\} \qquad (3.5)$$

where the transformations matrices are given by:

$$[T_{ri}] = \begin{bmatrix} \cos \psi & \sin \psi & 0 \\ -\sin \psi & \cos \psi & 0 \\ 0 & 0 & 1 \end{bmatrix} \qquad (3.6)$$

$$[T_{ur}] = \begin{bmatrix} \cos \beta_P & 0 & -sin\beta_P \\ 0 & 1 & 0 \\ \sin \beta_P & 0 & \cos \beta_P \end{bmatrix} \qquad (3.7)$$

$$[T_{cu}] = \begin{bmatrix} 1 & 0 & 0 \\ 0 & \cos \theta_0 & \sin \theta_0 \\ 0 & -\sin \theta_0 & \cos \theta_0 \end{bmatrix} \qquad (3.8)$$

The transformation between the deformed and cross-section systems $[T_{dc}]$ is derived later in this chapter.

3.1.2 Strain Energy Derivation

Consider the position of a point on the cross-section of a rotor blade before deformation with position vector given by

$$\vec{r}_0 = (h_x + x)\hat{I}_c + \eta \hat{J}_c + \zeta \hat{K}_c \qquad (3.9)$$

After deformation, the position vector is given by

$$\vec{R} = \vec{R}_0 + \vec{R}_E + \vec{R}_W \qquad (3.10)$$

84

where $\vec{R}_0$ represents deformed position of the cross section reference point, $\vec{R}_E$ represents deformation associated with the rigid rotation of the cross section, and $\vec{R}_W$ represents deformation associated with warping of the cross section. The position vectors are defined as follows:

$$\vec{R}_0 = (h_x + x + u_0)\hat{I}_c + v_0\hat{J}_c + w_0\hat{K}_c \tag{3.11}$$

$$\vec{R}_E = 0\hat{I}_c + \eta\hat{J}_c + \zeta\hat{K}_c \tag{3.12}$$

$$\vec{R}_W = W_u\hat{I}_c + W_\eta\hat{J}_c + W_\zeta\hat{K}_c \tag{3.13}$$

where W_u, W_η, and W_ζ are warping displacements defined as

$$W_u = u'\psi_{uA} + w'_{c_s}\psi_{uQ_\zeta} + \theta_\eta\psi_{uM_\eta} + v'_{c_s}\psi_{uQ_\eta} + \theta_\zeta\psi_{uM_\zeta} + \phi'\psi_{uT} \tag{3.14}$$

$$W_\eta = u'\psi_{\eta A} + w'_{c_s}\psi_{\eta Q_\zeta} + \theta_\eta\psi_{\eta M_\eta} + v'_{c_s}\psi_{\eta Q_\eta} + \theta_\zeta\psi_{\eta M_\zeta} + \phi'\psi_{\eta T} \tag{3.15}$$

$$W_\zeta = u'\psi_{\zeta A} + w'_{c_s}\psi_{\zeta Q_\zeta} + \theta_\eta\psi_{\zeta M_\eta} + v'_{c_s}\psi_{\zeta Q_\eta} + \theta_\zeta\psi_{\zeta M_\zeta} + \phi'\psi_{\zeta T} \tag{3.16}$$

where subscript s denotes shear strains due to shear deformation and θ is rotation due to bending. The warping terms represent nonclassical contributions to the displacements as a result of cross section deformation. The notation for the warping ψ_{ij} gives the displacement in the direction i associated with a load j, and the magnitude of the displacement in the i direction is shown to be proportional to the displacement associated with the load direction. The displacements associated with warping are in general small for beam structures, with only a few exceptions. The most well-known exception is the out-of-plane warping associated with torsion of noncircular beams (ψ_{uT} in the present formulation). With a completely general approach to anisotropic beam theory, any of the 18 warping terms shown above could be significant for a particular configuration. Thus, for the general approach, all of the warping terms would be maintained within the ordering scheme, even though for most practical cases all but a few terms could be eliminated.

However, rotorcraft aeroelastic analysis, based on one-dimensional beam modeling, generally only requires knowledge of the global blade behavior, and as such

85

the warping displacements need not be included explicitly in the aeroelastic formulation. The important contribution of warping has been shown in past studies to be a reduction in the effective beam stiffnesses. The warping unnecessarily complicates development of the one-dimensional analysis and will be eliminated except for some key terms which have been shown to be important, even for isotropic beams. The other effects of warping can be captured in a detailed cross section (local) analysis which is uncoupled from the beam (global) analysis.

The warping terms which are retained are the out-of-plane torsion-related warping ψ_{uT}, and the two out-of-plane shear-related warping terms ψ_{uQ_ζ} and ψ_{uQ_η}. If the Timoshenko-type shear deformation model is applied (the cross section is assumed to remain plane), then $\psi_{uQ_\zeta} = \zeta$ and $\psi_{uQ_\eta} = \eta$. The deformed position vector is then rewritten with $\vec{R}_w = [\phi'\psi_{uT} + v'_{c_s}\eta + w'_{c_s}\zeta]\hat{I}_c$ as

$$\vec{R} = (\{h_x + x + u_0, v_0, w_0\} + \{(\phi'\psi_{uT} + v'_{c_s}\eta + w'_{c_s}\zeta), \eta, \zeta\}[T_{dc}]) \begin{Bmatrix} \hat{I}_c \\ \hat{J}_c \\ \hat{K}_c \end{Bmatrix} \quad (3.17)$$

where T_{dc} is the transformation matrix between the deformed and cross-section coordinate systems, and will be derived in the next paragraph.

The sequence of rotations for transformation from the undeformed cross-section axis system to the deformed axis system is $\{\theta_\zeta, -\theta_\eta, \phi\}$ where θ_ζ is the Euler bending rotation in the lead-lag plane (given no pretwist), θ_η is the Euler bending rotation in the flapwise plane (given no pretwist), and ϕ is the elastic twist which may be a large angle. The transformation matrix is then defined as

$$[T_{dc}] = \begin{bmatrix} 1 & 0 & 0 \\ 0 & \cos\phi & \sin\phi \\ 0 & -\sin\phi & \cos\phi \end{bmatrix} \begin{bmatrix} 1 & 0 & -\theta_\eta \\ 0 & 1 & 0 \\ \theta_\eta & 0 & 1 \end{bmatrix} \begin{bmatrix} 1 & \theta_\zeta & 0 \\ -\theta_\zeta & 1 & 0 \\ 0 & 0 & 1 \end{bmatrix} \quad (3.18)$$

where the small angle assumption has been employed for the bending rotations.

86

The rotations may be written in terms of the cross-section kinematic variables as

$$\theta_\zeta = (v_{c,x} - \beta_{,x} w_c)\hat{J}_c \tag{3.19}$$

$$-\theta_\eta = (w_{c,x} + \beta_{,x} v_c)\hat{K}_c \tag{3.20}$$

which, when substituted into Eqn. 3.18, gives the transformation matrix as

$$[T_{dc}] = \begin{bmatrix} 1 & v_c' - w_c\theta_0' & w_c' + v_c\theta_0' \\[2mm] -(v_c' - w_c\theta_0')\cos\phi & \beta_c\sin\phi & \sin\phi \\ -(w_c' + v_c\theta_0')\sin\phi & +\cos\phi & \\[4mm] -(w_c' + v_c\theta_0')\cos\phi & \beta_c\cos\phi & \cos\phi \\ +(v_c' - w_c\theta_0')\sin\phi & -\sin\phi & \end{bmatrix} \tag{3.21}$$

where,

$$\beta_c = -(v_c' - w_c\theta_0')(w_c' + v_c\theta_0') \tag{3.22}$$

This transformation agrees with that of Kosmatka [55] if ϕ is assumed to be a small angle.

The strains are developed in terms of the displacements by substituting the derivatives of the position vectors into the strain component definitions as given in Wempner [80]. The position vectors have been defined in terms of the cross-section coordinates, and the derivatives were calculated as follows:

$$\vec{r}_{,x} = \{1, 0, 0\} \tag{3.23}$$

$$\vec{r}_{,\eta} = \{0, 1, 0\} \tag{3.24}$$

$$\vec{r}_{,\zeta} = \{0, 0, 1\} \tag{3.25}$$

$$\vec{R}_{,x} = \{G_{x1}, G_{x2}, G_{x3}\} \tag{3.26}$$

$$\vec{R}_{,\eta} = \{G_{\eta1}, G_{\eta2}, G_{\eta3}\} \tag{3.27}$$

$$\vec{R}_{,\zeta} = \{G_{\zeta1}, G_{\zeta2}, G_{\zeta3}\} \tag{3.28}$$

87

where the G_i terms are defined within the ordering scheme as:

$$G_{x1} = 1 + u'_c - \eta\kappa_\eta - \zeta\kappa_\zeta + \phi'\left[(\zeta v'_c + \eta w'_c - \eta v_c\theta'_0 - \zeta w_c\theta'_0)\cos\phi\right.$$
$$\left. + (\eta v'_c + \zeta w'_c + \zeta v_c\theta'_0 - \eta w_c\theta'_0)\sin\phi\right] + (\phi'\psi_{uT})' \qquad (3.29)$$

$$G_{x2} = v'_c - w_c\theta'_0 - \phi'[\zeta\cos\phi + \eta\sin\phi] \qquad (3.30)$$

$$G_{x3} = w'_c + v_c\theta'_0 + \phi'[\eta\cos\phi - \zeta\sin\phi] \qquad (3.31)$$

$$G_{\eta1} = v'_{c_s} - (v'_c - w_c\theta'_0)\cos\phi - (w'_c + v_c\theta'_0)\sin\phi + \phi'\psi_{uT,\eta} \qquad (3.32)$$

$$G_{\eta2} = \cos\phi + (v_cw_c\theta'^2_0 - v_cv'_c\theta'_0 + w_cw'_c\theta'_0 - v'_cw'_c)\sin\phi \qquad (3.33)$$

$$G_{\eta3} = \sin\phi \qquad (3.34)$$

$$G_{\zeta1} = w'_{c_s} - (w'_c + v_c\theta'_0)\cos\phi + (v'_c - w_c\theta'_0)\sin\phi + \phi'\psi_{uT,\zeta} \qquad (3.35)$$

$$G_{\zeta2} = -\sin\phi + (v_cw_c\theta'^2_0 - v_cv'_c\theta'_0 + w_cw'_c\theta'_0 - v'_cw'_c)\cos\phi \qquad (3.36)$$

$$G_{\zeta3} = \cos\phi \qquad (3.37)$$

and the curvatures are given by

$$\kappa_\eta = (v''_c - w_c\theta''_0 - 2w'_c\theta'_0 - v_c\theta'^2_0)\cos\phi +$$
$$(w''_c + v_c\theta''_0 + 2v'_c\theta'_0 - w_c\theta'^2_0)\sin\phi \qquad (3.38)$$

$$\kappa_\zeta = (w''_c + v_c\theta''_0 + 2v'_c\theta'_0 - w_c\theta'^2_0)\cos\phi -$$
$$(v''_c - w_c\theta''_0 - 2w'_c\theta'_0 - v_c\theta'^2_0)\sin\phi \qquad (3.39)$$

where κ_η is the curvature in the flapwise plane and κ_ζ is curvature in the lead-lag plane. The strain component definitions simplify, after substitution of the undeformed position vectors, to

$$\epsilon_{xx} = (\hat{R}_{,x} \cdot \hat{R}_{,x} - 1)/2 \qquad (3.40)$$

$$\epsilon_{x\eta} = (\hat{R}_{,x} \cdot \hat{R}_{,\eta}) \qquad (3.41)$$

$$\epsilon_{x\zeta} = (\hat{R}_{,x} \cdot \hat{R}_{,\zeta}) \qquad (3.42)$$

$$\epsilon_{\eta\eta} \approx \epsilon_{\zeta\zeta} \approx \epsilon_{\eta\zeta} \approx 0 \qquad (3.43)$$

where $\epsilon_{x\eta}$ and $\epsilon_{x\zeta}$ are the engineering form of the shear strains. The three nonzero strains are calculated by carrying out the dot products. These strains are shown after application of the ordering scheme in terms of the displacements defined in the cross-section system.

$$\epsilon_{xx} = u'_c + \frac{1}{2}(v'_c - w_c\theta'_0)^2 + \frac{1}{2}(w'_c + v_c\theta'_0)^2 - \eta\kappa_\eta - \zeta\kappa_\zeta + $$
$$\frac{1}{2}(\eta^2 + \zeta^2)\phi'^2 + (\phi'\psi_{uT})' \tag{3.44}$$

$$\epsilon_{x\eta} = v'_{c_s} + (\psi_{uT,\eta} - \zeta)\phi' \tag{3.45}$$

$$\epsilon_{x\zeta} = w'_{c_s} + (\psi_{uT,\zeta} + \eta)\phi' \tag{3.46}$$

These strains are defined in terms of the blade coordinate system through use of the transformation $[T_{cu}]$ as

$$\epsilon_{xx} = u' + \frac{1}{2}v'^2 + \frac{1}{2}w'^2 + \frac{1}{2}(\eta^2 + \zeta^2)\phi'^2 - v''[\eta\cos(\theta_0 + \phi) - \zeta\sin(\theta_0 + \phi)]$$
$$-w''[\eta\sin(\theta_0 + \phi) + \zeta\cos(\theta_0 + \phi)] + (\phi'\psi_{uT})' \tag{3.47}$$

$$\epsilon_{x\eta} = v'_s\cos(\theta_0 + \phi) + w'_s\sin(\theta_0 + \phi) + (\psi_{uT,\eta} - \zeta)\phi' \tag{3.48}$$

$$\epsilon_{x\zeta} = w'_s\cos(\theta_0 + \phi) - v'_s\sin(\theta_0 + \phi) + (\psi_{uT,\zeta} + \eta)\phi' \tag{3.49}$$

At this point a variable substitution is made which eliminates the kinematic contribution of foreshortening from the axial displacement. It has been shown by Kaza and Kvaternik [50] that this substitution provides the convenience of developing centrifugal stiffening terms associated with foreshortening in the kinetic energy formulation rather than in the strain energy formulation. The substitution is

$$u'_e = u' + \frac{1}{2}v'^2 + \frac{1}{2}w'^2 \tag{3.50}$$

where u'_e represents the elastic axial strain without kinematic contributions from transverse bending displacements. The contributions of these displacements will reappear in the formulation of kinetic energy when the variable substitution is carried through into that derivation. The strain components then become in final

form:

$$\epsilon_{xx} = u'_e + \frac{1}{2}(\eta^2 + \zeta^2)\phi'^2 + (\phi'\psi_{uT})' - v''[\eta\cos(\theta_0 + \phi) - \zeta\sin(\theta_0 + \phi)]$$
$$-w''[\eta\sin(\theta_0 + \phi) + \zeta\cos(\theta_0 + \phi)] \tag{3.51}$$

$$\epsilon_{x\eta} = v'_s\cos(\theta_0 + \phi) + w'_s\sin(\theta_0 + \phi) + (\psi_{uT,\eta} - \zeta)\phi' \tag{3.52}$$

$$\epsilon_{x\zeta} = w'_s\cos(\theta_0 + \phi) - v'_s\sin(\theta_0 + \phi) + (\psi_{uT,\zeta} + \eta)\phi' \tag{3.53}$$

The variation of the elastic strain energy is given by

$$\delta U = \int_0^R \iint_A \{\sigma_{xx}\delta\epsilon_{xx} + \sigma_{x\eta}\delta\epsilon_{x\eta} + \sigma_{x\zeta}\delta\epsilon_{x\zeta}\}\, d\eta d\zeta dx \tag{3.54}$$

and elastic stress-strain relationships employed in this formulation are given by

$$\left\{ \begin{array}{c} \sigma_{xx} \\ \sigma_{x\zeta} \\ \sigma_{x\eta} \end{array} \right\} = \left\{ \begin{array}{ccc} Q'_{11} & Q'_{15} & Q'_{16} \\ Q'_{15} & Q'_{55} & Q'_{56} \\ Q'_{16} & Q'_{56} & Q'_{66} \end{array} \right\} \left\{ \begin{array}{c} \epsilon_{xx} \\ \epsilon_{x\zeta} \\ \epsilon_{x\eta} \end{array} \right\} \tag{3.55}$$

where the Q'_{ij} represent the material stiffness at a location in the cross section. The material stiffnesses are an average value based on the individual ply material and orientation, and also depend on the orientation of the laminate with respect to the cross section axes. The stress-strain relations are substituted into the strain energy variational, followed by a second substitution of the strain-displacement relations (Eqns. 3.51-3.53) for the strains. After integrating over the area, the strain energy variation becomes

$$\delta U = \int_0^R \delta\hat{v}_i k_{ij}\hat{v}_j\, dx + \int_0^R \delta\hat{v}_i D_i\, dx \tag{3.56}$$

where $(i, j = 1, 9)$, and the strain vector is defined as:

$$\delta\hat{v}_i = \left\{ \begin{array}{ccccccccc} \delta u'_e & \delta v' & \delta v'' & \delta w' & \delta w'' & \delta\phi & \delta\phi' & \delta v'_s & \delta w'_s \end{array} \right\} \tag{3.57}$$

The first integral of Eqn. 3.56 represents the linear part of the strain energy and the second term represents the nonlinear contribution to the strain energy. The diagonal and nonzero off-diagonal terms of the symmetric linear cross section stiffness

90

matrix are listed as follows:

$$k_{11} = EA \tag{3.58}$$

$$k_{13} = -EA_c\cos\theta_1 \tag{3.59}$$

$$k_{15} = -EA_c\sin\theta_1 \tag{3.60}$$

$$k_{17} = EET + EA_{r^2}\theta_0' \tag{3.61}$$

$$k_{18} = EES_c\cos\theta_1 - EES_f\sin\theta_1 \tag{3.62}$$

$$k_{19} = EES_c\sin\theta_1 + EES_f\cos\theta_1 \tag{3.63}$$

$$k_{22} = 0 \tag{3.64}$$

$$k_{33} = EI_c\cos^2\theta_1 + EI_f\sin^2\theta_1 \tag{3.65}$$

$$k_{35} = EI_f\cos\theta_1\sin\theta_1 - EI_f\cos\theta_1\sin\theta_1 \tag{3.66}$$

$$k_{37} = ETC\cos\theta_1 - ETF\sin\theta_1 \tag{3.67}$$

$$k_{38} = (EFS_c + ECS_f)\cos\theta_1\sin\theta_1 \tag{3.68}$$

$$k_{39} = EFS_c\sin^2\theta_1 - ECS_f\cos^2\theta_1 \tag{3.69}$$

$$k_{44} = 0 \tag{3.70}$$

$$k_{55} = EI_f\cos^2\theta_1 + EI_c\sin^2\theta_1 \tag{3.71}$$

$$k_{57} = ETF\cos\theta_1 + ETC\sin\theta_1 \tag{3.72}$$

$$k_{58} = ECS_f\sin^2\theta_1 - EFS_c\cos^2\theta_1 \tag{3.73}$$

$$k_{59} = -(EFS_c + ECS_f)\cos\theta_1\sin\theta_1 \tag{3.74}$$

$$k_{66} = 0 \tag{3.75}$$

$$k_{77} = GJ \tag{3.76}$$

$$k_{88} = GA_c\cos^2\theta_1 + GA_f\sin^2\theta_1 \tag{3.77}$$

$$k_{89} = (GA_c - GA_f)\cos\theta_1\sin\theta_1 \tag{3.78}$$

$$k_{99} = GA_f\cos^2\theta_1 + GA_c\sin^2\theta_1 \tag{3.79}$$

with $\theta_1 = \theta_0 + \phi$ and the cross section integrals given as follows: the classical cross

91

section properties,

$$EA = \iint_A Q'_{11} \, d\eta \, d\zeta \qquad (3.80)$$

$$EA_c = \iint_A Q'_{11} \eta \, d\eta \, d\zeta \qquad (3.81)$$

$$EA_{r^2} = \iint_A Q'_{11} (\eta^2 + \zeta^2) \, d\eta \, d\zeta \qquad (3.82)$$

$$EI_c = \iint_A Q'_{11} \eta^2 \, d\eta \, d\zeta \qquad (3.83)$$

$$EI_f = \iint_A Q'_{11} \zeta^2 \, d\eta \, d\zeta \qquad (3.84)$$

$$GJ = \iint_A [Q'_{55} (\psi_{uT,\zeta} + \eta)^2 + Q'_{66} (\psi_{uT,\eta} - \zeta)^2$$
$$+ 2Q'_{56} \psi_{uT,\zeta} + \eta)(\psi_{uT,\eta} - \zeta)] \, d\eta \, d\zeta \qquad (3.85)$$

the shear-related stiffnesses,

$$GA_c = \iint_A Q'_{55} \, d\eta \, d\zeta \qquad (3.86)$$

$$GA_f = \iint_A Q'_{66} \, d\eta \, d\zeta \qquad (3.87)$$

the anisotropic material coupling stiffnesses,

$$EET = \iint_A Q'_{15} \psi_{uT,\zeta} + \eta) + Q'_{16} \psi_{uT,\eta} - \zeta) \, d\eta \, d\zeta \qquad (3.88)$$

$$ETC = \iint_A [Q'_{15} \psi_{uT,\zeta} + \eta) + Q'_{16} \psi_{uT,\eta} - \zeta)] \eta \, d\eta \, d\zeta \qquad (3.89)$$

$$ETF = \iint_A [Q'_{15} \psi_{uT,\zeta} + \eta) + Q'_{16} \psi_{uT,\eta} - \zeta)] \zeta \, d\eta \, d\zeta \qquad (3.90)$$

the shear-related anisotropic material coupling stiffnesses,

$$EES_c = \iint_A Q'_{15} \, d\eta \, d\zeta \qquad (3.91)$$

$$EES_f = \iint_A Q'_{16} \, d\eta \, d\zeta \qquad (3.92)$$

$$ECS_f = \iint_A Q'_{16} \eta \, d\eta \, d\zeta \qquad (3.93)$$

$$EFS_c = \iint_A Q'_{15} \zeta \, d\eta \, d\zeta \qquad (3.94)$$

and because symmetry in geometry and Q'_{11} is assumed about the chord line, the following section properties become zero,

$$\iint_A Q'_{11} \zeta \, d\eta \, d\zeta = 0 \qquad (3.95)$$

$$\iint_A Q'_{11} \eta\zeta \, d\eta \, d\zeta = 0 \qquad (3.96)$$

92

Anisotropic material properties containing ζ to the first power are not assumed to be zero because Q'_{15} and Q'_{16} may fluctuate greatly about the chord line. The shear-related properties are separated in the above organization of cross section properties because these parameters would not exist without considering shear deformation. It is shown that these properties couple the classical beam deformations with the shear deformations when anisotropic material layups are considered (Q'_{15} and Q'_{16} not zero). Also, the anisotropic material stiffnesses couple the classical beam deformations within themselves when anisotropic material layups are considered.

The possibility of material coupling of classical beam deformations with shear deformations makes it necessary to included these degrees of freedom in an anisotropic, rotating-beam, dynamic analysis. However, it may be possible to include the shear deformation effects implicitly using static condensation. The argument for static condensation of the linear stiffness matrix to eliminate the shear degrees of freedom is presented next. First, eliminate the second, fourth, and sixth rows and columns of k_{ij} because the strain energy terms associated with $\delta v', \delta w'$, and $\delta \phi$ are zero. The linear stiffness matrix k_{ij} can thus be reduced to a 6x6 coupled stiffness matrix with diagonal stiffnesses corresponding to an axial stiffness, two bending stiffnesses, a torsional stiffness, and two shear stiffnesses. For a static problem, the force-displacement relationship may be written as:

$$
\begin{bmatrix} Q_x \\ Q_y \\ Q_z \\ M_x \\ -M_y \\ M_z \end{bmatrix} = [k_{ij}] \begin{bmatrix} u'_e \\ v'_s \\ w'_s \\ \phi' \\ w'' \\ v'' \end{bmatrix}
\tag{3.97}
$$

where Q are forces in the directions indicated by subscripts and M are moments about directions indicated by subscripts. Notice that the displacement vector has

93

been temporarily rearranged to clarify the force part of the relationship. This relationship may be simplified for beam behavior by eliminating the shear-related degrees of freedom. As was shown by Hodges *et al.* [63] it is proper to assume the shear forces associated with the shear deformation are zero, but not the shear strains because of the presence of coupling terms. With Q_y and Q_z set to zero, the shear deformations may be removed through static condensation. This amounts to eliminating the rows and columns associated with shear from the compliance matrix rather than from the stiffness matrix. The compliance matrix is formulated by inverting the 6x6 cross-section stiffness matrix,

$$S_{ij} = k_{ij}^{-1}$$

and after elimination of the second and third rows and columns may be written as

$$\begin{bmatrix} u_e' \\ \phi' \\ w'' \\ v'' \end{bmatrix} = [S_{ij}'] \begin{bmatrix} Q_x \\ M_x \\ -M_y \\ M_z \end{bmatrix} \tag{3.98}$$

The bending-related compliance terms include the flexibility associated with any shear coupling present in the cross-section. The 4x4 compliance matrix is then inverted to obtain the desired 4x4 form of the fully-coupled cross-section stiffness matrix k_{ij}', which implicitly includes shear deformation effects. The term k_{ij} is thus replaced by k_{ij}' in Eqn. 3.56, and the vector of continuous displacement variations is reduced to

$$\delta \bar{v}_i = \left\{ \begin{array}{cccc} \delta u_e' & \delta v'' & \delta w'' & \delta \phi' \end{array} \right\} \tag{3.99}$$

This cross-section stiffness matrix is applicable to the dynamic problem assuming the dynamic effects associated with shear deformation are small.

Now, it may be further shown that the static condensation operation on the cross-section stiffness matrix serves only to reduce the effective stiffness properties

94

of the diagonal terms. Furthermore, the operation is independent of the twist angle θ_1 since it only involves the cross-section properties themselves. The reduced stiffness matrix can thus be written as

$$k'_{11} = \bar{E}A \tag{3.100}$$

$$k'_{12} = -\bar{E}A_\eta \cos\theta_1 \tag{3.101}$$

$$k'_{13} = -\bar{E}A_\eta \sin\theta_1 \tag{3.102}$$

$$k'_{14} = \bar{E}ET + \bar{E}A_{r2}\theta'_0 \tag{3.103}$$

$$k'_{22} = \bar{E}I_c \cos^2\theta_1 + \bar{E}I_f \sin^2\theta_1 \tag{3.104}$$

$$k'_{23} = \bar{E}I_f \cos\theta_1 \sin\theta_1 - \bar{E}I_f \cos\theta_1 \sin\theta_1 \tag{3.105}$$

$$k'_{24} = ETC \cos\theta_1 - ETF \sin\theta_1 \tag{3.106}$$

$$k'_{33} = \bar{E}I_f \cos^2\theta_1 + \bar{E}I_c \sin^2\theta_1 \tag{3.107}$$

$$k'_{34} = ETF \cos\theta_1 + ETC \sin\theta_1 \tag{3.108}$$

$$k'_{44} = \bar{G}J \tag{3.109}$$

where the classical stiffness terms EA, EI_f, EI_c, and GJ have been statically condensed at $\theta_1 = 0$ into the effective stiffness properties $\bar{E}A, \bar{E}I_f, \bar{E}I_c$, and $\bar{G}J$. Notice that the coupling stiffnesses related to anisotropic material properties, EET, ETC, and ETF, are unaffected by the condensation. The structural-based coupling properties (those based on twist and neutral-axis offsets) are affected because of their dependence on the classical beam stiffnesses. The important aspect of developing the cross-section stiffness matrix based on the effective stiffnesses is that it is possible to obtain the effective stiffnesses and coupling stiffnesses directly from sophisticated cross-section analyses. These analyses generally perform a static condensation or some equivalent operation internally, providing stiffnesses based on material compliance. These "effective" properties can then be adopted for the twisted blade using Eqns. 3.100-3.109.

The nonlinear stiffness matrix from Eqn. 3.56 can also be written in terms of

95

these effective beam properties, and is given as:

$$D_1 = EET v'' w'$$ (3.110)

$$D_2 = 0$$ (3.111)

$$D_3 = \bar{G}J\phi'w' + EET u'_e w' + \bar{G}Jv''w'^2 + 2ETC v''w'\cos\theta_1 +$$
$$ETF w'w''\cos\theta_1 - 2ETF v''w'\sin\theta_1 + ETC w'w''\sin\theta_1$$ (3.112)

$$D_4 = \bar{G}J\phi'v'' + EET u'_e v'' + \bar{G}Jv''^2 w' + ETC v''^2\cos\theta_1 +$$
$$ETF v''w''\cos\theta_1 - ETF v''^2\sin\theta_1 + ETC v''w''\sin\theta_1$$ (3.113)

$$D_5 = ETF v''w'\cos\theta_1 + ETC v''w'\sin\theta_1$$ (3.114)

$$D_6 = -ETF\phi'v''\cos\theta_1 - ETF v''^2 wp\cos\theta_1 + ETC\phi'w''\cos\theta_1 +$$
$$ETC v''w'w''\cos\theta_1 - \bar{E}I_f v''w''\cos^2\theta_1 + \bar{E}I_c v''w''\cos^2\theta_1 -$$
$$ETC\phi'v''\sin\theta_1 + \bar{E}A_\eta u'_e v''\sin\theta_1 - ETC v''^2 w'\sin\theta_1 -$$
$$ETF\phi'w''\sin\theta_1 - ETF v''w''w'\sin\theta_1 + \bar{E}I_f v''^2\cos\theta_1\sin\theta_1 -$$
$$\bar{E}I_c v''^2\cos\theta_1\sin\theta_1 - \bar{E}I_f w''^2\cos\theta_1\sin\theta_1 + \bar{E}I_c w''^2\cos\theta_1\sin\theta_1 +$$
$$\bar{E}I_f v''w''\sin^2\theta_1 - \bar{E}I_c v''w''\sin^2\theta_1$$ (3.115)

$$D_7 = \bar{G}Jv''w'$$ (3.116)

  (3.117)

where i of the D_i in this case correspond to the variational displacement vector minus the shear degrees of freedom:

$$\delta\tilde{v}_i = \left\{ \begin{array}{ccccccc} \delta u'_e & \delta v' & \delta v'' & \delta w' & \delta w'' & \delta\phi & \delta\phi' \end{array} \right\}$$ (3.118)

3.1.3 Kinetic Energy Derivation

The position of a point on the deformed blade as given by Eqn. 3.17 may be written using the blade reference displacements and neglecting the warping displacements

96

as

$$\vec{R} = (\{h_x + x + u, v, w\} + \{o, \eta, \zeta\}[T_{du}]) \begin{Bmatrix} \hat{I}_u \\ \hat{J}_u \\ \hat{K}_u \end{Bmatrix} \qquad (3.119)$$

where $[T_{du}]$ is the transformation between the deformed and undeformed-blade coordinate systems which is given by

$$[T_{du}] = [T_{dc}][T_{cu}] \qquad (3.120)$$

The velocity of a point on the deformed blade is written as

$$\vec{V} = \frac{\partial \vec{R}}{\partial t} + \vec{\Omega} \times \vec{R} \qquad (3.121)$$

where

$$\vec{\Omega} = \{\Omega_x, \Omega_y, \Omega_z\} \begin{Bmatrix} \hat{I}_u \\ \hat{J}_u \\ \hat{K}_u \end{Bmatrix} = \{0, 0, \Omega_0\}[T_{ri}]^T [T_{ru}]^T \begin{Bmatrix} \hat{I}_u \\ \hat{J}_u \\ \hat{K}_u \end{Bmatrix} \qquad (3.122)$$

and Ω_0 is the rotation rate at which the hub spins about the inertial z_i axis. If there is no precone then $\Omega_x = \Omega_y = 0$. After application of the ordering scheme, the velocity is given by

$$\vec{V} = \{V_x, V_y, V_z\} \begin{Bmatrix} \hat{I}_u \\ \hat{J}_u \\ \hat{K}_u \end{Bmatrix} \qquad (3.123)$$

$$
\begin{aligned}
V_x = {} & \dot{u} + w\Omega_y - v\Omega_z - (\Omega_z + \dot{v}')\eta \cos\theta_1 + (\Omega_y - \dot{w}')\zeta \cos\theta_1 + \eta\Omega_y \sin\theta_1 \\
& + \Omega_z \zeta \sin\theta_1 + \zeta \cos\theta_1 v'\dot{\phi} + \eta \sin\theta_1 v'\dot{\phi} - \eta \cos\theta_1 w'\dot{\phi} - \zeta \sin\theta_1 w'\dot{\phi} \\
& + \eta \sin\theta_1 \dot{w}' + \zeta \sin\theta_1 \dot{v}' \qquad (3.124)
\end{aligned}
$$

$$
\begin{aligned}
V_y = {} & \dot{v} - w\Omega_x + (h_x + x + u)\Omega_z - \Omega_z \eta v' \cos\theta_1 - \Omega_x \zeta \cos\theta_1 - \zeta\dot{\phi}\cos\theta_1 - \\
& \Omega_z \zeta w' \cos\theta_1 - \Omega_x \eta \sin\theta_1 - \eta\dot{\phi}\sin\theta_1 - \Omega_z \eta w' \sin\theta_1 + \Omega_z \zeta v' \sin\theta_1 (3.125)
\end{aligned}
$$

$$
\begin{aligned}
V_z = {} & \dot{w} + v\Omega_x - (h_x + x + u)\Omega_y + \Omega_x \eta \cos\theta_1 + \Omega_y \eta v' \cos\theta_1 + \eta\dot{\phi}\cos\theta_1 + \\
& \Omega_y \zeta v' \cos\theta_1 + \Omega_y \eta w' \sin\theta_1 - \zeta\dot{\phi}\sin\theta_1 - \Omega_x \zeta \sin\theta_1 - \Omega_y \zeta v' \sin\theta_1 (3.126)
\end{aligned}
$$

where $\theta_1 = \theta_0 + \phi$. After taking the variation of the velocity, the following substitutions, which are based on Eqn. 3.50, are made into $\vec{V}$ and $\delta\vec{V}$.

$$\dot{u} = \dot{u}_e - \int_0^x (v'\dot{v}' + w'\dot{w}') \, d\xi \qquad (3.127)$$

$$\delta u = \delta u_e - \int_0^x (v'\delta v' - w'\delta w') \, d\xi \qquad (3.128)$$

The variation of the blade kinetic energy is given by

$$\delta T = \int_0^R \iint_A \rho\vec{V} \cdot \delta\vec{V} \, d\eta d\zeta \, dx \qquad (3.129)$$

where ρ is the mass density of the blade. After substituting the velocity as defined in Eqn. 3.123 into the kinetic energy expression, calculating the velocity variation, and carrying out the dot product, the variation of the kinetic energy may be written as

$$\int_0^R m\{[T_u]_i \, \delta\hat{u}_i + [T_{\dot{u}}]_i \, \delta\hat{\dot{u}}_i + +T_F\} \, dx \qquad (3.130)$$

where $(i = 1,6)$ and the vector of displacement variations for the kinetic energy formulation is given by,

$$\delta\hat{u}_i = \{ \begin{array}{cccccc} \delta u_e & \delta v & \delta v' & \delta w & \delta w' & \delta\phi \end{array} \} \qquad (3.131)$$

The quantities $[T_u]_i$ and $[T_{\dot{u}}]_j$ represent groups of terms which may be functions of both u and $\dot{u}$. T_F represents additional terms in the kinetic energy which result from the integral part of the variation substitution for δu_e, and after application of the ordering scheme may be written as:

$$T_F = -(x + 2\dot{v}) \int_0^x (v'\delta v' + w'\delta w') \, d\xi + 2\delta v \int_0^x (v'\dot{v}' + w'\dot{w}') \, d\xi \qquad (3.132)$$

The contribution of T_F to the kinetic energy is then given by $\int_0^1 mT_F dx$ which after the appropriate substitutions gives

$$\int_0^R mT_F dx = \int_0^1 m[-(x + 2\dot{v}) \int_0^x (v'\delta v' + w'\delta w')d\xi + 2\delta v \int_0^x (v'\dot{v}' + w'\dot{w}') \, d\xi]dx \qquad (3.133)$$

98

Integration by parts yields a more convenient form for the foreshortening contribution to kinetic energy as

$$\int_0^R mT_F dx \;=\; -(F_A + F_{cor})(v' \delta v' + w' \delta w')$$
$$+2\delta v \int_0^x (v'\dot{v}' + w'\dot{w}')\, d\xi \qquad (3.134)$$

where

$$F_A \;=\; \int_x^R mx\, d\xi \qquad (3.135)$$

$$F_{cor} \;=\; \int_x^R 2m\dot{v}\, d\xi \qquad (3.136)$$

The terms associated with F_A reflect the centrifugal stiffening effects on the flap and lag equations while the terms associated with F_{cor} reflect the nonlinear Coriolis damping effects in those equations. The terms associated with F_A and F_{cor} are added to $T_{v_2'}$ and $T_{w_2'}$, which allows the linear contribution to the kinetic energy variation to be written as

$$\delta T_{lin} = \int_0^R \{ \delta \dot{u}_i m_{ij} \dot{u}_j + \delta \dot{u}_i c_{ij} \hat{u}_j + \delta u_i k_{ij} \hat{u}_j \}\, dx \qquad (3.137)$$

A more useful form of the above expression is obtained by integrating the variation in kinetic energy by parts over time. This can be done because in applying Hamilton's principle the variation in kinetic energy will be integrated in time. By temporarily switching the order of integration, the integration by parts can be performed.

$$\int_{t_1}^{t_2} \int_0^1 \delta u_i m_{ij} \dot{u}_j dx\, dt = \int_0^1 \int_{t_1}^{t_2} \delta u_i m_{ij} \dot{u}_j dt\, dx =$$
$$\int_0^1 \left(\delta u_i m_{ij} \dot{u}_j \Big|_{t_1}^{t_2} - \int_{t_1}^{t_2} \delta u_i m_{ij} \ddot{u}_j\, dt \right) dx = -\int_{t_1}^{t_2} \int_0^1 \delta u_i m_{ij} \ddot{u}_j\, dx\, dt \qquad (3.138)$$

After a similar operation on the damping term of Eqn. 3.137, the linear variation of kinetic energy becomes

$$\delta T_{lin} = \int_0^R \delta u_i \{ m_{ij} \ddot{u}_j + c_{ij} \dot{u}_j + k_{ij} \hat{u}_j \}\, dx \qquad (3.139)$$

99

with the vector of displacement variations for the kinetic energy formulation given by

$$\delta \hat{u}_i = \{ \ \delta u_e \quad \delta v \quad \delta v' \quad \delta w \quad \delta w' \quad \delta \phi \ \}^{\cdot} \tag{3.140}$$

m_{ij} is the mass matrix which includes rotational inertias, c_{ij} is the linear damping matrix, and k_{ij} is the linear stiffness matrix which contains the centrifugal stiffening terms of nonlinear origin.

3.2 Implementation

The linear parts of the strain and kinetic energies defined in Eqns. 3.56 and 3.139 were used to develop a p-version beam finite element so that the degree of polynomial approximation for the bending, torsion, and axial displacements may be independently selected. Integrations over the element length were performed symbolically to increase computational efficiency of the analysis. The final form of the rotating blade equations after application of Hamilton's principle in discretized form is given by

$$M_{ij}\ddot{q}_j + C_{ij}\dot{q}_j + K_{ij}q_j = 0 \tag{3.141}$$

where M_{ij}, C_{ij}, and K_{ij} are the element mass, damping, and stiffness matrices, respectively. q_j represents the vector of discrete displacements. The elements are assembled to form a global system which is solved using standard eigenvalue techniques to obtain modes and frequencies. Further description of the beam element formulation is provided in this section.

The present formulation is implemented as a beam finite element. Many past analyses for rotating blades have used this approach, but the order of polynomials used to approximate the displacements has varied. The analysis of Kosmatka [55] uses a quadratic torsion and axial approximation along with cubic Hermitian polynomials for bending. This set of assumptions provides the same level of accuracy

100

in the torsion and axial deformations as in the bending deformations. The analyses of Hong and Chopra [65,66] and Smith and Chopra [68] use similar displacement polynomials, but with a cubic axial approximation, developed as a mean for improving the axial mode predictions.

A higher-order element capability was developed for the dynamic analysis of beams in the GRASP code (Hodges *et. al.* [81]). In this code the user could independently increase the order of polynomial approximation of each displacement to match the physical characteristics of the beam. This is the so-called p-version finite element approach, and seems ideally suited for application to analysis of elastically-coupled beams because of the dramatic influence elastic couplings have on beam flexibility in some displacement modes. The study of Hinnant [82] demonstrated that, given proper modeling of the beam geometry, there is also substantial savings to be gained by use of p-version elements in terms of total number of degrees of freedom required to obtain an accurate solution.

3.2.1 Finite Element Discretization

The linear parts of the strain and kinetic energies as defined in Eqns. 3.56 and 3.139 are used to develop a p-version beam finite element. The continuous displacements which appear in these expressions are u, v, w, and ϕ, and are functions of both x and time. The continuous problem is discretized by introducing discrete degrees of freedom q_i which are related to the continuous displacements according to

$$u = \sum_{i=1}^{P_u} N_i^u q_i^u \qquad (3.142)$$

$$v = \sum_{i=1}^{P_v} N_i^v q_i^v \qquad (3.143)$$

$$w = \sum_{i=1}^{P_w} N_i^w q_i^w \qquad (3.144)$$

$$\phi = \sum_{i=1}^{P_\phi} N_i^\phi q_i^\phi \qquad (3.145)$$

where N_i are shape functions defined later in this section. Substitution of these equations into Eqns. 3.56 and 3.139 gives the strain and kinetic energies in terms of the discrete degrees of freedom. The virtual energy expression defined in Eqn. 3.1 may also be written in discretized form as

$$\delta \Pi = \int_{t_1}^{t_2} \left[\sum_{i=1}^{N} (\delta U_i - \delta T_i) \right] dt \tag{3.146}$$

where N is the number of spatial elements used to discretize the elastic blade. Each element is represented using the discrete displacements as

$$\delta U - \delta T = \delta q_i^T \left\{ M_{ij} \ddot{q}_j + C_{ij} \dot{q}_j + K_{ij} q_j \right\} \tag{3.147}$$

where the element mass, damping, and stiffness matrices are defined by

$$M_{ij} = \int_0^R B_{ik} m_{kl} B_{lj} \, dx \tag{3.148}$$

$$C_{ij} = \int_0^R B_{ik} c_{kl} B_{lj} \, dx \tag{3.149}$$

$$K_{ij} = \int_0^R (A_{ik} k_{kl} A_{lj} \, dx - B_{ik} k_{kl} B_{lj}) \, dx \tag{3.150}$$

where $B_{ik} = B_{lj}^T$ and $A_{ik} = A_{lj}^T$. B is a matrix of shape functions and shape function derivatives which satisfies the relationship

$$u_i = (D_T)_{ij} [\hat{u}_j] = (D_T)_{ij} [H_{jk} q_k] = B_{ik} q_k \tag{3.151}$$

where $\hat{u}_j$ is a vector of the continuous degrees of freedom u, v, w, and ϕ. D_T is a matrix of derivative operators associated with the kinetic energy formulation and H is a matrix of shape functions whose arrangement depends on the selection of discrete variables in q, and satisfies Eqns. 3.142-3.145. The definition of A_{ij} is similar to that of B_{ij} except that it is associated with the strain energy formulation. Thus, B may be replaced by A and subscripts of T may be replaced by V in Eqn. 3.151.

The discrete degrees of freedom are divided into two sets, external and internal. There are twelve external degrees of freedom which have physical significance as the

102

displacements and rotations associated with the ends of the beam finite element (six on each end). These deformations are depicted in Figure 3.3. The shape functions for N_i^u and N_i^ϕ are identical and have C^0-type continuity. There are two well-known linear polynomials used to define this set:

$$N_1^0 = 1 - \frac{x}{l} \tag{3.152}$$

$$N_2^0 = \frac{x}{l} \tag{3.153}$$

where $N_i^u = N_i^\phi = N_i^0$. The shape functions N_i^v and N_i^w require C^1-type continuity. These shape functions are given by:

$$N_1^1 = 2\frac{x^3}{l^3} - 3\frac{x^2}{l^2} + 1 \tag{3.154}$$

$$N_2^1 = \frac{x^3}{l^2} - 2\frac{x^2}{l} + x \tag{3.155}$$

$$N_3^1 = -2\frac{x^3}{l^3} + 3\frac{x^2}{l^2} \tag{3.156}$$

$$N_4^1 = \frac{x^3}{l^2} - \frac{x^2}{l} \tag{3.157}$$

where $N_i^v = N_i^w = N_i^1$.

The internal degrees of freedom have no physical significance, but are simply coefficients of the higher-order shape functions. The internal degrees of freedom serve to increase the accuracy of the transformation from the discrete problem having a finite number of degrees of freedom to the continuous problem having an infinite number of degrees of freedom. In the present formulation, the number of internal degrees of freedom is limited to four for the C^0-type displacements, and to two for the C^1-type displacements. There are, therefore, a total of six internal shape functions associated with each continuous displacement u, v, w, and ϕ. The additional C^0-type shape functions for u and ϕ are

$$N_3^0 = \sqrt{3}\,(\frac{x^2}{l^2} - \frac{x}{l}) \tag{3.158}$$

$$N_4^0 = \sqrt{5}\,(-2\frac{x^3}{l^3} + 3\frac{x^2}{l^2} - \frac{x}{l}) \tag{3.159}$$

$$N_5^0 = \sqrt{7}\left(5\frac{x^4}{l^4} - 10\frac{x^3}{l^3} + 6\frac{x^2}{l^2} - \frac{x}{l}\right) \tag{3.160}$$

$$N_6^0 = -42\frac{x^5}{l^5} + 105\frac{x^4}{l^4} - 90\frac{x^3}{l^3} + 30\frac{x^2}{l^2} - 3\frac{x}{l} \tag{3.161}$$

These shape functions are derived by Hinnant [82] based on satisfaction of two requirements: first, the higher order shape functions must be zero at the element boundaries, and second, they must be orthogonal with respect to their first derivative. The additional C^1-type shape functions for v and w are given by

$$N_5^1 = \sqrt{5}\left(\frac{x^4}{2l^4} - \frac{x^3}{l^3} + \frac{x^2}{2l^2}\right) \tag{3.162}$$

$$N_6^1 = \sqrt{7}\left(-\frac{x^5}{l^5} + 5\frac{x^4}{2l^4} - 2\frac{x^3}{l^3} + \frac{x^2}{2l^2}\right) \tag{3.163}$$

The derivation of these higher-order polynomials is similar to that of the C^0-type polynomials, only the functions must also have zero slope at the element boundaries, and must be orthogonal in their second derivative.

The arrangement of shape functions in the matrix of shape functions H depends on the arrangement of discrete degrees of freedom in q. To facilitate the element assembly process, the discrete unknowns were grouped with the first twelve external nodes together, followed by the twelve internal nodes ($4u$, $2v$, $2w$, and 4ϕ). The arrangement of the vector of discrete degrees of freedom is given as

$$q^T = \{\; u_1 \;\; v_1 \;\; w_1 \;\; \phi_1 \;\; -w_1' \;\; v_1' \;\; u_2 \;\; v_2 \;\; w_2 \;\; \phi_2 \;\; -w_2' \;\; v_2'$$

$$u_3 \;\; u_4 \;\; u_5 \;\; u_6 \;\; v_3 \;\; v_4 \;\; w_3 \;\; w_4 \;\; \phi_3 \;\; \phi_4 \;\; \phi_5 \;\; \phi_6 \;\} \tag{3.164}$$

Before the symbolic integrations of Eqns. 3.148-3.150 can be carried out, the mass, damping, and stiffness cross-section matrices (m, c, k, and k) must be defined as polynomials in x. The cross-section terms are functions of x because of the presence of the twist angle in many of the terms, which is itself a function of x. In the present formulation, it is desired to have the capability of accounting for changes in cross-section properties beyond that due to twist, such as taper, for example.

A beam element does not allow for such effects directly, so a quadratic polynomial curve fit was adapted to increase the accuracy of the element for changes in cross-section properties along its length.

The mass, damping, and stiffness matrices as given by Eqns. 3.148-3.150 were symbolically integrated to obtain 24 x 24 element matrices. These matrices were implemented in an analysis to determine the modes and frequencies of highly-twisted elastically-coupled rotor blades. As part of this implementation, the displacement approximations could be chosen for each continuous displacement independently. The external displacements represent the minimum number of degrees of freedom for each element, while the maximum is given by use of all twelve internal degrees of freedom. Any choice between 12 and 24 degrees of freedom per element could be accomodated in the analysis. The notation adopted for the present formulation is to select a "p" value which represents the number of internal degrees of freedom associated with a particular displacement. For example, an element with $p_u = 1$ and $p_\phi = 1$ uses the basic cubic hermitian polynomial approximation in bending (no internal degrees of freedom) and quadratic polynomial approximations in the axial and torsion displacements. This particular example happens to represent the most common approximation used in finite element rotor blade dynamic analysis because it gives an equivalent level of approximation in all displacement modes.

3.3   Analysis Application

The capabilities and limitations of the present analysis with respect to mode and frequency predictions of highly-twisted elastically-coupled beams are examined. The present analysis, referred to as CORBA (COmposite Rotating Beam Analysis) for clarity, is first verified for simple cases where the elastic coupling influences are small. The predictions of CORBA are then examined for cases where the

elastic coupling effects become significant. Convergence of the CORBA results was achieved using five beam elements with cubic polynomials for the bending displacements, and quadratic polynomials for the axial and torsion displacements. These approximations gave convergence in the most highly twisted rotating beams considered in this study, and were more than adequate for the untwisted cases.

3.3.1 Analysis Verification

Several cases were studied to verify CORBA predictions of modes and frequencies for rotating composite blades. Three of the case studies are presented in this paper. These three configurations, referred to as *Series 1*, were developed by Smith and Chopra [68] to investigate the effects of elastically coupled rotor blades for a soft-inplane hingeless rotor helicopter. The blade cross-section was designed to be representative of an actual rotor system with respect to stiffness and inertial properties. The main structural member of the rotor blade was a single cell composite box beam. The ply orientation of the box beam laminates was adjusted to produce the three configurations considered here. The first case is uncoupled (baseline), the second is extension-flap shear, flap bending-twist coupled (symmetric case), and the third is bending-shear, extension-twist coupled (anti-symmetric case). The terms "symmetric" and "anti-symmetric" refer to the orientation of laminates with respect to the bending axes of the box beam, but not to the laminates themselves. The individual laminates themselves are arranged in a symmetric configuration for all cases. The stiffness properties associated with each case, as reported by Smith and Chopra [68], are shown in Table 3.1. In this table, EA is the axial stiffness, GA_y and GA_z are the lag and flap shear stiffnesses, GJ is the torsional stiffness, and EI_y and EI_z are the flap and lag bending stiffnesses. k_{12} represents the extension-flap shear coupling, k_{13} the extension-lag shear coupling, k_{14} the extension-twist coupling, k_{25} the lag shear-flap bending coupling, k_{36} the

flap shear-lag bending coupling, k_{45} the flap bending-twist coupling, and finally k_{46} the lag bending-twist coupling. All the stiffnesses are shown to be nondimensionalized by appropriate factors of m_0 the mass per unit length, Ω the reference rotational velocity, and R the blade radius.

The rotating natural frequencies for each case as predicted by two analyses, UMARC and CORBA, are shown in Tables 3.2-3.4. All references to "UMARC" are understood to mean the version which has a 19 degree-of-freedom shear deformable beam element, unless otherwise indicated. The difference in predictions between CORBA and UMARC is shown to be less than one percent for all modes except the second flap mode of the anti-symmetric case where the difference is 1.35 percent. Comparison studies, not shown here, also showed good agreement between the two analyses for highly twisted blades, up to 90°. These correlations indicate that the present analysis has accurately captured the effects of rotation, twist, elastic coupling, and shear deformation.

Two more case studies, designated *Series 2*, were examined to determine the influence of higher amounts of elastic coupling on the frequency predictions of UMARC and CORBA. The cross-section geometry of these cases was a simple single cell box beam, without any nonstructural mass or secondary structure, and in one case the layup was arranged in an anti-symmetric configuration while the other was arranged in a symmetric configuration. The symmetric case had a $[15]_6$ layup of graphite epoxy material on the top and bottom walls while the sides had a layup of $[15/-15]_3$. The anti-symmetric layup was $[15]_6$ on top and $[-15]_6$ on the bottom wall, and one side was $[15]_6$ while the other side was $[-15]_6$. The box had an outside width of .953 inches and outside depth of .537 inches, and the specimens were 33.25 inches long. These cases were examined because a set of experimental results, presented by Chandra and Chopra [77], was available for correlation with the analytical predictions.

The cross-section mass and stiffness properties of these specimens were calculated using a two-dimensional analysis described in detail by Smith and Chopra [83]. This analysis accounts for shear deformation and the out-of-plane warping associated with torsion, but does not consider any other warping effects. The mass and stiffness properties developed by this analysis were used as input to both UMARC and CORBA.

The analytical and experimental results are listed in Table 3.5 for the anti-symmetric case and in Table 3.6 for the symmetric case. The importance of including the shear coupling effects for the anti-symmetric case is demonstrated by the overly stiff predictions shown for UMARC* (UMARC version without shear deformation). The frequency predictions of CORBA are shown to agree very well with those of UMARC in both cases. There is a small discrepancy in the predictions of the second lag modes, but this amounts to less than 4 percent. Of greater importance is the discrepancy of both beam analyses with respect to the experimental results. The correlation of CORBA with the experimental results is shown to be poor, particularly in the lag mode, for both the symmetric and anti-symmetric cases. The error is mostly likely caused by neglecting some important warping terms in the cross-section analysis.

3.3.2 Warping Influences on the Anti-Symmetric Beam

The cross-section analysis employed in the verification studies of the last section considered only the out-of-plane torsion-related warping. Account of this warping effect gave a much more flexible and accurate torsional stiffness value. Analogously, the shear stiffness of the beam is also decreased by warping of the cross-section. In this case, the majority of the effect is due to deformation of the cross-section associated with shear forces both inplane (anticlastic deformation) and out-of-plane. A simplified approach for including shear-related warping effects in a beam

is to reduce the effective shear stiffness by a factor K which represents the ratio of average shear stress over the cross-section to the shear stress at the centroid. This factor accounts for the near-parabolic distribution of shear stress through the cross section in the direction of the applied shear force, and is generally referred to as Timoshenko's shear correction factor. Since the amount of warping due to a shear load depends on the shape and material of the cross-section, so does the value of K. The value of K was determined, using the formulas derived by Cowper [84], as approximately 0.85 for the anti-symmetric box beam.

The influence of the shear stiffness effect on bending behavior was examined for the *Series 2* anti-symmetric box beam, but with variations of the laminate ply angles. The basic ply structure of the anti-symmetric box beam is $[\theta]_6$ on top and one side, and $[-\theta]_6$ on bottom and the other side, where $\theta = 15°$ for the baseline anti-symmetric configuration. The ply angle was varied from $\theta = 0°$ to $\theta = 45°$ for this study. The beam was considered non-rotating so as to isolate the elastic effects from the rotational effects.

For this study, the results of CORBA were compared with those of an anisotropic 3-D p-version finite element analysis developed by Hinnant [78]. The 3-D analysis used four brick elements to model the box beam. Convergence was achieved with ninth order polynomials for displacements along the length of the beam, cubic polynomials along the sides of the cross-section walls, and linear polynomials through the thickness of each laminate. The material properties of each brick finite element were determined by averaging the material properties for each ply in the laminate over the laminate thickness. For cases in which the box beam was twisted, each brick element was twisted in a continuous manner such that the finite element model did not differ from the physical model by more than one hundredth of an inch at any point.

Results of the ply angle sweep for the anti-symmetric box beam, both with and

without the shear correction factor applied, are illustrated in Figure 3.4, shown as a function of error in the CORBA analysis with respect to the 3-D analysis. The error in the first bending modes is shown to increase rapidly with ply angle, maximizing at about $\theta = 25°$, and then decrease with ply angle. This is consistent with what might be expected based on the Poisson effects because the Poisson's ratio of the box beam laminates follows a similar trend with ply angle. The cross-section warping is dependent on the Poisson's ratio, so errors associated with not including all the effects of warping are expected. The worst error is quite significant, about 16 percent in the first lag mode and about 6 percent in the first flap mode. The error in the second and third bending modes is shown to be higher, with error maximizing at about $\theta = 20°$. The shear correction factor is shown to greatly reduce these errors, giving a very accurate prediction in the flap modes.

In a second approach taken to account for all warping influences, the lag bending stiffness was determined through iteration (using the CORBA analysis) as that required to drive the first lag bending frequency to zero error. The error of the second and third lag bending modes associated with the new lag stiffness are illustrated in Figure 3.5. As shown, the error in the higher lag bending modes is reduced, with less than five percent error at $\theta = 30°$ where previously the error was in the 10 to 25 percent range. This is an important result because it shows that even in cases where the warping effects are significant, the frequencies of higher modes may be accurately predicted if the same is true of the fundamental modes. The result is not obvious because the importance of direct shear effects increases at higher modes (beam is effectively shorter). The rotating box beam with $[15]_6$ layup was then considered with the appropriate stiffness terms as developed in the nonrotating study. The results are shown in Table 3.7 to be greatly improved over those of Table 3.5, indicating that effects associated with rotation have a negligible influence on the accuracy of the frequency predictions.

3.3.3 Warping Influences on the Symmetric Beam

The symmetric box beam case was also examined as a function of ply angle in the nonrotating configuration. For the symmetric box beam case, the shear is uncoupled from bending and should have little effect on the bending frequencies. The plots of Figure 3.6 show that there is a dependency of the error (calculated with respect to the 3-D analysis results) on the ply orientation, just as there was for the anti-symmetric case. The error in the prediction of the fundamental torsion mode (which is coupled to the flap bending mode) is shown to increase with ply angle to a maximum at $\theta = 45°$, while the error in the lag mode (which is decoupled from torsion and flap) maximizes at about 25°. The error in the higher lag and flap modes does not follow the same path as the error in the fundamental lag mode with respect to the ply angle variations. The higher modes are shown to improve while the fundamental lag mode worsens for the ply angles above 30°.

A new torsional stiffness was determined which gave a zero error in the fundamental torsion mode. The procedure used was the same iterative procedure used previously to obtain the improved lag stiffnesses for the anti-symmetric case. It was found that the improvement to the torsional stiffness drove not only the fundamental torsion mode error to zero, but also drove the flap bending mode error to near zero because of the coupling between the two modes. The reverse was found not to be true, driving the flap bending mode to zero error did not correct the torsion mode error. Since both the fundamental torsion and flap bending modes could be corrected by adjusting a single stiffness value, the errors associated with the flap bending and torsion modes were likely from the same source, which was probably an alteration of the torsion-related warping function at the high ply angles.

An improved lag stiffness was also calculated using the iterative procedure. The error of the lag bending mode is attributed to out-of-plane warping associated

with bending since this mode is decoupled from all other modes.

Application of the refined torsion and lag bending stiffnesses improved predictions of the higher bending modes as shown in Figure 3.7. It is interesting that the error in the higher modes, after the corrections were applied, are lower at high ply angles where the beam is highly coupled and are worse at zero degrees ply angle where the beam is uncoupled.

3.3.4 Influence of Large Pretwist on Nonclassical Effects

Another important influence on composite blades is that of the built-in pretwist. The influence of pretwist could create problems for the approach of the present formulation because it is difficult to account for a global effect like pretwist in the local cross-section analysis. The study of Shield [85] illustrated the significant influence of pretwist on cross-section deformations of bars, and the study of Kosmatka [86] showed that pretwist has a significant influence on the cross-section deformations and extension-torsion behavior of solid and thin-wall airfoil sections. The static behavior of pretwisted elastically-coupled composite beams was studied by Iesan [53], Kosmatka and Dong [56], and Kosmatka [57]. These studies indicate that the elastic-coupling and nonclassical influences of shear-deformation and warping can be influenced by the pretwist of the beam. There are no known reports to date, however, indicating the magnitude of the effect that the pretwist may have on the dynamic behavior of elastically-coupled beams typical of rotor blades.

The influence of the pretwist on the nonclassical effects of shear deformation and warping were examined for the nonrotating symmetric and anti-symmetric box beam cases of *Series 2* with $\theta = 15°$. The error of the CORBA predictions as compared with the 3-D results are shown in Figure 3.8 for pretwist angles up to 90° in the anti-symmetric case. The change in error is small for the fundamental

modes, with error change less than five percent from the untwisted case, even in the extreme case of 90° of pretwist. The error in the higher lag modes is shown to be only slightly larger, with a change in the error from 9 to about 16 percent in the third lag mode. The change in error of both the fundamental and higher modes, as a function of pretwist, was negligible for the symmetric case.

3.3.5 Convergence Study

A convergence study was performed to determine if use of higher order elements is beneficial when beams are elastically coupled. A standard h-element is defined for purposes of the present discussion as one with cubic bending shape functions and quadratic axial and torsion displacement approximations. The equivalent p-version element of the present formulation has $p_u = 1$ and $p_\phi = 1$. Since this element is routinely used in rotor analyses, the convergence study will consider it a baseline for comparison. Elements with higher order than the standard are referenced by their addition to the displacement approximations. For example, "Std.+1w+1t" refers to a beam element with one order higher approximation in flap bending and torsion than the standard element.

A convergence study of a bending-twist-coupled untwisted composite box beam showed slow convergence of the third predominantly flap mode. The cause of this was probably due to the coupling between the bending and torsion modes. Various shape function approximation schemes were employed to determine an optimum for convergence of this particular mode. The results are illustrated in the plot of Figure 3.9 which shows that the "Std.+1w+1t" approximation scheme had the best convergence. Use of that approximation scheme decreased the total number of degrees of freedom from 32 to 22, assuming a 1 percent error criteria. This amounts to about a one-third reduction in global degrees of freedom which could relate to significant improvements in run times associated with analyses of

113

elastically-coupled blades.

The composite box beam considered in the above study was uniform and untwisted. A second study was conducted on the same beam with 40° of pretwist. In this case, the cross-section properties change as a function of x, and, as a result, the integrations were not exact. Again, various shape function approximation schemes were employed to determine an optimum for convergence of the third flapwise bending mode. The results are illustrated in the plot of Figure 3.10 which shows that there is no optimum. The convergence rates are also much shallower than those shown for the untwisted case in Figure 3.9. This is because in addition to the elastic coupling between flap and torsion modes, the pretwist introduces coupling between the bending modes. The only higher-order element which performed well had additonal order increases in both bending modes as well as torsion. However, for this twisted case, the higher order elements did nothing to improve efficiency, and in some cases even degraded it.

3.4 Summary

A dynamic analysis has been formulated for rotating pretwisted composite blades which exhibit anisotropic behavior. The present formulation incorporated the effects of shear deformation implicitly through elimination of the shear variables in the material compliance matrix. Results showed that this approach was able to capture the most significant effect of shear deformation, namely the reduction in effective bending stiffness that occurs when a substantial amount of bending-shear coupling is present in a beam. The difference between implicit and explicit use of shear degrees of freedom was shown to be less than 2 percent up to the second bending modes of some representative rotor blades, and less than 4 percent up to the second bending modes of some highly coupled box beam specimens.

The results of this study also showed that one-dimensional global dynamic anal-

ysis based on classical beam kinematics can accurately predict the bending and torsion frequencies of modes important to an aeroelastic analysis. However, the section properties used in the global analysis must account for the important non-classical effects associated with shear deformation, warping, and elastic couplings. These nonclassical effects were shown to have significant influence on the frequencies of the fundamental modes of highly coupled beam structures. Errors on the order of fifteen percent were reduced to less than five percent through account of the nonclassical effects. The influence of twist on the predictive capabilities of the analysis was shown to be small.

The present analysis (CORBA) was implemented using a p-version beam finite element. Both the advantages and disadvantages of this approach were discussed. The p-version element proved to be convenient for assuring a converged solution, and allowed the desired flexibility in tailoring the displacement approximations to the dynamic characteristics of a given beam configuration. Some degree of efficiency improvement was demonstrated for the uniform untwisted case, but efficiency does not appear to be an issue for more realistic rotor blade structures. Much of the efficiency of using higher order elements was shown to be lost for a highly twisted blade.

Table 3.1: Composite blade stiffnesses for *Series 1*.

Stiffness	Baseline	Sym.	Anti-Sym.
$EA/m_0\Omega^2 R^2$	378.1	378.1	378.1
$GA_y/m_0\Omega^2 R^2$	50.77	50.43	50.77
$GA_z/m_0\Omega^2 R^2$	25.85	25.85	25.85
$GJ/m_0\Omega^2 R^4$	.003822	.003815	.003796
$EI_y/m_0\Omega^2 R^4$	.008345	.008345	.008345
$EI_z/m_0\Omega^2 R^4$	.023198	.023198	.023198
$k_{12}/m_0\Omega^2 R^2$	0	-33.67	0
$k_{13}/m_0\Omega^2 R^2$	0	0	0
$k_{14}/m_0\Omega^2 R^3$	0	0	.3589
$k_{25}/m_0\Omega^2 R^3$	0	0	-.1794
$k_{36}/m_0\Omega^2 R^3$	0	0	.1796
$k_{45}/m_0\Omega^2 R^4$	0	-.001311	0
$k_{46}/m_0\Omega^2 R^4$	0	0	0

Table 3.2: Frequencies for the *Series 1* baseline.

CORBA (per rev)	UMARC (per rev)	Diff. (%)	Pred. Mode
0.749	0.747	0.23	1st lag
1.147	1.146	0.09	1st flap
3.398	3.389	0.26	2nd flap
4.338	4.315	0.53	2nd lag
4.590	4.590	0.01	1st tor.
7.459	7.416	0.58	3rd flap
13.61	13.60	0.08	2nd tor.

Table 3.3: Frequencies for the *Series 1* symmetric case.

CORBA (per rev)	UMARC (per rev)	Diff. %	Pred. Mode
0.749	0.747	0.23	1st lag
1.143	1.142	0.11	1st flap
3.354	3.346	0.25	2nd flap
4.338	4.314	0.55	2nd lag
4.590	4.590	0.01	1st tor.
13.63	13.62	0.08	2nd tor.

Table 3.4: Frequencies for the *Series 1* anti-symmetric case.

CORBA (per rev)	UMARC (per rev)	Diff. %	Pred. Mode
0.736	0.735	0.08	1st lag
1.142	1.141	0.07	1st flap
3.344	3.389	1.35	2nd flap
4.256	4.244	0.29	2nd lag
4.367	4.367	0.01	1st tor.

Table 3.5: Rotating frequencies of the *Series 2* anti-symmetric case at $\Omega = 1002$ RPM.

CORBA (Hz)	UMARC (Hz)	UMARC* (Hz)	Experiment (Hz)	CORBA[†] Diff. (%)	UMARC*[†] Diff. (%)	Pred. Mode
36.53	36.49	43.52	33.6	8.70	29.5	1st flap
53.89	53.73	62.57	46.6	15.65	34.3	1st lag
202.8	202.2	247.8	184.0	10.2	34.7	2nd flap
336.4	328.2	383.6				2nd lag
493.6	493.7	493.7				1st tor.

[†] Correlation with experimental results. * UMARC without shear deformation.

Table 3.6: Rotating frequencies of the *Series 2* symmetric case at $\Omega = 1002$ RPM.

CORBA (Hz)	UMARC (Hz)	Exp. (Hz)	CORBA[†] Diff. (%)	Pred. Mode
36.92	36.87	35.20	4.88	1st flap
62.79	62.45	53.80	16.7	1st lag
205.0	203.0	188.0	9.04	2nd flap
392.2	378.9			2nd lag
729.9	729.2			1st tor.

[†] Correlation with experimental results.

Table 3.7: Rotating frequencies of an anti-symmetric layup box beam at $\Omega = 1002$ RPM with refined stiffness properties.

CORBA (Hz)	Experiment (Hz)	CORBA Error (%)	Pred. Mode
34.78	33.60	3.50	1st flap
47.04	46.60	0.93	1st lag
190.4	184.0	3.46	2nd flap
293.4			2nd lag
493.6			1st tor.
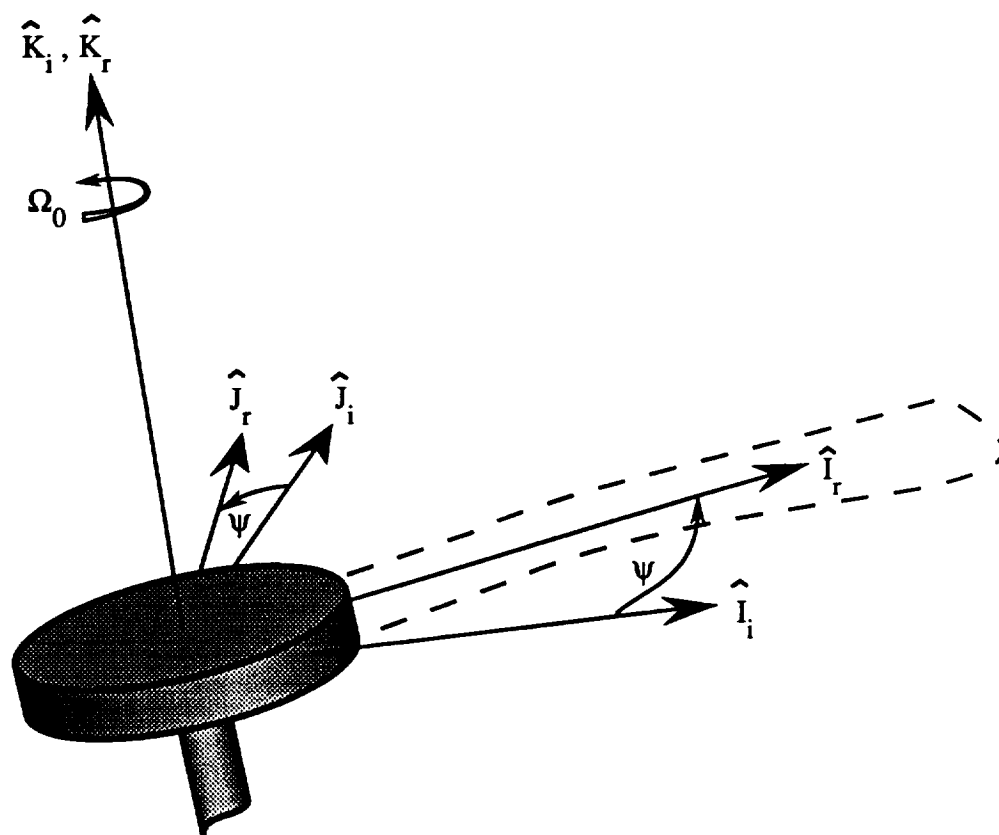
Figure 3.1: Geometry of the shaft and hub.
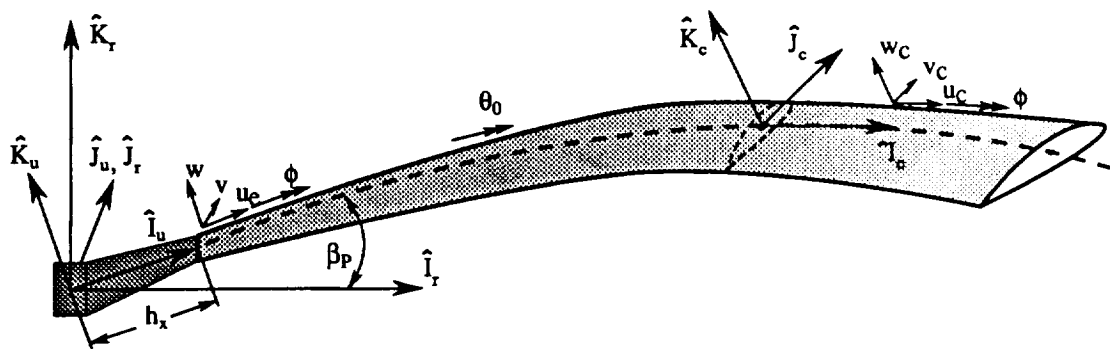
Figure 3.2: Geometry of the elastic blade.
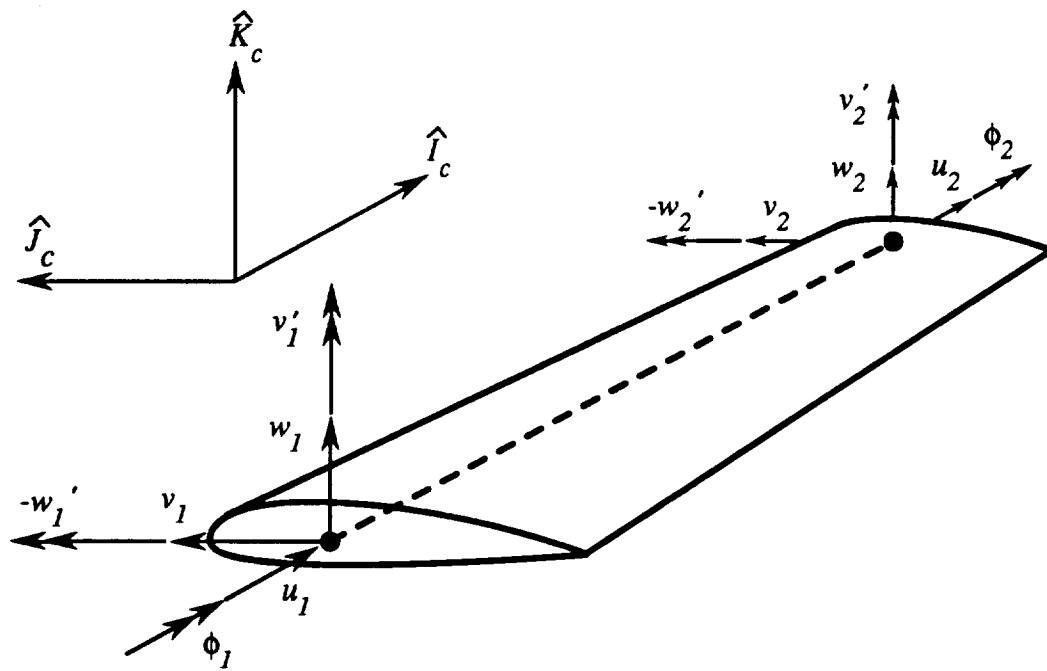
Figure 3.3: Beam element showing external discrete degrees of freedom.

(a) Fundamental modes.

(b) Second bending modes.

(c) Third bending modes.
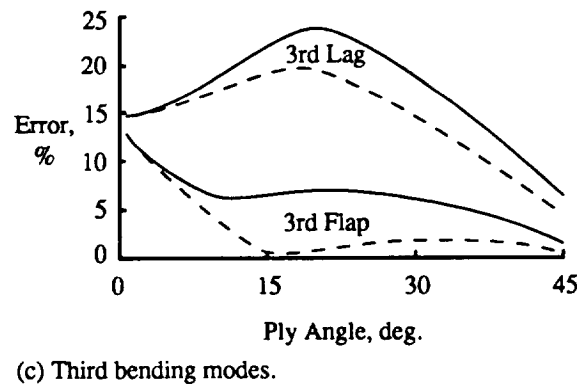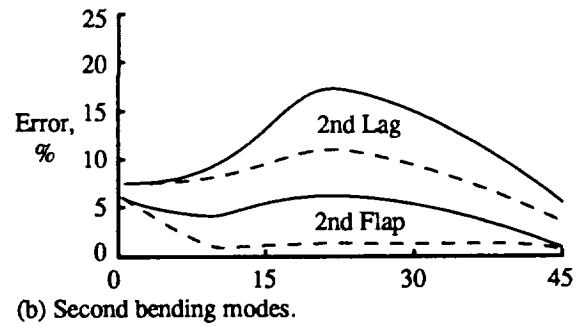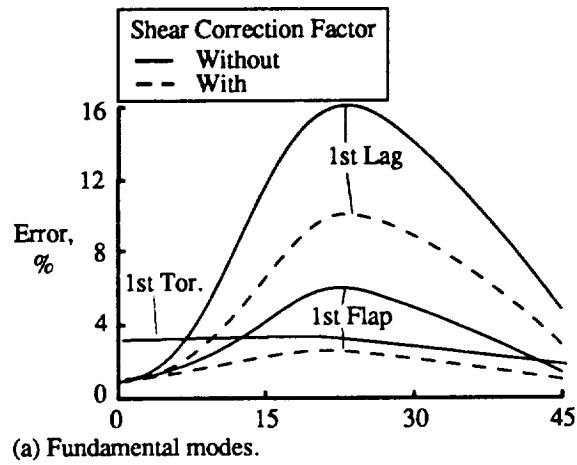
Figure 3.4: Error in frequency predictions as a function of ply angle for the anti-symmetric box beam.
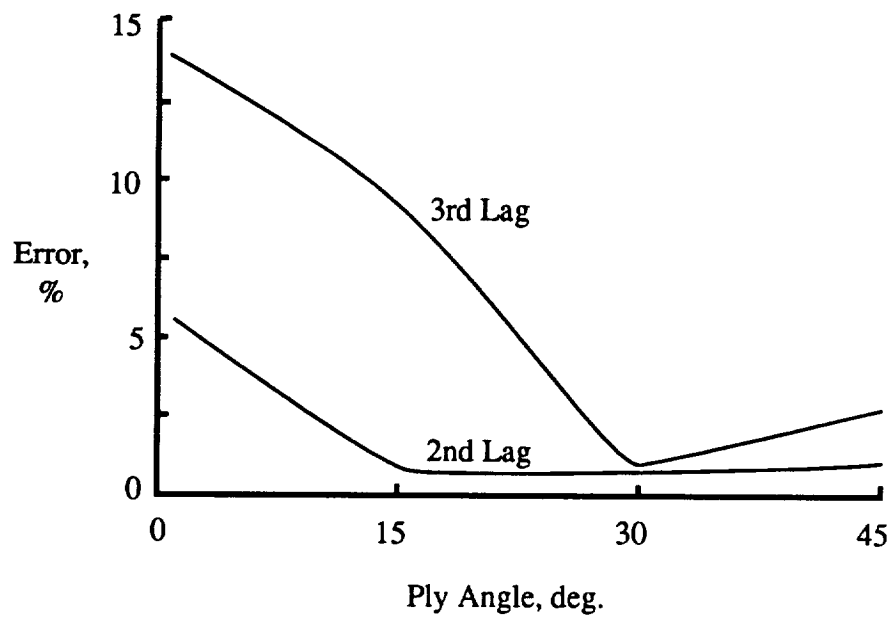
Figure 3.5: Error in lag mode bending frequency predictions after matching fundamental mode frequencies.
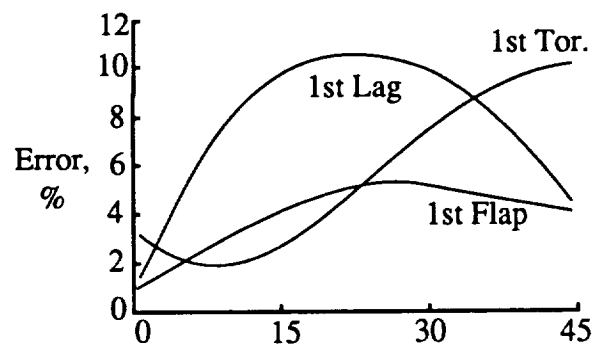
(a) Fundamental modes.
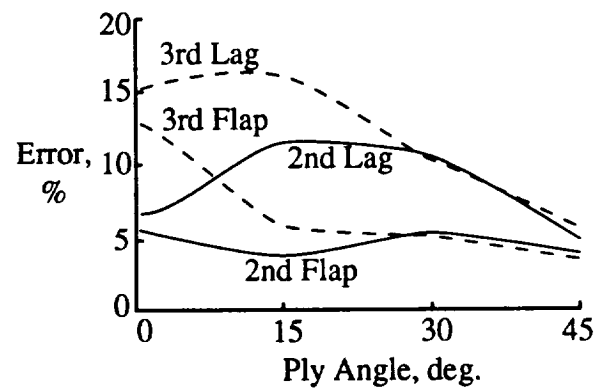
(b) Second and third bending modes.

Figure 3.6: Error in frequency predictions as a function of ply angle for the symmetric box beam.

125
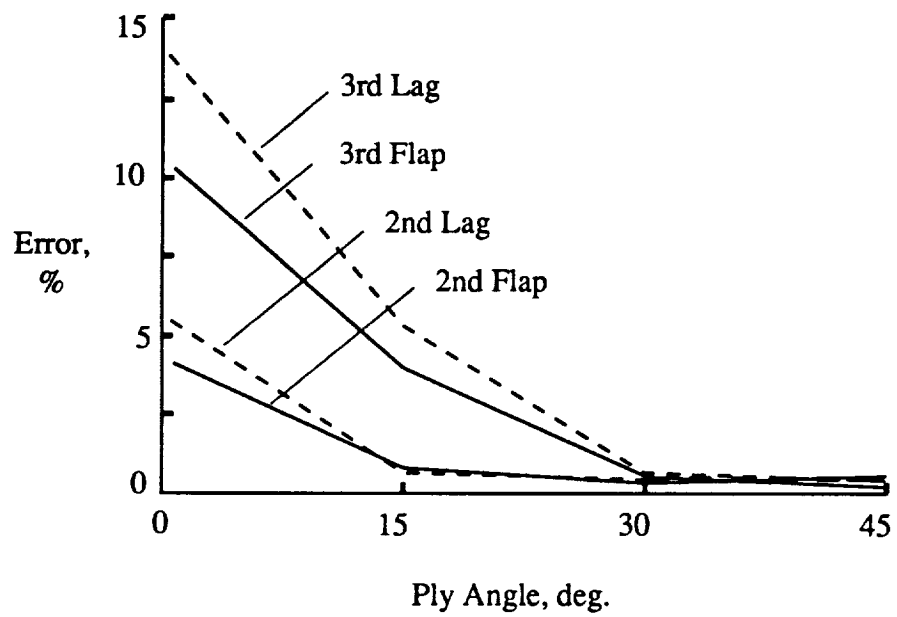
Figure 3.7: Error in higher mode bending frequency predictions after matching fundamental mode frequencies.

(a) Fundamental modes.

Pretwist in Box Beam, deg.
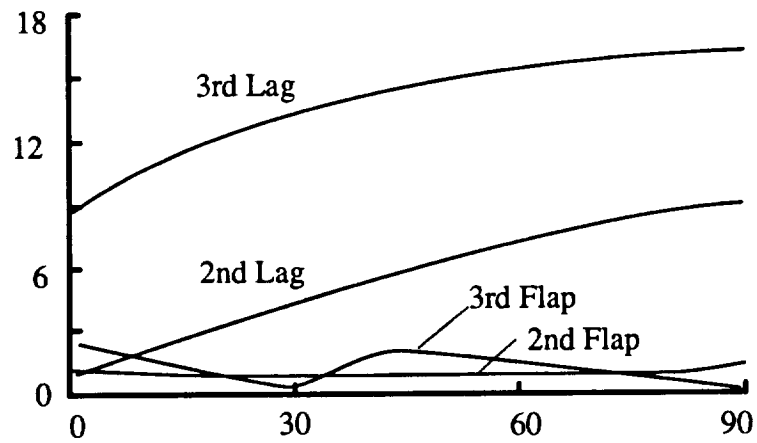
(b) Second and third bending modes.

Figure 3.8: Error in frequency predictions as a function of the anti-symmetric beam pretwist.
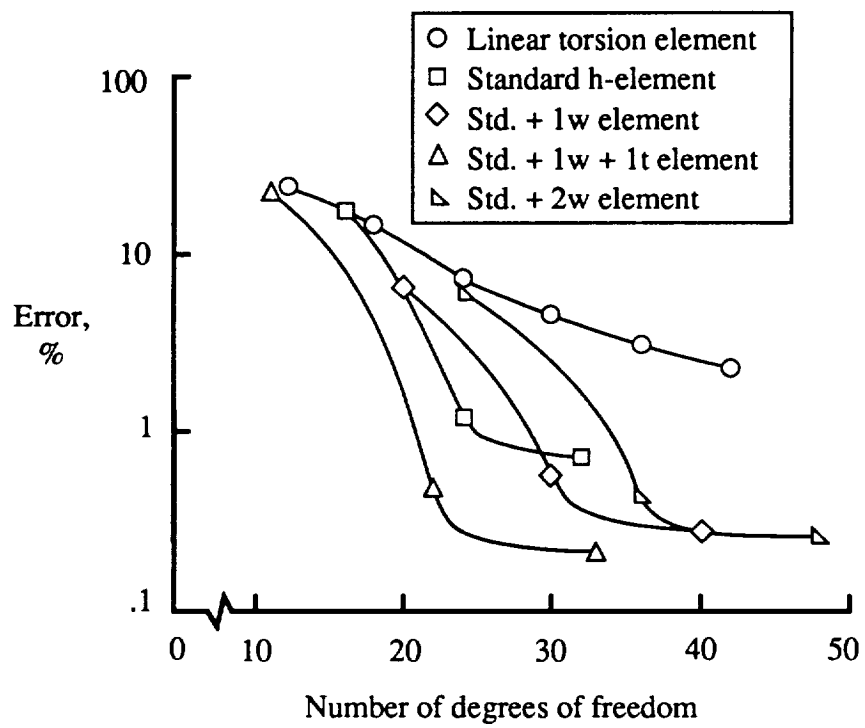
Figure 3.9: Convergence of the untwisted symmetric-case box beam.
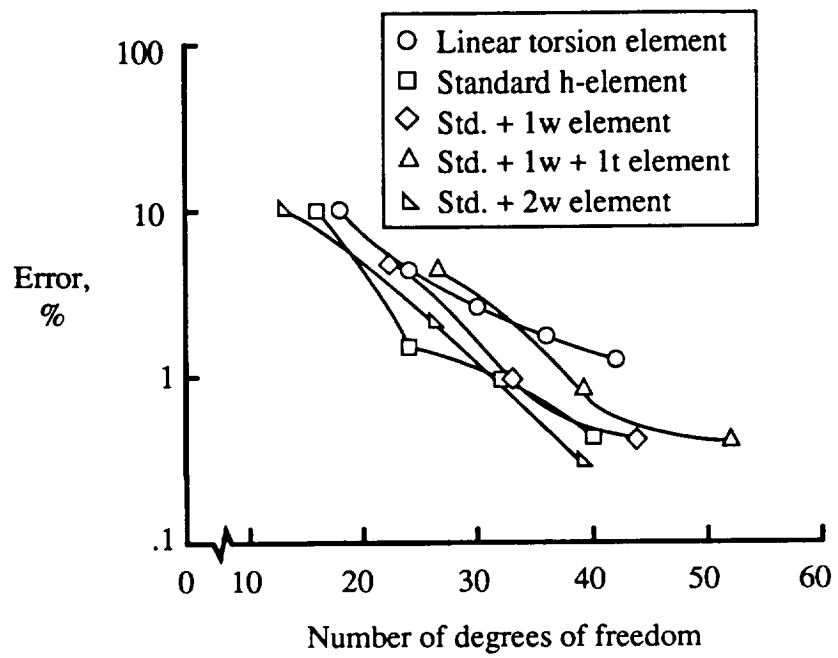
Figure 3.10: Convergence of the 40° twisted symmetric-case box beam.

129

Chapter 4

Structural Modeling of a Tiltrotor with Anisotropic Blades

The tiltrotor configuration requires several substantial modifications to the helicopter structural modeling which exists in UMARC. The modifications are necessary because of the large angle of attack of the pylon and requirements for additional hub-related degrees of freedom which do not currently exist in UMARC. It also has been determined that important terms for tiltrotor dyanmics, which are associated with rotor precone, do not appear in the current UMARC formulations. These terms will be included in the present derivations. The required changes are extensive enough that it is necessary to derive the new structural equations from basic principles. The derivation of the tiltrotor structural model, however, does follow the general guidelines of the derivation of the helicopter structural model used in UMARC. The significant similarities and differences between the helicopter and tiltrotor derivations are discussed throughout this chapter.

In the first part of this chapter, the tiltrotor modeling assumptions and frames of reference are introduced. Important considerations for a gimballed rotor system are included in this section. An energy formulation based on Hamilton's principle (used in UMARC formulations) is applied to the present model, resulting in sys-

tems of equations associated with the strain and kinetic energies. The formulation for elastic strain energy shows the differences related to precone between the past and present formulations. A new definition for blade foreshortening is defined as a result, and this definition is extended into the derivation of kinetic energy. The final linear mass, damping, and stiffness terms of the system are then defined.

4.1 The Tiltrotor Model

The fuselage motion is not considered in the present formulation. There are a number of tiltrotor wind tunnel tests based on cantilevered wing models to validate the theory before additional complexities associated with fuselage motion are added to the system. The tiltrotor is modeled as an elastic wing cantilevered to a fixed support. At the wing tip, a single rotor system is mounted to a rigid pylon which can rotate between airplane and hover modes as illustrated in Fig. 4.1. The rotor system consists of an arbitrary number of elastic blades, N_b. The wing and each blade are assumed to be elastic beams undergoing flap bending, lag bending, elastic twist, and axial deflections. The rotor pylon, though itself considered rigid, may pivot about the wing elastic axis, and may be set at any arbitrary angle with respect to the wing. In this dissertation, the pylon angle is 0° when the pylon points straight up (helicopter mode) and is 90° when the pylon points straight forward (airplane mode). The more common tiltrotor terminology in use today is just the opposite, 90° when the pylon points straight up (helicopter mode) and 0° when the pylon points straight forward (airplane mode). The different definition is used for the present derivation to be consistent with the equations of motion already established in the general purpose rotorcraft code known as UMARC. The pylon angle is closely related to the shaft angle of that code which is defined with 0° pointing straight up.

The types of rotor systems which can be accommodated in UMARC are the

131

bearingless, hingeless, and articulated rotor systems. Tiltrotors often use a gimbal rotor system which is considered in the present formulation.

4.2   Frames of Reference

The coordinate systems and transformations associated with the frames of reference used in the formulation of the tiltrotor structural model are defined in this section. For the present formulation, an inertial frame of reference is placed on the tiltrotor wing-tip on the wing before deformation as illustrated in Fig. 4.2. Note that the origin of this frame is at the pylon pivot point (point about which the pylon angle is defined) which is assumed to be close to or on the wing elastic axis at the wing tip.

The wing itself is flexible so a deformed-wing frame of reference is required to describe motion at the wing-tip. This motion is similar to the hub motion of a conventional helicopter if the pylon height is set to zero. Because of this similarity, the degrees of freedom associated with the transformation from the undeformed to the deformed wing reference frames are termed *hub* degrees of freedom. Five of the six hub degrees of freedom represented in the present formulation are analgous to the five original UMARC fuselage degrees of freedom. The original UMARC fuselage degrees of freedom for a helicopter configuration are given by x_f (translation positive aft), y_f (translation positive starboard), z_f (translation positive up), α_s (shaft pitch angle positive nose-down), and ϕ_s (roll angle positive starboard) while the new hub degrees of freedom are given by x_h (translation positive aft), y_h (translation positive starboard), z_h (translation positive up), α_h (pitch angle positive wing leading edge down), ϕ_h (roll angle positive for top of pylon moving starboard), and ζ_h (yaw angle positive for wing leading edge port). Note that these definitions are based on the starboard tiltrotor wing and rotor system. The inertial and deformed wing reference frames are illustrated in Figure 4.2.

132

The hub reference frame is offset from the deformed wing frame by the pylon height and is oriented in the same direction when the pylon angle is set to zero. The pylon angle α_p is assumed to be a large steady angle, and its effect on orientation of the hub frame is illustrated in Figure 4.3. While the hub frame remains fixed, a rotating blade frame rotates with the blade about the hub frame as illustrated in Fig. 4.4, and in the absense of precone or gimbal angle the vector I_r runs along the undeformed blade span.

A unique feature of tiltrotors is the common use of a gimbal rotor system. A gimbal rotor system acts like a ball joint at the center of rotation; the lead-lag behavior is similar to a hingeless rotor system and the flap behavior is similar to an articulated rotor system hinged at the center of rotation. It is convenient to visualize a gimbal reference frame as a fixed frame defined with the same origin as the hub frame, but oriented at angles β_{GC} and β_{GS} with respect to the hub frame as illustrated in Fig. 4.5. However, the gimbal flapping motion does not alter the swash-plate angle so the pitch angle of the rotating blade outboard of the pitch bearing remains unchanged by the gimbal flapping (ignoring any pitch-flap coupling for the time being). The fixed frame gimbal does not then provide a "proper" transformation for the physics of the system. The proper transformation is then to consider the gimbal flapping in the rotating system as a single degree of freedom β_G which always transforms into two fixed-system degrees of freedom regardless of the number of blades. The transformation is given by

$$\beta_G = \beta_{GC} \cos \psi + \beta_{GS} \sin \psi \qquad (4.1)$$

and because the gimbal angle is a function of time

$$\dot{\beta}_G = \dot{\beta}_{GC} \cos \psi + \dot{\beta}_{GS} \sin \psi + \beta_{GS} \Omega \cos \psi - \beta_{GC} \Omega \sin \psi \qquad (4.2)$$

The fixed system degrees of freedom associated with the gimbal are considered part of the hub set of degrees of freedom as a matter of convenience which gives a total

of eight hub terms. The gimbal may be locked out when articulated, hingeless, or bearingless rotor systems (which do not feature this motion) are modeled.

Following the above explanation, the next transformation in the sequence after the rotating-blade system is the undeformed blade system. From the rotating blade system a transformation is defined to the undeformed blade system through an angle previously defined in Chapter 3 as the precone angle. To account for the possibility of a gimbal rotor system, this transformation now includes the gimbal angle as defined in the rotating system. What was β_p now becomes $\beta_p + \beta_G$ as shown in Fig. 4.6.

The remaining two required reference frames, the cross-section reference frame and the deformed reference frame, were defined as part of the formulation of strain and kinetic energy in Chapter 3. The inertial reference frame of that formulation is essentially replaced by the sequence of reference systems from the present inertial system to the hub reference frame, and then the precone transformation is modified to include the gimbal angle.

The sequence of seven coordinate systems from the inertial to the deformed system is as follows (a notation of identification for each system is given in parenthesis): inertial (i), deformed-wing (w), hub (h), rotating (r), undeformed-blade (u), cross-section (c), and deformed-blade (d). The unit vector triads of each coordinate system are related to the triads of the previous coordinate system in the sequence through the following transformations:

$$
\left\{
\begin{array}{c}
\hat{I}_d \\
\hat{J}_d \\
\hat{K}_d
\end{array}
\right\}
= [T_{dc}]
\left\{
\begin{array}{c}
\hat{I}_c \\
\hat{J}_c \\
\hat{K}_c
\end{array}
\right\}
\tag{4.3}
$$

$$
\left\{
\begin{array}{c}
\hat{I}_c \\
\hat{J}_c \\
\hat{K}_c
\end{array}
\right\}
= [T_{cu}]
\left\{
\begin{array}{c}
\hat{I}_u \\
\hat{J}_u \\
\hat{K}_u
\end{array}
\right\}
\tag{4.4}
$$

$$\left\{ \begin{array}{c} \hat{I}_u \\ \hat{J}_u \\ \hat{K}_u \end{array} \right\} = [T_{ur}] \left\{ \begin{array}{c} \hat{I}_r \\ \hat{J}_r \\ \hat{K}_r \end{array} \right\} \tag{4.5}$$

$$\left\{ \begin{array}{c} \hat{I}_r \\ \hat{J}_r \\ \hat{K}_r \end{array} \right\} = [T_{rh}] \left\{ \begin{array}{c} \hat{I}_h \\ \hat{J}_h \\ \hat{K}_h \end{array} \right\} \tag{4.6}$$

$$\left\{ \begin{array}{c} \hat{I}_h \\ \hat{J}_h \\ \hat{K}_h \end{array} \right\} = [T_{hw}] \left\{ \begin{array}{c} \hat{I}_w \\ \hat{J}_w \\ \hat{K}_w \end{array} \right\} \tag{4.7}$$

$$\left\{ \begin{array}{c} \hat{I}_w \\ \hat{J}_w \\ \hat{K}_w \end{array} \right\} = [T_{wi}] \left\{ \begin{array}{c} \hat{I}_i \\ \hat{J}_i \\ \hat{K}_i \end{array} \right\} \tag{4.8}$$

The six transformation matrices required for the full sequence are defined as follows:

$$[T_{dc}] = \begin{bmatrix} 1 & v'_c - w_c\theta'_0 & w'_c + v_c\theta'_0 \\ \begin{array}{l} -(v'_c - w_c\theta'_0)\cos\phi \\ -(w'_c + v_c\theta'_0)\sin\phi \end{array} & \theta_0\sin\phi & \sin\phi \\ & + \cos\phi & \\ \begin{array}{l} -(w'_c + v_c\theta'_0)\cos\phi \\ +(v'_c - w_c\theta'_0)\sin\phi \end{array} & \theta_0\cos\phi & \cos\phi \\ & -\sin\phi & \end{bmatrix} \tag{4.9}$$

$$[T_{cu}] = \begin{bmatrix} 1 & 0 & 0 \\ 0 & \cos\theta_0 & \sin\theta_0 \\ 0 & -\sin\theta_0 & \cos\theta_0 \end{bmatrix} \tag{4.10}$$

$$[T_{ur}] = \begin{bmatrix} \cos\beta_{pg} & 0 & -\sin\beta_{pg} \\ 0 & 1 & 0 \\ \sin\beta_{pg} & 0 & \cos\beta_{pg} \end{bmatrix} \qquad (4.11)$$

$$[T_{rh}] = \begin{bmatrix} \cos\psi & \sin\psi & 0 \\ -\sin\psi & \cos\psi & 0 \\ 0 & 0 & 1 \end{bmatrix} \qquad (4.12)$$

$$[T_{hw}] = \begin{bmatrix} \cos\alpha_p & 0 & -\sin\alpha_p \\ 0 & 1 & 0 \\ \sin\alpha_p & 0 & \cos\alpha_p \end{bmatrix} \qquad (4.13)$$

$$[T_{wi}] = \begin{bmatrix} \cos\psi_h & \sin\psi_h & 0 \\ -\sin\psi_h & \cos\psi_h & 0 \\ 0 & 0 & 1 \end{bmatrix} \begin{bmatrix} \cos\alpha_h & 0 & -\sin\alpha_h \\ 0 & 1 & 0 \\ \sin\alpha_p & 0 & \cos\alpha_h \end{bmatrix}$$
$$\begin{bmatrix} 1 & 0 & 0 \\ 0 & \cos\phi_h & -\sin\phi_h \\ 0 & \sin\phi_h & \cos\phi_h \end{bmatrix} \qquad (4.14)$$

The transformation T_{dc} was derived previously in Chapter 3. The transformation T_{cu} accounts for pitch angle of the cross-section with respect to the plane of rotation. The pitch angle θ_0 is a combination of blade collective, cyclic, and pretwist, and is not assumed to be a small angle. T_{ur} accounts for the blade precone and gimbal angles, both of which are assumed to be of order ϵ and positive in the flap-up direction. As will be seen later in the derivation, β_G is a function of time while β_p is not. T_{rh} accounts for the blade rotation angle $\psi = \Omega t$ defined as a positive rotation about the $\hat{K}_r$ vector and is not a small angle. The transformation T_{hw} accounts for the steady pylon angle setting (at $0°$ the rotor points up for helicopter mode, at $90°$ the rotor points forward for airplane mode) which is not assumed to be a small angle. The final transformation accounts for deformation rotations of

the wing at the wing-tip, α_h, ϕ_h, and ζ_h. These three angles are of order ϵ.

Because all the coordinate systems are orthogonal, the above transformation matrices may be inverted by taking the transpose, producing the following relationships for the inverse transforms

$$[T_{cd}] \quad = [T_{dc}]^{-1} \quad = [T_{dc}]^T \tag{4.15}$$

$$[T_{uc}] \quad = [T_{cu}]^{-1} \quad = [T_{cu}]^T \tag{4.16}$$

$$[T_{ru}] \quad = [T_{ur}]^{-1} \quad = [T_{ur}]^T \tag{4.17}$$

$$[T_{hr}] \quad = [T_{rg}]^{-1} \quad = [T_{rh}]^T \tag{4.18}$$

$$[T_{wh}] \quad = [T_{hw}]^{-1} \quad = [T_{hw}]^T \tag{4.19}$$

$$[T_{iw}] \quad = [T_{wi}]^{-1} \quad = [T_{wi}]^T \tag{4.20}$$

The transformation from one frame to any other is accomplished by multiplying through the applicable part of the transformation sequence. For example, the transformation from the hub to the cross-section reference system is given by

$$\left\{ \begin{array}{c} \hat{I}_h \\ \hat{J}_h \\ \hat{K}_h \end{array} \right\} = [T_{hc}] \left\{ \begin{array}{c} \hat{I}_c \\ \hat{J}_c \\ \hat{K}_c \end{array} \right\} = [T_{hr}][T_{ru}][T_{uc}] \left\{ \begin{array}{c} \hat{I}_c \\ \hat{J}_c \\ \hat{K}_c \end{array} \right\} \tag{4.21}$$

and the transformation from the cross-section blade reference frame back to the hub frame is given by

$$\left\{ \begin{array}{c} \hat{I}_c \\ \hat{J}_c \\ \hat{K}_c \end{array} \right\} = [T_{ch}] \left\{ \begin{array}{c} \hat{I}_h \\ \hat{J}_h \\ \hat{K}_h \end{array} \right\} = [T_{cu}][T_{ur}][T_{rh}] \left\{ \begin{array}{c} \hat{I}_h \\ \hat{J}_h \\ \hat{K}_h \end{array} \right\}$$

$$= [T_{uc}]^T [T_{ru}]^T [T_{hr}]^T \left\{ \begin{array}{c} \hat{I}_h \\ \hat{J}_h \\ \hat{K}_h \end{array} \right\} \tag{4.22}$$

The transformations discussed above are used throughout the remaining sections to define displacements and velocities in the various reference frames.

4.3 Nondimensionalization and Ordering Scheme

The present formulation is developed in nondimensional form consistant with that used in UMARC. The physical quantities are nondimensionalized by reference parameters associated with the rotor system as follows:

$$\text{Length} \quad R \tag{4.23}$$

$$\text{Time} \quad \Omega^{-1} \tag{4.24}$$

$$\text{Mass/Length} \quad m_0 \tag{4.25}$$

$$\text{Velocity} \quad \Omega R \tag{4.26}$$

$$\text{Acceleration} \quad \Omega^2 R \tag{4.27}$$

$$\text{Force} \quad m_0 \Omega^2 R^2 \tag{4.28}$$

$$\text{Moment} \quad m_0 \Omega^2 R^3 \tag{4.29}$$

$$\text{Energy or Work} \quad m_0 \Omega^2 R^3 \tag{4.30}$$

The reference parameter m_0 is defined as the distributed mass of a uniform blade which has the same flap inertia as the blade under consideration (which may be nonuniform). This parameter is given by

$$m_0 = \frac{3 I_\beta}{R^3} = \frac{3 \int_0^R m r^2 dr}{R^3} \tag{4.31}$$

The present formulation is explicit and nonlinear. In this type of formulation, the number of terms can quickly become unmanagable. In general, an ordering scheme is adopted to reduce the number of nonlinear terms retained in the formulation. It identifies those terms which have little or no impact on the system under the geometric assumptions adopted. Terms of order ϵ^{n+2} are ignored when terms up to ϵ^n exist in the same energy expression, and ϵ is a quantity equivalent to the maximum bending rotation expected in the beam model. The ordering scheme used in the tiltrotor formulation is slightly different from that used in previous

138

formulations associated with UMARC. As elastic coupling in rotor blades can result in large elastic twist, the present ordering scheme considers elastic twist to be of order 1 rather than of order ϵ as it has in past formulations. The order of important nondimensional quantities associated with the tiltrotor formulation are listed as follows:

$$O(1) = \mu, \frac{x}{R}, \frac{h}{R}, \frac{m}{m_0}, \frac{\partial}{\partial\psi}, \frac{\partial}{\partial x},$$

$$\cos\psi, \sin\psi, \cos\theta_1, \sin\theta_1, \cos\alpha_p, \sin\alpha_p,$$

$$\theta_0, \theta_1, \phi \tag{4.32}$$

$$O(\epsilon) = \frac{v}{R}, \frac{w}{R}, \beta_p, \beta_{GC}, \beta_{GS}$$

$$\frac{\dot{x}_h}{R}, \frac{\dot{y}_h}{R}, \frac{\dot{z}_h}{R}, \alpha_h, \phi_h, \zeta_h, \dot{\alpha}_h, \dot{\phi}_h, \dot{\zeta}_h,$$

$$\frac{\eta_r}{R}, \frac{e_d}{R}, \frac{e_A}{R}, \frac{e_g}{R} \tag{4.33}$$

$$O(\epsilon^2) = \frac{u_e}{R} \tag{4.34}$$

4.4 Formulation Using Hamilton's Principle

The tiltrotor formulation is based on Hamilton's variational principle generalized for a nonconservative system which may be expressed as

$$\delta\Pi = \int_{t_1}^{t_2} (\delta U - \delta T - \delta W)\, dt = 0 \tag{4.35}$$

δU is the variation of the elastic strain energy, δT is the variation of kinetic energy, and δW is the work done by nonconservative forces which are of aerodynamic origin in the present system. The contributions to these energy expressions from the rotor blades, hub, and wing may be summed as

$$\delta U = \left(\sum_{m=1}^{N_b} \delta U_b \right) + \delta U_h + \delta U_w \tag{4.36}$$

$$\delta T = \left(\sum_{m=1}^{N_b} \delta T_b \right) + \delta T_h + \delta T_w \tag{4.37}$$

139

$$\delta W = \left(\sum_{m=1}^{N_b} \delta W_b \right) + \delta W_h + \delta W_w \tag{4.38}$$

where b refers to the blade, h to the hub, and w to the wing. The work is performed by the aeordynamic loads on the rotor blades which is considered later in Chapter 5. There is no contribution of the structural model to work, only the elastic strain (potential) energy and the kinetic energy (and associated mass, damping, and stiffness matrices) are derived in the present chapter. The elastic strain energy is the result of rotor blade and wing deformations. The elastic strain energy of the rotor blade with the hub fixed was derived in Chapter 3, but some modifications for the hub motion and rotor precone must be considered for these results to be valid. The wing structural model is the same as the rotor blade with $\Omega = 0$ so there is no need for a new formulation of elastic or kinetic energy for the wing contribution. The kinetic energy of the rotor system, which was derived in Chapter 3 for a fixed hub, is invalid for hub motion, and is thus reformulated with the hub motion included in the present chapter.

4.4.1   Formulation of Elastic Strain Energy

Blade Elastic Strain Energy

On the surface, it would not seem necessary to reconsider the elastic strain energy of the rotor blade as defined in Chapter 3 for the tiltrotor configuration. This is because the orientation of the rotor in space should not influence the elastic deformation which is defined relative to the undeformed blade. If the important influence of precone had been included properly in this formulation then this would indeed be the case. The present definition for nonlinear strain includes rigid body motion as was seen in the previous development of Chapter 3. There, a foreshortening strain variable, u_F, was defined so that the centrifugal stiffening effect associated with the kinematic contribution to rotor foreshortening was removed

from the strain energy formulation, and through the same variable substitution, reappeared in the kinetic energy formulation. Unfortunately, that formulation (like past UMARC formulations) does not account for the additional rigid body motions associated with precone. The orientation of the blade with respect to the hub plane influences the centrifugal force on the blade which, in the application of Hamilton's principle, appears first in the strain energy. The present section redefines the foreshortening substitution to include the precone influence and thereby improves the formulation by accounting for centrifugal-elastic coupling effects arising from the precone.

The fundamental kinematic variables from Chapter 3 were defined in the undeformed-blade coordinate system as u, v, and w. The undeformed-blade coordinate system may be preconed at an angle β_p with respect to the rotating blade coordinate system as shown in Figure 4.6. Three new kinematic variables are defined in this system as u_r, v_r, and w_r. The relationship between these new kinematic variables and the kinematic variables of the undeformed-blade coordinate system are given by the transformation T_{ur} as

$$u_r = u \cos \beta_p - w \sin \beta_p \qquad (4.39)$$

$$v_r = v \qquad (4.40)$$

$$w_r = w \cos \beta_p + u \sin \beta_p \qquad (4.41)$$

Since β_p is a small angle and u is an order of magnitude smaller than w, these relationships may be simplified to

$$u_r = u - w\beta_p \qquad (4.42)$$

$$v_r = v \qquad (4.43)$$

$$w_r = w \qquad (4.44)$$

Now, w may be defined as:

$$w = w_e + v\phi \qquad (4.45)$$

141

where w_e is the elastic flapwise deformation and $v\phi$ is the rigid body motion in the flap direction due to the combination of lag and twist deformation. The axial displacement for the precone-modified formulation is then written as

$$u_r = u - \beta_p(w_e + v\phi) \tag{4.46}$$

It is apparent then that the only significant influence of the precone is the shortening of the axial kinematic variable by the term $\beta_p(w_e + v\phi)$. Since this term modifies the blade extension, it will modify the blade stiffness via centrifugal forces, similar to the foreshortening discussed in Chapter 3.

Substitution of the new definition for axial displacement (Eqn. 4.46) into the position vector defined by Eqn. 3.17, taking derivatives defined by Eqns. 3.23-3.28, and substitution of these results into the strain definitions given by Eqns. 3.40-3.42 yields the precone-modified strains as:

$$\begin{aligned}
\epsilon_{xx} &= u' + \beta_p w' + \beta_p v\phi' + \beta_p v'\phi + \frac{1}{2}v'^2 + \frac{1}{2}w'^2 + \\
&\quad \frac{1}{2}(\eta^2 + \zeta^2)\phi'^2 + (\phi'\psi_{uT})' - v''[\eta\cos(\theta_0 + \phi) - \zeta\sin(\theta_0 + \phi)] \\
&\quad -w''[\eta\sin(\theta_0 + \phi) + \zeta\cos(\theta_0 + \phi)] \tag{4.47}
\end{aligned}$$

$$\epsilon_{x\eta} = v'_s\cos(\theta_0 + \phi) + w'_s\sin(\theta_0 + \phi) + (\psi_{uT,\eta} - \zeta)\phi' \tag{4.48}$$

$$\epsilon_{x\zeta} = w'_s\cos(\theta_0 + \phi) - v'_s\sin(\theta_0 + \phi) + (\psi_{uT,\zeta} + \eta)\phi' \tag{4.49}$$

where the kinematic variables are now defined in the rotating-blade coordinate system although the subscript r has been dropped.

Recall from Chapter 3 that the kinematic foreshortening of the rotor blade is removed from the potential energy formulation through the following substitution

$$u' = u'_e - \frac{1}{2}v'^2 - \frac{1}{2}w'^2 \tag{4.50}$$

and this was necessary to account for the rigid body displacements included in the definition of u. u is now modified to include the rigid body displacement

associated with the precone. The rigid-body motion contribution is then added to the definition of axial strain so that Eqn. 4.50 becomes

$$u' = u'_e - \frac{1}{2}v'^2 - \frac{1}{2}w'^2 - \beta_p(v'\phi + v\phi') \tag{4.51}$$

It then follows that

$$\delta u' = \delta u'_e - v'\delta v' - w'\delta w' - \beta_p(\phi\delta v' + v'\delta\phi + v\delta\phi' + \phi'\delta v) \tag{4.52}$$

$$u = u_e - \frac{1}{2}\int_0^x (v'^2 + w'^2)d\xi - \beta_p \int_0^x (v'\phi + v\phi')d\xi \tag{4.53}$$

$$\delta u = \delta u_e - \int_0^x (v'\delta v' + w'\delta w')d\xi -$$
$$\beta_p \int_0^x (\phi\delta v' + v'\delta\phi + v\delta\phi' + \phi'\delta v)d\xi \tag{4.54}$$

With these new definitions for the axial strain, the strain energy becomes

$$\epsilon_{xx} = u'_e + \beta_p w' + \frac{1}{2}(\eta^2 + \zeta^2)\phi'^2 + (\phi'\psi_{uT})' - v''[\eta\cos(\theta_0 + \phi) - \zeta\sin(\theta_0 + \phi)]$$
$$-w''[\eta\sin(\theta_0 + \phi) + \zeta\sin(\theta_0 + \phi)] \tag{4.55}$$

$$\epsilon_{x\eta} = v'_s\cos(\theta_0 + \phi) + w'_s\sin(\theta_0 + \phi) + (\psi_{uT,\eta} - \zeta)\phi' \tag{4.56}$$

$$\epsilon_{x\zeta} = w'_s\cos(\theta_0 + \phi) - v'_s\sin(\theta_0 + \phi) + (\psi_{uT,\zeta} + \eta)\phi' \tag{4.57}$$

where, again, the kinematic variables are now defined in the rotating-blade coordinate system although the subscript r has been dropped. The linear stiffness matrix terms defined by Eqns. 3.58-3.79 in Chapter 3 are now modified to

$$k_{11} = EA \tag{4.58}$$

$$k_{13} = -EA_\eta\cos\theta_1 \tag{4.59}$$

$$k_{15} = -EA_\eta\sin\theta_1 \tag{4.60}$$

$$k_{17} = EET + EA_{r2}\theta'_0 \tag{4.61}$$

$$k_{18} = EES_c\cos\theta_1 - EES_f\sin\theta_1 \tag{4.62}$$

$$k_{19} = EES_c\sin\theta_1 + EES_f\cos\theta_1 \tag{4.63}$$

$$k_{22} = EA\beta_p \tag{4.64}$$

143

$$k_{33} = EI_c \cos^2\theta_1 + EI_f \sin^2\theta_1 \tag{4.65}$$

$$k_{35} = EI_f \cos\theta_1 \sin\theta_1 - EI_f \cos\theta_1 \sin\theta_1 \tag{4.66}$$

$$k_{37} = ETC \cos\theta_1 - ETF \sin\theta_1 \tag{4.67}$$

$$k_{38} = (EFS_c + ECS_f) \cos\theta_1 \sin\theta_1 \tag{4.68}$$

$$k_{39} = EFS_c \sin^2\theta_1 - ECS_f \cos^2\theta_1 \tag{4.69}$$

$$k_{44} = 0 \tag{4.70}$$

$$k_{55} = EI_f \cos^2\theta_1 + EI_c \sin^2\theta_1 \tag{4.71}$$

$$k_{57} = ETF \cos\theta_1 + ETC \sin\theta_1 \tag{4.72}$$

$$k_{58} = ECS_f \sin^2\theta_1 - EFS_c \cos^2\theta_1 \tag{4.73}$$

$$k_{59} = -(EFS_c + ECS_f) \cos\theta_1 \sin\theta_1 \tag{4.74}$$

$$k_{66} = 0 \tag{4.75}$$

$$k_{77} = GJ \tag{4.76}$$

$$k_{88} = GA_c \cos^2\theta_1 + GA_f \sin^2\theta_1 \tag{4.77}$$

$$k_{89} = (GA_c - GA_f) \cos\theta_1 \sin\theta_1 \tag{4.78}$$

$$k_{99} = GA_f \cos^2\theta_1 + GA_c \sin^2\theta_1 \tag{4.79}$$

with $\theta_1 = \theta_0 + \phi$. The i, j of the stiffness matrix correspond the vector of displacement and displacement variation, respectively, where the displacement variation vector is given by

$$\delta \tilde{v}_i = \left\{ \begin{array}{ccccccccc} \delta u'_e & \delta v' & \delta v'' & \delta w' & \delta w'' & \delta\phi & \delta\phi' & \delta v'_s & \delta w'_s \end{array} \right\} \tag{4.80}$$

These terms agree with those developed in Chapter 3 except for the k_{22} stiffness. An investigation of this particular term showed a negligible influence on flap stiffness of typical rotor blades because the centrifugal-related flap stiffness is dominant. However, care must be exercised in the selection of an axial stiffness which is reasonable since an unreasonably large value may create an influence when precone is present in the system (an infinite axial stiffness will result in an infinite

144

flap stiffness). The stiffness matrix is still applicable to static condensation, as explained in Chapter 3, only there is an additional diagonal term which expands the matrix size to a 5 x 5. The reduced stiffness matrix is now given by

$$k'_{11} = \bar{E}A \tag{4.81}$$

$$k'_{12} = -\bar{E}A_\eta \cos\theta_1 \tag{4.82}$$

$$k'_{13} = -\bar{E}A_\eta \sin\theta_1 \tag{4.83}$$

$$k'_{14} = \bar{E}ET + \bar{E}A_{r^2}\theta'_0 \tag{4.84}$$

$$k'_{22} = \bar{E}I_c \cos^2\theta_1 + \bar{E}I_f \sin^2\theta_1 \tag{4.85}$$

$$k'_{23} = \bar{E}I_f \cos\theta_1 \sin\theta_1 - \bar{E}I_f \cos\theta_1 \sin\theta_1 \tag{4.86}$$

$$k'_{24} = \bar{E}TC \cos\theta_1 - \bar{E}TF \sin\theta_1 \tag{4.87}$$

$$k'_{33} = \bar{E}I_f \cos^2\theta_1 + \bar{E}I_c \sin^2\theta_1 \tag{4.88}$$

$$k'_{34} = \bar{E}TF \cos\theta_1 + \bar{E}TC \sin\theta_1 \tag{4.89}$$

$$k'_{44} = \bar{G}J \tag{4.90}$$

$$k'_{55} = EA\beta_p \tag{4.91}$$

and the corresponding vector of displacement variation is

$$\delta v_i = \left\{ \begin{array}{cccc} \delta u'_e & \delta v'' & \delta w'' & \delta \phi' \delta v' \end{array} \right\} \tag{4.92}$$

Hub Elastic Strain Energy

The strain energy contribution of the hub is given entirely by the gimbal system when hub springs are included. This is a very simple formulation given by

$$U_h = \frac{1}{2} K_{\beta_{GC}} \beta_{GC}^2 + \frac{1}{2} K_{\beta_{GS}} \beta_{GS}^2 \tag{4.93}$$

and the variation of the strain energy is then

$$\delta U_h = K_{\beta_{GC}} \beta_{GC} \delta\beta_{GC} + K_{\beta_{GS}} \beta_{GS} \delta\beta_{GS} \tag{4.94}$$

145

The other hub degrees of freedom do not have any direct elastic strain contribution. The strain energy associated with these motions come from the wing structure so elastic stiffness does not exist until the hub is assembled to the wing model. The assembly process will be discussed later in this chapter.

4.4.2 Formulation of Kinetic Energy

To reformulate the kinetic energy of the system with hub motion included, the contributions of hub motion to the total velocity must be considered. In this section, the velocity components in the three principle inertial frame directions are derived. There are two contributions to these velocities considered in the present derivation: the blade motion and the hub motion. As mentioned previously, the fuselage motion contribution is not considered, and is not required for development of a cantilevered wing tiltrotor model. The general expression of the velocity vector for the motion of the blade and hub together can be written relative to any frame of reference as

$$\vec{V} = \vec{V}_b + \vec{V}_h \qquad (4.95)$$

where $\vec{V}_b$ represents the blade contribution and $\vec{V}_h$ represents the hub contribution to the total velocity.

The contribution of the blade and hub velocities is determined by taking the time derivative of the position vector in the inertial frame. This approach eliminates the need to determine the time rate of change of a local rotating reference frame with respect to an inertial frame since the local frame in this case *is* the inertial frame. The position vector of an arbitrary point on the cross section of the deformed blade is given by:

$$\vec{R} = \{x_h \hat{I}_i, y_h \hat{J}_i, z_h \hat{K}_i\} + h\hat{K}_w + \{(x+u)\hat{I}_u, v\hat{J}_u, w\hat{K}_u\} + \{0, \eta\hat{J}_d, \zeta\hat{K}_d\} \quad (4.96)$$

146

which may be written entirely in the inertial reference frame as

$$\vec{R} = (\{x_h, y_h, z_h\} + \{0, 0, h\}[T_{wi}] + \{(x+u), v, w\}[T_{ui}]$$

$$+ \{0, \eta, \zeta\}[T_{di}]) \left\{ \begin{array}{c} \hat{I}_i \\ \hat{J}_i \\ \hat{K}_i \end{array} \right\} \tag{4.97}$$

The blade and hub degrees of freedom are functions of time as is the azimuth angle ψ which may be written as Ωt. The precone angle β_p is assumed to be constant. After carrying out the transformations and applying the ordering scheme, the velocity due to blade and hub motions is then defined by

$$\vec{V}_b + \vec{V}_h = \frac{\partial \vec{R}}{\partial t} = V_x \hat{I}_i + V_y \hat{J}_i + V_z \hat{K}_i \tag{4.98}$$

with V_x, V_y, and V_z provided as follows (note separation between terms provided to help delineate between $O(1)$, $O(\epsilon)$, and $O(\epsilon^2)$ contributions to each velocity)

$$V_x = -\cos\alpha_p \sin\psi\, x -$$

$\cos\alpha_p \cos\psi \cos\theta_1\, \eta - \dot{\alpha}_h \cos\alpha_p\, h - \cos\alpha_p \cos\psi\, v - \cos\alpha_p \sin\psi\, \dot{v} -$

$\sin\alpha_p\, \dot{w} - \dot{\alpha}_h \cos\psi \sin\alpha_p\, x - \dot{\beta}_{GC}\cos\psi \sin\alpha_p\, x - \dot{\beta}_{GS}\cos\psi \sin\alpha_p\, x +$

$\alpha_h \sin\alpha_p \sin\psi\, x + \dot{\beta}_{GC}\sin\alpha_p \sin\psi\, x - \dot{\beta}_{GS}\sin\alpha_p \sin\psi\, x + \dot{x}_h -$

$\cos\psi\, x\zeta_h - \sin\psi\, x\dot{z}_h + \cos\alpha_p \cos\psi \sin\theta_1\, \zeta +$

$\alpha_h \cos\psi \cos\theta_1\, \eta\sin\alpha_p + \alpha_h \dot{\alpha}_h h\sin\alpha_p + \dot{\alpha}_h \cos\theta_1\, \eta\sin\alpha_p \sin\psi -$

$\dot{\alpha}_h \cos\alpha_p\, \eta\sin\theta_1 + \beta_p \cos\alpha_p\, \eta\sin\psi \sin\theta_1 + 2\dot{\beta}_{GC}\cos\alpha_p \cos\psi\, \eta\sin\psi \sin\theta_1 -$

$\dot{\beta}_{GS}\cos\alpha_p \cos\psi\, \eta\sin\psi \sin\theta_1 - \cos\theta_1\, \eta\sin\alpha_p\, \dot{\theta}_1 + \cos\alpha_p\, \eta\sin\psi \sin\theta_1\, \dot{\theta}_1 -$

$\cos\alpha_p \sin\psi\, u + \cos\alpha_p \cos\psi\, \dot{u} + \alpha_h \cos\psi \sin\alpha_p\, v +$

$\dot{\alpha}_h \sin\alpha_p \sin\psi\, v + \alpha_h \sin\alpha_p \sin\psi\, \dot{v} - \cos\alpha_p \cos\psi \cos\theta_1\, \eta v' - \dot{\alpha}_h \cos\alpha_p\, w +$

$$\beta_p\cos\alpha_p\sin\psi\,w + 2\dot\beta_{GC}\cos\alpha_p\cos\psi\sin\psi\,w - \dot\beta_{GS}\cos\alpha_p\cos\psi\sin\psi\,w -$$

$$\dot\alpha_h\cos\alpha_p\,\dot w - \beta_p\cos\alpha_p\cos\psi\,\dot w - \beta_{GS}\cos\alpha_p\cos\psi\sin\psi\,\dot w -$$

$$\cos\alpha_p\cos\psi\,\eta\sin\theta_1\,\dot w' - \dot\alpha_h\beta_p\cos\alpha_p\,x - \alpha_h\dot\alpha_h\cos\alpha_p\cos\psi\,x -$$

$$\alpha_h\dot\beta_{GC}\cos\alpha_p\cos\psi\,x - \alpha_h\beta_{GS}\cos\alpha_p\cos\psi\,x + \alpha_h\beta_{GC}\cos\alpha_p\sin\psi\,x -$$

$$\dot\alpha_h\beta_{GS}\cos\alpha_p\sin\psi\,x - \alpha_h\dot\beta_{GS}\cos\alpha_p\sin\psi\,x + \beta_{GC}\beta_p\cos\alpha_p\cos\psi\sin\psi\,x -$$

$$\dot\beta_{GS}\beta_p\cos\alpha_p\cos\psi\sin\psi\,x + \cos\theta_1\,\eta\sin\psi\,\zeta_h + \sin\psi\,v\zeta_h - \cos\psi\,\dot v\zeta_h -$$

$$\cos\psi\cos\theta_1\,\eta\dot z_h - \cos\psi\,v\dot z_h + h\sin\alpha_p\,\zeta_h\dot z_h - \dot\alpha_h\beta_{GC}\cos\alpha_p\cos\psi\,x -$$

$$\cos\alpha_p\cos\psi\,x\zeta_h\dot z_h + \cos\alpha_p\cos\theta_1\,\eta\sin\psi\,v' + \cos\alpha_p\,\eta\sin\psi\sin\theta_1\,w' -$$

$$\dot\beta_{GC}\cos\alpha_p\,\cos^2\psi\eta\sin\theta_1 - \beta_{GS}\cos\alpha_p\,\cos^2\psi\eta\sin\theta_1 -$$

$$\dot\beta_{GC}\cos\alpha_p\,\cos^2\psi w - \beta_{GS}\cos\alpha_p\,\cos^2\psi w + \beta_{GS}\cos\alpha_p\,\sin^2\psi w -$$

$$\dot\beta_{GC}\beta_p\cos\alpha_p\,\cos^2\psi x - \beta_{GS}\beta_p\cos\alpha_p\,\cos^2\psi x - \beta_{GC}\dot\beta_{GC}\cos\alpha_p\,\cos^3\psi x -$$

$$\beta_{GC}\beta_{GS}\cos\alpha_p\,\cos^3\psi x + \beta_{GC}^2\cos\alpha_p\,\cos^2\psi\sin\psi\,x -$$

$$\beta_{GS}^2\cos\alpha_p\,\cos^2\psi\sin\psi\,x - \beta_{GC}\dot\beta_{GS}\cos\alpha_p\,\cos^2\psi\sin\psi\,x -$$

$$\beta_{GS}\dot\beta_{GS}\cos\alpha_p\cos\psi\,\sin^2\psi x - \beta_{GC}\cos\alpha_p\,\cos^2\psi\dot w +$$

$$\beta_{GS}\cos\alpha_p\,\eta\sin^2\psi\sin\theta_1 - \dot\beta_{GC}\beta_{GS}\cos\alpha_p\,\cos^2\psi\sin\psi\,x +$$

$$\beta_{GC}\beta_{GS}\cos\alpha_p\cos\psi\,\sin^2\psi x - \dot\alpha_h\cos\alpha_p\cos\theta_1\,\zeta + \beta_p\cos\alpha_p\cos\theta_1\sin\psi\,\zeta +$$

$$2\dot\beta_{GC}\cos\alpha_p\cos\psi\cos\theta_1\sin\psi\,\zeta - \dot\beta_{GS}\cos\alpha_p\cos\psi\cos\theta_1\sin\psi\,\zeta -$$

$$\alpha_h\cos\psi\sin\alpha_p\sin\theta_1\,\zeta - \dot\alpha_h\sin\alpha_p\sin\psi\sin\theta_1\,\zeta +$$

$$\cos\alpha_p\cos\theta_1\sin\psi\,\dot\theta_1\zeta + \sin\alpha_p\sin\theta_1\,\dot\theta_1\zeta +$$

$$\cos\alpha_p\cos\psi\sin\theta_1\,\dot v'\zeta - \cos\alpha_p\cos\psi\cos\theta_1\,\dot w'\zeta -$$

$$\sin\psi\sin\theta_1\,\zeta\zeta_h + \cos\psi\sin\theta_1\,\zeta\dot\zeta_h - \cos\alpha_p\sin\psi\sin\theta_1\,\zeta v' +$$

$$\cos\alpha_p\cos\theta_1\sin\psi\,\zeta w' - \dot\beta_{GC}\cos\alpha_p\,\cos^2\psi\cos\theta_1\,\zeta -$$

$$\beta_{GS}\cos\alpha_p\,\cos^2\psi\cos\theta_1\,\zeta + \beta_{GS}\cos\alpha_p\cos\theta_1\,\sin^2\psi\zeta \tag{4.99}$$

148

$$V_y = \cos\psi\, x +$$

$$\cos\alpha_p\, h\dot\phi - \cos\theta_1\, \eta\sin\dot\psi - \sin\psi\, v + \cos\psi\, \dot v + \cos\psi\, \dot\phi\sin\alpha_p\, x -$$

$$\dot\phi\sin\alpha_p\, \sin\psi\, x + \dot y_h - \cos\alpha_p\, \sin\psi\, x\zeta_h - h\sin\alpha_p\, \dot z_h + \cos\alpha_p\, \cos\psi\, x\dot z_h +$$

$$\sin\psi\, \sin\theta_1\, \zeta -$$

$$\cos\psi\, \cos\theta_1\, \eta\phi\sin\alpha_p - \dot\alpha_h h\phi\sin\alpha_p - \alpha_h h\dot\phi\sin\alpha_p -$$

$$\cos\theta_1\, \eta\dot\phi\sin\alpha_p\, \sin\psi - \beta_p\cos\psi\, \eta\sin\theta_1 + \cos\alpha_p\, \eta\dot\phi\sin\theta_1 -$$

$$\dot\beta_{GC}\cos\psi\, \eta\sin\psi\, \sin\theta_1 - 2\beta_{GS}\cos\psi\, \eta\sin\psi\, \sin\theta_1 - \cos\psi\, \eta\sin\theta_1\, \dot\theta_1 +$$

$$\cos\psi\, u + \sin\psi\, \dot u - \cos\psi\, \phi\sin\alpha_p\, v - \dot\phi\sin\alpha_p\, \sin\psi\, v -$$

$$\phi\sin\alpha_p\, \sin\psi\, \dot v - \cos\theta_1\, \eta\sin\psi\, \dot v' - \beta_p\cos\psi\, w +$$

$$\cos\alpha_p\, \dot\phi w - \dot\beta_{GC}\cos\psi\, \sin\psi\, w - 2\beta_{GS}\cos\psi\, \sin\psi\, w + \cos\alpha_p\, \phi\dot w -$$

$$\beta_p\sin\psi\, \dot w - \beta_{GC}\cos\psi\, \sin\psi\, \dot w - \eta\sin\psi\, \sin\theta_1\, \dot w' +$$

$$\dot\alpha_h\cos\alpha_p\, \cos\psi\, \phi x + \dot\beta_{GC}\cos\alpha_p\, \cos\psi\, \phi x + \beta_{GS}\cos\alpha_p\, \cos\psi\, \phi x +$$

$$\beta_p\cos\alpha_p\, \dot\phi x + \alpha_h\cos\alpha_p\, \cos\psi\, \dot\phi x + \beta_{GC}\cos\alpha_p\, \cos\psi\, \dot\phi x -$$

$$\dot\beta_{GC}\beta_p\cos\psi\, \sin\psi\, x - \beta_{GS}\beta_p\cos\psi\, \sin\psi\, x - \alpha_h\cos\alpha_p\, \phi\sin\psi\, x -$$

$$\beta_{GC}\cos\alpha_p\, \phi\sin\psi\, x + \dot\beta_{GS}\cos\alpha_p\, \phi\sin\psi\, x + \beta_{GS}\cos\alpha_p\, \dot\phi\sin\psi\, x -$$

$$\phi\dot\phi\sin\psi\, x + \beta_{GC}\beta_{GS}\sin\psi^3 x - \beta_{GS}\dot\beta_{GS}\sin\psi^3 x -$$

$$\cos\alpha_p\, \cos\psi\, \cos\theta_1\, \eta\zeta_h - \cos\alpha_p\, \cos\psi\, v\zeta_h - \cos\alpha_p\, \sin\psi\, \dot v\zeta_h -$$

$$\sin\alpha_p\, \dot w\zeta_h - \dot\beta_{GC}\cos\psi\, \sin\alpha_p\, x\zeta_h - \beta_{GS}\cos\psi\, \sin\alpha_p\, x\zeta_h +$$

$$\beta_{GC}\sin\alpha_p\, \sin\psi\, x\zeta_h - \dot\beta_{GS}\sin\alpha_p\, \sin\psi\, x\zeta_h - \cos\alpha_p\, \cos\theta_1\, \eta\sin\psi\, \dot z_h -$$

$$\eta\sin\alpha_p\, \sin\theta_1\, \dot z_h - \cos\alpha_p\, \sin\psi\, v\dot z_h - \sin\alpha_p\, w\dot z_h -$$

$$\beta_p\sin\alpha_p\, x\dot z_h - \beta_{GC}\cos\psi\, \sin\alpha_p\, x\dot z_h - \beta_{GS}\sin\alpha_p\, \sin\psi\, x\dot z_h -$$

$$\sin\psi\, x\zeta_h\dot z_h - \cos\psi\, \cos\theta_1\, \eta v' - \cos\psi\, \eta\sin\theta_1\, w' -$$

$$\beta_{GC} \cos^2\psi\eta\sin\theta_1 \; + \beta_{GC}\eta \, \sin^2\psi\sin\theta_1 \; - \dot{\beta}_{GS}\eta \, \sin^2\psi\sin\theta_1 \; -$$

$$\beta_{GC} \cos^2\psi w + \beta_{GC} \sin^2\psi w - \dot{\beta}_{GS} \sin^2\psi w -$$

$$\beta_{GS} \sin^2\psi\dot{w} - \beta_{GC}\dot{\beta}_{GC} \cos^2\psi\sin\psi \; x -$$

$$\dot{\beta}_{GS}\beta_p \sin^2\psi x - \beta_{GC}\beta_{GS} \cos^2\psi\sin\psi \; x +$$

$$\beta_{GC}\beta_p \sin^2\psi x + \beta_{GC}^2\cos\psi \, \sin^2\psi x - \dot{\beta}_{GC}\beta_{GS}\cos\psi \, \sin^2\psi x -$$

$$\beta_{GS}^2\cos\psi \, \sin^2\psi x - \beta_{GC}\dot{\beta}_{GS}\cos\psi \, \sin^2\psi x -$$

$$\beta_p\cos\psi \, \cos\theta_1 \, \zeta + \cos\alpha_p \, \cos\theta_1 \, \dot{\phi}\zeta - \dot{\beta}_{GC}\cos\psi \, \cos\theta_1 \, \sin\psi \, \zeta -$$

$$2\beta_{GS}\cos\psi \, \cos\theta_1 \, \sin\psi \, \zeta + \cos\psi \, \phi\sin\alpha_p \, \sin\theta_1 \, \zeta + \dot{\phi}\sin\alpha_p \, \sin\psi \, \sin\theta_1 \, \zeta -$$

$$\cos\psi \, \cos\theta_1 \, \dot{\theta}_1\zeta + ssh\sin\theta_1 \, \dot{v}'\zeta - cth\sin\psi \, \dot{w}'\zeta +$$

$$\cos\alpha_p \, \cos\psi \, \sin\theta_1 \, \zeta\zeta_h - \cos\theta_1 \, \sin\alpha_p \, \zeta\dot{\zeta}_h + \cos\alpha_p \, \sin\psi \, \sin\theta_1 \, \zeta\dot{\zeta}_h +$$

$$\cos\psi \, \sin\theta_1 \, \zeta v' - csh\cos\theta_1 \, \zeta w' - \beta_{GC} \, \cos^2\psi\cos\theta_1 \, \zeta +$$

$$\beta_{GC}\cos\theta_1 \, \sin^2\psi\zeta - \dot{\beta}_{GS}\cos\theta_1 \, \sin^2\psi\zeta \qquad (4.100)$$

$$V_z \;\; = \;\; \sin\alpha_p \, \sin\psi \, x$$

$$+\dot{z}_h + \cos\psi \, \cos\theta_1 \, \eta\sin\alpha_p \; + \beta_{GS}\cos\alpha_p \, \cos\psi \, x + \cos\psi \, \sin\alpha_p \, v +$$

$$\cos\alpha_p \, \dot{w} + \dot{\alpha}_h\cos\alpha_p \, \cos\psi \, x - \dot{\phi}_h\sin\psi \, x - \beta_{GC}\cos\alpha_p \, \sin\psi \, x - \cos\psi \, \phi_h x -$$

$$(\alpha_h\cos\alpha_p \, \cos\psi \, \cos\theta_1 \, \eta) - \cos\psi \, \cos\theta_1 \, \eta\dot{\phi}_h -$$

$$\dot{\alpha}_h\cos\alpha_p \, \cos\theta_1 \, \eta\sin\psi \; + \cos\theta_1 \, \eta\phi_h\sin\psi + \dot{\alpha}_h\eta\sin\alpha_p \, \sin\theta_1 \; -$$

$$\beta_p\eta\sin\alpha_p \, \sin\psi \, \sin\theta_1 \; + \cos\alpha_p \, \cos\theta_1 \, \eta\dot{\theta}_1 - \eta\sin\alpha_p \, \sin\psi \, \sin\theta_1 \, \dot{\theta}_1 +$$

$$\sin\alpha_p \, \sin\psi \, u - \cos\psi \, \sin\alpha_p \, \dot{u} - \cos\psi \, \phi_h v - \alpha_h\cos\alpha_p \, \cos\psi \, v -$$

$$\dot{\alpha}_h\cos\alpha_p \, \sin\psi \, v + \phi_h\sin\psi \, v - \cos\psi \, ps\dot{v} - \alpha_h\cos\alpha_p \, \sin\psi \, \dot{v} +$$

$$\sin\alpha_p \, \sin\psi \, \dot{v} - \cos\theta_1 \, \eta\sin\alpha_p \, \sin\psi \, v' + \cos\psi \, \cos\theta_1 \, \eta\sin\alpha_p \, \dot{v}' +$$

$$\dot\alpha_h \sin\alpha_p\, w - \beta_p \sin\alpha_p\, \sin\psi\, w + \alpha_h \sin\alpha_p\, \dot w + \beta_p \cos\psi\, \sin\alpha_p\, \dot w +$$

$$\cos\psi\, \eta \sin\alpha_p\, \sin\theta_1\, \dot w' + \dot\alpha_h \beta_p \sin\alpha_p\, x + \alpha_h \dot\alpha_h \cos\psi\, \sin\alpha_p\, x +$$

$$\cos\psi\, \phi_h \dot\phi_h \sin\alpha_p\, x - \alpha_h \cos\alpha_p\, \sin\psi\, x + \dot\alpha_h \cos\alpha_p\, x_h -$$

$$\dot\phi_h y_h - \alpha_h \cos\psi\, x\zeta_h - \cos\alpha_p\, \cos\psi\, \dot\phi_h x\zeta_h -$$

$$\dot\alpha_h \sin\psi\, x\zeta_h + \cos\alpha_p\, \phi_h \sin\psi\, x\zeta_h - \cos\alpha_p\, \cos\psi\, \phi_h x\dot\zeta_h -$$

$$\alpha_h \sin\psi\, x\dot\zeta_h + \dot\alpha_h \sin\alpha_p\, z_h - \beta_{GC} \cos\alpha_p\, \cos\psi\, \cos\theta_1\, \eta -$$

$$\beta_{GS} \cos\alpha_p\, \cos\theta_1\, \eta\sin\psi\ - \beta_{GC} \cos\alpha_p\, \cos\psi\, v - \beta_{GS} \cos\alpha_p\, \sin\psi\, v$$

$$+\beta_{GS} \cos\alpha_p\, \cos\psi\, \dot v - \beta_{GC} \cos\alpha_p\, \sin\psi\, \dot v - \beta_{GC} \sin\alpha_p\, \dot w +$$

$$-\dot\alpha_h \beta_{GC} \cos\psi\, \sin\alpha_p\, x - \alpha_h \beta_{GS} \cos\psi\, \sin\alpha_p\, x - \dot\alpha_h \beta_{GS} \sin\alpha_p\, \sin\psi\, x +$$

$$\alpha_h \beta_{GC} \sin\alpha_p\, \sin\psi\, x - \dot\alpha_h \cos\theta_1\, \sin\alpha_p\, \zeta + \beta_p \cos\theta_1\, \sin\alpha_p\, \sin\psi\, \zeta +$$

$$\alpha_h \cos\alpha_p\, \cos\psi\, \sin\theta_1\, \zeta + \beta_{GC} \cos\alpha_p\, \cos\psi\, \sin\theta_1\, \zeta + \cos\psi\, \dot\phi_h \sin\theta_1\, \zeta +$$

$$\cos\psi\, \sin\alpha_p\, \sin\theta_1\, \zeta + \dot\alpha_h \cos\alpha_p\, \sin\psi\, \sin\theta_1\, \zeta + \beta_{GS} \cos\alpha_p\, \sin\psi\, \sin\theta_1\, \zeta -$$

$$\phi_h \sin\psi\, \sin\theta_1\, \zeta + \cos\theta_1\, \sin\alpha_p\, \sin\psi\, \dot\theta_1 \zeta - \cos\alpha_p\, \sin\theta_1\, \dot\theta_1 \zeta -$$

$$\sin\alpha_p\, \sin\psi\, \sin\theta_1\, v'\zeta + \cos\psi\, \sin\alpha_p\, \sin\theta_1\, \dot v'\zeta + \cos\theta_1\, \sin\alpha_p\, \sin\psi\, w'\zeta -$$

$$\cos\psi\, \cos\theta_1\, \sin\alpha_p\, \dot w'\zeta - \eta\sin\alpha_p\, \sin\psi\, \sin\theta_1\, w' \qquad (4.101)$$

The variation of velocity is calculated from the above equations and placed in form similar to Eqn. 4.98 as

$$\delta\vec V_b + \delta\vec V_h = \delta V_x \hat I_i + \delta V_y \hat J_i + \delta V_z \hat K_i \qquad (4.102)$$

Variation of Kinetic Energy

The kinetic energy for the blade and hub system is given by

$$T = \frac{1}{2} \int_0^R \iint_A \rho_s \vec V \cdot \vec V\, d\eta\, d\zeta\, dx \qquad (4.103)$$

where $\hat V$ is the velocity as defined by Eqn. 4.98 and ρ_s is the mass density of any arbitrary point in the system. In the present formulation, the mass density of the

151

hub is zero because the mass of the pylon and rotor hub is considered part of the wing. The variation of the kinetic energy is given by

$$\delta T = \int_0^R \iint_A \rho_s \vec{V} \cdot \delta \vec{V} \, d\eta \, d\zeta \, dx \qquad (4.104)$$

Integration over the cross section area results in the following definitions for the mass constants of the blade:

$$m = \iint_A \rho_s \, d\eta \, d\zeta \qquad (4.105)$$

$$m e_g = \iint_A \rho_s \eta \, d\eta \, d\zeta \qquad (4.106)$$

$$m k_{m1}^2 = \iint_A \rho_s \zeta^2 \, d\eta \, d\zeta \qquad (4.107)$$

$$m k_{m2}^2 = \iint_A \rho_s \eta^2 \, d\eta \, d\zeta \qquad (4.108)$$

$$m k_m^2 = \iint_A \rho_s (\zeta^2 + \eta^2) \, d\eta \, d\zeta \qquad (4.109)$$

where m represents the blade mass per unit length, e_g is the mass center of gravity offset from the elastic axis which is positive forward, k_{m1} and k_{m2} are the flapwise and chordwise mass radii of gyration, respectively, and k_m is the torsional mass radius of gyration so that $m k_m^2$ represents the torsional mass moment of inertia about the elastic axis. Because a symmetrical airfoil is assumed about the chordline, the following integrations are zero:

$$\iint_A \rho_s \zeta \, d\eta \, d\zeta = 0 \qquad (4.110)$$

$$\iint_A \rho_s \zeta \eta \, d\eta \, d\zeta = 0 \qquad (4.111)$$

The nondimensional form of the kinetic energy, after the cross section integrations are carried out on the velocity dot product, is written as

$$\begin{aligned}
\frac{\delta T}{m_0 \Omega^2 R^3} = \int_0^R & m(T_F + T_u \delta u_e + T_{\dot{u}} \delta \dot{u}_e + T_v \delta v + T_{\dot{v}} \delta \dot{v} + T_w \delta w + T_{\dot{w}} \delta \dot{w} + \\
& T_\phi \delta \phi + T_{\dot{\phi}} \delta \dot{\phi} + T_{v'} \delta v' + T_{\dot{v}'} \delta \dot{v}' + T_{w'} \delta w' + T_{\dot{w}'} \delta \dot{w}' + \\
& T_{\dot{x}_h} \delta \dot{x}_h + T_{\dot{y}_h} \delta \dot{y}_h + T_{\dot{z}_h} \delta \dot{z}_h + T_{\alpha_h} \delta \alpha_h + T_{\dot{\alpha}_h} \delta \dot{\alpha}_h + \\
& T_{\phi_h} \delta \phi_h + T_{\dot{\phi}_h} \delta \dot{\phi}_h + T_{\zeta_h} \delta \zeta_h + T_{\dot{\zeta}_h} \delta \dot{\zeta}_h + \\
& T_{\beta_{GC}} \delta \beta_{GC} + T_{\dot{\beta}_{GC}} \delta \dot{\beta}_{GC} + T_{\beta_{GS}} \delta \beta_{GS} + T_{\dot{\beta}_{GS}} \delta \dot{\beta}_{GS}) \, dx \qquad (4.112)
\end{aligned}$$

where δT_F is the contribution associated with the foreshortening effect. The kinetic energy associated with this effect was derived in Chapter 3, but before proceeding with the kinetic energy formulation with hub included, the kinetic energy associated with T_F as modified for the precone is derived.

Kinetic Energy Associated with Foreshortening

The new form for the axial strain with precone included is given by Eqn. 4.51. The foreshortening contribution can then be written as

$$u'_F = \frac{1}{2}v'^2 + \frac{1}{2}w'^2 + \beta_p(v'\phi + v\phi') \qquad (4.113)$$

since $u' = u'_e - u'_F$. Substitution of this definition into the expressions for velocity and velocity variation give the foreshortening contribution as

$$T_F = -(x + 2\dot{v})\delta u_F + \dot{u}_F \delta v \qquad (4.114)$$

and the terms associated with u_F are given by

$$
\begin{aligned}
\delta u_F &= \int_0^x (v'\delta v' + w'\delta w')d\xi + \\
&\quad \beta_p \int_0^x (\phi\delta v' + v'\delta\phi + v\delta\phi' + \phi'\delta v)d\xi \qquad (4.115) \\
\dot{u}_F &= \int_0^x (v'\dot{v}' + w'\dot{w}')\,d\xi + \\
&\quad \beta_p \int_0^x (v'\dot{\phi} + \dot{v}'\phi + \dot{v}\phi' + v\dot{\phi}')d\xi \qquad (4.116)
\end{aligned}
$$

The contribution to the kinetic energy is then given by $\int_0^1 mT_F dx$ which, after the appropriate substitutions and application of the ordering scheme, gives

$$
\begin{aligned}
\int_0^1 mT_F dx &= \int_0^1 m[-(x + 2\dot{v})\int_0^x (v'\delta v' + w'\delta w')d\xi - \\
&\quad x\beta_p \int_0^x (\phi\delta v' + v'\delta\phi + v\delta\phi' + \phi'\delta v)d\xi + \\
&\quad 2\delta v \int_0^x (v'\dot{v}' + w'\dot{w}')\,d\xi]dx \qquad (4.117)
\end{aligned}
$$

As was the case in Chapter 3, integration by parts yields the convenient form for the foreshortening contribution. For the present case, the kinetic energy associated

153

with foreshortening becomes

$$\int_0^1 mT_F dx = -(F_A + F_{cor})(v'\delta v' + w'\delta w') - \beta_p F_A(\phi\delta v' + v'\delta\phi + v\delta\phi' + \phi'\delta v)$$

$$+2\delta v \int_0^x (v'\dot{v}' + w'\dot{w}')\,d\xi \tag{4.118}$$

where

$$F_A = \int_x^1 mx\,d\xi \tag{4.119}$$

$$F_{cor} = \int_x^1 2m\dot{v}\,d\xi \tag{4.120}$$

Comparing results with Chapter 3, the modifications to the formulation for precone are seen to add centrifugal stiffness contributions only and do not add contributions to the nonlinear Coriolis damping (within the ordering scheme).

Terms in the Kinetic Energy

Let $[T_u]_i$ represent the groups of terms which are the coefficients of $\delta\hat{u}_i$ and $[T_{\dot{u}}]_i$ represent the groups of terms which are the coefficients of $\delta\hat{\dot{u}}_i$ where

$$\delta\hat{u} = \{\delta u_e \ \delta v \ \delta w \ \delta\phi \ \delta v' \ \delta w'$$

$$\delta x_h \ \delta y_h \ \delta z_h \ \delta\alpha_h \ \delta\phi_h \ \delta\zeta_h \ \delta\beta_{GC} \ \delta\beta_{GS}\} \tag{4.121}$$

and

$$\delta\hat{\dot{u}}_i = \frac{d}{dt}\delta\hat{u}_i \tag{4.122}$$

Equation 4.112 can then be expressed more compactly as

$$\frac{\delta T}{m_0\Omega^2 R^3} = \int_0^R m([T_u]_i\delta\hat{u}_i + [T_{\dot{u}}]_i\delta\hat{\dot{u}}_i + T_F)\,dx \tag{4.123}$$

Through integration by parts, the following relationship is developed

$$\int_0^R [T_{\dot{u}}]_i\delta\hat{\dot{u}}_i = -\int_0^R \frac{d}{dt}([T_{\dot{u}}]_i)\delta\hat{u}_i \tag{4.124}$$

which may be used to further simplify Eqn. 4.123 to

$$\frac{\delta T}{m_0\Omega^2 R^3} = \int_0^R m([T_{\bar{u}}]_i\delta\hat{u}_i + T_F)\,dx \tag{4.125}$$

154

where

$$[T_{\bar{u}}]_i = [T_u]_i - \frac{d}{dt}[T_{\dot{u}}]_i \qquad (4.126)$$

so that the $[T_{\bar{u}}]_i$ include the additional acceleration terms gained by the integration by parts. The values for the $[T_{\bar{u}}]_i$ are derived as

$$
\begin{aligned}
T_u =\ & \ddot{\alpha}_h \cos\psi\, h - \cos\theta_1\, e_g \phi\dot{\phi} - \cos\alpha_p\, h\dot{\phi}_h \sin\psi\ - \\
& 2e_g \dot{\phi}\sin\theta_1\ - \ddot{u} + 2\dot{v} + x + 2\dot{\phi}_h \sin\alpha_p\, x\ - \\
& \cos\alpha_p \cos\psi\, \ddot{x}_h - \sin\psi\, \ddot{y}_h - \cos\psi\, \sin\alpha_p\, \ddot{z}_h + 2\cos\alpha_p\, x\dot{\zeta}_h\ + \\
& h\sin\alpha_p\, \sin\psi\, \ddot{\zeta}_h \qquad (4.127)
\end{aligned}
$$

$$
\begin{aligned}
T_v =\ & \cos\theta_1\, e_g - \cos\alpha_p \cos\psi\, h\ddot{\phi}_h + \cos\theta_1\, e_g \dot{\phi}^2\ + \\
& \cos\theta_1\, e_g \phi\ddot{\phi} - \ddot{\alpha}_h h\sin\psi\ - e_g \phi\sin\theta_1\ + \\
& e_g \ddot{\phi}\sin\theta_1\ + \cos\theta_1\, e_g \phi\ddot{\theta}_1 + e_g \sin\theta_1\, \ddot{\theta}_1 - 2\dot{u}\ + \\
& v - \ddot{v} + \phi_h \sin\alpha_p\, x - \ddot{phi}_h \sin\alpha_p\, x + \cos\alpha_p \sin\psi\, \ddot{x}_h\ - \\
& \cos\psi\, \ddot{y}_h + \sin\alpha_p \sin\psi\, \ddot{z}_h + \cos\alpha_p\, x\dot{\zeta}_h + \cos\psi\, h\sin\alpha_p\, \dot{\zeta}_h\ - \\
& \cos\alpha_p\, x\ddot{\zeta}_h \qquad (4.128)
\end{aligned}
$$

$$
\begin{aligned}
T_w =\ & -\cos\theta_1\, e_g \ddot{\phi} + e_g \dot{\phi}^2 \sin\theta_1\ + e_g \phi\ddot{\phi}\sin\theta_1\ - \\
& \cos\theta_1\, e_g \ddot{\theta}_1 + e_g \phi\sin\theta_1\, \ddot{\theta}_1 - \ddot{w} - \beta_p x + \alpha_h \cos\psi\, x\ - \\
& \ddot{\alpha}_h \cos\psi\, x + \beta_{GC} \cos\psi\, x - \ddot{\beta}_{GC} \cos\psi\, x - 2\dot{\beta}_{GS} \cos\psi\, x\ + \\
& 2\cos\alpha_p \cos\psi\, \dot{\phi}_h x + 2\dot{\alpha}_h \sin\psi\, x + 2\dot{\beta}_{GC} \sin\psi\, x\ + \\
& \beta_{GS} \sin\psi\, x - \ddot{\beta}_{GS} \sin\psi\, x - \cos\alpha_p\, \phi_h \sin\psi\, x + \cos\alpha_p\, \ddot{\phi}_h \sin\psi\, x\ + \\
& \sin\alpha_p\, \ddot{x}_h - \cos\alpha_p\, \ddot{z}_h + \sin\alpha_p \sin\psi\, x\zeta_h - 2\cos\psi\, \sin\alpha_p\, x\dot{\zeta}_h\ - \\
& \sin\alpha_p \sin\psi\, x\ddot{\zeta}_h \qquad (4.129)
\end{aligned}
$$

$$
\begin{aligned}
T_\phi =\ & -\cos^2\theta_1 k_{m2}^2 \phi - \cos^2\theta_1 k_{m2}^2 \ddot{\phi} + \cos\theta_1\, k_{m1}^2 \sin\theta_1\ - \\
& \cos\theta_1\, k_{m2}^2 \sin\theta_1\ + \cos\theta_1\, k_{m2}^2 \phi^2 \sin\theta_1\ + k_{m2}^2 \phi\sin^2\theta_1\ - \\
& k_{m2}^2 \ddot{\phi}\sin^2\theta_1 - \cos^2\theta_1 k_{m2}^2 \ddot{\theta}_1 - k_{m2}^2 \sin^2\theta_1 \ddot{\theta}_1\ - \\
& \ddot{\beta}_{GC} \cos\psi\, \cos\theta_1\, e_g x - \ddot{\beta}_{GS} \cos\theta_1\, e_g \sin\psi\, x + e_g \phi\ddot{\phi}\sin\theta_1\, x \qquad (4.130)
\end{aligned}
$$

155

$$T_{v'} = \cos^2\theta_1 k_{m2}^2 \phi\dot\phi + 3\cos\theta_1 k_{m2}^2 \dot\phi\sin\theta_1 -$$

$$3k_{m2}^2 \phi\dot\phi \sin^2\theta_1 - \cos\theta_1 e_g x + e_g \phi\sin\theta_1 x \tag{4.131}$$

$$T_{w'} = -\cos^2\theta_1 k_{m2}^2 \dot\phi + 4\cos\theta_1 k_{m2}^2 \phi\dot\phi\sin\theta_1 +$$

$$2k_{m2}^2 \dot\phi \sin^2\theta_1 - \cos\theta_1 e_g \phi x - e_g\sin\theta_1 x \tag{4.132}$$

$$T_{x_h} = \ddot\alpha_h\cos\alpha_p\, h - \cos\alpha_p \cos\psi \cos\theta_1 e_g \phi\dot\phi + \cos\theta_1 e_g \dot\phi\sin\alpha_p -$$

$$\cos\alpha_p \cos\theta_1 e_g\sin\psi - \cos\alpha_p \cos\theta_1 e_g \dot\phi^2\sin\psi -$$

$$\cos\alpha_p \cos\theta_1 e_g \phi\ddot\phi\sin\psi - 2\cos\alpha_p \cos\psi\, e_g \dot\phi\sin\theta_1 -$$

$$e_g \dot\phi^2\sin\alpha_p \sin\theta_1 - e_g \phi\ddot\phi\sin\alpha_p \sin\theta_1 +$$

$$\cos\alpha_p e_g \phi\sin\psi \sin\theta_1 - \cos\alpha_p e_g \ddot\phi\sin\psi \sin\theta_1 +$$

$$\cos\theta_1 e_g\sin\alpha_p \ddot\theta_1 - \cos\alpha_p \cos\theta_1 e_g \phi\sin\psi \ddot\theta_1 -$$

$$e_g \phi\sin\alpha_p \sin\theta_1 \ddot\theta_1 - \cos\alpha_p e_g\sin\psi \sin\theta_1 \ddot\theta_1 + \cos\alpha_p \cos\psi\, u +$$

$$2\cos\alpha_p \sin\psi\, \dot u - \cos\alpha_p \cos\psi\, \ddot u - \cos\alpha_p \sin\psi\, v + 2\cos\alpha_p \cos\psi\, \dot v +$$

$$\cos\alpha_p \sin\psi\, \ddot v + \sin\alpha_p \ddot w + \cos\alpha_p \cos\psi\, x - \alpha_h\cos\psi \sin\alpha_p\, x +$$

$$\ddot\alpha_h\cos\psi \sin\alpha_p\, x - \beta_{GC}\cos\psi \sin\alpha_p\, x + \ddot\beta_{GC}\cos\psi \sin\alpha_p\, x +$$

$$2\dot\beta_{GS}\cos\psi \sin\alpha_p\, x - 2\dot\alpha_h\sin\alpha_p \sin\psi\, x - 2\dot\beta_{GC}\sin\alpha_p \sin\psi\, x -$$

$$\beta_{GS}\sin\alpha_p \sin\psi\, x + \ddot\beta_{GS}\sin\alpha_p \sin\psi\, x - \ddot x_h - \sin\psi\, x\zeta_h +$$

$$2\cos\psi\, x\dot\zeta_h + \sin\psi\, x\ddot\zeta_h \tag{4.133}$$

$$T_{y_h} = \cos\psi \cos\theta_1 e_g - \cos\alpha_p\, h\ddot\phi_h + \cos\psi \cos\theta_1 e_g \dot\phi^2 +$$

$$\cos\psi \cos\theta_1 e_g \phi\ddot\phi - \cos\theta_1 e_g \phi\dot\phi\sin\psi -$$

$$\cos\psi\, e_g \dot\phi\sin\theta_1 + \cos\psi\, e_g \ddot\phi\sin\theta_1 - 2e_g \dot\phi\sin\psi \sin\theta_1 +$$

$$\cos\psi \cos\theta_1 e_g \phi\ddot\theta_1 + \cos\psi\, e_g\sin\theta_1 \ddot\theta_1 + \sin\psi\, u -$$

$$2\cos\psi\, \dot u - \sin\psi\, \ddot u + \cos\psi\, v + 2\sin\psi\, \dot v - \cos\psi\, \ddot v +$$

$$\cos\psi\, \phi_h\sin\alpha_p\, x - \cos\psi\, \ddot\phi_h\sin\alpha_p\, x + \sin\psi\, x + 2\dot\phi_h\sin\alpha_p \sin\psi\, x -$$

$$\ddot y_h + \cos\alpha_p \cos\psi\, x\zeta_h + 2\cos\alpha_p \sin\psi\, x\dot\zeta_h + h\sin\alpha_p \ddot\zeta_h -$$

$$\cos\alpha_p \, \cos\psi \, x\ddot{\zeta}_h \tag{4.134}$$

$$
\begin{aligned}
T_{z_h} \quad = \quad & -\cos\alpha_p \, \cos\theta_1 \, e_g\ddot{\phi} + \ddot{\alpha}_h h\sin\alpha_p \; - \\
& \cos\psi \, \cos\theta_1 \, e_g\phi\dot{\phi}\sin\alpha_p \; - \cos\theta_1 \, e_g\sin\alpha_p \, \sin\psi \; - \\
& \cos\theta_1 \, e_g\dot{\phi}^2\sin\alpha_p \, \sin\psi \; - \cos\theta_1 \, e_g\phi\ddot{\phi}\sin\alpha_p \, \sin\psi \; + \\
& \cos\alpha_p \, e_g\dot{\phi}^2\sin\theta_1 \; + \cos\alpha_p \, e_g\phi\ddot{\phi}\sin\theta_1 \; - \\
& 2\cos\psi \, e_g\dot{\phi}\sin\alpha_p \, \sin\theta_1 \; + e_g\phi\sin\alpha_p \, \sin\psi \, \sin\theta_1 \; - \\
& e_g\ddot{\phi}\sin\alpha_p \, \sin\psi \, \sin\theta_1 \; - \cos\alpha_p \, \cos\theta_1 \, e_g\ddot{\theta}_1 \; - \\
& \cos\theta_1 \, e_g\phi\sin\alpha_p \, \sin\psi \, \ddot{\theta}_1 + \cos\alpha_p \, e_g\phi\sin\theta_1 \, \ddot{\theta}_1 \; - \\
& e_g\sin\alpha_p \, \sin\psi \, \sin\theta_1 \, \ddot{\theta}_1 + \cos\psi \, \sin\alpha_p \, u + 2\sin\alpha_p \, \sin\psi \, \dot{u} \; - \\
& \cos\psi \, \sin\alpha_p \, \ddot{u} - \sin\alpha_p \, \sin\psi \, v + 2\cos\psi \, \sin\alpha_p \, \dot{v} + \sin\alpha_p \, \sin\psi \, \ddot{v} \; - \\
& \cos\alpha_p \, \ddot{w} + \alpha_h\cos\alpha_p \, \cos\psi \, x - \ddot{\alpha}_h\cos\alpha_p \, \cos\psi \, x + \beta_{GC}\cos\alpha_p \, \cos\psi \, x \; - \\
& \ddot{\beta}_{GC}\cos\alpha_p \, \cos\psi \, x - 2\dot{\beta}_{GS}\cos\alpha_p \, \cos\psi \, x + 2\cos\psi \, \dot{\phi}_h x \; + \\
& \cos\psi \, \sin\alpha_p \, x + 2\dot{\alpha}_h\cos\alpha_p \, \sin\psi \, x + 2\dot{\beta}_{GC}\cos\alpha_p \, \sin\psi \, x \; + \\
& \beta_{GS}\cos\alpha_p \, \sin\psi \, x - \ddot{\beta}_{GS}\cos\alpha_p \, \sin\psi \, x - \phi_h\sin\psi \, x \; + \\
& \ddot{\phi}_h\sin\psi \, x - \ddot{z}_h \tag{4.135}
\end{aligned}
$$

$$
\begin{aligned}
T_{\alpha_h} \quad = \quad & -\ddot{\alpha}_h h^2 + \cos\psi \, \cos\theta_1 \, e_g h\phi\dot{\phi} + \cos\theta_1 \, e_g h\sin\psi \; + \\
& \cos\theta_1 \, e_g h\dot{\phi}^2\sin\psi + \cos\theta_1 \, e_g h\phi\ddot{\phi}\sin\psi \; + \\
& 2\cos\psi \, e_g h\dot{\phi}\sin\theta_1 - e_g h\phi\sin\psi \, \sin\theta_1 \; + \\
& e_g h\ddot{\phi}\sin\psi \, \sin\theta_1 + \cos\theta_1 \, e_g h\phi\sin\psi \, \ddot{\theta}_1 \; + \\
& e_g h\sin\psi \, \sin\theta_1 \, \ddot{\theta}_1 - \cos\psi \, hu - 2h\sin\psi \, \dot{u} + \cos\psi \, h\ddot{u} \; + \\
& h\sin\psi \, v - 2\cos\psi \, h\dot{v} - h\sin\psi \, \ddot{v} - \cos\psi \, hx \; - \\
& \cos\psi \, \cos\theta_1 \, e_g\dot{\phi}x - 2\cos\psi \, h\dot{\phi}_h\sin\alpha_p \, x + h\phi_h\sin\alpha_p \, \sin\psi \, x \; - \\
& h\ddot{\phi}_h\sin\alpha_p \, \sin\psi \, x + \cos\psi \, e_g\dot{\phi}^2\sin\theta_1 \, x \; + \\
& \cos\psi \, e_g\phi\ddot{\phi}\sin\theta_1 \, x - \cos\psi \, \cos\theta_1 \, e_g\ddot{\theta}_1 x \; +
\end{aligned}
$$

$$\cos\psi\; e_g\dot\phi\sin\theta_1\;\ddot\theta_1 x - \cos\psi\;\ddot w x + \alpha_h\cos\psi\;^2 x^2 -$$

$$\ddot\alpha_h\cos\psi\;^2 x^2 + \beta_{GC}\cos\psi\;^2 x^2 - \ddot\beta_{GC}\cos\psi\;^2 x^2 -$$

$$2\dot\beta_{GS}\cos\psi\;^2 x^2 + 2\cos\alpha_p\;\cos\psi\;^2\dot\phi_h x^2 +$$

$$2\dot\alpha_h\cos\psi\;\sin\psi\; x^2 + 2\dot\beta_{GC}\cos\psi\;\sin\psi\; x^2 +$$

$$\beta_{GS}\cos\psi\;\sin\psi\; x^2 - \ddot\beta_{GS}\cos\psi\;\sin\psi\; x^2 -$$

$$\cos\alpha_p\;\cos\psi\;\phi_h\sin\psi\; x^2 + \cos\alpha_p\;\cos\psi\;\ddot\phi_h\sin\psi\; x^2 + \cos\alpha_p\; h\ddot x_h +$$

$$\cos\psi\;\sin\alpha_p\; x\ddot x_h + h\sin\alpha_p\;\ddot z_h - \cos\alpha_p\;\cos\psi\; x\ddot z_h +$$

$$\cos\alpha_p\; h\sin\psi\; x\zeta_h + \cos\psi\;\sin\alpha_p\;\sin\psi\; x^2\zeta_h - 2\cos\alpha_p\;\cos\psi\; hx\dot\zeta_h -$$

$$2\cos\psi\;^2\sin\alpha_p\; x^2\dot\zeta_h - \cos\alpha_p\; h\sin\psi\; x\ddot\zeta_h -$$

$$\cos\psi\;\sin\alpha_p\;\sin\psi\; x^2\ddot\zeta_h \qquad (4.136)$$

$$T_{\phi_h} \;=\; \cos\alpha_p\;\cos\psi\;\cos\theta_1\; e_g h - \cos\alpha_p\;^2 h^2\ddot\phi_h +$$

$$\cos\alpha_p\;\cos\psi\;\cos\theta_1\; e_g h\dot\phi^2 + \cos\alpha_p\;\cos\psi\;\cos\theta_1\; e_g h\phi\ddot\phi -$$

$$\cos\alpha_p\;\cos\theta_1\; e_g h\phi\dot\phi\sin\psi\; - \cos\alpha_p\;\cos\psi\; e_g h\dot\phi\sin\theta_1 +$$

$$\cos\alpha_p\;\cos\psi\; e_g h\ddot\phi\sin\theta_1\; - 2\cos\alpha_p\; e_g h\dot\phi\sin\psi\;\sin\theta_1 +$$

$$\cos\alpha_p\;\cos\psi\;\cos\theta_1\; e_g h\phi\ddot\theta_1 + \cos\alpha_p\;\cos\psi\; e_g h\sin\theta_1\;\ddot\theta_1 +$$

$$\cos\alpha_p\; h\sin\psi\; u - 2\cos\alpha_p\;\cos\psi\; h\dot u - \cos\alpha_p\; h\sin\psi\;\ddot u +$$

$$\cos\alpha_p\;\cos\psi\; hv + 2\cos\alpha_p\; h\sin\psi\;\dot v - \cos\alpha_p\;\cos\psi\; h\ddot v +$$

$$\cos\theta_1\; e_g\sin\alpha_p\; x + \cos\alpha_p\;\cos\psi\; h\phi_h\sin\alpha_p\; x -$$

$$2\cos\alpha_p\;\cos\psi\; h\ddot\phi_h\sin\alpha_p\; x + \cos\theta_1\; e_g\dot\phi^2\sin\alpha_p\; x +$$

$$\cos\theta_1\; e_g\phi\ddot\phi\sin\alpha_p\; x + \cos\alpha_p\; h\sin\psi\; x +$$

$$\cos\alpha_p\;\cos\theta_1\; e_g\ddot\phi\sin\psi\; x - \ddot\alpha_h h\sin\alpha_p\;\sin\psi\; x +$$

$$2\cos\alpha_p\; h\dot\phi_h\sin\alpha_p\;\sin\psi\; x - e_g\phi\sin\alpha_p\;\sin\theta_1\; x +$$

$$e_g\ddot\phi\sin\alpha_p\;\sin\theta_1\; x - \cos\alpha_p\; e_g\dot\phi^2\sin\psi\;\sin\theta_1\; x -$$

$$\cos\alpha_p\; e_g\phi\ddot\phi\sin\psi\;\sin\theta_1\; x + \cos\theta_1\; e_g\phi\sin\alpha_p\;\ddot\theta_1 x +$$

$$\cos\alpha_p \, \cos\theta_1 \, e_g \sin\psi \, \ddot\theta_1 x + e_g \sin\alpha_p \, \sin\theta_1 \, \ddot\theta_1 x -$$

$$\cos\alpha_p \, e_g \dot\phi \sin\psi \, \sin\theta_1 \, \dot\theta_1 x - 2\sin\alpha_p \, \dot u x + \sin\alpha_p \, v x -$$

$$\sin\alpha_p \, \ddot v x + \cos\alpha_p \, \sin\psi \, \ddot w x + \cos\psi^2 \dot\phi_h \sin\alpha_p{}^2 x^2 -$$

$$\cos\psi^2 \ddot\phi_h \sin\alpha_p{}^2 x^2 - \alpha_h \cos\alpha_p \, \cos\psi \, \sin\psi \, x^2 +$$

$$\ddot\alpha_h \cos\alpha_p \, \cos\psi \, \sin\psi \, x^2 - \beta_{GC} \cos\alpha_p \, \cos\psi \, \sin\psi \, x^2 +$$

$$\ddot\beta_{GC} \cos\alpha_p \, \cos\psi \, \sin\psi \, x^2 + 2\dot\beta_{GS} \cos\alpha_p \, \cos\psi \, \sin\psi \, x^2 -$$

$$2\cos\psi \, \dot\phi_h \sin\psi \, x^2 + 2\cos\psi \, \dot\phi_h \sin\alpha_p{}^2 \sin\psi \, x^2 -$$

$$2\dot\alpha_h \cos\alpha_p \, \sin\psi^2 x^2 - 2\dot\beta_{GC} \cos\alpha_p \, \sin\psi^2 x^2 -$$

$$\beta_{GS} \cos\alpha_p \, \sin\psi^2 x^2 + \ddot\beta_{GS} \cos\alpha_p \, \sin\psi^2 x^2 + \dot\phi_h \sin\psi^2 x^2 -$$

$$\ddot\phi_h \sin\psi^2 x^2 - \cos\alpha_p \, h \ddot y_h - \cos\psi \, \sin\alpha_p \, x \ddot y_h +$$

$$\sin\psi \, x \ddot z_h + \cos\alpha_p{}^2 \cos\psi \, h x \zeta_h + \cos\alpha_p \, \cos\psi^2 \sin\alpha_p \, x^2 \zeta_h +$$

$$2\cos\alpha_p{}^2 h \sin\psi \, x \dot\zeta_h + 2\cos\alpha_p \, \cos\psi \, \sin\alpha_p \, \sin\psi \, x^2 \dot\zeta_h +$$

$$\cos\alpha_p \, h^2 \sin\alpha_p \, \ddot\zeta_h - \cos\alpha_p{}^2 \cos\psi \, h x \ddot\zeta_h +$$

$$\cos\psi \, h \sin\alpha_p{}^2 x \ddot\zeta_h - \cos\alpha_p \, \cos\psi^2 \sin\alpha_p \, x^2 \ddot\zeta_h \qquad (4.137)$$

$$T_{\zeta_h} = -(\cos\psi \, \cos\theta_1 \, e_g h \sin\alpha_p) + \cos\alpha_p \, h^2 \ddot\phi_h \sin\alpha_p -$$

$$\cos\psi \, \cos\theta_1 \, e_g h \dot\phi^2 \sin\alpha_p - \cos\psi \, \cos\theta_1 \, e_g h \phi \ddot\phi \sin\alpha_p +$$

$$\cos\theta_1 \, e_g h \phi \dot\phi \sin\alpha_p \, \sin\psi + \cos\psi \, e_g h \dot\phi \sin\alpha_p \, \sin\theta_1 -$$

$$\cos\psi \, e_g h \ddot\phi \sin\alpha_p \, \sin\theta_1 + 2 e_g h \dot\phi \sin\alpha_p \, \sin\psi \, \sin\theta_1 -$$

$$\cos\psi \, \cos\theta_1 \, e_g h \phi \sin\alpha_p \, \ddot\theta_1 - \cos\psi \, e_g h \sin\alpha_p \, \sin\theta_1 \, \ddot\theta_1 -$$

$$h \sin\alpha_p \, \sin\psi \, u + 2\cos\psi \, h \sin\alpha_p \, \dot u + h \sin\alpha_p \, \sin\psi \, \ddot u -$$

$$\cos\psi \, h \sin\alpha_p \, v - 2h \sin\alpha_p \, \sin\psi \, \dot v + \cos\psi \, h \sin\alpha_p \, \ddot v +$$

$$\cos\alpha_p \, \cos\theta_1 \, e_g x - \cos\alpha_p{}^2 \cos\psi \, h \ddot\phi_h x + \cos\alpha_p \, \cos\theta_1 \, e_g \dot\phi^2 x +$$

$$\cos\alpha_p \, \cos\theta_1 \, e_g \phi \ddot\phi x - \cos\psi \, h \dot\phi_h \sin\alpha_p{}^2 x +$$

$$\cos\psi \, h \ddot\phi_h \sin\alpha_p{}^2 x - \ddot\alpha_h \cos\alpha_p \, h \sin\psi \, x - h \sin\alpha_p \, \sin\psi \, x -$$

$$\cos\theta_1 \, e_g \ddot{\phi} \sin\alpha_p \, \sin\psi \, x - 2h\dot{\phi}_h \sin\alpha_p{}^2 \sin\psi \, x -$$

$$\cos\alpha_p \, e_g \phi \sin\theta_1 \, x + \cos\alpha_p \, e_g \ddot{\phi} \sin\theta_1 \, x +$$

$$e_g \dot{\phi}^2 \sin\alpha_p \, \sin\psi \, \sin\theta_1 \, x + e_g \phi \ddot{\phi} \sin\alpha_p \, \sin\psi \, \sin\theta_1 \, x +$$

$$\cos\alpha_p \, \cos\theta_1 \, e_g \phi \dot{\theta}_1 x - \cos\theta_1 \, e_g \sin\alpha_p \, \sin\psi \, \dot{\theta}_1 x +$$

$$\cos\alpha_p \, e_g \sin\theta_1 \, \ddot{\theta}_1 x + e_g \phi \sin\alpha_p \, \sin\psi \, \sin\theta_1 \, \ddot{\theta}_1 x -$$

$$2\cos\alpha_p \, \ddot{u}x + \cos\alpha_p \, vx - \cos\alpha_p \, \ddot{v}x - \sin\alpha_p \, \sin\psi \, \ddot{w}x +$$

$$\cos\alpha_p \, \cos\psi^2 \phi_h \sin\alpha_p \, x^2 - \cos\alpha_p \, \cos\psi^2 \ddot{\phi}_h \sin\alpha_p \, x^2 +$$

$$\alpha_h \cos\psi \, \sin\alpha_p \, \sin\psi \, x^2 - \ddot{\alpha}_h \cos\psi \, \sin\alpha_p \, \sin\psi \, x^2 +$$

$$\beta_{GC} \cos\psi \, \sin\alpha_p \, \sin\psi \, x^2 - \ddot{\beta}_{GC} \cos\psi \, \sin\alpha_p \, \sin\psi \, x^2 -$$

$$2\dot{\beta}_{GS} \cos\psi \, \sin\alpha_p \, \sin\psi \, x^2 + 2\cos\alpha_p \, \cos\psi \, \dot{\phi}_h \sin\alpha_p \, \sin\psi \, x^2 +$$

$$2\dot{\alpha}_h \sin\alpha_p \, \sin\psi^2 x^2 + 2\dot{\beta}_{GC} \sin\alpha_p \, \sin\psi^2 x^2 +$$

$$\beta_{GS} \sin\alpha_p \, \sin\psi^2 x^2 - \ddot{\beta}_{GS} \sin\alpha_p \, \sin\psi^2 x^2 + \sin\psi \, x\ddot{x}_h +$$

$$h\sin\alpha_p \, \ddot{y}_h - \cos\alpha_p \, \cos\psi \, x\ddot{y}_h - \cos\alpha_p \, \cos\psi \, h\sin\alpha_p \, x\zeta_h +$$

$$\cos\alpha_p{}^2 \cos\psi^2 x^2 \zeta_h + \sin\psi^2 x^2 \zeta_h -$$

$$2\cos\alpha_p \, h\sin\alpha_p \, \sin\psi \, x\dot{\zeta}_h - 2\cos\psi \, \sin\psi \, x^2 \dot{\zeta}_h +$$

$$2\cos\alpha_p{}^2 \cos\psi \, \sin\psi \, x^2 \dot{\zeta}_h - h^2 \sin\alpha_p{}^2 \ddot{\zeta}_h +$$

$$2\cos\alpha_p \, \cos\psi \, h\sin\alpha_p \, x\ddot{\zeta}_h - \cos\alpha_p{}^2 \cos\psi^2 x^2 \ddot{\zeta}_h -$$

$$\sin\psi^2 x^2 \ddot{\zeta}_h \tag{4.138}$$

$$T_{\beta_{GC}} = -\cos\psi \, \cos\theta_1 \, e_g \ddot{\phi}x + \cos\psi \, e_g \dot{\phi}^2 \sin\theta_1 \, x +$$

$$\cos\psi \, e_g \phi \ddot{\phi} \sin\theta_1 \, x - \cos\psi \, \cos\theta_1 \, e_g \ddot{\theta}_1 x +$$

$$\cos\psi \, e_g \phi \sin\theta_1 \, \ddot{\theta}_1 x - \cos\psi \, \ddot{w}x - \dot{\beta}_{GS} x^2 +$$

$$\alpha_h \cos\psi^2 x^2 - \ddot{\alpha}_h \cos\psi^2 x^2 + \beta_{GC} \cos\psi^2 x^2 -$$

$$\ddot{\beta}_{GC} \cos\psi^2 x^2 - \dot{\beta}_{GS} \cos\psi^2 x^2 + 2\cos\alpha_p \, \cos\psi^2 \dot{\phi}_h x^2 +$$

$$2\dot{\alpha}_h \cos\psi \, \sin\psi \, x^2 + 2\dot{\beta}_{GC} \cos\psi \, \sin\psi \, x^2 +$$

$$\beta_{GS}\cos\psi \, \sin\psi \, x^2 - \ddot{\beta}_{GS}\cos\psi \, \sin\psi \, x^2 -$$

$$\cos\alpha_p \, \cos\psi \, \phi_h\sin\psi \, x^2 + \cos\alpha_p \, \cos\psi \, \ddot{\phi}_h\sin\psi \, x^2 +$$

$$\dot{\beta}_{GS}\sin\psi \,^2 x^2 + \cos\psi \, \sin\alpha_p \, x\ddot{x}_h - \cos\alpha_p \, \cos\psi \, x\ddot{z}_h +$$

$$\cos\psi \, \sin\alpha_p \, \sin\psi \, x^2\zeta_h - 2\cos\psi \,^2\sin\alpha_p \, x^2\dot{\zeta}_h -$$

$$\cos\psi \, \sin\alpha_p \, \sin\psi \, x^2\ddot{\zeta}_h \tag{4.139}$$

$$T_{\beta_{GS}} = -\cos\theta_1 \, e_g\ddot{\phi}\sin\psi \, x + e_g\dot{\phi}^2\sin\psi \, \sin\theta_1 \, x +$$

$$e_g\dot{\phi}\dot{\phi}\sin\psi \, \sin\theta_1 \, x - \cos\theta_1 \, e_g\sin\psi \, \ddot{\theta}_1 x +$$

$$e_g\dot{\phi}\sin\psi \, \sin\theta_1 \, \dot{\theta}_1 x - \sin\psi \, \ddot{w}x + \dot{\beta}_{GC}x^2 -$$

$$\dot{\beta}_{GC}\cos\psi \,^2 x^2 + \alpha_h\cos\psi \, \sin\psi \, x^2 - \ddot{\alpha}_h\cos\psi \, \sin\psi \, x^2 +$$

$$\beta_{GC}\cos\psi \, \sin\psi \, x^2 - \ddot{\beta}_{GC}\cos\psi \, \sin\psi \, x^2 -$$

$$2\dot{\beta}_{GS}\cos\psi \, \sin\psi \, x^2 + 2\cos\alpha_p \, \cos\psi \, \dot{\phi}_h\sin\psi \, x^2 +$$

$$2\dot{\alpha}_h\sin\psi \,^2 x^2 + \dot{\beta}_{GC}\sin\psi \,^2 x^2 + \beta_{GS}\sin\psi \,^2 x^2 -$$

$$\ddot{\beta}_{GS}\sin\psi \,^2 x^2 - \cos\alpha_p \, \phi_h\sin\psi \,^2 x^2 + \cos\alpha_p \, \ddot{\phi}_h\sin\psi \,^2 x^2 +$$

$$\sin\alpha_p \, \sin\psi \, x\ddot{x}_h - \cos\alpha_p \, \sin\psi \, x\ddot{z}_h + \sin\alpha_p \, \sin\psi \,^2 x^2\zeta_h -$$

$$2\cos\psi \, \sin\alpha_p \, \sin\psi \, x^2\dot{\zeta}_h - \sin\alpha_p \, \sin\psi \,^2 x^2\ddot{\zeta}_h \tag{4.140}$$

4.5 Structural Contributions to Mass, Damping, and Stiffness

The contributions of the structural model to the element mass, damping, and stiffness matrices is derived in this section based on the strain and kinetic energies formulated in the present chapter. The total energies produced by the hub and blade can be summed as

$$\delta U = \left[\sum_{m=1}^{N_b} \delta U_b\right] + \delta U_h \tag{4.141}$$

161

for the variation of elastic strain energy and as

$$\delta T = \left[\sum_{m=1}^{N_b} \delta T_b \right] + \delta T_h \tag{4.142}$$

for the variation of kinetic energy. Application of Hamilton's principle then gives the discretized form of the total energy as

$$\delta \Pi = \int_{\psi_I}^{\psi_F} (\delta U_i - \delta T_i - \delta W_i) \, d\psi = 0 \tag{4.143}$$

where i is the ith element of the rotor blade which is discretized into N_b elements. For the present section, the work contribution is zero (the structural model conserves energy).

The element for which the present structural matrices are defined is the same one used in the past UMARC formulations for metal blades which has 15 discrete degrees of freedom. It is possible to base the present anisotropic beam formulation on this element only because the static condensation process is used to eliminate the shear degrees of freedom from the strain energy formulation. The continuous degrees of freedom for the blade are related to the discrete degrees of freedom for this element as follows:

$$\hat{u} = [H_s] \, \hat{q} \tag{4.144}$$

$$\hat{u}' = [H_s'] \, \hat{q} \tag{4.145}$$

$$\hat{u}'' = [H_s''] \, \hat{q} \tag{4.146}$$

$$\dot{\hat{u}} = [H_s] \, \dot{\hat{q}} \tag{4.147}$$

$$\ddot{\hat{u}} = [H_s] \, \ddot{\hat{q}} \tag{4.148}$$

where the shape function matrix is defined as

$$[H_s] = \begin{bmatrix} H_u & 0 & 0 & 0 \\ 0 & H_b & 0 & 0 \\ 0 & 0 & H_b & 0 \\ 0 & 0 & 0 & H_\phi \end{bmatrix} \tag{4.149}$$

162

and the discrete (nodal) degrees of freedom are defined as

$$\hat{q} = [u_1 \ u_2 \ u_3 \ u_4 \ v_1 \ v_1' \ v_2 \ v_2' \ w_1 \ w_1' \ w_2 \ w_2' \ \phi_1 \ \phi_2 \ \phi_3] \qquad (4.150)$$

The shape function matrices are matrices of polynomials which satisfy Eqn. 3.151. H_u is a 4 x 1 matrix of C^0 continuous cubic polynomials, H_b is a 4 x 1 matrix of C^1 continuous cubic polynomials, and H_ϕ is a 3 x 1 matrix of C^0 continuous quadratic polynomials.

The hub degrees of freedom are already discrete, and may be written in matrix form as

$$\hat{x}_h = [x_h \ y_h \ z_h \ \alpha_h \ \phi_h \ \zeta_h \ \beta_{GC} \ \beta_{GS}] \qquad (4.151)$$

4.5.1 Blade Matrices

The total energy variation as given by Eqn. 4.143 contains variational terms of both the blade and the hub. The terms which are coefficients of the blade variational degrees of freedom $\delta \hat{q}$ constitute the blade equations, and the terms which are coefficients of the hub variational degrees of freedom $\delta \hat{x}_h$ constitute the hub equations. The present section deals with the blade equations which may be written in matrix form as:

$$\delta U_i - \delta T_i = \delta \hat{q}^T ([M_{bb}]\ddot{\hat{q}} + [C_{bb}]\dot{\hat{q}} + [K_{bb}]\hat{q} + [M_{bh}]\ddot{\hat{x}}_h + [C_{bh}]\dot{\hat{x}}_h + [K_{bh}]\hat{x}_h - F_b)_i \quad (4.152)$$

where the subscript b indicates association with the blade, h indicates association with the hub, and i indicates the ith element of N_b elements of which the blade has been discretized. Each of these matrices may be partitioned by the blade and hub degrees of freedom; (u, v, w, or ϕ) of the blade, and (x_h, y_h, z_h, α_h, ϕ_h, ζ_h, β_{GC},

or β_{GS}) of the hub which appear in the energy expressions. For example,

$$[M_{bb}] = \begin{bmatrix} M_{uu} & M_{uv} & M_{uw} & M_{u\phi} \\ M_{vu} & M_{vv} & M_{vw} & M_{v\phi} \\ M_{wu} & M_{wv} & M_{ww} & M_{w\phi} \\ M_{\phi u} & M_{\phi v} & M_{\phi w} & M_{\phi\phi} \end{bmatrix} \tag{4.153}$$

Based on the strain and kinetic energies derived in the present formulation, and after substitution of Eqns. 4.144-4.148, these matrix partitions are defined as follows: the blade-blade mass matrix is symmetric so that only the upper trianglular terms are listed as

$$M_{uu} = \int_0^1 m H_u^T H_u \, ds \tag{4.154}$$

$$M_{uv} = 0 \tag{4.155}$$

$$M_{uw} = 0 \tag{4.156}$$

$$M_{u\phi} = 0 \tag{4.157}$$

$$M_{vv} = \int_0^1 m H_b^T H_b \, ds \tag{4.158}$$

$$M_{vw} = 0 \tag{4.159}$$

$$M_{v\phi} = -\int_0^1 m e_g \sin\theta_1 H_b^T H_\phi \, ds \tag{4.160}$$

$$M_{ww} = \int_0^1 m H_b^T H_b \, ds \tag{4.161}$$

$$M_{w\phi} = \int_0^1 m e_g \cos\theta_1 H_b^T H_\phi \, ds \tag{4.162}$$

$$M_{\phi\phi} = \int_0^1 m k_m^2 H_\phi H_\phi \, ds \tag{4.163}$$

the blade-blade damping matrix is anti-symmetric so that $C_{ij} = -C_{ji}$ and the upper triangular terms are listed as

$$C_{uu} = 0 \tag{4.164}$$

$$C_{uv} = -\int_0^1 2m\Omega H_u{}^T H_b \, ds \tag{4.165}$$

$$C_{uw} = 0 \tag{4.166}$$

$$C_{u\phi} = 0 \tag{4.167}$$

$$C_{vv} = \int_0^1 2m\Omega e_g \cos\theta_1 H_b'^T H_b \, ds - \int_0^1 2m\Omega e_g \cos\theta_1 H_b^T H_b' \, ds \tag{4.168}$$

$$C_{vw} = -\int_0^1 2m\Omega\beta_p H_b^T H_b \, ds - \int_0^1 2m\Omega e_g \sin\theta_1 H_b^T H_b' \, ds \tag{4.169}$$

$$C_{v\phi} = 0 \tag{4.170}$$

$$C_{ww} = 0 \tag{4.171}$$

$$C_{w\phi} = 0 \tag{4.172}$$

$$C_{\phi\phi} = 0 \tag{4.173}$$

the blade-blade stiffness matrix is symmetric so that only the upper triangular terms are listed as

$$K_{uu} = \int_0^1 \bar{E}A H_u'^T H_u' \, ds \tag{4.174}$$

$$K_{uv} = -\int_0^1 \bar{E}A_c \cos\theta_1 H_u'^T H_b'' \, ds \tag{4.175}$$

$$K_{uw} = -\int_0^1 \bar{E}A_c \sin\theta_1 H_u'^T H_b'' \, ds \tag{4.176}$$

$$K_{u\phi} = \int_0^1 \bar{E}A_{r2}\theta_0' H_u'^T H_\phi' \, ds + \underline{\int_0^1 EET H_u'^T H_\phi' \, ds} \tag{4.177}$$

$$K_{vv} = \int_0^1 F_A H_b'^T H_b' \, ds - \int_0^1 m\Omega^2 H_b^T H_b \, ds$$
$$+ \int_0^1 (\bar{E}I_f \sin^2\theta_1 + \bar{E}I_c \cos^2\theta_1) H_b''^T H_b'' \, ds \tag{4.178}$$

$$K_{vw} = \int_0^1 (\bar{E}I_c - \bar{E}I_f)\sin\theta_1 \cos\theta_1 H_b''^T H_b'' \, ds \tag{4.179}$$

$$K_{v\phi} = \int_0^1 m\Omega^2 e_g \sin\theta_1 H_b^T H_\phi \, ds - \int_0^1 mx\Omega^2 e_g \sin\theta_1 H_b'^T H_\phi \, ds$$
$$+ \underline{\int_0^1 (ETC\cos\theta_1 - ETF\sin\theta_1) H_b''^T H_\phi' \, ds}$$
$$\underline{-\int_0^1 \beta_p F_A (H_b'^T H_\phi + H_b^T H_\phi') \, ds} \tag{4.180}$$

$$K_{ww} = \int_0^1 F_A H_b'^T H_b' \, ds + \int_0^1 (\bar{E}I_c \sin^2\theta_1 + \bar{E}I_f \cos^2\theta_1) H_b''^T H_b'' \, ds \tag{4.181}$$

$$K_{w\phi} = \int_0^1 mx\Omega^2 e_g \cos\theta_1 H_b'^T H_\phi \, ds +$$
$$\underline{\int_0^1 (ETF\cos\theta_1 + ETC\sin\theta_1) H_b''^T H_\phi' \, ds} \tag{4.182}$$

$$K_{\phi\phi} = \int_0^1 m\Omega^2 (k_{m2}^2 - k_{m1}^2) \cos 2\theta_0 H_\phi^T H_\phi \, ds + \int_0^1 \bar{G}J H_\phi'^T H_\phi \, ds \tag{4.183}$$

and the constant force terms are the same as those associated with the original
UMARC formulation, and are listed for completeness as

$$F_u = \int_0^1 mx\Omega^2 H_u{}^T\,ds \tag{4.184}$$

$$F_v = \int_0^1 m(\Omega^2 e_g\cos\theta_1 + \ddot{\theta}_0 e_g\sin\theta_1)H_b{}^T\,ds -$$
$$\int_0^1 mx\Omega^2 e_g\cos\theta_1 H_b{}'^T\,ds \tag{4.185}$$

$$F_w = -\int_0^1 m(\Omega^2\beta_p x + \ddot{\theta}_0 e_g\sin\theta_1)H_b{}^T\,ds -$$
$$\int_0^1 mx\Omega^2 e_g\sin\theta_1 H_b{}'^T\,ds \tag{4.186}$$

$$F_\phi = -\int_0^1 mk_m^2\ddot{\theta}_0 + m\Omega^2(k_{m2}^2 - k_{m1}^2)\sin\theta_1\cos\theta_1 H_\phi{}^T\,ds$$
$$-\int_0^1 m\Omega^2\beta_p e_g\cos\theta_1 x H_\phi{}^T\,ds \tag{4.187}$$

The underlined terms in the above equations are the additions to the blade-blade
structural matrices for the present formulation over those of the UMARC metal-
blade helicopter formulation. These terms account for the elastic coupling between
extension, bending, and twist deformations as well as the precone effect which cou-
ples lag bending and twist deformation. These terms represent significant contri-
butions to the original formulation because 1) it allows inclusion of elastic coupling
based on the classical beam element thereby reducing analytical modifications, and
2) accounts for the pitch-lag coupling due to precone which will be shown to have
a significant impact on tiltrotor stability predictions. The reduction in classical
beam stiffnesses due to coupling with shear deformations is accounted for by use
of the effective beam properties as indicated by the overbar on the terms affected.
The original form of the equations associated with these properties is unchanged
from the metal blade formulation. As shown, there are no modifications to the
original mass, damping, or force blade-blade system matrices.

166

The blade-hub matrices are also partitioned, for example:

$$[M_{bh}] = \begin{bmatrix} M_{ux_h} & M_{uy_h} & M_{uz_h} & M_{u\alpha_h} & M_{u\phi_h} & M_{u\zeta_h} & M_{u\beta_{GC}} & M_{u\beta_{GS}} \\ M_{vx_h} & M_{vy_h} & M_{vz_h} & M_{v\alpha_h} & M_{v\phi_h} & M_{v\zeta_h} & M_{v\beta_{GC}} & M_{v\beta_{GS}} \\ M_{wx_h} & M_{wy_h} & M_{wz_h} & M_{w\alpha_h} & M_{w\phi_h} & M_{w\zeta_h} & M_{w\beta_{GC}} & M_{w\beta_{GS}} \\ M_{\phi x_h} & M_{\phi y_h} & M_{\phi z_h} & M_{\phi\alpha_h} & M_{\phi\phi_h} & M_{\phi\zeta_h} & M_{\phi\beta_{GC}} & M_{\phi\beta_{GS}} \end{bmatrix} \qquad (4.188)$$

Based on the strain and kinetic energies derived in the present formulation, these matrix partitions are defined as follows: the nonzero terms of the blade-hub mass matrix are given by,

$$M_{v,\phi_h} = \int_0^1 mx\sin\alpha_p \, H_b{}^T \, ds \qquad (4.189)$$

$$M_{v,\zeta_h} = \int_0^1 mx\cos\alpha_p \, H_b{}^T \, ds \qquad (4.190)$$

$$M_{w,x_h} = -\int_0^1 m\sin\alpha_p \, H_b{}^T \, ds \qquad (4.191)$$

$$M_{w,z_h} = \int_0^1 m\cos\alpha_p \, H_b{}^T \, ds \qquad (4.192)$$

$$M_{\phi,x_h} = -\int_0^1 me_g\cos\theta_1\sin\alpha_p \, H_\phi{}^T \, ds \qquad (4.193)$$

$$M_{\phi,z_h} = \int_0^1 m\cos\alpha_p \, e_g\cos\theta_1 H_\phi{}^T \, ds \qquad (4.194)$$

$$M_{\phi,\phi_h} = -\int_0^1 mxe_g\sin\theta_1\sin\alpha_p \, H_\phi{}^T \, ds \qquad (4.195)$$

$$M_{\phi,\zeta_h} = -\int_0^1 mx\cos\alpha_p \, e_g\sin\theta_1 H_\phi{}^T \, ds \qquad (4.196)$$

the nonzero terms of the blade-hub damping matrix are given by,

$$C_{u,\phi_h} = -\int_0^1 2m\,x\sin\alpha_p \, H_u{}^T \, ds \qquad (4.197)$$

$$C_{u,\zeta_h} = -\int_0^1 2m\,x\cos\alpha_p \, H_u{}^T \, ds \qquad (4.198)$$

$$C_{v,\phi_h} = \int_0^1 2m\,xe_g\cos\theta_1\sin\alpha_p \, H_b'{}^T \, ds \qquad (4.199)$$

$$C_{v,\zeta_h} = \int_0^1 2m\,x\cos\alpha_p \, e_g\cos\theta_1 H_b'{}^T \, ds \qquad (4.200)$$

$$C_{w,\phi_h} = \int_0^1 2m\,xe_g\sin\theta_1\sin\alpha_p \, H_b'{}^T \, ds \qquad (4.201)$$

$$C_{w,\zeta_h} = \int_0^1 2m\,x\cos\alpha_p \, e_g\sin\theta_1 H_b'{}^T \, ds \qquad (4.202)$$

167

and all the terms of the blade-hub stiffness matrix are zero. Many terms from the energy expressions which appear to contribute to the system matrices are made zero by the following relationships:

$$\int_0^{2\pi} a(s)\cos\psi \ d\psi \ = \ 0 \tag{4.203}$$

$$\int_0^{2\pi} a(s)\sin\psi \ d\psi \ = \ 0 \tag{4.204}$$

$$\int_0^{2\pi} a(s)\cos\psi \sin\psi \ d\psi \ = \ 0 \tag{4.205}$$

Since these terms are summed over one rotor revolution in the coupled-trim and stability calculations (to be discussed in Chapters 6 and 7) the net influence is zero, and there is no need to include these terms in the system matrix calculations. All terms associated with the hub motion are new, and do not appear in the original UMARC formulation. There are, however, parallels between the formulations when the pylon angle is set to zero degrees (straight up like in helicopter mode). In this case the hub-related system matrices of the present formulation will match the fuselage-related system matrices of the original UMARC formulation, except that the hub (or fuselage) yawing degree of freedom, ζ_h, was not included there.

4.5.2   Hub Matrices

This section deals with the hub equations which may be written in matrix form as:

$$\Delta = \delta\hat{x}_h^T([M_{hb}]\hat{\ddot{q}} + [C_{hb}]\hat{\dot{q}} + [K_{hb}]\hat{q} + [M_{hh}]\hat{\ddot{x}}_h + [C_{hh}]\hat{\dot{x}}_h + [K_{hh}]\hat{x}_h - F_h) \tag{4.206}$$

where, again, the subscript b refers to the blade and h refers to the hub. These matrices are partitioned by the associated degrees of freedom in the hub and blade similar to the examples of the previous section. Based on the strain and kinetic energies derived in the present formulation, the matrix partitions are defined as

follows: the nonzero terms of the hub-blade mass matrix are given by,

$$M_{\phi_h,v} = \int_0^1 mx\sin\alpha_p \, H_b \, ds \tag{4.207}$$

$$M_{\zeta_h,v} = \int_0^1 mx\cos\alpha_p \, H_b \, ds \tag{4.208}$$

$$M_{x_h,w} = -\int_0^1 m\sin\alpha_p \, H_b \, ds \tag{4.209}$$

$$M_{z_h,w} = \int_0^1 m\cos\alpha_p \, H_b \, ds \tag{4.210}$$

$$M_{x_h,\phi} = -\int_0^1 me_g\cos\theta_1\sin\alpha_p \, H_\phi \, ds \tag{4.211}$$

$$M_{z_h,\phi} = \int_0^1 m\cos\alpha_p \, e_g\cos\theta_1 H_\phi \, ds \tag{4.212}$$

$$M_{\phi_h,\phi} = -\int_0^1 mxe_g\sin\theta_1\sin\alpha_p \, H_\phi \, ds \tag{4.213}$$

$$M_{\zeta_h,\phi} = -\int_0^1 mx\cos\alpha_p \, e_g\sin\theta_1 H_\phi \, ds \tag{4.214}$$

the nonzero terms of the hub-blade damping matrix are given by,

$$C_{\phi_h,u} = \int_0^1 2m \, x\sin\alpha_p \, H_u \, ds \tag{4.215}$$

$$C_{\phi_h,v} = \int_0^1 2m \, xe_g\cos\theta_1\sin\alpha_p \, H_b' \, ds \tag{4.216}$$

$$C_{\zeta_h,u} = \int_0^1 2m \, x\cos\alpha_p \, H_u \, ds \tag{4.217}$$

$$C_{\zeta_h,v} = \int_0^1 2m \, x\cos\alpha_p \, e_g\cos\theta_1 H_b' \, ds \tag{4.218}$$

$$C_{\phi_h,w} = \int_0^1 2m \, x(\beta_p\sin\alpha_p \, H_b - e_g\sin\theta_1\sin\alpha_p \, H_b') \, ds \tag{4.219}$$

$$C_{\zeta_h,w} = \int_0^1 2m \, x(\beta_p\cos\alpha_p \, H_b - \cos\alpha_p \, e_g\sin\theta_1 H_b') \, ds \tag{4.220}$$

$$C_{\phi_h,\phi} = \int_0^1 2m \, x\beta_p e_g\cos\theta_1\sin\alpha_p \, H_\phi \, ds \tag{4.221}$$

$$C_{\zeta_h,\phi} = \int_0^1 2m \, x\beta_p\cos\alpha_p \, e_g\cos\theta_1 H_\phi \, ds \tag{4.222}$$

and all the terms of the hub-blade stiffness matrix are zero.

The nonzero terms of the hub-hub mass matrix are given by,

$$M_{x_h,x_h} = \int_0^1 m \, ds \tag{4.223}$$

$$M_{x_h,\alpha_h} = -\int_0^1 m \cos\alpha_p \, h \, ds \tag{4.224}$$

169

$$M_{y_h,y_h} = \int_0^1 m\,ds \tag{4.225}$$

$$M_{y_h,\phi_h} = \int_0^1 m\cos\alpha_p\, h\,ds \tag{4.226}$$

$$M_{y_h,\zeta_h} = -\int_0^1 mh\sin\alpha_p\,ds \tag{4.227}$$

$$M_{z_h,z_h} = \int_0^1 m\,ds \tag{4.228}$$

$$M_{z_h,\alpha_h} = -\int_0^1 mh\sin\alpha_p\,ds \tag{4.229}$$

$$M_{\alpha_h,x_h} = -\int_0^1 m\cos\alpha_p\, h\,ds \tag{4.230}$$

$$M_{\alpha_h,z_h} = -\int_0^1 mh\sin\alpha_p\,ds \tag{4.231}$$

$$M_{\alpha_h,\alpha_h} = \int_0^1 m(h^2 + \cos^2\psi\, x^2)\,ds \tag{4.232}$$

$$M_{\alpha_h,\beta_{GC}} = \int_0^1 m\cos^2\psi\, x^2\,ds \tag{4.233}$$

$$M_{\phi_h,\phi_h} = \int_0^1 m(\cos^2\alpha_p\, h^2 + \cos^2\psi\sin^2\alpha_p\, x^2 + \sin^2\psi\, x^2)\,ds \tag{4.234}$$

$$M_{\phi_h,\zeta_h} = \int_0^1 m(-\cos\alpha_p\, h^2\sin\alpha_p + \cos\alpha_p\cos^2\psi\sin\alpha_p\, x^2)\,ds \tag{4.235}$$

$$M_{\phi_h,\beta_{GS}} = \int_0^1 m - \cos\alpha_p\sin^2\psi\, x^2\,ds \tag{4.236}$$

$$M_{\zeta_h,y_h} = -\int_0^1 mh\sin\alpha_p\,ds \tag{4.237}$$

$$M_{\zeta_h,\phi_h} = \int_0^1 m(-\cos\alpha_p\, h^2\sin\alpha_p + \cos\alpha_p\cos^2\psi\sin\alpha_p\, x^2)\,ds \tag{4.238}$$

$$M_{\zeta_h,\zeta_h} = \int_0^1 m(h^2\sin^2\alpha_p + \cos^2\alpha_p\cos^2\psi\, x^2 + \sin^2\psi\, x^2)\,ds \tag{4.239}$$

$$M_{\zeta_h,\beta_{GS}} = \int_0^1 m\sin\alpha_p\sin^2\psi\, x^2\,ds \tag{4.240}$$

$$M_{\beta_{GC},\alpha_h} = \int_0^1 m\cos^2\psi\, x^2\,ds \tag{4.241}$$

$$M_{\beta_{GC},\beta_{GC}} = \int_0^1 m\cos^2\psi\, x^2\,ds \tag{4.242}$$

$$M_{\beta_{GS},\phi_h} = -\int_0^1 m\cos\alpha_p\sin^2\psi\, x^2\,ds \tag{4.243}$$

$$M_{\beta_{GS},\zeta_h} = \int_0^1 m\sin\alpha_p\sin^2\psi\, x^2\,ds \tag{4.244}$$

$$M_{\beta_{GS},\beta_{GS}} = \int_0^1 m\sin^2\psi\, x^2\,ds \tag{4.245}$$

C-3

the nonzero terms of the hub-hub damping matrix are given by,

$$C_{\alpha_h,\phi_h} = \int_0^1 2m\cos\alpha_p \cos^2\psi \, x^2 \, ds \tag{4.246}$$

$$C_{\alpha_h,\zeta_h} = \int_0^1 2m\cos^2\psi \sin\alpha_p \, x^2 \, ds \tag{4.247}$$

$$C_{\alpha_h,\beta_{GS}} = \int_0^1 2m\cos^2\psi \, x^2 \, ds \tag{4.248}$$

$$C_{\phi_h,\alpha_h} = \int_0^1 2m\cos\alpha_p \sin^2\psi \, x^2 \, ds \tag{4.249}$$

$$C_{\phi_h,\beta_{GC}} = \int_0^1 2m\cos\alpha_p \sin^2\psi \, x^2 \, ds \tag{4.250}$$

$$C_{\zeta_h,\alpha_h} = \int_0^1 2m\sin\alpha_p \sin^2\psi \, x^2 \, ds \tag{4.251}$$

$$C_{\zeta_h,\beta_{GC}} = \int_0^1 2m\sin\alpha_p \sin^2\psi \, x^2 \, ds \tag{4.252}$$

$$C_{\beta_{GC},\phi_h} = \int_0^1 2m\cos\alpha_p \cos^2\psi \, x^2 \, ds \tag{4.253}$$

$$C_{\beta_{GC},\zeta_h} = \int_0^1 2m\cos^2\psi \sin\alpha_p \, x^2 \, ds \tag{4.254}$$

$$C_{\beta_{GC},\beta_{GS}} = \int_0^1 2m\cos^2\psi \, x^2 \, ds \tag{4.255}$$

$$C_{\beta_{GS},\alpha_h} = \int_0^1 2m\sin^2\psi \, x^2 \, ds \tag{4.256}$$

$$C_{\beta_{GS},\beta_{GC}} = -\int_0^1 2m\sin^2\psi \, x^2 \, ds \tag{4.257}$$

and the nonzero terms of the hub-hub stiffness matrix are given by,

$$K_{\alpha_h,\beta_{GC}} = -\int_0^1 \cos^2\psi \, x^2 \, ds \tag{4.258}$$

$$K_{\phi_h,\beta_{GS}} = \int_0^1 \cos\alpha_p \sin^2\psi \, x^2 \, ds \tag{4.259}$$

$$K_{\zeta_h,\beta_{GS}} = -\int_0^1 \sin\alpha_p \sin^2\psi \, x^2 \, ds \tag{4.260}$$

$$K_{\beta_{GC},\alpha_h} = -\int_0^1 \cos^2\psi \, x^2 \, ds \tag{4.261}$$

$$K_{\beta_{GC},\beta_{GC}} = \int_0^1 -\cos^2\psi \, x^2 \, ds + K_{\beta_{GC}} \tag{4.262}$$

$$K_{\beta_{GS},\zeta_h} = -\int_0^1 \sin\alpha_p \sin^2\psi \, x^2 \, ds \tag{4.263}$$

$$K_{\beta_{GS},\beta_{GS}} = -\int_0^1 \sin^2\psi \, x^2 \, ds + K_{\beta_{GS}} \tag{4.264}$$

Again, several terms from the energy expression are made zero because they have no net influence after integration around one revolution of the azimuth. It may

171

be surprising that there are nonzero blade-related terms in the hub-hub stiffness matrix. These terms do not add stiffness to the hub as they appear to do, but serve to cancel out the blade-related hub-hub mass contributions to stiffness which occur when those terms are transformed into a nonrotating reference frame. Notice the similar form of the blade-related mass and stiffness terms of the same indices. The blade-related mass terms are necessary because the blades contribute to the overall inertial properties of the hub. The natural process for these inertial terms is to contribute stiffness when a transformation from the rotating system to a fixed system takes place. The hub degrees of freedom are in a fixed system, but it is intuitive that there should be no stiffness contributions from the blade to the hub stiffnesses (in vacuum). The energy expressions take this into account by subtracting these stiffness contributions out, as is the role of the blade-related hub-hub stiffness terms listed above. The contributions from the hub strain energy are shown in the form of the stiffnesses $K_{\beta_{GC}}$ and $K_{\beta_{GS}}$. There is no strain energy associated with any of the other six degrees of freedom because they are, at present, free in space. The stiffness that will be associated with these degrees of freedom comes from the wing during the stability analysis matrix assembly process to be discussed in Chapter 7.

4.5.3 Wing Matrices

The wing is discretized as an elastic beam using the same beam element as that of the rotor blade. Because of this, the structural mass, damping, and stiffness matrices are the same as those for the rotor blade with a very few modifications. First, the wing is fixed so $\Omega = 0$. This makes all the structural contributions to the damping matrices zero also. Second, there is no precone so all terms containing β_p are zero. Third, there is no twist or control collective or cyclic to the value of θ_1 is zero. Fourth, the hub motions are self-contained in the wing matrices so there

are no wing-hub matrices. The wing system matrices are thus given as

$$[M_{ww}] = [M_{bb}], (\beta_p = \Omega = \theta_1 = 0) \tag{4.265}$$

$$[K_{ww}] = [K_{bb}], (\beta_p = \Omega = \theta_1 = 0) \tag{4.266}$$

$$[C_{ww}] = 0 \tag{4.267}$$

The motion of the wing is coupled to the hub (for stability calculations) by the six wing tip nodal displacements which correspond to six of the hub degrees as follows:

Wing dof	Hub dof	
u_1	$= -y_h$	(4.268)
v_1	$= x_h$	(4.269)
v_1'	$= \psi_h$	(4.270)
w_1	$= z_h$	(4.271)
w_1'	$= -\phi_h$	(4.272)
ϕ_1	$= -\alpha_h$	(4.273)

where $u_1, v_1, v_1', w_1, w_1'$, and ϕ_1 represent the discrete degrees of freedom at the wing tip. For trim and performance analysis, the wing is assumed to be rigid, and the hub degrees of freedom are fixed.
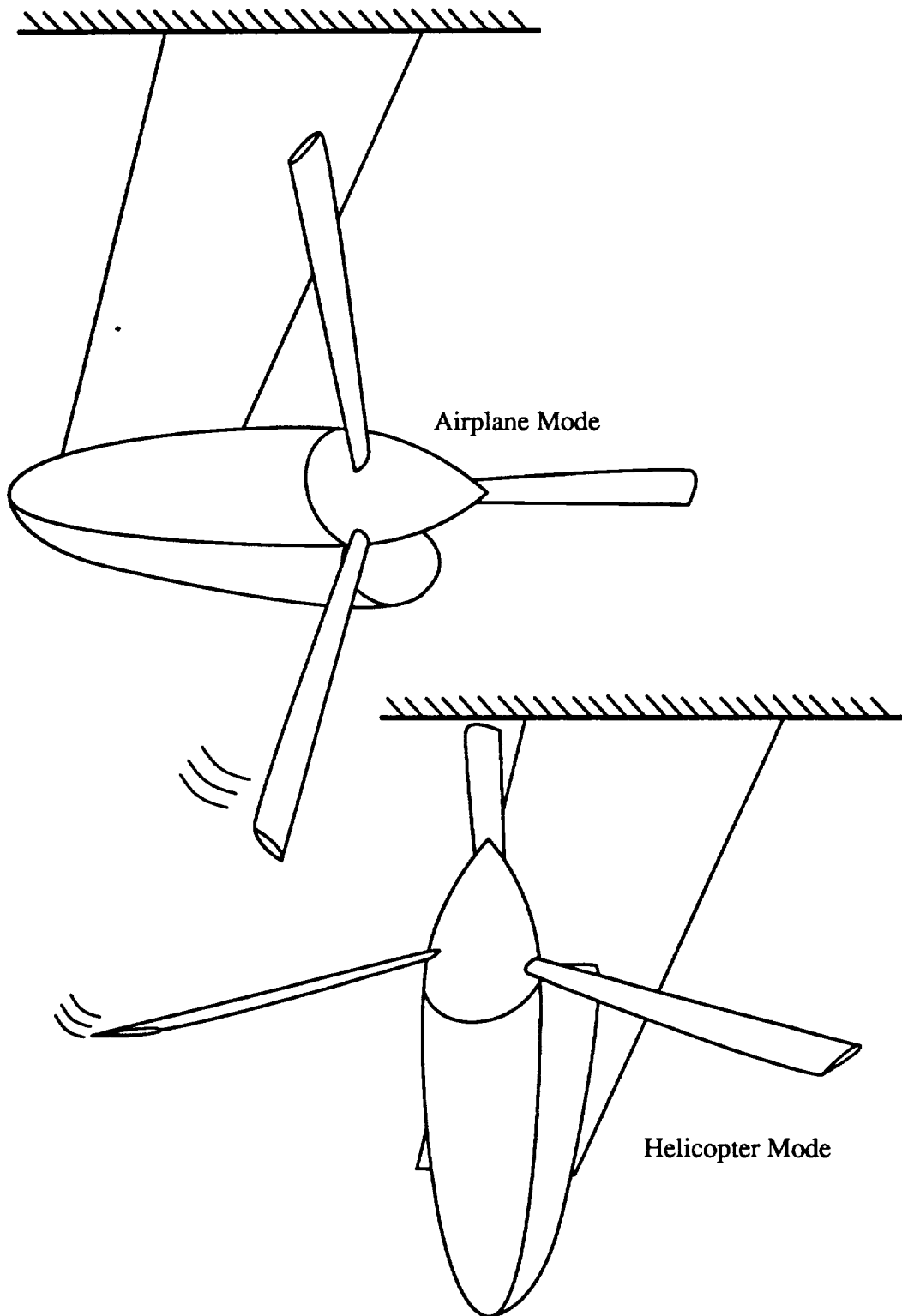
Figure 4.1: Basic tiltrotor configuration used for derivation of equations of motion.
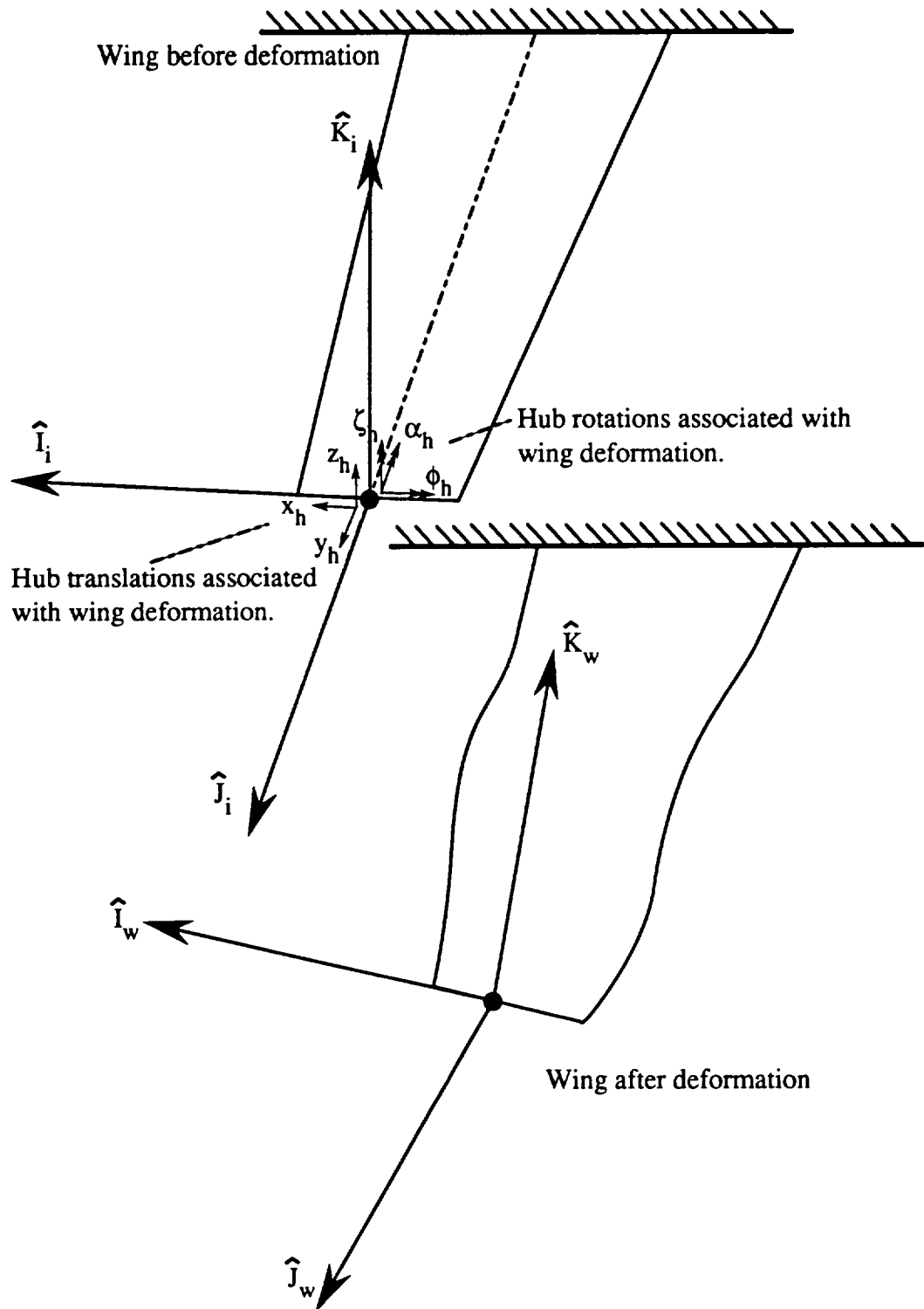
Figure 4.2: Tiltrotor coordinate system definition: inertial and wing reference frames showing hub motions.

175
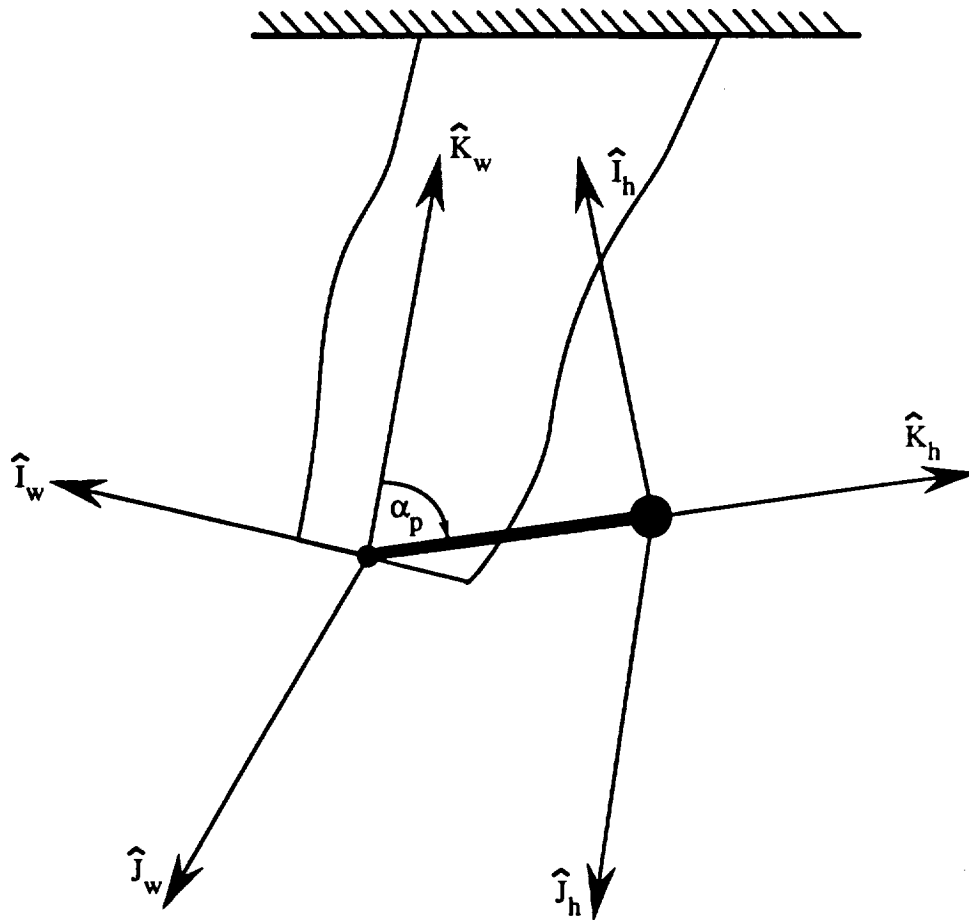
Figure 4.3: Tiltrotor coordinate system definition: wing and hub reference frames showing pylon angle and rigid pylon offset.
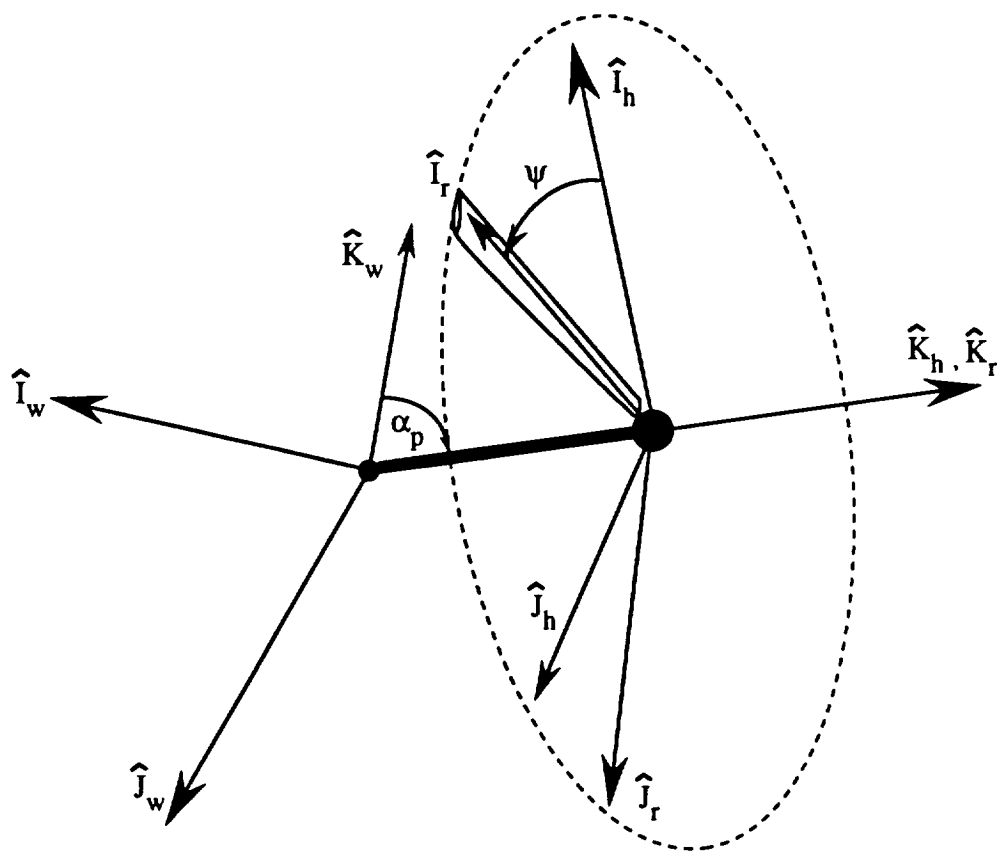
Figure 4.4: Tiltrotor coordinate system definition: wing, hub, and rotating-blade reference frames.
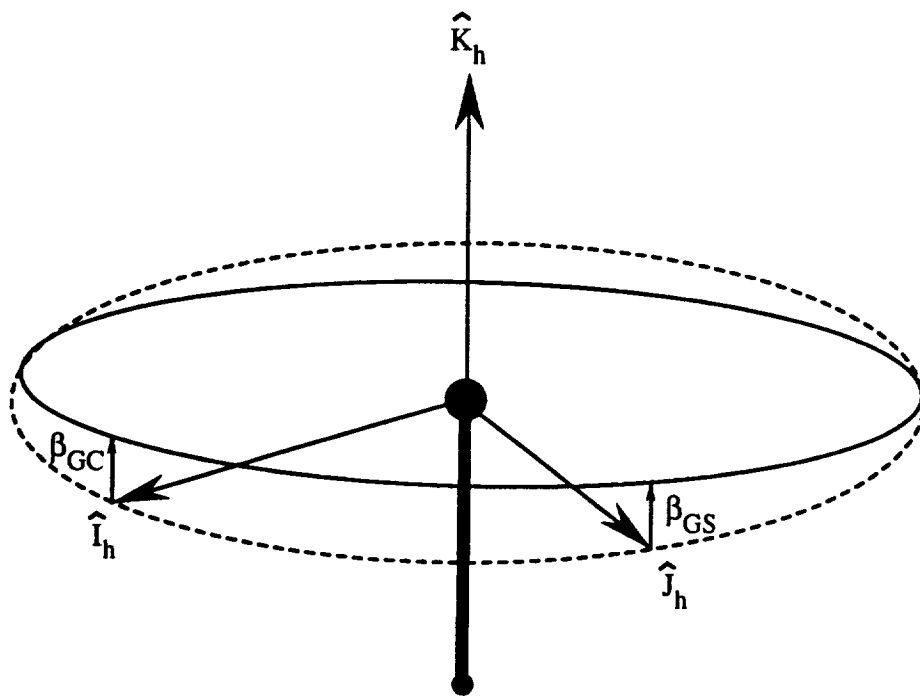
Figure 4.5: Tiltrotor coordinate system definition: hub and gimbal reference frames in fixed system.
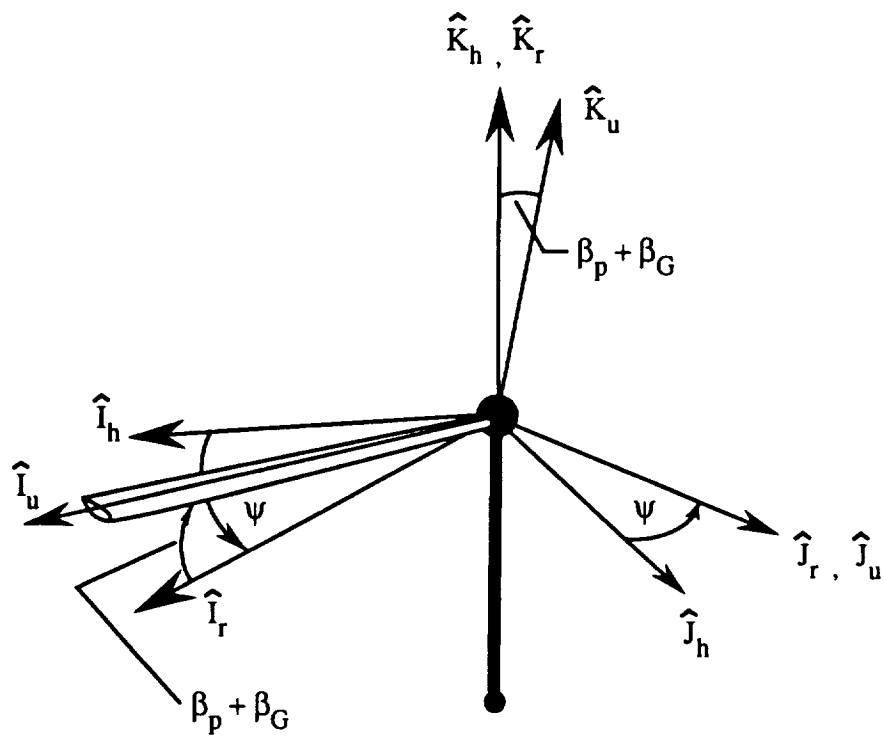
Figure 4.6: Tiltrotor coordinate system definition: hub, rotating-blade, and undeformed-blade reference frames showing precone and gimbal angles.

Chapter 5

Aerodynamic Modeling

The tiltrotor configuration requires several substantial modifications to the helicopter aerodynamic modeling as available in UMARC. The modifications are necessary because of the large angle of attack of the pylon and requirements for additional hub-related degrees of freedom for the tiltrotor model. The required changes are extensive, and thus it becomes necessary to derive the new aerodynamic system equations from basic principles. This derivation is performed in the current chapter.

The aerodynamic formulation is limited to the quasi-steady aerodynamics modeling. The quasi-steady aerodynamic analysis assumes the blade loads are a function of instantaneous blade section angle of attack at each blade spanwise location. Furthermore, the section lift, drag, and moment coefficients are based solely on static data associated with the airfoil of the particular spanwise location. The quasi-steady aerodynamic loading is dependent on the local velocities of the blade which are functions of the free-stream velocity, blade motion relative to an inertial frame, hub motion relative to an inertial frame, and the fuselage motion relative to an inertial frame. Fuselage motion, however, is not considered in the present formulation. It is apparent that the blade loads are motion dependent (functions of the hub and blade degrees of freedom), and as such they contribute to the system

mass, damping, and stiffness matrices as well as the load vector.

The aerodynamic forces are initially calculated in the deformed blade frame. This is particularly advantageous for a tiltrotor configuration because in the deformed frame, the high-inflow aerodynamics, which create difficulties for the aerodynamic modeling of rigid blade linear systems (because of high inflow angles), are treated in precisely the same manner as the helicopter low-inflow aerodynamics. The main difference between the helicopter and tiltrotor aerodyamics is in the transformation matrices which relate the blade loads and velocities in the deformed frame to an inertial frame of reference.

In the first section of this chapter, the local blade section velocities are derived in the deformed blade system. The aerodynamic loads associated with these velocities are defined in the following section, and are transformed into the inertial reference system. The work performed by the loads is derived in the next section, and Hamilton's principle is used to obtain the discretized finite-element matrices associated with the hub and blade degrees of freedom. The aerodynamic model for the wing is discussed in the final section of this chapter.

5.1   Derivation of Local Rotor Blade Velocities

The velocity components in the three principal deformed frame axes are derived using the same reference frames as those used to define the structural model in Chapter 4. There are three contributions to the velocities considered in the present derivation: the aircraft forward flight velocity, the blade motion, and the hub motion. As mentioned previously, the fuselage motion contribution is not considered in the present formulation. The general expression of the local velocity vector at a particular blade station can be written relative to any frame of reference as

$$\vec{V} = \vec{V_b} + \vec{V_h} - \vec{V_w} \tag{5.1}$$

181

where $\vec{V_b}, \vec{V_h},$ and $\vec{V_w}$ represent the blade, hub and relative wind contributions, respectively, to the total velocity. Each velocity vector will eventually be defined in the deformed blade reference frame, but it is advantageous to initially define each contribution in separate frames and transform the results into the deformed frame. The wind velocity and hub motions are initially defined in the inertial reference frame, while the blade motions are initially defined in the rotating reference frame.

The relative wind velocity is given by

$$\vec{V_w} = \mu \Omega R \, \hat{I_i} - \lambda_i \Omega R \, \hat{K_h} \tag{5.2}$$

where $\mu = V/\Omega R$ is defined as the advance ratio and λ_i is the induced flow produced by the thrusting rotor. The advance ratio in this case is defined in a slightly different form than that used in pure helicopter theory where $\mu = V \cos \alpha_s /\Omega R$. The induced flow is shown to be defined in the hub reference frame because thrust is defined perpendicular to the hub plane. The wind velocity is written in the inertial reference frame in vector form as

$$\vec{V_w} = (\{\mu \Omega R, 0, 0\} + \{0, 0, -\lambda_i \Omega R\}[T_{gi}]) \left\{ \begin{array}{c} \hat{I_i} \\ \hat{J_i} \\ \hat{K_i} \end{array} \right\} \tag{5.3}$$

The contribution of the blade and hub velocities is determined by taking the time derivative of the position vector in the inertial frame. This approach eliminates the need to determine the time rate of change of a local rotating reference frame with respect to an inertial frame since the local frame in this case *is* the inertial frame. The position vector of an arbitrary point on the cross section of the deformed blade is given by:

$$\vec{R} = \{x_h \hat{I_i}, y_h \hat{J_i}, z_h \hat{K_i}\} + h \hat{K_w} + \{(x+u)\hat{I_u}, v\hat{J_u}, w\hat{K_u}\} + \eta \hat{J_d} \tag{5.4}$$

which may be written entirely in the inertial reference frame as

$$\vec{R} = (\{x_h, y_h, z_h\} + \{0, 0, h\}[T_{wi}] + \{(x+u), v, w\}[T_{ui}]$$

182

$$+\{0,\eta,0\}[T_{di}]) \left\{ \begin{array}{c} \hat{I}_i \\ \hat{J}_i \\ \hat{K}_i \end{array} \right\} \tag{5.5}$$

The blade and hub degrees of freedom are functions of time as is the azimuth angle ψ which may be written as Ωt. The precone angle β_p is assumed to be constant. The velocity due to blade and hub motions is then defined by

$$\vec{V}_b + \vec{V}_h = \frac{\partial \vec{R}}{\partial t} = V_{b_x}\hat{I}_i + V_{b_y}\hat{J}_i + V_{b_z}\hat{K}_i \tag{5.6}$$

The wind velocity as defined by Eqn. 5.3 is then subtracted from the hub and blade velocity contributions. The total velocity is then transformed into the deformed frame as follows

$$\begin{aligned} \vec{V}_b + \vec{V}_h - \vec{V}_w &= (\{V_{b_x}, V_{b_y}, V_{b_z}\} + \{-\mu\Omega R, 0, 0\} \\ &\quad + \{0, 0, \lambda_i \Omega R\}[T_{hi}]) \ [T_{id}] \left\{ \begin{array}{c} \hat{I}_d \\ \hat{J}_d \\ \hat{K}_d \end{array} \right\} \end{aligned} \tag{5.7}$$

which is simplified to the notation

$$\vec{V}_{bhw} = U_r \hat{I}_d + U_t \hat{J}_d + U_p \hat{K}_d \tag{5.8}$$

where U_r, U_t, and U_p have been nondimensionalized by the rotor tip speed ΩR. In these expressions the following substitution is made to account for kinematic pitch-lag and pitch-flap coupling which may be produced by the gimbal rotor system controls geometry:

$$\theta_1 = \theta_1 + k_\beta \beta_G + k_\zeta \zeta_h \tag{5.9}$$

After application of the ordering scheme, and substitution for the rotating frame gimbal angle β_G in terms of fixed frame gimbal angles β_{GC} and β_{GS} (as defined by Eqns. 4.1 and 4.2), the velocity components are defined in terms of the blade and hub degrees of freedom. These velocities are listed in the equations to follow.

183

Each velocity component is separated into constant (subscript c), linear (subscript l), and nonlinear parts (subscript nl), and the linear part is written as a coefficient of the system degree of freedom with which it is associated. The radial component of velocity, which is positive moving from root to tip, is given by

$$U_r = R_c + R_l + R_{nl} \tag{5.10}$$

and

$$R_c = \lambda\beta_p - \mu\cos\alpha_p\,\cos\psi - \eta_r\cos\theta_1 + \mu\beta_p\sin\alpha_p \tag{5.11}$$

$$R_l = R_u + R_v + R_{v'} + \ldots + R_{\dot{\beta}_{GC}} + R_{\dot{\beta}_{GS}}$$

$$R_u = 0 \tag{5.12}$$

$$R_v = -1 \tag{5.13}$$

$$R_{v'} = \mu\cos\alpha_p\,\sin\psi + x \tag{5.14}$$

$$R_w = 0 \tag{5.15}$$

$$R_{w'} = \lambda + \mu\beta_p\cos\alpha_p\,\cos\psi + \mu\sin\alpha_p \tag{5.16}$$

$$R_{\dot{u}} = 1 \tag{5.17}$$

$$R_{\dot{v}} = 0 \tag{5.18}$$

$$R_{\dot{w}} = 0 \tag{5.19}$$

$$R_{\dot{v}'} = -\eta_r\cos\theta_1 \tag{5.20}$$

$$R_{\dot{w}'} = -\eta_r\sin\theta_1 \tag{5.21}$$

$$R_\phi = \eta_r\sin\theta_1 \tag{5.22}$$

$$R_{\dot{\phi}} = 0 \tag{5.23}$$

$$R_{\alpha_h} = \mu(\cos\psi\,\sin\alpha_p + \beta_p\cos\alpha_p) \tag{5.24}$$

$$R_{\phi_h} = 0 \tag{5.25}$$

$$R_{\zeta_h} = \mu\sin\psi \tag{5.26}$$

$$R_{\beta_{GC}} = \lambda\cos\psi + \mu\cos\psi \, \sin\alpha_p + \eta_r\sin\psi \, \sin\theta_1 \qquad (5.27)$$

$$R_{\beta_{GS}} = \lambda\sin\psi + \mu\sin\alpha_p \, \sin\psi - \eta_r\cos\psi \, \sin\theta_1 \qquad (5.28)$$

$$R_{\dot{x}_h} = -(\beta_p\sin\alpha_p - \cos\psi \, \cos\alpha_p) \qquad (5.29)$$

$$R_{\dot{y}_h} = \sin\psi \qquad (5.30)$$

$$R_{\dot{z}_h} = (\cos\psi \, \sin\alpha_p + \beta_p\cos\alpha_p) \qquad (5.31)$$

$$R_{\dot{\alpha}_h} = -h\cos\psi - \eta_r\cos\psi \, \sin\theta_1 \qquad (5.32)$$

$$R_{\dot{\phi}_h} = h\cos\alpha_p \, \sin\psi + \eta_r(\sin\psi \, \cos\alpha_p \, \sin\theta_1 - \cos\theta_1 \, \sin\alpha_p) \qquad (5.33)$$

$$R_{\dot{\zeta}_h} = -\eta_r\cos\alpha_p \, \cos\theta_1 - h\sin\alpha_p \, \sin\psi - \eta_r\sin\alpha_p \, \sin\psi \, \sin\theta_1 \qquad (5.34)$$

$$R_{\dot{\beta}_{GC}} = -\eta_r\cos\psi \, \sin\theta_1 \qquad (5.35)$$

$$R_{\dot{\beta}_{GS}} = -\eta_r\sin\psi \, \sin\theta_1 \qquad (5.36)$$

$$R_{nl} = 0 \qquad (5.37)$$

R_{nl} is given a zero value using the ordering scheme. As will be shown later in this chapter, the radial component of velocity only contributes to the aerodynamic forces through the drag terms which are at least an order of magnitude smaller than the lift terms. The tangential component of velocity, which is positive moving from leading to trailing edge, is given by

$$U_t = T_c + T_l + T_{nl} \qquad (5.38)$$

and

$$T_c = \mu\cos\alpha_p \, \cos\theta_1 \, \sin\psi + \lambda\sin\theta_1 + \mu\beta_p\cos\alpha_p \, \cos\psi \, \sin\theta_1 +$$
$$\mu\sin\alpha_p \, \sin\theta_1 + x\cos\theta_1 \qquad (5.39)$$

$$T_l = T_u + T_v + T_{v'} + \ldots + T_{\dot{\beta}_{GC}} + T_{\dot{\beta}_{GS}}$$
$$T_u = \cos\theta_1 \qquad (5.40)$$

185

$$T_v = \beta_p \sin\theta_1 \tag{5.41}$$

$$T_{v'} = -\lambda\beta_p\cos\theta_1 - \mu\cos\theta_1\left(\beta_p\sin\alpha_p - \cos\psi\,\cos\alpha_p\right) \tag{5.42}$$

$$T_w = -\beta_p\cos\theta_1 \tag{5.43}$$

$$T_{w'} = -\lambda\beta_p\sin\theta_1 - \mu\sin\theta_1\left(\beta_p\sin\alpha_p - \cos\psi\,\cos\alpha_p\right) \tag{5.44}$$

$$T_{\dot{u}} = 0 \tag{5.45}$$

$$T_{\dot{v}} = \cos\theta_1 \tag{5.46}$$

$$T_{\dot{w}} = \sin\theta_1 \tag{5.47}$$

$$T_{\dot{v}'} = 0 \tag{5.48}$$

$$T_{\dot{w}'} = 0 \tag{5.49}$$

$$T_\phi = -\mu\cos\alpha_p\,\sin\theta_1\sin\psi + \lambda\cos\theta_1 + \mu\beta_p\cos\psi\,\cos\theta_1\cos\alpha_p +$$
$$\mu\sin\alpha_p\,\cos\theta_1 - x\sin\theta_1 \tag{5.50}$$

$$T_{\dot\phi} = 0 \tag{5.51}$$

$$T_{\alpha_h} = -\mu\beta_p\cos\psi\,\sin\alpha_p\,\sin\theta_1 + \mu(\cos\alpha_p\,\sin\theta_1 - \cos\theta_1\,\sin\alpha_p\,\sin\psi) \tag{5.52}$$

$$T_{\phi_h} = 0 \tag{5.53}$$

$$T_{\zeta_h} = \mu\cos\psi\,\cos\theta_1 - \mu\beta_p\sin\psi\,\sin\theta_1 - \lambda\cos\theta_1\,k_\zeta -$$
$$\mu\beta_p\cos\alpha_p\,\cos\psi\,\cos\theta_1\,k_\zeta - \mu\cos\theta_1\,\sin\alpha_p\,k_\zeta \tag{5.54}$$

$$T_{\beta_{GC}} = \mu\cos\alpha_p\,\cos\psi\,^2\sin\theta_1 - x\sin\psi\,\sin\theta_1 + \lambda\cos\psi\,\cos\theta_1\,k_\beta +$$
$$\mu\beta_p\cos\alpha_p\,\cos\psi\,^2\cos\theta_1\,k_\beta + \mu\cos\psi\,\cos\theta_1\,\sin\alpha_p\,k_\beta \tag{5.55}$$

$$T_{\beta_{GS}} = \mu\cos\alpha_p\,\cos\psi\,\sin\psi\,\sin\theta_1 + \cos\psi\,\sin\theta_1\,x + \lambda\cos\theta_1\,\sin\psi\,k_\beta +$$
$$\mu\beta_p\cos\alpha_p\,\cos\psi\,\cos\theta_1\,\sin\psi\,k_\beta + \mu\cos\theta_1\,\sin\alpha_p\,\sin\psi\,k_\beta \tag{5.56}$$

$$T_{\dot{x}_h} = -\beta_p\cos\alpha_p\,\cos\psi\,\sin\theta_1 - (\cos\alpha_p\,\cos\theta_1\,\sin\psi + \sin\alpha_p\,\sin\theta_1) \tag{5.57}$$

$$T_{\dot{y}_h} = \cos\psi\,\cos\theta_1 - \beta_p\sin\psi\,\sin\theta_1 \tag{5.58}$$

$$T_{\dot{z}_h} = -\beta_p\cos\psi\,\sin\alpha_p\,\sin\theta_1 + (\cos\alpha_p\,\sin\theta_1 - \cos\theta_1\,\sin\alpha_p\,\sin\psi) \tag{5.59}$$

$$T_{\dot\alpha_h} = h(\cos\theta_1\,\sin\psi + \beta_p\cos\psi\,\sin\theta_1) + x(\cos\psi\,\sin\theta_1 + \beta_p\cos\theta_1\,\sin\psi) \tag{5.60}$$

$$T_{\dot\phi_h} = h\cos\alpha_p \cos\psi \cos\theta_1 - \beta_p h\cos\alpha_p \sin\psi \sin\theta_1 +$$

$$x\beta_p\cos\alpha_p \cos\psi \cos\theta_1 - x(\sin\psi \cos\alpha_p \sin\theta_1 - \cos\theta_1 \sin\alpha_p) \quad (5.61)$$

$$T_{\dot\zeta_h} = -h\cos\psi \cos\theta_1 \sin\alpha_p + \beta_p h\sin\alpha_p \sin\psi \sin\theta_1 + x\cos\alpha_p \cos\theta_1$$

$$-x\beta_p\cos\psi \cos\theta_1 \sin\alpha_p + x\sin\alpha_p \sin\psi \sin\theta_1 \quad (5.62)$$

$$T_{\dot\beta_{GC}} = x\cos\psi \sin\theta_1 \quad (5.63)$$

$$T_{\dot\beta_{GS}} = x\sin\psi \sin\theta_1 \quad (5.64)$$

$$T_{nl} = \beta_{GC}\cos\psi \sin\theta_1\, v + \beta_{GS}\sin\psi \sin\theta_1\, v - \lambda\beta_{GC}\cos\psi \cos\theta_1\, v' -$$

$$\mu\beta_{GC}\cos\psi \cos\theta_1 \sin\alpha_p\, v' - \lambda\beta_{GS}\cos\theta_1 \sin\psi\, v' -$$

$$\mu\beta_{GS}\cos\theta_1 \sin\alpha_p \sin\psi\, v' + \cos\theta_1\, vv' - \beta_{GC}\cos\psi \cos\theta_1\, w -$$

$$\beta_{GS}\cos\theta_1 \sin\psi\, w - \lambda\beta_{GC}\cos\psi \sin\theta_1\, w' -$$

$$\mu\beta_{GC}\cos\psi \sin\alpha_p \sin\theta_1\, w' - \lambda\beta_{GS}\sin\psi \sin\theta_1\, w' -$$

$$\mu\beta_{GS}\sin\alpha_p \sin\psi \sin\theta_1\, w' + \sin\theta_1\, vw' +$$

$$\mu\beta_{GC}^2\cos\alpha_p \cos\psi\,^3\cos\theta_1\, k_\beta +$$

$$2\mu\beta_{GC}\beta_{GS}\cos\alpha_p \cos\psi\,^2\cos\theta_1 \sin\psi\, k_\beta +$$

$$\mu\beta_{GS}^2\cos\alpha_p \cos\psi \cos\theta_1 \sin\psi\,^2 k_\beta + \beta_{GC}\cos\psi \cos\theta_1\, \dot w k_\beta +$$

$$\beta_{GS}\cos\theta_1 \sin\psi\, \dot w k_\beta + \mu\beta_{GC}\cos\alpha_p \cos\psi\,^2\cos\theta_1\, w' k_\beta +$$

$$\mu\beta_{GS}\cos\alpha_p \cos\psi \cos\theta_1 \sin\psi\, w' k_\beta +$$

$$\beta_{GC}\dot\beta_{GC}\cos\psi\,^2\cos\theta_1\, x k_\beta + \beta_{GC}\beta_{GS}\cos\psi\,^2\cos\theta_1\, x k_\beta -$$

$$\beta_{GC}^2\cos\psi \cos\theta_1 \sin\psi\, x k_\beta + \dot\beta_{GC}\beta_{GS}\cos\psi \cos\theta_1 \sin\psi\, x k_\beta +$$

$$\beta_{GS}^2\cos\psi \cos\theta_1 \sin\psi\, x k_\beta + \beta_{GC}\dot\beta_{GS}\cos\psi \cos\theta_1 \sin\psi\, x k_\beta -$$

$$\beta_{GC}\beta_{GS}\cos\theta_1 \sin\psi\,^2 x k_\beta + \beta_{GS}\dot\beta_{GS}\cos\theta_1 \sin\psi\,^2 x k_\beta -$$

$$\mu\beta_{GC}\cos\psi \sin\psi \sin\theta_1\, \zeta_h - \mu\beta_{GS}\sin\psi\,^2\sin\theta_1\, \zeta_h -$$

$$\mu\cos\theta_1 \sin\psi\, v'\zeta_h - \mu\sin\psi \sin\theta_1\, w'\zeta_h -$$

187

$$\mu\beta_{GC}\cos\alpha_p\,\cos\psi\,^2\cos\theta_1\,k_\zeta\zeta_h -$$

$$\mu\beta_{GS}\cos\alpha_p\,\cos\psi\,\cos\theta_1\,\sin\psi\,k_\zeta\zeta_h - \cos\theta_1\,\dot{w}k_\zeta\zeta_h -$$

$$\mu\cos\alpha_p\,\cos\psi\,\cos\theta_1\,w'k_\zeta\zeta_h - \dot{\beta}_{GC}\cos\psi\,\cos\theta_1\,xk_\zeta\zeta_h -$$

$$\beta_{GS}\cos\psi\,\cos\theta_1\,xk_\zeta\zeta_h + \beta_{GC}\cos\theta_1\,\sin\psi\,xk_\zeta\zeta_h -$$

$$\dot{\beta}_{GS}\cos\theta_1\,\sin\psi\,xk_\zeta\zeta_h + \cos\psi\,^2\cos\theta_1\,x\zeta_h^2 +$$

$$\cos^2\alpha_p\,\cos\theta_1\,\sin\psi\,^2x\zeta_h^2 + \cos\alpha_p\,\sin\alpha_p\,\sin\psi\,\sin\theta_1\,x\zeta_h^2 +$$

$$\beta_{GC}\cos\psi\,h\sin\alpha_p\,\sin\psi\,\sin\theta_1\,\dot{\zeta}_h + \beta_{GS}h\sin\alpha_p\,\sin\psi\,^2\sin\theta_1\,\dot{\zeta}_h +$$

$$\cos\psi\,\sin\alpha_p\,\sin\theta_1\,v\dot{\zeta}_h + \cos\theta_1\,h\sin\alpha_p\,\sin\psi\,v'\dot{\zeta}_h -$$

$$\cos\psi\,\cos\theta_1\,\sin\alpha_p\,w\dot{\zeta}_h + h\sin\alpha_p\,\sin\psi\,\sin\theta_1\,w'\dot{\zeta}_h -$$

$$\beta_{GC}\cos\psi\,^2\cos\theta_1\,\sin\alpha_p\,x\dot{\zeta}_h - \beta_{GS}\cos\psi\,\cos\theta_1\,\sin\alpha_p\,\sin\psi\,x\dot{\zeta}_h +$$

$$\beta_{GC}\cos\psi\,\cos\theta_1\,\sin\alpha_p\,\sin\psi\,xk_\beta\dot{\zeta}_h +$$

$$\beta_{GS}\cos\theta_1\,\sin\alpha_p\,\sin\psi\,^2xk_\beta\dot{\zeta}_h - \cos\theta_1\,\sin\alpha_p\,\sin\psi\,xk_\zeta\zeta_h\dot{\zeta}_h \qquad (5.65)$$

The perpendicular component of velocity, which is positive moving down through the rotor, is given by

$$U_p = P_c + P_l + P_{nl} \qquad (5.66)$$

and

$$
\begin{aligned}
P_c ={}& \lambda\cos\theta_1 + \mu\beta_p\cos\alpha_p\,\cos\psi\,\cos\theta_1 + \beta_p\eta_r + \mu\cos\theta_1\,\sin\alpha_p \\
& -\mu\cos\alpha_p\,\sin\psi\,\sin\theta_1 + \eta_r\dot{\theta}_1 - x\sin\theta_1 \qquad (5.67)
\end{aligned}
$$

$$P_l = P_u + P_v + P_{v'} + \ldots + P_{\dot{\beta}_{GC}} + P_{\dot{\beta}_{GS}}$$

$$P_u = -\sin\theta_1 \qquad (5.68)$$

$$P_v = \beta_p\cos\theta_1 \qquad (5.69)$$

$$P_{v'} = \lambda\beta_p\sin\theta_1 + \mu\sin\theta_1\,(\beta_p\sin\alpha_p - \cos\psi\,\cos\alpha_p) \qquad (5.70)$$

$$P_w = \beta_p\sin\theta_1 \qquad (5.71)$$

188

$$P_{w'} = -\lambda\beta_p\cos\theta_1 + \eta_r - \mu\cos\theta_1\,(\beta_p\sin\alpha_p - \cos\psi\,\cos\alpha_p\,) \qquad (5.72)$$

$$P_{\dot{u}} = 0 \qquad (5.73)$$

$$P_{\dot{v}} = -\sin\theta_1 \qquad (5.74)$$

$$P_{\dot{w}} = \cos\theta_1 \qquad (5.75)$$

$$P_{\dot{v}'} = 0 \qquad (5.76)$$

$$P_{\dot{w}'} = 0 \qquad (5.77)$$

$$P_{\phi} = -\mu\cos\alpha_p\,\sin\theta_1\cos\psi - \lambda\sin\theta_1 - \mu\beta_p\cos\psi\,\sin\theta_1\cos\alpha_p -$$
$$\mu\sin\alpha_p\,\sin\theta_1 - x\cos\theta_1 \qquad (5.78)$$

$$P_{\dot{\phi}} = 0 \qquad (5.79)$$

$$P_{\alpha_h} = \mu\cos\alpha_p\,\cos\theta_1 - \mu\sin\alpha_p\,(\beta_p\cos\psi\,\cos\theta_1 - \sin\psi\,\sin\theta_1\,) \qquad (5.80)$$

$$P_{\phi_h} = 0 \qquad (5.81)$$

$$P_{\zeta_h} = -\mu(\cos\psi\,\sin\theta_1 + \beta_p\cos\theta_1\,\sin\psi\,) + \mu\cos\alpha_p\,\cos\theta_1\,\sin\psi\,k_\zeta$$
$$+x\cos\theta_1\,k_\zeta \qquad (5.82)$$

$$P_{\beta_{GC}} = \mu\cos\alpha_p\,\cos\psi^{\,2}\cos\theta_1 + \cos\psi\,\eta_r - x\cos\theta_1\,\sin\psi -$$
$$\mu\cos\alpha_p\,\cos\psi\,\cos\theta_1\,\sin\psi\,k_\beta - x\cos\psi\,\cos\theta_1\,k_\beta \qquad (5.83)$$

$$P_{\beta_{GS}} = \mu\cos\alpha_p\,\cos\psi\,\cos\theta_1\,\sin\psi + \eta_r\sin\psi + x\cos\psi\,\cos\theta_1 -$$
$$\mu\cos\alpha_p\,\cos\theta_1\,\sin\psi^{\,2}k_\beta - x\cos\theta_1\,\sin\psi\,k_\beta \qquad (5.84)$$

$$P_{\dot{x}_h} = -\beta_p\cos\alpha_p\,\cos\psi\,\cos\theta_1 + (\sin\psi\,\cos\alpha_p\,\sin\theta_1 - \cos\theta_1\,\sin\alpha_p\,) \qquad (5.85)$$

$$P_{\dot{y}_h} = -(\cos\psi\,\sin\theta_1 + \beta_p\cos\theta_1\,\sin\psi\,) \qquad (5.86)$$

$$P_{\dot{z}_h} = \cos\alpha_p\,\cos\theta_1 - \sin\alpha_p\,(\beta_p\cos\psi\,\cos\theta_1 - \sin\psi\,\sin\theta_1\,) \qquad (5.87)$$

$$P_{\dot{\alpha}_h} = -\eta_r\sin\psi + h(\beta_p\cos\psi\,\cos\theta_1 - \sin\psi\,\sin\theta_1\,) + x\cos\psi\,\cos\theta_1$$
$$-x\beta_p\sin\psi\,\sin\theta_1 \qquad (5.88)$$

$$P_{\dot{\phi}_h} = -\cos\alpha_p\,\cos\psi\,\eta_r - h\cos\alpha_p\,(\cos\psi\,\sin\theta_1 + \beta_p\cos\theta_1\,\sin\psi\,) -$$
$$x\beta_p\cos\alpha_p\,\cos\psi\,\sin\theta_1 - x(\cos\alpha_p\,\cos\theta_1\,\sin\psi + \sin\alpha_p\,\sin\theta_1\,) \qquad (5.89)$$

$$P_{\dot{\zeta}_h} = \cos\psi\, \eta_r \sin\alpha_p \ + h\sin\alpha_p \left(\cos\psi\, \sin\theta_1 \ + \beta_p\cos\theta_1\, \sin\psi \right) +$$

$$x\beta_p\cos\psi\, \sin\alpha_p\, \sin\theta_1 \ - x\left(\cos\alpha_p\, \sin\theta_1 \ - \cos\theta_1\, \sin\alpha_p\, \sin\psi \right) \qquad (5.90)$$

$$P_{\dot{\beta}_{GC}} = x\cos\psi\, \cos\theta_1 \qquad (5.91)$$

$$P_{\dot{\beta}_{GS}} = x\cos\theta_1\, \sin\psi \qquad (5.92)$$

$$P_{nl} = \beta_{GC}\cos\psi\, \cos\theta_1 v + \beta_{GS}\cos\theta_1\sin\psi\, v +$$

$$\lambda\beta_{GC}\cos\psi\, \sin\theta_1 v' + \mu\beta_{GC}\cos\psi\, \sin\alpha_p\, \sin\theta_1 v' +$$

$$\lambda\beta_{GS}\sin\psi\, \sin\theta_1 v' + \mu\beta_{GS}\sin\alpha_p\, \sin\theta_1 v' -$$

$$\sin\theta_1 vv' + \beta_{GC}\cos\psi\, \sin\theta_1 w +$$

$$\beta_{GS}\sin\psi\, \sin\theta_1 w - \lambda\beta_{GC}\cos\psi\, \cos\theta_1 w' -$$

$$\mu\beta_{GC}\cos\psi\, \cos\theta_1\sin\alpha_p\, w' - \lambda\beta_{GS}\cos\theta_1\sin\psi\, w' -$$

$$\mu\beta_{GS}\cos\theta_1\sin\alpha_p\, \sin\psi\, w' + \cos\theta_1 vw' -$$

$$\beta_{GC}\cos\psi\, \cos\theta_1\dot{v}k_\beta - \mu\beta_{GC}\cos\alpha_p\, \cos^2\psi\cos\theta_1 v'k_\beta -$$

$$\mu\beta_{GS}\cos\alpha_p\, \cos\psi\, \cos\theta_1\sin\psi\, v'k_\beta - \mu\beta_{GS}\cos\theta_1\, \sin^2\psi\zeta_h +$$

$$\mu\sin\psi\, \sin\theta_1 v'\zeta_h - \mu\cos\theta_1\sin\psi\, w'\zeta_h -$$

$$\mu\beta_{GC}\, \cos^2\psi\cos\theta_1 k_\beta\zeta_h - \mu\beta_{GS}\cos\psi\, \cos\theta_1\sin\psi\, k_\beta\zeta_h +$$

$$\cos\theta_1\dot{v}k_\zeta\zeta_h + \mu\cos\alpha_p\, \cos\psi\, \cos\theta_1 v'k_\zeta\zeta_h +$$

$$\cos\alpha_p\, \cos\theta_1\sin\alpha_p\, \sin\psi\, x\zeta_h{}^2 - \cos^2\psi\sin\theta_1 x\zeta_h{}^2 -$$

$$\cos^2\alpha_p\, \sin^2\psi\sin\theta_1 x\zeta_h{}^2 + \mu\cos\psi\, \cos\theta_1 k_\zeta\zeta_h{}^2 +$$

$$\beta_{GC}\cos\psi\, \cos\theta_1 h\sin\alpha_p\, \sin\psi\, \dot{\zeta}_h + \beta_{GS}\cos\theta_1 h\sin\alpha_p\, \sin^2\psi\dot{\zeta}_h +$$

$$\cos\psi\, \cos\theta_1\sin\alpha_p\, v\dot{\zeta}_h - h\sin\alpha_p\, \sin\psi\, \sin\theta_1 v'\dot{\zeta}_h +$$

$$\cos\psi\, \sin\alpha_p\, \sin\theta_1 w\dot{\zeta}_h + \cos\theta_1 h\sin\alpha_p\, \sin\psi\, w'\dot{\zeta}_h +$$

$$\beta_{GC}\, \cos^2\psi\sin\alpha_p\, \sin\theta_1 x\dot{\zeta}_h + \beta_{GS}\cos\psi\, \sin\alpha_p\, \sin\psi\, \sin\theta_1 x\dot{\zeta}_h +$$

$$\beta_{GC}\, \cos^2\psi\cos\theta_1 h\sin\alpha_p\, k_\beta\dot{\zeta}_h + \beta_{GS}\cos\psi\, \cos\theta_1 h\sin\alpha_p\, \sin\psi\, k_\beta\dot{\zeta}_h -$$

$$\beta_{GC}\cos\alpha_p\,\cos\psi\,\cos\theta_1 x k_\beta\dot{\zeta}_h - \beta_{GS}\cos\alpha_p\,\cos\theta_1\sin\psi\,x k_\beta\dot{\zeta}_h +$$

$$\cos\alpha_p\,\cos\theta_1 x k_\zeta\zeta_h\dot{\zeta}_h - \beta_{GS}\cos\theta_1\sin\psi\,\dot{v}k_\beta -$$

$$\mu\beta_{GC}\cos\psi\,\cos\theta_1\sin\psi\,\zeta_h + \beta_{GS}\cos\psi\,\cos\theta_1 h\sin\alpha_p\,\sin\psi\,k_\beta\dot{\zeta}_h -$$

$$\cos\psi\,\cos\theta_1 h\sin\alpha_p\,k_\zeta\zeta_h\dot{\zeta}_h \qquad\qquad (5.93)$$

5.2 Quasi-Steady Airloads

Since the blade velocity is defined in the deformed blade system, the quasi-steady airloads based on two-dimensional strip theory are identical for tiltrotor and helicopter configurations. Only the contributions to the velocity components U_r, U_t, and U_p are changed. The following generic airload expressions are derived in the UMARC theory manual (Ref. 79), and are applicable in the present formulation. The nondimensional blade forces are written in the deformed reference frame

$$(\bar{L})_C = \frac{\gamma\bar{V}^2}{6a}C_l \qquad\qquad (5.94)$$

$$(\bar{D})_C = \frac{\gamma\bar{V}^2}{6a}C_d \qquad\qquad (5.95)$$

$$(\bar{M}_{ac})_C = \frac{\gamma\bar{V}^2 c}{6aR}C_m \qquad\qquad (5.96)$$

with the aerodynamic coefficients defined at the quarter-chord position by

$$C_l = c_0 + c_1\alpha \qquad\qquad (5.97)$$

$$C_d = d_0 + d_1\,|\alpha| + d_2\alpha^2 \qquad\qquad (5.98)$$

$$C_m = f_0 + f_1\alpha \qquad\qquad (5.99)$$

where c_0 is the zero-angle lift coefficient, c_1 is the lift curve slope, d_0 is the viscous drag coefficient, f_0 is the zero-angle pitching moment about the aerodynamic center, d_1 and d_2 are coefficients used to curve-fit drag polar data, and f_1 is the moment slope. In the present theory, it is assumed that the aerodynamic center is

191

sufficiently close to the quarter-chord that the quarter-chord may be used to define the aerodynamic coefficients. Under this assumption, the parameter f_1 should be zero. It should also be noted that the coefficient d_1 does not have a physical significance as do d_0 and d_2 in defining the two-dimensional drag, but is provided as a means for improving the curve fit of drag polar data. The coefficients defined above are valid only for incompressible attached flow conditions. Compressibility effects are accounted for by application of the Prandtl-Glauert factor to c_1

$$c_1 = \frac{c_1 \mid_{M=0}}{\sqrt{1 - M^2}} \tag{5.100}$$

This correction is valid only for subsonic conditions with $M \leq 0.9$.

The blade forces of Eqns. 5.94-5.96 may be expressed in the deformed reference frame (about the elastic axis) as

$$(\bar{L}_w)_C = \frac{\gamma \bar{V}^2}{6a}(C_l \cos \alpha + C_d \sin \alpha) \tag{5.101}$$

$$(\bar{L}_v)_C = \frac{\gamma \bar{V}^2}{6a}(C_l \sin \alpha - C_d \cos \alpha) \tag{5.102}$$

$$(\bar{L}_u)_C = \frac{\gamma \bar{V}^2}{6a}(-C_d \sin \Lambda) \tag{5.103}$$

$$(\bar{M}_\phi)_C = \frac{\gamma \bar{V}^2}{6a}(\frac{c}{R}C_m) - e_d(\bar{L}_w)_C \tag{5.104}$$

The following approximations are valid in the deformed reference frame:

$$\sin \alpha \simeq \alpha \simeq -\frac{U_P}{U_T} \tag{5.105}$$

$$\cos \alpha \simeq 1 \tag{5.106}$$

$$\bar{V} \simeq U_T \tag{5.107}$$

$$\sin \Lambda \simeq \frac{U_R}{U_T} \tag{5.108}$$

The approximations of Eqns. 5.105-5.108 and the expressions for the aerodynamic coefficients in Eqns. 5.97-5.99 are substituted into the expressions for rotor forces from Eqns. 5.101-5.104:

$$(\bar{L}_w)_C = \frac{\gamma}{6a}(c_0 U_T^2 - (c_1 + d_0)U_T U_P + d_1 \mid U_P \mid U_P) \tag{5.109}$$

192

$$(\bar{L}_v)_C = \frac{\gamma}{6a}(-d_0 U_T{}^2 - (c_0 U_P - d_1\,|U_P|)U_T + (c_1 - d_2)U_P{}^2) \quad (5.110)$$

$$(\bar{L}_u)_C = \frac{\gamma}{6a}(-d_0 U_R U_T) \quad (5.111)$$

$$(\bar{M}_\phi)_C = \frac{\gamma}{6a}\frac{c}{R}(f_0(U_T{}^2 + U_P{}^2) - f_1 U_T U_P) - e_d(\bar{L}_w)_C \quad (5.112)$$

The aerodynamic forces of the deformed frame may be transformed into the undeformed system via the transformation matrices defined previously in this Chapter

$$\left\{ \begin{array}{c} (L_u^A)_C \\ (L_v^A)_C \\ (L_w^A)_C \end{array} \right\} = [T_{ud}] \left\{ \begin{array}{c} (\bar{L}_u)_C \\ (\bar{L}_v)_C \\ (\bar{L}_w)_C \end{array} \right\} \quad (5.113)$$

$$(M_\phi^A)_C = (\bar{M}_\phi)_C \quad (5.114)$$

These equations for the circulatory lift and pitching moments can be modified to account for reverse flow and Mach effects as described in the following sections.

5.2.1 Reverse Flow

In helicopter mode at high forward flight velocities it is possible for the inboard blade section to experience reverse flow. This occurs when the forward flight velocity exceeds the local rotational velocity. When this occurs, the aerodynamic center of a typical airfoil shifts from approximately the quarter chord to approximately the three-quarter chord position. More exactly, the velocity terms derived in the previous sections may be modified by the following equations if $U_T < 0$:

$$e_d{}^R = e_d + \frac{c}{2R} \quad (5.115)$$

$$\eta_r{}^R = -e_d{}^R \quad (5.116)$$

where the superscript R indicates the reverse flow value.

5.2.2 Mach Number Perturbations

The blade forces are modified by the local Mach number as well as the angle of attack. Perturbations in the local Mach number and angle of attack must be

193

taken into account for an accurate stability solution. The perturbation of the lift coefficient may be written as

$$\delta C_l = \frac{\partial C_l}{\partial \alpha}\delta\alpha + \frac{\partial C_l}{\partial M}\delta M \tag{5.117}$$

The perturbations of angle of attack and Mach number are given by

$$\alpha = -\frac{U_P}{U_T} \tag{5.118}$$

$$\delta\alpha = -\frac{U_P\delta U_T - U_T\delta U_P}{U_T{}^2} \tag{5.119}$$

$$M = \frac{M_{tip}}{V_{tip}}V = M_{tip}\frac{U_T}{\Omega R} \tag{5.120}$$

$$\delta M = M_{tip}\frac{\delta U_T}{\Omega R} \tag{5.121}$$

Assuming the Prandtl-Glauert modification of Eqn. 5.100 applies, the derivatives of the lift coefficients are given by

$$\frac{\partial C_l}{\partial \alpha} = \frac{c_1\mid_{M=0}}{\sqrt{1-M^2}} \tag{5.122}$$

$$\frac{\partial C_l}{\partial M} = -\frac{1}{2}\frac{\partial C_l}{\partial \alpha}(1-M^2)\alpha \tag{5.123}$$

These equations give additional terms to the lift forces so that the new forces are given by

$$(\bar{L}_w)_C = \frac{\gamma}{6a}(c_0 U_T{}^2 - (c_1 + d_0)U_T U_P + d_1\mid U_P\mid U_P$$
$$+ c_2 M_{tip}U_T(U_T{}^2 + U_P{}^2)) \tag{5.124}$$

$$(\bar{L}_v)_C = \frac{\gamma}{6a}(-d_0 U_T{}^2 - (c_0 U_P - d_1\mid U_P\mid)U_T + (c_1 - d_2)U_P{}^2$$
$$- c_2 M_{tip}U_P(U_T{}^2 + U_P{}^2)) \tag{5.125}$$

$$(\bar{L}_u)_C = \frac{\gamma}{6a}(-d_0 U_R U_T) \tag{5.126}$$

$$(\bar{M}_\phi)_C = \frac{\gamma}{6a}\frac{c}{R}(f_0(U_T{}^2 + U_P{}^2) - f_1 U_T U_P) - e_d(\bar{L}_w)_C \tag{5.127}$$

where the additional perturbation terms contain c_2 and

$$c_2 = -\frac{1}{2}\alpha\sqrt{1-M^2}\,c_1\mid_{M=0} \tag{5.128}$$

194

The variation of the lift coefficient with respect to Mach number is needed, and can be obtained either from experimental data or from analytical relations. The experimental data are generally available as part of the typical 2-D airfoil data in the form of lift coefficient as a function of Mach number. The applicable value of $\frac{\partial C_l}{\partial M}$ can be calculated from this data using finite difference techniques.

5.2.3 Noncirculatory Airloads

The noncirculatory contribution to rotor blade forces, arising from pitch and plunge motions of the local airfoil section, are derived in this section. For a basic airfoil undergoing pitch and plunge motion in the presence of an oncoming headwind, the noncirculatory lift and moment forces are given by [87]

$$L_{NC} = \rho \pi b^2 (\ddot{h} - a_h b \ddot{\alpha}) + \rho \pi b^2 U \dot{\alpha} \tag{5.129}$$

$$= L_2 + L_3 \tag{5.130}$$

$$M_{NC} = a_h b L_2 - (\frac{1}{2} - a_h) b L_3 - \frac{\rho \pi b^4}{8} \ddot{\alpha} \tag{5.131}$$

For the airfoil section of a general rotor, including the tiltrotor, the following definitions apply and define the forces about the elastic axis

$$U = \Omega R(x + \mu \sin \psi \cos \alpha_p) \tag{5.132}$$

$$a_h b = e_d + \frac{c}{4} \tag{5.133}$$

$$\ddot{h} = -\ddot{w} \tag{5.134}$$

$$\ddot{\alpha} = \ddot{\theta}_1 \tag{5.135}$$

$$\dot{\alpha} = \dot{\theta}_1 \tag{5.136}$$

$$b = \frac{c}{2} \tag{5.137}$$

The noncirculatory airloads act on in the undeformed blade reference frame. Substitution of the above Eqns. 5.132-5.137 into Eqns. 5.129-5.131 gives the noncircu-

latory airload contributions as

$$(L_w^A)_{NC} = \frac{1}{2}\rho\pi c^2(-\ddot{w} + (\frac{c}{4} + e_d)\ddot{\theta}_1 + \Omega R(x + \mu\sin\psi\cos\alpha_p)\dot{\theta}_1) \qquad (5.138)$$

$$(M_\phi^A)_{NC} = \frac{1}{4}\rho\pi c^2((\frac{c}{4} + e_d)\ddot{w} - (\frac{c}{4} + e_d)^2\ddot{\theta}_1 - \Omega R(\frac{c}{2} + e_d)(x + \mu\sin\psi\cos\alpha_p)\dot{\theta}_1$$
$$- \frac{c^2\ddot{\theta}_1}{32}) \qquad (5.139)$$

The nondimensional form of these equations, as required to add with the nondimensional circulatory airloads derived previously, are obtained by dividing the lift by $m_0\Omega^2 R$ and the moment by $m_0\Omega^2 R^2$, yielding

$$(L_w^A)_{NC} = \frac{\gamma\pi\frac{c}{R}}{12a}(-\frac{\ddot{w}}{R} + (\frac{c}{4R} + \frac{e_d}{R})\ddot{\theta}_1 + (x + \mu\sin\psi\cos\alpha_p)\dot{\theta}_1) \qquad (5.140)$$

$$(M_\phi^A)_{NC} = \frac{\gamma\pi\frac{c}{R}}{12a}(\frac{c}{4R} + \frac{e_d}{R}(\frac{\ddot{w}}{R} - \ddot{\theta}_1) - \frac{c}{2R} + \frac{e_d}{R}(x + \mu\sin\psi\cos\alpha_p)\dot{\theta}_1$$
$$- \frac{c^2\ddot{\theta}_1}{32R^2}) \qquad (5.141)$$

The total airloads in the undeformed blade reference frame are then given by

$$L_u^A = (L_u^A)_C \qquad (5.142)$$

$$L_v^A = (L_v^A)_C \qquad (5.143)$$

$$L_w^A = (L_w^A)_C + (L_w^A)_{NC} \qquad (5.144)$$

$$M_\phi^A = (M_\phi^A)_C + (M_\phi^A)_{NC} \qquad (5.145)$$

5.3   Finite Element Discretization of Work

All the work done in the system is a result of the aerodynamic forces of the rotor system. Although the airloads originate at the blades, net rotor forces are developed which are dependent on the blade, gimbal, and hub motion, resulting in contributions to the mass, damping, and stiffness system matrices. As mentioned previously, the gimbal degrees of freedom are for convenience considered part of the hub motion since they too are defined in a nonrotating frame. The finite element

196

formulation for the work done by the hub and rotor system is then written as

$$\delta W = \left[\sum_{m=1}^{N_b} \delta W_b\right] + \delta W_h \tag{5.146}$$

where δW_b represents the work performed by perturbations of the blade degrees of freedom and δW_h represents work performed by perturbations of the hub degrees of freedom. Work is represented mathematically as

$$\delta W_b = \int_0^R (L_u^A \delta u + L_v^A \delta v + L_w^A \delta w + M_\phi^A \delta \phi) dx \tag{5.147}$$

L_u^A, L_v^A, L_w^A, and M_ϕ^A are the distributed aerodynamic forces acting in the rotating blade reference frame. Similarly, the work done on the hub is expressed as

$$\delta W_h = F_{x_h} \delta x_h + F_{y_h} \delta y_h + F_{z_h} \delta z_h + M_{\alpha_h} \delta \alpha_h + M_{\phi_h} \delta \phi_h + M_{\zeta_h} \delta \zeta_h$$

$$+ M_{\beta_{GC}} \delta \beta_{GC} M_{\beta_{GS}} \delta \beta_{GS} \tag{5.148}$$

where each force and moment is the net load acting on the associated hub degree of freedom. For the present formulation it is convenient to write these net forces and moments as the sum of a set of distributed forces and moments acting along the blade.

$$F_{x_h} = \sum_{m=1}^{N_b} \int_0^R F_{x_h}^A dx \tag{5.149}$$

$$F_{y_h} = \sum_{m=1}^{N_b} \int_0^R F_{y_h}^A dx \tag{5.150}$$

$$F_{z_h} = \sum_{m=1}^{N_b} \int_0^R F_{z_h}^A dx \tag{5.151}$$

$$M_{\alpha_h} = \sum_{m=1}^{N_b} \int_0^R M_{\alpha_h}^A dx \tag{5.152}$$

$$M_{\phi_h} = \sum_{m=1}^{N_b} \int_0^R M_{\phi_h}^A dx \tag{5.153}$$

$$M_{\zeta_h} = \sum_{m=1}^{N_b} \int_0^R M_{\zeta_h}^A dx \tag{5.154}$$

$$M_{\beta_{GC}} = \sum_{m=1}^{N_b} \int_0^R M_{\beta_{GC}}^A dx \tag{5.155}$$

$$M_{\beta_{GS}} = \sum_{m=1}^{N_b} \int_0^R M_{\beta_{GS}}^A dx \qquad (5.156)$$

Each of the distributed loads is designated by a superscript A to differentiate it from the other loads. The distributed aerodynamic blade loads L_u^A, L_v^A, L_w^A, and M_ϕ^A are transformed into the reference frame of the associated hub degree of freedom. This transformation is given by

$$\begin{Bmatrix} F_{x_h}^A \\ F_{y_h}^A \\ F_{z_h}^A \\ M_{\alpha_h}^A \\ M_{\phi_h}^A \\ M_{\zeta_h}^A \\ M_{\beta_{GC}}^A \\ M_{\beta_{GS}}^A \end{Bmatrix} = T_{FL} \begin{Bmatrix} L_u^A \\ L_v^A \\ L_w^A \\ M_\phi^A \end{Bmatrix} \qquad (5.157)$$

The transformation T_{FL} is not part of the regular transformation sequence introduced in the beginning of this chapter, but it is derived in the following section. Also, the present T_{FL} matrix is different from that associated with the original UMARC formulation because of the three additional hub forces: $M_{\zeta_h}^A, M_{\beta_{GC}}^A$, and $M_{\beta_{GS}}^A$.

5.3.1 Derivation of the T_{FL} Matrix

The transformation of the blade airloads into the nonrotating frames is described in this section. Six of the eight required force components, $F_{x_h}^A$, $F_{y_h}^A$, $F_{z_h}^A$, $M_{\phi_h}^A$, $M_{\alpha_h}^A$, and $M_{\zeta_h}^A$ are defined in the inertial frame while the remaining two, $M_{\beta_{GC}}^A$ and $M_{\beta_{GS}}^A$, are defined in the hub system.

The three directional forces are transformed into the inertial frame by

$$
\left\{ \begin{array}{c} F^A_{x_h} \\ F^A_{y_h} \\ F^A_{z_h} \end{array} \right\} = T_{iu} \left\{ \begin{array}{c} L^A_u \\ L^A_v \\ L^A_w \end{array} \right\} \tag{5.158}
$$

which, after application of the ordering scheme, gives terms up to second order. There are many more second-order terms in the present formulation than in the UMARC formulations because the ordering scheme of the present formulation assumes that the fuselage degrees of freedom are of $O(\epsilon)$ rather than $O(\epsilon^{\frac{3}{2}})$. There are enough additional second-order terms that it is impractical to list them all. Only the first-order terms are listed:

$$
\begin{aligned}
F^A_{x_h} &= -L^A_w \alpha_h \cos\alpha_p + L^A_u \cos\alpha_p \, \cos\psi \, - \\
& L^A_w \beta_p \cos\alpha_p \, \cos\psi \, - L^A_w \beta_{GC} \cos\alpha_p \, \cos^2\psi - L^A_w \sin\alpha_p \, - \\
& L^A_u \beta_p \sin\alpha_p \, - L^A_u \alpha_h \cos\psi \, \sin\alpha_p \, - L^A_u \beta_{GC} \cos\psi \, \sin\alpha_p \, + \\
& -L^A_v \cos\alpha_p \, \sin\psi \, - L^A_w \beta_{GS} \cos\alpha_p \, \cos\psi \, \sin\psi \, + L^A_v \alpha_h \sin\alpha_p \, \sin\psi \, - \\
& L^A_u \beta_{GS} \sin\alpha_p \, \sin\psi \, - L^A_v \cos\psi \, \zeta_h - L^A_u \sin\psi \, \zeta_h \tag{5.159}
\end{aligned}
$$

$$
\begin{aligned}
F^A_{y_h} &= L^A_v \cos\psi \, + L^A_w \cos\alpha_p \, \phi_h + L^A_u \cos\psi \, \phi_h \sin\alpha_p \, + \\
& L^A_u \sin\psi \, - L^A_w \beta_p \sin\psi \, - L^A_w \beta_{GC} \cos\psi \, \sin\psi \, - \\
& L^A_v \phi_h \sin\alpha_p \, \sin\psi \, - L^A_w \beta_{GS} \sin^2\psi \, + \\
& L^A_u \cos\alpha_p \, \cos\psi \, \zeta_h - L^A_w \sin\alpha_p \, \zeta_h - L^A_v \cos\alpha_p \, \sin\psi \, \zeta_h \tag{5.160}
\end{aligned}
$$

$$
\begin{aligned}
F^A_{z_h} &= L^A_w \cos\alpha_p \, + L^A_u \beta_p \cos\alpha_p \, + L^A_u \alpha_h \cos\alpha_p \, \cos\psi \, + \\
& L^A_u \beta_{GC} \cos\alpha_p \, \cos\psi \, - L^A_v \cos\psi \, \phi_h - L^A_w \alpha_h \sin\alpha_p \, + \\
& L^A_u \cos\psi \, \sin\alpha_p \, - L^A_w \beta_p \cos\psi \, \sin\alpha_p \, - \\
& L^A_w \beta_{GC} \cos^2\psi \sin\alpha_p \, - L^A_v \alpha_h \cos\alpha_p \, \sin\psi \, +
\end{aligned}
$$

$$L_u^A \beta_{GS} \cos\alpha_p \sin\psi - L_u^A \phi_h \sin\psi -$$

$$L_v^A \sin\alpha_p \sin\psi - L_w^A \beta_{GS} \cos\psi \sin\alpha_p \sin\psi \qquad (5.161)$$

The next transformation involves the inertial frame moments which have contributions from both the blade moment and the blade forces.

$$\begin{Bmatrix} -M_{\phi_h}^A \\ -M_{\alpha_h}^A \\ M_{\zeta_h}^A \end{Bmatrix} = T_{id} \begin{Bmatrix} \bar{M}_\phi^A \\ 0 \\ 0 \end{Bmatrix} + r_{iu} \times \{ L_u^A \hat{I}_u + L_v^A \hat{J}_u + L_w^A \hat{K}_u \} \qquad (5.162)$$

where r_{iu} is the position vector defined from the origin of the inertial reference frame to an arbitrary point on the blade elastic axis in the undeformed frame. Note the negative signs on $M_{\phi_h}^A$ and $M_{\alpha_h}^A$ indicating that these moments are in the opposite direction of the normal right-hand rule convention for orthogonal transformations. The position vector is defined as

$$r_{iu} = \{0, 0, h\} \begin{Bmatrix} \hat{I}_w \\ \hat{J}_w \\ \hat{K}_w \end{Bmatrix} + \{x + u, v, w\} \begin{Bmatrix} \hat{I}_u \\ \hat{J}_u \\ \hat{K}_u \end{Bmatrix} \qquad (5.163)$$

which may be written in the inertial frame as

$$r_{iu} = (\{0, 0, h\}[T_{wi}] + \{x + u, v, w\}[T_{ui}]) \begin{Bmatrix} \hat{I}_i \\ \hat{J}_i \\ \hat{K}_i \end{Bmatrix} \qquad (5.164)$$

After carrying out the cross product of Eqn. 5.162 and application of the ordering scheme, the inertial frame aerodynamic moments are listed up to first order as

$$-M_{\phi_h}^A = \bar{M}_\phi^A \alpha_h \cos\psi \sin\alpha_p + \bar{M}_\phi^A \beta_{GC} \cos\psi \sin\alpha_p -$$

$$L_v^A \alpha_h \cos\psi \, h \sin\alpha_p - 2L_w^A \beta_{GC} \cos\alpha_p \cos\psi \, h \sin\psi +$$

$$\bar{M}_\phi^A \beta_{GS} \sin\alpha_p \sin\psi - L_u^A \alpha_h h \sin\alpha_p \sin\psi -$$

$$2L_w^A \beta_{GS} \cos\alpha_p \, h \sin\psi^2 + L_v^A \sin\alpha_p \, u -$$

200

$$L_w^A \cos\alpha_p \sin\psi \; u - L_w^A \cos\alpha_p \cos\psi \; v - L_u^A \sin\alpha_p \; v +$$

$$\bar{M}_\phi^A \cos\alpha_p \sin\psi \; v' + L_v^A \cos\alpha_p \cos\psi \; w +$$

$$L_u^A \cos\alpha_p \sin\psi \; w + \bar{M}_\phi^A \sin\alpha_p \; w' + L_v^A \alpha_h \cos\alpha_p \; x +$$

$$L_v^A \beta_{GC} \cos\alpha_p \cos^2\psi \; x - L_u^A \beta_{GC} \cos\alpha_p \cos\psi \sin\psi \; x +$$

$$L_w^A \alpha_h \sin\alpha_p \sin\psi \; x - L_u^A \beta_{GS} \cos\alpha_p \sin^2\psi \; x + L_u^A \cos\psi \; h\zeta_h +$$

$$\bar{M}_\phi^A \sin\psi \; \zeta_h - L_v^A h\sin\psi \; \zeta_h - L_w^A \cos\psi \; x\zeta_h +$$

$$L_v^A \beta_{GS} \cos\alpha_p \cos\psi \sin\psi \; x \qquad\qquad (5.165)$$

$$-M_{\alpha_h}^A = 2L_w^A \beta_{GC} \cos^2\psi \; h - \bar{M}_\phi^A \cos\psi \; \phi_h \sin\alpha_p +$$

$$L_v^A \cos\psi \; h\phi_h \sin\alpha_p + 2L_w^A \beta_{GS} \cos\psi \; h\sin\psi +$$

$$L_u^A h\phi_h \sin\alpha_p \sin\psi + L_w^A \cos\psi \; u - L_w^A \sin\psi \; v -$$

$$\bar{M}_\phi^A \cos\psi \; v' - L_u^A \cos\psi \; w + L_v^A \sin\psi \; w +$$

$$L_u^A \beta_{GC} \cos^2\psi \; x - L_v^A \cos\alpha_p \; \phi_h x +$$

$$L_v^A \beta_{GC} \cos\psi \sin\psi \; x + L_u^A \beta_{GS} \cos\psi \sin\psi \; x -$$

$$L_w^A \phi_h \sin\alpha_p \sin\psi \; x + L_v^A \beta_{GS} \sin^2\psi \; x -$$

$$\bar{M}_\phi^A \cos\alpha_p \cos\psi \; \zeta_h + L_v^A \cos\alpha_p \cos\psi \; h\zeta_h +$$

$$L_u^A \cos\alpha_p \; h\sin\psi \; \zeta_h + L_v^A \sin\alpha_p \; x\zeta_h -$$

$$L_w^A \cos\alpha_p \sin\psi \; x\zeta_h \qquad\qquad (5.166)$$

$$M_{\zeta_h}^A = \bar{M}_\phi^A \alpha_h \cos\alpha_p \cos\psi +$$

$$\bar{M}_\phi^A \beta_{GC} \cos\alpha_p \cos\psi - L_v^A \alpha_h \cos\alpha_p \cos\psi \; h -$$

$$L_u^A \cos\psi \; h\phi_h + \bar{M}_\phi^A \beta_{GS} \cos\alpha_p \sin\psi -$$

$$L_u^A \alpha_h \cos\alpha_p \; h\sin\psi - \bar{M}_\phi^A \phi_h \sin\psi + L_v^A h\phi_h \sin\psi +$$

$$2L_w^A \beta_{GC} \cos\psi \; h\sin\alpha_p \sin\psi +$$

$$2L_w^A \beta_{GS} h\sin\alpha_p \sin^2\psi + L_v^A \cos\alpha_p \; u +$$

$$L_w^A \sin\alpha_p \sin\psi\, u - L_u^A \cos\alpha_p\, v + L_w^A \cos\psi\, \sin\alpha_p\, v -$$

$$\bar{M}_\phi^A \sin\alpha_p \sin\psi\, v' - L_v^A \cos\psi\, \sin\alpha_p\, w -$$

$$L_u^A \sin\alpha_p \sin\psi\, w + \bar{M}_\phi^A \cos\alpha_p\, w' + L_w^A \cos\psi\, \phi_h x -$$

$$L_v^A \alpha_h \sin\alpha_p\, x - L_v^A \beta_{GC} \cos^2\psi\, \sin\alpha_p\, x +$$

$$L_w^A \alpha_h \cos\alpha_p \sin\psi\, x + L_u^A \beta_{GC} \cos\psi\, \sin\alpha_p \sin\psi\, x -$$

$$L_v^A \beta_{GS} \cos\psi\, \sin\alpha_p \sin\psi\, x + L_u^A \beta_{GS} \sin\alpha_p \sin^2\psi\, x \qquad (5.167)$$

In similar fashion, the gimbal moments are given by

$$\left\{ \begin{array}{c} M_{\beta_{GS}}^A \\ -M_{\beta_{GC}}^A \\ M_{\zeta_h}^A \end{array} \right\} = T_{hd} \left\{ \begin{array}{c} \bar{M}_\phi^A \\ 0 \\ 0 \end{array} \right\} + r_{hu} \times \{ L_u^A \hat{I}_u + L_v^A \hat{J}_u + L_w^A \hat{K}_u \} \qquad (5.168)$$

where only the moment $-M_{\beta_{GC}}^A$ is a negative moment in the transformation sense. The third moment is a repeat of the previous torque moment derived in Eqn. 5.165, and is simply used as a place-holder and check on the previous work. The position vector is now defined as

$$r_{hu} = (\{x + u, v, w\}[T_{uh}]) \left\{ \begin{array}{c} \hat{I}_h \\ \hat{J}_h \\ \hat{K}_h \end{array} \right\} \qquad (5.169)$$

and after substituting this expression into Eqn. 5.168, carrying out the cross product, and applying the ordering scheme, the gimbal moments are listed up to first order as

$$\begin{aligned} M_{\beta_{GS}}^A = {}& L_w^A \sin\psi\, u + L_w^A \cos\psi\, v - \\ & \bar{M}_\phi^A \sin\psi\, v' - L_v^A \cos\psi\, w - \\ & L_u^A \sin\psi\, w - L_v^A \beta_{GC} \cos^2\psi\, x + \\ & L_u^A \beta_{GC} \cos\psi\, \sin\psi\, x - L_v^A \beta_{GS} \cos\psi\, \sin\psi\, x + \\ & L_u^A \beta_{GS} \sin^2\psi\, x \end{aligned} \qquad (5.170)$$

$$-M_{\beta GC}^A \;=\; L_w^A \cos\psi\; u - L_w^A \sin\psi\; v -$$

$$\bar{M}_\phi^A \cos\psi\; v' - L_u^A \cos\psi\; w +$$

$$L_v^A \sin\psi\; w + L_u^A \beta_{GC} \cos^2\psi\; x +$$

$$L_v^A \beta_{GC} \cos\psi\; \sin\psi\; x + L_u^A \beta_{GS} \cos\psi\; \sin\psi\; x +$$

$$L_v^A \beta_{GS} \sin^2\psi\; x \qquad\qquad (5.171)$$

Taking the coefficients of L_u^A, L_v^A, L_w^A, and $\bar{M}_\phi^A$ from Eqns. 5.159-5.161, Eqns. 5.165-5.167, and Eqns. 5.170-5.171 gives the transformation matrix as

$$T_{FL} = (T_{FL})_0 + (T_{FL})_q + (T_{FL})_{x_h} + (T_{FL})_{q^2} + (T_{FL})_{qx_h} + (T_{FL})_{x_h^2} \qquad (5.172)$$

where the subscript 0 indicates the constant terms, subscripts q and x_h indicate linear terms associated with the blade and hub degrees of freedom, respectively, and q^2, qx_h, and x_h^2 indicate terms nonlinear in the blade and hub degrees of freedom. The nonlinear parts of the T_{FL} matrix did not exist in past UMARC formulations. Again, the nonlinear parts of T_{FL} contains numerous of terms with the present ordering scheme. It is not practical to show these terms considering the small contributions they have on the system, but these terms have been included in the analysis associated with the present theory. Errors associated with coding these terms by hand are avoided by deriving the equations using symbolic manipulation software in which the equations may be written in FORTRAN form and pasted directly into the files comprising the analysis. The constant and linear contributions to the T_{FL} matrix are listed as follows:

$$(T_{FL})_0 =$$

$$\begin{bmatrix}
\cos\alpha_p \cos\psi - \beta_p \sin\alpha_p & -\cos\alpha_p \sin\psi & -\beta_p \cos\alpha_p \cos\psi - \sin\alpha_p & 0 \\[4pt]
\sin\psi & \cos\psi & -\beta_p \sin\psi & 0 \\[4pt]
\beta_p \cos\alpha_p + \cos\psi \sin\alpha_p & -\sin\alpha_p \sin\psi & \cos\alpha_p - \beta_p \cos\psi \sin\alpha_p & 0 \\[4pt]
-\cos\psi\, h & \sin\psi\,(h + x\beta_p) & \cos\psi\,(h\beta_p + x) & -\sin\psi \\[4pt]
\cos\alpha_p\, h\sin\psi & \cos\alpha_p \cos\psi\,(h + x\beta_p) + x\sin\alpha_p & -\cos\alpha_p \sin\psi\,(x + h\beta_p) & \beta_p \sin\alpha_p - \cos\alpha_p \cos\psi \\[4pt]
-h\sin\alpha_p \sin\psi & -\cos\psi \sin\alpha_p\,(h + x\beta_p) + x\cos\alpha_p & \sin\alpha_p \sin\psi\,(x + h\beta_p) & \beta_p \cos\alpha_p + \cos\psi \sin\alpha_p \\[4pt]
0 & x\beta_p \sin\psi & x\cos\psi & -\sin\psi \\[4pt]
0 & -x\beta_p \cos\psi & x\sin\psi & \cos\psi
\end{bmatrix}$$

$$(T_{FL})_q =$$

$$\begin{bmatrix}
0 & 0 & 0 & 0 \\[4pt]
0 & 0 & 0 & 0 \\[4pt]
0 & 0 & 0 & 0 \\[4pt]
-\cos\psi\, w & \sin\psi\, w & \cos\psi\, u - \sin\psi\, v & -\cos\psi\, v' \\[4pt]
-v\sin\alpha_p + w\cos\alpha_p \sin\psi & u\sin\alpha_p + w\cos\alpha_p \cos\psi & -u\cos\alpha_p \sin\psi - v\cos\alpha_p \cos\psi & v'\cos\alpha_p \sin\psi + w'\sin\alpha_p \\[4pt]
-v\cos\alpha_p - w\sin\alpha_p \sin\psi & u\cos\alpha_p - w\cos\psi \sin\alpha_p & u\sin\alpha_p \sin\psi + v\cos\psi \sin\alpha_p & -v'\sin\alpha_p \sin\psi + w'\cos\alpha_p \\[4pt]
-w\cos\psi & \sin\psi\, w & \cos\psi\, u - \sin\psi\, v & -\cos\psi\, v' \\[4pt]
-\sin\psi\, w & -\cos\psi\, w & \sin\psi\, u + \cos\psi\, v & -\sin\psi\, v'
\end{bmatrix}$$

$$(T_{FL})_{x_h} =$$

$$\begin{bmatrix}
-\sin\alpha_p(\alpha_h\cos\psi + \beta_{GC}\cos\psi + \beta_{GS}\sin\psi) - \sin\psi\,\zeta_h & -\cos\psi(\beta_{GS}\sin\alpha_p + \zeta_h) + \sin\psi\sin\alpha_p(\alpha_h + \beta_{GC}) \\[4pt]
\cos\psi(\phi_h\sin\alpha_p + \cos\alpha_p\,\zeta_h) & -\sin\psi(\phi_h\sin\alpha_p + \cos\alpha_p\,\zeta_h) \\[4pt]
\cos\alpha_p\cos\psi(\alpha_h + \beta_{GC}) + \sin\psi(\beta_{GS}\cos\alpha_p - \phi_h) & \beta_{GS}\cos\alpha_p\cos\psi - \cos\psi\,\phi_h - \cos\alpha_p\sin\psi(\alpha_h + \beta_{GC}) \\[4pt]
h\sin\psi(\phi_h\sin\alpha_p + \cos\alpha_p\,\zeta_h) & h\cos\psi\,\phi_h\sin\alpha_p + x\beta_{GS} - x\cos\alpha_p\,\phi_h + h\cos\alpha_p\cos\psi\,\zeta_h + x\sin\alpha_p\,\zeta_h \\[4pt]
h(\cos\psi\,\zeta_h - \alpha_h\sin\alpha_p\sin\psi) & \alpha_h(-h\cos\psi\sin\alpha_p + x\cos\alpha_p) + x\beta_{GC}\cos\alpha_p - h\sin\psi\,\zeta_h \\[4pt]
-h(\cos\psi\,\phi_h + \alpha_h\cos\alpha_p\sin\psi) & h(\phi_h\sin\psi - \alpha_h\cos\alpha_p\cos\psi) - x\sin\alpha_p(\alpha_h - \beta_{GC}) \\[4pt]
0 & x\beta_{GS} \\[4pt]
0 & -x\beta_{GC}
\end{bmatrix}$$

$$\begin{bmatrix}
-\alpha_h\cos\alpha_p - \beta_{GC}\cos\alpha_p & 0 \\[4pt]
-\beta_{GS} + \cos\alpha_p\,\phi_h - \sin\alpha_p\,\zeta_h & 0 \\[4pt]
-\alpha_h\sin\alpha_p - \beta_{GC}\sin\alpha_p & 0 \\[4pt]
h\beta_{GC} - x\sin\psi(\phi_h\sin\alpha_p + \cos\alpha_p\,\zeta_h) & -\cos\psi(\phi_h\sin\alpha_p + \cos\alpha_p\,\zeta_h) \\[4pt]
-h\beta_{GS}\cos\alpha_p - x\cos\psi(\beta_{GS}\sin\alpha_p + \zeta_h) + x\sin\psi(\alpha_h\sin\alpha_p + \beta_{GC}\sin\alpha_p) & \cos\psi(\alpha_h\sin\alpha_p + \beta_{GC}\sin\alpha_p) + \sin\psi(\beta_{GS}\sin\alpha_p + \zeta_h) \\[4pt]
h\beta_{GS}\sin\alpha_p - x\cos\psi(\beta_{GS}\cos\alpha_p + \phi_h) + x\sin\psi(\alpha_h\cos\alpha_p + \beta_{GC}\cos\alpha_p) & \cos\psi(\alpha_h\cos\alpha_p + \beta_{GC}\cos\alpha_p) + \sin\psi(\beta_{GS}\cos\alpha_p - \phi_h) \\[4pt]
0 & 0 \\[4pt]
0 & 0
\end{bmatrix}$$

5.3.2 Discretization of the Blade Equations

As previously discussed, the contributions of work are divided into work done on the blade and work done on the hub. The work done on the blade results in the blade equations which also have hub motion contributions, and the work done on

the hub results in the hub equations which also have blade motion contributions. This section will address the blade-blade and blade-hub equations which result from the variation of work done on the blade. The nondimensional form of the work is

$$\delta W_b = \frac{\gamma}{6} \int_0^R \delta \hat{u}^T \hat{L}^A dr \tag{5.173}$$

where

$$\delta \hat{u}^T = [u \; v \; w \; \phi]^T \tag{5.174}$$

$$\hat{L}^A = [L_u^A \; L_v^A \; L_w^A \; M_\phi^A]^T \tag{5.175}$$

The aerodynamic force vector, $\hat{L}^A$, can be expressed as a sum of constant, linear, and nonlinear contributions of the blade and hub motion. This is written as

$$\hat{L}^A = (\hat{L}^A)_0 + (\hat{L}^A)_q + (\hat{L}^A)_{x_h} + (\hat{L}^A)_{q^2} + (\hat{L}^A)_{qx_h} + (\hat{L}^A)_{x_h^2} \tag{5.176}$$

where 0 refers to the constant terms, q to the blade discretized displacement vector, and x_h to the hub displacement vector. The displacement vector, $\hat{u}$, may be discretized in terms of the spatial shape functions matrix, $[H_s]$, and the blade discrete degrees of freedom vector, $\hat{q}$ as

$$\hat{u} = [H_s] \hat{q} \tag{5.177}$$

$$\hat{u}' = [H_s'] \hat{q} \tag{5.178}$$

$$\dot{\hat{u}} = [H_s] \dot{\hat{q}} \tag{5.179}$$

The shape function matrix is defined as

$$[H] = \begin{bmatrix} H_u & 0 & 0 & 0 \\ 0 & H_b & 0 & 0 \\ 0 & 0 & H_b & 0 \\ 0 & 0 & 0 & H_\phi \end{bmatrix} \tag{5.180}$$

205

where the shape functions H_u, H_b, and H_ϕ are the same as those discussed in Chapter 4. The discrete degrees of freedom are defined as

$$\hat{q} = [u_1 \ u_2 \ u_3 \ u_4 \ v_1 \ v_1' \ v_2 \ v_2' \ w_1 \ w_1' \ w_2 \ w_2' \ \phi_1 \ \phi_2 \ \phi_3] \qquad (5.181)$$

and the vector of fuselage displacements is defined as

$$\hat{x}_h = [x_h \ y_h \ z_h \ \alpha_h \ \phi_h \ \zeta_h \ \beta_{GC} \ \beta_{GS}] \qquad (5.182)$$

The linear terms, $(\hat{L}^A)_q$ and $(\hat{L}^A)_{x_h}$, of the aerodynamic force vector may written as a sum of coefficient matrices such that

$$
\begin{aligned}
(\hat{L}^A)_q + (\hat{L}^A)_{x_h} &= [A_u]\hat{u} + [A_{u'}]\hat{u}' + [A_{\dot{u}}]\hat{\dot{u}} \\
&\quad + [A_{\ddot{u}}]\hat{\ddot{u}} + [A_{x_h}]\hat{x}_h + [A_{\dot{x}_h}]\hat{\dot{x}}_h
\end{aligned}
\qquad (5.183)
$$

Substitution of Eqns. 5.177-5.183 into the expression for virtual work Eqn. 5.173 yields the element blade-blade and blade-hub mass, damping, and stiffness matrices and load vectors.

$$
\begin{aligned}
\delta W_b &= \delta \hat{q}^T ([M_{bb}^A]\hat{\ddot{q}} + [C_{bb}^A]\hat{\dot{q}} + [K_{bb}^A]\hat{q} + [C_{bh}^A]\hat{\dot{x}}_h + [K_{bh}^A]\hat{x}_h \\
&\quad + [Q_b^A]_0 + [Q_b^A]_{q^2} + [Q_b^A]_{qx_h} + [Q_b^A]_{x_h^2})
\end{aligned}
\qquad (5.184)
$$

where the system matrices are defined as

$$\left[M_{bb}^A\right] = \frac{\gamma}{6} l \int_0^1 [H_s]^T [A_{\ddot{u}}][H_s] \, ds \qquad (5.185)$$

$$\left[C_{bb}^A\right] = \frac{\gamma}{6} l \int_0^1 [H_s]^T [A_{\dot{u}}][H_s] \, ds \qquad (5.186)$$

$$\left[K_{bb}^A\right] = \frac{\gamma}{6} l \int_0^1 ([H_s]^T [A_u][H_s] + [H_s']^T [A_{u'}][H_s']) \, ds \qquad (5.187)$$

$$\left[C_{bh}^A\right] = \frac{\gamma}{6} l \int_0^1 [H_s]^T [A_{\dot{x}_h}] \, ds \qquad (5.188)$$

$$\left[K_{bh}^A\right] = \frac{\gamma}{6} l \int_0^1 [H_s]^T [A_{x_h}] \, ds \qquad (5.189)$$

$$\left[Q_b^A\right]_0 = \frac{\gamma}{6} l \int_0^1 [H_s]^T [L^A]_0 \, ds \qquad (5.190)$$

$$\left[Q_b^A\right]_{q^2} = \frac{\gamma}{6} l \int_0^1 [H_s]^T [L^A]_{q^2} \, ds \qquad (5.191)$$

$$\left[Q_b^A\right]_{qx_h} = \frac{\gamma}{6} l \int_0^1 [H_s]^T [L^A]_{qx_h} \, ds \tag{5.192}$$

$$\left[Q_b^A\right]_{x_h^2} = \frac{\gamma}{6} l \int_0^1 [H_s]^T [L^A]_{x_h^2} \, ds \tag{5.193}$$

In the above set of equations, γ is the Lock number and l is the nondimensional element length. The subscripts bb refer to blade-blade matrices while the subscripts bh refer to the blade-hub matrices. The constant load vector $[Q_b^A]_0$ is used in the blade response analysis to determine the deflected trim position of the blade. The nonlinear load vectors $[Q_b^A]_{q^2}$, $[Q_b^A]_{qx_h}$, and $[Q_b^A]_{x_h^2}$ are linearized about the deflected trim position and can also contribute to the stiffness and damping matrices.

5.3.3 Discretization of the Hub Equations

This section will derive the hub-blade and hub-hub equations which result from the variation of work done by the blade forces on the hub. The work performed on the hub was given in Eqn. 5.148 as

$$\delta W_h = F_{x_h}\delta x_h + F_{y_h}\delta y_h + F_{z_h}\delta z_h + M_{\alpha_h}\delta \alpha_h + M_{\phi_h}\delta \phi_h + M_{\zeta_h}\delta \zeta_h$$
$$+ M_{\beta_{GC}}\delta \beta_{GC} + M_{\beta_{GS}}\delta \beta_{GS}$$

which after substitution of Eqns. 5.149-5.156 may be written as

$$\delta W_h = \sum_{m=1}^{N_b} \int_0^R (F_{x_h}^A\delta x_h + F_{y_h}^A\delta y_h + F_{z_h}^A\delta z_h + M_{\alpha_h}^A\delta \alpha_h + M_{\phi_h}^A\delta \phi_h + M_{\zeta_h}^A\delta \zeta_h$$
$$+ M_{\beta_{GC}}^A\delta \beta_{GC} M_{\beta_{GS}}^A\delta \beta_{GS}) \, dx \tag{5.194}$$

$$= \sum_{m=1}^{N_b} \int_0^R \delta \hat{x}_h^T \hat{F}_h^A \, dr \tag{5.195}$$

where

$$\hat{x}_h = [\delta x_h \; \delta y_h \; \delta z_h \; \delta \alpha_h \; \delta \phi_h \; \delta \zeta_h \; \delta \beta_{GC} \; \delta \beta_{GS}]^T \tag{5.196}$$

$$\hat{F}_h^A = [F_{x_h}^A \; F_{y_h}^A \; F_{z_h}^A \; M_{\alpha_h}^A \; M_{\phi_h}^A \; M_{\zeta_h}^A \; M_{\beta_{GC}}^A \; M_{\beta_{GS}}^A]^T \tag{5.197}$$

The transformation of the aerodynamic loads from the blade to the hub is then given by

$$\hat{F}_h^A = [T_{FL}]\hat{L}^A \tag{5.198}$$

with $[T_{FL}]$ defined by Eqn. 5.172. To determine the linear and nonlinear contributions to the system mass, damping, and stiffness matrices, and the constant and nonlinear contributions to the system load vector, the hub aerodynamic force vector $\hat{F}_h^A$ is divided into several parts as

$$\hat{F}_h^A = (\hat{F}_h^A)_0 + (\hat{F}_h^A)_q + (\hat{F}_h^A)_{x_h} + (\hat{F}_h^A)_{q^2} + (\hat{F}_h^A)_{qx_h} + (\hat{F}_h^A)_{x_h^2} \tag{5.199}$$

and by using the T_{FL} transformation matrix, each part is defined as

$$(\hat{F}_h^A)_0 = (\hat{L}^A)_0 (T_{FL})_0 \tag{5.200}$$

$$(\hat{F}_h^A)_q = (\hat{L}^A)_0 (T_{FL})_q + (\hat{L}^A)_q (T_{FL})_0 \tag{5.201}$$

$$(\hat{F}_h^A)_{x_h} = (\hat{L}^A)_0 (T_{FL})_{x_h} + (\hat{L}^A)_{x_h} (T_{FL})_0 \tag{5.202}$$

$$(\hat{F}_h^A)_{q^2} = (\hat{L}^A)_0 (T_{FL})_{q^2} + (\hat{L}^A)_q (T_{FL})_q + (\hat{L}^A)_{q^2} (T_{FL})_0 \tag{5.203}$$

$$(\hat{F}_h^A)_{qx_h} = (\hat{L}^A)_q (T_{FL})_{x_h} + (\hat{L}^A)_{x_h} (T_{FL})_q \tag{5.204}$$

$$(\hat{F}_h^A)_{x_h^2} = (\hat{L}^A)_0 (T_{FL})_{x_h^2} + (\hat{L}^A)_{x_h} (T_{FL})_{x_h} + (\hat{L}^A)_{x_h^2} (T_{FL})_0 \tag{5.205}$$

Based on the above equations, the linear contributions to the force vector may be written as

$$(\hat{F}_h^A)_L = (\hat{L}^A)_0 (T_{FL})_q + (\hat{L}^A)_q (T_{FL})_0 + (\hat{L}^A)_0 (T_{FL})_{x_h} + (\hat{L}^A)_{x_h} (T_{FL})_0 \tag{5.206}$$

To arrive at the linear contribution to the damping and stiffness matrices, the linear transformation contributions need to be written as coefficients of displacements. Let

$$(\hat{L}^A)_0 (T_{FL})_q = (T_{FL})_0^u \hat{u} + (T_{FL})_0^{u'} \hat{u}' \tag{5.207}$$

$$(\hat{L}^A)_0 (T_{FL})_{x_h} = (T_{FL})_0^{x_h} \hat{x}_h \tag{5.208}$$

Recalling that the linear blade lift terms may be written as coefficients of displacements as given by Eqn. 5.183, the linear force vector is then given by

$$\begin{aligned}
(\hat{F}_h^A)_L &= (T_{FL})_0^u \hat{u} + (T_{FL})_0^{u'} \hat{u}' \\
&\quad + (T_{FL})_0 ([A_u]\hat{u} + [A_{u'}]\hat{u}' + [A_{\dot{u}}]\hat{\dot{u}} + [A_{\ddot{u}}]\hat{\ddot{u}}) \\
&\quad + (T_{FL})_0^{x_h} \hat{x}_h + (T_{FL})_0 ([A_{x_h}]\hat{x}_h + [A_{\dot{x}_h}]\hat{\dot{x}}_h)
\end{aligned} \tag{5.209}$$

Substitution of Eqns. 5.177-5.183 into the expression for the hub virtual work (Eqn. 5.195) yields the element hub-blade and hub-hub damping and stiffness matrices and load vectors.

$$\delta W_h = \sum_{m=1}^{N_b} \delta \hat{x}_h^T ([C_{hb}^A]\hat{\dot{q}} + [K_{hb}^A]\hat{q} + [C_{hh}^A]\hat{\dot{x}}_h + [K_{hh}^A]\dot{x}_h$$
$$+ [Q_h^A]_0 + [Q_h^A]_{q^2} + [Q_h^A]_{qx_h} + [Q_h^A]_{x_h^2}) \tag{5.210}$$

where the system matrices are defined as

$$\left[M_{hb}^A\right] = \frac{\gamma}{6}l\int_0^1 (T_{FL})_0[A_{\ddot{u}}][H_s]\,ds \tag{5.211}$$

$$\left[C_{hb}^A\right] = \frac{\gamma}{6}l\int_0^1 (T_{FL})_0[A_{\dot{u}}][H_s]\,ds \tag{5.212}$$

$$\left[K_{hb}^A\right] = \frac{\gamma}{6}l\int_0^1 (T_{FL})_0^u[H_s] + (T_{FL})_0^{u'}[H_s']$$
$$+ ((T_{FL})_0[A_u][H_s] + (T_{FL})_0[A_{u'}][H_s'])\,ds \tag{5.213}$$

$$\left[C_{hh}^A\right] = \frac{\gamma}{6}l\int_0^1 (T_{FL})_0[A_{\dot{x}_h}]\,ds \tag{5.214}$$

$$\left[K_{hh}^A\right] = \frac{\gamma}{6}l\int_0^1 (T_{FL})_0^{x_h} + (T_{FL})_0[A_{x_h}]\,ds \tag{5.215}$$

$$\left[Q_h^A\right]_0 = \frac{\gamma}{6}l\int_0^1 (F_h^A)_0\,ds \tag{5.216}$$

$$\left[Q_h^A\right]_{q^2} = \frac{\gamma}{6}l\int_0^1 (F_h^A)_{q^2}\,ds \tag{5.217}$$

$$\left[Q_h^A\right]_{qx_h} = \frac{\gamma}{6}l\int_0^1 (F_h^A)_{qx_h}\,ds \tag{5.218}$$

$$\left[Q_h^A\right]_{x_h^2} = \frac{\gamma}{6}l\int_0^1 (F_h^A)_{x_h^2}\,ds \tag{5.219}$$

5.3.4 Nonlinear Force Contributions

Contributions to the mass, damping, and stiffness matrices are obtained from the nonlinear force vectors defined in Eqns. 5.190-5.193 for the blade and in Eqns. 5.216-5.219 for the hub. The procedure described here for obtaining the nonlinear contributions is the same as that used in the UMARC formulations, only the expanded displacement vector for the hub is used and there are additional nonlinear components of the force transformation matrix T_{FL}. The force

vector Q is written for the ith element as a sum of constant and nonlinear parts as

$$[Q]_i = [Q_0]_i + [Q_{NL}]_i \qquad (5.220)$$

The nonlinear element load vector is linearized about the deflected trim position using a first order Taylor series expansion. For each nonlinear element load vector

$$[Q_{NL}]_i = ([Q_{NL}] \mid_0 + \frac{\partial [Q_{NL}]}{\partial \hat{q}} \hat{q} + \frac{\partial [Q_{NL}]}{\partial \dot{\hat{q}}} \dot{\hat{q}} + \frac{\partial [Q_{NL}]}{\partial \hat{x}_h} \hat{x}_h + \frac{\partial [Q_{NL}]}{\partial \dot{\hat{x}}_h} \dot{\hat{x}}_h)_i \qquad (5.221)$$

Similar to Eqn. 5.183, the nonlinear contributions of the blade aerodynamic forces may be written in coefficient form as

$$
\begin{aligned}
[L^A]_{nl} &= [L^A]_{q^2} + [L^A]_{qx_h} + [L^A]_{x_h^2} \\
&= [A_u]_{nl}\hat{u} + [A_{u'}]_{nl}\hat{u}' + [A_{\dot{u}}]_{nl}\dot{\hat{u}} + \\
&\quad [A_{x_h}]_{nl}\hat{x}_h + [A_{\dot{x}_h}]_{nl}\dot{\hat{x}}_h
\end{aligned}
\qquad (5.222)
$$

where after linearization about the deflected trim position, the nonlinear A matrices are defined as:

$$[A_u]_{nl} = \left[\frac{\partial}{\partial u}[L^A]_{nl} \quad \frac{\partial}{\partial v}[L^A]_{nl} \quad \frac{\partial}{\partial w}[L^A]_{nl} \quad \frac{\partial}{\partial \phi}[L^A]_{nl} \right] \qquad (5.223)$$

$$[A_{u'}]_{nl} = \left[\frac{\partial}{\partial u'}[L^A]_{nl} \quad \frac{\partial}{\partial v'}[L^A]_{nl} \quad \frac{\partial}{\partial w'}[L^A]_{nl} \quad \frac{\partial}{\partial \phi'}[L^A]_{nl} \right] \qquad (5.224)$$

$$[A_{\dot{u}}]_{nl} = \left[\frac{\partial}{\partial \dot{u}}[L^A]_{nl} \quad \frac{\partial}{\partial \dot{v}}[L^A]_{nl} \quad \frac{\partial}{\partial \dot{w}}[L^A]_{nl} \quad \frac{\partial}{\partial \dot{\phi}}[L^A]_{nl} \right] \qquad (5.225)$$

$$[A_{x_h}]_{nl} = \frac{\partial}{\partial \hat{x}_h}[L^A]_{nl} \qquad (5.226)$$

$$[A_{\dot{x}_h}]_{nl} = \frac{\partial}{\partial \dot{\hat{x}}_h}[L^A]_{nl} \qquad (5.227)$$

After substitution into the blade work equation, the nonlinear blade-blade and blade-hub damping and stiffness matrices are given by:

$$\left[C_{bb}^A \right]_{nl} = -\frac{\gamma}{6} l \int_0^1 [H_s]^T [A_{\dot{u}}]_{nl} [H_s] \, ds \qquad (5.228)$$

$$\left[K_{bb}^A \right]_{nl} = -\frac{\gamma}{6} l \int_0^1 ([H_s]^T [A_u]_{nl} [H_s] + [H'_s]^T [A_{u'}]_{nl} [H'_s]) \, ds \qquad (5.229)$$

210

$$\left[C^A_{bh} \right]_{nl} = -\frac{\gamma}{6} l \int_0^1 [H_s]^T [A_{\dot{x}_h}]_{nl} \, ds \tag{5.230}$$

$$\left[K^A_{bh} \right]_{nl} = -\frac{\gamma}{6} l \int_0^1 [H_s]^T [A_{x_h}]_{nl} \, ds \tag{5.231}$$

$$\tag{5.232}$$

which can be added to the linear stiffness matrices for stability analysis.

The nonlinear contributions to the hub equations is more difficult because of the involvement of the force transformation matrix T_{FL}. The nonlinear forces on the hub are written as:

$$(\hat{F}^A_h)_{nl} = [T_{FL}][L^A]_{nl}$$
$$= (\hat{F}^A_h)_{q^2} + (\hat{F}^A_h)_{qx_h} + (\hat{F}^A_h)_{x_h^2} \tag{5.233}$$

After substitution of Eqns. 5.203-5.205 into the above expression, and linearizing about the deflected trim position, the nonlinear forces may be written in coefficient form as:

$$(\hat{F}^A_h)_{nl} = [T_{FL}]_0([A_u]_{nl}\hat{u} + [A_{u'}]_{nl}\hat{u}') + (A^h_u)_{nl}\hat{u} + [A^h_{u'}]_{nl}\hat{u}' +$$
$$[T_{FL}]_0[A_{\dot{u}}]_{nl}\hat{\dot{u}} + [A^h_{\dot{u}}]_{nl}\hat{\dot{u}} +$$
$$[T_{FL}]_0[A_{x_h}]_{nl}\hat{x}_h + [A^h_{x_h}]_{nl}\hat{x}_h +$$
$$[T_{FL}]_0[A_{\dot{x}_h}]_{nl}\hat{\dot{x}}_h + [A^h_{\dot{x}_h}]_{nl}\hat{\dot{x}}_h \tag{5.234}$$

with the new hub-related nonlinear A matrices given by:

$$\left[A^h_u \right]_{nl} = (\hat{L}^A)_0 \frac{\partial}{\partial \hat{u}}(T_{FL})_{q^2} + (\hat{L}^A)_q \frac{\partial}{\partial \hat{u}}(T_{FL})_q + \frac{\partial}{\partial \hat{u}}(\hat{L}^A)_q(T_{FL})_q \tag{5.235}$$

$$\left[A^h_{u'} \right]_{nl} = (\hat{L}^A)_0 \frac{\partial}{\partial \hat{u}'}(T_{FL})_{q^2} + (\hat{L}^A)_q \frac{\partial}{\partial \hat{u}'}(T_{FL})_q + \frac{\partial}{\partial \hat{u}'}(\hat{L}^A)_q(T_{FL})_q \tag{5.236}$$

$$\left[A^h_{\dot{u}} \right]_{nl} = (\hat{L}^A)_0 \frac{\partial}{\partial \hat{\dot{u}}}(T_{FL})_{q^2} + (\hat{L}^A)_q \frac{\partial}{\partial \hat{\dot{u}}}(T_{FL})_q + \frac{\partial}{\partial \hat{\dot{u}}}(\hat{L}^A)_q(T_{FL})_q \tag{5.237}$$

$$\left[A^h_{x_h} \right]_{nl} = (\hat{L}^A)_0 \frac{\partial}{\partial \hat{x}_h}(T_{FL})_{q^2} + (\hat{L}^A)_q \frac{\partial}{\partial \hat{x}_h}(T_{FL})_q + \frac{\partial}{\partial \hat{x}_h}(\hat{L}^A)_q(T_{FL})_q \tag{5.238}$$

$$\left[A^h_{\dot{x}_h} \right]_{nl} = (\hat{L}^A)_0 \frac{\partial}{\partial \hat{\dot{x}}_h}(T_{FL})_{q^2} + (\hat{L}^A)_q \frac{\partial}{\partial \hat{\dot{x}}_h}(T_{FL})_q + \frac{\partial}{\partial \hat{\dot{x}}_h}(\hat{L}^A)_q(T_{FL})_q \tag{5.239}$$

Substitution of these terms into the appropriate energy expression for the hub gives the nonlinear contributions to the hub-blade and hub-hub damping and stiffness matrices as:

$$\left[C_{hb}^A\right]_{nl} = -\frac{\gamma}{6}l\int_0^1 (T_{FL})_0[A_{\dot u}]_{nl}[H_s] + [A_{\dot u}^h]_{nl}[H_s]\,ds \tag{5.240}$$

$$\left[K_{hb}^A\right]_{nl} = -\frac{\gamma}{6}l\int_0^1 (T_{FL})_0[A_u]_{nl}[H_s] + (T_{FL})_0[A_{u'}]_{nl}[H_s']$$

$$+[A_u^h]_{nl}[H_s] + (T_{FL})_0[A_{u'}^h]_{nl}[H_s'])\,ds \tag{5.241}$$

$$\left[C_{hh}^A\right]_{nl} = -\frac{\gamma}{6}l\int_0^1 (T_{FL})_0[A_{\dot x_h}]_{nl} + [A_{\dot x_h}^h]_{nl}\,ds \tag{5.242}$$

$$\left[K_{hh}^A\right]_{nl} = -\frac{\gamma}{6}l\int_0^1 (T_{FL})_0[A_{x_h}]_{nl} + [A_{x_h}^h]_{nl}\,ds \tag{5.243}$$

$$\tag{5.244}$$

5.4 Wing Aerodynamics

As is the case with the wing structural model, the wing aerodynamic model parallels that of the blade. Only linear aerodynamics are considered for the wing, and then only for inclusion in the stability analysis. For stability, the constant load vector is not considered, so the wing aerodynamic contribution to the wing system matrices is given by the linear blade-blade matrices with appropriate substitutions. The substitutions begin with definition of the local velocity vectors. Here, the wing acts the same as the blade when $\psi = 90°$ and $\alpha_p = 0°$. Of course, the rotational velocity and precone are zero for the wing. Also, the term θ_1 for the wing is the sum of the wing incidence angle and the fuselage angle of attack. With these substitutions, the velocity components for the wing are given by: $(U_r)_w$, $(U_t)_w$, and $(U_p)_w$ which are defined as follows:

The radial component of velocity is given by

$$(U_r)_w = (R_c)_w + (R_l)_w \tag{5.245}$$

with

$$(R_c)_w \;=\; 0 \tag{5.246}$$

$$(R_l)_w \;=\; (R_u)_w + (R_v)_w + (R_{v'})_w + \ldots + (R_{\dot\phi})_w$$

$$(R_u)_w \;=\; 0 \tag{5.247}$$

$$(R_v)_w \;=\; 0 \tag{5.248}$$

$$(R_{v'})_w \;=\; \mu \tag{5.249}$$

$$(R_w)_w \;=\; 0 \tag{5.250}$$

$$(R_{w'})_w \;=\; 0 \tag{5.251}$$

$$(R_{\dot u})_w \;=\; 1 \tag{5.252}$$

$$(R_{\dot v})_w \;=\; 0 \tag{5.253}$$

$$(R_{\dot w})_w \;=\; 0 \tag{5.254}$$

$$(R_{\dot v'})_w \;=\; 0 \tag{5.255}$$

$$(R_{\dot w'})_w \;=\; 0 \tag{5.256}$$

$$(R_\phi)_w \;=\; 0 \tag{5.257}$$

$$(R_{\dot\phi})_w \;=\; 0 \tag{5.258}$$

The tangential component of velocity is given by

$$(U_t)_w = (T_c)_w + (T_l)_w \tag{5.259}$$

with

$$(T_c)_w \;=\; \mu \cos\theta_1 \tag{5.260}$$

$$(T_l)_w \;=\; (T_u)_w + (T_v)_w + (T_{v'})_w + \ldots + (T_{\dot\phi})_w$$

$$(T_u)_w \;=\; \cos\theta_1 \tag{5.261}$$

$$(T_v)_w = 0 \tag{5.262}$$

$$(T_{v'})_w = 0 \tag{5.263}$$

$$(T_w)_w = 0 \tag{5.264}$$

$$(T_{w'})_w = 0 \tag{5.265}$$

$$(T_{\dot{u}})_w = 0 \tag{5.266}$$

$$(T_{\dot{v}})_w = \cos\theta_1 \tag{5.267}$$

$$(T_{\dot{w}})_w = \sin\theta_1 \tag{5.268}$$

$$(T_{\dot{v}'})_w = 0 \tag{5.269}$$

$$(T_{\dot{w}'})_w = 0 \tag{5.270}$$

$$(T_\phi)_w = -\mu\sin\theta_1 \tag{5.271}$$

$$(T_{\dot{\phi}})_w = 0 \tag{5.272}$$

The perpendicular component of velocity is given by

$$(U_p)_w = (P_c)_w + (P_l)_w \tag{5.273}$$

and

$$(P_c)_w = \mu\sin\theta_1 \tag{5.274}$$

$$(P_l)_w = (P_u)_w + (P_v)_w + (P_{v'})_w + \ldots + (P_{\dot{\phi}})_w$$

$$(P_u)_w = 0 \tag{5.275}$$

$$(P_v)_w = 0 \tag{5.276}$$

$$(P_{v'})_w = 0 \tag{5.277}$$

$$(P_w)_w = 0 \tag{5.278}$$

$$(P_{w'})_w = 0 \tag{5.279}$$

$$(P_{\dot{u}})_w = 0 \tag{5.280}$$

$$(P_{\dot{v}})_w = -\sin\theta_1 \tag{5.281}$$

$$(P_{\dot{w}})_w = \cos\theta_1 \tag{5.282}$$

$$(P_{\dot{v}'})_w = 0 \tag{5.283}$$

$$(P_{\dot{w}'})_w = 0 \tag{5.284}$$

$$(P_{\phi})_w = \mu\cos\theta_1 \tag{5.285}$$

$$(P_{\dot{\phi}})_w = 0 \tag{5.286}$$

These velocity components can then be used to form the aerodynamic contributions to the wing mass, damping, and stiffness element matrices using the derivation provided in this chapter for the blade-blade equations. The corrections provided in those sections for including Mach number perturbations and noncirculatory airloads are also applicable to the wing aerodynamic model.

Chapter 6

Vehicle Trim and Blade Response Analysis

Vehicle trim refers to an equilibrium of forces and moments on the aircraft, including the rotor steady force contributions. The rotor system loads depend on the blade response, so the determination of the airframe trim and blade response is coupled together. Thus, the procedure is referred to as "coupled trim", and is an important part of rotor analysis.

The present chapter is divided into three major parts: 1) formulation of the vehicle equilibrium equations, 2) formulation and solution of the blade response equations, and 3) discussion of the coupled trim procedure. While much of the solution procedures discussed in the present chapter are similar to those used in UMARC, there are some new requirements for the present tiltrotor formulation. The major modifications for the present formulation are as follows: the definition of new tiltrotor-related vehicle trim equations, the creation of a new rigid-blade high-inflow analysis for estimating initial controls, capability of recalculating the Jacobian matrix in the coupled trim procedure, and estimation of elastic blade twist in both the rigid-blade and elastic blade analyses.

6.1 Vehicle Trim Equations

The vehicle trim equations consist of the definition of two vectors describing the state of trim: the vehicle force residuals $\hat{F}$ and the trim unknowns $\hat{\theta}$ which will be referred to as the control vector. The force residuals define the equilibrium balance of the rotor hub forces and the airframe forces which are functions of the trim unknowns and the blade response. The trim unknowns are the quantities to be solved for in the coupled trim procedure. The lengths of these vectors are the same and depend on the flight condition and associated assumptions which can be made in regard to the force balance. For the tiltrotor model of the present formulation, three trim options are offered, and are classified as: free-flight, wind tunnel, and axisymmetric trim. General free-flight trim considers equilibrium about a convenient point in the vehicle and assumes symmetric level flight. This option includes a balance of forces from the rotor, wing, horizontal tail, and the fuselage. Wind tunnel trim for the tiltrotor configuration assumes a cantilevered wing and rotor model, and excludes consideration of the airframe (fuselage, wing, and horizontal tail) forces. Axisymmetric trim is a highly simplified scheme applicable to the hover and axial flight cases in which only the rotor thrust balance is considered.

6.1.1 Free-Flight Trim

For the tiltrotor free-flight trim scheme, symmetric level flight is assumed. This implies that only one of the rotor systems need be considered and that the opposite rotor is a mirror image of the one under consideration. Under this assumption, the vehicle roll and yaw moments and the vehicle side forces balance by definition, independent of the actual loads on the rotor, wing, horizontal tail, and fuselage. The free-flight trim may be used to solve the trim equations for any of the tiltrotor flight modes: hover, helicopter forward flight, conversion mode, or high-speed axial flight. However, simplified trim schemes are available and may be desirable for

flight conditions where a reduced set of unknowns can be used.

A side view of the free-flight geometry is shown in Figure 6.1 (other views are not necessary because of the assumption of symmetry). As shown, the steady rotor thrust, drag, and pitch moment contribute to the aircraft equilibrium which is established at a point in the fuselage which has the same x and z coordinates as the pylon pivot point. Aerodynamic loads from the tail section, wing, and rotor are also considered, and the wing and tail may each have incidence angles built-in which are added to the angle of attack of the fuselage. Lateral and roll moments on the aircraft are balanced by the assumed symmetry of the flight condition, but to restrain flapping to a minimum, lateral flapping moment at the rotor itself (M_x, not shown in figure) must be zero. The forward component of thrust balances with the aircraft and rotor drags while the wing lift and vertical component of rotor thrust must balance with the vehicle weight. The rotor side force and rotor torque balance due to symmetry. The force equilibrium is written in terms of a vector of force residuals $\hat{F}$ in which

$$\hat{F} = 0 \tag{6.1}$$

when trim is complete. There are four force residuals for the tiltrotor symmetric free-flight trim which are given by

$$F_1 = D_f + D_w + D_t - (T\sin\alpha_p - H\cos\alpha_p) \tag{6.2}$$

$$F_2 = L_f + L_w + L_t + (T\cos\alpha_p + H\sin\alpha_p) - W \tag{6.3}$$

$$F_3 = M_y + (M_y)_f - W(z_w \sin\alpha_f + x_w \cos\alpha_f) - D_f z_w +$$
$$M_w + M_t - D_t(z_w - z_t) - L_t(x_t - x_w) + hH \tag{6.4}$$

$$F_4 = M_x \tag{6.5}$$

These equations are derived from the force and moment diagram illustrated in Figure 6.1, and all quantities are in nondimensional form. F_1 and F_2 represent the vertical and horizontal force residuals, respectively, F_3 represents the longitudinal

218

(pitch) moment residual, and F_4 represents the lateral moment residual about the rotor hub. T, H, M_x, and M_y are the rotor thrust, drag, roll moment, and pitch moment, respectively. These forces are balanced by the lift, drag, and moments (L, D, M) associated with the fuselage, wing, and horizontal tail (subscripts f, w, and t), and by the vehicle weight, W. x_t and x_w indicate the longitudinal distance between the fuselage center of gravity and the quarter chord position of the tail and wing, respectively. Similarly, z_t and z_w indicate vertical height above the fuselage center of gravity of the tail and wing, respectively. The fuselage forces appearing in the residual equations are defined as follows:

$$D_f = \frac{\mu^2}{2} \frac{\gamma N_b}{3\sigma a} \frac{f}{A} \tag{6.6}$$

$$D_w = \frac{\mu^2}{2} \frac{\gamma N_b}{3\sigma a} S_w (C_d)_w \tag{6.7}$$

$$D_t = \frac{\mu^2}{2} \frac{\gamma N_b}{3\sigma a} S_t (C_d)_t \tag{6.8}$$

$$L_f = \frac{\mu^2}{2} \frac{\gamma N_b}{3\sigma a} S_t (C_l)_f \tag{6.9}$$

$$L_w = \frac{\mu^2}{2} \frac{\gamma N_b}{3\sigma a} S_w (C_{l_\alpha})_w (\alpha_f + (\alpha_0)_w) \tag{6.10}$$

$$L_t = \frac{\mu^2}{2} \frac{\gamma N_b}{3\sigma a} S_t (C_{l_\alpha})_t (\alpha_f + (\alpha_0)_t) \tag{6.11}$$

$$(M_y)_f = \frac{\mu^2}{2} \frac{\gamma N_b}{3\sigma a} C_{M_f} \tag{6.12}$$

$$M_w = \frac{\mu^2}{2} \frac{\gamma N_b}{3\sigma a} S_w (C_m)_w c_w \tag{6.13}$$

$$M_t = \frac{\mu^2}{2} \frac{\gamma N_b}{3\sigma a} S_t (C_m)_t c_t \tag{6.14}$$

and the rotor forces are calculated in the hub plane based on a finite element in time solution. In the above equations, γ represents the Lock number, N_b is the number of blades, a is the reference lift curve slope of the rotor blades, σ is the blade solidity, f/A is the fuselage flat plate area, α_0 is the incidence angle of the wing or tail with respect to the fuselage (angle of attack when α_f is zero), and C_{M_f} is the fuselage pitch moment coefficient without the wing or horizontal tail included.

The unknown quantities to be determined in the coupled trim procedure are given in vector form as

$$\hat{\theta}^T = [\alpha_f \ \theta_{75} \ \theta_{1c} \ \theta_{1s}] \tag{6.15}$$

where α_s is the fuselage angle of attack which is the same as the rotor shaft tilt when the rotor pylon angle is at $0°$. The remaining three controls govern the rotor blade pitch as a function of azimuth, and can be written for any blade radial station as

$$\theta(x, \psi) = \theta_{75} + \theta_x + \theta_{1c}\cos\psi + \theta_{1s}\sin\psi \tag{6.16}$$

where θ_{75} is the pitch angle defined at the 75% radial station (essentially the collective pitch setting defined at $.75R$), θ_x is the difference in pitch between the 75% radial station and the radial station at x which is given by the built-in blade twist (twist may be nonlinear), and θ_{1c} and θ_{1s} are the cyclic pitch angles.

6.1.2 Wind Tunnel Trim

For the tiltrotor configuration, wind tunnel trim refers to a cantilevered wing and rotor system. Here, there is no need to include fuselage, wing, or tail forces in the force residual calculations. There is no fuselage angle of attack, and the pylon is set at a steady value given by α_P. The force residual equations for this configuration are greatly simplified as compared to the free-flight case, and are given by:

$$F_1 = T - T_i \tag{6.17}$$

$$F_2 = M_y \tag{6.18}$$

$$F_3 = M_x \tag{6.19}$$

F_1 is the thrust residual which is the difference between the calculated thrust T based on a current value of the collective pitch setting and the desired thrust level T_i (an input parameter). F_2 and F_3 are the pitch and roll moment residuals at the rotor hub. These residuals determine the level of cyclic pitch in the rotor system

220

which is nonzero when an antisymmetric flow condition exists (α_P not at $0°$ or $90°$).

The unknown quantities to be determined in the wind tunnel coupled trim procedure are given in vector form as

$$\hat{\theta}^T = [\theta_{75} \; \theta_{1c} \; \theta_{1s}] \tag{6.20}$$

where the fuselage angle of attack α_f, has been dropped from the vector of unknowns as defined for the free-flight case.

6.1.3   Axisymmetric Trim

Simplified trim procedures are available for the two tiltrotor flight conditions in which flow through the rotor is perfectly-symmetric (independent of azimuth station), axisymmetric hover and high-speed axial flight. In the context of the analytical tiltrotor model, axisymmetric hover is a free-flight condition which assumes that the vehicle center of gravity aligns with the rotor thrust axis such that no cyclic control is required to balance vehicle forces and moments. Axial flight is a wind-tunnel trim case in which the pylon angle is set to $90°$ (airplane mode). Only one force residual equation is required for these two cases as is given by:

$$F_1 = T - T_i \tag{6.21}$$

where T is the calculated thrust based on a current value of the collective and T_i is the desired thrust level. T_i is an input parameter defined as the desired value of thrust in the axial flight case and $T_i = W$ in the hover case. There is only one term in the corresponding vector of unknowns:

$$\hat{\theta}^T = [\theta_{75}] \tag{6.22}$$

221

6.2 Blade Response Equations

An integral part of the coupled trim scheme is the solution of the steady blade response, as this impacts the hub force calculations. The steady rotor response is calculated for a fixed hub, so only the blade-related equations defined in Chapters 4 and 5 (hub and wing equations involved only in the stability analysis) are used, and within these equations the hub motion terms are neglected such that:

$$\hat{\dot{x}}_h = 0 \tag{6.23}$$

$$\hat{\ddot{x}}_h = 0 \tag{6.24}$$

For the tiltrotor configuration, the hub displacements are not members of the vector of unknown trim parameters so it may also be assumed that

$$\hat{x}_h = 0 \tag{6.25}$$

in the calculation of the steady blade response. The blade response is then defined by the solution of:

$$\int_0^{2\pi} (\delta \hat{q}_b^G)^T ([M_{bb}^G] \hat{\ddot{q}}_b^G + [C_{bb}^G] \hat{\dot{q}}_b^G + [K_{bb}^G] \hat{q}_b^G - \hat{F}_b^G) \, d\psi = 0 \tag{6.26}$$

where the blade-blade structural and aerodynamic element matrices defined in Chapters 4 and 5 have been combined and assembled into respective global matrices as indicated by the superscript G. The assembly process is described in more detail in Chapter 7. For free flight trim, the blade force vector includes contributions of the fuselage angle of attack.

To reduce computation time, the blade response equations are solved using normal modes. The free vibration modes for the blade are calculated based on the structural contributions to the global mass and stiffness matrices:

$$[M_{bb}^G]^S \hat{\ddot{q}}_b^G + [K_{bb}^G]^S \hat{q}_b^G = 0 \tag{6.27}$$

where the superscript S indicates contributions only from the structural model, and the matrix terms are calculated based on $\theta_{75} = 0$. This system is solved using standard eigenvalue techniques for a desired number of model degrees of freedom, generally 6 to 8. All eigenvalues of this system are positive real numbers, and the eigenvectors are real and orthogonal. The global displacements are related to the new set of modal displacements as:

$$\hat{q}_b^G = [\Phi]\hat{p}_b \tag{6.28}$$

where $[\Phi]$ is the N^G x m modal matrix, and N^G is the number of blade global degrees of freedom and m is the number of modes. After substitution of this relationship into Eqn. 6.26, the modal response equations are expressed as:

$$\int_0^{2\pi} (\delta\hat{p}_b)^T ([M_{bb}^p]\hat{\ddot{p}}_b + [C_{bb}^p]\hat{\dot{p}}_b + [K_{bb}^p]\hat{p}_b - \hat{F}_b^p)\, d\psi = 0 \tag{6.29}$$

where

$$[M_{bb}^p] = [\Phi]^T \left[M_{bb}^G\right] [\Phi] \tag{6.30}$$

$$[C_{bb}^p] = [\Phi]^T \left[C_{bb}^G\right] [\Phi] \tag{6.31}$$

$$[K_{bb}^p] = [\Phi]^T \left[K_{bb}^G\right] [\Phi] \tag{6.32}$$

$$[F_b^p] = [\Phi]^T \left[F_b^G\right] \tag{6.33}$$

defines the modal mass, damping, and stiffness matrices.

6.2.1   Finite Element in Time

Solution of Eqn. 6.29 requires a numerical integration method such as Runge-Kutta or finite element in time. The procedure used in the present formulation is the finite element in time method, and is no different than that procedure used in the UMARC formulations. As a matter of completeness, however, some of the details of the procedure are established in the present section.

A temporal finite element based on Hamilton's principle is used to discretize the azimuthal dependence (periodic part) of the blade response equations. The normal mode degrees of freedom p_b are approximated with 5th order Lagrangian C^0-continuous polynomials (6 nodes per time element).

The damping and stiffness matrices of the blade response equations contain periodic terms, but the mass matrix does not. Application of the finite element in time procedure is then facilitated by an integration of the response equations by parts. Eqn. 6.29 may be written as:

$$\int_0^{2\pi} \left\{ \begin{array}{c} \delta \hat{p}_b \\ \delta \hat{\dot{p}}_b \end{array} \right\}^T \left\{ \begin{array}{c} \hat{F}_b^p - [C]_b^p \hat{\dot{p}}_b - [K]_b^p \hat{p}_b \\ [M]_b^p \hat{\dot{p}}_b \end{array} \right\} d\psi = \left\{ \begin{array}{c} \delta \hat{p}_b \\ \delta \hat{\dot{p}}_b \end{array} \right\}^T \left\{ \begin{array}{c} [M]_b^p \hat{\dot{p}}_b \\ 0 \end{array} \right\} \Bigg|_0^{2\pi} \quad (6.34)$$

where the right hand side of the equation is zero because periodicity for the system is enforced such that

$$\hat{p}(2\pi) = \hat{p}(0) \quad (6.35)$$

The response equations may then be written as

$$\int_0^{2\pi} \delta \hat{y}^T [Q] \, d\psi = 0 \quad (6.36)$$

where

$$\hat{y} = \left\{ \begin{array}{c} \delta \hat{p}_b \\ \delta \hat{\dot{p}}_b \end{array} \right\} \quad (6.37)$$

and

$$[Q] = \left\{ \begin{array}{c} \hat{F}_b^p - [C]_b^p \hat{\dot{p}}_b - [K]_b^p \hat{p}_b \\ [M]_b^p \hat{\dot{p}}_b \end{array} \right\} \quad (6.38)$$

At this stage, the matrix $[Q]$ is nonlinear since it contains $\hat{F}_b^p$. Using a procedure analogous to spatial discretization, the interval of one rotor revolution 2π is divided into several time (azimuthal) elements as shown in Fig. 6.2. The blade response equations are then expressed as a sum of the response over each time interval as:

$$\sum_{i=1}^{N_t} \int_{\psi_i}^{\psi_i+1} \delta \hat{y}_i^T [Q]_i \, d\psi = 0 \quad (6.39)$$

224

where N_t is the number of time elements used. The response may be linearized using a first-order Taylor series expansion about a set of steady state values $\hat{y}_0$ which represent the current blade response estimate. The linearized response is written as:

$$\sum_{i=1}^{N_t} \int_{\psi_i}^{\psi_{i+1}} \delta \hat{y}_i^T ([Q(y_0)]_i + [K_t(\hat{y}_0)]_i \Delta \hat{y}_i)\, d\psi = 0 \qquad (6.40)$$

where

$$[K_t]_i = \begin{bmatrix} \frac{\partial F_b^G}{\partial \dot{p}_b} - [K]_b^G & \frac{\partial F_b^G}{\partial \dot{p}_b} - [C]_b^G \\ 0 & [M]_b^G \end{bmatrix} \qquad (6.41)$$

For the ith element, the time variation of the modal displacement vector can be expressed in terms of the temporal shape functions and the temporal discrete displacements as:

$$\hat{p}_b(\psi) = [H_t(s)]\hat{\xi} \qquad (6.42)$$

where s is the local time coordinate defined as:

$$s = \frac{\psi - \psi_i}{\psi_{i+1} - \psi_i} \qquad (6.43)$$

and $\psi_{i+1} - \psi_i$ is the time span of the ith element. The number of shape functions in the matrix $[H]_t$ depends on the level of approximation, but generally the default approximation used in the current formulation is 6 nodes per element which yields a set of six 5th-order polynomials. This family of polynomials is derived in Ref. 79. The response equations can then be written in terms of the discrete unknowns as:

$$\sum_{i=1}^{N_t} \int_{\psi_i}^{\psi_{i+1}} \delta \hat{\xi}_i^T [N]^t ([Q]_i + [K_t]_i [N] \Delta \hat{\xi}_i)\, d\psi = 0 \qquad (6.44)$$

where

$$N = \left\{ \begin{array}{c} [H_t(\psi)] \\ [\dot{H}_t(\psi)] \end{array} \right\} \qquad (6.45)$$

After summation and assembly of the elements (which follows the same procedures as that of the spatial elements) and conversion from a set of element degrees of

225

freedom to a set of global degrees of freedom, the response equations may be written as:

$$[Q]^G + [K]_t^G \Delta \hat{\xi}^G = 0 \qquad (6.46)$$

which is solved subject to the boundary conditions:

$$\hat{\xi}(0) = \hat{\xi}(2\pi) \qquad (6.47)$$

$$\dot{\hat{\xi}}(0) = \dot{\hat{\xi}}(2\pi) \qquad (6.48)$$

6.3 Coupled Trim Procedure

The coupled trim procedure used for the tiltrotor formulation is similar to that used in UMARC, but a few modifications have been added. New segments of the procedure are the different initial controls and modifications to facilitate convergence of blades with large twist deformations. For the initial controls estimate of a tiltrotor configuration, a new rigid-blade flap analysis is formulated which accounts for high-inflow, large steady pylon angles, large blade twist, and the airframe forces (wing and horizontal tail) when free flight is considered. For the convergence of blades with large twist, the coupled trim procedure is modified so that a twist deformation estimate may be added to the initial controls estimate and the Jacobian may be recalculated at given intervals in the procedure.

The basic procedure of the present coupled trim solution is shown in Fig. 6.3. The objective is to balance the rotor and airframe forces, driving the force residual equations to zero. It is advantageous to start the procedure with a good estimate of the initial controls for two reasons: 1) the procedure involves nonlinear equations and so it is possible to obtain an unrealistic or divergent solution 2) the procedure is computationally intensive and the number of iterations needed to achieve the converged solution depends on the closeness of the initial guess to the final solution. Based on the initial controls, the blade response equations are solved yielding

an initial set of rotor forces and the blade responses (velocity and displacement associated with each discrete degree of freedom). A Jacobian matrix is formulated to determine a new set of controls required to drive the force residual to zero. The blade response and rotor forces associated with the new set of controls is then calculated. This process continues until convergence of both the blade response and vehicle force residuals is obtained. A new Jacobian is never recalculated during the iteration cycle in previous versions of the UMARC analysis, but as shown the Jacobian may be recalculated in the present formulation. The new procedure also calls for interactive support of the user when large twist deformations are involved. A divergent process may be encountered in such situations which requires restarting of the analysis with an improved estimate of the elastic twist. This estimate may be gained from observations of early coupled trim iterations.

6.3.1 Initial Controls Estimate

As mentioned previously, it is advantageous to start the coupled trim procedure with a good estimate of the initial controls. A reasonably good approximation of the initial controls (including fuselage angle of attack for free flight) may be obtained with a rigid flapping blade analysis. Although a rigid-blade analysis including both flap and lag motions is formulated in Chapter 2, it assumes axial flight, and is, therefore, not applicable to the general tiltrotor configuration. A new rigid-blade analysis is formulated based on a flap-only rigid-blade and lift-curve-slope aerodynamics. Because this model is applicable for the general tiltrotor configuration, including free-flight conversion modes, the development is quite involved. The formulation of the rigid-blade controls-estimate analysis is thus provided in Appendix B.

227

6.3.2 Blade Steady Periodic Response

The blade steady periodic response is obtained from solution of the global finite element in time matrices defined by Eqn. 6.46, with initial conditions defined by Eqns. 6.47 and 6.48. These equations represent a time discretized nonlinear set of algebraic equations which are solved iteratively using Newton's method. Recall that the solution vector is written as a sum of steady and perturbations quantities such that

$$\hat{\xi} = \hat{\xi}_0 + \Delta \hat{\xi} \tag{6.49}$$

The steady global solution update for each iteration is thus given by

$$\hat{\xi}^G_{i+1} = \hat{\xi}^G_i + \Delta \hat{\xi}^G_i \tag{6.50}$$

where convergence is obtained when $\Delta \xi^G_i \approx 0$. In the coupled-trim procedure, this iterative solution is coupled with the solution of the force residual equations such that both the blade steady periodic response $\hat{\xi}^G$ and blade control vector $\hat{\theta}$ are obtained simultaneously.

6.3.3 Computation of Blade and Hub Loads

Solution of the force residual equations requires the contribution of the hub loads which come from conversion of the rotating blade loads into the fixed frame. The rotating blade loads are calculated in the present formulation using a force summation method involving integration of the local blade inertial and aerodynamic forces along the span. Aerodynamic contributions to the blade loads are defined in Chapter 5. Intertial contributions to the blade loads are defined in UMARC formulations and are listed in Ref. 79. Since the hub is fixed in the coupled trim procedure, the inertial loads depend only on the deformation associated with the blade itself so that the tiltrotor and helicopter equations are identical. The equations for the inertial contributions to the blade loads are nonlinear, and require

knowledge of the blade displacements, velocities, and accelerations. The displacement and velocity information are products of the finite element in time solution. The blade accelerations are calculated from rearrangement of Eqn. 6.26 as:

$$\ddot{q}_b^G = [M_{bb}^G]^{-1}(\hat{F}_b^G - [C_{bb}^G]\dot{q}_b^G - [K_{bb}^G]\hat{q}_b^G) \tag{6.51}$$

The inertial and aerodynamic contributions to each of the three force and moment directions are summed as:

$$L_u = L_u^A + L_u^I \tag{6.52}$$

$$L_v = L_v^A + L_v^I \tag{6.53}$$

$$L_w = L_w^A + L_w^I \tag{6.54}$$

$$M_u = M_\phi^A + M_\phi^I \tag{6.55}$$

$$M_v = M_\phi^A v' + M_v^I \tag{6.56}$$

$$M_w = M_\phi^A w' + M_w^I \tag{6.57}$$

where the loads are defined in the undeformed blade system. The rotating blade forces and moments at the root are then obtained by integration along the blade span:

$$F_x = \int_0^R L_u \, dr \tag{6.58}$$

$$F_y = \int_0^R L_v \, dr \tag{6.59}$$

$$F_z = \int_0^R L_w \, dr \tag{6.60}$$

$$M_x = \int_0^R (M_u + L_w v - L_v w) \, dr \tag{6.61}$$

$$M_y = \int_0^R (M_v - L_w(r + u) + L_u w) \, dr \tag{6.62}$$

$$M_z = \int_0^R (M_w + L_v(r + u) - L_u v) \, dr \tag{6.63}$$

The fixed frame loads are defined in the hub plane, and are calculated using the Fourier coordinate transformation as:

$$F_x^H = \sum_{m=1}^{N_b} (F_x^m \cos\psi_m - F_y^m \sin\psi_m - \beta_p F_z^m \cos\psi_m) \tag{6.64}$$

$$F_y^H = \sum_{m=1}^{N_b} (F_x^m \sin\psi_m + F_y^m \cos\psi_m - \beta_p F_z^m \sin\psi_m) \qquad (6.65)$$

$$F_z^H = \sum_{m=1}^{N_b} (F_z^m + \beta_p F_x^m) \qquad (6.66)$$

$$M_x^H = \sum_{m=1}^{N_b} (M_x^m \cos\psi_m - M_y^m \sin\psi_m - \beta_p M_z^m \cos\psi_m) \qquad (6.67)$$

$$M_y^H = \sum_{m=1}^{N_b} (M_x^m \sin\psi_m + M_y^m \cos\psi_m - \beta_p M_z^m \sin\psi_m) \qquad (6.68)$$

$$M_z^H = \sum_{m=1}^{N_b} (M_z^m + \beta_p M_x^m) \qquad (6.69)$$

where m designates the mth blade of N_b blades, F are the hub shear forces, and M are the hub moments. The hub shear forces and moments may be periodic, and are therefore expressed in terms of harmonics. Any periodic functions may be expanded in a Fourier series as

$$f(\psi) = f_0 + \sum_{n=1}^{\infty} (f_{nc} \cos n\psi + f_{ns} \sin n\psi) \qquad (6.70)$$

where f_0 is a steady term and n denotes the nth harmonic. Expansion of the hub forces and moments in a Fourier series gives the steady hub force and moment terms required for the force residual equations (T, H, M_x, and M_y while Y and Q are also gained, but not required due to symmetry). The harmonic terms give the vibratory loads of the system.

6.3.4 Inflow Update

Just as the definition of advance ratio is modified for the tiltrotor configuration to exclude the angle of attack, so is the definition of the inflow. Normally, the inflow has an induced-flow component and a forward velocity component. The component of inflow due to forward flight velocity is accounted for in the present formulation with sine and cosine terms in the equations of motion and aerodynamic force calculations. The induced inflow, λ_i, depends on the rotor thrust T (the zeroth

230

harmonic of F_z^H), and is updated accordingly on each iteration of the coupled trim procedure. Two inflow models are available for the tiltrotor inflow calculations, but these do not include the interference of the wing or fuselage on the flow. The simplest is a uniform induced inflow distribution given by

$$\lambda_i = 1.15\sqrt{\frac{C_T}{2}} \tag{6.71}$$

which is adequate for high speed axial flight where the thrust generation is fairly uniform across the disk and the induced inflow velocity is a very small (almost insignificant) part of the total velocity through the rotor. A more complex model developed by Gessow [91] is used for hover:

$$\lambda_i = \frac{\sigma(c_1)_i}{16}(-1 + \sqrt{1 + \frac{32\theta x}{\sigma(c_1)_i}}) \tag{6.72}$$

where $(c_1)_i$ is the local lift curve slope corrected for Mach and stall effects. This model is important for tiltrotors because the blades generally are highly twisted such that some part of the blade span is influenced by stall. Inflow distributions for several blade linear twist distributions are compared in Fig. 6.4 which show the large differences between uniform and nonuniform hover distribution models. This plot also shows the effects of stall at high blade twists, as noted by the increase in collective angle required to produce the desired thrust. Also, while low twist blades have fairly uniform inflow on the outer one-half of the span (even using the nonuniform inflow model), the highly-twisted blades have very nonlinear distributions of inflow which should be accounted for in the hover aerodynamics.

6.3.5 Computation of Jacobian and Controls Update

The residual force equations are satisfied by changing the control vector $\hat{\theta}$ such that the rotor forces required to balance the residual force equations are obtained. Some of the airframe forces, of course, also shift with changes in the control vector, as does the blade response which, in turn, influence the rotor forces. The nonlinearity

of the problem requires careful selection of the control vector increments such that numerical stability is maintained. To this end, the airframe force residual vector $\hat{F}$ is linearized about the current control vector setting $\hat{\theta}_i$ such that

$$\hat{F}(\hat{\theta}_i + \Delta\hat{\theta}_i) = \hat{F}(\hat{\theta}_i) + [J]\Delta\hat{\theta}_i = 0 \qquad (6.73)$$

where $[J]$ is the vehicle Jacobian matrix given by

$$[J] = \frac{\partial \hat{F}}{\partial \hat{\theta}}\Big|_{\hat{\theta}=\hat{\theta}_0} \qquad (6.74)$$

The Jacobian matrix is obtained numerically by sequential perturbation of each control parameter in the control vector, generally about 5 percent of the current value, which after calculation of blade response, blade loads, and hub loads, results in an associated residual vector. The Jacobian matrix is then approximated as

$$[J] = \frac{\hat{F}(\hat{\theta} + \Delta\hat{\theta}) - \hat{F}(\hat{\theta})}{\Delta\hat{\theta}} \qquad (6.75)$$

where $\Delta\hat{\theta}$ are the control perturbations. This matrix is calculated using the initial control settings to begin the coupled trim procedure, but may be recalculated using the current control vector of any iteration desired. Recalculation of the Jacobian is only desirable when the initial control settings are faulty as may be the case when large twist deformations are experienced.

Rearrangement of Eqn. 6.73 gives the desired increment in the controls vector as

$$\Delta\hat{\theta}_i = -[J]\hat{F}(\hat{\theta}_i) \qquad (6.76)$$

and the control vector is updated as

$$\hat{\theta}_{i+1} = \hat{\theta}_i + (1 - R)\Delta\hat{\theta}_i \qquad (6.77)$$

where R is a damping factor used to maintain numerical stability and $0 < R < 1$. R is typically set to decay exponentially as the number of iterations increases. The default value for the present formulation is

$$R = e^{-\frac{i}{40}} \qquad (6.78)$$

6.3.6 Converged Blade Response and Vehicle Trim

Convergence of the coupled trim solution is achieved when both the force residual equations and the blade response equations are satisfied. Convergence of the blade response is defined by the scalar sum of azimuthal blade tip deflections between successive iterations which must be less than a specified tolerance:

$$\frac{\sqrt{\sum_{j=1}^{N_\psi}(q_{i+1} - q_i)^2}}{\sqrt{\sum_{j=1}^{N_\psi} q_{i+1}^2}} < \epsilon_1 \qquad (6.79)$$

where N_ψ is the number of global temporal Gaussian points. Similarly, for the force residual convergence, the magnitude of the force vector must be less than a specified tolerance:

$$\sqrt{\sum_{i=1}^{n} F_i^2} < \epsilon_2 \qquad (6.80)$$

where n is the number of force residuals in the force residual vector for the type of trim scheme used.

A typical convergence tolerance for ϵ_1 is .005 which represent a 0.5 percent change in the response magnitude between successive iterations. A typical value for ϵ_2 is .0001.

6.3.7 Large Twist Deformations

Convergence problems may be experienced for blades where the elastic twist deformation is substantial. Convergence is more sensitive to twist than to other blade deformations because twist has a much more significant impact on the blade angle of attack and aerodynamic loads. Examples of blade designs which might experience convergence problems are designs which are subject to large twist changes such as torsionally-soft or extension-twist-coupled blades. Most convergence problems can be overcome with an accurate estimate of the final twist deformation which can be determined by just a few iterations of the coupled trim procedure.

The initial control estimates do not include blade elastic twist deformation, but modifications to the trim procedure allow an estimate of the twist deformation to be included in the initial controls analysis. In the present formulation, the twist deformation is approximated by a linear distribution based on an input value for the 75-percent radial station, ϕ_{75}. The twist deformation at any given radial position is then written as

$$\phi = \frac{x}{.75}\phi_{75} \tag{6.81}$$

which is combined with the built-in twist in the rigid-blade analysis. The control estimate will then include the twist estimate such that, in general, the collective estimate θ_{75} without twist included is reduced by an amount approximately equal to ϕ_{75} when twist is included. However, the estimate is an improvement on the simpler approximation $(\theta_{75})_{new} = (\theta_{75})_{old} - \phi_{75}$ because the rigid-blade analysis is able to account for the change in twist all along the blade span which may have an influence on the collective as well as the other controls in the control vector.

The elastic blade coupled trim procedure generally begins with a zero deformation vector. Without including the initial twist deformation, the Jacobian calculated from the initial response will not reflect the twist approximation, and this will adversely affect the coupled trim procedure. The twist approximation is thus extended to the elastic blade trim by initializing the twist part of the deformation vector as

$$\phi_i = \frac{x_i}{.75}\phi_{75} \tag{6.82}$$

where i represents the gaussian point and x_i is the radial station associated with the gauss point. This estimate may also be held fixed for a specified number of iterations before being relaxed, thereby soothing the elastic blade bending response which tends to move erratically when large twist deformations are encountered.

The second modification for improving convergence in the coupled trim procedure, as discussed previously, is recalculation of the Jacobian at specified intervals

234

of iterations. Using the initial twist estimate in conjunction with the recalculation of the Jacobian should enable convergence to be reached for any realistic blade design, vehicle configuration, and flight condition. A typical scenario for obtaining convergence of a difficult problem is described in the following paragraph.

Assume an extension-twist-coupled blade with 40 degrees of linear nose-down twist is modeled on a tiltrotor configuration in hover. The initial control estimate gives θ_{75} at about 13 degrees which is an angle of attack of about 7 degrees because the inflow angle is calculated at 6 degrees. The initial control estimate is a very good one if the blade is torsionally rigid, but the elastic twist for this blade is high, say 15 degrees nose-up at the 75-percent radial station ($\phi_{75} = 15°$). The elastic coupled trim procedure is begun and the Jacobian is calculated. On the second iteration after calculation of the Jacobian, the large twist gives a negative angle of attack at the .75R station. The force residual shows that the total pitch angle here is too high, and, with the Jacobian, attempts to decrease the collective to account for this. However, the control step size on the first few iterations is highly damped. The controls cannot move as quickly as the deformations, so large positive thrust is produced. On subsequent iterations, the coupled trim eventually overcompensates for the large positive thrust with a very large negative step size in the collective setting, which results in a large negative thrust. The coupled trim begins to oscillate between increasingly larger values of positive and negative thrust, becoming unstable rapidly, and further computation is stopped. During the first few iterations, however, the elastic twist is shown to be about 12 degrees at .75R which seems reasonable for the blade considered. This twist is then used as input to linearly estimate the controls, and the procedure is begun again. This time the control estimate analysis predicts a collective setting of 1 degree because it accounts for the 12 degrees of nose-up estimated elastic twist. The elastic blade coupled trim also uses the twist estimate, and it is specified to keep the estimate

as the actual twist deformation for the first three iterations after the Jacobian is calculated. When the actual twist deformation is produced on the fourth iteration of coupled trim, the blade response is sufficiently converged that there are only small changes in the blade response and control vectors. Both begin to converge, but the elastic twist eventually moves up to 15 degrees at .75R. The force residual changes as the twist deformation increases such that the natural position of the collective setting should be -1 degree, but the step size is always a percentage of the current control value so it cannot cross over a zero point. The coupled trim must be stopped and restarted with a larger estimate for the elastic twist, say 17 degrees, so that the initial collective estimate has a negative value. Now, convergence will be achieved.
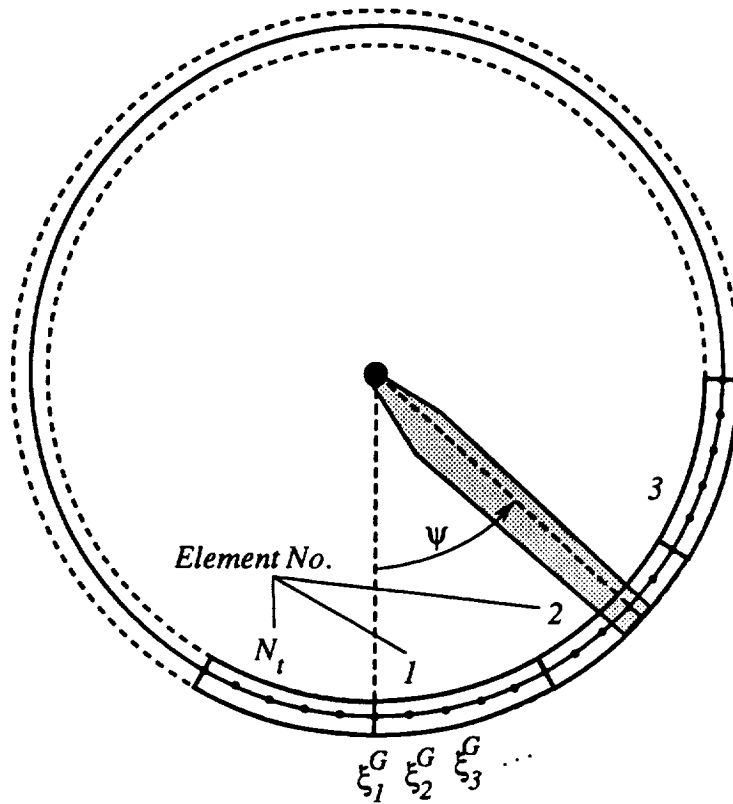
Figure 6.1: Rotor and airframe forces on a tiltrotor in free flight.
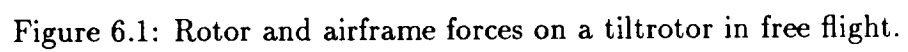
Figure 6.2: Discretization of azimuth into time elements.
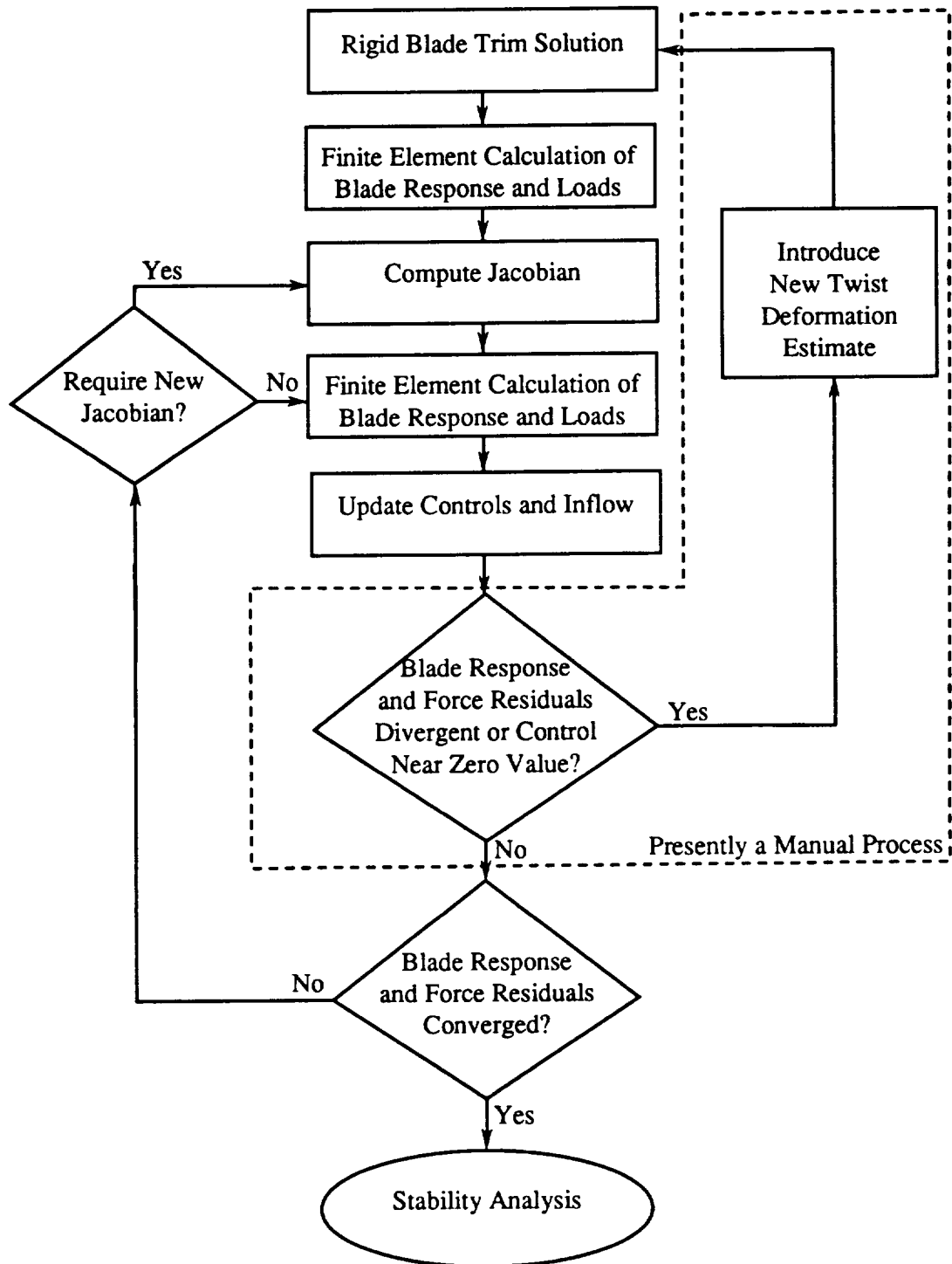
Figure 6.3: Coupled trim procedure as modified for the present formulation.
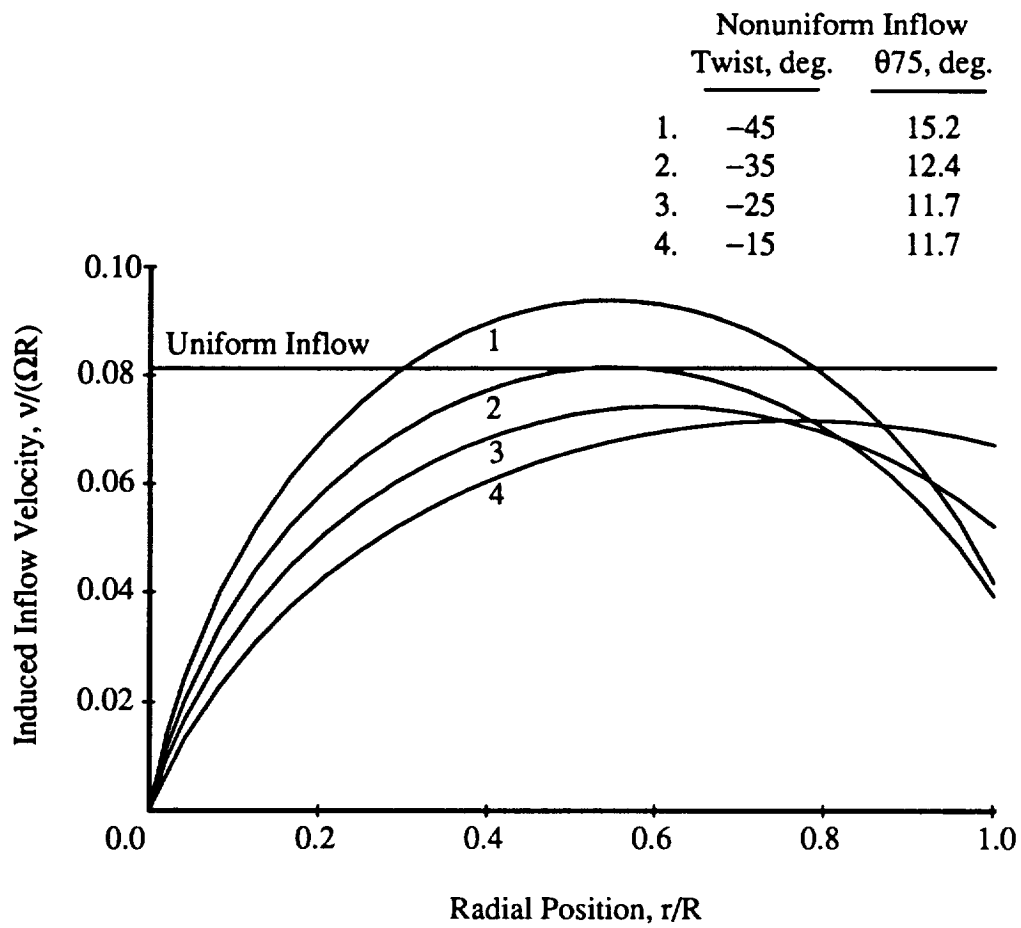
239

Figure 6.4: Uniform and nonuniform induced inflow distributions in hover for blades with various twists.

Chapter 7

Stability Analysis

This chapter addresses the procedures implemented for determination of tiltrotor stability characteristics. There are substantial modifications required to the UMARC formulations regarding the assembly of the global system matrices, but the stability analyses themselves are relatively unchanged. This chapter also discusses the importance of the engine drive train dynamics on tiltrotor system stability, and shows how these effects are incorporated in the present formulation. Dynamic inflow, which has been considered in UMARC formulations, is not included.

The UMARC formulations consider both a linearized eigenanalysis and a transient response analysis for determination of system stability. In the linearized eigenanalysis, the nonlinear differential equations are derived for the perturbed motion of the system, and are then linearized about the deflected trim position. An eigenvalue analysis is performed on the homogeneous form of these equations to determine the system stability characteristics. For periodic equations, a Floquet transition matrix or a constant-coefficient approximation is used to obtain the system equations in suitable form for the eigenanalysis. Advantages of the linearized eigenanalysis are that damping of high-frequency modes can be accurately estimated, the effects of rigid-body motions can be included in the stability cal-

culations, and the method is computationally efficient. The disadvantage is that highly nonlinear effects such as flow separation and dynamic stall are lost in the calculations. These effects are captured in the transient response analysis in which the blade motion is integrated over time. After the transient response is calculated, a damping estimation method such as "moving block" is then used to estimate the damping of the system modes. Disadvantages of this method are loss of accuracy in the determination of damping of high-frequency and high-damping modes, sensitivity of system nonlinearities to control perturbations, and high computational time.

Application of linearized eigenanalysis appears suitable for most of the practical range of tiltrotor dynamics problems since the most common form of tiltrotor instability (whirl flutter) occurs in high-speed axial flight. For this flight condition, the equations of motion have constant coefficients. Thus, there is no need to consider Floquet theory or use constant coefficient approximations for most cases. For the tiltrotor configuration, the isolated blade stability is not important because the hub motion is coupled with the elastic wing modes, and has a large influence on the system damping. The present formulation considers only linearized eigenanalysis in the fixed frame.

7.1 Assembly of the System Equations

Assembly of the system equations is based on application of Hamilton's principle given by Eqns. 4.35-4.38. The system matrices defined in Chapters 4 and 5 are derived by assuming the degrees of freedom (state variables) $\hat{q}$, $\hat{x}_h$, and q_w are small perturbations about the deflected trim position:

$$\hat{q} = (\hat{q})_0 + \Delta\hat{q} \tag{7.1}$$

$$\hat{x}_h = (\hat{x}_h)_0 + \Delta\hat{x}_h \tag{7.2}$$

$$\hat{q} = (\hat{q}_w)_0 + \Delta\hat{q}_w \tag{7.3}$$

where subscript 0 indicates the steady values and Δ indicates a small perturbation. The variational quantities are then given by:

$$\delta\hat{q} = \delta(\hat{q})_0 + \delta\Delta\hat{q} \tag{7.4}$$

$$\delta\hat{x}_h = \delta(\hat{x}_h)_0 + \delta\Delta\hat{x}_h \tag{7.5}$$

$$\delta\hat{q} = \delta(\hat{q}_w)_0 + \delta\Delta\hat{q}_w \tag{7.6}$$

but for the converged trim solution the variation of the steady value must be zero by definition so that

$$\delta\hat{q} = \delta\Delta\hat{q} \tag{7.7}$$

$$\delta\hat{x}_h = \delta\Delta\hat{x}_h \tag{7.8}$$

$$\delta\hat{q} = \delta\Delta\hat{q}_w \tag{7.9}$$

The work and energies associated with the perturbation motion can also be written as a sum of steady and perturbation quantities which gives the following form for the variation of Hamilton's principle:

$$\int_{t_1}^{t_2} (\delta U_0 - \delta T_0 - \delta W_0)\, dt + \int_{t_1}^{t_2} (\delta\Delta U_0 - \delta\Delta T_0 - \delta\Delta W_0)\, dt = 0 \tag{7.10}$$

However, the steady state trim solution satisfies the equation

$$\int_{t_1}^{t_2} (\delta U_0 - \delta T_0 - \delta W_0)\, dt = 0 \tag{7.11}$$

so the energy variation corresponding to the perturbation motion becomes:

$$\int_{t_1}^{t_2} (\delta\Delta U_0 - \delta\Delta T_0 - \delta\Delta W_0)\, dt = 0 \tag{7.12}$$

Thus, the perturbation symbol may be dropped from the equations with the understanding that all the state variables represent perturbation quantities after the trim solution is reached.

243

Following the application of Hamilton's principle, the blade, hub, and wing matrices are defined in Chapters 4 and 5. These element matrices are classified as follows:

$[M_{bb}]$ Blade-blade structural mass matrix

$[C_{bb}]$ Blade-blade structural damping matrix

$[K_{bb}]$ Blade-blade structural stiffness matrix

$[F_b]$ Blade structural load vector with nonlinear terms

$[M_{bh}]$ Blade-hub structural mass matrix

$[C_{bh}]$ Blade-hub structural damping matrix

$[K_{bh}]$ Blade-hub structural stiffness matrix

$[M_{hb}]$ Hub-blade structural mass matrix

$[C_{hb}]$ Hub-blade structural damping matrix

$[K_{hb}]$ Hub-blade structural stiffness matrix

$[M_{hh}]$ Hub-hub structural mass matrix

$[C_{hh}]$ Hub-hub structural damping matrix

$[K_{hh}]$ Hub-hub structural stiffness matrix

$[M_{ww}]$ Wing structural mass matrix

$[C_{ww}]$ Wing structural damping matrix

$[K_{ww}]$ Wing structural stiffness matrix

$\left[M_{bb}^A\right]$ Blade-blade aerodynamic mass matrix

$\left[C_{bb}^A\right]$ Blade-blade aerodynamic damping matrix

$\left[K_{bb}^A\right]$ Blade-blade aerodynamic stiffness matrix

$\left[F_b^A\right]$ Blade aerodynamic load vector

$\left[M_{bh}^A\right]$ Blade-hub aerodynamic mass matrix

$\left[C_{bh}^A \right]$ Blade-hub aerodynamic damping matrix

$\left[K_{bh}^A \right]$ Blade-hub aerodynamic stiffness matrix

$\left[M_{hb}^A \right]$ Hub-blade aerodynamic mass matrix

$\left[C_{hb}^A \right]$ Hub-blade aerodynamic damping matrix

$\left[K_{hb}^A \right]$ Hub-blade aerodynamic stiffness matrix

$\left[C_{hh}^A \right]$ Hub-hub aerodynamic damping matrix

$\left[K_{hh}^A \right]$ Hub-hub aerodynamic stiffness matrix

$\left[M_{ww}^A \right]$ Wing aerodynamic mass matrix

$\left[C_{ww}^A \right]$ Wing aerodynamic damping matrix

$\left[K_{ww}^A \right]$ Wing aerodynamic stiffness matrix

$\left[C_{bb}^A \right]_{nl}$ Blade-blade nonlinear aerodynamic damping matrix

$\left[K_{bb}^A \right]_{nl}$ Blade-blade nonlinear aerodynamic stiffness matrix

$\left[C_{bh}^A \right]_{nl}$ Blade-hub nonlinear aerodynamic damping matrix

$\left[K_{bh}^A \right]_{nl}$ Blade-hub nonlinear aerodynamic stiffness matrix

$\left[C_{hb}^A \right]_{nl}$ Hub-blade nonlinear aerodynamic damping matrix

$\left[K_{hb}^A \right]_{nl}$ Hub-blade nonlinear aerodynamic stiffness matrix

$\left[C_{hh}^A \right]_{nl}$ Hub-hub nonlinear aerodynamic damping matrix

$\left[K_{hh}^A \right]_{nl}$ Hub-hub nonlinear aerodynamic stiffness matrix

The blade part of the matrices corresponds to the 15 discrete blade degrees of freedom $\hat{q}$, the hub part of the matrices corresponds to the 8 hub degrees of freedom $\hat{x}_h$, and the wing part of the matrices corresponds to the 15 discrete wing degrees of freedom $\hat{q}_w$. The terms of these matrices are as yet not integrated over the element length. Also, the blade equations are derived in a rotating coordinate system while the hub and wing equations are derived in a fixed coordinate system. This difference needs to be resolved before a stability solution can be performed.

245

7.1.1 Element Integration

Calculation of the element matrices requires integration over the length of the beam element and is performed numerically. A 6-point Gauss quadrature procedure is used in UMARC (and also in the present analysis) which gives the integration of a typical term in the element matrices as:

$$\int_0^1 F(s)\,ds = \sum_{j=1}^{6} w_j F(s_j) \tag{7.13}$$

where w_j is the weighting factor at the jth quadrature point and s_j is the position of the jth quadrature point. A 6-point formula is used because it offers the best compromise between accuracy and numerical efficiency for the integration of polynomials associated with the present formulation.

The numerical integration technique is highly compatible with tiltrotor blades because these blades typically have large twists. Since the beam properties are defined in the local cross-section reference frame, but are converted to an untwisted reference frame, integration of an element with large twist can introduce significant errors, particularly if the beam properties and twist vary along the element span. A linear interpolation scheme has been introduced in the present formulation to account for beam property and twist variations within an element. Properties for the beam elements may be designated at each node point. During the Gaussian integration, the properties at each of the 6 Gauss point locations are estimated as

$$F(s_j) = F(0) + \frac{s_j}{l}(F(l) - F(0)) \tag{7.14}$$

where $F(0)$ is a typical beam property at the first node point, $F(l)$ is a typical beam property at the second node point, and l is the element length. In previous UMARC formulations, a beam property is assumed constant over the element length, and if nonlinear twist is used, the twist is also assumed constant over the element length.

Following integration, the structural, aerodynamic, and nonlinear aerodynamic contributions of the common matrix types are summed to produce the total element matrices. The total element matrices are now designated by a superscript e as:

$[M^e_{bb}]$ Blade-blade total element mass matrix

$[C^e_{bb}]$ Blade-blade total element damping matrix

$[K^e_{bb}]$ Blade-blade total element stiffness matrix

$[F^e_b]$ Blade total load vector with nonlinear terms

$[M^e_{bh}]$ Blade-hub total element mass matrix

$[C^e_{bh}]$ Blade-hub total element damping matrix

$[K^e_{bh}]$ Blade-hub total element stiffness matrix

$[M^e_{hb}]$ Hub-blade total element mass matrix

$[C^e_{hb}]$ Hub-blade total element damping matrix

$[K^e_{hb}]$ Hub-blade total element stiffness matrix

$[M^e_{hh}]$ Hub-hub total element mass matrix

$[C^e_{hh}]$ Hub-hub total element damping matrix

$[K^e_{hh}]$ Hub-hub total element stiffness matrix

$[M^e_{ww}]$ Wing total element mass matrix

$[C^e_{ww}]$ Wing total element damping matrix

$[K^e_{ww}]$ Wing total element stiffness matrix

7.1.2 Assembly of the Element Matrices

Assembly of the elements involves conversion from local element nodes and local degrees of freedom to global nodes and global degrees of freedom. The blade elements are assembled end-to-end with the second local node of one element corresponding to the first local node of the following element. Each overlap defines

247

one global node. Following the approach of past UMARC formulations, the blade elements are assembled from the blade tip to the root so that global node 1 is at the blade tip and global node $N_e + 1$ is at the center of rotation. The assembly process associated with conversion of the blade element degrees of freedom to the blade global degrees of freedom is a standard finite element technique described in several references (Ref. 89 for example). This process gives the global blade-blade, blade-hub, hub-blade, and hub-hub matrices which are listed as:

$[M_{BB}]$ Blade-blade global mass matrix

$[C_{BB}]$ Blade-blade global damping matrix

$[K_{BB}]$ Blade-blade global stiffness matrix

$[F_B]$ Blade global load vector with nonlinear terms

$[M_{BH}]$ Blade-hub global mass matrix

$[C_{BH}]$ Blade-hub global damping matrix

$[K_{BH}]$ Blade-hub global stiffness matrix

$[M_{HB}]$ Hub-blade global mass matrix

$[C_{HB}]$ Hub-blade global damping matrix

$[K_{HB}]$ Hub-blade global stiffness matrix

$[M_{HH}]$ Hub-hub global mass matrix

$[C_{HH}]$ Hub-hub global damping matrix

$[K_{HH}]$ Hub-hub global stiffness matrix

The same procedure is repeated for the wing element matrices to obtain the global wing matrices:

$[M_{WW}]$ Wing global mass matrix

$[C_{WW}]$ Wing global damping matrix

$[K_{WW}]$ Wing global stiffness matrix

248

The global blade displacement vector contains 9 x $(N_e + 1)$ displacements before application of boundary conditions, and may be written as:

$$\hat{q}_B = \{u_1 \; v_1 \; v_1' \; w_1 \; w_1' \; \phi_1 \; u_2 \; \phi_2 \; u_3 \; u_4 \; v_2 \; v_2' \; w_2 \; w_2' \; \phi_3$$

$$\ldots u_{(3N_e+1)} \; v_{(N_e+1)} \; v_{(N_e+1)}' \; w_{(N_e+1)} \; w_{(N_e+1)}' \; \phi_{(2N_e+1)}\} \qquad (7.15)$$

A similar global displacement vector is obtained for the wing $\hat{q}_W$, but the degrees of freedom correspond to the number of elements selected for the wing which may be different from the number of elements selected for the blade. The global hub displacement vector $\hat{x}_H$ is the same as the element displacement vector $\hat{x}_h$.

Application of the appropriate boundary conditions reduces the size of the displacement vector and the appropriate rows and columns of the system matrices are eliminated. For a hingeless rotor system, the blade is cantilevered at the root so all six kinematic variables associated with node $N_e + 1$ are assumed to be zero. As hinges are incorporated into the model, as for an articulated rotor system, the appropriate constraints are relaxed. The wing is assumed to be cantilevered at the root, so all six degrees of freedom there are constrained.

Following assembly, application of boundary conditions, and summation over N_b blades, the system equations may be written in matrix form as:

$$\begin{Bmatrix} (\delta \hat{q}_B)_1 \\ (\delta \hat{q}_B)_2 \\ \vdots \\ (\delta \hat{q}_B)_{N_b} \\ \delta \hat{x}_H \end{Bmatrix}^T \left(\begin{bmatrix} (M_{BB})_1 & 0 & \cdots & 0 & (M_{BH})_1 \\ 0 & (M_{BB})_2 & \cdots & 0 & (M_{BH})_2 \\ \vdots & \vdots & \ddots & \vdots & \vdots \\ 0 & 0 & \cdots & (M_{BB})_{N_b} & (M_{BH})_{N_b} \\ (M_{HB})_1 & (M_{HB})_2 & \cdots & (M_{HB})_{N_b} & M_{HH} \end{bmatrix} \begin{Bmatrix} (\hat{\ddot{q}}_B)_1 \\ (\hat{\ddot{q}}_B)_2 \\ \vdots \\ (\hat{\ddot{q}}_B)_{N_b} \\ \hat{\ddot{x}}_H \end{Bmatrix} \right.$$

249

$$+ \begin{bmatrix} (C_{BB})_1 & 0 & \cdots & 0 & (C_{BH})_1 \\ 0 & (C_{BB})_2 & \cdots & 0 & (C_{BH})_2 \\ \vdots & \vdots & \cdots & \vdots & \vdots \\ 0 & 0 & \cdots & (C_{BB})_{N_b} & (C_{BH})_{N_b} \\ (C_{HB})_1 & (C_{HB})_2 & \cdots & (C_{HB})_{N_b} & C_{HH} \end{bmatrix} \begin{Bmatrix} (\dot{\hat{q}}_B)_1 \\ (\dot{\hat{q}}_B)_2 \\ \vdots \\ (\dot{\hat{q}}_B)_{N_b} \\ \dot{\hat{x}}_H \end{Bmatrix}$$

$$+ \begin{bmatrix} (K_{BB})_1 & 0 & \cdots & 0 & (K_{BH})_1 \\ 0 & (K_{BB})_2 & \cdots & 0 & (K_{BH})_2 \\ \vdots & \vdots & \cdots & \vdots & \vdots \\ 0 & 0 & \cdots & (K_{BB})_{N_b} & (K_{BH})_{N_b} \\ (K_{HB})_1 & (K_{HB})_2 & \cdots & (K_{HB})_{N_b} & K_{HH} \end{bmatrix} \begin{Bmatrix} (\hat{q}_B)_1 \\ (\hat{q}_B)_2 \\ \vdots \\ (\hat{q}_B)_{N_b} \\ \hat{x}_H \end{Bmatrix}$$

$$= \begin{Bmatrix} (F_B)_1 \\ (F_B)_2 \\ \vdots \\ (F_B)_{N_b} \\ 0 \end{Bmatrix} \tag{7.16}$$

The nonlinear contributions to the force vectors are linearized using a Taylor Series expansion for each of the N_b blades:

$$F_B = \frac{\partial F_B}{\partial \hat{q}_B} \hat{q}_B + \frac{\partial F_B}{\partial \dot{\hat{q}}_B} \dot{\hat{q}}_B \tag{7.17}$$

and the system equations can then be expressed as:

$$\begin{bmatrix} M_{RR} & M_{RH} \\ M_{HR} & M_{HH} \end{bmatrix} \begin{Bmatrix} \ddot{\hat{q}}_R \\ \ddot{\hat{x}}_H \end{Bmatrix} + \begin{bmatrix} C_{RR} & C_{RH} \\ C_{HR} & C_{HH} \end{bmatrix} \begin{Bmatrix} \dot{\hat{q}}_R \\ \dot{\hat{x}}_H \end{Bmatrix}$$

$$+ \begin{bmatrix} K_{RR} & K_{RH} \\ K_{HR} & K_{HH} \end{bmatrix} \begin{Bmatrix} \hat{q}_R \\ \hat{x}_H \end{Bmatrix} = 0 \tag{7.18}$$

250

where

$$M_{RR} = \begin{bmatrix} (M_{BB})_1 & 0 & \cdots & 0 \\ 0 & (M_{BB})_2 & \cdots & 0 \\ \vdots & \vdots & \ddots & \vdots \\ 0 & 0 & \cdots & (M_{BB})_{N_b} \end{bmatrix} \tag{7.19}$$

$$C_{RR} = \begin{bmatrix} (C_{BB} - \frac{\partial F_B}{\partial \dot{q}_B})_1 & 0 & \cdots & 0 \\ 0 & (C_{BB} - \frac{\partial F_B}{\partial \dot{q}_B})_2 & \cdots & 0 \\ \vdots & \vdots & \ddots & \vdots \\ 0 & 0 & \cdots & (C_{BB} - \frac{\partial F_B}{\partial \dot{q}_B})_{N_b} \end{bmatrix} \tag{7.20}$$

$$K_{RR} = \begin{bmatrix} (K_{BB} - \frac{\partial F_B}{\partial q_B})_1 & 0 & \cdots & 0 \\ 0 & (K_{BB} - \frac{\partial F_B}{\partial q_B})_2 & \cdots & 0 \\ \vdots & \vdots & \ddots & \vdots \\ 0 & 0 & \cdots & (K_{BB} - \frac{\partial F_B}{\partial q_B})_{N_b} \end{bmatrix} \tag{7.21}$$

$$\dot{q}_R = \{(\hat{q}_B)_1^T \ (\hat{q}_B)_2^T \ \cdots \ (\hat{q}_B)_{N_b}^T\} \tag{7.22}$$

The wing system equations are not yet included in the system. The hub and rotor system equations given by Eqn. 7.18 are next transformed into normal mode space before the wing system equations are added in to complete the system.

7.1.3 Normal Mode Transformation

Due to the size of the finite element matrices associated with N_b elastic blades, the computational effort is reduced by transforming the blade equations into normal mode space. This typically reduces the number of degrees of freedom from about 40-100 to about 6-8 per blade. The normal mode transformation of the present formulation is exactly the same as for past UMARC formulations. Some of the details of this process are given in this section for completeness.

After a trimmed solution is obtained, the deformed blade mode shapes are calculated. These modes are obtained using an eigenanalysis on the blade structural

system using the mean deflected trim position over one rotor revolution, and therefore include blade couplings associated with the nonlinear structural terms. The resulting modes are then used to transform the rotor displacement vector into the modal space:

$$
\hat{q}_R = \left\{ \begin{array}{c} (\delta\hat{q}_B)_1 \\ (\delta\hat{q}_B)_2 \\ \vdots \\ (\delta\hat{q}_B)_{N_b} \end{array} \right\} = \begin{bmatrix} \Phi & & & \\ & \Phi & & \\ & & \ddots & \\ & & & \Phi \end{bmatrix} \hat{q}_R = \left\{ \begin{array}{c} (\delta\hat{p}_B)_1 \\ (\delta\hat{p}_B)_2 \\ \vdots \\ (\delta\hat{p}_B)_{N_b} \end{array} \right\} = [\Phi]\,\hat{p}_R \qquad (7.23)
$$

The blade-related matrices are then transformed into modal space as:

$$
\begin{bmatrix} \bar{M}_{RR} & \bar{M}_{RH} \\ \bar{M}_{HR} & M_{HH} \end{bmatrix} \left\{ \begin{array}{c} \ddot{\hat{p}}_R \\ \ddot{\hat{x}}_H \end{array} \right\} + \begin{bmatrix} \bar{C}_{RR} & \bar{C}_{RH} \\ \bar{C}_{HR} & C_{HH} \end{bmatrix} \left\{ \begin{array}{c} \dot{\hat{p}}_R \\ \dot{\hat{x}}_H \end{array} \right\}
$$

$$
+ \begin{bmatrix} \bar{K}_{RR} & \bar{K}_{RH} \\ \bar{K}_{HR} & K_{HH} \end{bmatrix} \left\{ \begin{array}{c} \hat{p}_R \\ \hat{x}_H \end{array} \right\} = 0 \qquad (7.24)
$$

where the transformations are given by:

$$
\bar{M}_{RR} = [\Phi]^T M_{RR} [\Phi] \qquad (7.25)
$$

$$
\bar{M}_{RH} = [\Phi]^T M_{RH} \qquad (7.26)
$$

$$
\bar{M}_{HR} = M_{HR} [\Phi] \qquad (7.27)
$$

$$
\bar{C}_{RR} = [\Phi]^T C_{RR} [\Phi] \qquad (7.28)
$$

$$
\bar{C}_{RH} = [\Phi]^T C_{RH} \qquad (7.29)
$$

$$
\bar{C}_{HR} = C_{HR} [\Phi] \qquad (7.30)
$$

$$
\bar{K}_{RR} = [\Phi]^T K_{RR} [\Phi] \qquad (7.31)
$$

$$
\bar{K}_{RH} = [\Phi]^T K_{RH} \qquad (7.32)
$$

$$
\bar{K}_{HR} = K_{HR} [\Phi] \qquad (7.33)
$$

7.1.4 Addition of the Wing Equations

Modal reduction of the blade-hub system equations does not affect the hub degrees of freedom as shown by Eqn. 7.24. The discrete wing degrees of freedom at the wing tip and six of the eight hub degrees of freedom are the same as discussed in Chapter 4. The relationship between the common wing and hub degrees of freedom is given by:

$$\text{Wing dof} \qquad \text{Hub dof}$$

$$u_1 \;=\; -y_h \tag{7.34}$$

$$v_1 \;=\; x_h \tag{7.35}$$

$$v_1' \;=\; \psi_h \tag{7.36}$$

$$w_1 \;=\; z_h \tag{7.37}$$

$$w_1' \;=\; -\phi_h \tag{7.38}$$

$$\phi_1 \;=\; -\alpha_h \tag{7.39}$$

where $u_1, v_1, v_1', w_1, w_1'$, and ϕ_1 represent the discrete degrees of freedom at the wing tip. Using a procedure analogous to the summation of the element matrices, the wing system matrices can be summed with the hub-related matrices to produce a new set of coupled hub-wing matrices. The procedure is represented mathematically as:

$$\bar{M}_{WW} \;=\; M_{HH} \oplus M_{WW} \tag{7.40}$$

$$\bar{C}_{WW} \;=\; C_{HH} \oplus C_{WW} \tag{7.41}$$

$$\bar{K}_{WW} \;=\; K_{HH} \oplus K_{WW} \tag{7.42}$$

$$\hat{x}_W \;=\; \left\{ \begin{array}{c} \beta_{GC} \\ \beta_{GS} \\ \hat{q}_W \end{array} \right\} \tag{7.43}$$

253

where $\oplus$ is used to indicate the procedure of adding finite element matrices with common global degrees of freedom. The new WW (with bar) matrices contain two more rows and columns than the old WW matrices, and these rows and columns correspond to β_{GC} and β_{GS} from the HH matrices. The rest of the HH matrices (which correspond to the remaining 6 hub degrees of freedom) are added into the first six rows and columns of the old WW matrix (which correspond to the wing tip degrees of freedom). Rows and/or columns of the HH matrices are first rearranged to align with the wing tip discrete degrees of freedom to facilitate the assembly process. The hub-blade and blade-hub matrices are modified as:

$$\bar{M}_{RH} \;\rightarrow\; \bar{M}_{RW} \tag{7.44}$$

$$\bar{M}_{HR} \;\rightarrow\; \bar{M}_{WR} \tag{7.45}$$

$$\bar{M}_{RH} \;\rightarrow\; \bar{M}_{RW} \tag{7.46}$$

$$\bar{M}_{HR} \;\rightarrow\; \bar{M}_{WR} \tag{7.47}$$

$$\bar{M}_{RH} \;\rightarrow\; \bar{M}_{RW} \tag{7.48}$$

$$\bar{M}_{HR} \;\rightarrow\; \bar{M}_{WR} \tag{7.49}$$

where $\rightarrow$ is used to indicate a transformation of rows, columns, and signs such that the hub-related matrices correspond to the wing matrices and are consistent with Eqns. 7.34-7.39. The new matrices are filled with rows and columns of zeros where there is no coupling between the rotor system and the wing degrees of freedom beyond those associated with the wing tip. The resulting coupled rotor-wing system equations are given by:

$$\begin{bmatrix} \bar{M}_{RR} & \bar{M}_{RW} \\ \bar{M}_{WR} & \bar{M}_{WW} \end{bmatrix} \left\{ \begin{array}{c} \mathring{p}_R \\ \mathring{x}_W \end{array} \right\} + \begin{bmatrix} \bar{C}_{RR} & \bar{C}_{RW} \\ \bar{C}_{WR} & \bar{C}_{WW} \end{bmatrix} \left\{ \begin{array}{c} \mathring{p}_R \\ \mathring{x}_W \end{array} \right\}$$
$$+ \begin{bmatrix} \bar{K}_{RR} & \bar{K}_{RW} \\ \bar{K}_{WR} & \bar{K}_{WW} \end{bmatrix} \left\{ \begin{array}{c} \hat{p}_R \\ \hat{x}_W \end{array} \right\} = 0 \tag{7.50}$$

7.1.5 Engine Drive Train Dynamics

The importance of modeling the tiltrotor engine drive train dynamics accurately in high-speed axial flight mode is discussed in Ref. 35. It is concluded in this reference that the dynamic behavior of a typical system with engine, transmission, and governor modeled is much like that of a windmilling rotor system, with some influence of the engine inertia and damping. The interconnect shaft is shown to have a significant influence on the antisymmetric tiltrotor dynamics, but these modes are not considered in the present formulation. Based on the results of Ref. 35, a windmilling rotor system is employed as the drive train model in the present formulation, and is used for stability analysis of the tiltrotor in axial flight.

For a windmilling rotor, a rotational degree of freedom about the shaft is introduced, and is unconstrained with respect to the wing. In axial flight, the hub degree of freedom ϕ_h corresponds to a rotation about the shaft, and is thus used to model the windmilling rotor system. The assembly process described in the above section is modified so that ϕ_h is not constrained to the corresponding wing tip motion. This is tantamount to replicating the wing-assembly procedure with 5 hub degrees of freedom instead of 6, where the hub degree of freedom ϕ_h no longer corresponds to the wing tip degree of freedom w'_1. The result is one additional global degree of freedom in the wing displacement vector:

$$
\hat{x}_W = \left\{ \begin{array}{c} \phi_h \\ \beta_{GC} \\ \beta_{GS} \\ \hat{q}_W \end{array} \right\} \tag{7.51}
$$

There is also one additional row and column in each of the WW system matrices, one additional column in the RW matrices, and one additional row in the WR system matrices of Eqn. 7.50.

A more advanced engine drive train model may now be obtained by including

255

the appropriate inertia, damping, and stiffness properties associated with ϕ_h. This model could itself have several degrees of freedom which are coupled to the rotor system, through ϕ_h, using an assembly process analogous to that used to couple the wing and rotor systems. Such a model is not considered in the present formulation.

7.2 Stability Analysis Procedure

The stability analysis procedure from this point on is unmodified from previous UMARC formulations except for the much larger size of the global system equations due to the elastic wing model. The system equations are next transformed into first order form for efficient stability eigenanalysis. Here, a system state vector Y is defined as:

$$\hat{Y} = \left\{ \begin{array}{c} \hat{\dot{p}}_R \\ \hat{\dot{x}}_W \\ \hat{p}_R \\ \hat{x}_W \end{array} \right\} \tag{7.52}$$

The system equations are then written in first order form as:

$$\begin{bmatrix} \bar{M}_{RR} & \bar{M}_{RW} & 0 & 0 \\ \bar{M}_{WR} & \bar{M}_{WW} & 0 & 0 \\ 0 & 0 & I & 0 \\ 0 & 0 & 0 & I \end{bmatrix} \hat{\dot{Y}}$$

$$+ \begin{bmatrix} \bar{C}_{RR} & \bar{C}_{RW} & \bar{K}_{RR} & \bar{K}_{RW} \\ \bar{C}_{WR} & \bar{C}_{WW} & \bar{K}_{WR} & \bar{K}_{WW} \\ I & 0 & 0 & 0 \\ 0 & I & 0 & 0 \end{bmatrix} \hat{Y} = 0 \tag{7.53}$$

256

Multiplication of Eqn. 7.53 by the matrix

$$
\begin{bmatrix}
\begin{bmatrix} \bar{M}_{RR} & \bar{M}_{RW} \\ \bar{M}_{WR} & \bar{M}_{WW} \end{bmatrix}^{-1} & \begin{bmatrix} 0 & 0 \\ 0 & 0 \end{bmatrix} \\[2em]
\begin{bmatrix} 0 & 0 \\ 0 & 0 \end{bmatrix} & \begin{bmatrix} I & 0 \\ 0 & I \end{bmatrix}
\end{bmatrix}
\tag{7.54}
$$

gives the desired first order form of the system equations as

$$
\dot{\hat{Y}} = [A(\psi, \hat{Y}_0)]\hat{Y}
\tag{7.55}
$$

The stability matrix $\hat{A}$ is shown to be a function of both the azimuth location ψ and the trim solution vector $\hat{Y}_0$. At this point the blade-related parts of the system equations are formulated in a rotating frame. Since the wing-related parts of the system equations are formulated in a fixed frame, it is advantageous to transform the blade-related parts also into a fixed frame.

7.2.1 Fixed Coordinate Transformation

The fixed coordinate transformation implemented in past UMARC formulations as well as the present formulation involves two steps: transformation of the blade-related rotating frame coordinates to fixed coordinates and transformation of the blade equations into fixed frame equations. The blade-related rotating frame coordinates are related to the fixed frame coordinates $\hat{\xi}$ as

$$
\hat{p}_R = [A_b]\hat{\xi}
\tag{7.56}
$$

where

$$
\hat{\xi} = \begin{Bmatrix} \xi^{(1)} \\ \xi^{(2)} \\ \vdots \\ \xi^{(m)} \end{Bmatrix}
\tag{7.57}
$$

and m is the number of modes used to represent the blade response. Each element in the above column vector represents another column vector of fixed frame coordinates for the kth modal displacement of the blade:

$$\xi^{(k)} = \left\{ \begin{array}{c} \xi_0 \\ \xi_{1c} \\ \xi_{2c} \\ \vdots \\ \xi_{ns} \\ \xi_{n/2} \end{array} \right\} \tag{7.58}$$

Each $\xi^{(k)}$ has length N_b so that the length of $\bar{\xi}$ is mN_b. The transformation matrix A_b is written as

$$[A_b] = \left[\begin{array}{cccc} a_b & 0 & \ldots & 0 \\ 0 & a_b & \ldots & 0 \\ 0 & 0 & \ddots & 0 \\ 0 & 0 & \ldots & a_b \end{array} \right] \tag{7.59}$$

where each column represents a blade mode considered for the stability analysis and

$$a_b = \left\{ \begin{array}{ll} \{1, \cos\psi_b, \ldots, \cos(n\psi_b), \sin\psi_b, \ldots, \sin(n\psi_b), (-1)^b\} & \text{if } N_b \text{ even} \\ \{1, \cos\psi_b, \ldots, \cos(n\psi_b), \sin\psi_b, \ldots, \sin(n\psi_b)\} & \text{if } N_b \text{ odd} \end{array} \right. \tag{7.60}$$

$$n = \left\{ \begin{array}{ll} \frac{N_b-2}{2} & \text{if } N_b \text{ even} \\ \frac{N_b-1}{2} & \text{if } N_b \text{ odd} \end{array} \right. \tag{7.61}$$

Because $[A_b]$ is a function of time, the derivatives of the modal displacement vectors are written as:

$$\hat{p} = \hat{A}_b \hat{\xi} + \hat{\dot{A}}_b \hat{\xi} = \hat{A}_b \hat{\dot{\xi}} + \hat{B}_b \hat{\xi} \tag{7.62}$$

$$\hat{\ddot{p}} = \hat{A}_b \hat{\ddot{\xi}} + 2\hat{\dot{A}}_b \hat{\dot{\xi}} + \hat{\ddot{A}}_b \hat{\xi}$$

$$= \hat{A}_b \hat{\ddot{\xi}} + 2\hat{B}_b \hat{\dot{\xi}} + \hat{C}_b \hat{\xi} \tag{7.63}$$

258

The blade equations (system equations which are coefficients of $\delta\hat{p}$) are then transformed into the fixed frame using the following operations:

$$\frac{1}{N_b} \sum_{m=1}^{N_b} (\text{Eqn}) \tag{7.64}$$

$$\frac{2}{N_b} \sum_{m=1}^{N_b} (\text{Eqn}) \cos(k\psi_m) \tag{7.65}$$

$$\frac{2}{N_b} \sum_{m=1}^{N_b} (\text{Eqn}) \sin(k\psi_m) \tag{7.66}$$

$$\frac{1}{N_b} \sum_{m=1}^{N_b} (\text{Eqn})(-1)^m \tag{7.67}$$

for each of the k blades.

After substitution of the fixed frame transformations given by Eqns. 7.62- 7.63 and the fixed frame equation transformations given by Eqns. 7.64-7.67, the system equations given by Eqn. 7.50 then become

$$\begin{bmatrix} \bar{M}_{R_fR_f} & \bar{M}_{R_fW} \\ \bar{M}_{WR_f} & \bar{M}_{WW} \end{bmatrix} \left\{ \begin{array}{c} \ddot{\hat{\xi}} \\ \ddot{\hat{x}}_W \end{array} \right\} + \begin{bmatrix} \bar{C}_{R_fR_f} & \bar{C}_{R_fW} \\ \bar{C}_{WR_f} & \bar{C}_{WW} \end{bmatrix} \left\{ \begin{array}{c} \dot{\hat{\xi}} \\ \dot{\hat{x}}_W \end{array} \right\}$$

$$+ \begin{bmatrix} \bar{K}_{R_fR_f} & \bar{K}_{R_fW} \\ \bar{K}_{WR_f} & \bar{K}_{WW} \end{bmatrix} \left\{ \begin{array}{c} \hat{\xi} \\ \hat{x}_W \end{array} \right\} = 0 \tag{7.68}$$

where the following definitions for the new fixed-frame blade-related matrices apply:

$$\bar{M}_{R_fR_f} = \frac{1}{N_b} \sum_{m=1}^{N_b} [H_b][\bar{M}_{RR}][A_b] \tag{7.69}$$

$$\bar{C}_{R_fR_f} = \frac{1}{N_b} \sum_{m=1}^{N_b} [H_b](2[\bar{M}_{RR}][B_b] + [\bar{C}_{RR}][A_b]) \tag{7.70}$$

$$\bar{K}_{R_fR_f} = \frac{1}{N_b} \sum_{m=1}^{N_b} [H_b]([\bar{M}_{RR}][C_b] + [\bar{C}_{RR}][B_b] + [\bar{K}_{RR}][A_b]) \tag{7.71}$$

$$\bar{M}_{R_fW} = \frac{1}{N_b} \sum_{m=1}^{N_b} [H_b][\bar{M}_{RW}] \tag{7.72}$$

$$\bar{C}_{R_fW} = \frac{1}{N_b} \sum_{m=1}^{N_b} [H_b][\bar{C}_{RW}] \tag{7.73}$$

$$\bar{K}_{R_fW} = \frac{1}{N_b} \sum_{m=1}^{N_b} [H_b][\bar{K}_{RW}] \qquad (7.74)$$

$$\bar{M}_{WR_f} = \frac{1}{N_b} \sum_{m=1}^{N_b} [\bar{M}_{WR}][A_b] \qquad (7.75)$$

$$\bar{C}_{WR_f} = \frac{1}{N_b} \sum_{m=1}^{N_b} (2[\bar{M}_{WR}][B_b] + [\bar{C}_{WR}][A_b]) \qquad (7.76)$$

$$\bar{K}_{WR_f} = \frac{1}{N_b} \sum_{m=1}^{N_b} ([\bar{M}_{WR}][C_b] + [\bar{C}_{WR}][B_b] + [\bar{K}_{WR}][A_b]) \qquad (7.77)$$

and

$$[H_b] = \begin{bmatrix} h_b & & \\ & \ddots & \\ & & h_b \end{bmatrix} \qquad (7.78)$$

which is a mN_b x m matrix where m is the number of modes and

$$h_b = \begin{Bmatrix} 1 \\ 2\cos(\psi_b) \\ 2\cos(2\psi_b) \\ \vdots \\ 2\cos(n\psi_b) \\ 2\sin(\psi_b) \\ 2\sin(2\psi_b) \\ \vdots \\ 2\sin(n\psi_b) \\ (-1)^b \end{Bmatrix} \qquad (7.79)$$

which has length N_b. This system of equations may also be converted to first order form using the procedure described in the previous section. The resulting system is then written in first order form as

$$\dot{\hat{Y}}_f = [A_f(\psi)]\hat{Y}_f \qquad (7.80)$$

where $[A_f(\psi)]$ is the fixed-frame stability matrix and $\hat{Y}_f$ is the fixed-frame vector

260

of state variables:

$$\hat{Y}_f = \left\{ \begin{array}{c} \hat{\xi} \\ \hat{x}_W \\ \hat{\xi} \\ \hat{x}_W \end{array} \right\}$$ (7.81)

If the rotor system is aligned for axial or hover flight, then the matrix $[A_f]$ is not a function of ψ, and Eqn. 7.80 may be solved using standard eigenvalue analysis techniques. Solution gives the damping and frequencies of the rotor and wing modes associated with the system. If the tiltrotor is in conversion mode or helicopter forward flight mode then the matrix $[A_f]$ *is* a function of ψ, and steps must be taken to account for the periodicity of the system before a solution may be obtained.

7.2.2 Floquet Theory

The linearized first order system given by Eqn. 7.80 may contain periodic terms because of the azimuthal change in aerodynamic forces associated with forward flight and/or application of cyclic pitch controls. Stability characteristics of a linear periodic system may be determined using Floquet theory. Formulations of Floquet theory for finite element based stability analysis are presented in Refs. 67 and 88, and these derivations represent the formulations used in the current analysis. Details of the basic relations developed in these formulations are presented in Ref. 79, and an outline of the procedure is presented in this section.

The system of equations including wing motion is placed in first order form as

$$\hat{Y} = [A]\hat{Y}$$ (7.82)

The solution to this system must be expressible as a linear combination of the state variables at time ψ_0 such that

$$\hat{Y}(\psi) = [\Phi(\psi, \psi_0)]\hat{Y}(\psi_0)$$ (7.83)

where the Φ matrix is known as the state transition matrix, and by definition:

$$[\Phi(\psi_0, \psi_0)] = [I] \tag{7.84}$$

Substitution of Eqn. 7.82 into Eqn. 7.83 gives

$$[\dot{\Phi}] = [A][\Phi] \tag{7.85}$$

The rotorcraft equations are periodic with a period of 2π so that

$$[A(\psi + 2\pi)] = [A(\psi)] \tag{7.86}$$

and the transition matrix may be expressed as

$$[\Phi(\psi, \psi_0)] = [P(\psi)]e^{[B(\psi - \psi_0)]} \tag{7.87}$$

where $[P]$ is a periodic matrix of period 2π and $[P(\psi_0)] = [I]$. The exponential decay or growth of the system solution is shown to depend only on the matrix $[B]$. The discrete Floquet transition matrix is defined as:

$$[Q] = [\Phi(\psi_0 + 2\pi, \psi_0)] \tag{7.88}$$

which may be written as

$$[Q] = e^{2\pi[B]} \tag{7.89}$$

Let $[\Lambda]$ be the eigenvalue matrix (Jordan form) of $[B]$, and $[S]$ be the corresponding modal matrix. Then $[B] = [S][\Lambda][S]^{-1}$ and

$$[Q] = e^{2\pi[B]} = [S]e^{2\pi[\Lambda]}[S]^{-1} \tag{7.90}$$

Thus, $[S]$ is also the modal matrix of $[Q]$, and the eigenvalue matrix associated with the Floquet transition matrix is

$$[\Theta] = e^{2\pi[\Lambda]} \tag{7.91}$$

or

$$[\Lambda] = \frac{1}{2\pi}\ln[\Theta] \tag{7.92}$$

262

The system is unstable if the real part of any eigenvalue is greater then zero $(Re(\Lambda_i) > 0)$.

The Floquet transition matrix Q can be computed by integrating Eqn. 7.85 over one rotor revolution starting with the initial conditions given by Eqn. 7.84.

The eigenvalues of $[B]$ determine the system stability, but these eigenvalues are shown to be the same as the eigenvalues of the Floquet transition matrix $[Q]$:

$$\theta_k = Re(\theta_k) + iIm(\theta_k) = e^{2\pi(\alpha_k + i\omega_k)} \qquad (7.93)$$

The Floquet stability eigenvalues are thus given by the kth eigenvalue of $[Q]$ as

$$\alpha_k = \frac{1}{2\pi}\ln\sqrt{Re^2(\theta_k) + Im^2(\theta_k)} \qquad (7.94)$$

$$\omega_k = \frac{1}{2\pi}\tan^{-1}\left(\frac{Im(\theta_k)}{Re(\theta_k)}\right) \pm n\Omega; n = 0, 1, 2, \ldots \qquad (7.95)$$

where α_k and ω_k are the decay rate and Floquet frequency of the kth mode, respectively. The frequency is shown to be multivalued; the sum of a principle part and an integer multiple of the rotor rotational velocity. Determination of the frequency value which corresponds to the physical system requires additional effort. One approach is to use results of a constant coefficient approximation (discussed in next section) to determine this frequency.

It should be noted that the stability of a tiltrotor system must be assessed in a fixed frame because of the large influence of the wing motion on the rotor system. Application of the Floquet theory in the fixed frame increases the size of the transition matrix by a factor of N_b^2 since all blades must be considered simultaneously.

7.2.3 Constant Coefficient Approximation

Much of the derivations presented in this research has assumed that the system modeled is moderately nonlinear. This assumption reduces the size and complexity

of the system equations, and allows the basic qualities of the nonlinear system to be captured in the linear solution. In an analogous manner, it may be assumed that in certain flight modes that the system is periodic, but not highly periodic. The basic qualities of the periodicity may then be captured by averaging the system stability matrix over one rotor revolution, and the resulting system is greatly simplified as the stability matrix becomes a matrix of constant terms only. The constant coefficient approximation to the stability matrix is given by:

$$[A_{fc}] = \frac{1}{2\pi} \int_0^{2\pi} [A_f] \, d\psi \qquad (7.96)$$

and the new system of equations given by

$$\dot{\hat{Y}} = [A_{fc}] \, \hat{Y} \qquad (7.97)$$

may be solved using standard eigenvalue analysis.

The constant coefficient approximation generally gives an accurate representation of the system stability of helicopters for advance ratios under 0.3. For tiltrotor application, the constant coefficient approximation should be accurate over most of the flight envelope because conversion to an axial flight mode occurs at advance ratios less than 0.3. Once in axial flight, the periodicity disappears due to the symmetry of the rotor with respect to the oncoming flow.

The advantage of the constant coefficient approximation compared to Floquet theory is more than mere computational efficiency. The nature of Floquet theory is such that the frequencies of the Floquet eigenvalues do not represent the physical frequencies of the system modes. It is, therefore, very difficult to identify the mode which is associated with the damping part of the eigenvalue. The constant coefficient approximation aids in this process (even in flight modes where the approximation is poor) since the frequencies do match the frequencies of the physical system.

Chapter 8

Results and Discussion

This chapter addresses results obtained using the elastic-blade tiltrotor analysis as developed in Chapters 4 - 7. This chapter can de divided into three major sections. The first section presents correlations of the present analysis with results from flight tests and other analyses as reported in the open literature. Correlation efforts include controls, performance predictions in hover and cruise flights, frequency and damping predictions of wing and rotor modes in airplane mode, and vibratory bending moments in conversion mode. The second section presents an investigation of bending-twist-coupled rotor blades designed to expand the tiltrotor whirl flutter boundaries. Here, the adverse pitch-lag dynamics associated with rotor precone are shown to be negated by the elastic bending-twist-coupled rotor blade, thereby improving tiltrotor stability. The third section presents an investigation of extension-twist-coupled rotor blades designed to improve the aerodynamic performance of tiltrotors in hover and cruise flight modes. Here, large amounts of elastic twist are used to obtain an improved twist distribution for the hover flight mode while maintaining an optimum twist distribution in cruise mode. The elastic twist in hover is different from cruise because of the variation in rotor speeds between the helicopter and airplane flight modes.

8.1 Baseline Design

The rotor and wing configuration used for validation of the present analysis, and as a baseline for performance and stability comparisons of elastically-coupled blade designs, is the Bell-designed, full-scale, gimballed, stiff-inplane model as tested in the NASA Ames 40- by 80-Foot Wind Tunnel [31]. Much of the data needed to describe this system are reported in Chapter 2, Tables 2.1-2.3. Additional plots describing the blade twist, elastic axis offsets, mass, and stiffness distributions are shown in Figs. 8.1 - 8.6. This series of plots indicate, by a darkened symbol, the values input for the endpoints of each of the five beam elements used to model the blade. Linear interpolation was used to obtain the value of each parameter at the six gauss points (used for numerical integration within each of the beam elements) so it is appropriate to connect each darkened symbol with a straight line. It should be noted that the data shown in these plots are an approximation of the distributions illustrated in reference 31, conformed to the spanwise node point locations of the present model. The baseline rotor system also has positive pitch-flap coupling with δ_3 = -22.5° and a rotor precone of 2.5°. Plots illustrating the wing elastic axis offsets, mass, and stiffness distributions are shown in Figs. 8.7 - 8.9. Linear interpolation is not used for the wing because there is little variation of the spanwise properties, so the parameter values in these plots are shown to be constant within each beam element.

8.2 Validation

The objective of this section is to build confidence in the present elastic-blade tiltrotor analysis by showing an acceptable level of agreement with other analyses as well as experimental results. The capabilities of the present tiltrotor analysis extends to all free-flight modes of operation for performance and loads calculations,

but only to a coupled cantilevered wing and rotor system for stability calculations. The correlation efforts of the present section will address all of these predictive capabilities. An important note for this section is that the definition of the pylon angle is changed to be consistant with past definitions. Here, the pylon angle at zero degrees designates airplane mode while the pylon angle at 90 degrees designates helicopter mode. Recall that the original formulation uses an opposite definition for the pylon angle to be consistant with the helicopter definition of rotor shaft tilt.

8.2.1 Blade Frequencies

The bending frequencies and mode shapes of the baseline elastic rotor blade trimmed at $V/\Omega R = 0.7$ are shown in Fig. 8.10. The left side of the figure shows the results reported in reference 31 while the right side shows the results obtained with the present analysis. As shown, the rotor system trims to about the same θ_{75} in each analysis (1.3% difference), and the frequencies of the first three predominantly-bending modes are in good agreement. The analysis of reference 31 considers only uncoupled torsion, so there is no torsion participation in the bending mode shapes (shown on the right side of the figure) which is not the case with the present analysis.

The analysis of reference 31 considers a rigid pitch motion uncoupled from the elastic torsion modes, and the elastic torsion motion is uncoupled from the blade bending motion as well. A rigid-body torsion mode may be created in the present analysis by using a torsion spring at the blade root. However, the elastic torsional stiffness of the beam elements must be much greater than the torsion spring or else the rigid-body motion will disappear and couple with the first-elastic mode. As shown in Fig. 8.11, the frequency of the rigid pitch and first elastic modes are very close, so they will not both exist in the present torsionally-coupled analysis or in

267

C-4

the physical system. The rigid-body motion is not considered in the baseline model of the present analysis because this mode cannot in reality be decoupled from the elastic motion. Further, an objective of this chapter is to investigate potential use of elastic blade couplings (bending-twist, extension-twist) which requires an accurate model of the blade torsional stiffness. It is, therefore, undesirable to define a baseline design with a rigid body torsion mode that can only be simulated by use of torsionally-stiff outboard beam elements. The baseline design for the present analysis will be based on the the torsion properties defined in reference 31 which produces the torsion mode shape and frequency shown on the right side of Fig. 8.11. The elastic predominantly-torsion mode shapes and frequencies are in good agreement between the two analyses.

Predicited variations in the first three elastic blade frequencies with velocity (airplane-mode) are shown in Fig. 8.12 for both the the present analysis and the analysis of reference 31. The bending stiffnesses are highly influenced by the forward flight velocity because large increases in the collective setting are required as the speed increases, and this tends to place more of the stiffer chord bending stiffness of the blade in the flap direction and tends to place more of the softer flap bending stiffness of the blade in the lag direction. Thus, the first mode, which is predominantly inplane, is shown to decrease in frequency as velocity increases, and the second mode, which is predominantly a flap mode, is shown to increase in frequency as velocity increases. The agreement in predictions between the two analyses is shown to be good, with the higher modes in closer agreement than the lower mode. The first bending modes are sensitive to the stiffness distributions at the root end of the blade, but the stiffnesses of the baseline design varies drastically at the root, so some discrepancy in modeling between the two analyses is understandable.

8.2.2 Stability in High-Speed Axial Flight

The discussion to this point has shown that the structural modeling of the tiltrotor system in the present analysis is accurate. There is also an indication that the basic aerodynamic modeling is satisfactory because of the agreement in collective position (θ_{75}) at the design cruise velocity. With these correlations, the dynamic system stability in cruise flight with the elastic wing included is now compared.

The dynamics of the baseline wing and rotor system are illustrated in Fig. 8.13 which is a root locus plot comparing the results presented in reference 31 to those of the present analysis. The range of velocity sweep in this plot is from 0 to 400 knots. The two flap modes $\beta+1$ and $\beta-1$ are the fixed-system eigenvalues for the gimbal flap motion while the β flap mode is the elastic coning motion. The fixed-frame elastic flap modes are not shown since comparable results are not available from reference 31. Modes with frequencies greater than 3/rev are also not shown. The root locus plot shows good agreement for both the frequency and damping of the modes, and similar movement as a result of the velocity sweep. The largest discrepancy between the two analyses is that the low frequency lag mode $(\zeta-1)$ in the present analysis couples strongly at low velocity with the wing beam mode as those frequencies cross. This does not occur with the analysis of reference 31. A closer examination of damping in the wing modes is shown in Figs. 8.14 and 8.15. The plot of Fig. 8.14 shows predictions of the wing beam mode damping ratio as a function of velocity (airplane mode), and includes full-scale experimental results as reported in reference 31. Whirl flutter is predicted to occur at about 305 knots by the analysis of reference 31, and at about 285 knots by the present analysis (about 7 percent difference). The damping ratio predictions are not in good agreement over the entire velocity sweep because the damping ratio of the present analysis has a spike which occurs when the $\zeta-1$ mode couples with the wing beam mode. This transfer of damping from the rotor lag motion to the wing beam mode when

the frequencies of those modes cross agrees with results discussed previously in Chapter 2. The wing beam mode damping ratio predictions of both analyses agree satisfactorily with the experimental data. Damping of the wing chord and pitch modes is shown as a function of velocity in Fig. 8.15. The damping predictions are shown to agree well near the velocities at which these modes become unstable.

Further validation of the present analysis is offered by observing predictive changes resulting from rotor parameter variations. An important parameter in tiltrotor dynamics, which will be discussed in more detail in the following sections of this chapter, is the rotor precone. As the rotor precone is lowered, the wing beam bending mode damping is observed in Fig. 8.16 to increase at higher velocities (expanding the flutter envelope). This trend is predicted by both of the analyses. Variation of the blade torsional frequency also has a significant effect on tiltrotor dynamics. The predicted trends for damping of the wing-beam mode with increase in blade torsional frequency are shown in Fig. 8.17. Similar trends are observed between predictions of the two analyses, but differences in the flutter velocity grow with increases in the blade torsional stiffness. These differences are attributable to the difference in modeling of the negative pitch-lag coupling associated with rotor precone. In the analysis of reference 31, the pitch-lag coupling is estimated from basic uncoupled-torsion dynamics and is modeled as a kinematic feedback parameter while, in the present analysis, the pitch-lag coupling is a natural occurance of the elastic blade dynamics.

Because the torsional dynamics do have a significant effect on the wing damping, it is also necessary to investigate the effects of the torsional modes which differ for the two baseline designs. Recall from previous discussion that the rigid body mode used in the analysis of reference 31 must be omitted in the present analysis in favor of an accurate modeling of the first elastic torsion blade mode. The rigid-body mode can be simulated in the present analysis with a torsion spring

and torsionally-stiff outboard beam sections. The difference in wing beam mode damping associated with each torsion model, the rigid-pitch mode at 4.8/rev and the first-elastic torsion mode at 5.7/rev, are shown in Fig. 8.18. The flutter velocity associated with the rigid torsion case is shown to be about 5 percent lower than that associated with the 1st elastic mode case.

8.2.3 Stability in Helicopter, Conversion, and Airplane Modes

The capabilities of the present analysis are assessed in helicopter, conversion, and airplane modes using a cantilevered elastic wing and elastic blade rotor model. Some additional input parameters for this model are illustrated in Fig. 8.19 which were reported in reference 31.

The conversion corridor extends from aircraft velocities of about 90 knots to about 170 knots. Up to 90 knots, the wing is near stall and the rotors provide the necessary lift forces. The pylon orientation is at or near 90 degrees until the lower conversion bounds is reached. The pylon then begins to rotate over, reaching zero degrees by the time the aircraft reaches about 140 knots. Rotor rotation rate is held constant during this period. Once the pylon is fully converted, the rotor rotation speed is then dropped for high-speed cruise flight, which is generally 15 to 20 percent less then the hover rotor speed. There is a significant drop in the rotor disc loading (C_T/σ) in moving from hover into airplane flight which has a significant impact on the tiltrotor pitch dynamics as will be discussed later in this chapter. The rotor model of the present analysis was trimmed to the disc loading illustrated in Fig. 8.19 at several velocities. The rotor speed and pylon angles, also illustrated in the figure, were input for each velocity point as well. Notice the abrupt change in rotor rotation rate from 563 rpm in helicopter mode to 458 rpm in cruise mode over a velocity range of about 20 knots. This change represents a rotor speed ratio of

271

1.23 used in helicopter mode because the nondimensional input parameters for the present rotor model were based on the cruise rotor speed. The trimmed collective, as calculated by the present analysis and as reported in reference 31, are illustrated as a function of velocity in Fig. 8.20, and the associated damping of the wing modes are illustrated in Fig. 8.21. The data reported in reference 31 for these two plots are based on a constant rotor speed (no rotor speed perturbation degree-of-freedom) and no blade torsion degree-of-freedom. These assumptions have an influence on the results, so the validity of comparing these particular results with the present analysis calculations are suspect. However, as these are the only such results available in helicopter and conversion mode operation for this tiltrotor model, the comparison is attempted. The trimmed-collective settings shown in Fig. 8.20 are similar, with the present analysis generally predicting about 2° to 5° higher collective. The higher collective predicted by the present analysis is attributed to the torsional flexibility of that model. The wing modes damping trends shown in Fig. 8.21 also show agreement considering the difference in analytical assumptions used in obtaining these results.

8.2.4   Performance

The plots of Figs. 8.22 and 8.23 compare the performance predictions of the present analysis to results of full-scale XV-15 flight tests for hover and cruise flights, respectively. This comparison is valid because of the similarity of the present analysis rotor model to the XV-15 rotor system. The test data are taken from reference 90. The hover measurements are for an isolated XV-15 rotor system (no wing/body interference effect). The present analysis is shown in Fig. 8.22 to agree well with the test data for the hover figure of merit. Maximum error is about 4 percent which is less than the variation of the test data. A Gessow-Meyers [91] inflow distribution was used for the hover analysis. One might note that the figure of merit is generally

272

much higher for a tiltrotor aircraft than for a conventional rotorcraft because of the high disc loading for a tiltrotor. Thus, the profile power is a smaller percentage of the total power required to hover, so the tiltrotor hover efficiency is less sensitive to airfoil drag characteristics than conventional helicopters. Based on the gross design weight of the XV-15, the C_T/σ is .1145 at sea level. The predictions for cruise propeller efficiency, shown in Fig. 8.23, also agree well with the test results at low disc loadings, but the analysis slightly under-predicts the efficiency at high disc loadings. The flight test data also reflect the large changes in velocity required to achieve the various disc loadings. The predictions differ from the experimental results by at most 8 percent which is also about the range in variation of the test data. A typical operating point for the XV-15 is at $C_T/\sigma = .05$ [90].

8.2.5 Free-Flight Trim and Blade Loads

The final part of the validation section addresses capability of the analysis to predict free-flight trim conditions and blade loads. As mentioned previously, the present analysis does not yet have the capability of assessing stability for free-flight because the fuselage degrees of freedom are not yet included in the stability analysis. Additional parameters required to develop the free-flight model are given in reference 13, and are listed in nondimensional form in table 8.1. The trim values obtained with the present analysis are illustrated in Fig. 8.24. Here, the tiltrotor in helicopter mode is shown to have a forward (nose-down) tilt of the fuselage and forward tilt of the tip path plane (indicated by cyclic pitch θ_{1s}). Each of these tilts increases with velocity to increase thrust in the forward-flight direction. The collective pitch remains about the same because the wing loading decreases the rotor thrust requirement about the same amount that the forward tilt increases the rotor thrust requirement. As forward flight velocity continues to increase, the pylon angle is lowered which greatly decreases the tilt of the fuselage and tip-path

plane. The collective angle also decreases because of the increased flow through the rotor with the increased shaft tilt. As the inflow continues to increase, the collective trend eventually reverses as larger collectives are required to maintain a positive blade angle of attack on top of the larger inflow angles. This is true in spite of the decreased thrust requirements from the rotor as the aircraft begins to enter airplane flight mode. The horizontal tail controls of the aircraft become dominant in maintaining pitch moment equilibrium, so cyclic is no longer required to produce nose-down moment. However, the cyclic pitch in conversion mode must increase with velocity because of the large edgewise flow through the rotor system. Without cyclic control here, a large fuselage-pitch-up moment would be created by the rotor system. As the pylon angle approaches zero degrees (airplane mode), the cyclic pitch quickly falls to zero while the collective continues to increase with the inflow. The fuselage pitch angle is shown to fall to about zero degrees as the 3 degrees of wing incidence provides adequate lift in high speed flight. While the control sequence described above seems plausible, no controls data from flight tests could be found for comparison. The data shown previously in Fig. 8.20 for the collective angle of a cantilevered wing and rotor system is closely related to the collective trim controls of the free-flight analysis shown in Fig. 8.24.

Blade loads associated with the above trim conditions are illustrated in Fig. 8.25, and are compared with flight test data of the XV-15 reported in reference 90. The test data were obtained at $r/R = 0.35$ while the analysis shows calculations at $r/R = .40$ because of modeling considerations. The trend of increasing vibratory blade bending moment with velocity for helicopter and conversion modes are predicted by the present analysis. The actual values agree well for part of the lower end of the velocity range considered at each pylon angle, but in general the analytical bending moments increase at a faster rate than the experimental results. This rate is decreased for the 30° pylon angle because the rotor speed decreases

274

from 563 rpm to 458 rpm over the velocity range considered. In airplane mode
(0° pylon angle) the vibratory loads are much smaller because there is little or
no edgewise flow and cyclic controls are nearly zero. The predicted vibratory mo-
ments therefore approach zero. The larger flight test moments for this mode are
attributed to nonuniform airflow about the rotor azimuth such as may be caused by
wing/fuselage interference, gusts, or a non-straight-and-level flight path. It should
be noted that some of the analytical beam-bending results shown in Fig. 8.25 are
sensitive to the selection of the horizontal-tail incidence angle which may vary from
0 to 6 degrees. This angle was not precisely known for any particular flight condi-
tion. The curves associated with the conversion angles can be shifted by about 5
knots in either direction based on selection of the horizontal-tail incidence angle.

8.2.6   Summary of Validation Results

The results of the validation section show that the present analysis is reasonably
accurate in predictions of loads, performance, and stability for an elastic-blade,
gimballed, baseline tiltrotor. Important effects related to the elasticity of the blade,
such as the precone/torsional-stiffness influence were also shown to be accurately
predicted. Results from Chapter 3 showed that the elastic rotating beam model
was accurate in predictions of frequencies for elastically-coupled rotor blades. Com-
bining the results of the present chapter with those of Chapter 3, it is reasonable
to assume that the present analysis will accurately predict loads, performance, and
stability of tiltrotors with elastically-coupled rotor blades.

8.3   Bending-Twist-Coupled Rotor Blade

The present section focuses on means for increasing the velocity at which tiltrotor
whirl flutter occurs in high-speed airplane-mode flight. Many of the parameters

which influence whirl flutter were examined in Chapter 2. This chapter did not, however, consider the elasticity of the rotor blade which has been shown to greatly influence tiltrotor stability characteristics. Important blade parameters which affect stability are the rotor precone and blade torsional stiffness. The potential for using a bending-twist-coupled rotor blade to offset the adverse precone effect is examined in the present section.

8.3.1 Precone Effect

The baseline cantilevered wing and rotor system instability was shown in the previous section to be defined by the wing-beam-bending-mode damping. Instability of this mode is shown in Fig. 8.16 to occur at higher velocities (expanding the flutter envelope) as the rotor precone is lowered. Similarly, the instability of this mode is shown in Fig. 8.17 to occur at higher velocities as the blade torsional stiffness is increased. The cause of these trends is the coupling of the elastic blade lag and pitch motions due to the rotor precone. This adverse effect is clearly explained in reference 31, but must to some extent be repeated here for completeness.

Consider the rotor system in hover. Here the rotor disc loading is high, so to offset large blade bending moments, rotor precone is introduced. As shown in Fig. 8.26a, the precone gives a component of centrifugal force which opposes the lift force. With ideal precone these forces balance, and there is no net bending moment imposed on the rotor blade (at least for some desired spanwise location on the blade). Now, consider the rotor system in airplane cruise. The disc loading is shown in Fig. 8.19 to decrease by an order of magnitude compared to the hover value. The centrifugal force component perpendicular to the blade also decreases because of the lowered rotor speed in cruise, but only by about 66 percent ($\frac{1}{1.23^2}$). Thus, in cruise there is a significant imbalance of centrifugal force tending to bend the rotor blade back (flap down). This imbalance creates a torsion moment about

the blade inboard sections proportional to the lag bending deflection as illustrated in Fig. 8.26b.

Now consider the static torsion balance of the rotor blade. The net flap moment due to aerodynamic and centrifugal forces has a torsional component proportional to lag which must be balanced by the blade torsional stiffness:

$$M_\beta \eta + I_\theta \omega_\theta^2 \theta = 0 \qquad (8.1)$$

where M_β is the net bending moment nondimensionalized by $I_\beta \Omega^2$, η is the lag deflection nondimensionalized by R, I_θ is the torsional inertia nondimensionalized by I_β, ω_θ is the torsional frequency nondimensionalized by Ω, and θ is the local torsional deflection. If the blade is considered to be semi-rigid such that the lag and torsional deflections occur at the root of the blade, then an effective kinematic pitch-lag coupling term can be defined as

$$K_{P_\eta} = -\frac{\theta}{\eta} = \frac{M_\beta}{I_\theta \omega_\theta^2} \qquad (8.2)$$

where $K_{P_\eta} > 0$ gives lag-back/pitch-down coupling. The flap moment at the blade root is given by

$$M_\beta = \gamma \int \frac{L}{ac} r\,dr - \beta_p - \beta_{trim} \qquad (8.3)$$

where L is the blade lift at a given spanwise position, β_p is the precone angle, and β_{trim} is the elastic coning angle. In hover, the precone is selected to balance the lift so M_β is small and K_{P_η} is small. In cruise, the precone term dominates so the kinematic pitch-lag coupling can be estimated by:

$$K_{P_\eta} = \frac{\beta_p}{I_\theta \omega_\theta^2} \qquad (8.4)$$

Therefore, the precone and torsional stiffness determine the pitch-lag coupling, and this coupling happens to have a significant effect on tiltrotor stability in high-speed flight. The effective kinematic coupling of the baseline system is estimated in reference 31 to be -0.3 which is considered a high value.

277

In the present analysis, there is no need to estimate kinematic pitch-lag coupling. The equations of motion derived in Chapter 4 include the precone effect naturally as part of the elasticity of the rotating beam.

8.3.2 Positive Pitch-Lag Coupling

From the discussion of the previous section, it seems rather obvious that if positive pitch-lag coupling were introduced into the rotor system to offset the negative pitch-lag coupling introduced by rotor precone, then the stability characteristics would improve. There are two methods which may readily be used to introduce positive pitch-lag coupling (lag-back/pitch-down): kinematic coupling in the control system and elastic bending-twist coupling in the rotor blade.

Certain aspects of kinematic coupling in the control system may limit use of this approach, at least for stiff-inplane rotor systems such as the baseline gimballed rotor system. The virtual lag hinge of stiff-inplane rotor systems can be well removed from the control attachment point (pitch bearing location) of the blade such that the lag deflection experienced at the control system is very small. This may be a problem with tiltrotors since the blades are short and stiff to begin with. With lag deflections at the control system small compared to outboard lag deflections, the control system pitch-lag coupling will not be able to compete with the precone effect. The elastic lag deflection of the baseline rotor blade is shown in airplane mode at the normal cruise velocity in Fig. 8.27. It is shown that the lag deflection anywhere inboard of 30 percent is an order of magnitude less than the deflection at the tip, and the virtual lag hinge is at about 40 percent. Thus, the lag deflection associated with the control system (located at about 10 percent) is much smaller than the lag deflection associated with the precone effect (a summation of lag deflections along the blade span). Another adverse aspect of using the control system to create positive pitch-lag coupling is the constraints on

278

control system parameters for rotor flapping and handling qualities. The manner in which the control system is used to obtain kinematic pitch-lag coupling is to alter the pitch horn cant angle, pitch link cant angle, pitch bearing spanwise location, pitch horn length, or radial location of the pitch horn to pitch link attachment point so that elastic lag motion will create blade pitch. The geometry of these parameters is illustrated in Fig. 8.28. The problem associated with changes in the control system is that these parameters also control the pitch-flap coupling of the rotor system which is generally set to constrain rotor flap motion. Handling qualities will also be influenced by the control system changes which introduces additional constraints on the amount of pitch-lag kinematic coupling which may be obtained for the system.

The addition of pitch-lag coupling through design of a bending-twist-coupled rotor blade has some advantages as well as disadvantages as compared to the control system approach. The disadvantage is that an entirely new rotor blade must be designed which may have different frequencies compared to the baseline design, and the blade design must incorporate anisotropic layups of composite materials for which there is relatively little experience in usage at a production level. Because of the large built-in twist of tiltrotor blades, it is not possible to decouple structural lag-bending-twist and flap-bending-twist, so both pitch-lag and pitch-flap couplings exist simultaneously. For gimballed systems, this is not a problem because the fundamental flap mode is the gimbal-flapping mode which is unaffected by the elasticity of the blade. Thus, an advantage of the bending-twist-coupled rotor blade is that gimbal flapping is uncoupled from the pitch-lag coupling which is not the case for the control system approach. Another advantage of the bending-twist-coupled blade approach is that the pitch-lag coupling is proportional to the local lag deflection rather than the lag deflection at one particular inboard section. The amount of positive pitch-lag coupling which can be created should

279

therefore be on the order of that associated with the precone effect.

The basic concept of a bending-twist-coupled rotor blade used in tiltrotor cruise mode is illustrated in Fig. 8.29. An untwisted blade is used in the diagram to clarify the deformations. The collective pitch in tiltrotor cruise $(V/\Omega R)$ is about 46° at the 75 percent spanwise station. At the 40 percent location of the virtual lag hinge, the pitch angle due to blade twist is 11° higher, so for purposes of illustrating the bending-twist-coupled rotor blade on an untwisted blade, the blade chord is rotated to 57° with respect to the plane of rotation. Now, define flatwise bending as bending of the rotor blade in a plane perpendicular to the chord. On conventional helicopters this is referred to as flapwise bending (bending perpendicular to the plane of rotation). For the present configuration it is seen that flatwise bending has a larger inplane (in the plane of rotation) component than out-of plane (flapwise) component. Therefore, to create pitch-lag coupling in the rotor system, the blade should be flatwise-bending-twist coupled. Chordwise-bending-twist coupling can also contribute, but as velocity and, therefore, collective increase, this elastic coupling would have a diminishing effect on pitch-lag coupling.

The manner in which flatwise-bending-twist coupling may be introduced into a rotor blade is addressed next. An anisotropic layup of off-axis composite plies in the primary structure of the blade is one of the most effective ways to create this type of elastic coupling. A simple truss analogy is shown in Fig. 8.30 to help explain exactly why bending-twist coupling is created with off-axis composite plies. As shown, a rotor blade section is assumed to be composed of a composite laminate rotated off-axis in the same direction on both the upper and lower surfaces. at a particular section of the blade undergoing flap-down bending, the bending moment can be translated into a force-couple such that the upper surface has a tension force and the lower surface has a compressive force. Looking only at the upper surface, the composite material may be modeled as a simple truss with two crossing rod

members. One rod is extensionally-stiff and represents the fiber direction, and the other rod is extensionally flexible and represents the matrix direction. A tension force on this model can be seen to not only extend the truss, but also to shear it in the direction of the flexible rod member. The shear strains are consistent along the entire upper surface of the airfoil, creating a shear flow which tends to twist the blade nose-down. The lower surface is in compression rather than tension. The material fiber direction on this surface is the same as the lower surface, so in compression the shear flow is in the opposite direction from the upper surface, and also produces nose-down twist. The bending-twist coupling illustrated in the figure is flatwise-bending-up-nose-up which is just the opposite of what is desired for the tiltrotor blade to offset the precone pitch-lag effect. Flatwise-bending-up-nose-down coupling is created by reversing the fiber angles illustrated in the diagram.

8.3.3   Investigation of Bending-Twist-Coupled Blades

To develop guidelines for realistic magnitudes of bending-twist coupling, a NACA 0012 airfoil section composed entirely of graphite/epoxy composite weave material is considered. The airfoil cross section, illustrated in Fig. 8.31, is shown to have a chord length the same as that the baseline tiltrotor blade. The laminate material properties are listed in table 8.2, and the laminate thickness is selected to give flatwise-bending stiffness and torsional stiffness within range of the baseline blade when the material plies are oriented at 0° (the cross-ply of the weave would be at 90°). There are approximately 18 plies of weave material in the laminate as shown in Fig. 8.32. Here, two cases to be considered are illustrated. In *case 1* the entire laminate may be rotated off-axis at an angle labeled α. In *case 2* only half the plies (every other laminate) may be rotated off-axis at an angle labeled α while all the remaining laminates (designated β) stay at 0°. *Case 2* is considered to add the

281

reality of structural constraints which may limit the amount of primary structure which can be used to create bending-twist coupling. The flatwise and torsional stiffnesses are plotted as a function of off-axis ply angle, α, in Fig. 8.33. This plot shows that the flatwise and torsional stiffnesses associated with both cases are within the range of those respective stiffnesses associated with the baseline blade. The range of the stiffnesses of the baseline account for variations of the stiffnesses from about 40% span out to the tip. The tendency for increases in ply angle is to reduce the flatwise bending stiffness and increase the torsion stiffness. At high ply angles the bending and torsion stiffnesses of the composite blade models are shown to leave the baseline range, which is an indication that the blade stiffnesses may create a structural or dynamic problem. The magnitude of the bending-twist-coupling stiffness increases with ply angle until reaching a peak at about 25° as shown in Fig. 8.34. The location of the peak makes sense because the coupling is zero at 0° and 45°. One would then expect a maximum about half way between these two points. A convenient way to characterize the magnitude of the bending-twist coupling is to relate it to the bending and torsion stiffnesses to which it is related. To this end, a coupling parameter is defined as

$$\lambda = \frac{K_{34}}{EI_f + GJ} \tag{8.5}$$

where K_{34} is the flatwise-bending-twist coupling stiffness. This parameter relates the amount of bending-twist coupling that can realistically be designed into a blade to the bending and torsional stiffnesses themselves. As the amount of bending or torsion stiffness increases, it is easier to add a greater magnitude of coupling into the design, and this is reflected by the coupling parameter. A plot of the coupling parameter λ is shown as a function of ply angle for the two composite blade cases in Fig. 8.35. This plot is very similar to that of Fig. 8.34, indicating that the parameter is consistent with magnitude of coupling in the blade, even though the bending and torsion stiffnesses are changing as the ply angle increases. A realistic

282

value for the coupling parameter can be determined by comparing the plot of Fig. 8.33 with that of Fig. 8.35. Figure 8.33 shows that for *case 1* the stiffnesses leave the baseline range at a ply angle of about 12°, and for *case 2* the stiffnesses leave the baseline range at a ply angle of about 20°. Using these respective angles as constraints, from Fig. 8.35 the coupling parameter is limited to $\lambda = .25$ for *case 1* and to $\lambda = .12$ for *case 2*. These numbers may then be used as guidelines for preliminary design of a rotor blade based on a set of baseline uncoupled stiffnesses. The coupling parameter of *case 1* shows the upper limit of how much coupling can be added to the blade without significantly altering its baseline characteristics. The coupling parameter of *case 2* is a more conservative number which accounts not only for the constraints of *case 1*, but also for the likelihood that all structure in the blade cannot be used to create coupling.

The influence of flatwise-bending-twist coupling on the stability of the baseline system was then investigated. The coupling parameters are used to define the flatwise-bending-twist coupling stiffness distribution of the baseline blade based on the baseline classical beam stiffnesses. The classical beam stiffnesses themselves are not altered, so the baseline blade frequencies are retained. This procedure isolates the influence on stability by the addition of elastic coupling into the blade.

The plot of Fig. 8.36 shows the damping of the wing beam mode damping as a function of velocity for three value of the coupling parameter. The baseline design is uncoupled, so $\lambda = 0$ for this case. For the remaining two cases the indicated value of λ and the baseline flatwise-bending and torsion stiffnesses were used to calculate K_{34} at each blade station outboard of 40% span. There was no structural coupling for the inner 40% span because it may be desirable not to have coupling in the high-stress root section. The velocity at which the system becomes unstable is shown to increase with the magnitude of coupling. The flutter velocity of about 250 knots is increased to about 360 knots at $\lambda = .10$, an increase of 44 percent. The

plot of Fig. 8.37 illustrates the sensitivity of flutter velocity to the point at which coupling is initiated (blade coupled from initiation point out to tip). This plot is based entirely on the $\lambda = .05$ coupling. The baseline design is, again, uncoupled so the initiation point is given a value of r/R = 1.0. The previously obtained result is established at r/R = 0.4, and the flutter velocity increases. Reduction of the initiation point to r/R = 0.2 is shown to greatly increase the flutter velocity, indicating that the coupling has the greatest effect at the inboard sections of the blade. This result seems reasonable considering that the bending slope for the fundamental bending mode has the greatest values in this section of the blade. The increase in flutter velocity for this case is about 56 percent over the baseline design.

Although no kinematic pitch-lag coupling is considered in the present analysis, it is possible to calculate an effective kinematic coupling based on the elastic twist of the blade tip. The kinematic pitch-lag coupling then becomes a function of velocity because of the change in collective pitch, which places increasingly more of the flatwise-bending in the lag direction. The effective pitch-lag coupling was calculated based on an untwisted version of the baseline blade, and the results are plotted in Fig. 8.38. The effective coupling associated with the $\lambda = .05$ case (40% initiation) is shown to be on the order of 0.3 which is considered a large value, and has about the same magnitude as the negative pitch-lag coupling calculated for the precone effect in reference 31. The effective kinematic pitch-lag coupling for the $\lambda = .10$ case is even larger, reaching a maximum of about 0.8. Thus, very large values of pitch-lag coupling can be obtained using elastic flatwise-bending-twist coupling in the rotor blade.

The impact of bending-twist coupling on tiltrotor performance and blade loads is investigated next. The cruise performance in airplane mode at $V/\Omega R = .7$ is plotted as a function of disc loading in Fig. 8.39. While an untwisted blade is shown

(as a reference) to have an adverse effect on cruise performance, the bending-twist-coupled blade is shown to have the same performance as the baseline blade. The hover figure of merit is plotted as a function of disc loading in Fig. 8.40. Here, the untwisted version of the baseline blade is shown to have slightly improved performance over the baseline blade. The bending-twist-coupled blade has virtually the same performance as the baseline with slightly better figure of merits at low disc loadings and slightly lower figure of merits at high disc loadings. Root bending moments in the lag and flap directions are plotted as a function of azimuth station in Fig. 8.41. The flight mode here is conversion with the pylon at 75° and a velocity of 100 knots. The bending moments predicted for the coupled and baseline blades are shown to be virtually the same for both directions.

From the previous discussions of this section, the use of flatwise-bending-twist-coupled blades are shown to have a very favorable influence on stability without creating adverse effects on performance or blade loads. The potential impact of coupling on blade dynamics and strength have been avoided in the investigation by considering only magnitudes of elastic coupling which can be obtained without significant changes in baseline stiffness properties.

8.4 Extension-Twist-Coupled Rotor Blade

This section focuses on means for improving tiltrotor performance through passive blade twist control. The twist distribution of a blade is altered by elastically coupling the blade extension and twist modes. Extension-twist coupling is effective for tiltrotors because in changing from hover to forward flight there is a significant decrease in rotor speed and a significant increase in inflow through the rotor disc. The large change in inflow makes it desirable to have a change in twist distribution so that more of the blade span is maintained at an optimum angle of attack. The large change in rotor speed provides a mechanism, the change in centrifugal force,

by which to alter the twist using extension-twist coupling.

8.4.1 Optimum Twist Distributions

The twist distribution of the baseline tiltrotor blade is the same as that of the XV-15 and is plotted in Fig. 8.1. This twist distribution is based on a compromise of the twist desired for hover and that design for high-speed cruise. An investigation of the optimum twist distribution for each flight mode, hover and cruise, was performed based on both linear and nonlinear distributions. One difficulty encountered with this investigation was the classification of the nonlinear twist distribution. The baseline twist distribution is nonlinear, but can be accurately approximated by a series of two linear distributions joined at the 40% radius. The nonlinear twist distribution is then defined by the baseline twist from 0 to the 40% span followed by a linear twist rate from 40% to the blade tip. The linear approximation of the baseline twist outboard of $.4R$ is $30°/R$ ($18°$ over a span of $.6R$). It should be noted that all twists and twist rates are defined as positive for nose-down twist (moving from root to tip). A plot of the power required for cruise is shown in Fig. 8.42 as a function of twist rate for both the linear and nonlinear twist distributions. The power required is shown as a percentage change relative to the baseline (XV-15) power required, with a negative change indicating improved performance. The performance associated with the nonlinear twist distribution is shown to match that associated with the baseline XV-15 twist at $30°/R$ as expected. The optimum nonlinear twist is shown to improve performance by only one percent at a rate of $42°/R$ while the optimum linear twist distribution is shown to improve performance by one-half percent at about $50°/R$. From these results it appears that the baseline twist is very close to an optimum value for cruise, and that a nonlinear twist distribution is only slightly more desirable, from a performance standpoint, than a linear twist distribution.

286

A plot of the power required for hover is shown in Fig. 8.43 as a function of twist rate for both the linear and nonlinear twist distributions. Again, the power required is shown as a percentage change relative to the baseline (XV-15) power required, with a negative change indicating improved performance. The performance associated with the nonlinear twist distribution is shown to match that associated with the baseline XV-15 twist at $30°/R$ as expected. The optimum nonlinear twist is shown to improve performance by about six percent at a twist rate of $12°/R$ while the optimum linear twist distribution is shown to improve performance by about 11 percent at a twist rate of $25°/R$. From these results it appears that the baseline twist is very far from an optimum value for hover, and that a linear twist distribution is much more desirable, from a performance standpoint, than a nonlinear twist distribution.

8.4.2 Design of Extension-Twist-Coupled Blades

It is difficult to define an extension-twist-coupled rotor blade in terms of the base-line tiltrotor blade because there are several aspects of this coupling that require non-traditional design methodology. Definition of an axial stiffness for a rotor blade, as is required for this type of coupling, is itself non-traditional. In most rotorcraft analyses, rotor blades are assumed to be rigid in extension. The introduction of extension-twist elastic coupling also creates bending-shear coupling between the two bending directions. For example, the bending stiffness in the flatwise-bending plane is coupled to the shear stiffness in the chordwise-bending plane. The bending-shear coupling, as shown in Chapter 3, significantly reduces the effective bending stiffness of the structure. Unless high stiffness laminates are used efficiently in the blade primary structure, it is unlikely that the extension-twist-coupled blade design can maintain baseline bending stiffness values, and still achieve desired twist deformation goals. By efficiency here it is meant that all

or most of the primary structure must contribute to the desired coupling effect. Another differentiating aspect of the extension-twist-coupled blade design is an increase in blade tip-mass. An increase in blade tip-mass is necessary to increase the centrifugal forces which act as the twist deformation mechanism. With both increased tip mass and bending-shear coupling, the fundamental frequencies of an extension-twist-coupled blade almost certainly must deviate from that associated with the baseline rotor blade.

Representative guidelines for establishing stiffness properties of an extension-twist-coupled blade are based on the same Gr/E material used for the bending-twist-coupled blade and the same cross section model shown in Fig. 8.31. The laminate thickness is reduced by one-half in order to reduce the extension stiffness to values which can be effective in an extension-twist-coupled blade. The laminate considered is shown in the top of Fig. 8.32, except only half the plies exist in the present model (9 instead of 18 plies). For an extension-twist coupled blade, the laminate on the lower surface is rotated in the opposite direction to the laminate on the upper surface, so it is understood that an angle oriented at $+\alpha$ on the upper surface is opposed by a laminate oriented at $-\alpha$ on the lower surface. Based on these assumptions, the flatwise-bending and torsion stiffnesses associated with an extension-twist-coupled blade are plotted as a function of off-axis ply angle in Fig. 8.44. This plot shows that the flatwise-bending stiffness is reduced by a factor of about one-half to one-third that obtained for the baseline and bending-twist-coupled blades. The torsional stiffness is also lowered, but remains in a range close to that used in the baseline blade. Extension and extension-twist-coupling stiffnesses are plotted as a function of off-axis ply angle in Fig. 8.45. The extension-twist-coupling stiffness reaches a maximum around 22.5°, and the extension stiffness is seen to drop rapidly with increases in the ply angles. Realistic values of coupling stiffness are not extracted from the baseline blade stiffnesses,

as was the case for the bending-twist-coupled blade, and instead are derived from the airfoil cross section model itself. The problem here is that the rotor system frequencies will change, but the frequencies of the rotor blade will change anyway with the addition of tip mass (as is required to obtain large twist changes). The loss here is that deviations from the baseline stiffness values will create unknown deviations in the stability of the system simply from changes in blade frequencies. The effect on stability of adding the extension-twist-coupling alone will not be known.

An analytical model of an extension-twist-coupled blade is based on the cross section model discussed in the previous paragraph. The blade sections outboard of 20 percent span are considered to be elastically coupled while the blade section inboard of 20 percent span is considered to be uncoupled and built up to withstand high loads. The stiffness values for the coupled sections of the blade are obtained for a laminate ply angle of $\alpha = 20°$ because of the large amount of extension-twist-coupling obtained at this angle. The extension stiffness associated with this ply angle is 232 which is the value used for the coupled blade sections. For the uncoupled root section, this stiffness is increased to 500. The extension-twist stiffness K_{14} can reach as high as .5 as shown in Fig. 8.45, but to account for reductions in coupling due to uncoupled structural components in the cross section, a conservative value of -.2 is used in the coupled sections of the blade model (the negative sign gives the proper direction for the desired twist deformation as shall be discussed shortly). The chordwise and flatwise bending stiffnesses are set to one-half of the baseline values shown in Figs. 8.5 and 8.6, respectively. Torsional stiffness by the guideline is about .0022, a low value which is desirable for obtaining large twists. The torsional stiffness for the analytical model is set at .0044 using the conservative approach adopted for the coupling stiffness. Values for the root element of the analytical model (0 - .2 r/R) are unchanged from the baseline case.

With the stiffnesses now established for the extension-twist-coupled blade, the amount of twist deformation can only be further increased with additional tip mass. To maintain realistic values for the tip mass, the mass contribution of a steel tip mass with a cross section of 15 in² is determined as a function of its length. A plot of the running mass at the blade tip versus the tip mass length is shown in Fig. 8.46. The finite element model assumes a linear distribution over the blade segment so the value of the running mass at the tip node is about twice what the value would be if it were constant over the segment. The weight added to the blade is also shown in the plot. Reasonably large twists were obtained using tip mass values of 8 to 12 which are shown to add between 19 and 26 pounds per blade (114-156 lbs. to total system). Three extension-twist-coupled blade cases were considered for the present investigation. Each case differed only by the tip mass value, using 8, 10, and 12, respectively. The mass distributions for the three cases are plotted in Fig. 8.47.

The twist design of the three extension-twist-coupled blade cases is considered next. For the twist design, the optimum twist distribution for cruise mode will be obtained as determined from Fig. 8.37. This is done because airplane cruise mode is generally considered the more important flight mode, where the most time in flight is spent, and is thus where optimum efficiency is required. The optimum twist distribution for this flight mode (as defined by the rigid blade study) is obtained by calculating the elastic twist at the cruise rotor speed, and adding this twist to the the undeformed (zero rpm) twist distribution. The twist distributions of the three extension-twist cases are compared to the baseline twist distributions for cruise mode in Fig. 8.48 and for the undeformed (starting) condition in Fig. 8.49. The twist distributions of the three extension-twist cases in cruise mode are shown to be identical as expected, with a twist rate in the outboard sections just slightly higher than the baseline twist distribution. Little deviation from the baseline twist

distribution was expected because the baseline twist was shown in Fig. 8.36 to be very close to an optimum for performance. The undeformed twists for the three cases demonstrate the increase twist associated with increased tip mass. Comparing Figs. 8.48 and 8.49, one can determine that twist deformations obtained at the blade tip are 12, 16, and 22 degrees for the tip-mass cases of 8, 10, and 12, respectively. The twist distributions obtained for the hover mode are illustrated in Fig. 8.50. Here, the twist distributions do not follow a consistent pattern where the twist rate on the outboard end (the untwisting) becomes increasingly smaller with increased tip-mass as one might expect. The centrifugal flattening (propeller pitching moment) works against the extension-twist coupling, attempting to further twist rather than untwist the blade. This is because the pitch angle of all the blade sections are positive with respect to the plane of rotation as required to produce the lift needed from the rotor system in hover. The centrifugal flattening effect attempts to pitch the outboard sections in a nose-down sense (into the plane of rotation) which tends to increase the negative twist of the blade. This effect increases with the tip-mass which helps explain why the hover twist distributions in Fig. 8.50 are as shown.

8.4.3 Investigation of Extension-Twist-Coupled Blades

The performance associated with the hover and cruise flight modes are shown for the three extension-twist-coupled blade cases in Fig. 8.51. Based on the deformed twist distributions shown in Fig. 8.48 and the performance estimate provided in Fig. 8.36, the performance of the extension-twist-coupled designs in cruise should be about the same and should improve relative to the baseline by about one percent. This is indeed shown to be the case in Fig. 8.51. For hover, the performance improvement should be no greater then 10 percent which is shown to be the improvement associated with the optimum linear twist in Fig. 8.37. The actual

deformed twist distribution obtained for the hover case is close to the nonlinear twist case shown in that figure. Based on that curve, and the twist rate for the outboard blade sections in hover (23-26 $\deg/R$), the performance improvement should be about 3 to 4 percent. The actual performance improvement predictions for these cases range from 6 to 7.5 percent with the tip-mass of 10 showing the greatest improvement. The additional improvements here are attributed to the flap deformation associated with the increased tip-mass over the baseline value. The flap deformation is in the negative direction since the precone is selected based on the baseline mass distribution. As the tip-mass increases, the additional centrifugal force bends the blade down which is tantamount to reducing the precone on the baseline blade. With the blade closer to the plane of rotation the lift is more aligned with the desired direction of thrust and the efficiency is increased. The performance improvement associated with adding tip-mass to the baseline blade (without extension-twist-coupling) is shown in Fig. 8.52 to be about one percent. The extension-twist-coupled blades are more flexible in bending so the performance improvement due to the tip-mass increase should be even greater for them.

The performance results of Fig. 8.51 are promising, but the stability of the extension-twist-coupled blades must be investigated next. First, the stability of the extension-twist-coupled blades without the precone effect is considered. The beam wing mode damping is plotted as a function velocity in Fig. 8.53, and shows that the velocity at which flutter occurs is significantly reduced by the increased tip-mass. One reason for this decrease is the reduced frequency of the wing torsion mode created by the additional rotor mass. The reduction in torsion frequency brings the wing beam and torsion mode frequencies closer together which is very destabilizing as discussed in Chapter 2. Wing frequencies are plotted as a function of velocity in Fig. 8.54 for three cases of the uncoupled baseline blade. The case of additional tip-mass added to the baseline blade is shown to decrease the torsional

frequency much more than the beam frequency. An increase in the wing torsional stiffness by 20 percent is shown to increase the wing torsional frequency back to near its baseline value over most of the velocity range considered. The effect on wing beam mode damping for these cases is shown in Fig. 8.55. Here, the flutter velocity is shown to decrease significantly with increased tip mass similar to the results shown in Fig. 8.53 for the extension-twist-coupled blades. The addition of wing torsional stiffness to the baseline plus increased tip mass case is shown to increase the flutter velocity by about two-thirds of the difference between that case and the baseline case. These results indicate that most of the reduction in flutter velocity with increases in tip mass is attributable to the change in the wing torsional frequency.

The additional destabilizing effects of rotor precone ($\beta_p = 1.5°$) are illustrated in Fig. 8.56 which show that the extension-twist-coupled blades on the baseline system have very low flutter velocities. These results are shown for $\beta_p = 1.5°$ instead of $\beta_p = 2.5°$ because the additional blade mass decreases the ideal precone for hover. These poor results should be expected because of the increase in centrifugal forces associated with the additional tip mass which, in turn, amplify the precone effect. The precone effect will naturally be high in extension-twist-coupled blades since both the precone and coupling effects are highly sensitive to the centrifugal loads. It seems from these results that an extension-twist-coupled blade set must have zero or very near zero precone. Whether or not the coupled blades, which tend to be weak in bending, can survive the increased bending loads associated with lower precone is another question. The present investigation does not include a stress analysis, so this question will remain unanswered.

Table 8.1: Parameters for the baseline free-flight model.

Parameter	Analysis Variable	Value
c_W	ct/sigma	0.088
S_w	wing_area	1.08
S_t	tail_area	.32
C_{l_w}	lift_slope_wing	6.0
C_{l_t}	lift_slope_tail	6.0
C_{d_w} [1]	cd_wing	.0
C_{d_t} [1]	cd_tail	.0
C_{m_w}	cmac_wing	-.00
C_{m_t}	cmac_tail	-.00
xcg_w	wing_xcg	.02
zcg_w	wing_zcg	.1
xcg_t	horiz_tail_xcg	1.8
zcg_t	horiz_tail_zcg	.05
α_w	wing_fixed_angle	3.0°
α_t [2]	tail_fixed_angle	3.0°
c_w	wing_chord	.42
c_t	horiz_tail_chord	.313
f_A	parasite_drag_area	0.025

[1] Wing and tail drag included in parasite drag area.

[2] 3.0° nominal, can vary 0 to +6 degrees.

Table 8.2: Material properties for IM7/3501 Gr/E woven cloth.

Property	Value
E_{11} (psi)	11.64
E_{22} (psi)	11.64
E_{33} (psi)	1.62554
G_{12} (psi)	0.909
G_{13} (psi)	0.909
G_{23} (psi)	0.909
ν_{12}	0.0466
ν_{13}	0.320
ν_{23}	0.320
ρ (pci)	0.05781
$t_{ply}(in)$	.014
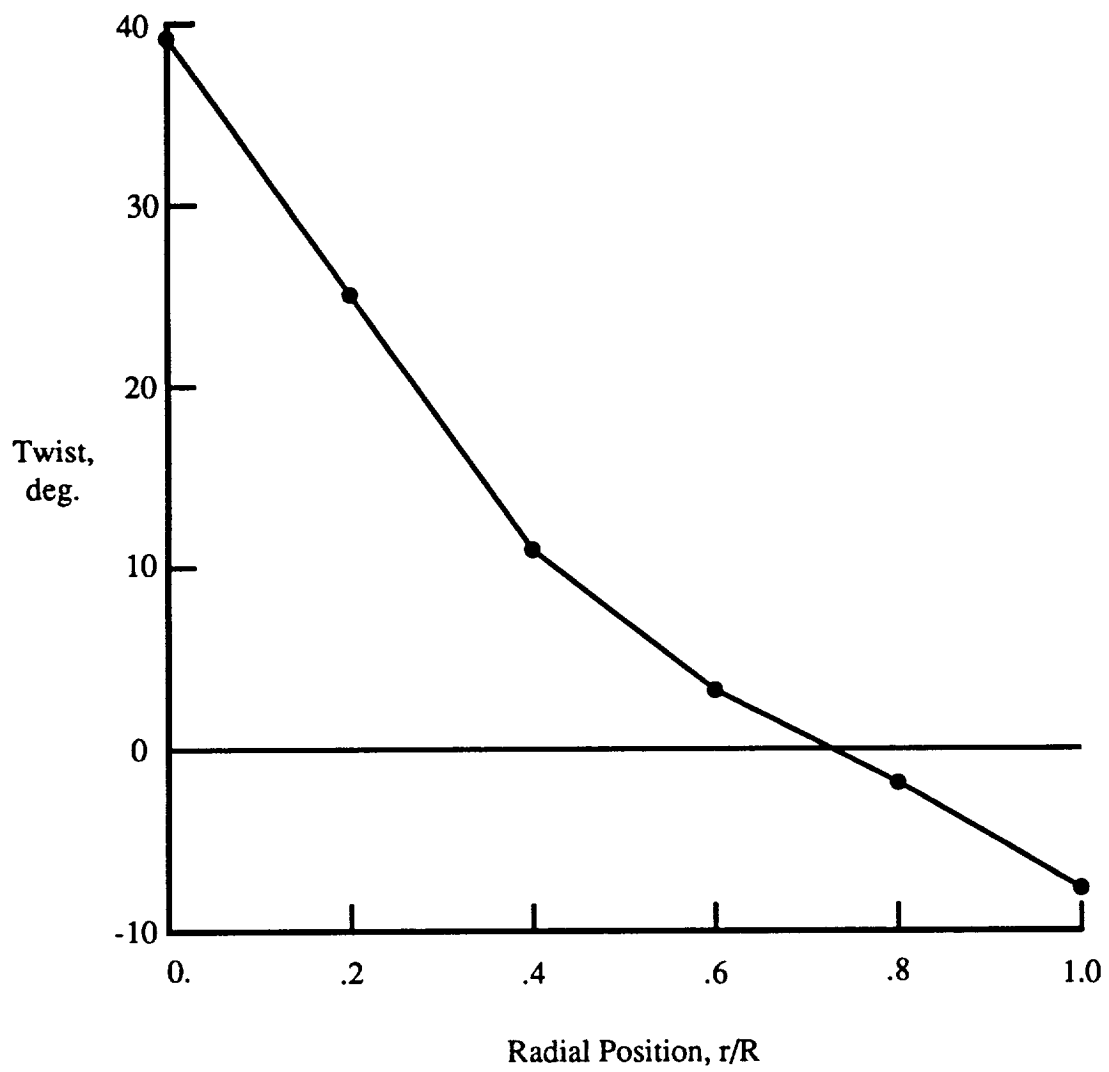
Figure 8.1: Baseline rotor blade twist distribution.
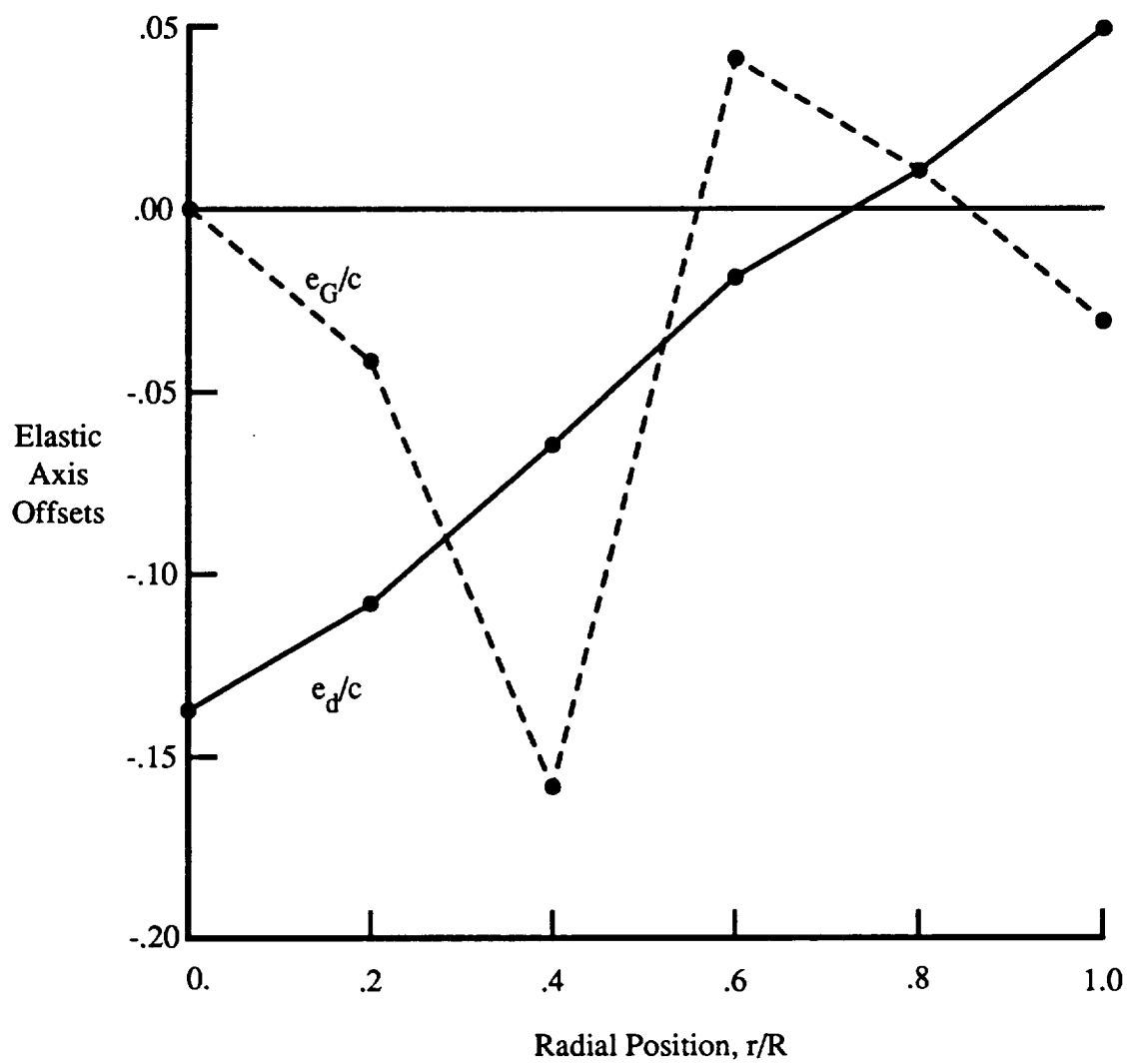
Figure 8.2: Baseline rotor blade elastic axis offset distributions.
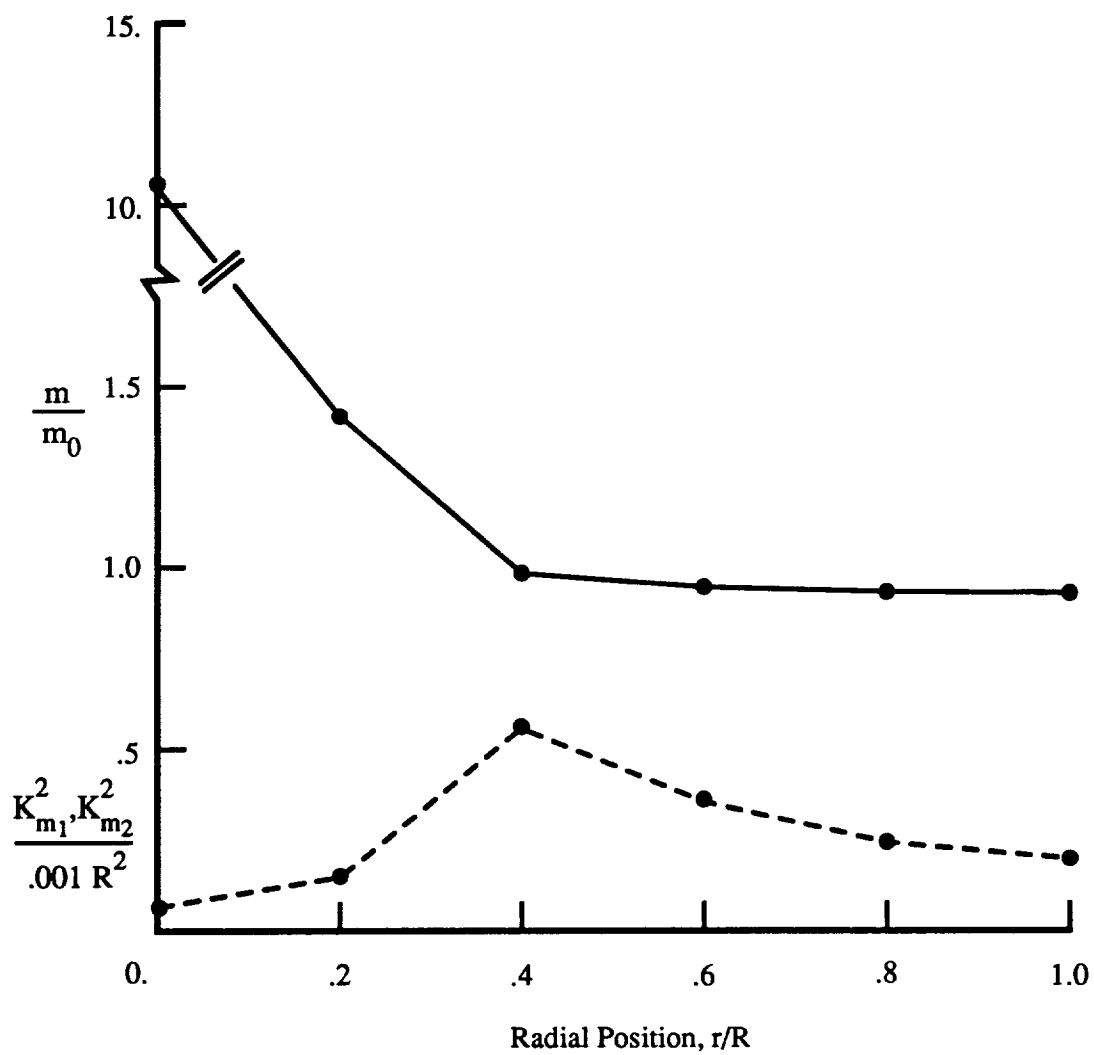
Figure 8.3: Baseline rotor blade mass and mass radius of gyration distributions.

298

$$\frac{GJ}{m_0\Omega^2R^4}$$

Radial Position, r/R
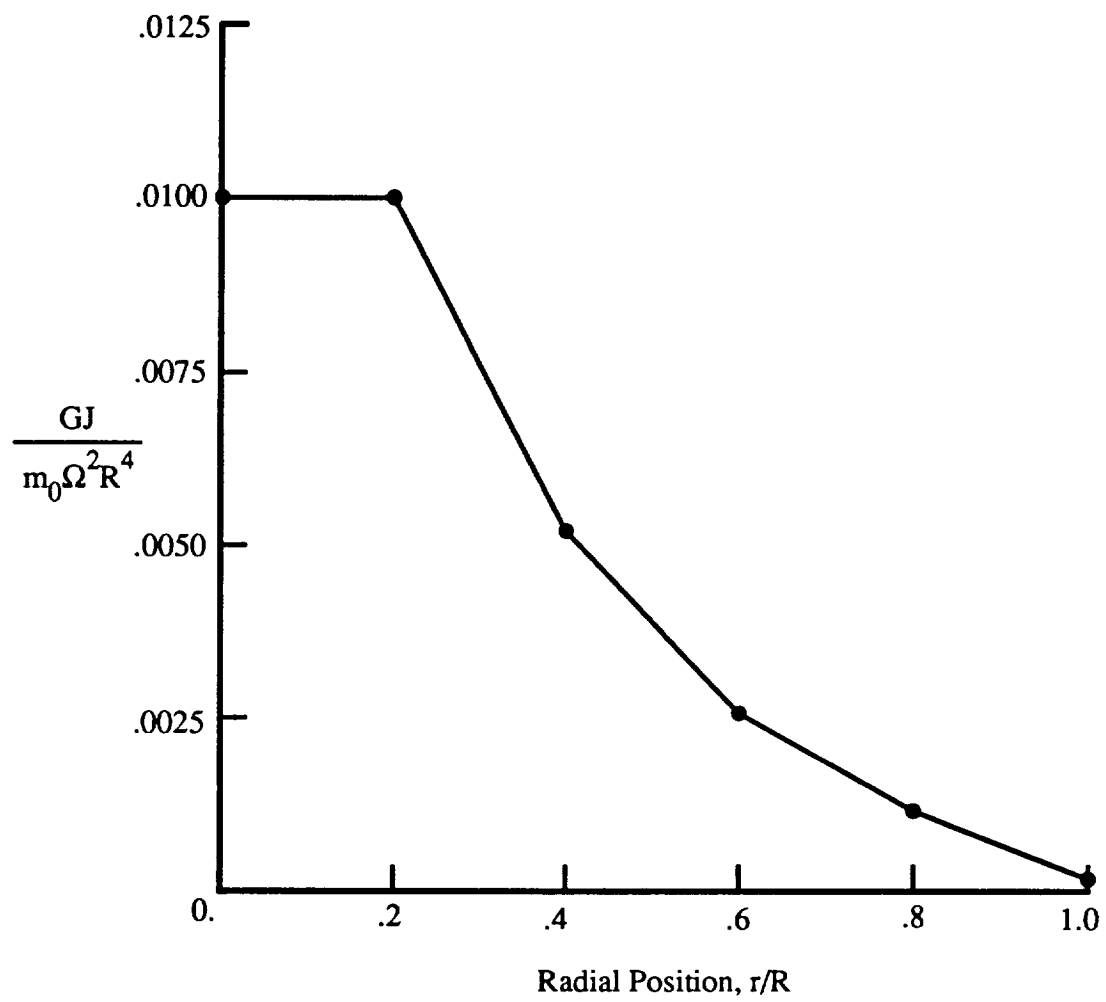
Figure 8.4: Baseline rotor blade torsional stiffness distribution.

$$\frac{EI_\zeta}{m_0\Omega^2R^4}$$

Radial Position, r/R
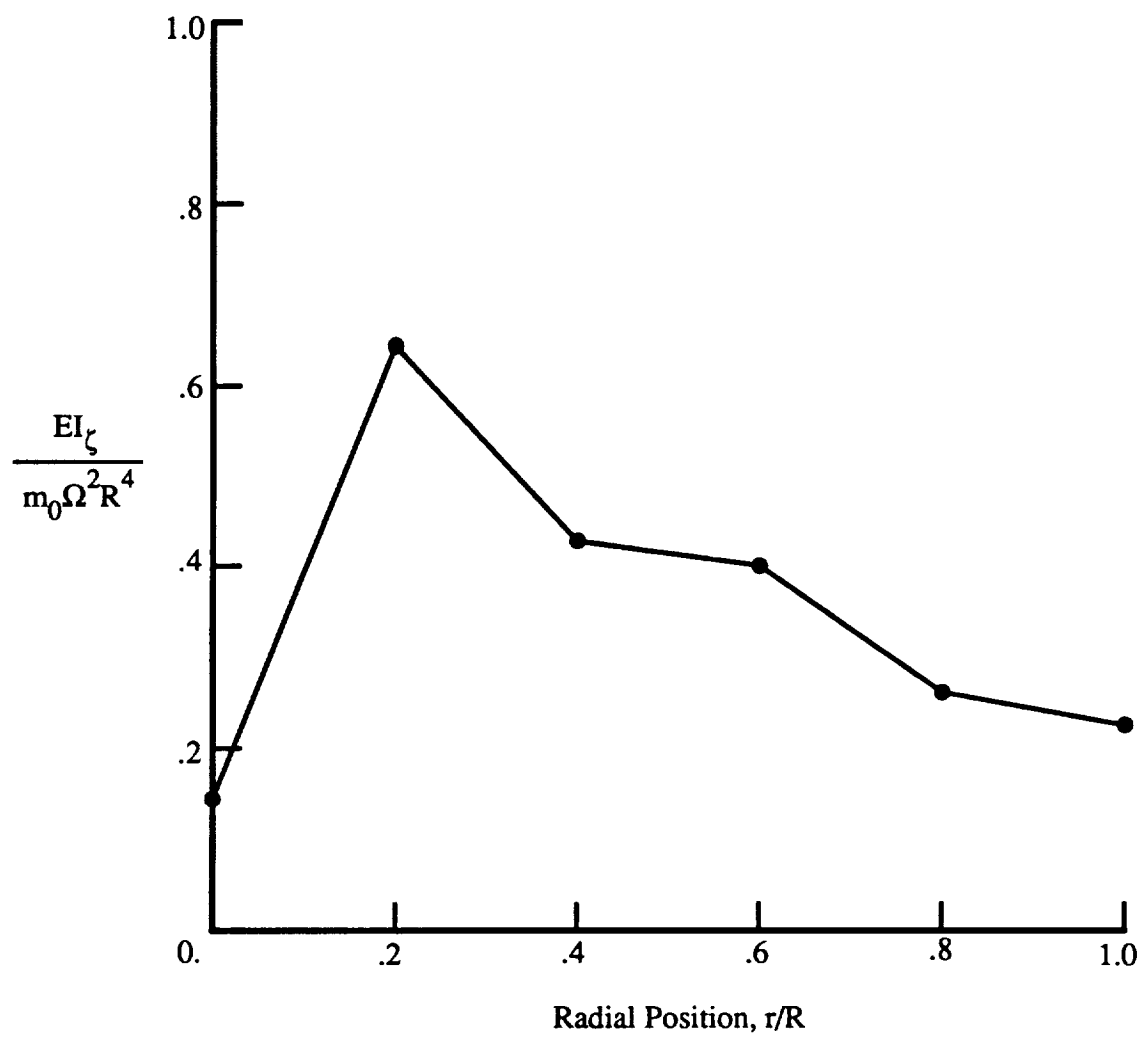
Figure 8.5: Baseline rotor blade chordwise bending stiffness distribution.
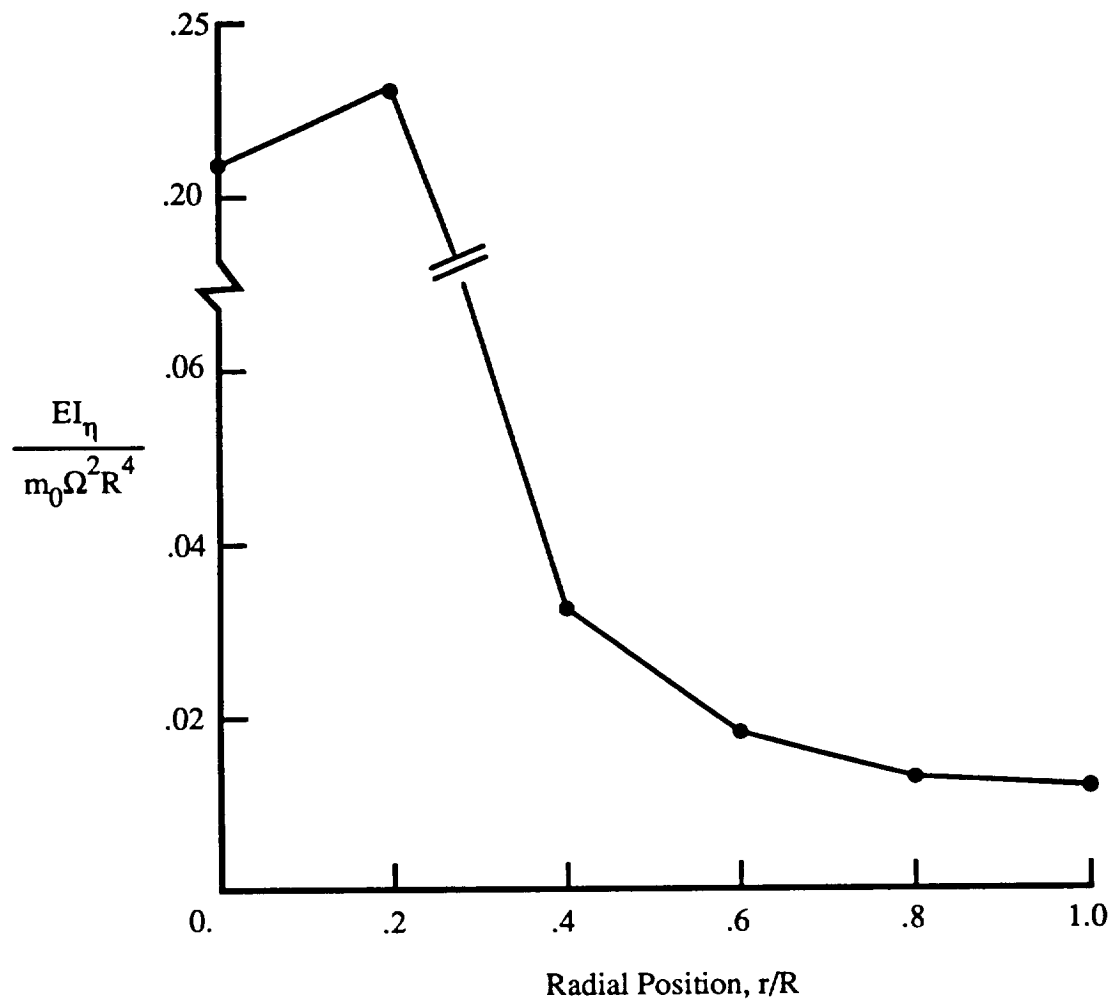
Figure 8.6: Baseline rotor blade flapwise bending stiffness distribution.
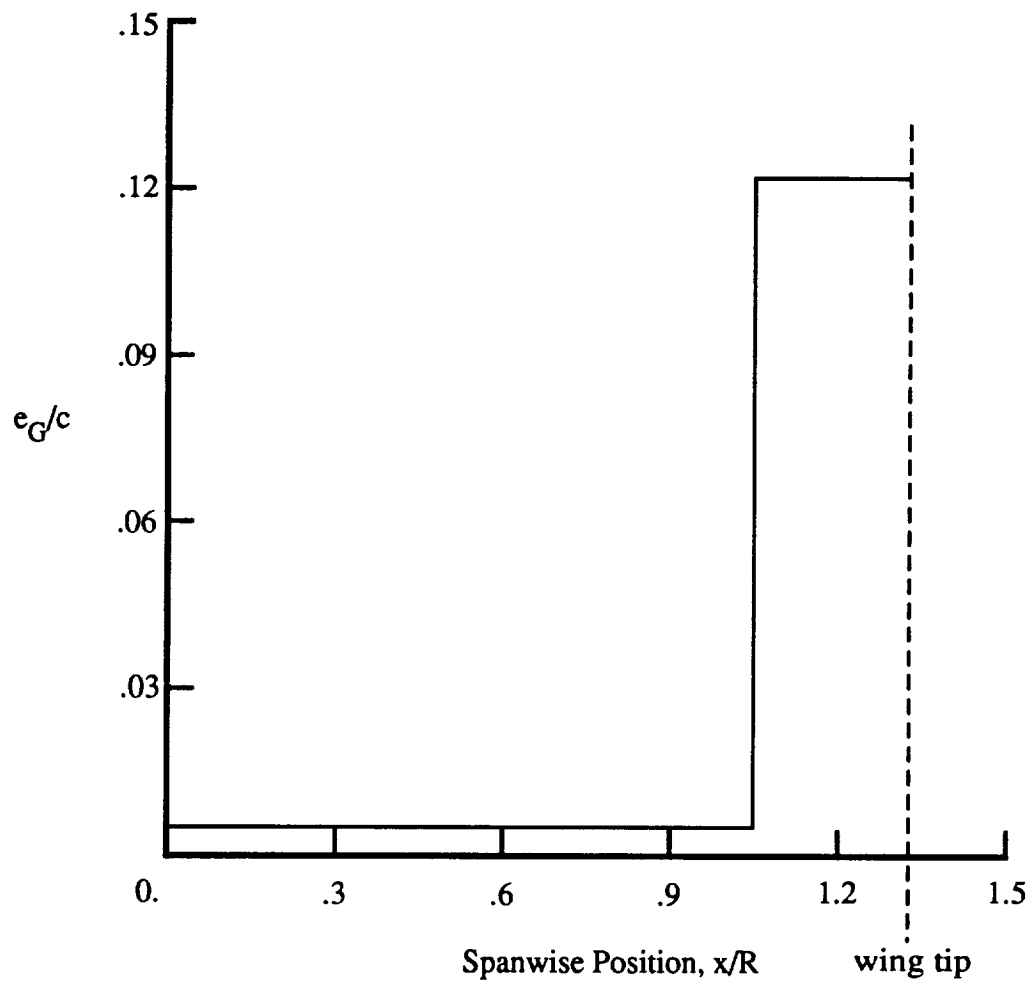
Figure 8.7: Baseline-wing center-of-gravity-axis forward of elastic-axis.
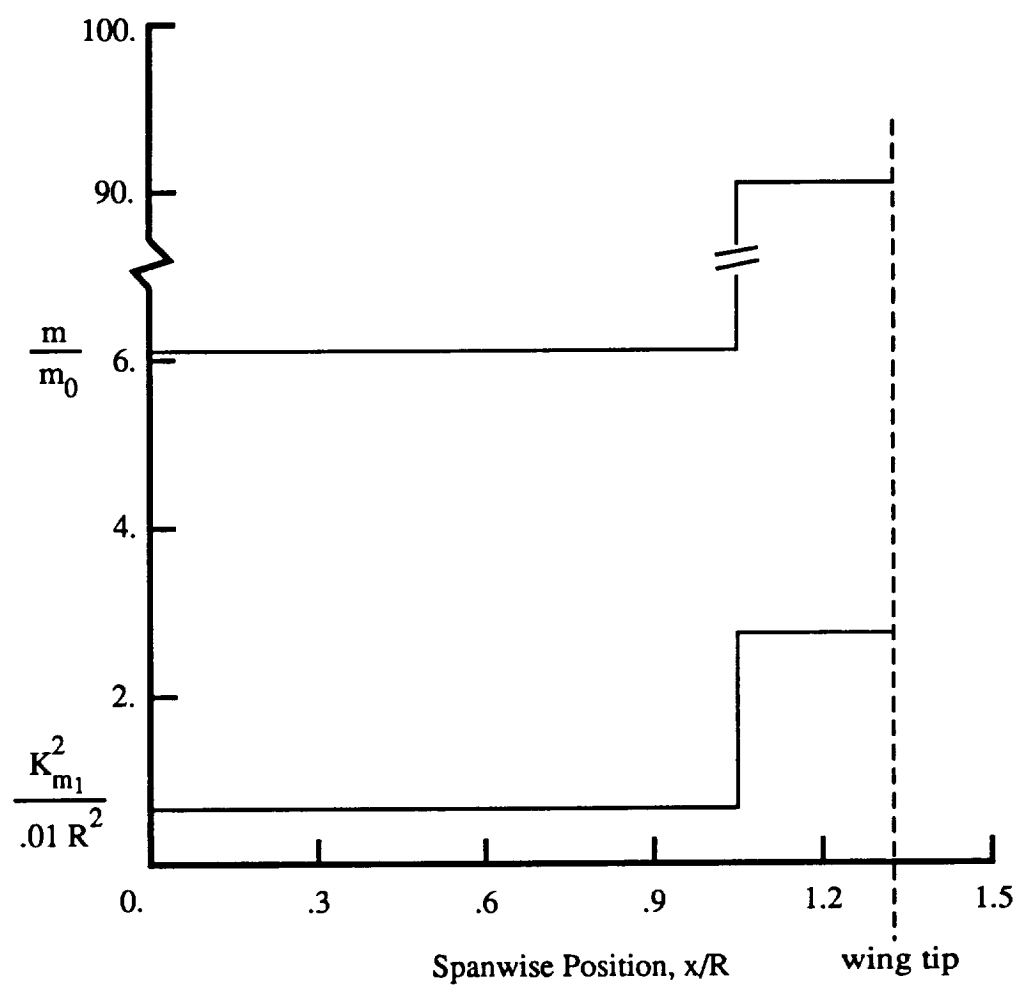
Figure 8.8: Baseline-wing mass and mass radius of gyration distributions.
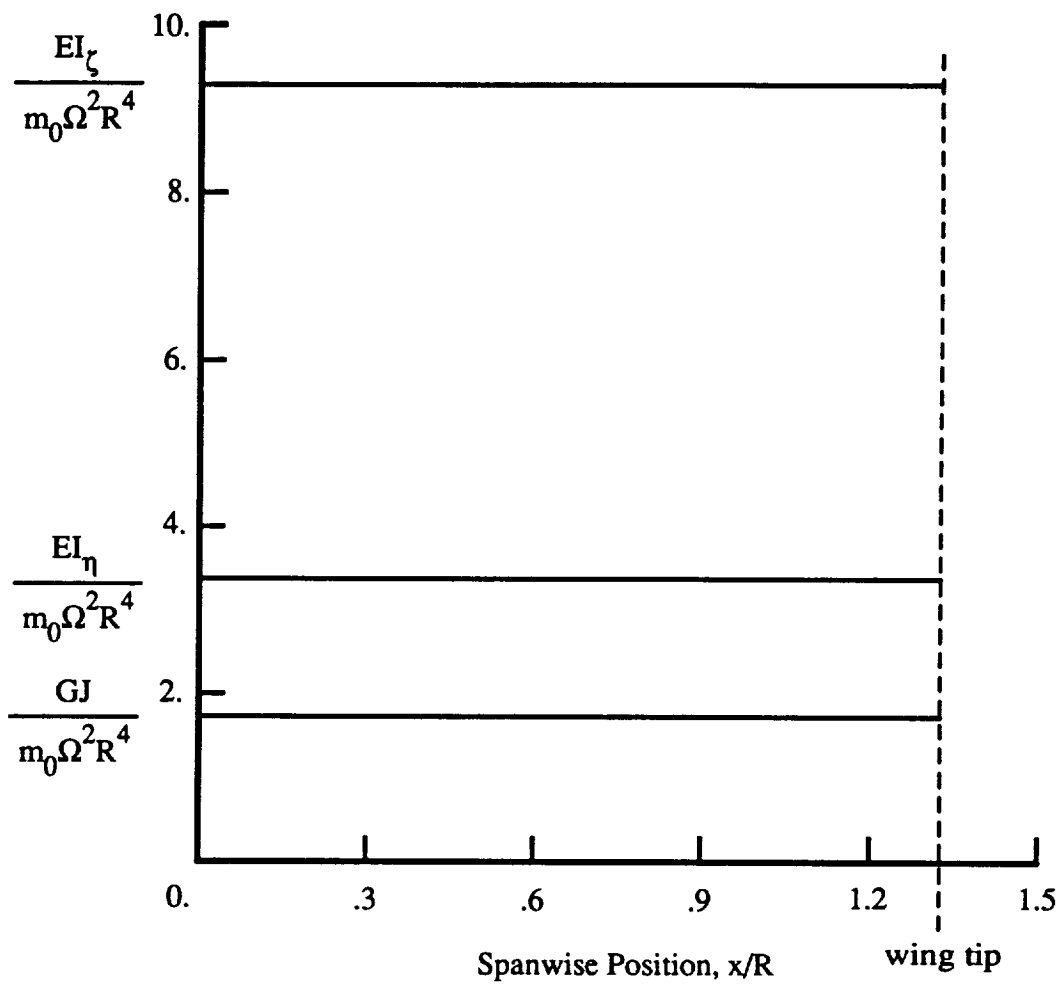
Figure 8.9: Baseline-wing torsion and bending stiffnesses distribution.
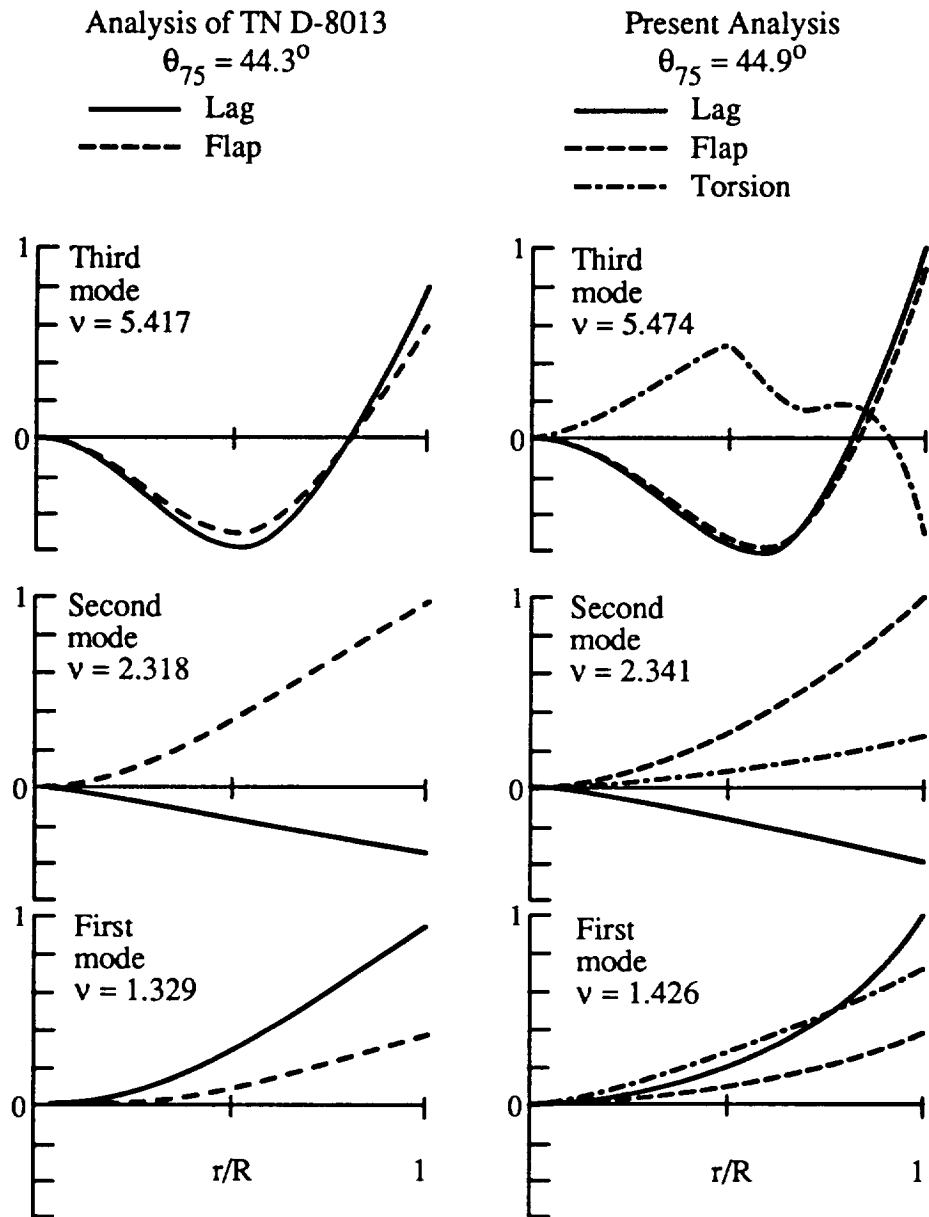
Figure 8.10: Comparison of rotor blade predominantly-bending mode shapes and frequencies at $V/(\Omega R) = 0.7$ ($V = 240$ knots).

Analysis of TN D-8013
$\theta_{75} = 44.3^o$

Rigid pitch
$\omega = 4.8$

First elastic
$\omega = 5.70$

r/R

Second elastic
$\omega = 12.77$

Present Analysis
$\theta_{75} = 44.9^o$

First elastic
$\omega = 5.73$

r/R

Second elastic
$\omega = 11.25$
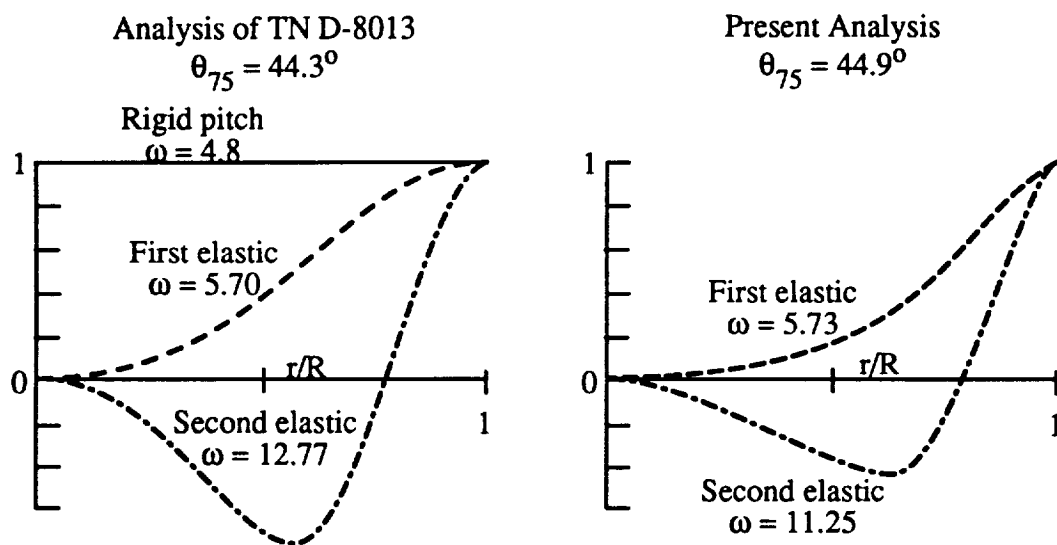
Figure 8.11: Comparison of rotor blade predominantly-torsion mode shapes and frequencies at $V/(\Omega R) = 0.7$ (V = 240 knots).
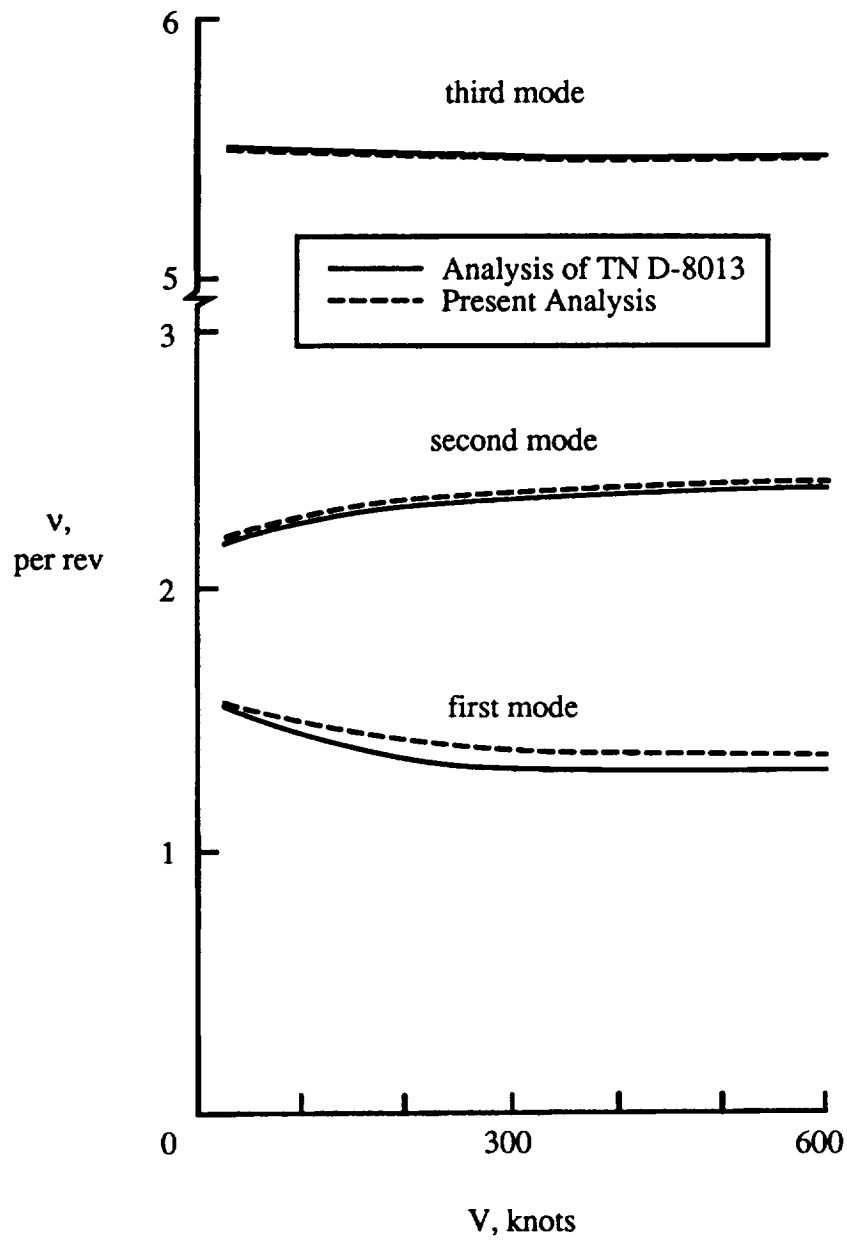
Figure 8.12: Comparison of rotating blade-bending mode frequencies at $\Omega = 458$ rpm.
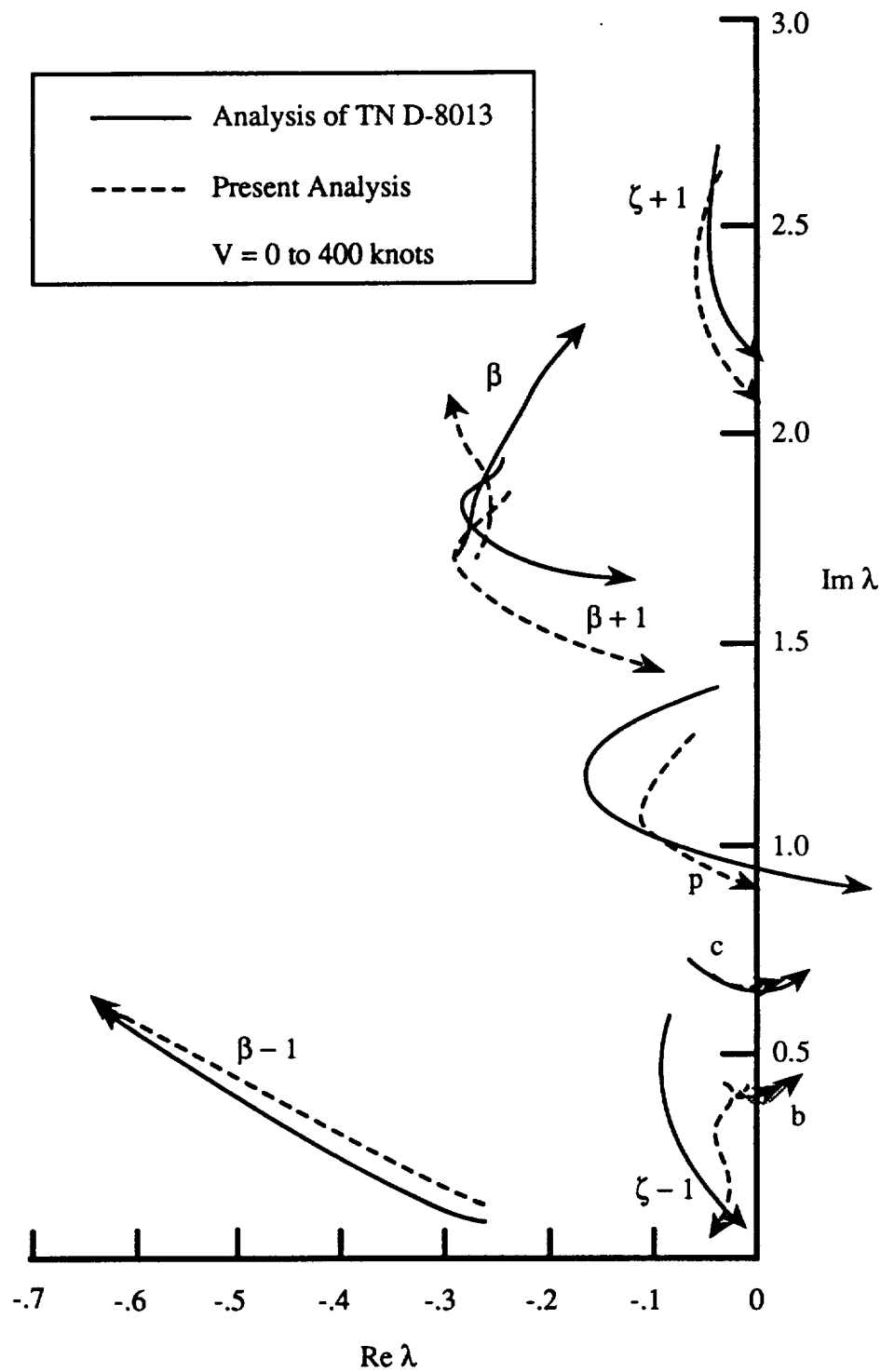
Figure 8.13: Comparison of root locus for cruise velocity sweep, windmilling rotor.
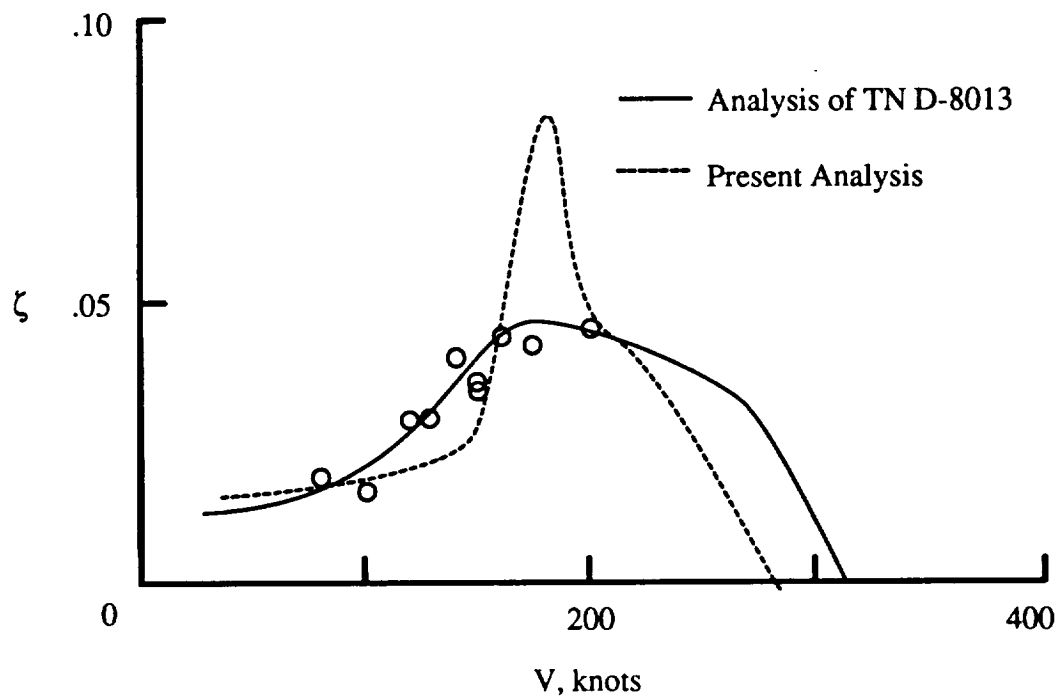
Figure 8.14: Comparison of wing beam mode damping ratio including full-scale test results.
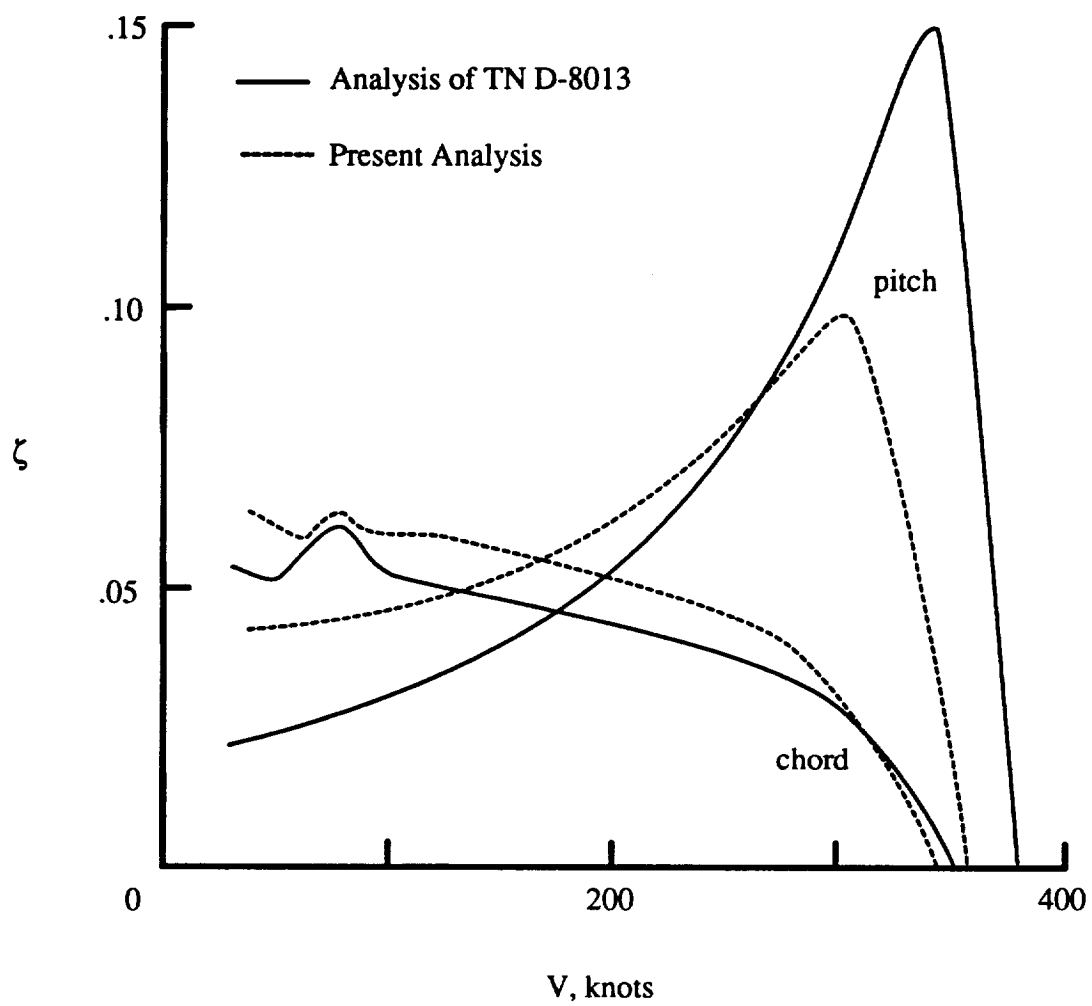
Figure 8.15: Comparison of wing-chord and wing-pitch mode damping ratios.
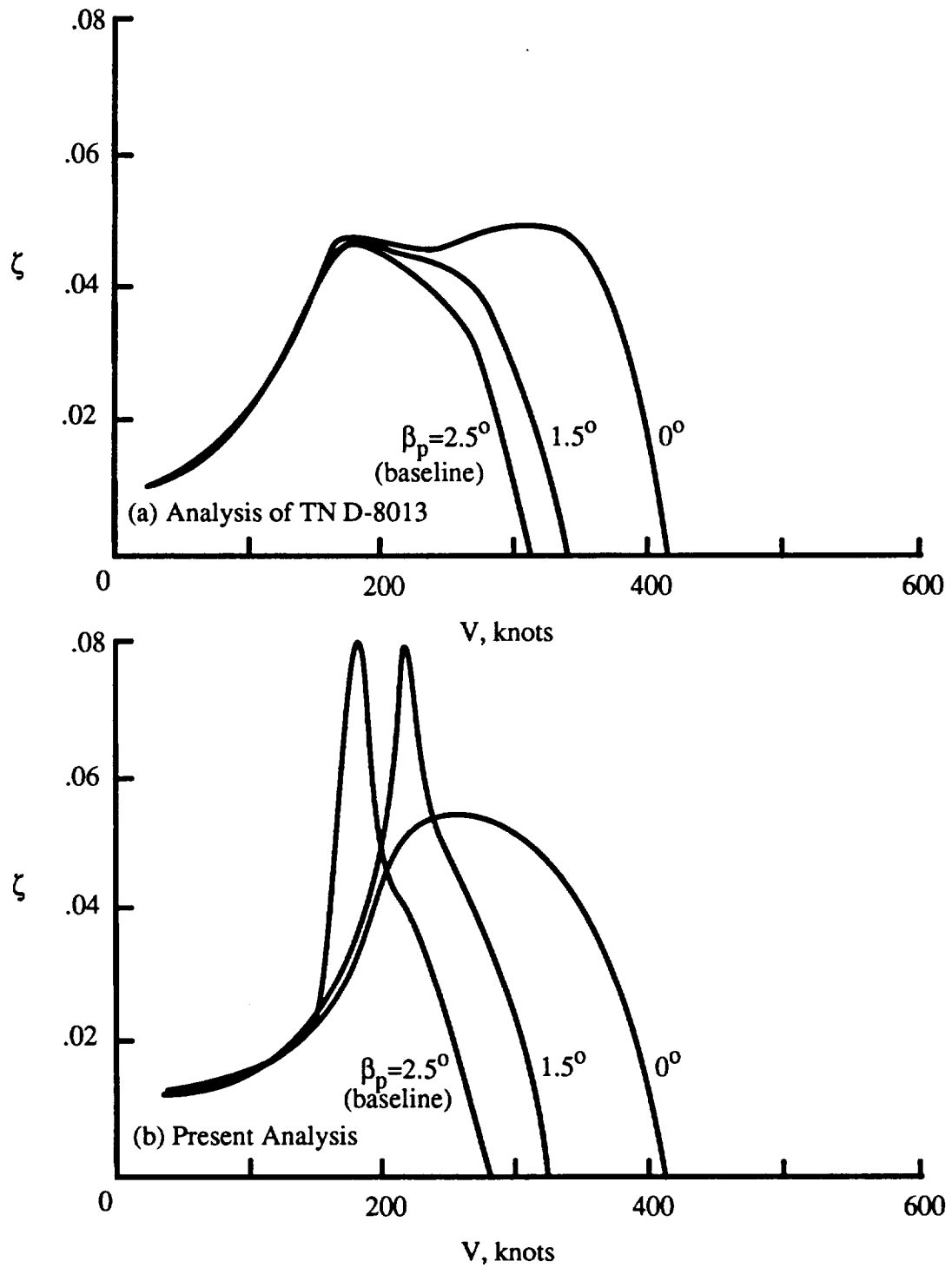
Figure 8.16: Comparison of wing beam mode damping ratio as a function of rotor precone. (a) Results from TN D-8013. (b) Results from the present analysis.
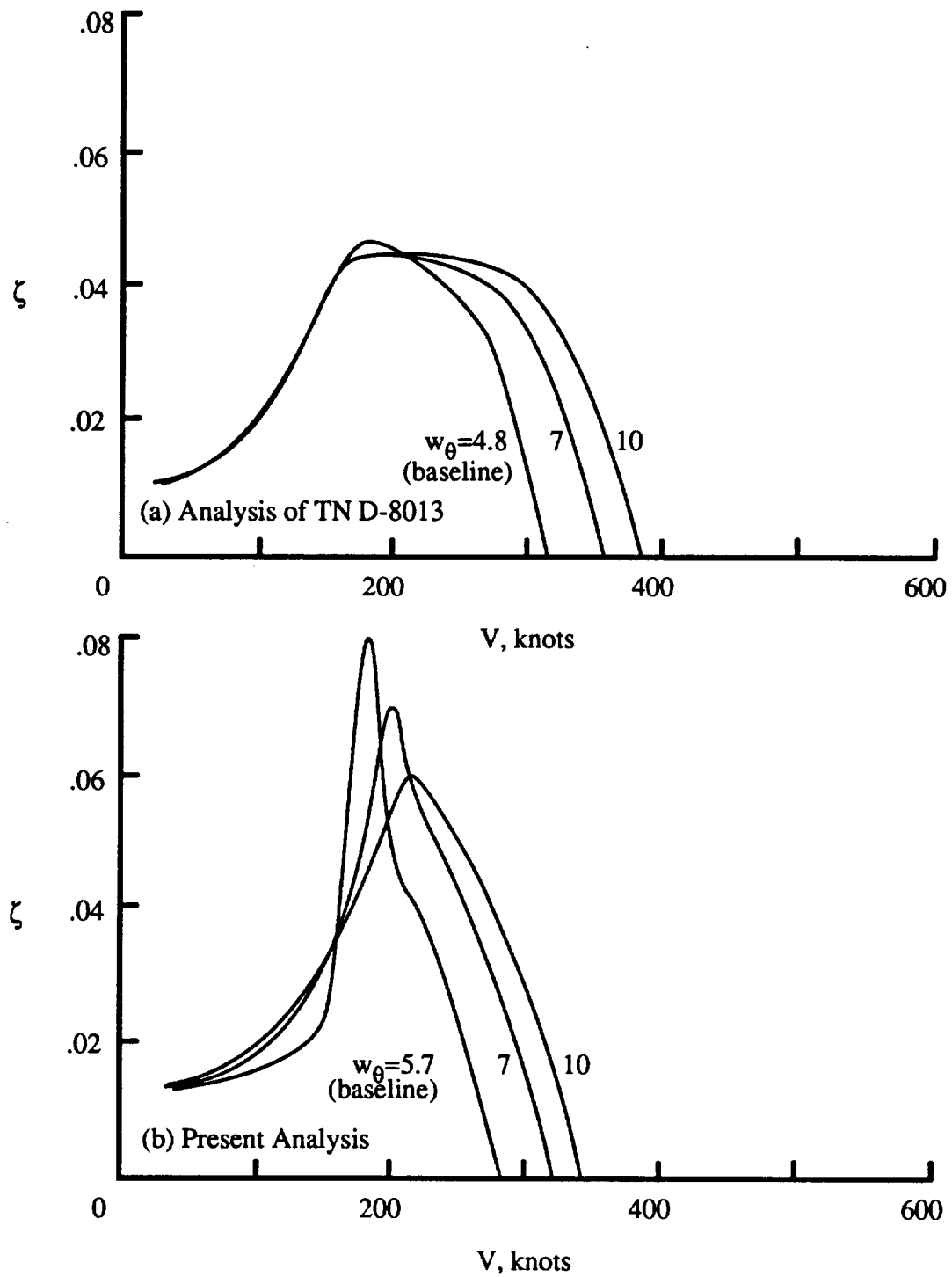
Figure 8.17: Comparison of wing beam mode damping ratio as a function of blade torsional frequency. (a) Results from TN D-8013. (b) Results from the present analysis.

312
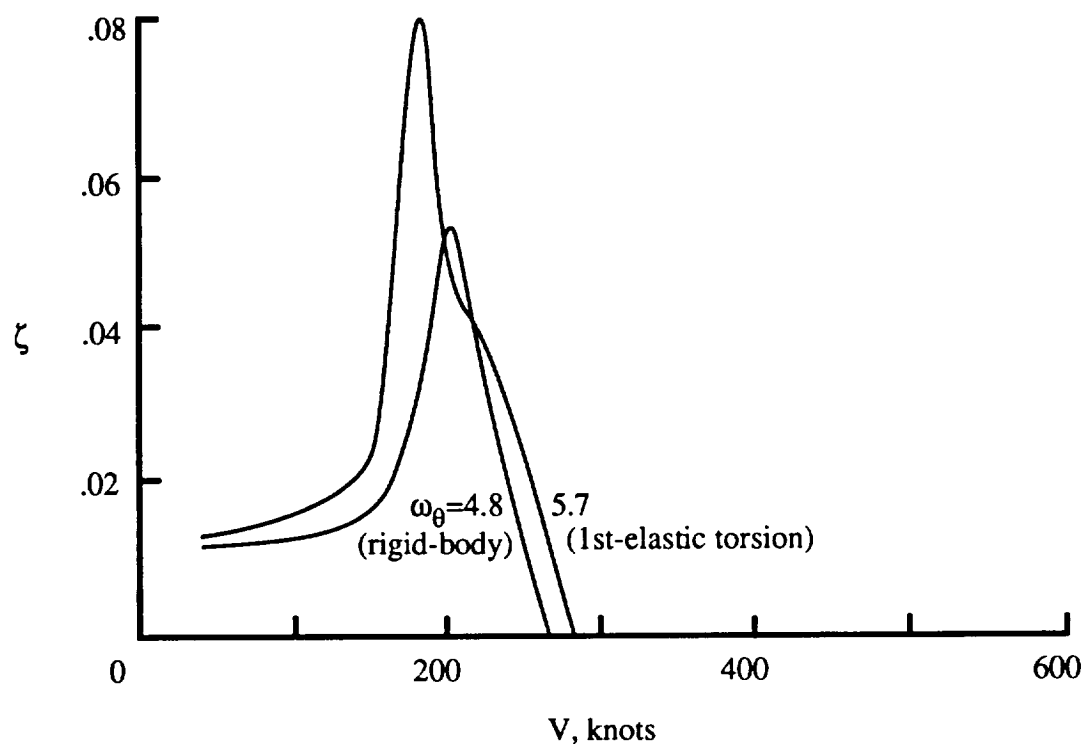
Figure 8.18: Comparison of wing beam mode damping ratio as a function of blade torsion mode selection.

313
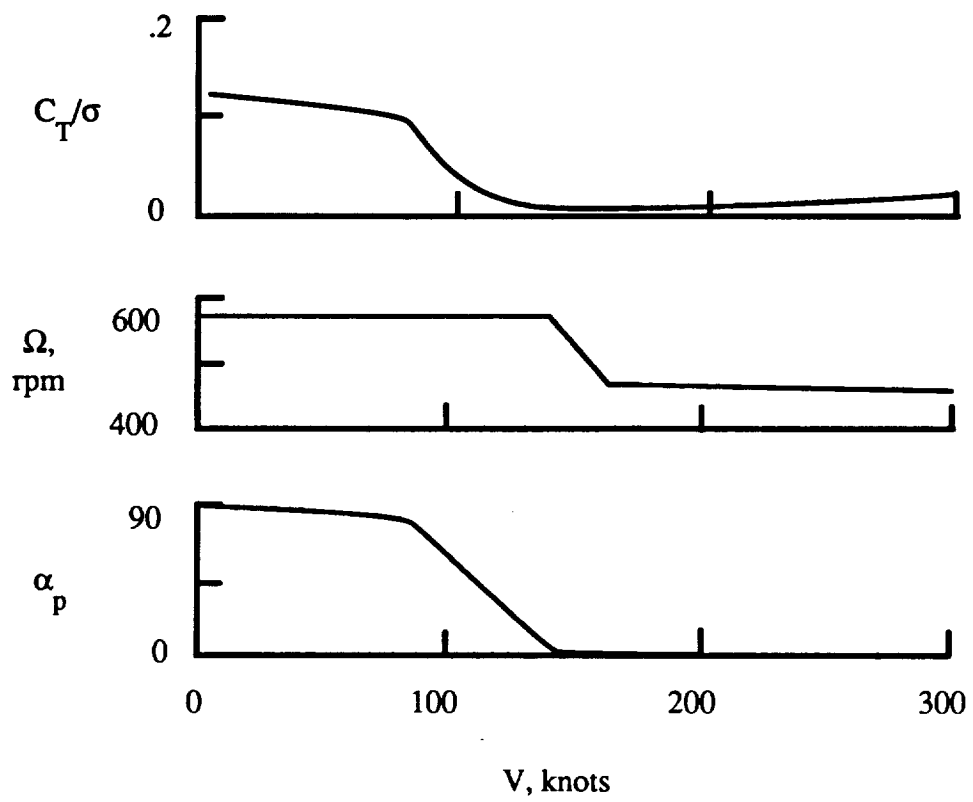
Figure 8.19: Gimballed rotor system input parameters for helicopter, conversion, and airplane flight modes.
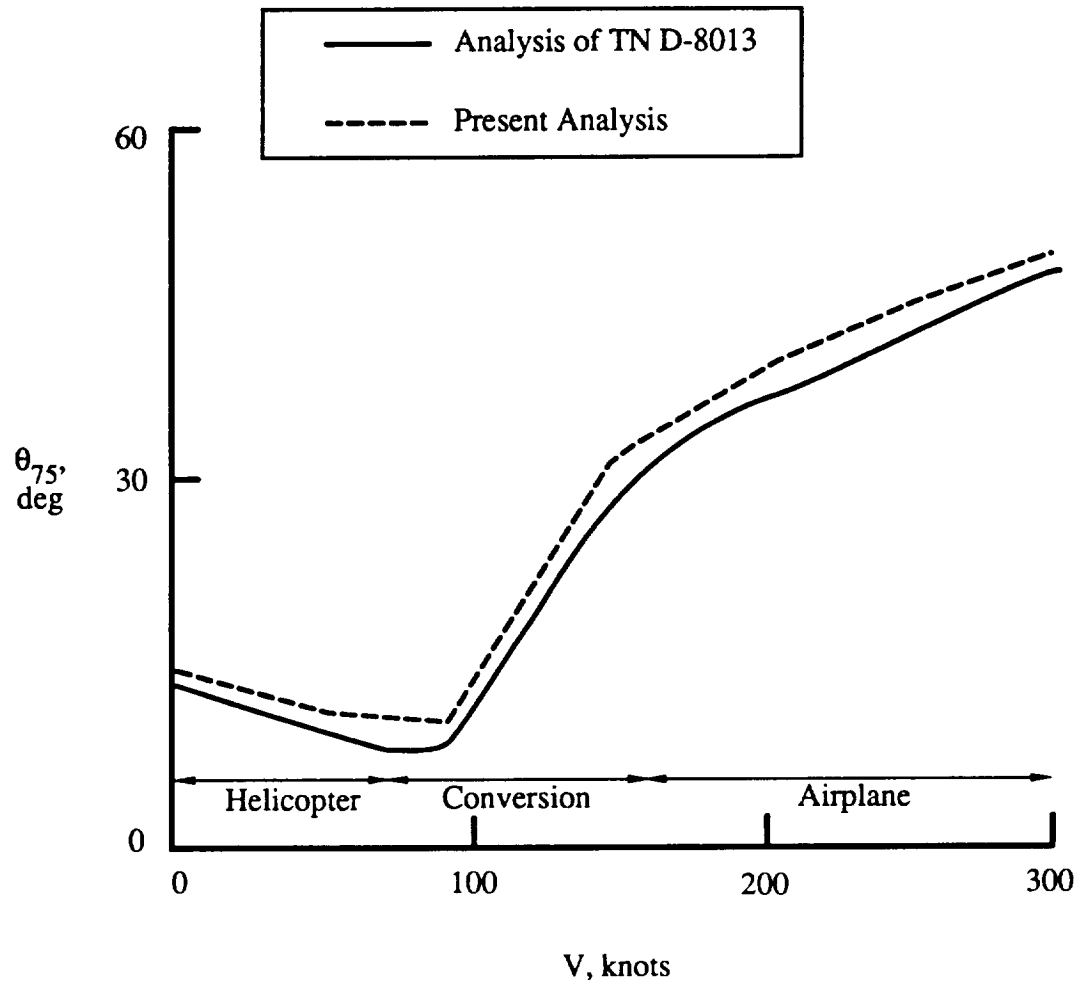
Figure 8.20: Comparison of rotor system trim collective for helicopter, conversion, and airplane flight modes.
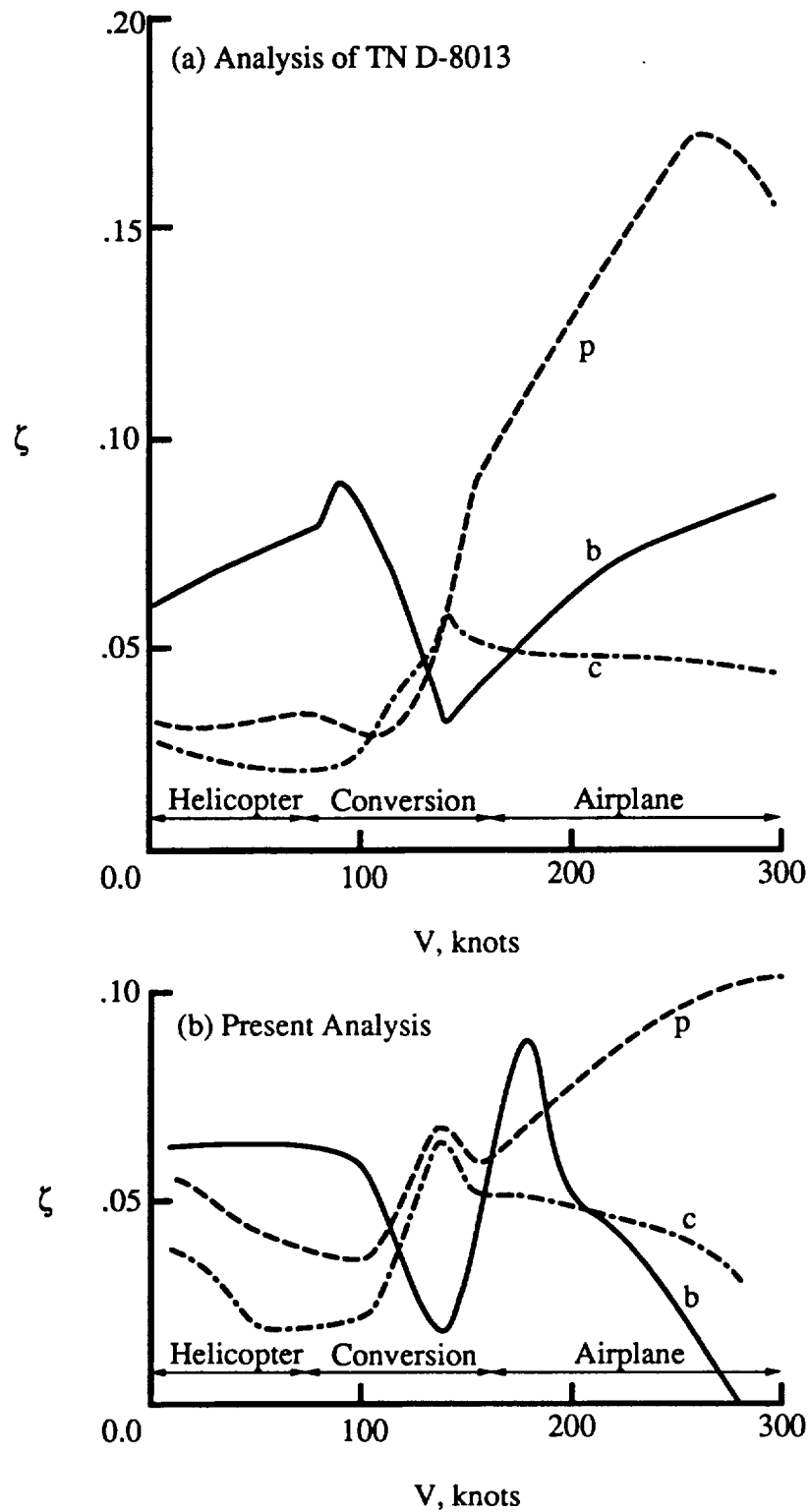
Figure 8.21: Comparison of wing-mode damping for helicopter, conversion, and airplane flight modes.
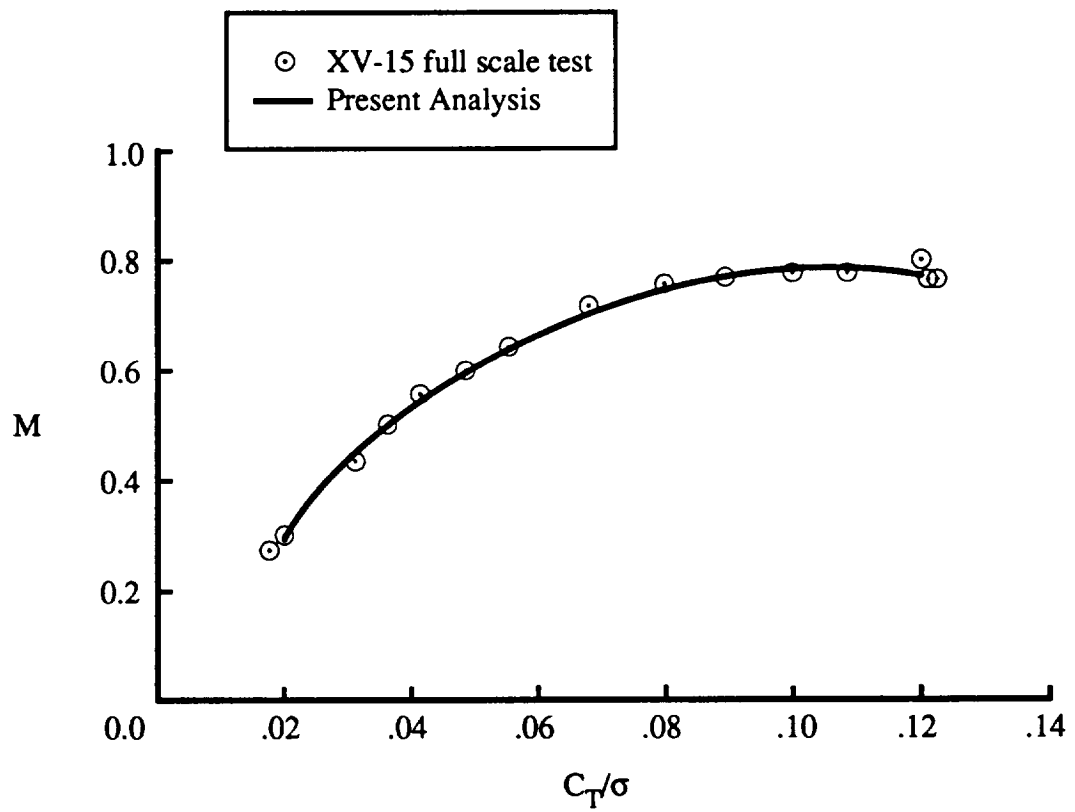
Figure 8.22: Comparison of hover figure of merit predictions with full-scale XV-15 test results.
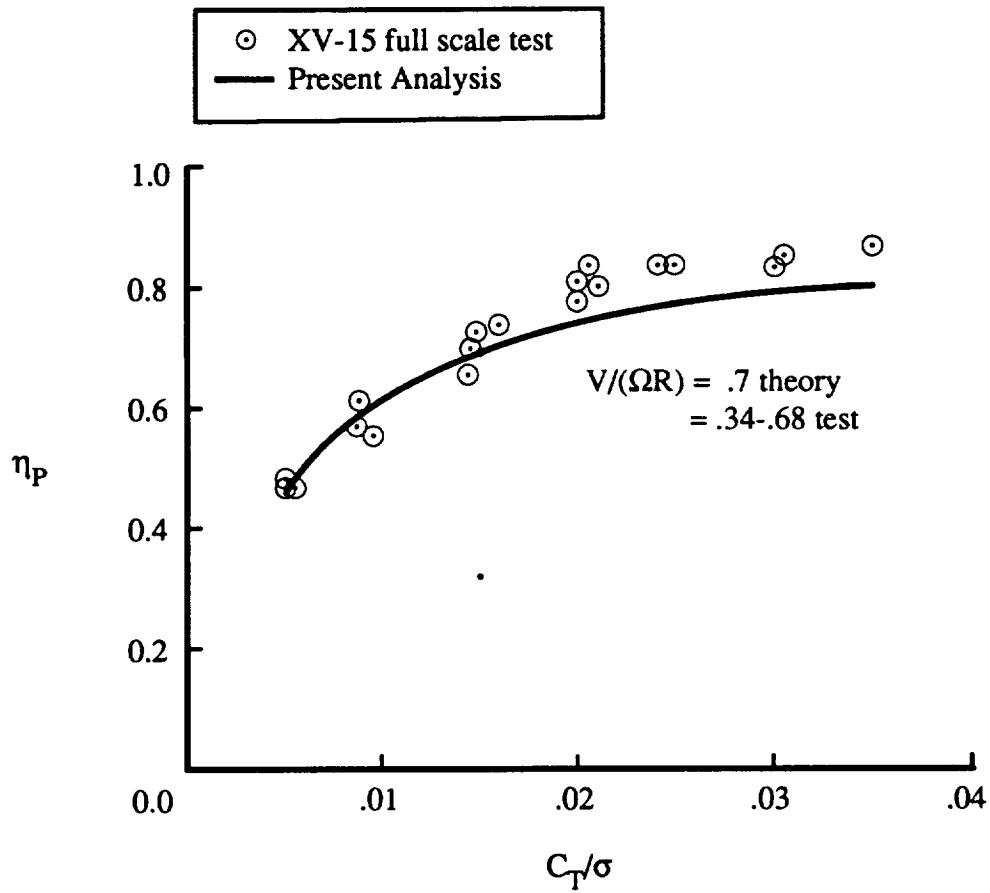
Figure 8.23: Comparison of cruise propeller efficiency predictions with full-scale XV-15 test results.
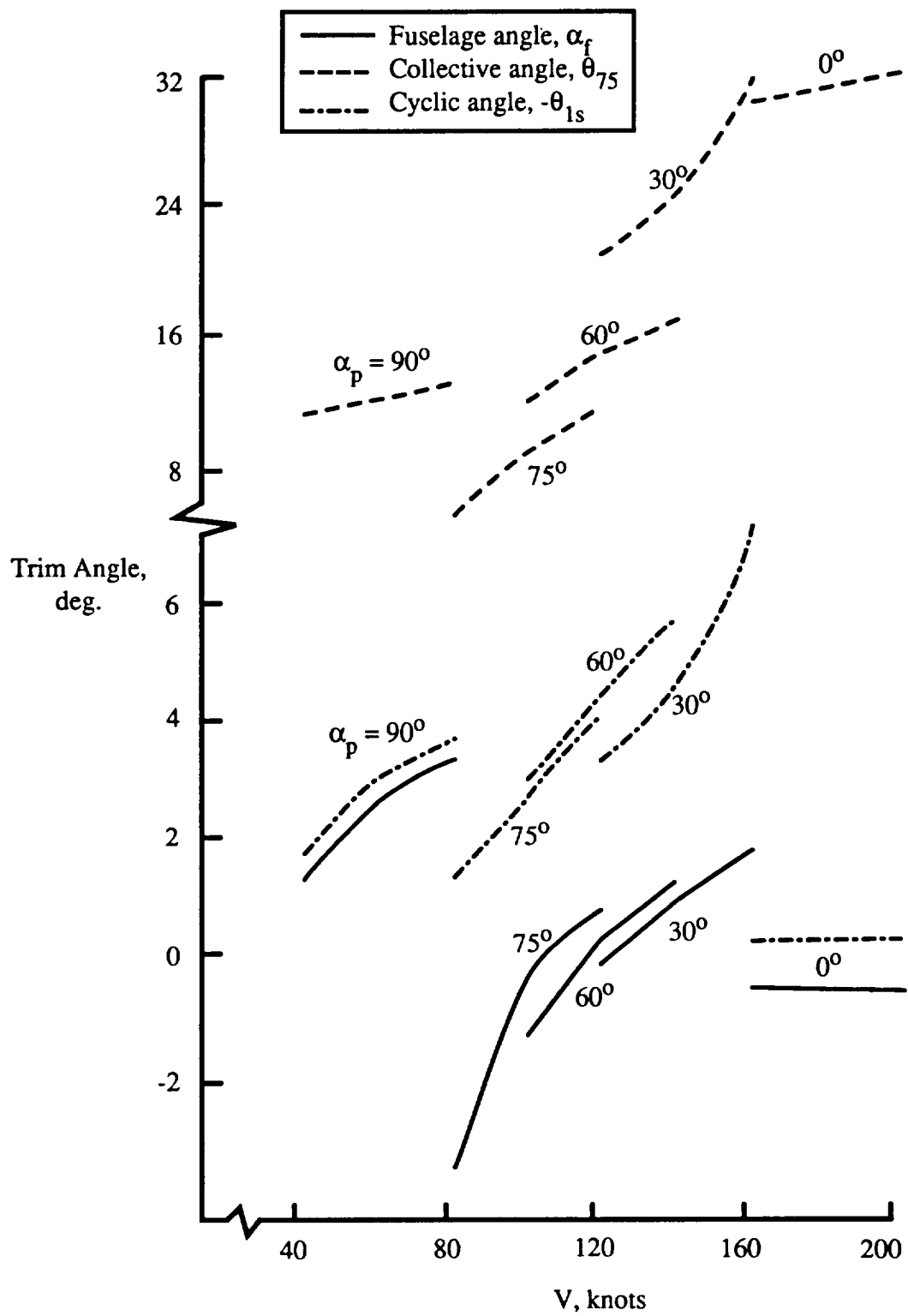
Figure 8.24: Free-flight predicted trim angles.
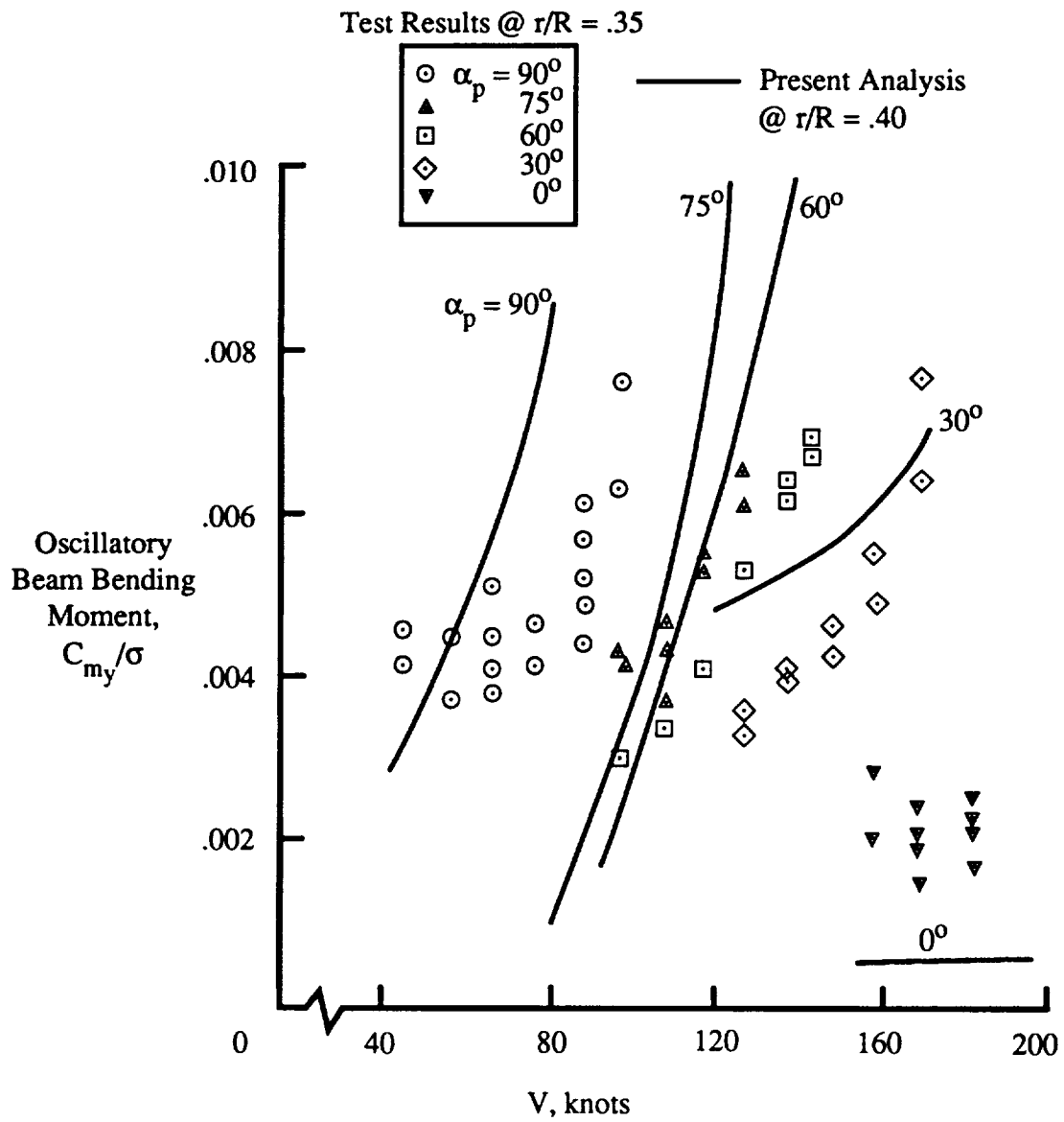
Figure 8.25: Comparison of free-flight blade bending moment predictions with flight test results.
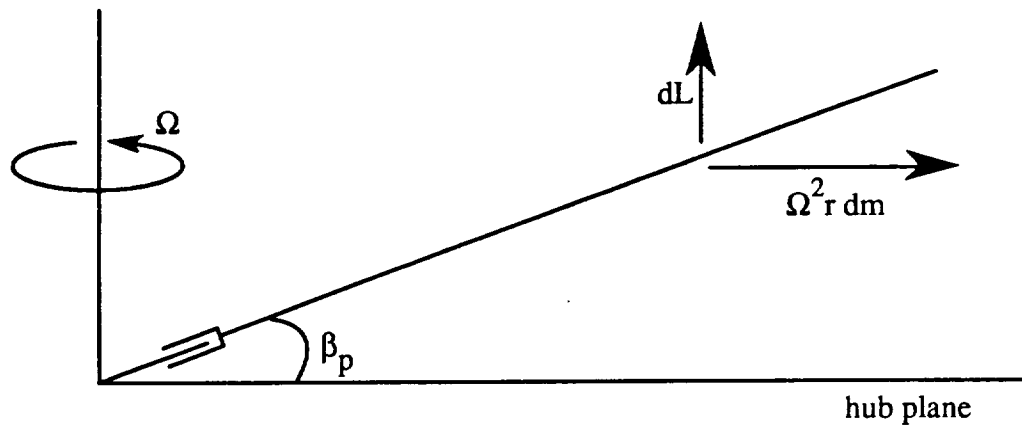
(a) Equilibrium of lift and centrifugal forces.
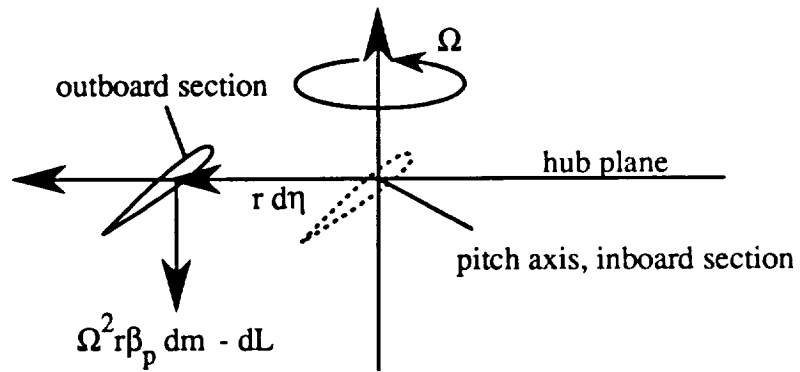
(b) Torsion about inboard sections due to lag motion.

Figure 8.26: Cause of tiltrotor adverse pitch-lag dynamics.
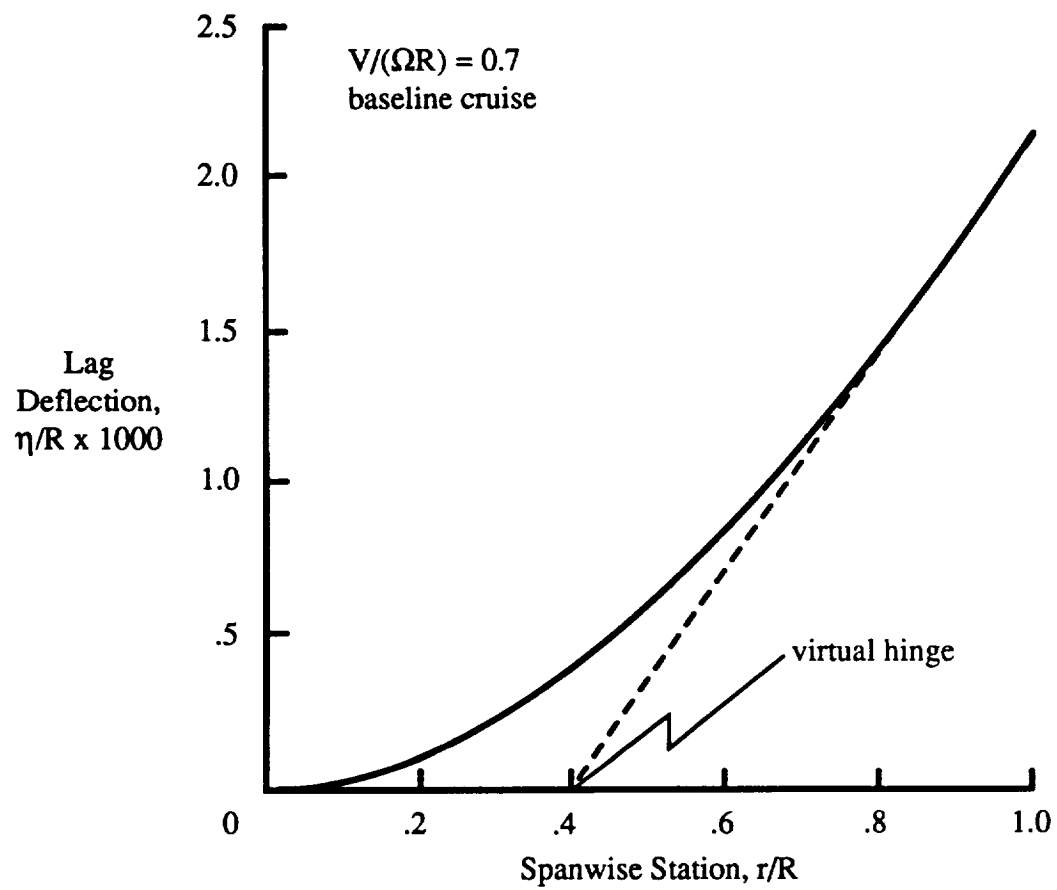
Figure 8.27: Elastic lag deflection of baseline rotor blade in cruise mode.
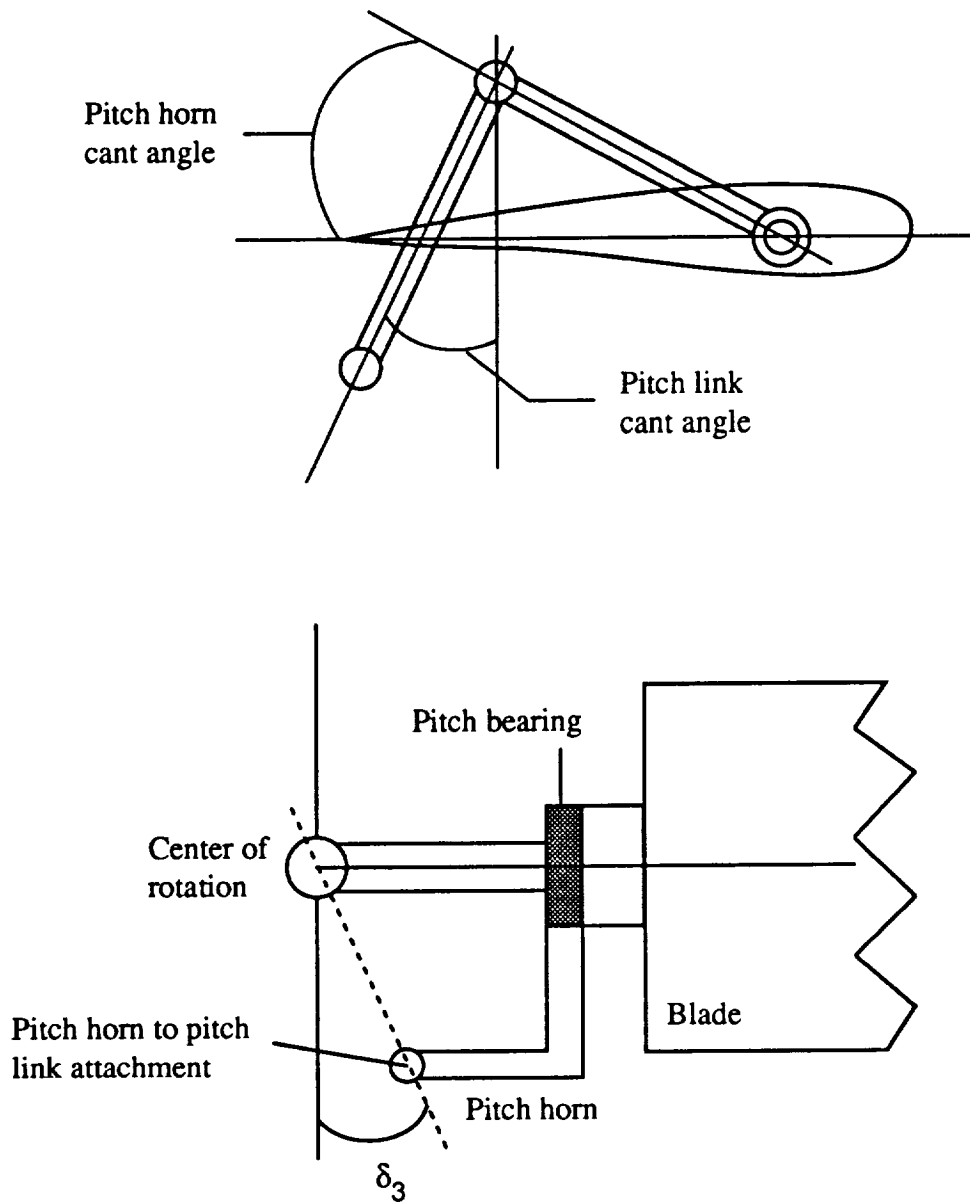
Figure 8.28: Control system parameters used to introduce kinematic couplings.

323
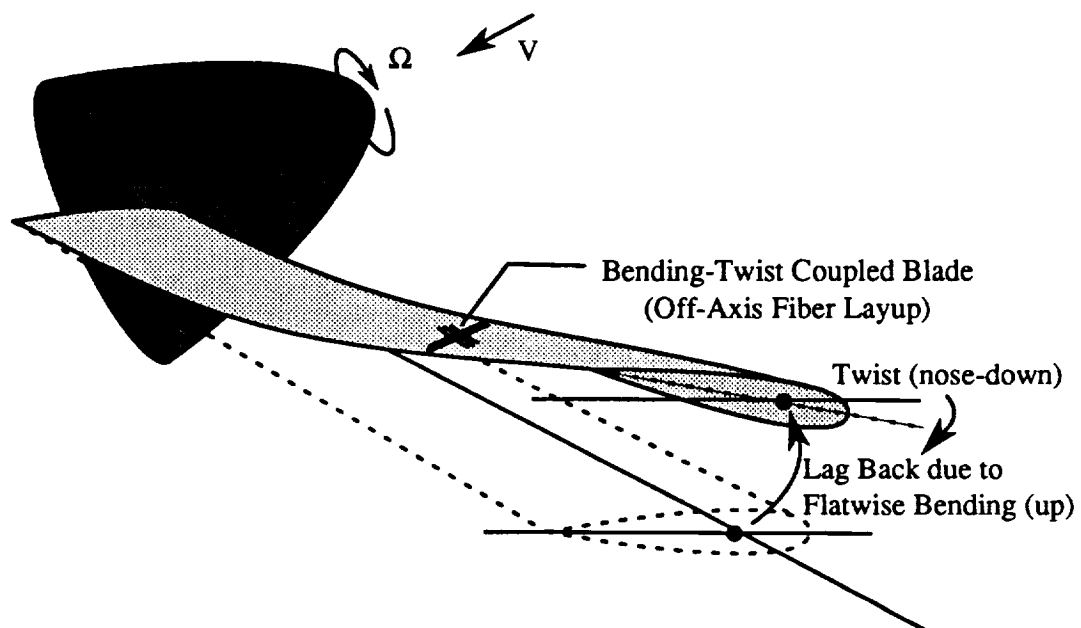
Figure 8.29: Bending-twist-coupled tiltrotor blade.
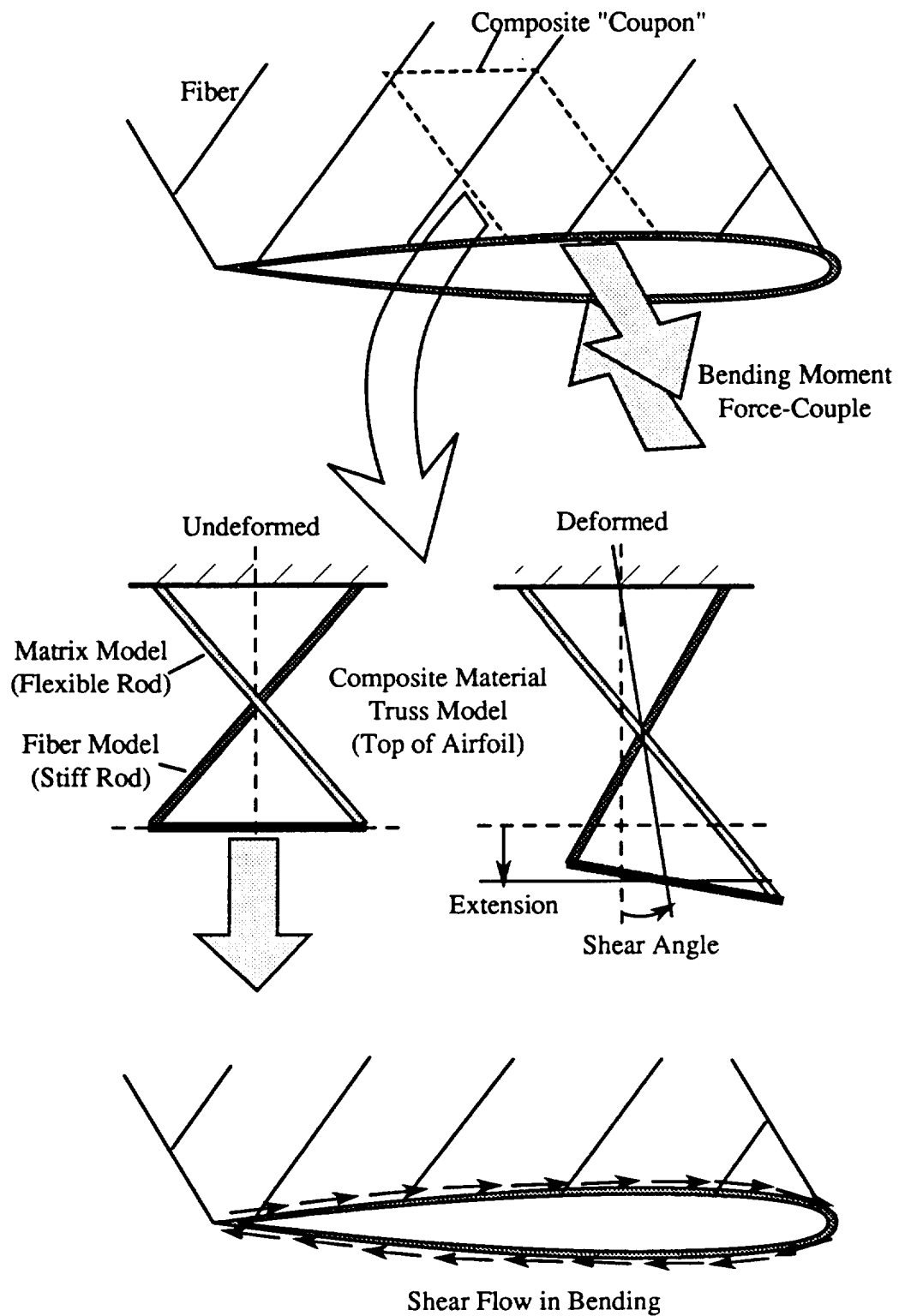
Figure 8.30: Composite material truss model used to explain elastic coupling in blade.

thickness = .224 in.
(18 plies x .0124 in./ply)

Chord = 14 in.
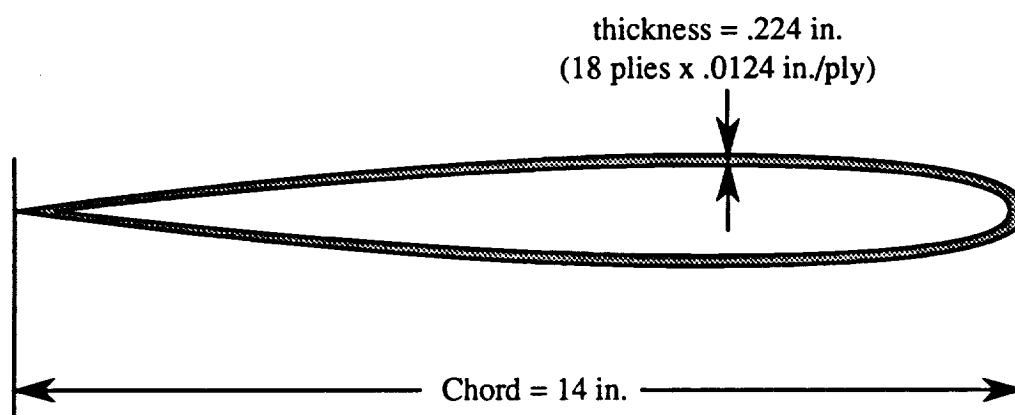
Figure 8.31: Cross section of a NACA 0012 airfoil section and associated dimensions for the composite blade analytical model.
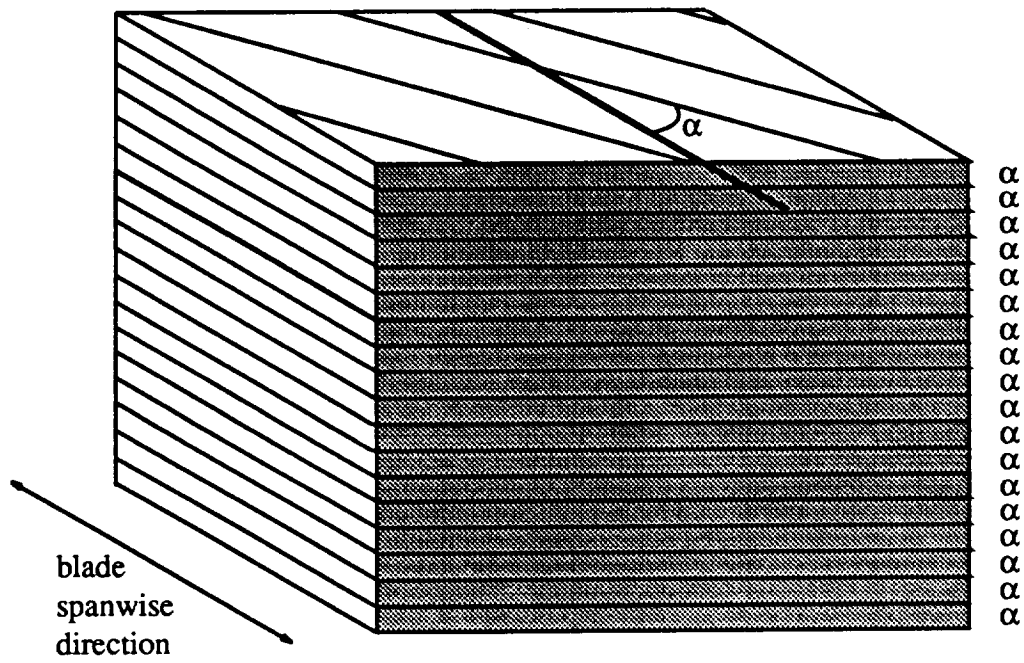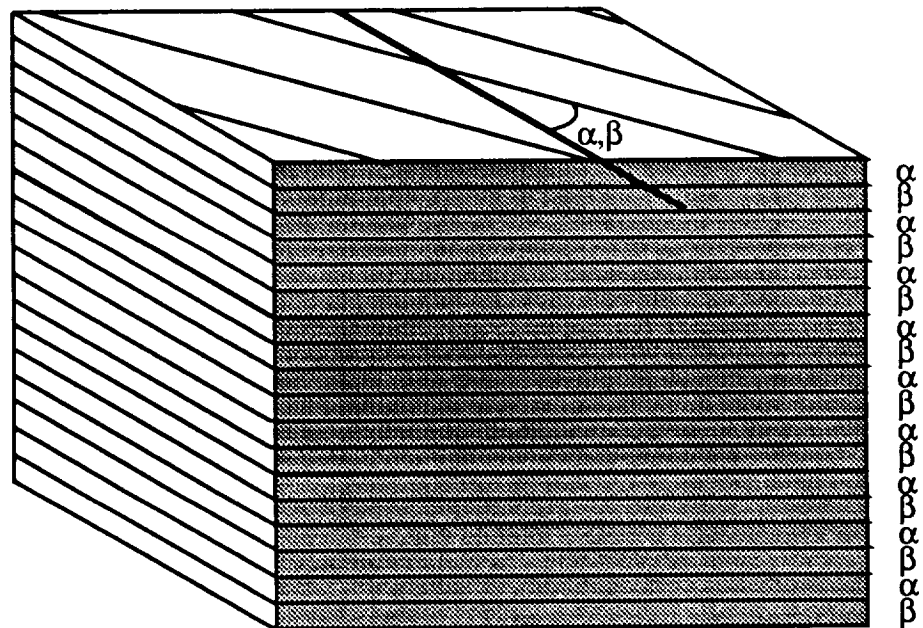
Figure 8.32: Two laminate cases considered for the composite blade analytical model.
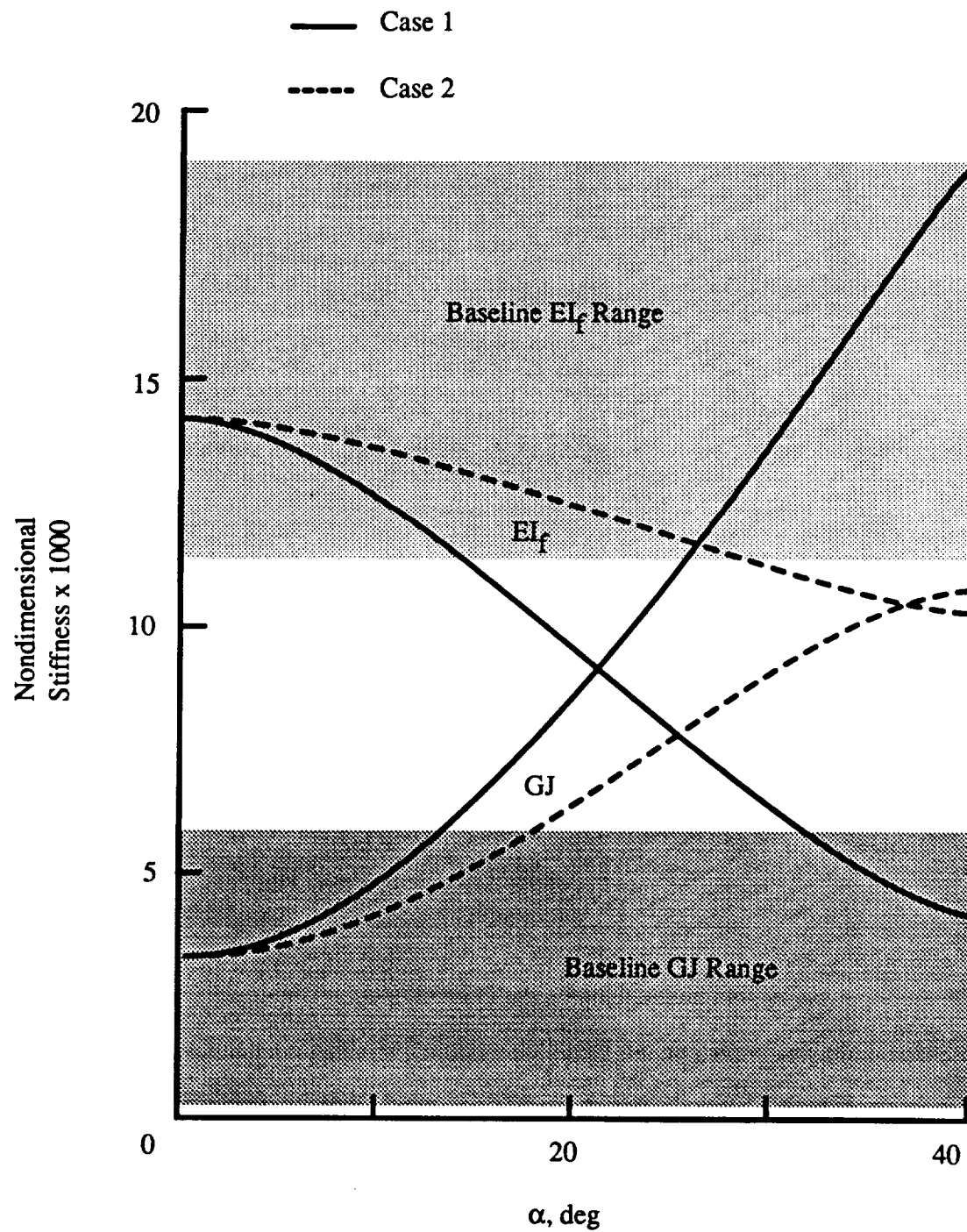
Figure 8.33: Blade stiffnesses as a function of off-axis ply angle for the bending-twist-coupled blade.
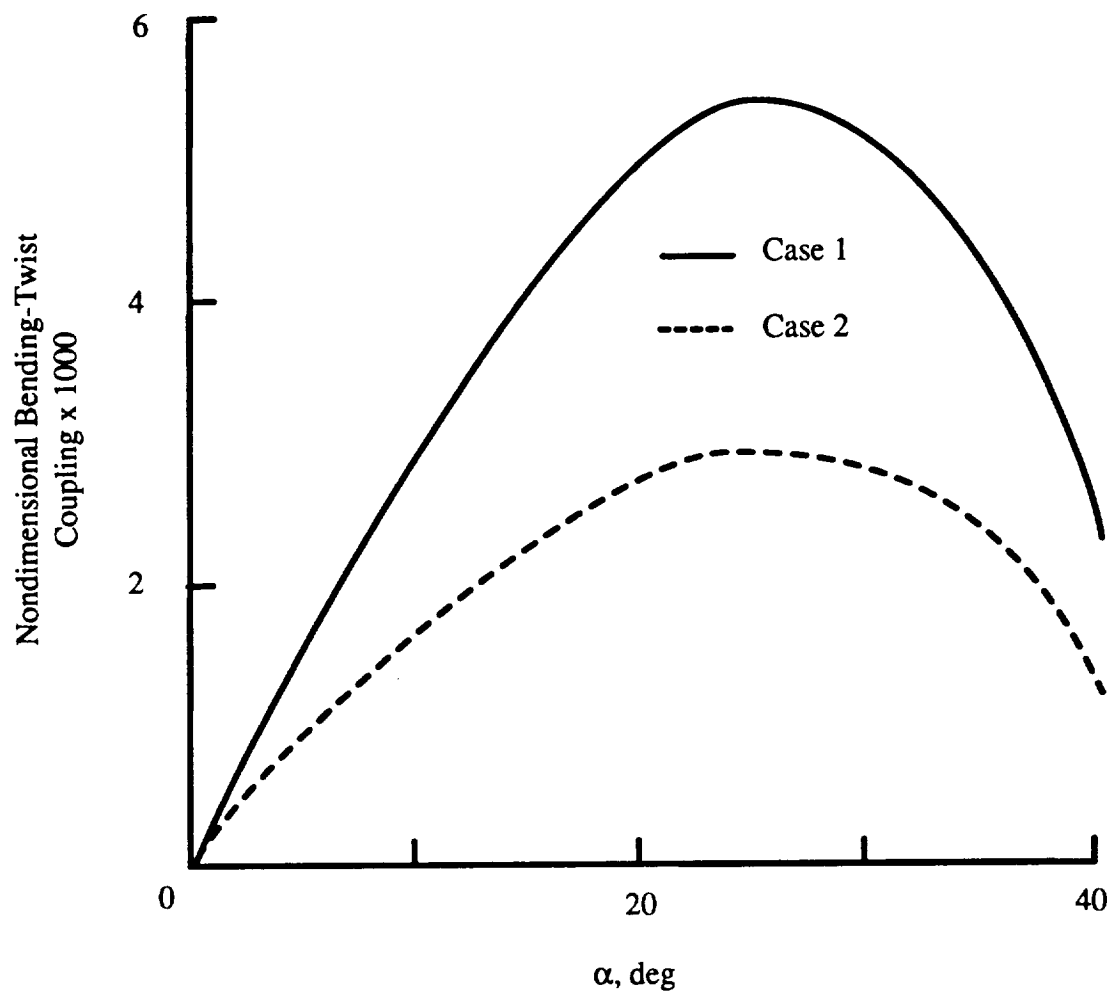
Figure 8.34: Blade flatwise-bending-twist-coupling stiffness as a function of off-axis ply angle.
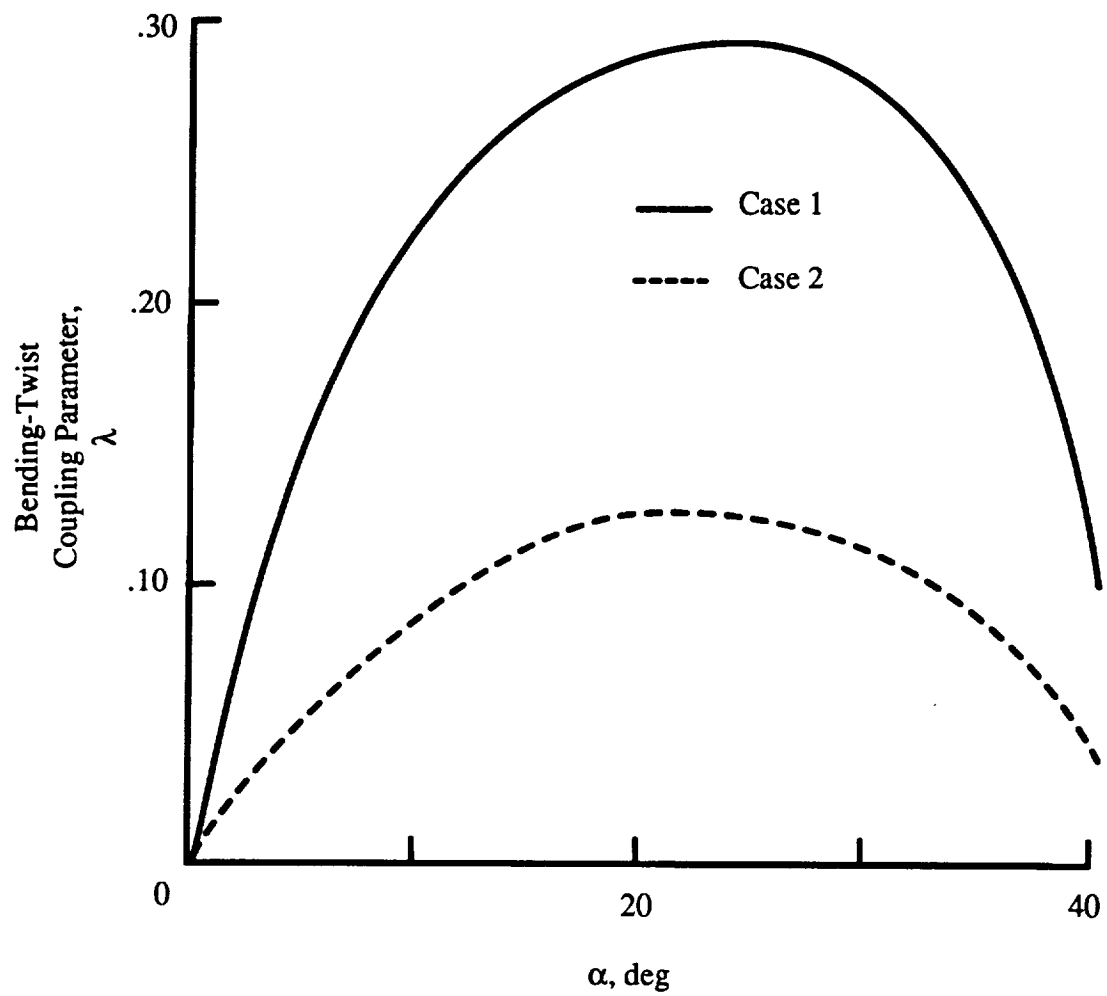
Figure 8.35: Blade flatwise-bending-twist-coupling parameter as a function of off-axis ply angle.
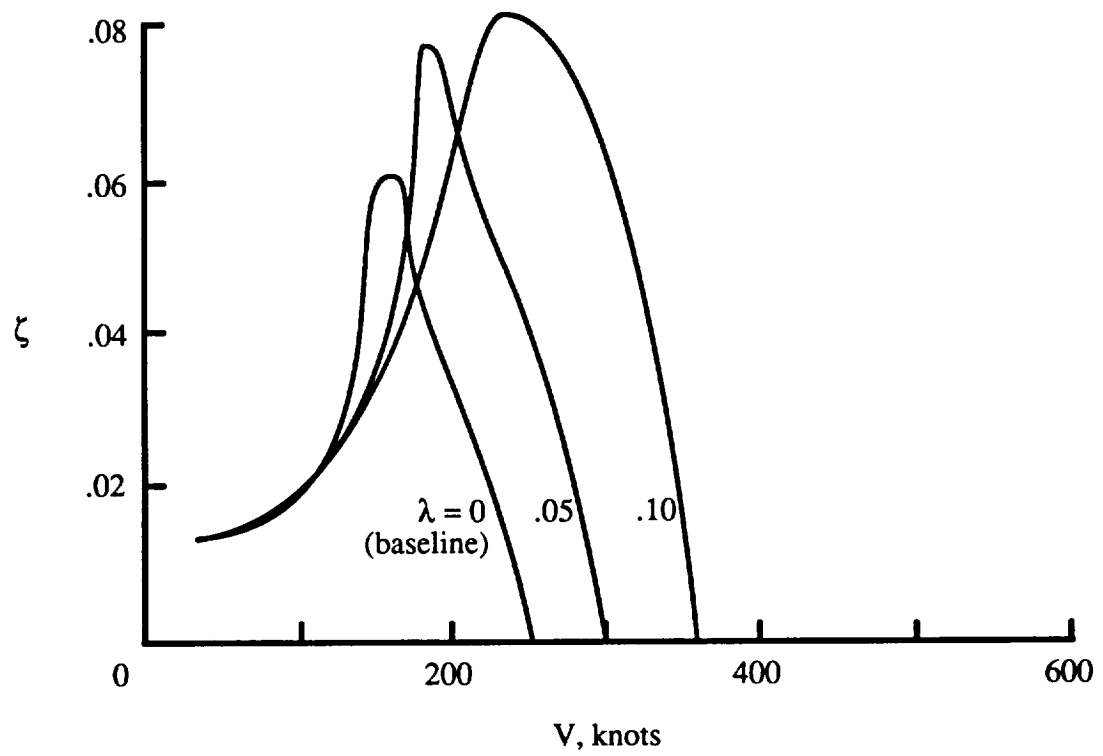
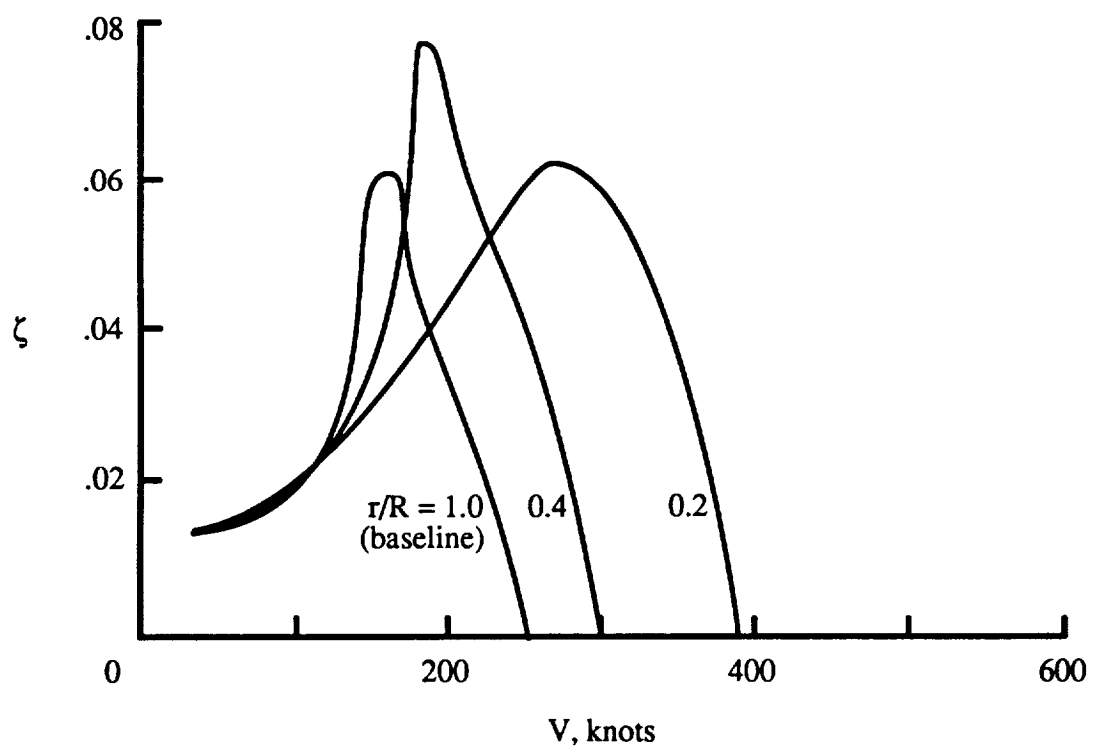Figure 8.36: Influence of blade bending-twist-coupling parameter on wing beam-mode damping.

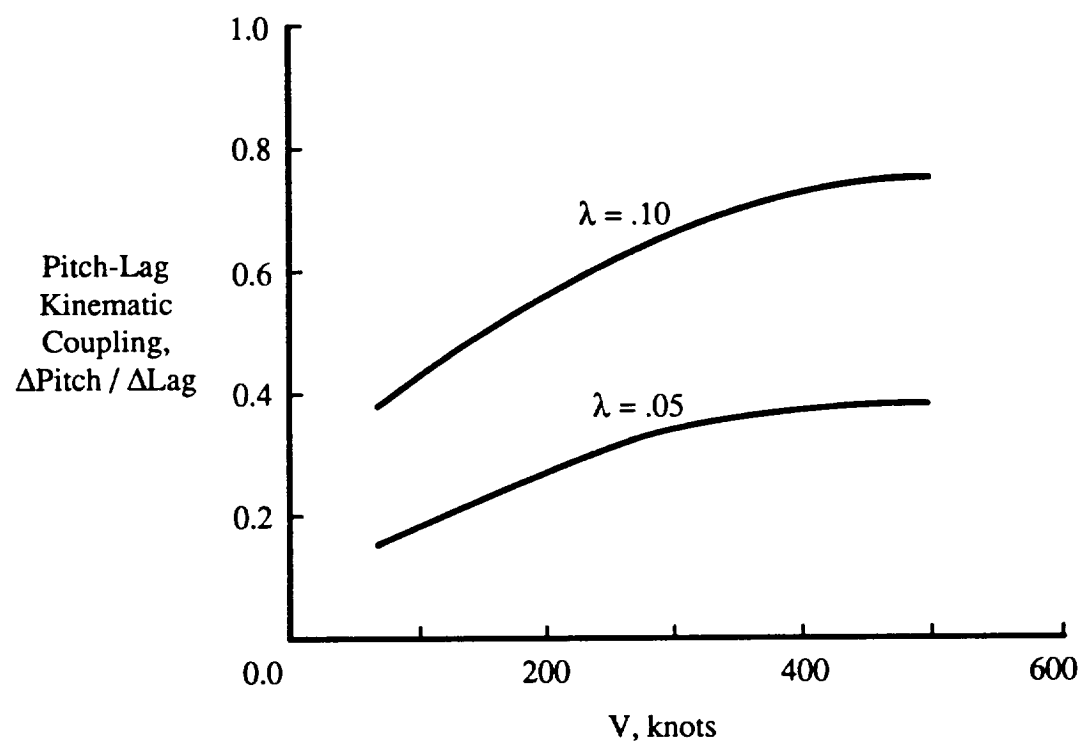Figure 8.37: Influence of blade bending-twist-coupling spanwise-initiation on wing beam-mode damping.

Figure 8.38: Effective kinematic pitch-lag coupling for a bending-twist-coupled tiltrotor blade.
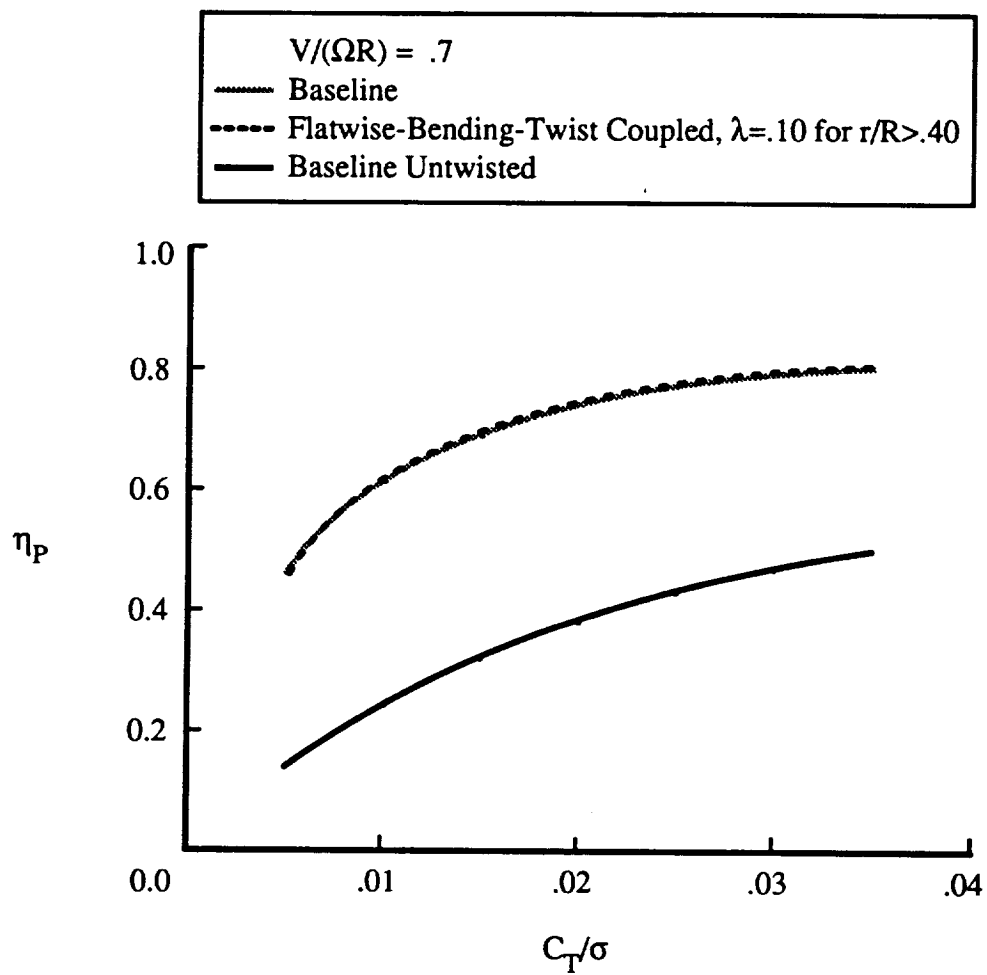
Figure 8.39: Cruise performance comparison for a bending-twist-coupled blade design.
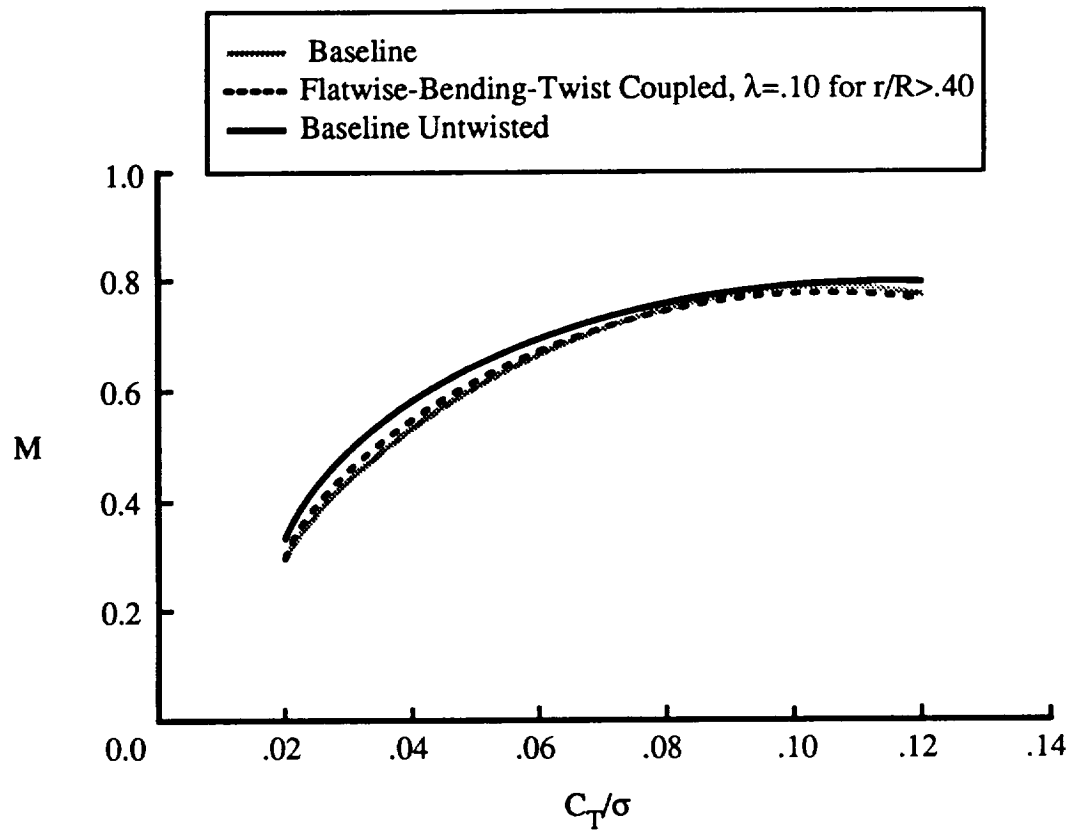
Figure 8.40: Hover performance comparison for a bending-twist-coupled blade design.
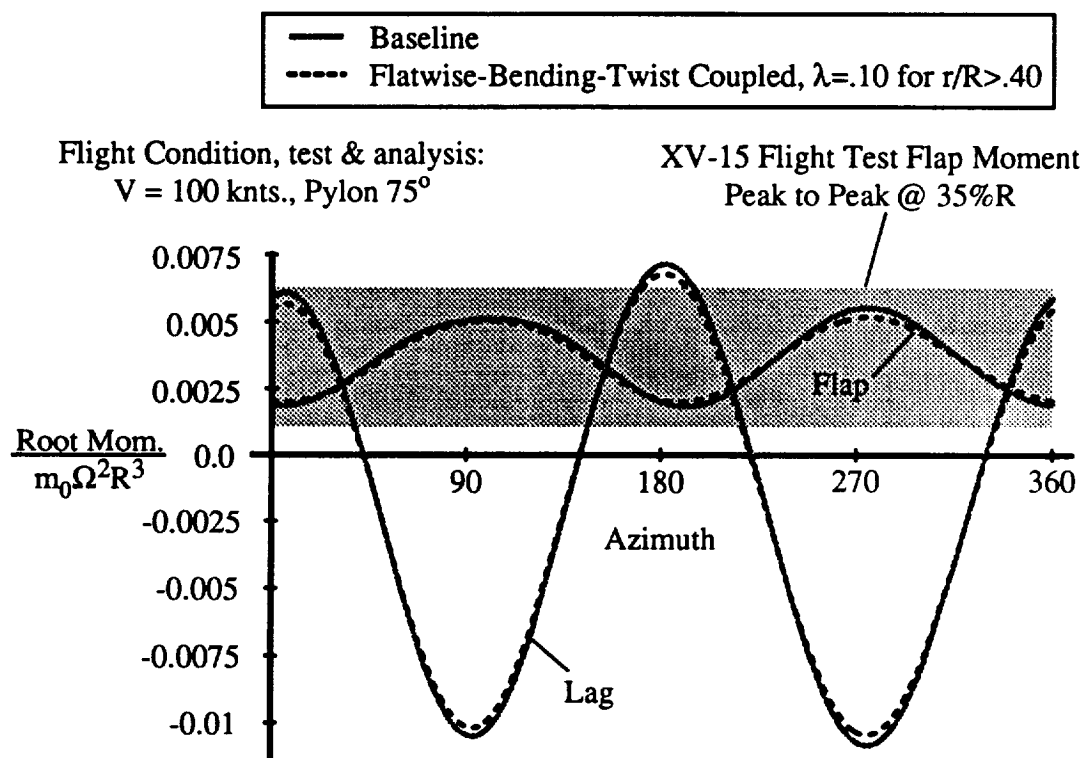
Figure 8.41: Root-end bending moment comparison for a bending-twist-coupled blade design.
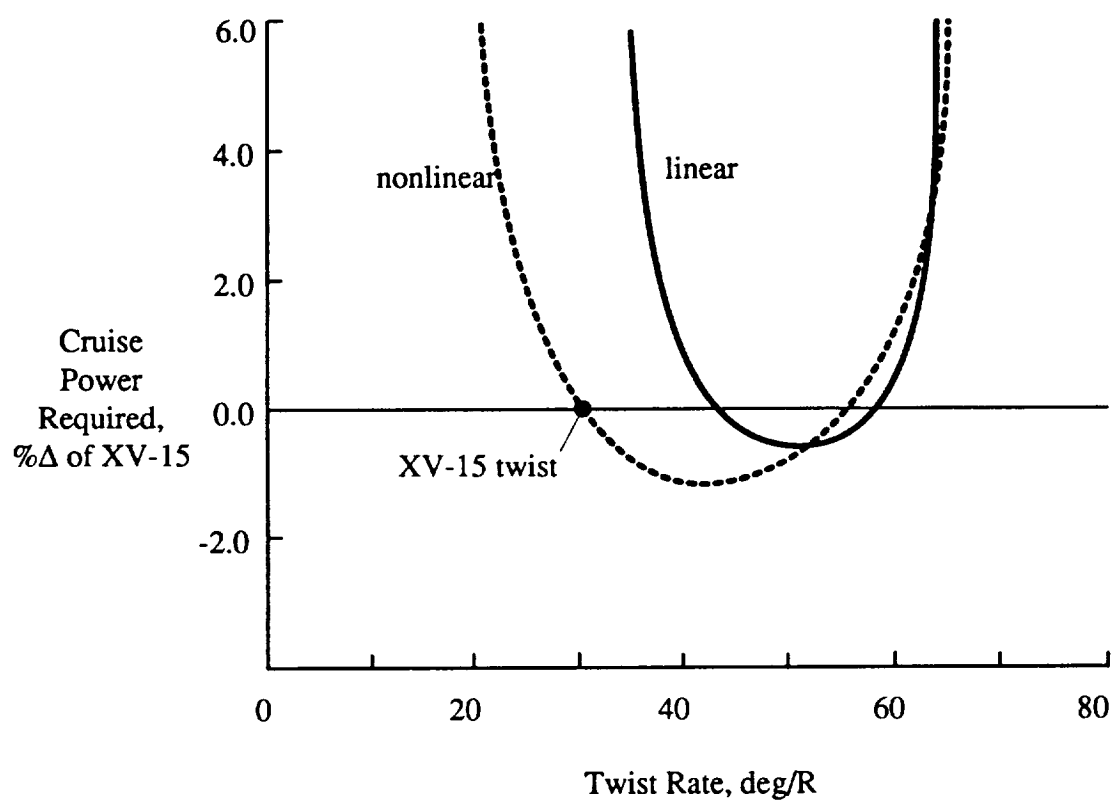
Figure 8.42: Cruise performance as a function blade twist.
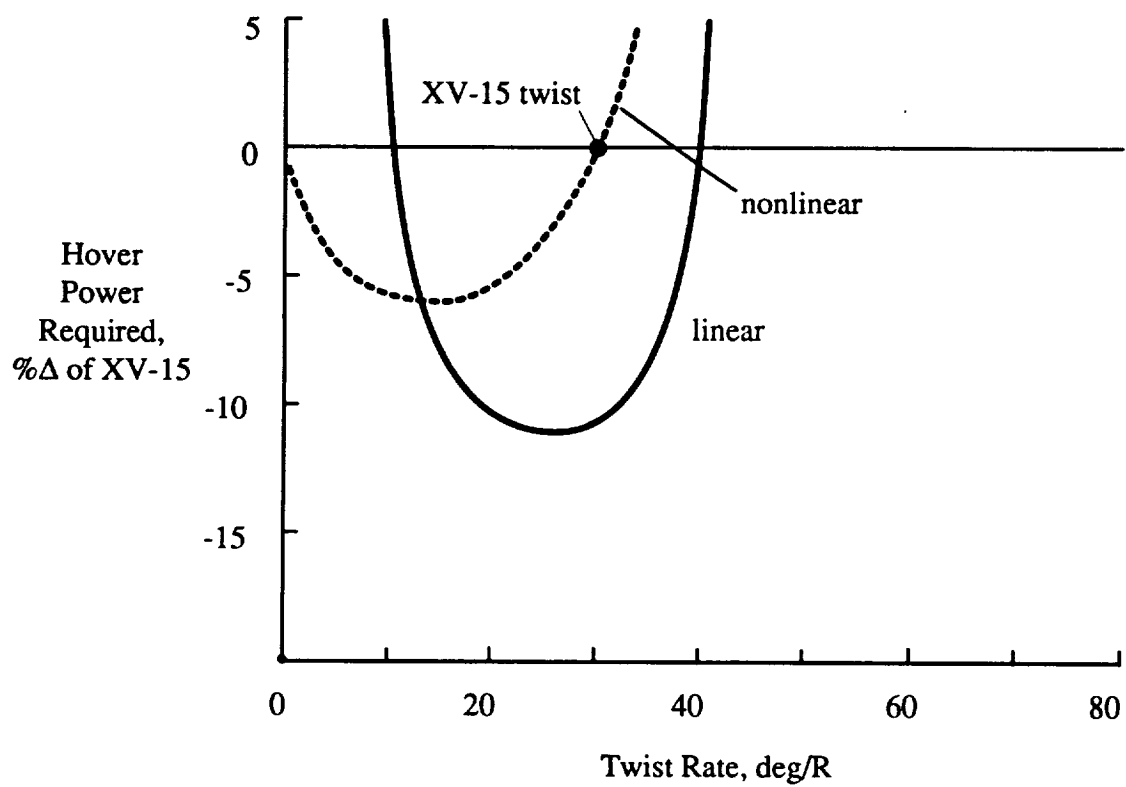
Figure 8.43: Hover performance as a function blade twist.

338
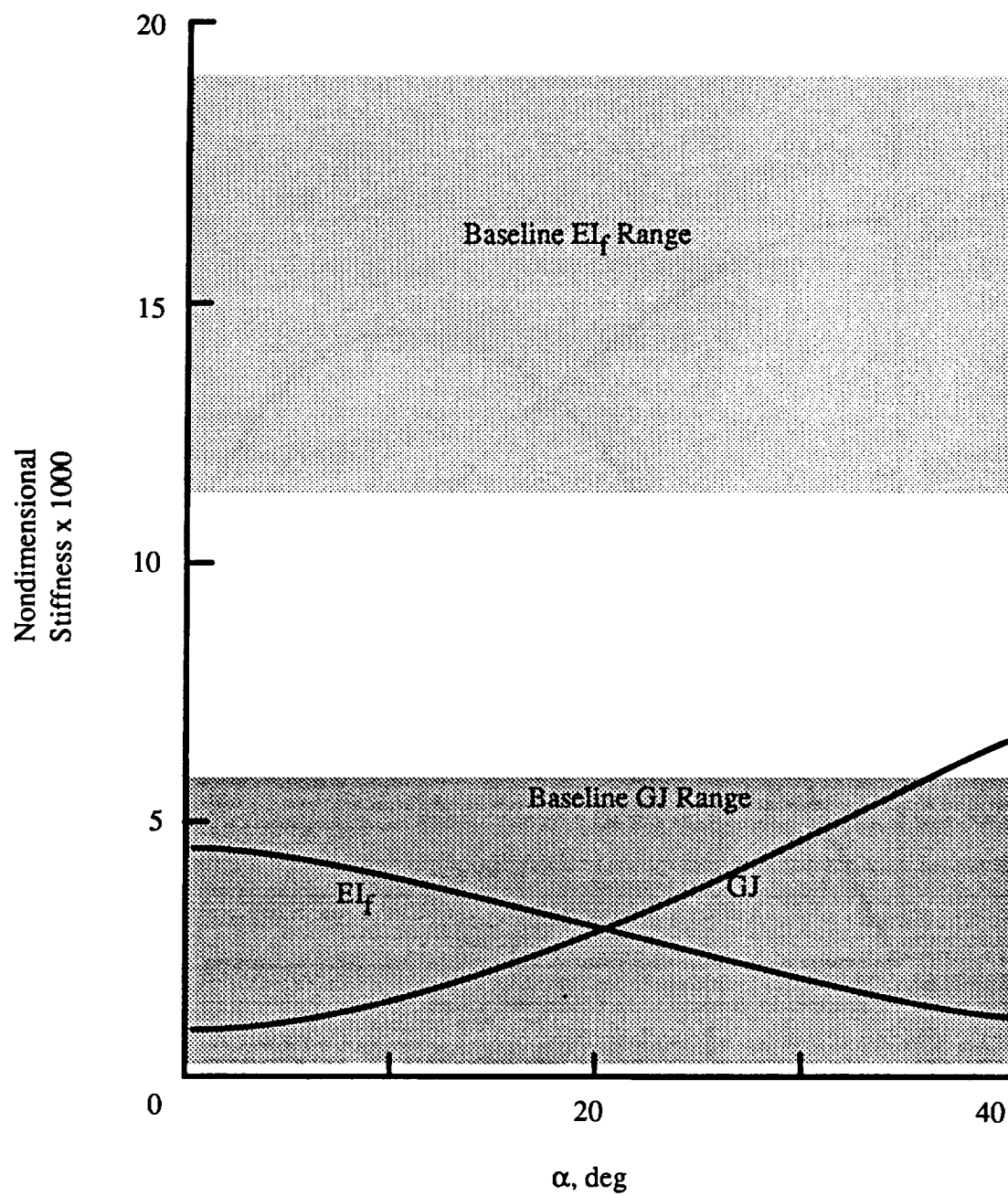
Figure 8.44: Flatwise bending and torsional stiffnesses for a representative extension-twist-coupled blade.
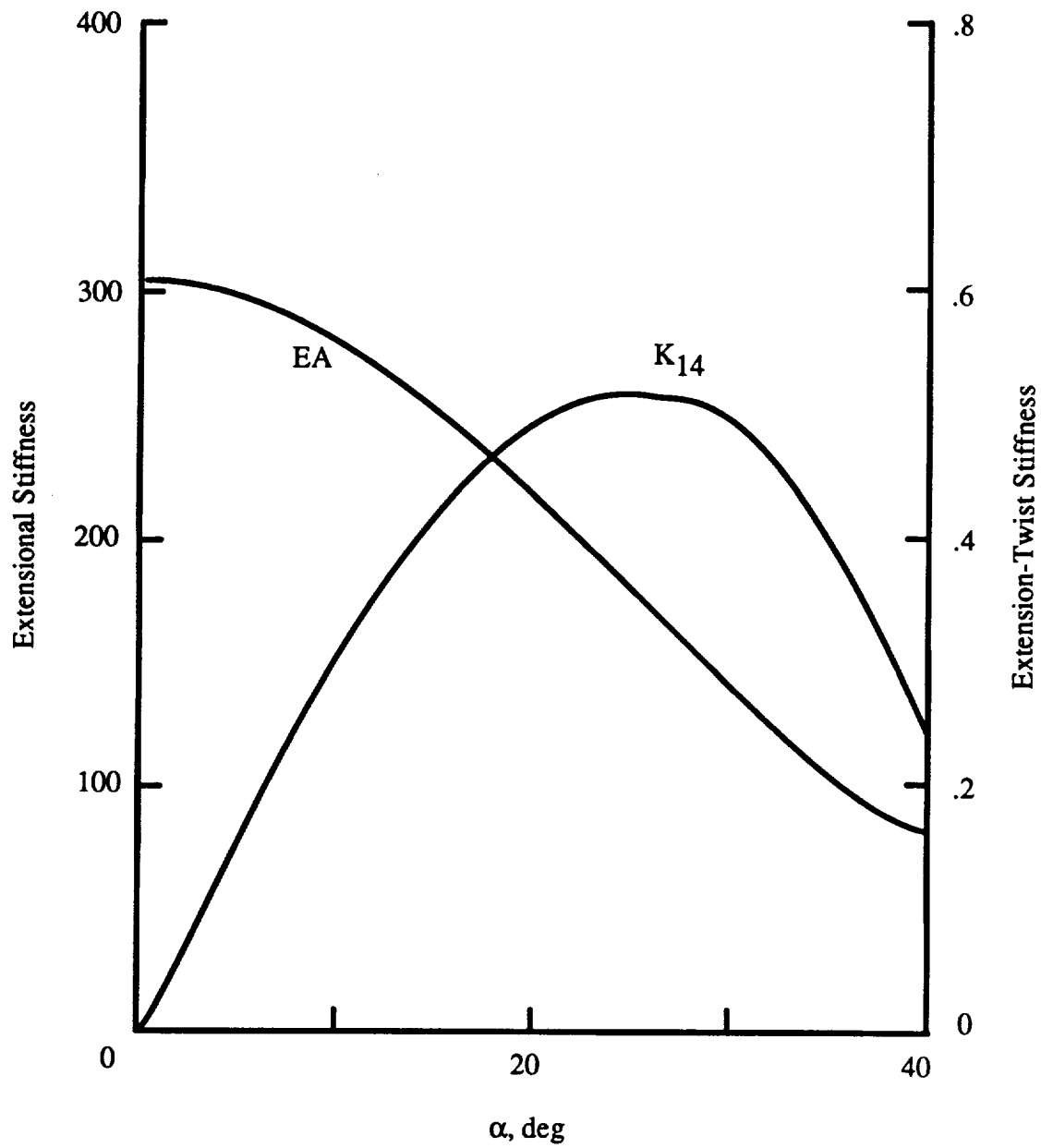
Figure 8.45: Extension and extension-twist stiffnesses for a representative extension-twist-coupled blade.
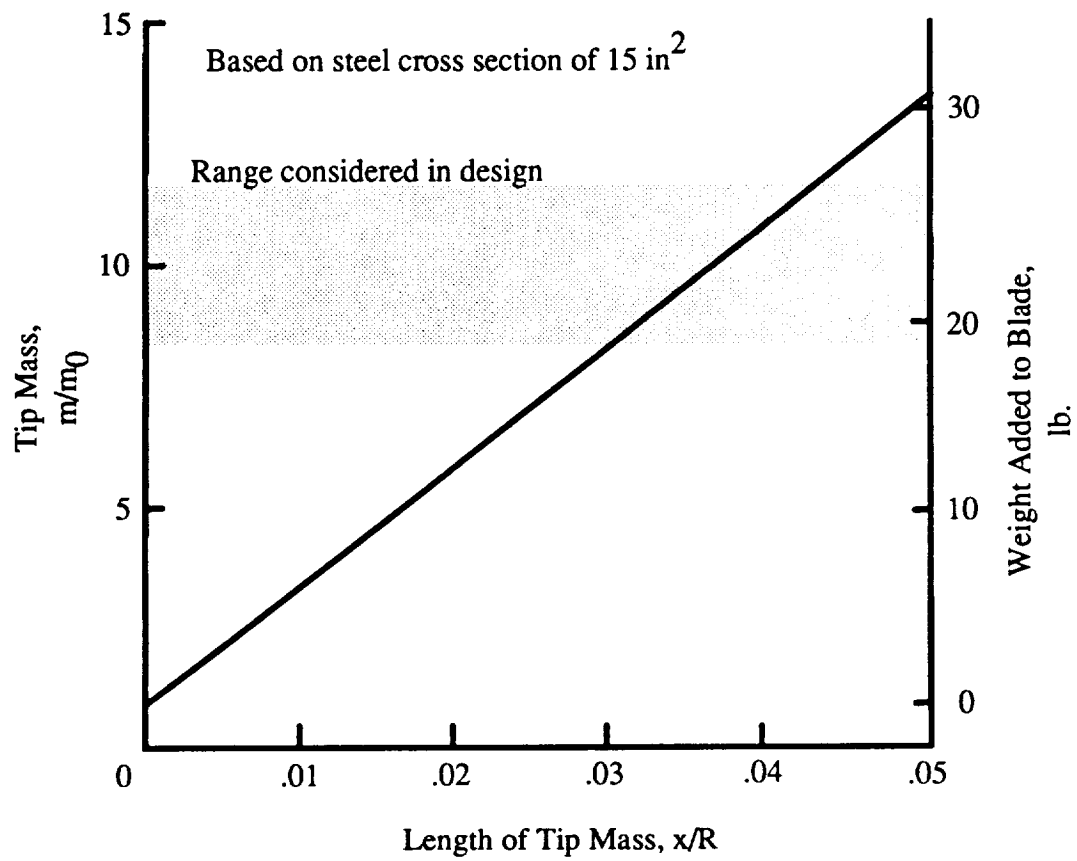
Figure 8.46: Tip mass for a representative extension-twist-coupled blade based on a steel cross section.
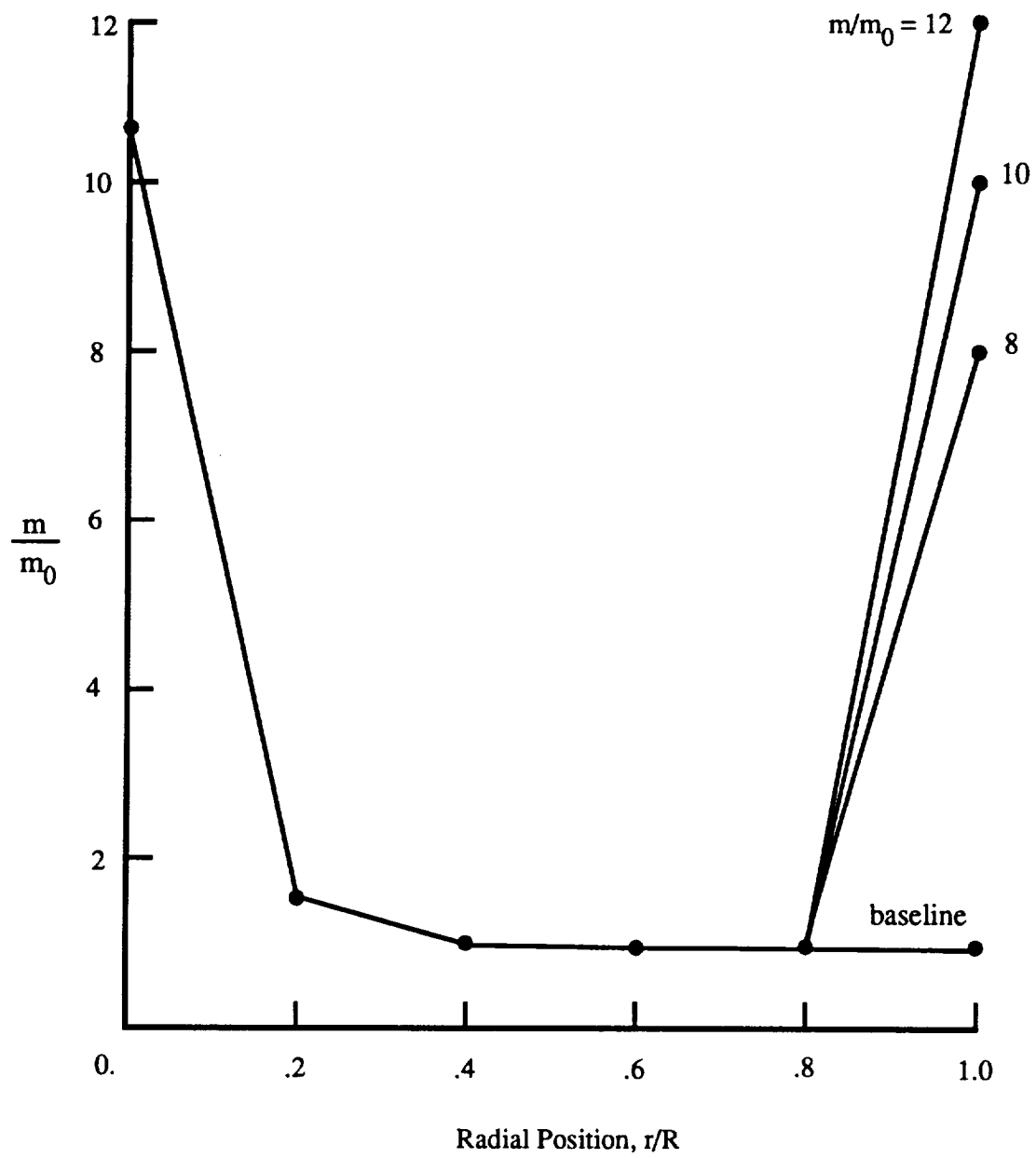
Figure 8.47: Mass distribution of the extension-twist-coupled blade cases.
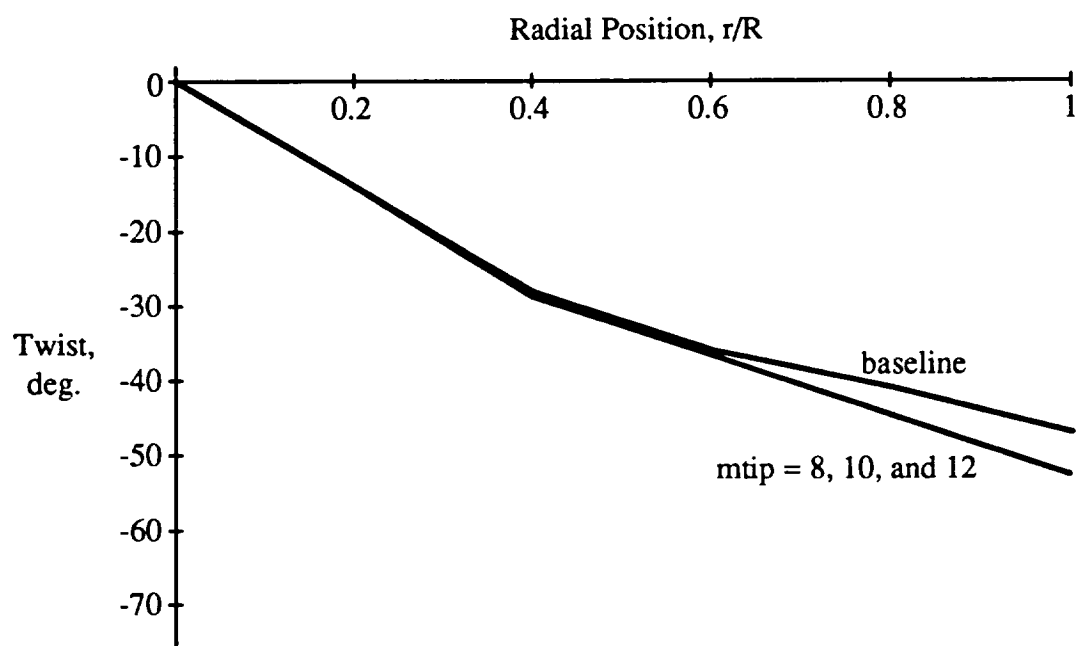
Figure 8.48: Extension-twist-coupled blade twist distributions in cruise mode (100% reference rpm).
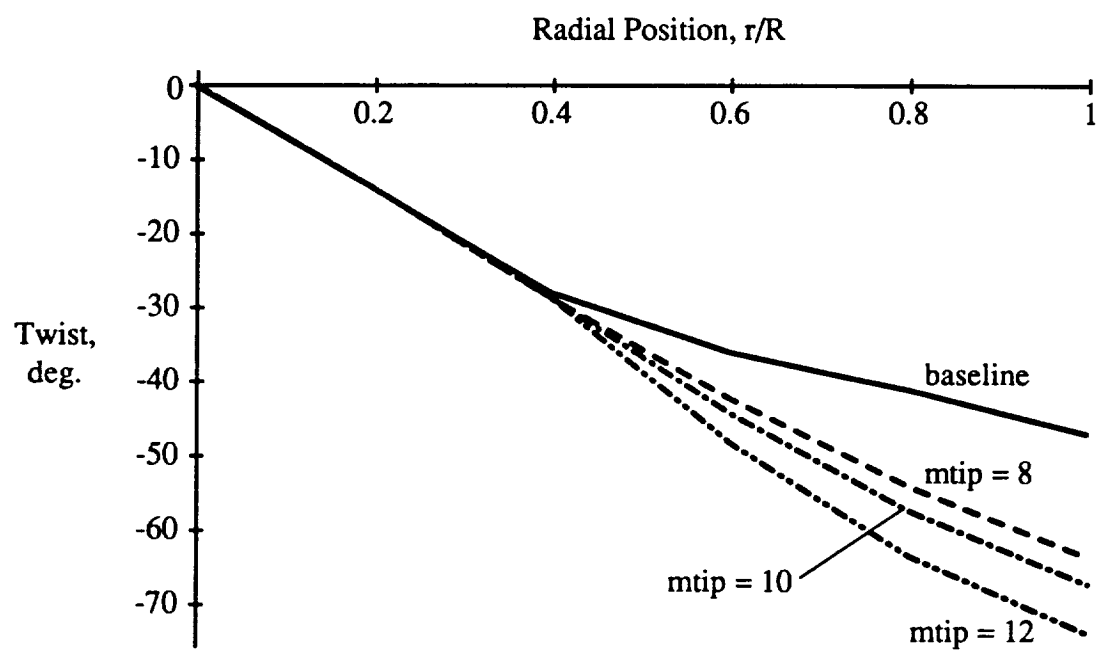
Figure 8.49: Extension-twist-coupled blade twist distributions before deformation (nonrotating).
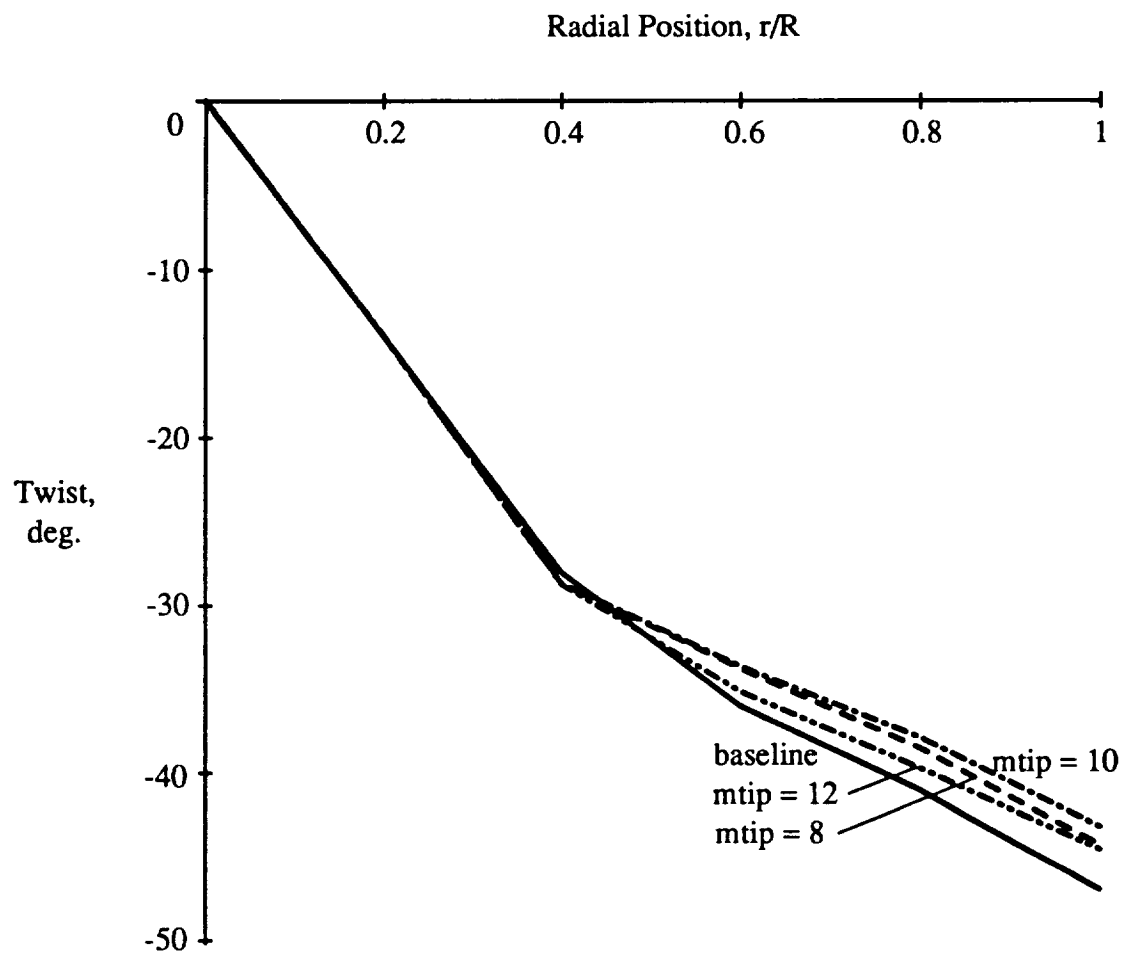
Figure 8.50: Extension-twist-coupled blade twist distributions in hover mode (123% reference rpm).
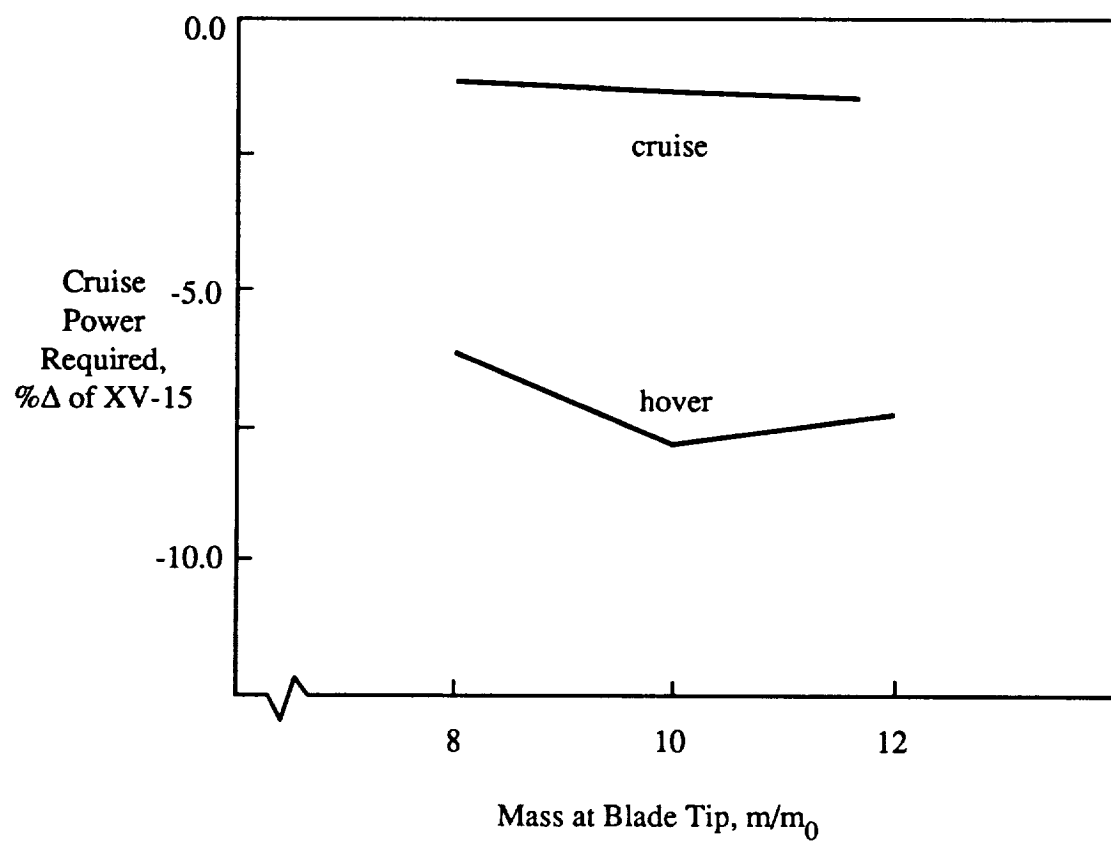
Figure 8.51: Performance comparisons for extension-twist-coupled blade designs.
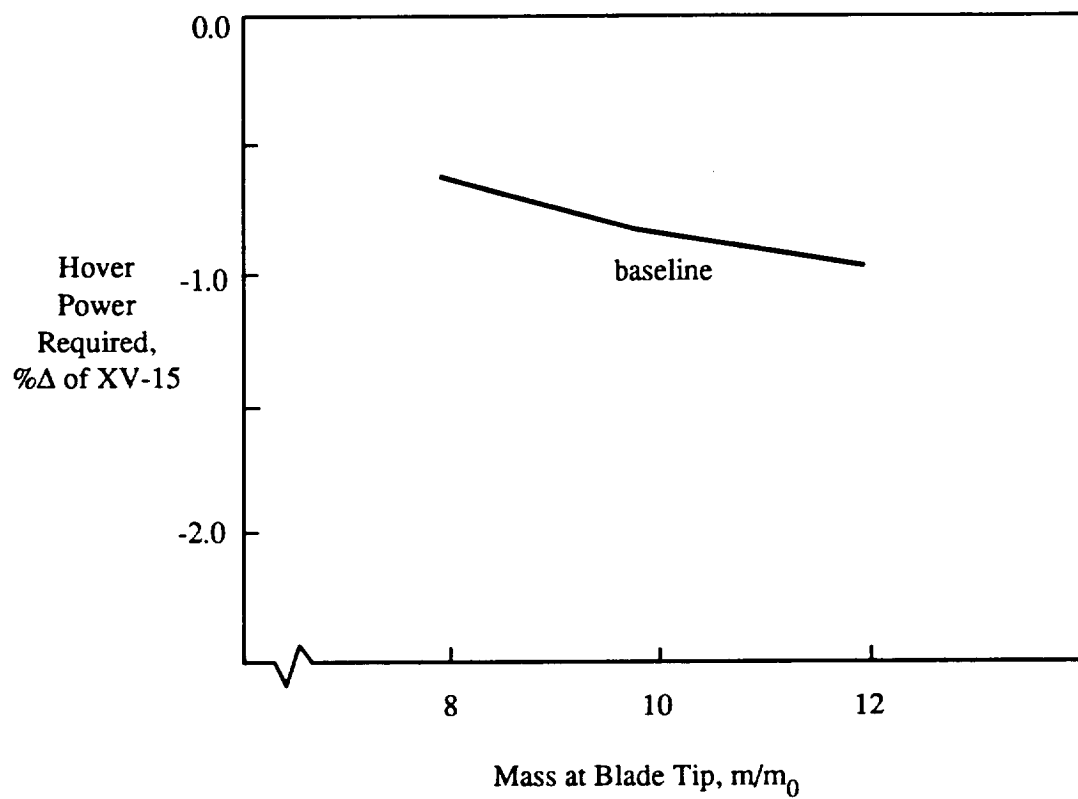
Figure 8.52: Hover performance improvement associated with increased tip mass on the baseline blade.
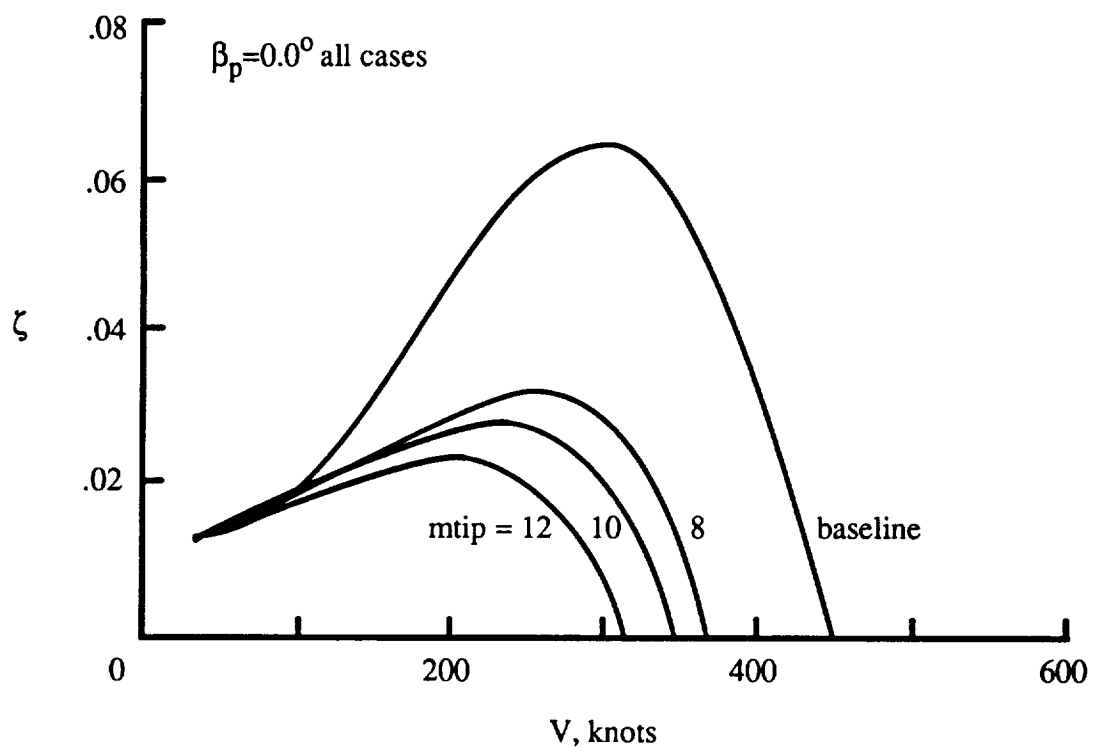
Figure 8.53: Influence of blade extension-twist-coupling on wing beam-mode damping with rotor precone at 0.0°.
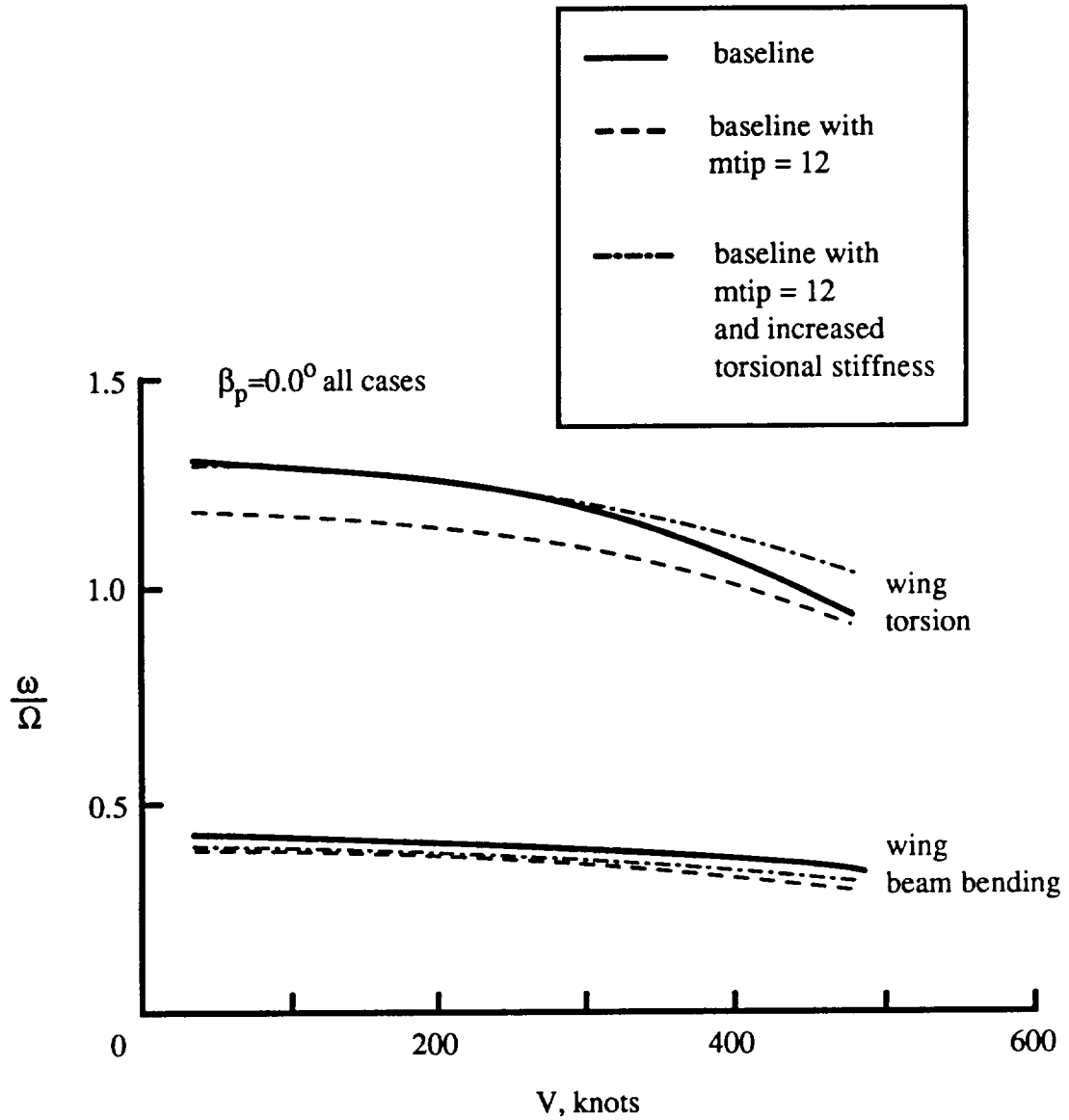
Figure 8.54: Wing beam and torsion frequencies associated with the modified baseline cases, in airplane mode.

349
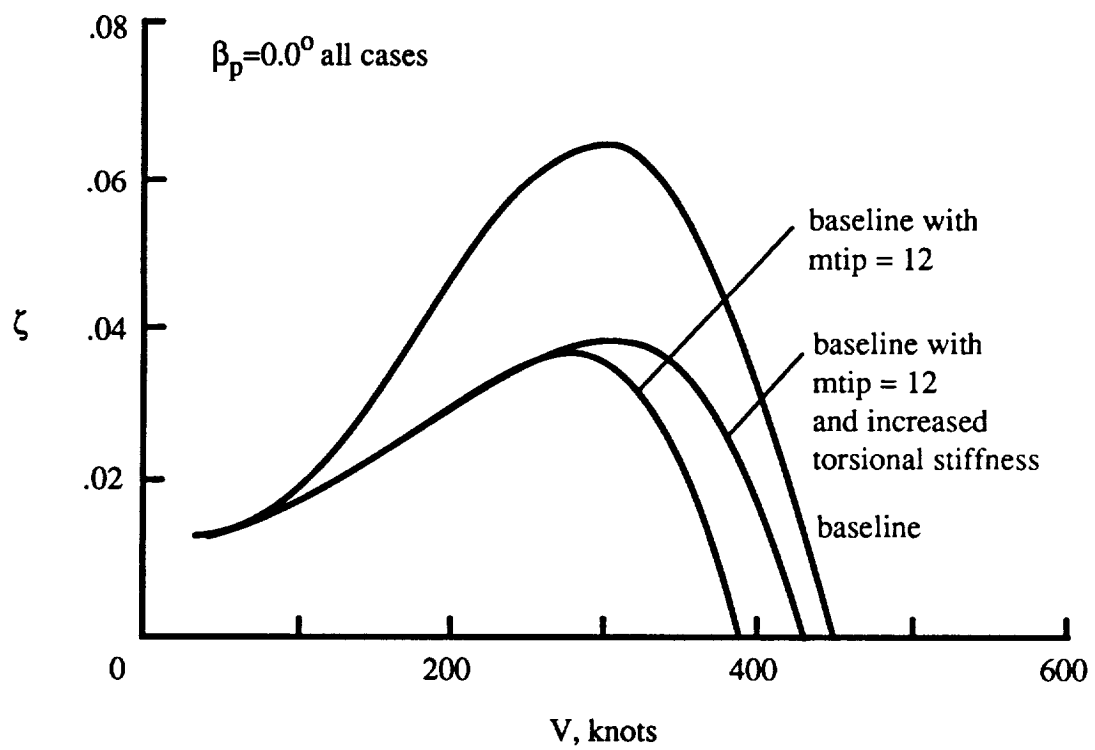
Figure 8.55: Wing beam mode damping associated with the modified baseline cases, in airplane mode.
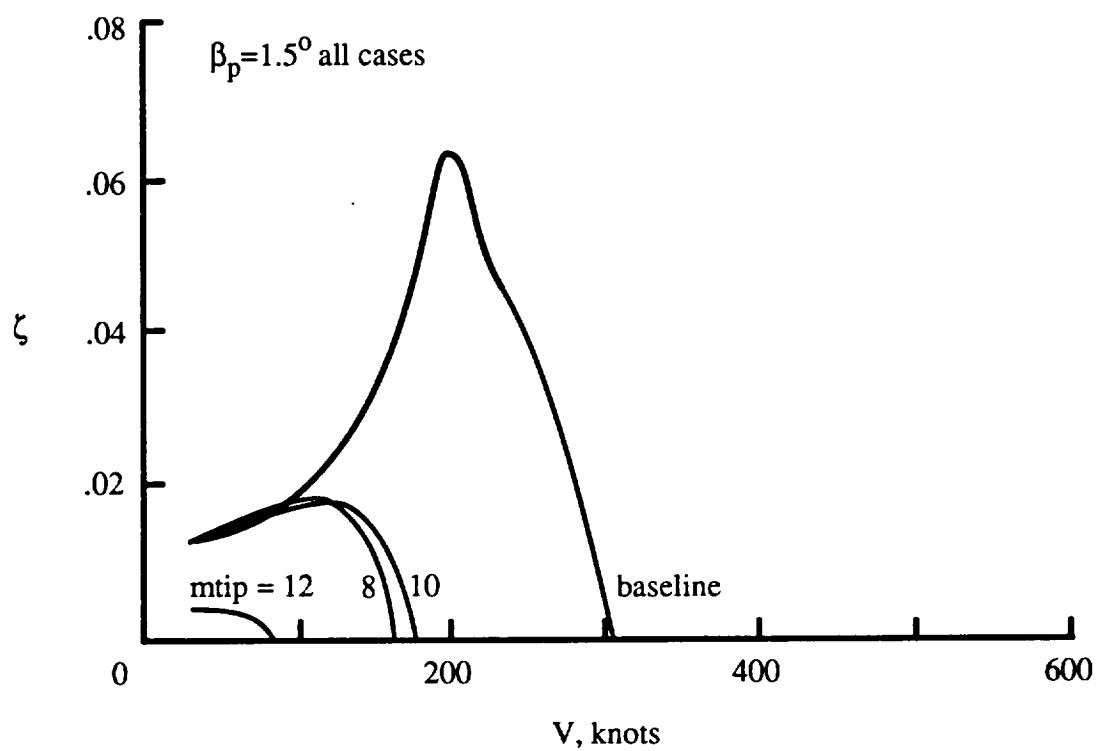
Figure 8.56: Influence of blade extension-twist-coupling on wing beam-mode damping with rotor precone at 1.5°.

Chapter 9

Conclusions and

Recommendations

The research efforts presented in this dissertation may be divided into four main parts. First, a simple rigid-blade, elastic wing, axial-flight tiltrotor analysis was developed and used to investigate fundamental trends related to the whirl flutter instability. Second, an anisotropic rotating beam analysis was developed and used to investigate the accuracy of an implicit shear deformation model for highly-coupled and highly-twisted rotor blades. Third, the system equations were derived for the analytical model of a fully-coupled, anisotropic blade or wing, tiltrotor in free-flight or in a wind tunnel. Fourth, the loads, performance, and stability characteristics of some example elastically-coupled rotor blades were investigated and compared with those characteristics of a baseline system. This chapter presents the major conclusions reached for each of these four parts of the present research, and includes recommendations for future research in the final section.

352

9.1   Fundamental Study of Whirl Flutter

The influences of several key system design parameters on tiltrotor aeroelastic stability in the high-speed axial flight mode were examined in Chapter 2. The findings of this investigation have substantiated earlier work performed by other researchers as well as identified some new trends and the physical reasonings behind them. Some of the important past conclusions which have been substantiated are as follows:

1. Beam and torsion frequency separation has a large influence on stability of the wing beam mode.

2. Negative δ_3 is more effective than positive δ_3 with respect to stability considerations for a stiff-inplane rotor system.

The results of this study have also identified and explained at least two important effects which have not been previously discussed in the open literature:

1. Lag frequency tuning appears to be a practical method for increasing axial flight flutter velocities. The blade lag frequency may be selected to reduce the coupling of the $\beta-1$ and wing beam modes, thereby increasing the wing beam mode damping.

2. An increase in forward wing sweep is destabilizing. This is because of an increase in the rotor destabilizing force components in the beam and chord directions. The wing frequency changes associated with the reorientation of the pylon with sweep have a stabilizing influence on the beam mode, but this effect is dominated by the rotor force changes.

9.2 Dynamic Analysis of Pretwisted Elastically-Coupled Rotor Blades

A dynamic analysis was formulated for rotating pretwisted composite blades which exhibit anisotropic behavior in Chapter 3. This formulation incorporated the effects of shear deformation implicitly through elimination of the shear variables in the material compliance matrix. The major results of this study are listed as follows:

1. The implicit shear deformation model was able to capture the most significant effect of shear deformation, namely the reduction in effective bending stiffness that occurs when a substantial amount of bending-shear coupling is present in a beam. The difference between implicit and explicit use of shear degrees of freedom was shown to be less than 2 percent up to the second bending modes of some representative rotor blades, and less than 4 percent up to the second bending modes of some highly coupled box beam specimens.

2. One-dimensional global dynamic analysis based on classical beam kinematics can accurately predict the bending and torsion frequencies of modes important to an aeroelastic analysis. However, the section properties used in the global analysis must account for the important nonclassical effects associated with shear deformation, warping, and elastic couplings. These nonclassical effects were shown to have significant influence on the frequencies of the fundamental modes of highly coupled beam structures. Errors on the order of fifteen percent were reduced to less than five percent through accounting of the nonclassical effects.

3. The influence of twist on the predictive capabilities of the analysis was shown to be small.

4. The analysis of Chapter 3 was implemented using a p-version beam finite element. Both the advantages and disadvantages of this approach were discussed.

The p-version element proved to be convenient for assuring a converged solution, and allowed the desired flexibility in tailoring the displacement approximations to the dynamic characteristics of a given beam configuration. Some degree of efficiency improvement was demonstrated for the uniform untwisted case, but efficiency does not appear to be an issue for more realistic rotor blade structures. Much of the efficiency of using higher order elements was shown to be lost for a highly twisted blade.

9.3 Development of the Aeroelastic Tiltrotor Theory

The theoretical development presented in this dissertation represents the first known attempt to include both anisotropic blade and tiltrotor configuration modeling capabilities in a general purpose rotorcraft analysis. Several specialized features were developed for this system which include an anisotropic beam model with implicit shear deformation for highly-coupled and highly-twisted rotor blades, a hub model with six degrees-of-freedom plus gimbal capability, large pylon-tilt angles, an aeroelastic wing model, and a fully-coupled aeroelastic trim and response capability for tiltrotors in free-flight or in a wind tunnel. The derivation of these features were presented in Chapters 4 through 7. The following conclusions are based on this study:

1. The present formulation shows that the rigid-body rotation associated with precone contributes significant elastic pitch-lag coupling terms not included in past UMARC formulations. These terms are essential for accurate prediction of stability of most tiltrotor configurations.

2. Numerical integration is an effective analytical technique for the spanwise spatial integration of beam finite element models of highly-twisted blades. Linear

355

interpolation at the numerical quadrature points, based on element end-node properties provides a high level of accuracy compared to constant-property elements.

9.4 Validation and Application of the Aeroelastic Tiltrotor Analysis

This research represents the first known investigation of the aeroelastic loads, response, performance, and stability of tiltrotors with elastically-coupled rotor blades. The first part of the investigation focuses on validation of the tiltrotor model for a baseline case. The second part of the investigation considers the potential for increasing the baseline tiltrotor flutter velocity using bending-twist-coupled rotor blades. This part of the investigation also considers the influence of bending-twist coupling on performance and blade loads. The third and final part of the investigation considers the potential for improving the aerodynamic performance of tiltrotors using extension-twist-coupled rotor blades. This part of the investigation also considers the influence of extension-twist coupling on stability. The following summaries and conclusions are based on these investigations discussed in Chapter 8:

9.4.1 Validation of the Aeroelastic Tiltrotor Analysis

Validation efforts show that the present analysis is satisfactory with respect to its predictions of loads, response, performance, and stability in all three modes of tiltrotor operation: helicopter, conversion, and airplane flight modes. In high-speed airplane flight mode, the present analysis predictions for a baseline configuration produced the following conclusions:

1. Coupled bending mode shapes are in good agreement with predictions of the reference 31 analysis.

2. Cruise collective is only 1.3 percent different from prediction of the reference 31 analysis.

3. Predictions of wing and blade frequencies and damping are in good agreement with results presented in reference 31. Predictions of wing beam mode damping also compare favorably with experimental results.

4. Whirl flutter is predicted to occur at about 305 knots by the analysis of reference 31, and at about 285 knots by the present analysis (about 7 percent difference).

5. Agreement in flutter predictions between the present analysis and the reference 31 analysis is less then 7 percent for the parametric variations considered of the baseline precone and blade torsional frequency.

6. Propeller efficiency predictions agree well with XV-15 flight test data. A maximum of 8 percent difference was predicted which is within the range of the test data variations.

Predictions by the present analysis for a baseline design in helicopter, conversion, and airplane flight modes produced the following conclusions:

1. Predicted collective pitch agreed within 5 degrees of the predicted values of reference 31 in spite of differing analytical assumptions for the blade torsional stiffness in these cases.

2. Damping of the wing modes (torsion, beam, and chord) follows similar trends through conversion mode as those of the reference 31 analysis.

3. Propeller efficiency predictions agree well with XV-15 isolated-rotor test data. A maximum of 4 percent difference was predicted which is less than the range of the test data variations.

4. Blade bending loads trends with respect to pylon angle and flight mode agree well with XV-15 flight test data. Agreement of load magnitudes were also good over some of the velocity range considered for each pylon angle. The load

357

predictions were found to be very sensitive to the selection of the tail incidence angle.

9.4.2 Investigation of Bending-Twist-Coupled Blades

This investigation showed that elastic bending-twist coupling of the rotor blade is a very effective means for increasing the flutter velocity of a tiltrotor. The following conclusions were reached as part of the bending-twist-coupled rotor blade investigation:

1. The negative pitch-lag coupling created by the rotor precone effect significantly reduces the flutter velocity of tiltrotors in airplane flight mode.

2. The introduction of positive pitch-lag coupling via rotor blade elastic bending-twist coupling can significantly increase the flutter velocity of a baseline system. Flutter velocities were increased by as much as 44 percent.

3. The use of elastic bending-twist coupling rather than control mechanisms to introduce positive pitch-lag coupling has distinct advantages: greater magnitudes of pitch-lag coupling may be obtained and there is no associated influence on the pitch-gimbal coupling.

4. The magnitudes of bending-twist coupling required to significantly improve the tiltrotor stability characteristics are physically obtainable and well within the range of realistic rotor designs.

5. The magnitudes of bending-twist coupling required to significantly improve the tiltrotor stability characteristics have a negligible influence on tiltrotor hover and cruise performance.

6. The magnitudes of bending-twist coupling required to significantly improve the tiltrotor stability characteristics have a negligible influence on conversion-mode blade bending loads.

358

9.4.3 Investigation of Extension-Twist-Coupled Blades

This investigation showed that passive blade twist control via elastic extension-twist coupling of the rotor blade has the capability of significantly improving tiltrotor aerodynamic performance, particularly in the hover mode. This approach was shown to have a detrimental impact on stability characteristics, however, because increased mass of the rotor system reduces the wing torsional frequency and increased centrifugal force worsens the precone effect. The stability of an extension-twist-coupled rotor blade could be made acceptable by: 1) increasing wing torsional stiffness, or 2) reducing the rotor precone. The following conclusions were reached as part of the extension-twist-coupled rotor blade investigation:

1. Optimum blade twist distributions for hover and airplane cruise were determined assuming independent design for each flight mode. The optimum twist distribution predicted for hover was $25°/R$ (nose-down) linear and the associated performance improvement was about 11 percent better than that associated with the baseline twist distribution. The optimum twist distribution predicted for cruise was a nonlinear distribution composed of the baseline twist from 0 to $.4R$ and $42°/R$ (nose-down) linear from $.4R$ to the tip. The associated cruise performance improvement was about 1 percent better than that associated with the baseline twist distribution. These results showed that significant performance improvements may be gained by changing blade twist between the hover and cruise flight modes rather than using a single blade twist compromised for both flight modes.

2. Extension-twist-coupled blade designs depend on high levels of centrifugal forces to produce necessary twist changes. These designs generally result in increased tip-mass compared to an uncoupled design.

3. Extension-twist-coupled blade designs do not generally result in reduced torsional stiffness compared to uncoupled designs because anisotropic laminates used to produce desired coupling have high off-axis ply angles.

4. Example extension-twist-coupled designs improved performance predictions for hover by 6 to 7.5 percent and for cruise by about 1 percent. The associated twist deformation change between hover and cruise range from 8 to 10 degrees measured at the blade tip.

5. Stability characteristics of the basic extension-twist-coupled designs in airplane mode are unacceptable. Reductions in flutter velocity range from 40 to 75 percent for the 1.5° precone case. About one-half of this reduction is attributable to the decrease in wing torsional frequency due to increased rotor mass, and the rest is attributable to increased precone effect associated with the increased centrifugal forces.

6. Stability characteristics of the basic extension-twist-coupled designs can be made acceptable if the following parameters can be achieved within the design constraints: an increase in wing torsional stiffness on the order of 20 percent or a reduction of rotor precone to near zero.

9.5 Recommendations for Future Research

The research presented in this dissertation shows that promising improvements in tiltrotor aeroelastic performance may be gained through elastic tailoring of the rotor blade. However, there are several areas where the investigations were limited by the capabilities of the present analysis. The following section suggests enhancements for the present analysis as well as recommendations for future research in the area of elastically-coupled rotor blades.

1. The present analysis assumes a straight elastic axis for the blade. Many modern tiltrotor design studies consider some type of swept blades for the purpose of reducing drag divergence effects at high speeds. The UMARC general purpose rotorcraft code, on which the present analysis is based, already has a swept elastic axis capability. It is anticipated that these modifications may be introduced into

the tiltrotor analysis with little difficulty.

2. The present analysis has a limited free-flight model. It is planned to rederive the equations of Chapters 4 and 5 with fuselage motion terms included. The inclusion of the fuselage motion will allow the analysis to include the antisymmetric wing modes and to predict stability more accurately in free-flight.

3. The present analysis has a limited drive-train model. It has been shown by other researchers that the drive-train dynamics can have a significant impact on tiltrotor stability predictions. The present model considers only two cases: a constant rotor speed (no speed perturbation) and a zero-frequency speed perturbation (no stiffness associated with rotor speed perturbations). A drive train dynamics model is planned to be added to the system which would allow specification of torsional stiffness, damping, and inertia associated with the drive system and the rotor speed perturbation.

4. The present analysis has no wing-download model. The rotor in hover imparts downward flow on the wing which increases the effective weight of the system by about 7 percent. The actual download depends on several parameters of the wing such as area, flap excursions, and incidence angle. Relatively simple models have been developed for predicting the download which can be included in the present analysis.

5. The present analysis has no wing/body interference model. The presence of the wing and fuselage interfere with the airflow through the rotor system, thereby altering the angle of attack on the rotor blade. Therefore, even in symmetric flight conditions such as airplane axial flight, the rotor will experience asymmetric flow patterns which may contribute greatly to the dynamic loads on the system. The difficulties associated with including some type of interference model have not yet been investigated.

6. The present research does not consider hingeless and bearingless rotor tiltro-

tor systems. These types of rotor systems have been considered for tiltrotors in the past, so the influence of elastic coupling on blades of theses systems should be investigated.

7. The present research does not use formal optimization techniques in designing elastically-coupled blades. It is evident from the discussion on elastic tailoring that many trade-offs must be considered. Certain assumptions were made in the present investigations so as to account for strength and manufacturability constraints. The performance and stability characteristics of these designs may be improved if these constraints were defined more rigorously through formal optimization techniques.

8. The present research does not investigate the effects of elastic coupling on blade transient response. The system response to gust loading is a very important aspect of tiltrotor design, especially for a civil version of this aircraft. The large disc area makes the tiltrotor very sensitive to gust loads which can produce uncomfortable accelerations at the passenger seating locations. It may be possible to improve this response using elastically-coupled rotor blades. Investigations of the use of active controls to alleviate gust response is another worthy research topic.

9. Experimental verification of the elastically-coupled tiltrotor blade concepts is required. There is very little data currently available, so it is not possible to judge the accuracy of the present analytical predictions when blades are elastically-coupled. Data on blade loads, performance, and stability are required, especially stability data near the flutter boundary.

Appendix A

Rigid Blade Tiltrotor Analysis-Math Model Development

The equations of motion are derived for a tiltrotor cantilvered wing model in the axial flight mode. The derivation consists of five parts: the formulation of the blade structural model based on a three-bladed gimballed rotor system with hub motions included, the formulation of the rotor aerodynamics and associated contributions to the system matrices, formulation of an elastic finite element wing structural model, formulation of the wing aerodynamics and associated wing system matrices, and coupling of the wing and rotor/hub systems. The formulation for the rotor system equations of motion follows closely the formulation presented in Ref. 31. The new part of the present formulation is the coupling of the rotor equations with a wing finite element model rather than a wing modal representation. Forward wing sweep is incorporated in the wing finite element formulation to allow that effect to be studied.

A.1 Rotor and Hub Structural Model

Consider a blade system rotating on a rigid pylon as illustrated in Fig. A.1. The fundamental blade flap and lag motions are considered, and the pylon motion at the pivot point has six associated degrees of freedom. The pivot point is located a distance h behind the blade hub, and the rotor is shown to be oriented symmetrically with respect to the oncoming flow (tiltrotor axial flight mode). The translational degrees of freedom at the pylon pivot are x_P, y_P, and z_P which represent the vertical, lateral, and longitudinal motions, respectively, and the rotational degrees of freedom at the pylon pivot are α_x, α_y, and α_z which represent the pylon yaw, pitch, and roll motions, respectively. There are six rotor forces defined at the rotor hub (in a fixed reference frame) which can be translated back to the pylon pivot. These forces have both inertial and aerodynamic origins from the blade system.

The rotor system is assumed to be three-bladed with a gimballed hub. There are two degrees of freedom per blade which are associated with the fundamental flap and lag blade modes, defined relative to the hub plane. These modes are assumed to be uncoupled which can be a poor approximation of the elastic motion of a tiltrotor blade because of the high twist and high collective pitch typically associated with these blades. However, in this case the predominant flap motion is a rigid body rotation about the center of rotation because of the presence of the gimbal. Thus, an assumption of uncoupled flap and lag motions should not have a major influence on the present model which does not consider all the elastic blade motion. It has been shown in other investigations such as Kvaternik [16] that accurate representations of basic tiltrotor dynamics may be achieved without inclusion of the lag motion at all. Rigid pitch motion of the blade about its feathering axis is also considered. The steady pitch is a sum of the root collective and built-in blade twist. A perturbation of the pitch motion is associated with a

$C \cdot 5$

small change in the control inputs and with kinematic pitch/flap coupling (δ_3 flap hinge skew angle). The rotor is assumed to rotor freely on the shaft (windmilling state) such that no torque is transmitted to the pylon pivot, and pylon pivot roll motion does not influence rotor rotation rate. This state is modeled after the equations of motion are transformed into the fixed frame, by assuming a zero frequency for the collective lag mode. The initial equations of motion for the rotor system with hub motions included are derived in the rotating reference frame for a constant rotational speed Ω.

The equations of motion for the blade in the rotating reference frame with the pylon pivot motions included are given in Ref. 31 in nondimensional form as:

$$I_\beta^*(\ddot{\beta} + \nu_\beta^2 \beta) + I_{\beta\alpha}^*[-(\ddot{\alpha}_y - 2\ddot{\alpha}_x)\cos\psi_m + (\ddot{\alpha}_x + 2\ddot{\alpha}_y)\sin\psi_m] + S_\beta^* \ddot{z}_P$$
$$= \frac{\gamma M_F}{ac} \tag{A.1}$$

$$I_\zeta^*(\ddot{\zeta} + \nu_\zeta^2 \zeta) + S_\zeta^*[(\ddot{x}_P + h\ddot{\alpha}_y)\sin\psi_m - (\ddot{y}_P - h\ddot{\alpha}_x)\cos\psi_m] - I_{\zeta\alpha}^* \ddot{\alpha}_z$$
$$= \frac{\gamma M_L}{ac} \tag{A.2}$$

where the M_F and M_L represent the pure flap and pure lag components of the distributed aerodynamic forces:

$$M_F = \int_0^R F_z r \, dr \tag{A.3}$$

$$M_L = \int_0^R F_x r \, dr \tag{A.4}$$

and the inertia constants are nondimensionalized by the rigid-blade flap inertia I_b ($I_\beta^* = I_\beta/I_b$ for example) and are defined in terms of the blade section mass and the blade mode shapes:

$$I_b = \int_0^R r^2 m \, dr \tag{A.5}$$

$$I_\beta = \int_0^R \eta_\beta^2 m \, dr \tag{A.6}$$

$$I_{\beta\alpha} = \int_0^R \eta_\beta m r \, dr \tag{A.7}$$

365

$$S_\beta = \int_0^R \eta_\beta m \, dr \tag{A.8}$$

$$I_\zeta = \int_0^R \eta_\zeta^2 m \, dr \tag{A.9}$$

$$I_{\zeta\alpha} = \int_0^R \eta_\zeta m r \, dr \tag{A.10}$$

$$S_\zeta = \int_0^R \eta_\zeta m \, dr \tag{A.11}$$

The blade flap bending mode is represented by η_β and the lag bending mode is represented by η_ζ, and the mode shape values are $\eta_\beta = r$ for rigid flap motion and $\eta_\zeta = r$ for rigid lag motion. Coriolis inertial coupling is neglected in these equations because these forces are small compared to the aerodynamic forces associated with high inflow aerodynamics, where the forces in the lag direction are of the same magnitude as the flap direction.

The equations of motion are transformed into the fixed frame using the Fourier coordinate transformation based on three blades:

$$I_{\beta_0}^*(\ddot\beta_0 + \nu_{\beta_0}^2 \beta_0) + S_{\beta_0}^* \ddot z_P = \frac{\gamma M_{F_0}}{ac} \tag{A.12}$$

$$I_\beta^* \left[\ddot\beta_{1C} + 2\dot\beta_{1S} + (\nu_\beta^2 - 1)\beta_{1C} \right] + I_{\beta\alpha}^*(-\ddot\alpha_y + 2\dot\alpha_x) = \frac{\gamma M_{F_{1C}}}{ac} \tag{A.13}$$

$$I_\beta^* \left[\ddot\beta_{1S} - 2\dot\beta_{1C} + (\nu_\beta^2 - 1)\beta_{1S} \right] + I_{\beta\alpha}^*(\ddot\alpha_x + 2\dot\alpha_y) = \frac{\gamma M_{F_{1S}}}{ac} \tag{A.14}$$

$$I_{\zeta_0}^*(\ddot\zeta_0 + \nu_{\zeta_0}^2 \zeta_0) - I_{\zeta_0\alpha}^* \ddot\alpha_z = \frac{\gamma M_{L_0}}{ac} \tag{A.15}$$

$$I_\zeta^* \left[\ddot\zeta_{1C} + 2\dot\zeta_{1S} + (\nu_\zeta^2 - 1)\zeta_{1C} \right] + S_\zeta^*(-\ddot y_P + h\ddot\alpha_x) = \frac{\gamma M_{L_{1C}}}{ac} \tag{A.16}$$

$$I_\zeta^* \left[\ddot\zeta_{1S} - 2\dot\zeta_{1C} + (\nu_\zeta^2 - 1)\zeta_{1S} \right] + S_\zeta^*(\ddot x_P + h\ddot\alpha_y) = \frac{\gamma M_{L_{1S}}}{ac} \tag{A.17}$$

The frequencies and inertial parameters in the fixed frame are shown to vary among the equations of motion associated with the fixed frame degrees of freedom. This is so because the root constraint conditions vary for a gimballed rotor system based on the rotor mode involved. For the gimballed rotor, in the collective flapping mode and the cyclic lag modes the blade acts as if it were cantilevered, while in the cyclic flap modes the blade acts as if it were hinged at the center of rotation. In

366

collective lag mode, the blade acts as if it were cantilevered if the rotor is assumed to turn at constant speed, but for a windmilling rotor the blade is free to rotate about the shaft so that

$$\nu_{\zeta_0} = 0 \tag{A.18}$$

$$I^*_{\zeta_0} = 1 \tag{A.19}$$

$$I^*_{\zeta_0 \alpha} = 1 \tag{A.20}$$

The flap aerodynamic moments in the fixed frame are given by:

$$M_{F_0} = \frac{1}{N} \sum_m M_{F_m} \tag{A.21}$$

$$M_{F_{1C}} = \frac{2}{N} \sum_m M_{F_m} \cos \psi_m \tag{A.22}$$

$$M_{F_{1S}} = \frac{2}{N} \sum_m M_{F_m} \sin \psi_m \tag{A.23}$$

A.2 Rotor Aerodynamic Model

The rotor aerodynamics are based on linear strip theory with the section lift and drag defined as:

$$L = \frac{1}{2} \rho c (u_T^2 + u_P^2) c_l \tag{A.24}$$

$$D = \frac{1}{2} \rho c (u_T^2 + u_P^2) c_d \tag{A.25}$$

where c_l and c_d are the local blade section lift and drag coefficients, respectively. The velocity components are defined with respect to the hub plane as illustrated in Fig. A.2, which also illustrates definition of the angle of attack, inflow angle, and pitch angle of the blade section. Resolving the section aerodynamic forces into the hub plane, and nondimensionalizing by ac gives the blade loads as:

$$\frac{F_z}{ac} = U(u_T \frac{c_l}{2a} - u_P \frac{c_d}{2a}) \tag{A.26}$$

$$\frac{F_x}{ac} = U(u_P \frac{c_l}{2a} + u_T \frac{c_d}{2a}) \tag{A.27}$$

$$\frac{F_r}{ac} = U u_R \frac{c_d}{2a} - \beta \frac{F_z}{2a} \tag{A.28}$$

367

and the net blade flap and lag moment are defined by substitution of these expressions into Eqns. A.3 and A.4. The hub forces in the fixed frame are also desired because these forces act on the wing. In coefficient form, the required hub forces are defined in terms of the blade section forces as:

$$\frac{C_T}{\sigma a} = \frac{1}{N}\sum_m \int_0^1 \frac{F_z}{ac}\,dr \tag{A.29}$$

$$\frac{2C_H}{\sigma a} = \frac{2}{N}\sum_m (\cos\psi_m \int_0^1 \frac{F_r}{ac}\,dr + \sin\psi_m \int_0^1 \frac{F_x}{ac}\,dr) \tag{A.30}$$

$$\frac{2C_Y}{\sigma a} = \frac{2}{N}\sum_m (\sin\psi_m \int_0^1 \frac{F_r}{ac}\,dr - \cos\psi_m \int_0^1 \frac{F_x}{ac}\,dr) \tag{A.31}$$

$$\frac{C_Q}{\sigma a} = \frac{1}{N}\sum_m \int_0^1 \frac{F_x}{ac}r\,dr \tag{A.32}$$

$$\frac{2C_{M_x}}{\sigma a} = \frac{2}{N}\sum_m \sin\psi_m \int_0^1 \frac{F_r}{ac}r\,dr \tag{A.33}$$

$$\frac{2C_{M_y}}{\sigma a} = -\frac{2}{N}\sum_m \cos\psi_m \int_0^1 \frac{F_r}{ac}r\,dr \tag{A.34}$$

Evaluation of the force integrals requires substitution of the aerodynamic parameters in terms of perturbation quantities which result from blade and hub motion The damping and stiffness associated with these perturbations ultimately determine the stability of the system. Each velocity component may be written as a sum of steady and small perturbation parts where the steady parts are given by:

$$u_T = \Omega r \tag{A.35}$$

$$u_P = V + \nu \tag{A.36}$$

$$u_R = 0 \tag{A.37}$$

where it can be shown that for high inflow:

$$\nu = \frac{C_T}{2V} \tag{A.38}$$

The perturbation parts of the velocities are produced by the blade and hub motion as:

$$\delta u_T = r(\overset{*}{\alpha}_z - \overset{*}{\zeta}) - h(\overset{*}{\alpha}_y \sin\psi_m + \overset{*}{\alpha}_x \cos\psi_m) +$$

$$V(\alpha_y \sin \psi_m + \alpha_x \cos \psi_m) + \overset{*}{\overset{*}{y}}_P \cos \psi_m - \overset{*}{\overset{*}{x}}_P \sin \psi_m \qquad \text{(A.39)}$$

$$\delta u_P = r(\overset{*}{\beta} - \overset{*}{\alpha}_y \cos \psi_m + \overset{*}{\alpha}_x \sin \psi_m) + \overset{*}{z}_P \qquad \text{(A.40)}$$

$$\delta u_R = h(-\overset{*}{\alpha}_y \cos \psi_m - \overset{*}{\alpha}_x \sin \psi_m) + \nu(\alpha_y \cos \psi_m - \alpha_x \sin \psi_m)$$

$$- \overset{*}{y}_P \sin \psi_m - \overset{*}{x}_P \cos \psi_m \qquad \text{(A.41)}$$

To facilitate integration of the terms involving these perturbations quantities, the tangential and perpendicular velocity perturbation components are written as:

$$\delta u_T = r \delta u_{T_A} + \delta u_{T_B} \qquad \text{(A.42)}$$

$$\delta u_P = r \delta u_{P_B} + \delta u_{P_A} \qquad \text{(A.43)}$$

The other aerodynamic parameter perturbations are given by:

$$\delta c_l = \frac{\partial c_l}{\partial \alpha} \delta \alpha + \frac{\partial c_l}{\partial M} \delta M \qquad \text{(A.44)}$$

$$\delta c_d = \frac{\partial c_d}{\partial \alpha} \delta \alpha + \frac{\partial c_d}{\partial M} \delta M \qquad \text{(A.45)}$$

$$\delta \alpha = \delta \theta - \frac{u_T \delta u_p - u_p \delta u_t}{U^2} \qquad \text{(A.46)}$$

$$\delta U = \frac{u_T \delta u_T - u_p \delta u_P}{U} \qquad \text{(A.47)}$$

$$\delta M = M_{tip} \delta U \qquad \text{(A.48)}$$

$$\delta \theta = \theta - K_P \beta \qquad \text{(A.49)}$$

Substitution of the perturbation quantities into the integral force equations results in some rather lengthy and complicated expressions which may be simplified by expanding the force equations in terms of a set of aerodynamic coefficients defined in Ref. 31. These terms represent parts of the force integrations which are coefficients of the various control and velocity perturbations, such that:

$$\int_0^1 \frac{F_z}{ac} r \, dr = M_0 + M_\mu \delta u_{T_B} + M_\zeta \delta u_{T_A} + M_\lambda \delta u_{P_A} + M_\beta \delta u_{P_B} + M_\theta \delta \theta \qquad \text{(A.50)}$$

$$\int_0^1 \frac{F_x}{ac} dr = H_0 + H_\mu \delta u_{T_B} + H_\zeta \delta u_{T_A} + H_\lambda \delta u_{P_A} + H_\beta \delta u_{P_B} + H_\theta \delta \theta \qquad \text{(A.51)}$$

$$\int_0^1 \frac{F_z}{ac} dr = T_0 + T_\mu \delta u_{T_B} + T_\zeta \delta u_{T_A} + T_\lambda \delta u_{P_A} + T_\beta \delta u_{P_B} + T_\theta \delta \theta \qquad \text{(A.52)}$$

369

$$\int_0^1 \frac{F_x}{ac} r \, dr = Q_0 + Q_\mu \delta u_{Q_B} + Q_\zeta \delta u_{Q_A} + Q_\lambda \delta u_{P_A} + Q_{\dot\beta} \delta u_{P_B} + Q_\theta \delta\theta \quad \text{(A.53)}$$

$$\int_0^1 \frac{F_r}{ac} \, dr = R_\mu \delta u_R - \beta \frac{C_T}{\sigma a} \quad \text{(A.54)}$$

where the aerodynamic coefficients M, H, T, Q, and R represent flap moment, in-plane drag force, thrust force, torque moment, and blade radial force, respectively. The subscripts of these terms designate the source of the force or moment - 0 is the trim value, μ is hub inplane velocity, $\dot\zeta$ is blade rotational velocity, $\dot\beta$ is flap velocity, λ is hub longitudinal or inflow velocity, and θ is pitch control.

The blade forces are then transformed into the fixed frame to obtain the final aerodynamic force relationships in terms of the forward flight velocity and the blade and hub motions as:

$$M_{F_0} = M_0 + M_\zeta(\ddot\alpha_z - \dot\zeta_0) + M_{\dot\beta} \dot\beta_0$$
$$M_\lambda \ddot{z}_P + M_\theta(\theta_0 - K_P\beta_0) \quad \text{(A.55)}$$

$$M_{F_{1C}} = M_\mu[-h \dot\alpha_x + V\alpha_x + \ddot{y}_P] +$$
$$M_\zeta(\dot\zeta_{1C} - \dot\zeta_{1S}) + M_{\dot\beta}(\dot\beta_{1C} + \beta_{1S} - \ddot\alpha_y) +$$
$$M_\theta(\theta_{1C} - K_P\beta_{1C}) \quad \text{(A.56)}$$

$$M_{F_{1S}} = M_\mu[-h \dot\alpha_y + V\alpha_y - \ddot{x}_P] +$$
$$M_\zeta(-\dot\zeta_{1S} + \dot\zeta_{1C}) + M_{\dot\beta}(\dot\beta_{1S} - \beta_{1C} + \ddot\alpha_x) +$$
$$M_\theta(\theta_{1S} - K_P\beta_{1S}) \quad \text{(A.57)}$$

$$-M_{L_0} = Q_0 + Q_\zeta(\ddot\alpha_z - \dot\zeta_0) + Q_{\dot\beta} \dot\beta_0$$
$$Q_\lambda \ddot{z}_P + Q_\theta(\theta_0 - K_P\beta_0) \quad \text{(A.58)}$$

$$-M_{L_{1C}} = Q_\mu[-h \dot\alpha_x + V\alpha_x + \ddot{y}_P] +$$
$$Q_\zeta(\dot\zeta_{1C} - \dot\zeta_{1S}) + Q_{\dot\beta}(\dot\beta_{1C} + \beta_{1S} - \ddot\alpha_y) +$$
$$Q_\theta(\theta_{1C} - K_P\beta_{1C}) \quad \text{(A.59)}$$

$$-M_{L_{1S}} = Q_\mu[-h \dot\alpha_y + V\alpha_y - \ddot{x}_P] +$$
$$Q_\zeta(-\dot\zeta_{1S} + \dot\zeta_{1C}) + Q_{\dot\beta}(\dot\beta_{1S} - \beta_{1C} + \ddot\alpha_x) +$$

$$Q_\theta(\theta_{1S} - K_P\beta_{1S}) \qquad\qquad\qquad\qquad \text{(A.60)}$$

Substitution of these expressions into Eqns. A.12-A.17 and grouping terms as coefficients of the blade and pylon degrees of freedom complete the equations of motion for the rotor system.

As stated earlier, the net force and moments in the fixed frame are also required as these forces act on the wing, and those expressions will be needed when the wing formulation is coupled with the rotor/pylon system. After substitution of the perturbation quantities into the integral force expressions given by Eqns. A.29-A.34, and carrying out the integrations, the blade forces are transformed into the fixed frame to obtain the final hub forces in terms of the forward flight velocity and the blade and hub motions as:

$$\frac{C_T}{\sigma a} = T_0 + T_\zeta(\overset{*}{\alpha}_z - \overset{*}{\zeta}_0) + T_{\dot\beta}\overset{*}{\beta}_0 + T_\lambda\overset{*}{z}_P + T_\theta(\theta_0 - K_P\beta_0) \qquad \text{(A.61)}$$

$$\frac{2C_H}{\sigma a} = (H_\mu + R_\mu)[-h\,\overset{*}{\alpha}_y + V\alpha_y - \overset{*}{x}_P] +$$

$$\qquad\qquad H_\zeta(-\overset{*}{\zeta}_{1S} + \zeta_{1C}) + H_{\dot\beta}(\overset{*}{\beta}_{1S} + \overset{*}{\alpha}_x) +$$

$$\qquad\qquad H_\theta(\theta_{1S} - K_P\beta_{1S}) - H_{\dot\beta}\beta_{1C} \qquad\qquad \text{(A.62)}$$

$$\frac{2C_Y}{\sigma a} = -(H_\mu + R_\mu)[-h\,\overset{*}{\alpha}_x + V\alpha_x + \overset{*}{y}_P] -$$

$$\qquad\qquad H_\zeta(-\overset{*}{\zeta}_{1C} - \zeta_{1C}) - H_{\dot\beta}(\overset{*}{\beta}_{1C} + \overset{*}{\alpha}_y) -$$

$$\qquad\qquad H_\theta(\theta_{1C} - K_P\beta_{1C}) - H_{\dot\beta}\beta_{1S} \qquad\qquad \text{(A.63)}$$

$$\frac{C_Q}{\sigma a} = Q_0 + Q_\zeta(\overset{*}{\alpha}_z - \overset{*}{\zeta}_0) + Q_{\dot\beta}\overset{*}{\beta}_0 + Q_\lambda\overset{*}{z}_P + Q_\theta(\theta_0 - K_P\beta_0) \quad \text{(A.64)}$$

There is also an inertial force contribution to the hub forces which must be added to the above aerodynamic contributions:

$$\left(\frac{C_T}{\sigma a}\right)_{int} = -\frac{S^*_{\beta_0}}{\gamma}\overset{**}{\beta}_0 - \frac{M^*_b}{\gamma}\overset{**}{z}_P \qquad\qquad \text{(A.65)}$$

$$\left(\frac{2C_H}{\sigma a}\right)_{int} = -\frac{S^*_\zeta}{\gamma}\overset{**}{\zeta}_{1S} - \frac{2}{\gamma}M^*_b(\overset{**}{x}_P + h\,\overset{**}{\alpha}_y) \qquad \text{(A.66)}$$

$$\left(\frac{2C_Y}{\sigma a}\right)_{int} = \frac{S^*_\zeta}{\gamma}\overset{**}{\zeta}_{1C} - \frac{2}{\gamma}M^*_b(\overset{**}{y}_P - h\,\overset{**}{\alpha}_x) \qquad \text{(A.67)}$$

$$\left(\frac{C_Q}{\sigma a}\right)_{in} = -\frac{I_{\zeta 0\alpha}^*}{\gamma}\ddot{\zeta}_0 - \frac{I_0^*}{\gamma}\ddot{\alpha}_z \tag{A.68}$$

Rather than carry out the aerodynamic integral expressions for the hub moment terms C_{M_x} and C_{M_y}, and then adding in a set of inertial contributions, these moments may be expressed as the result of a spring moment which includes both the aerodynamic and inertial contributions:

$$\frac{2C_{M_x}}{\sigma a} = \frac{I_\beta^*}{\gamma}(\nu_\beta^2 - 1)\beta_{1S} \tag{A.69}$$

$$\frac{2C_{M_y}}{\sigma a} = -\frac{I_\beta^*}{\gamma}(\nu_\beta^2 - 1)\beta_{1C} \tag{A.70}$$

It is seen from these expressions that the hub moments are zero when the in-vacuum flap frequency $\nu_\beta = 1$ such as the case of an articulated rotor hinged at the center of rotation, and the hub moments increase as the flap frequency increases for given values of the flap angles.

All that remains for development of the aerodynamic contributions is definition and evaluation of the integral expressions for the aerodynamic coefficients. These expressions are provided in Ref. 31, and are evaluated numerically in the present analysis. The numerical integration is performed by discretizing the blade into several segments, and then summing up the aerodynamic contribution of each segment. A trim procedure is implemented based on changes in collective pitch until a desired rotor thrust level is obtained, usually zero for a windmilling rotor. The numerical approach allows changes in the blade section aerodynamics to be considered, including the influence of stall and compressibility. Numerical integration of the aerodynamic coefficients requires definition of $\frac{c_{l_\alpha}}{2a}$, $\frac{c_l}{2a}$, $\frac{c_{d_\alpha}}{2a}$, $\frac{c_d}{2a}$, $\frac{Mc_{l_M}}{2a}$, and $\frac{Mc_{d_M}}{2a}$ at each blade segment which are based on the local pitch, inflow, and attack angles and local Mach number. The following analytical expressions, defined in Ref. 31, are used for the unstalled lift parameters and include Mach number corrections:

$$\frac{c_{l_\alpha}}{2a} = \frac{1}{2}(1 - M^2)^{-\frac{1}{2}} \tag{A.71}$$

372

$$\frac{c_l}{2a} = \frac{\alpha}{2}(1 - M^2)^{-\frac{1}{2}} \tag{A.72}$$

$$\frac{c_l}{2a} + \frac{Mc_{l_M}}{2a} = \frac{\alpha}{2}(1 - M^2)^{-\frac{3}{2}} \tag{A.73}$$

where the stall point is defined as $12°$. The Mach number in these expressions is truncated at 0.95 to prevent numerical problems near $M = 1$. The unstalled drag parameters are defined as:

$$c_d = .0065 - .0216\alpha + .4\alpha^2 + \Delta c_d \tag{A.74}$$

$$\Delta c_d = .43(M + |\alpha| / .26 - .9) \text{ for } |\alpha| > \alpha_{d_v} \tag{A.75}$$

$$\Delta c_d = 0 \text{ otherwise} \tag{A.76}$$

$$\alpha_{d_v} = .26(.9 - M) \tag{A.77}$$

For stalled flow, the following approximations are used:

$$c_l = sgn(\alpha) \tag{A.78}$$

$$c_d = 2\sin^2\alpha \tag{A.79}$$

A.3   Wing Structural Model

The wing structural model is based on a finite element formulation of a standard Euler beam undergoing beam (vertical) bending, chordwise bending, and torsion (see Fig. A.3). The extensional degree of freedom (translation along wing span) is not considered as the wing is assumed to be rigid in this direction. The wing continuous degrees of freedom are given by

$$\hat{u} = \{w \ v \ \phi\} \tag{A.80}$$

which are related to the discrete degrees of freedom for one element:

$$\hat{q} = \{w_1 \ v_1 \ \phi_1 \ \theta_{z_1} \ \theta \ y_1 \ w_2 \ v_2 \ \phi_2 \ \theta_{z_2} \ \theta \ y_2\} \tag{A.81}$$

373

as

$$\hat{u} = [H]\,\hat{q} \qquad\qquad (A.82)$$

where $[H]$ is a matrix of shape functions. The standard shape functions are applied here, a set of four Hermitian polynomials $[H_b]$ for the bending degrees of freedom and a set of two linear polynomials $[H_\theta]$ for the torsion degree of freedom such that the matrix of shape functions may be written as:

$$[H] = \begin{bmatrix} H_b^1 & 0 & 0 & 0 & H_b^2 & H_b^3 & 0 & 0 & 0 & H_b^4 \\ 0 & H_b^1 & 0 & H_b^2 & 0 & 0 & H_b^3 & 0 & H_b^4 & 0 \\ 0 & 0 & H_\theta^1 & 0 & 0 & 0 & 0 & H_\theta^2 & 0 & 0 \end{bmatrix} \qquad (A.83)$$

The strain energy for the linear beam theory is defined in several references and is defined in terms of the beam continuous degrees of freedom of the present formulation as:

$$V = \frac{1}{2}\int_0^l [EI_c(v'')^2 + EI_b(w'')^2 + GJ(\theta')^2]\,dx \qquad (A.84)$$

The kinetic energy is formulated on the assumption that the center of gravity may be offset from the elastic axis by a distance y. The translational velocity of an arbitrary point on the beam cross section is written as:

$$\dot{u}_x = 0 \qquad\qquad (A.85)$$

$$\dot{u}_y = \dot{v} \qquad\qquad (A.86)$$

$$\dot{u}_z = \dot{w} + y\dot{\phi} \qquad\qquad (A.87)$$

In matrix form, the accelerations of an arbitrary point may be written as:

$$\hat{\ddot{u}} = \begin{bmatrix} \ddot{u}_y \\ \ddot{u}_z \end{bmatrix} = \begin{bmatrix} 0 & 1 & 0 \\ 1 & 0 & y \end{bmatrix} \begin{bmatrix} \ddot{w} \\ \ddot{v} \\ \ddot{\phi} \end{bmatrix} \qquad (A.88)$$

374

The variation of the kinetic energy is then given by:

$$T = \int_V \rho \, \delta \hat{u}^T \, \ddot{\hat{u}} \, dV = \int_0^l \delta \hat{u}^T \left[\iint_A \rho \begin{bmatrix} 1 & 0 & y \\ 0 & 1 & 0 \\ y & 0 & y^2 \end{bmatrix} dA \right] \ddot{\hat{u}} \, dx \qquad (A.89)$$

For the structural model, Hamilton's principle is applied in its conservative form:

$$\int_{t_1}^{t_2} \delta(T - V) \, dt = 0 \qquad (A.90)$$

into which are substituted the appropriate expressions for the strain and kinetic energy and the discrete relations to the continuous degrees of freedom. Following these substitutions, the structural mass and stiffness matrices may be expressed as:

$$\left[M^S \right] = \int_0^l [H]^T [M_s][H] \, dx \qquad (A.91)$$

$$\left[K^S \right] = \int_0^l [H]^T [K_s][H] \, dx \qquad (A.92)$$

where

$$[M_s] = \begin{bmatrix} m & 0 & S_\alpha \\ 0 & m & 0 \\ S_\alpha & 0 & I_\theta \end{bmatrix} \qquad (A.93)$$

$$[K_s] = \begin{bmatrix} EI_b & 0 & 0 \\ 0 & EI_c & 0 \\ 0 & 0 & GJ \end{bmatrix} \qquad (A.94)$$

These integrations are performed symbolically, and result in the 10 x 10 beam element structural mass and stiffness matrices.

375

A.4 Wing Aerodynamic Model

The wing aerodynamic model is based on the quasi-steady lift approximation:

$$\alpha_{eff} = \alpha_0 + \phi - \frac{\dot{w}}{U} \tag{A.95}$$

where w and ϕ represent two of the three continuous degrees of freedom for the wing, and U is the free stream velocity. The components of aerodynamic force may then be written as:

$$L_w = qcc_{l_a}(\alpha_0 + \phi - \frac{\dot{w}}{U}) \tag{A.96}$$

$$L_v = 0 \tag{A.97}$$

$$M_\phi = L_w\,e \tag{A.98}$$

where e is the chordwise distance of the elastic axis behind the aerodynamic center. These forces may be expressed with aerodynamic coefficient matrices as:

$$\left\{\begin{array}{c} L_w \\ L_v \\ M_\phi \end{array}\right\} = [A_0]\left\{\begin{array}{c} \alpha_0 \\ 0 \\ \alpha_0 \end{array}\right\} + [A_1]\left\{\begin{array}{c} w \\ v \\ \phi \end{array}\right\} + [A_2]\left\{\begin{array}{c} \dot{w} \\ \dot{v} \\ \dot{\phi} \end{array}\right\} \tag{A.99}$$

where

$$[A_1] = \begin{bmatrix} 0 & 0 & qcc_{l_a} \\ 0 & 0 & 0 \\ 0 & 0 & qcec_{l_a} \end{bmatrix} \tag{A.100}$$

$$[A_2] = \begin{bmatrix} -qcc_{l_a}/U & 0 & 0 \\ 0 & 0 & 0 \\ -qcec_{l_a}/U & 0 & 0 \end{bmatrix} \tag{A.101}$$

and $[A_0] = [A_1]$. The variation of work done by the aerodynamic forces may be written as

$$\delta W = \int_0^l \{\delta w\ \ \delta v\ \ \delta\phi\} \left\{\begin{array}{c} L_w \\ L_v \\ M_\phi \end{array}\right\} dx \tag{A.102}$$

376

which, after substitution of the aerodynamic coefficient expressions and the relations between the discrete and continuous degrees of freedom, leads to the aerodynamic damping and stiffness matrices:

$$\left[C^A\right] = \int_0^l [H]^T[A_1][H]\,dx \tag{A.103}$$

$$\left[K^A\right] = \int_0^l [H]^T[A_2][H]\,dx \tag{A.104}$$

These integrations are performed symbolically, and result in the 10 x 10 beam element aerodynamic damping and stiffness matrices. Application of Hamilton's principle in the nonconservative form (work included) shows that the aerodynamic matrices may be subtracted from the structural matrices to give the total mass, damping, and stiffness matrices for the wing as:

$$[M_w] = [M^S] \tag{A.105}$$

$$[C_w] = [C^S] - [C^A] \tag{A.106}$$

$$[K_w] = [K^S] - [K^A] \tag{A.107}$$

A.5 Wing Aerodynamic Model with Sweep

With sweep included in the wing, the aerodynamic contribution to the system matrices must be modified. Consider the elastic wing swept back at an angle Λ as illustrated in Fig. A.4. The quasi-steady lift approximation is now written as

$$\alpha_{eff} = \alpha_0 + \phi\cos\Lambda - \frac{\dot{w}}{U} - w'\sin\Lambda \tag{A.108}$$

where a continuous degrees of freedom w' is now required for the formulation. The vector of continuous degrees of freedom and the associated shape function matrix used for the structural model must be modified to reflect this new requirement. The new relationship between the continuous and discrete degrees of freedom is written as:

$$\hat{u}^A = \{w\ v\ \phi\ v'\ w'\} \tag{A.109}$$

377

which are related to the discrete degrees of freedom for one element:

$$\hat{q} = \{w_1 \ v_1 \ \phi_1 \ \theta_{z_1} \ \theta \ y_1 \ w_2 \ v_2 \ \phi_2 \ \theta_{z_2} \ \theta \ y_2\} \tag{A.110}$$

as

$$\hat{u}^A = [H^A]\hat{q} \tag{A.111}$$

where $[H^A]$ is the new matrix of shape functions for the swept wing formulation:

$$[H^A] = \begin{bmatrix} H_b^1 & 0 & 0 & 0 & H_b^2 & H_b^3 & 0 & 0 & 0 & H_b^4 \\ 0 & H_b^1 & 0 & H_b^2 & 0 & 0 & H_b^3 & 0 & H_b^4 & 0 \\ 0 & 0 & H_\theta^1 & 0 & 0 & 0 & 0 & H_\theta^2 & 0 & 0 \\ 0 & (H_b^1)' & 0 & (H_b^2)' & 0 & 0 & (H_b^3)' & 0 & (H_b^4)' & 0 \\ (H_b^1)' & 0 & 0 & 0 & (H_b^2)' & (H_b^3)' & 0 & 0 & 0 & (H_b^4)' \end{bmatrix} \tag{A.112}$$

To be compatible with the new vector of continuous displacements, the work is now expressed as:

$$\delta W = \int_0^l \{\delta w \ \delta v \ \delta \phi \ \delta v' \ \delta w'\} \begin{Bmatrix} L_w \\ L_v \\ M_\phi \\ M_z \\ M_y \end{Bmatrix} dx \tag{A.113}$$

The components of aerodynamic force are, again, written with aerodynamic coefficient matrices:

$$\begin{Bmatrix} L_w \\ L_v \\ M_\phi \\ M_z \\ M_y \end{Bmatrix} = [A_3] \begin{Bmatrix} \alpha_0 \\ 0 \\ \alpha_0 \\ 0 \\ 0 \end{Bmatrix} + [A_4] \begin{Bmatrix} w \\ v \\ \phi \\ v' \\ w' \end{Bmatrix} + [A_5] \begin{Bmatrix} \dot{w} \\ \dot{v} \\ \dot{\phi} \\ \dot{v}' \\ \dot{w}' \end{Bmatrix} \tag{A.114}$$

378

where the new matrices are 5 x 5 rather then 3 x 3, and are listed as follows:

$$
[A_4]^{\cdot} = \begin{bmatrix} 0 & 0 & qcc_{l_\alpha}\cos\Lambda & 0 & qcc_{l_\alpha}\sin\Lambda \\ 0 & 0 & 0 & 0 & 0 \\ 0 & 0 & qcec_{l_\alpha}\cos\Lambda & 0 & qcec_{l_\alpha}\sin\Lambda \\ 0 & 0 & 0 & 0 & 0 \\ 0 & 0 & 0 & 0 & 0 \end{bmatrix} \tag{A.115}
$$

$$
[A_5] = \begin{bmatrix} -qcc_{l_\alpha}/U & 0 & 0 & 0 & 0 \\ 0 & 0 & 0 & 0 & 0 \\ -qecc_{l_\alpha}/U & 0 & 0 & 0 & 0 \\ 0 & 0 & 0 & 0 & 0 \\ 0 & 0 & 0 & 0 & 0 \end{bmatrix} \tag{A.116}
$$

with $[A_3] = [A_4]$. The variation of work done by the aerodynamic forces then leads to the aerodynamic damping and stiffness matrices:

$$
\left[C^A\right] = \int_0^l [H^A]^T [A_4][H^A]\,dx \tag{A.117}
$$

$$
\left[K^A\right] = \int_0^l [H^A]^T [A_5][H^A]\,dx \tag{A.118}
$$

which may be subtracted from the structural matrices as before. The structural wing matrices are not influenced by the wing sweep.

Wing sweep also modifies the lift curve slope. For a shear wing, where the airfoil section is assumed to rotate with the sweep and remain perpendicular to the elastic axis, the effective lift curve slope becomes:

$$
(c_{l_\alpha})_{eff} = (c_{l_\alpha})\cos\Lambda \tag{A.119}
$$

and for a standard swept wing, where the airfoil remains aligned with the free stream, the effective lift curve slope becomes:

$$
(c_{l_\alpha})_{eff} = (c_{l_\alpha})\cos^2\Lambda \tag{A.120}
$$

379

A.6 Coupling of the Wing and Rotor Systems

The wing is coupled to the rotor through the discrete degrees of freedom at the wing tip. There are two ways in which the coupling occurs: 1) the rotor system degrees of freedom at the pylon pivot point are related to the discrete degrees of freedom at the wing tip and 2) the rotor hub forces, which are written in terms of the rotor perturbation parameters, perform work on the wing.

The discrete displacements at the wing tip may be written as:

$$\hat{q}_t = \{\delta w_2 \ \delta v_2 \ \delta \phi_2 \ \delta v_2' \ \delta w_2'\} \tag{A.121}$$

where the subscript 2 indicates association with the second node of the wing tip beam element. With sweep introduced into the wing, these are related to the pylon pivot degrees of freedom (x_P, y_P, z_P , α_x, α_y, and α_z) as:

$$x_P = w_2 \tag{A.122}$$

$$y_P = v_2 \sin \Lambda \tag{A.123}$$

$$z_P = v_2 \cos \Lambda \tag{A.124}$$

$$\alpha_x = v_2' \tag{A.125}$$

$$\alpha_y = \phi_2 \cos \Lambda - w_2' \sin \Lambda \tag{A.126}$$

$$\alpha_z = -\phi_2 \sin \Lambda - w_2' \cos \Lambda \tag{A.127}$$

and these relationships are substituted into the rotor system equations (Eqns. A.12-A.17 and Eqns. A.55-A.60) and the net hub force equations (Eqns. A.66-A.68).

Work is performed on the wing by the rotor hub forces, but only on the wing

tip. After a transformation for the wing sweep, the work may be written as:

$$\delta W = \{\delta w_2 \ \delta v_2 \ \delta \phi_2 \ \delta v_2' \ \delta w_2'\} \left\{ \begin{array}{c} H \\ T\cos\Lambda + Y\sin\Lambda \\ (M_y + hH)\cos\Lambda + Q\sin\Lambda \\ M_z - hY \\ -Q\cos\Lambda + (M_y + hH)\sin\Lambda \end{array} \right\} \qquad (\text{A.128})$$

There is no integration here since the degrees of freedom are discrete. The work is nondimensionalized by dividing through by $(\frac{N}{2}I_b\Omega^2)$ which gives the coefficient form of the rotor hub forces:

$$\frac{\delta W}{\frac{N}{2}I_b\Omega^2} = \delta\hat{q}_t(\frac{2\gamma}{\sigma a}) \left\{ \begin{array}{c} C_H \\ C_T\cos\Lambda + C_Y\sin\Lambda \\ (C_{M_y} + \bar{h}C_H)\cos\Lambda + C_Q\sin\Lambda \\ C_{M_z} - \bar{h}C_Y \\ -C_Q\cos\Lambda + (C_{M_y} + \bar{h}C_H)\sin\Lambda \end{array} \right\} \qquad (\text{A.129})$$

Substitution of the expressions for the hub forces into the above equations yields the work performed on the wing tip beam element in terms of the wing tip and blade perturbation motions. Writing this system as coefficients of the wing and blade motion yields damping and stiffness matrices which may be added to those associated with the rotor system (Eqns. A.12-A.17 and Eqns. A.55-A.60).

The wing and rotor system equations may then be assembled using standard finite element techniques where the parts of each matrix associated with common global degrees of freedom are added together. The rotor matrices are already in global form because they are written in terms of the discrete wing tip degrees of freedom. The wing matrices are assembled based on conversion of the element degrees of freedom into global degrees of freedom, but, as only one element is associated with the wing tip node, the five degrees of freedom at that location are already global. The common global degrees of freedom for the rotor and wing systems are those five degrees of freedom associated with the wing tip node.

381

A.7 Listing of the Rotor/Wing Matrices

The final inertial and aerodynamic rotor/wing matrices are listed in the form used in the rigid-blade analysis. The notation appearing in the listing is as follows: $mroti(i,j)$ is the mass matrix which has only inertial contributions, $crotf(i,j)$ is the aerodynamic damping matrix, $croti(i,j)$ is the inertial damping matrix, $krotf(i,j)$ is the aerodynamic stiffness matrix, and $kroti(i,j)$ is the inertial stiffness matrix. The element matrices are separated by aerodynamic and inertial contributions so that one of these effects may be easily excluded from the analysis if so desired. The two contributions are simply added together if both are desired. The numbering i or j associated with each degrees of freedom is

$$1 = w_2$$
$$2 = v_2$$
$$3 = \phi_2$$
$$4 = v_2'$$
$$5 = w_2'$$
$$6 = \beta_{1c}$$
$$7 = \beta_{1s}$$
$$8 = \zeta_{1c}$$
$$9 = \zeta_{1s}$$
$$10 = \beta_0$$
$$11 = \zeta_0$$

where the first 5 are the discrete degrees of freedom associated with the wing tip and the last 6 are the rotor system fixed frame degrees of freedom. Some of the parameters appearing in the listing are defined as follows:

$$\text{csl} = \cos \Lambda$$

382

$$\text{snl} \quad = \quad \sin \Lambda$$

$$\text{Mbstar} \quad = \quad M_b^*$$

$$\text{Szstar} \quad = \quad S_\zeta^*$$

$$\text{Sb0star} \quad = \quad S_{\beta_0}^*$$

$$\text{Ibastar} \quad = \quad I_{\beta\alpha}^*$$

$$\text{Ibetstar} \quad = \quad I_\beta^*$$

$$\text{Iz0star} \quad = \quad I_{\zeta_0}^*$$

$$\text{Izetstar} \quad = \quad I_\zeta^*$$

$$\text{Iz0astar} \quad = \quad I_{\zeta_0\alpha}^*$$

$$\text{nubeta} \quad = \quad \nu_\beta$$

$$\text{kp} \quad = \quad \text{kinematic pitch-flap coupling}$$

$$\text{hmu} \quad = \quad \text{Aerodynamic coefficient } H_\mu$$

$$\text{tth} \quad = \quad \text{Aerodynamic coefficient } T_\theta$$

and the remaining terms can be understood from these examples. The term *autorot* has a value of 1 if constant rotor speed assumption is desired (no rotor speed perturbation degree of freedom) and has a value of 0 otherwise. The nonzero contributions to the rotor wing matrices are now listed as:

```
mroti(1,1)  = 2*Mbstar;

mroti(1,3)  = 2*Mbstar*csl*h;

mroti(1,5)  = 2*Mbstar*h*snl;

mroti(1,9)  = Szstar;

mroti(2,2)  = 2*Mbstar*csl^2 + 2*Mbstar*snl^2;

mroti(2,4)  = -2*Mbstar*h*snl;

mroti(2,8)  = -(Szstar*snl);

mroti(2,10) = 2*Sb0star*csl;
```

```
mroti(3,1) = 2*Mbstar*csl*h;

mroti(3,3) = 2*Mbstar*csl^2*h^2 + 2*I0star*autorot*snl^2;

mroti(3,5) = -2*I0star*autorot*csl*snl + 2*Mbstar*csl*h^2*snl;

mroti(3,9) = Szstar*csl*h;

mroti(3,11) = 2*Iz0astar*autorot*snl;

mroti(4,2) = -2*Mbstar*h*snl;

mroti(4,4) = 2*Mbstar*h^2;

mroti(4,8) = Szstar*h;

mroti(5,1) = 2*Mbstar*h*snl;

mroti(5,3) = -2*I0star*autorot*csl*snl + 2*Mbstar*csl*h^2*snl;

mroti(5,5) = 2*I0star*autorot*csl^2 + 2*Mbstar*h^2*snl^2;

mroti(5,9) = Szstar*h*snl;

mroti(5,11) = -2*Iz0astar*autorot*csl;

mroti(6,3) = -(Ibastar*csl);

mroti(6,5) = -(Ibastar*snl);

mroti(6,6) = Ibetstar;

mroti(7,4) = Ibastar;

mroti(7,7) = Ibetstar;

mroti(8,2) = -(Szstar*snl);

mroti(8,4) = Szstar*h;

mroti(8,8) = Izetstar;

mroti(9,1) = Szstar;

mroti(9,3) = Szstar*csl*h;

mroti(9,5) = Szstar*h*snl;

mroti(9,9) = Izetstar;

mroti(10,2) = Sb0star*csl;

mroti(10,10) = Ib0star;
```

```
mroti(11,3) = Iz0astar*autorot*snl;

mroti(11,5) = -(Iz0astar*autorot*csl);

mroti(11,11) = Iz0star;


crotf(1,1) = gamma*hmu;

crotf(1,3) = csl*gamma*h*hmu;

crotf(1,4) = -(gamma*hbd);

crotf(1,5) = gamma*h*hmu*snl;

crotf(1,7) = -(gamma*hbd);

crotf(1,9) = gamma*hzd;

crotf(2,2) = gamma*hmu*snl^2 - 2*csl^2*gamma*tlam;

crotf(2,3) = -(csl*gamma*hbd*snl) + 2*csl*gamma*snl*tzd;

crotf(2,4) = -(gamma*h*hmu*snl);

crotf(2,5) =( -(gamma*hbd*snl^2) - 2*csl^2*gamma*tzd)*autorot;

crotf(2,6) = gamma*hbd*snl;

crotf(2,8) = -(gamma*hzd*snl);

crotf(2,10) = -2*csl*gamma*tbd;

crotf(2,11) = 2*csl*gamma*tzd;

crotf(3,1) = csl*gamma*h*hmu;

crotf(3,2) = -2*autorot*csl*gamma*qlam*snl;

crotf(3,3) = csl^2*gamma*h^2*hmu + 2*autorot*gamma*qzd*snl^2;

crotf(3,4) = -(csl*gamma*h*hbd);

crotf(3,5) = csl*gamma*h^2*hmu*snl - 2*autorot*csl*gamma*qzd*snl;

crotf(3,7) = -(csl*gamma*h*hbd);

crotf(3,9) = csl*gamma*h*hzd;

crotf(3,10) = -2*autorot*gamma*qbd*snl;

crotf(3,11) = 2*autorot*gamma*qzd*snl;
```

```
crotf(4,2) = -(gamma*h*hmu*snl);

crotf(4,3) = csl*gamma*h*hbd;

crotf(4,4) = gamma*h^2*hmu;

crotf(4,5) = gamma*h*hbd*snl;

crotf(4,6) = -(gamma*h*hbd);

crotf(4,8) = gamma*h*hzd;

crotf(5,1) = gamma*h*hmu*snl;

crotf(5,2) = 2*autorot*csl^2*gamma*qlam;

crotf(5,3) = csl*gamma*h^2*hmu*snl - 2*autorot*csl*gamma*qzd*snl;

crotf(5,4) = -(gamma*h*hbd*snl);

crotf(5,5) = 2*autorot*csl^2*gamma*qzd + gamma*h^2*hmu*snl^2;

crotf(5,7) = -(gamma*h*hbd*snl);

crotf(5,9) = gamma*h*hzd*snl;

crotf(5,10) = 2*autorot*csl*gamma*qbd;

crotf(5,11) = -2*autorot*csl*gamma*qzd;

crotf(6,2) = -(gamma*mmu*snl);

crotf(6,3) = csl*gamma*mbd;

crotf(6,4) = gamma*h*mmu;

crotf(6,5) = gamma*mbd*snl;

crotf(6,6) = -(gamma*mbd);

crotf(6,8) = gamma*mzd;

crotf(7,1) = gamma*mmu;

crotf(7,3) = csl*gamma*h*mmu;

crotf(7,4) = -(gamma*mbd);

crotf(7,5) = gamma*h*mmu*snl;

crotf(7,7) = -(gamma*mbd);

crotf(7,9) = gamma*mzd;
```

386

```
crotf(8,2) = -(gamma*qmu*snl);

crotf(8,3) = csl*gamma*qbd;

crotf(8,4) = gamma*h*qmu;

crotf(8,5) = gamma*qbd*snl;

crotf(8,6) = -(gamma*qbd);

crotf(8,8) = gamma*qzd;

crotf(9,1) = gamma*qmu;

crotf(9,3) = csl*gamma*h*qmu;

crotf(9,4) = -(gamma*qbd);

crotf(9,5) = gamma*h*qmu*snl;

crotf(9,7) = -(gamma*qbd);

crotf(9,9) = gamma*qzd;

crotf(10,2) = -(csl*gamma*mlam);

crotf(10,3) = autorot*gamma*mzd*snl;

crotf(10,5) = -(autorot*csl*gamma*mzd);

crotf(10,10) = -(gamma*mbd);

crotf(10,11) = gamma*mzd;

crotf(11,2) = -(csl*gamma*qlam);

crotf(11,3) = autorot*gamma*qzd*snl;

crotf(11,5) = -(autorot*csl*gamma*qzd);

crotf(11,10) = -(gamma*qbd);

crotf(11,11) = gamma*qzd;


croti(6,4) = 2*Ibastar;

croti(6,7) = 2*Ibetstar;

croti(7,3) = 2*Ibastar*csl;

croti(7,5) = 2*Ibastar*snl;
```

```
croti(7,6) = -2*Ibetstar;

croti(8,9) = 2*Izetstar;

croti(9,8) = -2*Izetstar;


krotf(1,3) = -(V*gamma*hmu);

krotf(1,6) = gamma*hbd;

krotf(1,7) = gamma*hth*kp;

krotf(1,8) = -(gamma*hzd);

krotf(2,4) = V*gamma*hmu*snl;

krotf(2,6) = -(gamma*hth*kp*snl);

krotf(2,7) = gamma*hbd*snl;

krotf(2,9) = -(gamma*hzd*snl);

krotf(2,10) = 2*csl*gamma*kp*tth;

krotf(3,3) = -(V*csl*gamma*h*hmu);

krotf(3,6) = csl*gamma*h*hbd;

krotf(3,7) = csl*gamma*h*hth*kp;

krotf(3,8) = -(csl*gamma*h*hzd);

krotf(3,10) = 2*autorot*gamma*kp*qth*snl;

krotf(4,4) = -(V*gamma*h*hmu);

krotf(4,6) = gamma*h*hth*kp;

krotf(4,7) = -(gamma*h*hbd);

krotf(4,9) = gamma*h*hzd;

krotf(5,3) = -(V*gamma*h*hmu*snl);

krotf(5,6) = gamma*h*hbd*snl;

krotf(5,7) = gamma*h*hth*kp*snl;

krotf(5,8) = -(gamma*h*hzd*snl);

krotf(5,10) = -2*autorot*csl*gamma*kp*qth;
```

388

```
krotf(6,4) = -(V*gamma*mmu);

krotf(6,6) = gamma*kp*mth;

krotf(6,7) = -(gamma*mbd);

krotf(6,9) = gamma*mzd;

krotf(7,3) = -(V*gamma*mmu);

krotf(7,6) = gamma*mbd;

krotf(7,7) = gamma*kp*mth;

krotf(7,8) = -(gamma*mzd);

krotf(8,4) = -(V*gamma*qmu);

krotf(8,6) = gamma*kp*qth;

krotf(8,7) = -(gamma*qbd);

krotf(8,9) = gamma*qzd;

krotf(9,3) = -(V*gamma*qmu);

krotf(9,6) = gamma*qbd;

krotf(9,7) = gamma*kp*qth;

krotf(9,8) = -(gamma*qzd);

krotf(10,10) = gamma*kp*mth;

krotf(11,10) = gamma*kp*qth;


kroti(3,6) = -(Ibastar*csl) + Ibastar*csl*nubeta^2;

kroti(4,7) = Ibastar - Ibastar*nubeta^2;

kroti(5,6) = -(Ibastar*snl) + Ibastar*nubeta^2*snl;

kroti(6,6) = -Ibetstar + Ibetstar*nubeta^2;

kroti(7,7) = -Ibetstar + Ibetstar*nubeta^2;

kroti(8,8) = -Izetstar + Izetstar*nuzeta^2;

kroti(9,9) = -Izetstar + Izetstar*nuzeta^2;

kroti(10,10) = Ib0star*nub0^2;
```

```
kroti(11,11) = Iz0star*nuz0^2;
```

A.8   Listing of the Wing Element Matrices

The final wing element matrices with both aerodynamic and structural contributions are listed in the form used in the rigid-blade analysis. The notation appearing in the listing is as follows: $m(i,j)$ is the mass matrix which has only inertial contributions, $c(i,j)$ is the damping matrix which has both structural and aerodynamic contributions, and $k(i,j)$ is the stiffness matrix which also has both structural and aerodynamic contributions. The numbering i or j associated with each degree of freedom is:

$$1 = w_1$$
$$2 = v_1$$
$$3 = \phi_1$$
$$4 = v_1'$$
$$5 = w_1'$$
$$6 = w_2$$
$$7 = v_2$$
$$8 = \phi_2$$
$$9 = v_2'$$
$$10 = w_2'$$

where the first 5 are the discrete degrees of freedom associated with node 1 (node closer to wing root) and the last 5 are the discrete degrees of freedom associated with node 2. Some of the parameters appearing in the listing are defined as follows:

mcg   =   mass per unit length

Salf = 1st mass moment of inertia about elastic axis per unit length

Icg = 2nd mass moment of inertia about elastic axis per unit length

R = blade radius

l = element length

Cla = wing lift curve slope

cord = blade chord, c/R

qou = dynamic pressure over free stream velocity, q/U

sdamp = structural damping

eic = EI_c

eif = EI_b

gj = GJ

The nonzero contributions to the wing matrices are now listed as follows:

Wing element mass matrix:

m(1,1) = 13*R^2*l*mcg/35;

m(1,3) = 7*R*Salf*l/20;

m(1,5) = -11*R*l^2*mcg/210;

m(1,6) = 9*R^2*l*mcg/70;

m(1,8) = 3*R*Salf*l/20;

m(1,10) = 13*R*l^2*mcg/420;

m(2,2) = 13*R^2*l*mcg/35;

m(2,4) = 11*R*l^2*mcg/210;

m(2,7) = 9*R^2*l*mcg/70;

m(2,9) = -13*R*l^2*mcg/420;

m(3,1) = 7*R*Salf*l/20;

```
m(3,3) = Icg*l/3;

m(3,5) = -(Salf*l^2)/20;

m(3,6) = 3*R*Salf*l/20;

m(3,8) = Icg*l/6;

m(3,10) = Salf*l^2/30;

m(4,2) = 11*R*l^2*mcg/210;

m(4,4) = l^3*mcg/105;

m(4,7) = 13*R*l^2*mcg/420;

m(4,9) = -(l^3*mcg)/140;

m(5,1) = -11*R*l^2*mcg/210;

m(5,3) = -(Salf*l^2)/20;

m(5,5) = l^3*mcg/105;

m(5,6) = -13*R*l^2*mcg/420;

m(5,8) = -(Salf*l^2)/30;

m(5,10) = -(l^3*mcg)/140;

m(6,1) = 9*R^2*l*mcg/70;

m(6,3) = 3*R*Salf*l/20;

m(6,5) = -13*R*l^2*mcg/420;

m(6,6) = 13*R^2*l*mcg/35;

m(6,8) = 7*R*Salf*l/20;

m(6,10) = 11*R*l^2*mcg/210;

m(7,2) = 9*R^2*l*mcg/70;

m(7,4) = 13*R*l^2*mcg/420;

m(7,7) = 13*R^2*l*mcg/35;

m(7,9) = -11*R*l^2*mcg/210;

m(8,1) = 3*R*Salf*l/20;

m(8,3) = Icg*l/6;
```

392

```
m(8,5)  = -(Salf*l^2)/30;

m(8,6)  = 7*R*Salf*l/20;

m(8,8)  = Icg*l/3;

m(8,10) = Salf*l^2/20;

m(9,2)  = -13*R*l^2*mcg/420;

m(9,4)  = -(l^3*mcg)/140;

m(9,7)  = -11*R*l^2*mcg/210;

m(9,9)  = l^3*mcg/105;

m(10,1) = 13*R*l^2*mcg/420;

m(10,3) = Salf*l^2/30;

m(10,5) = -(l^3*mcg)/140;

m(10,6) = 11*R*l^2*mcg/210;

m(10,8) = Salf*l^2/20;

m(10,10) = l^3*mcg/105;
```

Wing damping matrix:

```
c(1,1)  = 13*Cla*R^2*cord*l*qou/35 + sdamp_w;

c(1,5)  = -11*Cla*R*cord*l^2*qou/210;

c(1,6)  = 9*Cla*R^2*cord*l*qou/70;

c(1,10) = 13*Cla*R*cord*l^2*qou/420;

c(2,2)= sdamp_v;

c(3,1)  = 7*Cla*R*cord*e*l*qou/20;

c(3,3)  = sdamp_phi;

c(3,5)  = -(Cla*cord*e*l^2*qou)/20;

c(3,6)  = 3*Cla*R*cord*e*l*qou/20;

c(3,10) = Cla*cord*e*l^2*qou/30;
```

```
c(5,1) = -11*Cla*R*cord*l^2*qou/210;

c(5,5) = Cla*cord*l^3*qou/105;

c(5,6) = -13*Cla*R*cord*l^2*qou/420;

c(5,10) = -(Cla*cord*l^3*qou)/140;

c(6,1) = 9*Cla*R^2*cord*l*qou/70;

c(6,5) = -13*Cla*R*cord*l^2*qou/420;

c(6,6) = 13*Cla*R^2*cord*l*qou/35 + sdamp_w;

c(6,10) = 11*Cla*R*cord*l^2*qou/210;

c(7,7) = sdamp_v;

c(8,1) = 3*Cla*R*cord*e*l*qou/20;

c(8,5) = -(Cla*cord*e*l^2*qou)/30;

c(8,6) = 7*Cla*R*cord*e*l*qou/20;

c(8,8) = sdamp_phi;

c(8,10) = Cla*cord*e*l^2*qou/20;

c(10,1) = 13*Cla*R*cord*l^2*qou/420;

c(10,5) = -(Cla*cord*l^3*qou)/140;

c(10,6) = 11*Cla*R*cord*l^2*qou/210;

c(10,10) = Cla*cord*l^3*qou/105;
```

Wing stiffness matrix:

```
k(1,1) = 12*R^2*eif/l^3 - Cla*R^2*cord*q*snl/2;

k(1,3) = -7*Cla*R*cord*l*q*csl/20;

k(1,5) = -6*R*eif/l^2 + Cla*R*cord*l*q*snl/10;

k(1,6) = -12*R^2*eif/l^3 + Cla*R^2*cord*q*snl/2;

k(1,8) = -3*Cla*R*cord*l*q*csl/20;

k(1,10) = -6*R*eif/l^2 - Cla*R*cord*l*q*snl/10;
```

```
k(2,2) = 12*R^2*eic/l^3;

k(2,4) = 6*R*eic/l^2;

k(2,7) = -12*R^2*eic/l^3;

k(2,9) = 6*R*eic/l^2;

k(3,1) = -(Cla*R*cord*e*q*snl)/2;

k(3,3) = gj/l - Cla*cord*e*l*q*csl/3;

k(3,5) = Cla*cord*e*l*q*snl/12;

k(3,6) = Cla*R*cord*e*q*snl/2;

k(3,8) = -(gj/l) - Cla*cord*e*l*q*csl/6;

k(3,10) = -(Cla*cord*e*l*q*snl)/12;

k(4,2) = 6*R*eic/l^2;

k(4,4) = 4*eic/l;

k(4,7) = -6*R*eic/l^2;

k(4,9) = 2*eic/l;

k(5,1) = -6*R*eif/l^2 + Cla*R*cord*l*q*snl/10;

k(5,3) = Cla*cord*l^2*q*csl/20;

k(5,5) = 4*eif/l;

k(5,6) = 6*R*eif/l^2 - Cla*R*cord*l*q*snl/10;

k(5,8) = Cla*cord*l^2*q*csl/30;

k(5,10) = 2*eif/l + Cla*cord*l^2*q*snl/60;

k(6,1) = -12*R^2*eif/l^3 - Cla*R^2*cord*q*snl/2;

k(6,3) = -3*Cla*R*cord*l*q*csl/20;

k(6,5) = 6*R*eif/l^2 - Cla*R*cord*l*q*snl/10;

k(6,6) = 12*R^2*eif/l^3 + Cla*R^2*cord*q*snl/2;

k(6,8) = -7*Cla*R*cord*l*q*csl/20;

k(6,10) = 6*R*eif/l^2 + Cla*R*cord*l*q*snl/10;

k(7,2) = -12*R^2*eic/l^3;
```

```
k(7,4) = -6*R*eic/l^2;

k(7,7) = 12*R^2*eic/l^3;

k(7,9) = -6*R*eic/l^2;

k(8,1) = -(Cla*R*cord*e*q*snl)/2;

k(8,3) = -(gj/l) - Cla*cord*e*l*q*csl/6;

k(8,5) = -(Cla*cord*e*l*q*snl)/12;

k(8,6) = Cla*R*cord*e*q*snl/2;

k(8,8) = gj/l - Cla*cord*e*l*q*csl/3;

k(8,10) = Cla*cord*e*l*q*snl/12;

k(9,2) = 6*R*eic/l^2;

k(9,4) = 2*eic/l;

k(9,7) = -6*R*eic/l^2;

k(9,9) = 4*eic/l;

k(10,1) = -6*R*eif/l^2 - Cla*R*cord*l*q*snl/10;

k(10,3) = -(Cla*cord*l^2*q*csl)/30;

k(10,5) = 2*eif/l - Cla*cord*l^2*q*snl/60;

k(10,6) = 6*R*eif/l^2 + Cla*R*cord*l*q*snl/10;

k(10,8) = -(Cla*cord*l^2*q*csl)/20;

k(10,10) = 4*eif/l;
```
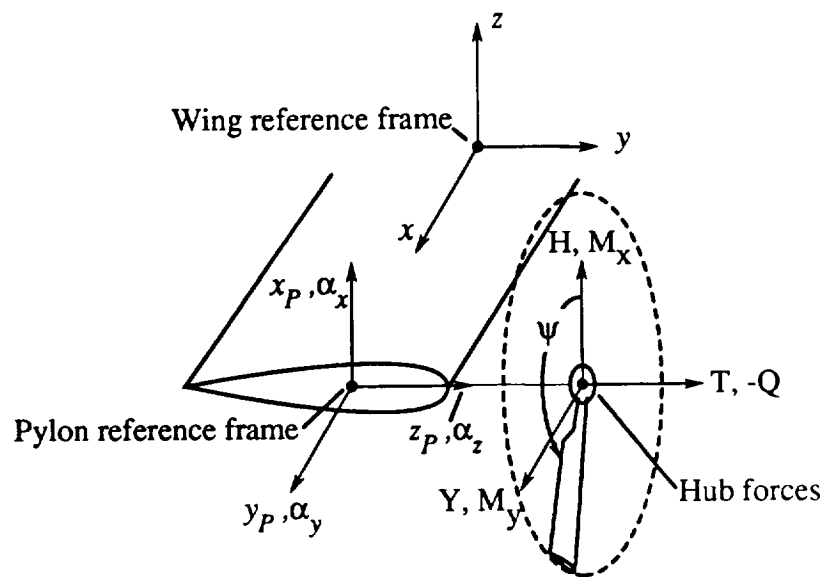
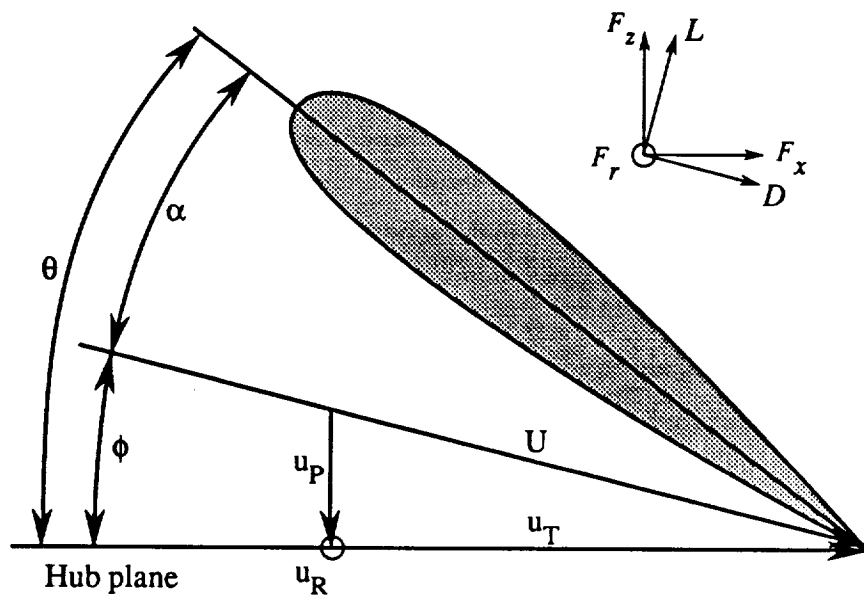Figure A.1: Wing and rotor model showing pylon pivot degrees of freedom and rotor hub forces.

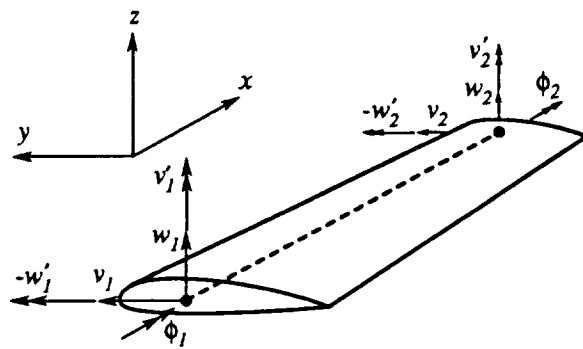Figure A.2: Velocity and force components on a representative blade section.

Figure A.3: Continuous and discrete degrees of freedom associated with a wing element.
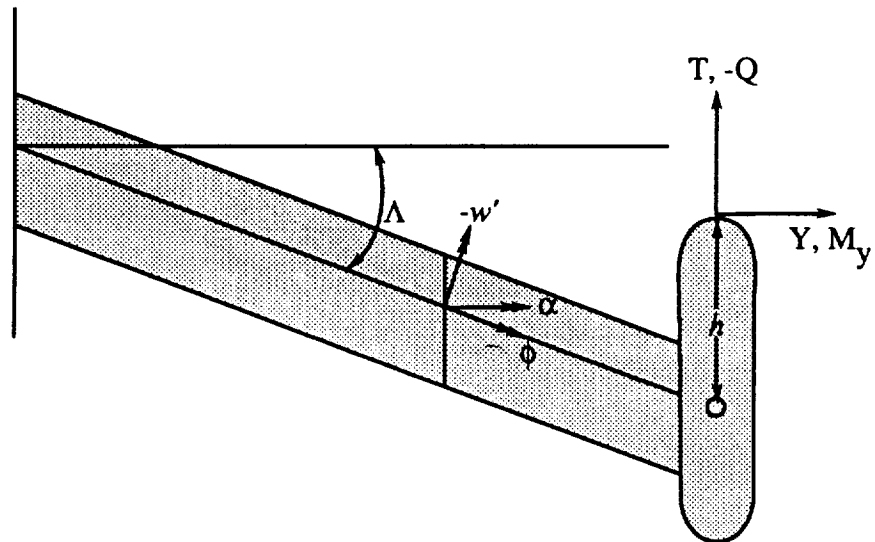
Figure A.4: Geometry of the swept wing configuration.

Appendix B

Rigid Blade Flap Model
Including Free-Flight

The objective of the rigid-blade flap analysis is to provide initial estimates (to be used for the elastic blade coupled trim procedure) for the blade collective and cyclic controls θ_{75}, θ_{1c}, and θ_{1s}, and the fuselage angle of attack, α_f, if free-flight trim is considered. If the elastic-coupled-trim is for a cantilevered wing model, then α_f is not required and the procedure is simplified. The rigid-blade analysis consists of three parts: 1) estimation of the fuselage angle of attack and the rotor thrust based on the gross airframe forces, but not including rotor hub forces other than thrust and not including blade flap motion, 2) estimation of the collective setting required to obtain the estimated rotor thrust from (1), and 3) with the initial guesses for fuselage angle of attack and the collective setting, solve simultaneously the coupled rotor/fuselage system with rotor flap motion included, resulting in an estimation of the four desired values θ_{75}, θ_{1c}, and θ_{1s}, and α_f plus the rotor flapping unknowns β_0, β_{1c}, and β_{1s}.

B.1 Estimate of Fuselage Angle of Attack and Rotor Thrust

If free-flight is not required, then a rotor thrust estimate is provided directly as input, the fuselage angle is set to zero, and the analysis of the present section is skipped. Otherwise, an initial approximation for α_f is obtained from a balance of forces on the fuselage. The hub forces from the rotor are not known, but the rotor thrust can be estimated since it must balance the aircraft drag and weight. The lift on the wing and horizontal tail depend on α_f, so even this initial estimate is an iterative process. The lift and drag contributions from the wing and horizontal tail are calculated as:

$$D_f = \frac{\mu^2}{2}\frac{\gamma N_b}{3\sigma a}\frac{f}{A} \tag{B.1}$$

$$D_w = \frac{\mu^2}{2}\frac{\gamma N_b}{3\sigma a}S_w(C_d)_w \tag{B.2}$$

$$D_t = \frac{\mu^2}{2}\frac{\gamma N_b}{3\sigma a}S_t(C_d)_t \tag{B.3}$$

$$L_w = \frac{\mu^2}{2}\frac{\gamma N_b}{3\sigma a}S_w(C_{l_\alpha})_w(\alpha_f + (\alpha_0)_w) \tag{B.4}$$

$$M_w = \frac{\mu^2}{2}\frac{\gamma N_b}{3\sigma a}S_w(C_m)_w c_w \tag{B.5}$$

$$M_t = \frac{\mu^2}{2}\frac{\gamma N_b}{3\sigma a}S_t(C_m)_t c_t \tag{B.6}$$

$$T_{fh} = D_f + D_w + D_t \tag{B.7}$$

$$T_r = T_{fh}/\sin\alpha_p \ , \text{ if } \sin\alpha_p \neq 0 \text{ (conversion, airplane modes)} \tag{B.8}$$

$$T_r = W \ , \text{ if } \sin\alpha_p = 0 \text{ (helicopter mode)} \tag{B.9}$$

$$T_{fv} = T\cos\alpha_p \ , \text{ if } \sin\alpha_p \neq 0 \text{ (conversion, airplane modes)} \tag{B.10}$$

$$T_{fv} = W \ , \text{ if } \sin\alpha_p = 0 \text{ (helicopter mode)} \tag{B.11}$$

where the lift and drag formulas for the wing, tail, and fuselage are the same as those used in the elastic blade trim equations, T_r is the estimate of rotor thrust, T_{fh} is the horizontal component of rotor thrust which must balance the drag forces,

and T_{fv} is the vertical component of rotor thrust which must balance with the airframe lift forces. The drag forces are made to balance by setting the horizontal component of rotor thrust equal to the sum of drags. Based on the pylon angle, this then defines the thrust and the vertical component of the thrust which is used to define a force residual in the vertical direction:

$$F_1 = W - L_w - L_t - T_{fv} \tag{B.12}$$

The lift contribution of the horizontal tail is calculated from the pitch moment balance:

$$L_t = (M_w + M_t - D_t(z_w - z_t) - W x_w - W \alpha_f z_w - D_f z_w)/(x_t - x_w) \tag{B.13}$$

because it is assumed that the elevator angle of the tail may be set to produce this balance. A Jacobian is calculated from the force residual equation:

$$J = T_{fh} + T_{fh} \cos^2 \alpha_p / \sin^2 \alpha_p + L_w/\alpha_f + L_t/\alpha_f \tag{B.14}$$

and is used to calculate the new estimate for α_f as:

$$(\alpha_f)_{new} = (\alpha_f)_{old} + F_1/J \tag{B.15}$$

B.2 Derivation of Blade and Hub Forces

Following convergence, the next step is to determine the collective setting required to produce the rotor thrust T_r. This calculation is also an iterative process, and the aerodynamic model of the rotor forces must first be formulated.

The rotor fixed-frame (hub) forces are calculated based on a rigid-blade-flapping model with flap frequency ν_β and a high-inflow aerodynamic model. The local velocities on a blade section at some spanwise station along the blade are defined as:

$$U_t = t_c + t_w w + t_{w'} w' + t_{\dot{w}} \dot{w} \tag{B.16}$$

$$U_p = p_c + p_w w + p_{w'} w' + p_{\dot{w}} \dot{w} \tag{B.17}$$

where U_t is the tangential velocity component, U_p is the perpendicular (upward) velocity component; subscript c denotes constant values, w and w' indicate dependence of the local velocity on displacement w, and $\dot{w}$ indicates dependence of the local velocity on blade flap velocity. The velocity components are defined as:

$$t_c = \mu\cos\alpha_p\cos\theta_1\sin\psi + \mu\beta_p\cos\alpha_p\cos\psi\sin\theta_1 + \lambda\sin\theta_1 +$$

$$\mu\sin\alpha_p\sin\theta_1 + x\cos\theta_1 \tag{B.18}$$

$$t_w = -\beta_p\cos\theta_1 \tag{B.19}$$

$$t_{w'} = -\mu\sin\theta_1\left(\cos\alpha_p\cos\theta_1\sin\psi + \sin\alpha_p\sin\theta_1\right) \tag{B.20}$$

$$t_{\dot{w}} = \sin\theta_1 \tag{B.21}$$

$$p_c = \mu\beta_p\cos\alpha_p\cos\psi\cos\theta_1 + \lambda\cos\theta_1 + \mu\cos\theta_1\sin\alpha_p -$$

$$\mu\cos\alpha_p\sin\psi\sin\theta_1 - x\sin\theta_1 \tag{B.22}$$

$$p_w = -\beta_p\sin\theta_1 \tag{B.23}$$

$$p_{w'} = -\mu\cos\theta_1\left(\cos\alpha_p\cos\theta_1\sin\psi + \sin\alpha_p\sin\theta_1\right) \tag{B.24}$$

$$p_{\dot{w}} = \cos\theta_1 \tag{B.25}$$

and the blade displacement w is defined in terms of the flap angle β such that:

$$w = x\beta \tag{B.26}$$

$$w' = \beta \tag{B.27}$$

$$\dot{w} = x\dot{\beta} \tag{B.28}$$

The control angle θ is substituted for in terms of its harmonic components as:

$$\theta = \theta_{75} + \theta_{1c}\cos\psi + \theta_{1s}\sin\psi \tag{B.29}$$

Now, assuming the blade produces only lift proportional to the nominal lift curve slope a, the forces on the blade along the chord line and perpendicular to it are given by:

$$v_{b0} = \frac{\gamma}{6}u_p^2 \tag{B.30}$$

404

$$w_{b0} = -\frac{\gamma}{6}u_t u_p \tag{B.31}$$

which may be transformed into the hub plane as:

$$F_x = -v_{b0}\cos\theta_1 + w_{b0}\sin\theta_1 \tag{B.32}$$

$$F_z = v_{b0}\sin\theta_1 + w_{b0}\cos\theta_1 \tag{B.33}$$

$$F_r = -\beta F_z \tag{B.34}$$

The rotor forces are calculated by transforming the following integrals into the fixed system:

$$T = \int_0^1 F_z \, dx \tag{B.35}$$

$$H = \int_0^1 (F_x\sin\psi + F_r\cos\psi) \, dx \tag{B.36}$$

$$M_x = \int_0^1 xF_z\sin\psi \, dx \tag{B.37}$$

$$M_y = \int_0^1 xF_z\cos\psi \, dx \tag{B.38}$$

and the flap moment equilibrium on the blade is given by:

$$M_\beta = \int_0^1 xF_z \, dx \tag{B.39}$$

which can be written as

$$M_\beta = M_0 + M_{1c}\cos\psi + M_{1s}\sin\psi \tag{B.40}$$

where M_0 represents the constant terms, and M_{1c} and M_{1s} represent the coefficients of the periodic terms $\cos\psi$ and $\sin\psi$, respectively. The final terms in these force equations (4 hub forces and 3 flapping moments) are listed in the following section.

B.3   Listing of the Hub Force and Blade Moment Expressions

The integrations of Eqns. B.35-B.40 result in seven lengthy expressions of the four hub forces and three blade moments, all in the rotating frame and containing the

seven unknowns.

The complete equation of motion for blade flapping is given by:

$$\ddot{\beta} + \nu_\beta^2 \beta = \gamma M_\beta + \frac{\omega_{\beta_0}^2}{\Omega^2}\beta_p \qquad (B.41)$$

which in nondimensional form and after substitution of the flap angle in terms of harmonics:

$$\beta = \beta_0 + \beta_{1c}\cos\psi + \beta_{1s}\sin\psi \qquad (B.42)$$

may be written as three equations which are coefficients of the periodic terms:

$$\beta_0 = \frac{1}{\nu_\beta^2}(\gamma M_0 + \omega_{\beta_0}^2 \beta_p) \qquad (B.43)$$

which is uncoupled from the cyclic equations:

$$\frac{\nu_{\beta^2} - 1}{\gamma}\beta_{1c} = M_{1c} \qquad (B.44)$$

$$\frac{\nu_{\beta^2} - 1}{\gamma}\beta_{1s} = M_{1s} \qquad (B.45)$$

The cyclic equations are coupled because M_{1c} and M_{1s} each contain terms with both β_{1c} and β_{1s}. The actual terms of the aerodynamic moments are listed as follows: the steady moment is written as

$$M_0 = \sum_{i=1}^{14} b_i \qquad (B.46)$$

with the coefficients given as follows

$$b_1 = -(\lambda_i \cos^3\theta_{75})/6. \qquad (B.47)$$

$$b_2 = -(\mu \cos^3\theta_{75} sp)/6. \qquad (B.48)$$

$$b_3 = \cos^2\theta_{75} \sin\theta_{75}/8. \qquad (B.49)$$

$$b_4 = \mu^2\cos^2\alpha_p \cos^2\theta_{75} \sin\theta_{75}/8. \qquad (B.50)$$

$$b_5 = -(\lambda_i \cos\theta_{75} \sin^2\theta_{75})/6. \qquad (B.51)$$

$$b_6 = -(\mu \cos\theta_{75}\sin\alpha_p \sin^2\theta_{75})/6. \qquad (B.52)$$

$$b_7 = \sin^3\theta_{75}/8. \tag{B.53}$$

$$b_8 = \mu^2\cos^2\alpha_p \sin^3\theta_{75}/8. \tag{B.54}$$

$$b_9 = \mu\cos\alpha_p \cos^3\theta_{75}\theta_{1s}/6. \tag{B.55}$$

$$b_{10} = \lambda_i\mu\cos\alpha_p \cos^2\theta_{75} \sin\theta_{75}\theta_{1s}/8. \tag{B.56}$$

$$b_{11} = \mu^2\cos\alpha_p \cos^2\theta_{75}\sin\alpha_p \sin\theta_{75}\theta_{1s}/8. \tag{B.57}$$

$$b_{12} = \mu\cos\alpha_p \cos\theta_{75} \sin^2\theta_{75}\theta_{1s}/6. \tag{B.58}$$

$$b_{13} = \lambda_i\mu\cos\alpha_p \sin^3\theta_{75}\theta_{1s}/8. \tag{B.59}$$

$$b_{14} = \mu^2\cos\alpha_p \sin\alpha_p \sin^3\theta_{75}\theta_{1s}/8. \tag{B.60}$$

the cosine moment is written as

$$M_{1c} = \sum_{i=15}^{32} b_i \tag{B.61}$$

with

$$b_{15} = -(\beta_{1s} \cos^3\theta_{75})/8. \tag{B.62}$$

$$b_{16} = -(\mu\beta_0\cos\alpha_p \cos^3\theta_{75})/6. \tag{B.63}$$

$$b_{17} = -(\mu\beta_p\cos\alpha_p \cos^3\theta_{75})/6. \tag{B.64}$$

$$b_{18} = \mu\beta_0\beta_p{}^2\cos\alpha_p \cos^3\theta_{75}/6. \tag{B.65}$$

$$b_{19} = -(\mu^2\beta_{1s}\cos^2\alpha_p \cos^3\theta_{75})/8. \tag{B.66}$$

$$b_{20} = -(\beta_{1s} \cos\theta_{75} \sin^2\theta_{75})/8. \tag{B.67}$$

$$b_{21} = -(\mu\beta_0\cos\alpha_p \cos\theta_{75} \sin^2\theta_{75})/6. \tag{B.68}$$

$$b_{22} = -(\mu\beta_p\cos\alpha_p \cos\theta_{75} \sin^2\theta_{75})/6. \tag{B.69}$$

$$b_{23} = \mu\beta_0\beta_p{}^2\cos\alpha_p \cos\theta_{75} \sin^2\theta_{75}/6. \tag{B.70}$$

$$b_{24} = -(\mu^2\beta_{1s}\cos^2\alpha_p \cos\theta_{75} \sin^2\theta_{75})/8. \tag{B.71}$$

$$b_{25} = \cos^3\theta_{75}\theta_{1c}/8. \tag{B.72}$$

$$b_{26} = \mu^2\cos^2\alpha_p \cos^3\theta_{75}\theta_{1c}/8. \tag{B.73}$$

$$b_{27} = \lambda_i \cos^2\theta_{75} \sin\theta_{75}\theta_{1c}/6. \tag{B.74}$$

$$b_{28} = \mu \cos^2\theta_{75} \sin\alpha_p \, \sin\theta_{75}\theta_{1c}/6. \tag{B.75}$$

$$b_{29} = \cos\theta_{75} \sin^2\theta_{75}\theta_{1c}/8. \tag{B.76}$$

$$b_{30} = \mu^2\cos^2\alpha_p \, \cos\theta_{75} \sin^2\theta_{75}\theta_{1c}/8. \tag{B.77}$$

$$b_{31} = \lambda_i \sin^3\theta_{75}\theta_{1c}/6. \tag{B.78}$$

$$b_{32} = \mu\sin\alpha_p \, \sin^3\theta_{75}\theta_{1c}/6. \tag{B.79}$$

and the sine moment is written as

$$M_{1s} = \sum_{i=33}^{50} b_i \tag{B.80}$$

with

$$b_{33} = \beta_{1c} \cos^3\theta_{75}/8. \tag{B.81}$$

$$b_{34} = -(\lambda_i\mu\cos\alpha_p \, \cos^3\theta_{75})/4. \tag{B.82}$$

$$b_{35} = -(\mu^2\beta_{1c}\cos^2\alpha_p \, \cos^3\theta_{75})/8. \tag{B.83}$$

$$b_{36} = -(\mu^2\cos\alpha_p \, \cos^3\theta_{75}sp)/4. \tag{B.84}$$

$$b_{37} = \mu\cos\alpha_p \, \cos^2\theta_{75} \sin\theta_{75}/3. \tag{B.85}$$

$$b_{38} = \beta_{1c} \cos\theta_{75} \sin^2\theta_{75}/8. \tag{B.86}$$

$$b_{39} = -(\lambda_i\mu\cos\alpha_p \, \cos\theta_{75} \sin^2\theta_{75})/4. \tag{B.87}$$

$$b_{40} = -(\mu^2\beta_{1c}\cos^2\alpha_p \, \cos\theta_{75} \sin^2\theta_{75})/8. \tag{B.88}$$

$$b_{41} = -(\mu^2\cos\alpha_p \, \cos\theta_{75}\sin\alpha_p \, \sin^2\theta_{75})/4. \tag{B.89}$$

$$b_{42} = \mu\cos\alpha_p \, \sin^3\theta_{75}/3. \tag{B.90}$$

$$b_{43} = \cos^3\theta_{75}\theta_{1s}/8. \tag{B.91}$$

$$b_{44} = 3\mu^2\cos^2\alpha_p \, \cos^3\theta_{75}\theta_{1s}/16. \tag{B.92}$$

$$b_{45} = \lambda_i \cos^2\theta_{75} \sin\theta_{75}\theta_{1s}/6. \tag{B.93}$$

$$b_{46} = \mu \cos^2\theta_{75}\sin\alpha_p \, \sin\theta_{75}\theta_{1s}/6. \tag{B.94}$$

$$b_{47} = \cos\theta_{75} \sin^2\theta_{75}\theta_{1s}/8. \tag{B.95}$$

$$b_{48} = 3\mu^2\cos^2\alpha_p \, \cos\theta_{75} \sin^2\theta_{75}\theta_{1s}/16. \tag{B.96}$$

$$b_{49} = \lambda_i \sin^3\theta_{75}\theta_{1s}/6. \tag{B.97}$$

$$b_{50} = \mu\sin\alpha_p \ \sin^3\theta_{75}\theta_{1s}/6. \tag{B.98}$$

The four hub force expressions, currently written in the rotating hub plane, must be converted to a fixed frame. The Fourier coordinate transformation into the fixed frame depends on the number of blades, but, as this rigid-blade analysis only provides an estimate of control parameters and the aerodynamic model is based only on a representative lift curve slope, it is adequate to assume an arbitrary number of blades to represent the tip-path-plane tilt for any typical N_b bladed system. This assumption greatly simplifies the hub force equations. The transformation to fixed frame is based on a three-bladed system, and the resulting hub forces are written as follows: the rotor thrust is given by

$$T = \frac{\gamma N_b}{6} \sum_{i=1}^{14} a_i \tag{B.99}$$

where

$$a_1 = -(\lambda_i \cos^3\theta_{75})/2. \tag{B.100}$$

$$a_2 = -(\mu \cos^3\theta_{75}sp)/2. \tag{B.101}$$

$$a_3 = \cos^2\theta_{75} \sin\theta_{75}/3. \tag{B.102}$$

$$a_4 = \mu^2\cos^2\alpha_p \ \cos^2\theta_{75} \sin\theta_{75}/2. \tag{B.103}$$

$$a_5 = -(\lambda_i \cos\theta_{75} \sin^2\theta_{75})/2. \tag{B.104}$$

$$a_6 = -(\mu \cos\theta_{75}\sin\alpha_p \ \sin^2\theta_{75})/2. \tag{B.105}$$

$$a_7 = \sin^3\theta_{75}/3. \tag{B.106}$$

$$a_8 = \mu^2\cos^2\alpha_p \ \sin^3\theta_{75}/2. \tag{B.107}$$

$$a_9 = \mu\cos\alpha_p \ \cos^3\theta_{75}\theta_{1s}/2. \tag{B.108}$$

$$a_{10} = \lambda_i\mu\cos\alpha_p \ \cos^2\theta_{75} \sin\theta_{75}\theta_{1s}/2. \tag{B.109}$$

$$a_{11} = \mu^2\cos\alpha_p \ \cos^2\theta_{75}\sin\alpha_p \ \sin\theta_{75}\theta_{1s}/2. \tag{B.110}$$

$$a_{12} = \mu\cos\alpha_p \ \cos\theta_{75} \sin^2\theta_{75}\theta_{1s}/2. \tag{B.111}$$

$$a_{13} = \lambda_i \mu \cos\alpha_p \ \sin^3\theta_{75}\theta_{1s}/2. \tag{B.112}$$

$$a_{14} = \mu^2 \cos\alpha_p \ \sin\alpha_p \ \sin^3\theta_{75}\theta_{1s}/2. \tag{B.113}$$

and the rotor drag force is given by

$$H = \frac{\gamma N_b}{6} \sum_{i=15}^{34} a_i \tag{B.114}$$

where

$$a_{15} = 3.\lambda_i\beta_{1c} \cos^3\theta_{75}/4. \tag{B.115}$$

$$a_{16} = 3.\mu\beta_{1c} \cos^3\theta_{75}sp/4. \tag{B.116}$$

$$a_{17} = -(\beta_{1c} \cos^2\theta_{75} \sin\theta_{75})/3. \tag{B.117}$$

$$a_{18} = \lambda_i\mu\cos\alpha_p \ \cos^2\theta_{75} \sin\theta_{75}/2. \tag{B.118}$$

$$a_{19} = \mu^2\cos\alpha_p \ \cos^2\theta_{75}\sin\alpha_p \ \sin\theta_{75}/2. \tag{B.119}$$

$$a_{20} = 3.\lambda_i\beta_{1c} \cos\theta_{75} \sin^2\theta_{75}/4. \tag{B.120}$$

$$a_{21} = 3.\mu\beta_{1c} \cos\theta_{75}\sin\alpha_p \ \sin^2\theta_{75}/4. \tag{B.121}$$

$$a_{22} = -(\beta_{1c} \sin^3\theta_{75})/3. \tag{B.122}$$

$$a_{23} = \lambda_i\mu\cos\alpha_p \ \sin^3\theta_{75}/2. \tag{B.123}$$

$$a_{24} = \mu^2\cos\alpha_p \ \sin\alpha_p \ \sin^3\theta_{75}/2. \tag{B.124}$$

$$a_{25} = \lambda_i \cos^3\theta_{75}\theta_{1s}/4. \tag{B.125}$$

$$a_{26} = \mu \cos^3\theta_{75}\sin\alpha_p \ \theta_{1s}/4. \tag{B.126}$$

$$a_{27} = \lambda_i^2 \cos^2\theta_{75} \sin\theta_{75}\theta_{1s}/2. \tag{B.127}$$

$$a_{28} = \lambda_i\mu \cos^2\theta_{75}\sin\alpha_p \ \sin\theta_{75}\theta_{1s} \tag{B.128}$$

$$a_{29} = \mu^2 \cos^2\theta_{75}\sin^2\alpha_p \ \sin\theta_{75}\theta_{1s}/2. \tag{B.129}$$

$$a_{30} = \lambda_i \cos\theta_{75} \sin^2\theta_{75}\theta_{1s}/4. \tag{B.130}$$

$$a_{31} = \mu \cos\theta_{75}\sin\alpha_p \ \sin^2\theta_{75}\theta_{1s}/4. \tag{B.131}$$

$$a_{32} = \lambda_i^2 \sin^3\theta_{75}\theta_{1s}/2. \tag{B.132}$$

$$a_{33} = \lambda_i\mu\sin\alpha_p \ \sin^3\theta_{75}\theta_{1s} \tag{B.133}$$

410

$$a_{34} = \mu^2 \sin^2\alpha_p \, \sin^3\theta_{75}\theta_{1s}/2. \qquad (B.134)$$

The roll and pitch moments in the fixed frame may be written in terms of the flapping restraint as they were in the rigid-blade analysis of Chapter 2:

$$M_x = \frac{\gamma N_b}{6}(\nu_\beta^2 - 1)\beta_{1s} \qquad (B.135)$$

$$M_y = -\frac{\gamma N_b}{6}(\nu_\beta^2 - 1)\beta_{1c} \qquad (B.136)$$

B.4 Estimate of Collective

An iterative process is used to establish an initial value for the collective trim based on achieving the desired level of thrust on the rigid-blade. The residual equation here is simply

$$F_1 = T - T_r \qquad (B.137)$$

where T is the calculated thrust based on the current value of θ_{75} and T_r is the desired thrust level calculated from the first part of this analysis. The new value of the collective is calculated from the analytical Jacobian:

$$J = \frac{\partial T}{\partial \theta_{75}} = \frac{\gamma N_b}{6} \sum_{i=1}^{14} \frac{\partial a_i}{\partial \theta_{75}} \qquad (B.138)$$

$$(\theta_{75})_{new} = (\theta_{75})_{old} + F_1/J \qquad (B.139)$$

Convergence here results in the estimate for the collective setting, and ends the analysis for the axisymmetric hover and axial flight cases. For these cases, only the fuselage angle of attack and collective setting are required. Otherwise, the analysis continues to determine the appropriate cyclic control values.

411

B.5 Coupled Rotor/Airframe and Flapping Blade Analysis

For conversion and airplane mode, an appropriate starting value for the collective and fuselage angle of attack are now known. Using these initial values, a new process is begun considering equilibrium of the entire airframe with the four hub forces included and blade flapping included. There are seven unknowns in this sequence: the three pitch controls, θ_{75}, θ_{1c}, and θ_{1s}, the fuselage angle of attack α_f, and the three flap angles, β_0, β_{1c}, and β_{1s}. Values for the unknowns θ_{1c}, θ_{1s}, β_{1c}, and β_{1s} are initially set to small values (.01 rad). The value of β_0 is obtained throughout the iterative process by Eqn. B.43 using the current values of θ_{75} and θ_{1s}. The new values of the remaining unknowns are obtained through formulation of a numerical 6 x 6 Jacobian matrix and 6 force residual equations. Airframe forces and rotor forces are combined to write the equilibrium of the aircraft as:

$$F_1 = 2T_{fh} - (D_w + D_f + D_t) \tag{B.140}$$

$$F_2 = W - (L_w + L_t + 2T_{fv}) \tag{B.141}$$

$$F_3 = 2M_y + 2hH + M_w + M_t - L_t(x_t - x_w) -$$
$$D_t(z_w - z_t) - Wx_w - Wz_w\alpha_f - D_f z_w \tag{B.142}$$

$$F_4 = M_x \tag{B.143}$$

$$F_5 = \frac{(\nu_\beta^2 - 1)}{\gamma}\beta_{1s} - M_{1c} \tag{B.144}$$

$$F_6 = \frac{(\nu_\beta^2 - 1)}{\gamma}\beta_{1c} - M_{1s} \tag{B.145}$$

where F_1 represents the horizontal force equilibrium, F_2 represents the vertical force equilibrium, F_3 represents the pitch moment equilibrium, F_4 represents the roll equilibrium of the rotor in the fixed system, and F_5 and F_6 represent the cyclic moment balances of the blade in the rotating frame which primarily influence the unknowns β_{1c} and β_{1s}. A Jacobian matrix is numerically generated by calculating

the change in the six force residuals due to individual perturbations of the six independent unknowns (β_0 is dependent). The new controls are written in terms of the previous iteration as:

$$(\hat{\theta})_{new} = (\hat{\theta})_{old} + (1 - R)[J]^{-1}\hat{F} \qquad \text{(B.146)}$$

where $\hat{\theta}$ is a vector of the six independent unknowns and $\hat{F}$ is a vector of the six force residuals, and R is a parameter used to control numerical damping. The iteration process continues until convergence is reached, determined by the magnitude of the force residual vector:

$$Mag(F) = \sqrt{\sum_{i=1}^{6} F_i^2} \qquad \text{(B.147)}$$

$$Mag(F) < .000001 \text{ for convergence} \qquad \text{(B.148)}$$

The convergence of the problem is controlled by the application of appropriate damping factors on the step size taken by the unknowns, and by recalculation of the Jacobian matrix after a selected number of iterations.

References

1. McVeigh, M.A., Rosenstein, H.J., and McHugh, F.J.: Aerodynamic Design of the XV-15 Advanced Composite Tilt Rotor Blade. Presented at the 39th Annual Forum of the American Helicopter Society, St. Louis, Missouri, May 1983.

2. Farrell, M.K.: Aerodynamic Design of the V-22 Osprey Proprotor. Presented at the 45th Annual Forum of the American Helicopter Society, Boston, Massechusetts, May 1989.

3. Felker, F.F.: A Review of Tilt Rotor Download Research. 14th European Rotorcraft Forum, Milano, Italy, September 1988.

4. Huston, R.J., Golub, R.A., and Yu, J.C.: Noise Considerations for Tiltrotor. Presented at the AIAA/ASME/SAE/ASEE 25th Joint Propulsion Conference, Maonterey, CA, July 1989.

5. Edwards, B.D.: External Noise of the XV-15 Tiltrotor Aircraft. NASA Contractor Report 187463, May 1991.

6. Gaffey, T.M., Yen, J.G., and Kvaternik, R.G.: Analysis and Model Tests of the Proprotor Dynamics of a Tilt-Proprotor VTOL Aircraft. U.S. Air Force V/STOL Technology and Planning Conference, Las Vegas, Nv, September 1969

7. V/STOL Study - Research Aircraft Design. Bell Helicopter Company, Fort Worth, Tx, NASA CR 114442, June 1972.

8. Johnson, W.: Optimum Control Alleviation of Tilting Proprotor Gust Response. *Journal of Aircraft*, Vol. 14, No. 3, March 1977, pp. 301-308.

9. Johnson, W.: Recent Developments in the Dynamics of Advanced Rotor Systems, NASA TM 86669, March 1985.

10. Bilger, J.M., Marr, R.L., and Zahedi, A.: Results of Structural Dynamic Testing of the XV-15 Tilt Rotor Research Aircraft. *Journal of the American Helicopter Society*, Vol. 27, No. 2, April 1982.

11. Quigley, H.C. and Koenig, D.G.: A Flight Study of the Dynamic Stability of a Tilting-Rotor Convertiplane, NASA TN D-778, April 1961.

12. Abbott, F.T., Jr., Kelly, H.N., and Hampton, K.D.: Investigation of 1/8-Size Dynamic-Aeroelastic Model of the Lockheed Electra Airplane in the Langley Transonic Dynamics Tunnel, NASA TM SX-456, November 1960.

13. Tilt Rotor Project Office Staff, Matin Maisel, Coordinator: Tilt Rotor Research Aircraft Familiarizaiton Document: NASA TM X-62, 407, January 1975.

14. Johnson, W.: An Assessment of the Capability To Calculate Tilting Prop-Rotor Aircarft Perfomance, Loads, and Stability, NASA TP 2291, March 1984.

15. Popelka, D, Sheffler, M., and Bilger, J.: Correlation of Stability Test Results and Analysis for the 1/5 Scale V-22 Aeroelastic Model, Presented at the 41st Annual Forum of the American Helicopter Society, Fort Worth, Texas, May 1985.

16. Kvaternik, R.G.: Studies in Tilt-Rotor VTOL Aircraft Aeroelasticity. Ph.D. Thesis, Case Western Reserve Univ., 1973.

17. Ormiston, R.A.: Rotor-Fuselage Dynamic Coupling Charactersitics of Helicopter Air and Ground Resonance. Presented at the American Helicopter

Society/Nanjing Aeronautical Institute Vertical Flight Technology Seminar, Nanjing, China, November 1985.

18. Smith, E.C.: Aeroelastic Response and Aeromechanical Stability of Helicopters with Elastically Coupled Composite Rotor Blades. Ph.D. Thesis, Department of Aerospace Engineering, University of Maryland, College Park, Maryland, 1992.

19. Nixon, M.W.: Extension-Twist Coupling of Composite Circular Tubes With Application to Tilt Rotor Blade Design, Proceedings of the AIAA / ASME / ASCE / AHS 28th Structures, Structural Dynamic and Materials Conference, AIAA Paper No. 87-0772, Monterrey, California, April 1987.

20. Taylor, E.S. and Browne, K.A.: Vibration Isolation of Aircraft Power Plants, *Journal of the Aeronautical Sciences*, Vol. 6, Dec. 1938, pp. 43-49.

21. Richardson, J.R. and Naylor, H.F.W.: Whirl Flutter of Propellers with Hinged Blades. Rep. No. 24, Engineering Research Associates, Toronto, Canada, 1962.

22. Richardson, J.R., McKillop, J.A., Naylor, H.F.W., and Bandler, P.A.: Whirl Flutter of Propellers with Flexible Twisted Blades. Rep. No. 43, Engineering Research Associates, Toronto, Canada, 1962.

23. Reed, W. H., III: Propeller-Rotor Whirl Flutter: A State-of-the-Art Review. J. Sound Vib, Vol. 4, No. 3, November 1966, pp. 526-544.

24. Young, M.I. and Lytwyn, R.T.: The Influence of Blade Flapping Restraint on the Dynamic Stability of Low Disk Loading Propeller-Rotors. Proceedings of the American Helicopter Society 23rd Annual National Forum, Washington, D.C., May 1967, pp. 38-54.

25. Wernicke, K.G. and Gaffey, T.M.: Review and Discussion of "The Influence of Blade Flapping Restraint on the Dynamic Stability of Low Disk Loading Propeller-Rotors". Proceedings of the American Helicopter Society 23rd Annual National Forum, Washington, D.C., May 1967, pp. 55-60.

26. Edenborough, H.K.: Investigation of Tilt-Rotor VTOL Aircraft Rotor-Pylon Stability. *Journal of Aircraft*, Vol. 5, No. 6, March-April 1968.

27. DeLarm, Leon: Whirl Flutter and Divergence Aspects of Tilt-Wing and Tilt-Rotor Aircraft. U.S. Air Force V/STOL Technology Planning Conference, Las Vegas, Nevada, September 1969.

28. Kaza, K. R. V.: Effect of Steady State Coning Angle and Damping on Whirl Flutter Stability. *Journal of Aircraft*, Vol. 10, No. 11, November 1973, pp. 664-669.

29. Kvaternik, R.G.: Experimental and Analytical Studies in Tilt-Rotor Aeroelasticity. Presented at the AHS/NASA Ames Specialists' Meeting on Rotorcraft Dynamics, Moffett Field, CA, February 1974.

30. Kvaternik, R.G.: A Review of Some Tilt-Rotor Aeroelastic Research at NASA-Langley. *Journal of Aircraft*, Vol. 13, No. 5, May 1976, pp. 357-363.

31. Johnson, W.: Dynamics of Tilting Proprotor Aircraft in Cruise Flight. NASA TN D-7677, May 1974.

32. Johnson, W.: Analytical Model for Tilting Proprotor Aircraft Dynamics, Including Blade Torsion and Coupled Bending Modes, and Conversion Mode Operation. NASA TM X-62,369, August 1974.

33. Johnson, W.: Analytical Modeling Requirements for Tilting Proprotor Aircraft Dynamics. NASA TN D-8013, July 1975.

34. Johnson, W.: A Comprehensive Analytical Model of Rotorcraft Aerodynamics and Dynamics. NASA TM 81182, 81183, and 81184, 1980.

35. Johnson, W.: The Influence of Engine/Transmission/Governor on Tilting Proprotor Aircraft Dynamics. NASA TM X-62,455, June 1975.

36. Johnson, W.: Comparison of Calculated and Measured Blade Loads on a Full-Scale Tilting Proprotor in a Wind Tunnel, NASA TM 81228, 1980.

37. Johnson, W.: Assessment of Aerodynamic and Dynamic Models in a Comprehensive Analysis for Rotorcraft, *Computer and Math Journal*, May 1985.

38. Acree, C.W., Jr., and Tischler, M. B.: Identification of XV-15 Aeroelastic Modes Using Frequency-Domain Methods. Vertica Vol. 13, No. 1 pp. 51-62, 1989.

39. Johnson, W.: A Comprehensive Analytical Model of Rotorcraft Aerodynamics and Dynamics. Johnson Aeronautics, Palo Alto, CA, 1988.

40. Kottapalli, S. and Meza, V.: Analytical Aeroelastic Stability Considerations and Conversion Loads for an XV-15 Tilt-Rotor in a Wind Tunnel Simulation. AIAA Paper No. 92-2258, Presented at the 33rd Structures, Structural Dynamics, and Materials Conference, Dallas, Texas, April 1992.

41. Alexander, H.R., Maizel, M.D., and Giulianetti, D.J.: The Development of Advanced Technology Blades for Tiltrotor Aircraft. Eleventh European Rotorcraft Form, London, England, September 1985.

42. Bauchau, O.A., Lowey, R.G., and Bryan, P.S.: An Approach to Ideal Twist Distribution in Tilt Rotor VTOL Blade Designs. RTC Report No. D-86-2, Rensselaer Polytechnic Institute, Troy, New York, July 1986.

43. Nasu, K.: Tilt-Rotor Flutter Control in Cruise Flight. NASA TM 88315, December 1986.

44. Houbolt, J.C. and Brooks, G.W.: Differential Equations of Motion for Combined Flapwise Bending, Chordwise Bending, and Torsion of Twisted Nonuniform Rotor Blades, NACA Report 1346, 1956.

45. Hodges, D.H. and Ormiston, R.A.: Nonlinear Equations for Bending of Rotating Beams with Application to Linear Flap-Lag Stability, NASA TM X-2770, May 1973.

46. Peters, D.A. and Ormiston, R.A.: The Effects of Second Order Blade Bending on the Angle of Attack of Hingeless Rotor Blades, *Journal of the American Helicopter Society*, Vol. 18, No. 4, October 1973.

47. Hodges, D.H. and Dowell, E.H.: Nonlinear Equations of Motion for the Elastic Bending and Torsion of Twisted Non-Uniform Rotor Blades: NASA TN D-7818, December 1974.

48. Bauchau, O.A. and Liu, S.P.: Finite Element Based Modal Analysis of Helicopter Rotor Blades, Vertica, Vol. 13, No. 2, 1989.

49. Bauchau, O.A. and Guernsey, D.: On the Choice of Appropriate Bases for Nonlinear Dynamic Modal Analysis, Proceedings of the American Helicopter society International Technical Specialists' Meeting on Rotorcrat Basic Research, Atlanta Georgia, March 25-27, 1991.

50. Kaza, K.R., and Kvaternik, R.G.: Nonlinear Aeroelastic Equations for Combined Flapwise Bending, Chordwise Bending, Torsion, and Extension of Twisted, Nonuniform Rotor Blades in Forward Flight, NASA TM 74059, 1977.

51. Hodges, D.H. and Atilgan, A.R.: Asymptotical Modeling of Initially Curved and Twisted Composite Rotor Blades, *Proceedings of the AHS International Technical Specialists' Meeting on Rotorcraft Basic Research*, Atlanta, Georgia, March 25-27, 1991.

52. Reissner, E. and Tsai, W.T.: Pure Bending, Stretching, and Twisting of Anisotropic Cylindrical Shells. *Journal of Applied Mechanics*, March 1972, pp. 148-154.

53. Iesan, D.: Saint-Venant's Problem for Inhomgeneous and Anisotropic Elastic Bodies. *Journal of Elasticity*, Vol. 6, 1976, pp. 277-294.

54. Giavotto, V., Borri, M., Mantegazza, P., and Ghiringhelli, G.: Anisotropic Beam Theory and Applications. Computers and Structures, Vol. 6, No. 1-4, 1983, pp. 403-413.

55. Kosmatka, J.B.: Structural Dynamic Modeling of Advanced Composite Propellers by the Finite Element Method, Ph.D. Dissertation, University of California, Los Angeles, 1986.

56. Kosmatka, J.B. and Dong, S. B.: Saint-Venant Solutions for Prismatic Anisotropic Beams, *International Journal of Solids and Structures*, Vol. 28, No. 7, 1991, pp. 917-938.

57. Kosmatka, J.B.: Extension-Bend-Twist Coupling Behavior of Thin-Walled Advanced Composite Beams with Initial Twist," *Proceedings of the 32nd Structures, Structural Dynamics, and Materials Conference*, Baltimore, MD, AIAA Paper No. 91- 1023-CP, Vol. 2, 1991, pp. 1037-1049.

58. Kosmatka, J.B.: Analysis of Composite Rotor Blades Via Saint Venant's Elasticity Solutions, *Presented at the 14th European Rotorcraft Forum*, Milano, Italy, 1988.

59. Kosmatka, J.B., and Ie, C.: On the Vibration Behavior of Shear-Deformable Prismatic Beams Including In-Plane Cross-Section Deformations, *Proceedings of the 32nd Structures, Structural Dynamics, and Materials Conference*, Baltimore, MD, AIAA Paper No. 91-1201-CP, Vol. 2, 1991, pp. 1462-1474.

60. Mansfield, E.H. and Sobey, A.J.: The Fibre Composite Helicopter Blade, Part 1: Stiffness Properties, Part 2: Prospects for Aeroelastic Tailoring. Aeronatuical Quarterly, May 1979, pp. 413-449.

61. Rehfield, L.W.: Design Analysis Methodology for Composite Rotor Blades. Seventh DoD/NASA Conference of Fibrous Composites in Structural Design, Denver, CO, June 1985.

62. Rehfield, L.W., Atilgan, A.R., and Hodges, D.H.: Non-Classical Behavior of Thin- Walled Composite Beams With Closed Cross Sections, *Journal of the American Helicopter Society*, Vol. 35, (2), 1990.

63. Hodges, R.V., Nixon, M.W., and Rehfield, L.W.: Comparison of Composite Rotor Blade Models: A Coupled-Beam Analysis and an MSC / NASTRAN Finite-Element Model, NASA TM 89024, 1987.

64. Nixon, M.W.: Analytical and Experimental Investigations of Extension-Twist-Coupled Structures, George Washington University Masters Thesis, Hampton, VA, 1989.

65. Hong, C.H. and Chopra, I.: Aeroelastic Stability Analysis of a Composite Rotor Blade, *Journal of the American Helicopter Society*, Vol. 30, No. 2, 1985, pp.57-67.

66. Hong, C.H. and Chopra, I.: Aeroelastic Stability Analysis of a Composite Bearingless Rotor Blade, *Journal of the American Helicopter Society*, Vol. 31, No. 4, 1985, pp. 29-35.

67. Panda, B. and Chopra, I.: Dynamics of Composite Rotor Blades in Forward Flight, Vertica, Vol. 11, No. 1/2, January 1987.

68. Smith, E.C., and Chopra, I.C.: Aeroelastic Response and Blade Loads of a Composite Rotor in Forward Flight," *Proceedings of the 33rd Structures, Structural Dynamics, and Materials Conference*, Dallas, Tx, AIAA Paper No. 92-2566, 1992.

69. Rand, O.: Periodic Response of Thin-Walled Composite Blades: Proceedings of the 30th AIAA/ASME/ASCE/AHS/ASC Structures, Structural Dynamics and Materials Conference, Mobile, Alabama, April 1989.

70. Rand, O.: Theoretical Modeling of Composite Rotating Beams, TAE Report No. 633 Technion - Israel Institute of Technology, Haifa, Israel, October 1988.

71. Fulton, M.: Applications of Composite Rotor Stability to Extension-Twist Coupled Blades, Proceedings of the 33rd AIAA/ASME/ASCE/AHS/ASC Structures, Structural Dynamics and Materials Conference, Dallas Texas, April 1992.

72. Hodges, D.H.: A Mixed Variational Formulation Based on Exact Intrinsic Equations for Dynamics of Moving Beams, *International Journal of Solids and Structures*, Vol. 26, No. 11, pp. 1253-1273.

73. Yuan, K.A., Friedmann, P.P., and Venkatesan, C., A New Aeroelastic Model for Composite Rotor Blades with Straight and Swept Tips, Proceedings of the 33rd AIAA/ASME/ASCE/AHS/ASC Structures, Structural Dynamics and Materials Conference, Dallas Texas, April 1992.

74. Minguet, P. and Dugundji, J.: Experiments and Analysis for Composite Blades Under Large Deflections, *AIAA Journal*, Vol. 28, No. 9, September 1990.

75. Minguet, P. and Dugundji, J.: Static and Dynamic Behavior of Composite Helicopter Rotor Blades Under Large Deflection, Ph.D. Dissertation, Massachusetts Institute of Technology, Cambridge, Massachusetts, 1989.

76. Schneider, J. and Wilkerson, J.: Advanced Rotorcraft V/STOL Technology Needs for the High Speed Rotorcraft. AIAA/AHS/ASEE Aircraft Design, Systems and Operations Conference, Dayton, OH, September 1990.

77. Chandra, R., and Chopra, I.: Experimental Theoretical Investigation of the Vibration Characteristics of Rotating Composite Box-Beams, *Presented at the American Helicopter Society National Technical Specialists' Meeting on Rotorcraft Dynamics*, Arlington, Tx, 1989.

78. Hinnant, H.E.: A Curvilinear, Anisotropic, p-Version, Brick Finite Element Based on Geometric Entities, *Proceedings of the 33rd Structures, Structural Dynamics, and Materials Conference*, Dallas, Tx, AIAA Paper No. 92-2329, 1992.

79. University of Maryland Advanced Rotor Code (UMARC) Theory Manual, University of Maryland, Dept. of Aerospace Engineering, College Park, MD, 1991.

80. Wempner, G.: *Mechanics of Solids with Applications to Thin Bodies*, 1st edition, McGraw-Hill Book Co., New York, N.Y, 1981.

81. Hodges, D.H., Hopkins, A.S., Kunz, D.L., and Hinnant, H.E.: "General Rotorcraft Aeromechanical Stability Program (GRASP) Theory Manual," NASA TM 102255, 1990.

82. Hinnant, H.E.: "Derivation of a Tapered p-Version Beam Finite Element," NASA TP 2931, 1989.

83. Smith, E.C. and Chopra, I.: "Formulation and Evaluation of an Analytical Model for Composite Box-Beams," *Journal of the American Helicopter Society*, Vol. 36, No. 3, 1990, pp. 22-35.

84. Cowper, G.R., "The Shear Coefficient in Timoshenko's Beam Theory," *Journal of Applied Mechanics*, June 1966, pp. 335-340.

85. Shield, R. T.: "Extension and Torsion of Elastic Bars with Initial Twist," *ASME Journal of Applied Mechanics*, Vol. 49, 1982, pp. 779-786.

86. Kosmatka, J.B.:"On the Behavior of Pretwisted Beams with Irregular Cross Sections," *ASME Journal of Applied Mechanics*, Vol. 59, 1992, pp. 146-152.

87. Fung, Y.C., *An Introduction to the Theory of Aeroelasticity*, Dover Publications Inc., N.Y., 1960.

88. Jang, J., "Ground and Air Resonance of Bearingless Rotors in Hover and Forward Flight, " PH.D. Dissertation, University of Maryland, College Park, Maryland, 1988.

89. Bathe, Klaus-Jurgen, *Finite Element Procedures in Engineering Analysis*, Prentice-Hall, Inc., Englewood Cliffs, New Jersey, Copyright 1982.

90. Johnson, W., Lau, Benton H., and Bowles, J.V.: Calculated Performance, Stability, and Maneuverability of High Speed Tilting Proprotor Aircraft, *Vertica*, Vol. 11, No. 1/2, 1987, pp. 317-339.

91. Gessow, A., and Meyers, G.C.: *Aerodynamics of the Helicopter*, Frederick Ungar Publishing Co., New York, Copyright 1952.